Lawrence Berkeley National Laboratory
Recent Work

Title
Earth Sciences Division Annual Report 1992

Permalink
https://escholarship.org/uc/item/0n2569jb

Author
Lawrence Berkeley National Laboratory

Publication Date
1993-09-01

eScholarship.org Powered by the California Digital Library
University of California

LBL-33000
UC-403

Annual Report 1992

REFERENCE COPY
Does Not
Circulate
Copy 1
Bldg. 50 Library.
LBL-33000

Earth Sciences Division

September 1993

LAWRENCE BERKELEY LABORATORY
UNIVERSITY OF CALIFORNIA
BERKELEY, CALIFORNIA 94720

Prepared for the U.S. Department of Energy under Contract No. DE-AC03-76SF00098

DISCLAIMER

This document was prepared as an account of work sponsored by the United States Government. Neither the United States Government nor any agency thereof, nor The Regents of the University of California, nor any of their employees, makes any warranty, express or implied, or assumes any legal liability or responsibility for the accuracy, completeness, or usefulness of any information, apparatus, product, or process disclosed, or represents that its use would not infringe privately owned rights. Reference herein to any specific commercial product, process, or service by its trade name, trademark, manufacturer, or otherwise, does not necessarily constitute or imply its endorsement, recommendation, or favoring by the United States Government or any agency thereof, or The Regents of the University of California. The views and opinions of authors expressed herein do not necessarily state or reflect those of the United States Government or any agency thereof or The Regents of the University of California and shall not be used for advertising or product endorsement purposes.

This report has been reproduced directly from the best available copy.

Lawrence Berkeley Laboratory is an Equal Opportunity Employer

DISCLAIMER

This document was prepared as an account of work sponsored by the United States Government. While this document is believed to contain correct information, neither the United States Government nor any agency thereof, nor the Regents of the University of California, nor any of their employees, makes any warranty, express or implied, or assumes any legal responsibility for the accuracy, completeness, or usefulness of any information, apparatus, product, or process disclosed, or represents that its use would not infringe privately owned rights. Reference herein to any specific commercial product, process, or service by its trade name, trademark, manufacturer, or otherwise, does not necessarily constitute or imply its endorsement, recommendation, or favoring by the United States Government or any agency thereof, or the Regents of the University of California. The views and opinions of authors expressed herein do not necessarily state or reflect those of the United States Government or any agency thereof or the Regents of the University of California.

EARTH SCIENCES DIVISION ANNUAL REPORT 1992

Lawrence Berkeley Laboratory
University of California
Berkeley, California 94720

September 1993

Prepared for the U.S. Department of Energy under Contract No. DE-AC03-76SF00098

ACKNOWLEDGMENTS

This work was supported through U.S. Department of Energy Contract No. DE-AC03-76SF00098 by (1) the DOE Director, Office of Energy Research, (i) Office of Basic Energy Sciences, Geosciences Program, and (ii) Office of Health and Environmental Research, Subsurface Science Program and Environmental Sciences Division; (2) the DOE Director, Office of Civilian Radioactive Waste Management, Office of Facilities Siting and Development; (3) the DOE Assistant Secretary for Conservation and Renewable Energy, Office of Renewable Energy; (4) the DOE Assistant Secretary for Fossil Energy, Office of Oil, Gas and Shale Technologies; (5) the DOE Director, Office of Environmental Restoration and Waste Management, (i) Office of Environmental Restoration and (ii) Office of Technology Development; (6) U.S. Government Offices in (i) Bureau of Reclamation, (ii) Environmental Protection Agency, (iii) Geological Survey, and (iv) National Science Foundation; (7) the State of California; and (8) national and international grants from private and public institutions.

CONTENTS

INTRODUCTION

Scientists and engineers of the Earth Sciences Division, following the mission of a multipurpose National Laboratory, conduct research on a wide variety of topics relevant to the nation's energy development programs. This report summarizes the activities for 1992. The Earth Sciences Division has unique expertise in several research areas, due in part to the special resources and facilities available at the Lawrence Berkeley Laboratory and in part to the Laboratory's commitment to technical and scientific excellence. Furthermore, interlaboratory cooperation within the U.S. Department of Energy system and collaboration with other research institutions give Division personnel access to unmatched intellectual and technological resources for the study of complex subsurface properties, processes, and problems.

Much of the Division's research deals with the physical and chemical properties and processes in the earth's crust, from the partially saturated, low-temperature near-surface environment to the high-temperature environments characteristic of regions where magmatic-hydrothermal processes are active. Strengths in laboratory and field instrumentation, numerical modeling, and *in situ* measurement allow study of the transport of mass and heat through geologic media—studies that now include the appropriate chemical reactions and the hydraulic-mechanical complexities of fractured rock systems. Related laboratory and field investigations address the effects of temperature, pressure, stresses, pore fluids, and fractures on the elastic and electrical properties of rock masses. These studies are concerned with rock behavior in the brittle and ductile crustal regimes, and they drive the development of improved geomechanical and geophysical tools and techniques for mapping and characterizing heterogeneity in the subsurface. Program initiatives on special topics of research are generated in response to needs. Of recent note are Division efforts involving the application of isotope geochemistry to the study of geodynamic processes and earth history, the development of improved methods for high-resolution imaging of the subsurface, and the use of advanced technologies for characterizing processes that occur in the shallow subsurface, where contaminants now intrude and where remedial action is required.

This Annual Report presents summaries of selected representative research activities grouped according to the principal disciplines of the Earth Sciences Division: Geology and Geochemistry, Geophysics and Geomechanics, and Reservoir Engineering and Hydrogeology. We are proud to be able to bring you this report, which we hope will convey not only a description of the Division's scientific activities but also a sense of the enthusiasm and excitement present today in the Earth Sciences.

GEOLOGY AND GEOCHEMISTRY

Investigators in the Geology and Geochemistry group primarily study causes and results of chemical reactions in the earth's crust. These reactions result from interactions between subsurface aqueous fluids and the surrounding soil and rock, causing chemical alteration of the solids and changes in the chemistry of the fluids. Since many of these reactions occur during the movement of fluids, our studies are quite germane to the disposal and isolation of radioactive and toxic wastes. Successful containment of waste species depends strongly on arresting the movement of dissolved chemical species in groundwater. In this respect, specific investigations in areas of isotope geochemistry, radiochemistry, inorganic chemistry, and surface chemistry are all applicable to reactive chemical transport models. Field-oriented research pertinent to chemical transport encompasses the coupling of hydrology with isotope geology, aqueous analytical chemistry, chemical-species modeling, and hydrochemistry. Projects emphasizing geochemical and chemical modeling of nuclear waste repositories focus on how both radionuclide and major groundwater species react and migrate under conditions close to and away from the repository.

The group also conducts basic research on processes that occur in the earth's crust and oceans, including examination of isotopic evidence for interactions of components within the crust and between the crust and mantle and studies pertinent to the thermodynamics of chemical species in aqueous systems. The geochemistry of geothermal systems and the paleoclimatic implications of isotopic variations are also under investigation. Members participate in the Continental Scientific Drilling program and in studies to define the occurrence and movement of radon and its parent radioisotopes in rock and soil. Research is also in progress on interfacial chemical reactions that address both solid-liquid and solid-gas reactions on mineral surfaces.

Correlation of the Na/K Ratio in Geothermal Well Waters with the Thermodynamic Properties of Low Albite and Potash Feldspar

J. A. Apps and G. M. Chang

For many years, the element concentration ratio, Na/K, in the liquid aqueous phase has been used to estimate the source region temperature of hot springs and geothermal effluents. It possesses the advantage that it is unaffected by transient boiling or condensation, and is affected only slowly by conductive cooling, although Fournier and Truesdell (1973) recommended its use only where source region temperatures are greater than 150°C.

The thermochemical basis for the Na/K geothermometer is not well defined. Usually, discussion centers on the "exchange" reaction between plagioclase (low albite) and potash feldspar (adularia or microcline);

$$NaAlSi_3O_8 + K^+ = KAlSi_3O_8 + Na^+ \quad (1)$$

where

$$\log K(T) = \frac{[Na^+]}{[K^+]} \quad (2)$$

Attempts to reconcile field observations with calculations based on published thermodynamic properties of the participating species have not been particularly successful.

The coexistence of secondary low albite and potash feldspar in geothermal systems is frequently mentioned in the literature. Tomasson and Kristmannsdottir (1972), in discussing mineral alteration in the geothermal area of Reykjanes, Iceland, refer to the occasional presence of albitized plagioclase as well as the sporadic occurrence of newly formed potash feldspar in all geothermal holes. Mehegan and Robinson (1982) and Viereck et al. (1982) describe secondary hydrothermal alteration in the Reydarfjordur drill core from Eastern Iceland. Low albite and adularia coexist in most of the intersected volcaniclastic rocks, whereas authigenic albite replaces primary plagioclase crystals in some of the interdigitated basaltic flows. Browne and Ellis (1970) noted the presence of adularia and secondary albite in hydrothermally altered intermediate and acid lavas and volcaniclastic rocks intersected by boreholes in the Ohaki-Broadlands hydrothermal area in New Zealand. On the Kamchatka Peninsula, Naboko et al. (1965) refer to secondary adularia and albite in dacitic and andestic volcaniclastics of the Pauzhetka geothermal field, whereas Trukhin and Petrova (1974) describe alteration zones containing secondary albite and adularia in andesitic lavas and andesitic and dacitic tuffs of the Bolshe-Bann geothermal field. In contrast, mineralogical studies of cores penetrating sea floor basalts, between ~ 4°C and 70°C, never mention the coexistence of low albite with potash feldspar, although frequent reference is made to the presence of the latter, sometimes replacing plagioclase. Plagioclase is usually replaced by secondary clays instead of low albite. Analcime is commonly observed as an authigenic phase, although it is rarely observed in basalts saturated with meteoric waters at similar temperatures.

Because extensive mineralogical observations confirm the coexistence of secondary low albite and potash feldspar in geothermal fields, it is reasonable to assume that the Na/K ratio in the aqueous phase reflects a close approach to chemical equilibrium between these two minerals, particularly at temperatures greater than 150°C, where the Na/K geothermometer has proven to be most reliable.

COMPARISON OF NA/K, PREDICTED FROM THERMODYNAMIC DATA, WITH FIELD DATA

Several comprehensive internally consistent compilations of thermodynamic data of minerals have been published in which $\Delta H^\circ_{f,298}$ or $\Delta G^\circ_{f,298}$, of both low albite and potash feldspar (adularia or microcline) are included (Helgeson et al., 1978; Robie et al., 1979; Berman, 1988; Holland and Powell, 1990). Their properties are based on calorimetry and high temperature; i.e., > 400°C, phase equilibria with coexisting minerals. Helgeson et al. also used the Na/K ratio from gas field brines to correlate the properties of the two feldspars. Recently, Kiseleva et al. (1990) redetermined $\Delta H^\circ_{f,298}$ for microline using high-temperature lead borate melt calorimetry.

In Figure 1, the calculated values of log $K(T)$ for Eq. (1) from all five sources are compared with the analytical determinations of the Na/K ratio in well waters from geothermal fields and deep water-saturated formations from around the world. Field temperatures were measured down hole or computed from well discharge data. The log $K(T)$ values are calculated along the water saturation curve, employing the entropies cited by Robie et al. (1979) and Maier-Kelley heat capacity functions, cited by Helgeson et al. (1978), for low albite and potash feldspar. The thermodynamic properties for the ionic species, Na^+ and K^+, are those given by Shock and Helgeson (1988). The uncertainties are estimated from those given in the cited references.

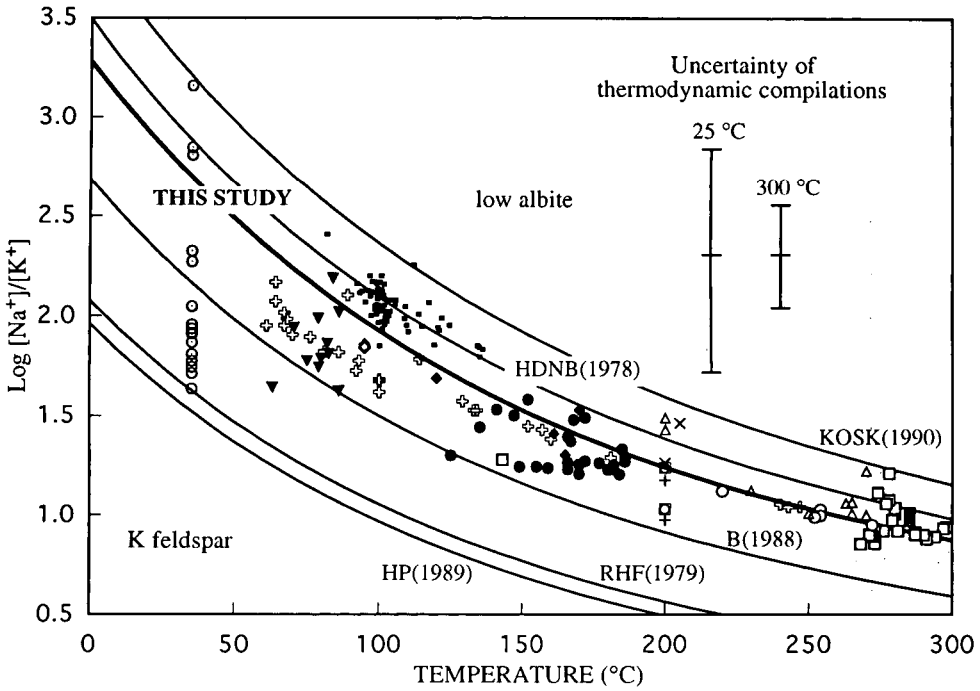

Figure 1. Log[Na^+]/[K^+], as a function of temperature, calculated from thermodynamic compilations (labeled by initials of authors' surnames and date) and well waters (symbols): ✣, Iceland; New Zealand (⊠, Kawerau; □, Ohaki-Broadlands; ⊡ Orakeikorako; ×, Rotorua; ○, Tauhara; +, Waiotapu; △, Wairakei); United States (◇, Cajon Pass, CA; ■, Kettleman Dome, CA; ⊙, Savannah River, SC); Russia (◆, Bolshe Bann; ▼, Paratunka; ●, Pauzhetka). [XBL 933-357]

Although mineralogical studies from most sites selected for the correlation describe the presence of authigenic low albite and potash feldspar, there is no assurance that the recovered groundwaters originated where low albite and potash feldspar coexisted. Some sampled well waters may have been mixtures from several producing zones. In spite of these uncertainties the field data are generally consistent and can be fitted by a univariant curve, positioned as indicated in Figure 1 to within ± 0.2 log(Na^+)/(K^+), or 1 kJ in ΔG_r° for reaction (1) at 25° and 2 kJ at 300°C. This contrasts with an uncertainty of nearly 3.5 kJ for the log $K(T)$ predicted from calorimetry or phase equilibrium measurements. The fitted curve follows closely the equation proposed by Fournier (1981) for the Na/K geothermometer, and the data reported by Il'in et al. (1979) for the Pauzhetka geothermal field, but it does not fit their data from the lower-temperature Paratunka field in the same region.

The precision of Na/K predictions using either calorimetric and/or high-temperature phase equilibrium data do not do justice to the quality of routinely obtainable field measurements. Groundwater analyses may therefore have the potential for calibrating thermodynamic data, provided that rigorous control is maintained over sampling and analysis procedures.

The chemical analyses of geothermal wells below 200°C reported by Arnorsson et al. (1983) include Al^{3+}. The saturation indices of low albite and potash feldspar can therefore be computed for those well waters, and their solubility products can be compared with those predicted from calorimetry and high-temperature phase equilibria. The results, illustrated in Figure 2, show the saturation indices referenced to the data by Berman (1988), who used the thermodynamic properties of low albite taken from Hemingway and Robie (1977). The saturation indices of both feldspars show trends toward supersaturation below 100°C. This trend might indicate that the sampled waters originated at temperatures higher than those measured and were not in equilibrium with the local environment, a condition reflecting the uncertain validity of Na/K ratio in the low-temperature domain. In spite of the scatter, the saturation indices suggest that $\Delta G_{f,298}^\circ$ of low albite might be more nearly correct than that of potash feldspar in Berman's database.

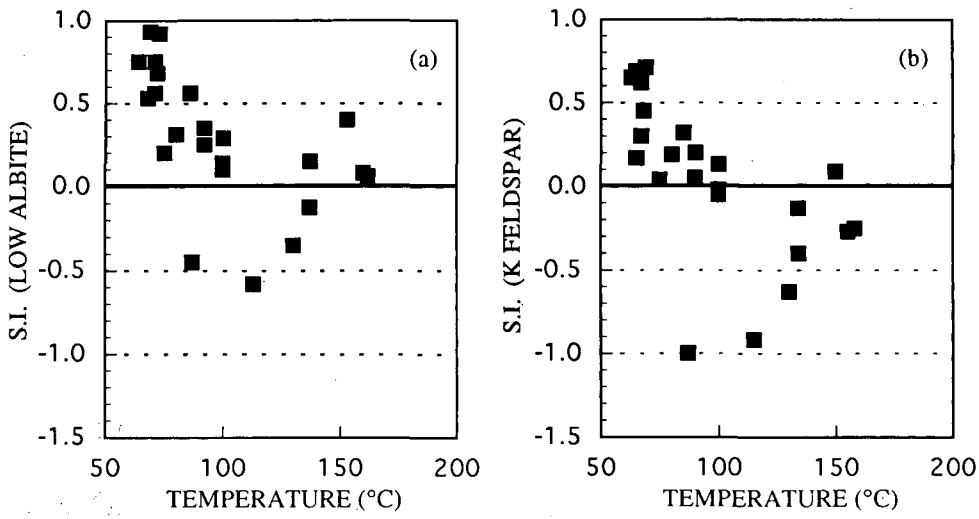

Figure 2. Saturation indices for **(a)** low albite and **(b)** potash feldspar as a function of temperature, calculated from well waters in Iceland from data by Arnorsson et al. (1983). [XBL 933-348]

ADJUSTMENT OF $\Delta G^{\circ}_{f,298}$ FOR POTASH FELDSPAR

A correction to $\Delta G^{\circ}_{f,298}$ for potash feldspar alone using the field correlation of Na/K yields a revised value of -3748.6 ± 3.7 kJ·mol^{-1}, which is more negative than that of Robie et al. (1979), -3742.3 ± 3.4 kJ·mol^{-1}, or that of Berman (1988), -3745.4 kJ·mol^{-1}, but is much less negative than -3754.2 ± 3.7 kJ·mol^{-1} calculated from $\Delta H^{\circ}_{f,298}$ of microcline determined by Kiseleva et al. (1990).

REFERENCES

Arnorsson, S., Gunnlaugsson, E., and Svavarsson, H., 1983. The chemistry of geothermal waters in Iceland, II. Mineral equilibria and independent variables controlling water compositions. Geochim. Cosmochim. Acta, v. 47, p. 547–566.

Berman, R.G., 1988. Internally-consistent thermodynamic data for minerals in the system Na_2O-K_2O-CaO-MgO-FeO-Fe_2O_3-Al_2O_3-SiO_2-H_2O-CO_2. J. Petrol., v. 29, p.445–522.

Browne, P.R.L., and Ellis, A.J., 1970. The Ohaki-Broadlands hydrothermal area, New Zealand: Mineralogy and related geochemistry. Am. J. Sci., v. 269, p.97–131.

Fournier, R.O., 1981. Application of water geochemistry to geothermal exploration and reservoir engineering. *In* L. Rybach and L.J.P. Muller (eds.), Geothermal Systems: Principles and Case Histories (Chapter 4). John Wiley and Sons, Ltd., New York

Fournier, R.O., and Truesdell, A.H., 1973. An empirical Na-K-Ca geothermometer for natural waters. Geochim. Cosmochim. Acta, v. 37, p. 1255–1275.

Helgeson, H.C., Delany, J.M., Nesbitt, H.W., and Bird, D.K., 1978. Summary and critique of the thermodynamic properties of rock forming minerals. Am. J. Sci., v. 278-A, p. 1–229.

Hemingway, B.S., and Robie, R.A., 1977. Enthalpies of formation of low albite ($NaAlSi_3O_8$), gibbsite ($Al(OH)_3$) and $NaAlO_2$: Revised values for $\Delta G^{\circ}_{f,298}$ and $\Delta G^{\circ}_{f,298}$ of some alumino-silicate minerals. J. Res. U.S. Geol. Surv., v. 5, p. 413–429.

Holland, T.J.B., and Powell, R., 1990. An enlarged and updated internally consistent thermodynamic dataset with uncertainties and correlations: The system K_2O-Na_2O-CaO-MgO-MnO-FeO-Fe_2O_3-Al_2O_3-TiO_2-SiO_2-C-H_2-O_2. J. Metamorphic Geol., v. 8, p. 89–124.

Il'in, V.A., Kononov, B.G., Polyak, B.G., and Kozlovtseva, S.V., 1979. Hydrochemical estimation of deep rock temperatures. Geochem. Int., v. 1979, p. 119–132.

Kiseleva, I.A., Ogorodova, L.P., Siderov, Yu.I., and Khodakovskiy, I.L., 1990. Thermodynamic properties of alkali feldspars. Geochem. Int., v. 1990, p. 93–100.

Mehegan, J.M., and Robinson, P.T., 1982. Secondary mineralization and hydrothermal alteration in the Reydarfjordur drill core, Eastern Iceland. J. Geophys. Res., v. 87, p. 6511–6524.

Naboko, S.I., Karpov, G.A., and Roznikova, A.P., 1965. Gidrotermal'nyi metamorphizm porod i mineralo-

obrazovanie[Hydrothermal metamorphism of rocks and mineralization]. *In* Pauzhetskie Goryachie Vody na Kamchatka. Nauka, Moscow, p. 76–118.

Robie, R.A., Hemingway, B.S., and Fisher, J.R., 1979. Thermodynamic properties of minerals and related substances at 298.15 K and 1 bar (10^5 Pascals) pressure and at higher temperature. U.S. Geol. Surv. Bull. 1452.

Shock, E., and Helgeson, H.C., 1988. Calculation of thermodynamic and transport properties of aqueous species at high pressures and temperatures: Correlation algorithms for ionic species and equation of state prediction to 5 kb and 1000°C. Geochim. Cosmochim. Acta, v. 2, p. 2009–2036.

Tomasson, J., and Kristmannsdottir, H., 1972. High temperature alteration minerals and thermal brines, Reykjanes, Iceland. Contrib. Mineral. Petrol., v. 36, p. 123–134.

Trukhin, Yu., P., and Petrova, V.V., 1974. Geochemical effect of hydrothermal metasomatism and variation in the composition of thermal solutions with time (based on Bolshe-Banny geothermal deposit of Kamchatka). *In* S.I. Naboko (ed.), Gidrotermal'nye Mineraloobrazuyushchio Rastvory Oblastei Aktivnogo Vulkanizma (Hydrothermal Mineral-Forming Solutions in the Areas of Active Volcanism). Nauka Publishers, Siberian Branch Novosibirisk, 1974. Translated from Russian and published for the U.S. Department of the Interior and the National Science Foundation by Amerind Publishing Co. Pvt. Ltd., New Delhi, 1982, p. 274–285.

Viereck, L.G., Griffin, B.J., Schmincke, H.-U., and Pritchard, R.G., 1982. Volcaniclastic rocks of the Reydarfjordur drill hole, Eastern Iceland 2. Alteration. J. Geophys. Res. v. 87, p. 6459–6476.

Numerical Simulations of Precipitation of Quartz and Calcite Accompanying Solute Transport in a Temperature Gradient

C. L. Carnahan

The computer program THCVP simulates one-dimensional advective-dispersive transport of reactive chemicals with coupling from precipitation-dissolution reactions to fluid flow by means of changes in porosity and hydraulic conductivity (Carnahan, 1991, 1992a). The program was used to simulate deposition of quartz and calcite in the presence of steady gradients of temperature. The spatial distributions of deposition turned out to be quite different for the two minerals. The differences can be explained by interaction between the gradient of temperature and the temperature dependences of the solubility products of quartz and calcite.

CHEMICAL SYSTEMS SIMULATED

The deposition of quartz is described by the equilibrium between solid quartz and the single solution species, silicic acid:

$$SiO_2(s) + 2H_2O(l) = Si(OH)_4 \ . \qquad (R1)$$

The equilibrium concentration of silicic acid is affected only by temperature. The deposition of calcite involves equilibria among the solid and multiple solution species:

$$CaCO_3(s) + H_2O(l) = Ca^{2+} + HCO_3^- + OH^- , \qquad (R2)$$

$$HCO_3^- + OH^- = CO_3^{2-} + H_2O(l), \qquad (R3)$$

$$HCO_3^- + H_2O(l) = H_2CO_3 + OH^- , \qquad (R4)$$

$$H_2O(l) = H^+ + OH^- . \qquad (R5)$$

These equilibria are affected by temperature, pH, and activities of calcium and carbonate species in solution.

To account for their variations with temperature, the equilibrium constants for reactions R1–R5 were calculated by the thermodynamic relation of Clarke and Glew (1966), truncated after four terms:

$$\log K(T) = A + \frac{C}{T} + D \log T + ET , \qquad (1)$$

where $K(T)$ is an equilibrium constant for a chemical reaction evaluated at absolute temperature T. The coefficients A, C, D, and E are related to the changes of standard entropy, enthalpy, and heat capacity for the reaction. Table 1 lists values of the coefficients for Eq. (1) that were used in the simulations. Variations of the equilibrium constants for reactions R1–R5 from 30° to 90°C are shown in Figure 1.

Table 1. Coefficients for Eq. (1).

Reactions	A	C	D	E
$SiO_2(s) + 2H_2)(l) = Si(OH)_4$	1.881	−1560.	0.	-2.028×10^{-3}
$CaCO_3(s) + H_2O(l) = Ca^{2+} + HCOS(\_,3) + OH^-$	−29.08	−2383.	13.75	-3.051×10^{-2}
$HCOS(\_,3) + OH^- = COS(_2\_,3) + H_2O(l)$	154.095	−3086.9	−60.29	3.051×10^{-2}
$HCOS(\_,3) + H_2O(l) = H_2CO_3 + OH^-$	−40.25	−522.0	13.54	4.150×10^{-3}
$H_2O(l) = H^+ + OH^-$	−76.985	−1506.4	31.25	-3.110×10^{-2}

SIMULATIONS OF MINERAL DEPOSITION

The two chemical systems were simulated in the presence of a steady gradient of temperature. In each case, the inner boundary ($x = 0$) of the spatial domain is held at 90°C and the outer boundary ($x = 1$ m) is held at 30°C. Temperature varies linearly in space between these two limits and is constant in time. Fluid flow is driven by a constant gradient of hydraulic head equal to −0.1. Complete details of the simulations and their results are given elsewhere (Carnahan, 1992b).

Quartz-Water System

The initial porosity of the spatial domain is 0.05, and the initial Darcy flux is 1×10^{-5} m/s. The fluid phase initially occupying the domain contains silicic acid in equilibrium with quartz, and the concentration of silicic acid at a given location is determined by the temperature at that location. Starting at time zero, silicic acid in equilibrium with quartz at 90°C flows into the domain at $x = 0$. The solubility of quartz decreases as temperature decreases (see curve R1 in Figure 1), so a negative gradient of silicic acid concentration exists in the domain from $x = 0$ to $x = 1$. The gradient of concentration creates a flux of silicic acid from hotter to colder regions of the domain, and quartz precipitates in response to its decreasing solubility.

With passage of time, significant quantities of quartz are deposited, as shown in Figure 2. Porosity is reduced throughout the spatial domain, but particularly near the inlet; at $x = 0.02$ m, the amount of deposited quartz asymptotically approaches the pore capacity. At larger distances from the inlet, amounts of precipitate asymptotically ap-

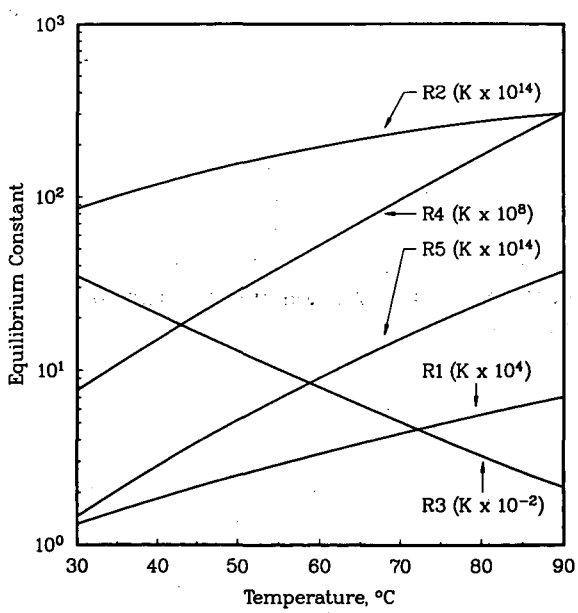

Figure 1. Scaled equilibrium constants vs. temperature for reactions R1–R5. [XBL 933-349]

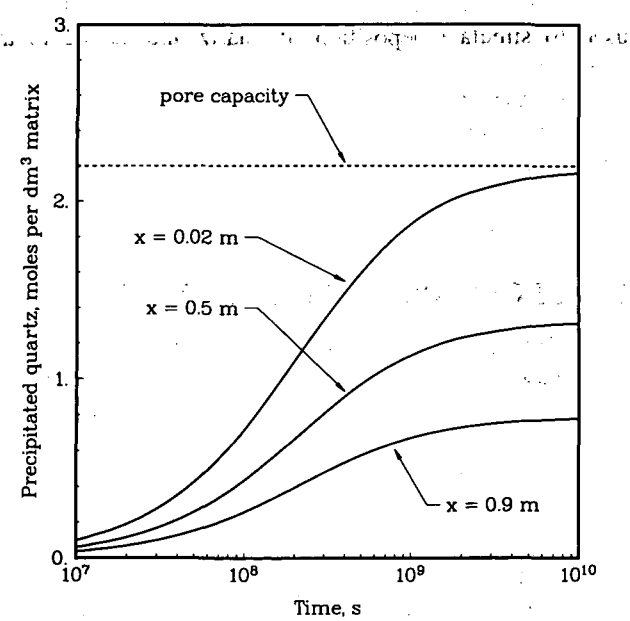

Figure 2. Deposited quartz vs. time at several distances. [XBL 933-350]

proach lower limits. The Darcy flux through the domain as a function of time is shown in Figure 4. It is evident that the fluid flow system has not achieved a steady-state condition at a simulated elapsed time of 1×10^{10} s; instead, the system appears to be asymptotically approaching a state of zero flow.

Calcite-Water System

In this case, the initial porosity of the spatial domain is 0.01, and the initial Darcy flux is 1×10^{-5} m/s. The fluid phase initially occupying the domain contains calcium and carbonate species in equilibrium with calcite at a fixed hydroxide concentration of 9×10^{-5} mole/dm^3 and at a temperature determined by location. Starting at time zero, solution in equilibrium with calcite at 90°C flows into the domain at $x = 0$. The hydroxide concentration of this solution is about 1.5×10^{-4} mole/dm^3.

As in the case of quartz, the solubility of calcite decreases with decreasing temperature (see curve R2 in Figure 1), and calcite is deposited in the spatial domain. In contrast to the case of quartz, the deposition of calcite is lightest near the inlet and is more uniformly distributed through the spatial domain. These features are evident in the deposition histories shown in Figure 3. The Darcy flux through the domain as a function of time is shown in Figure 4. As in the case of quartz deposition, the fluid flow has not achieved a steady-state condition at a simulated elapsed time of 1×10^{10} s and appears to be asymptotically approaching a state of zero flow. However, the distribution of chemical species within the spatial domain quickly reaches a steady state. Profiles of the steady-state concentrations of simulated species are shown in Figure 5.

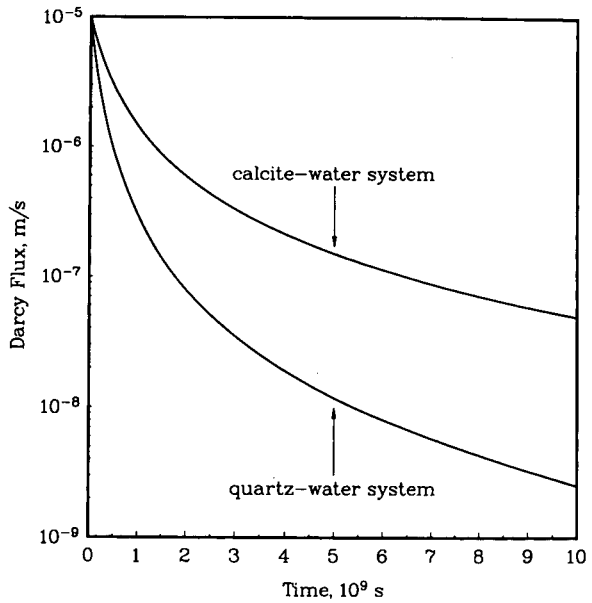

Figure 4. Darcy fluxes vs. time during deposition of quartz and calcite. [XBL 933-352]

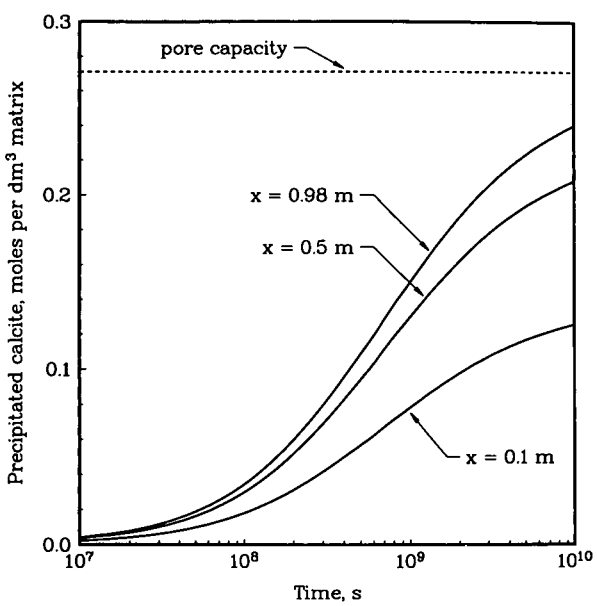

Figure 3. Deposited calcite vs. time at several distances. [XBL 933-351]

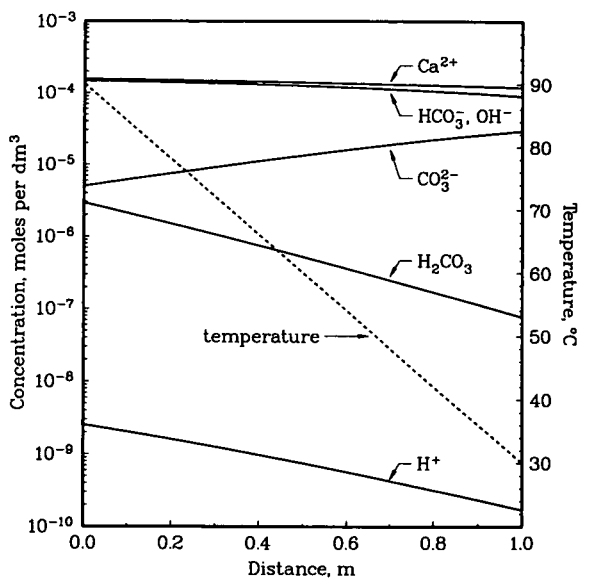

Figure 5. Profiles of steady-state concentrations of solution species in equilibrium with calcite and profile of temperature vs. distance during deposition of calcite. [XBL 933-353]

DISCUSSION

The most evident difference in the behaviors of the quartz-water and calcite-water systems is the difference in mode of deposition of the solid phases: quartz is deposited more heavily near the inlet of the spatial domain, whereas calcite is deposited more heavily away from the inlet. Specifically, the amount of quartz precipitated at $x = 0.02$ m equals 98% of the theoretical pore capacity, with initial porosity of 0.05, at the simulated time 1×10^{10} s, whereas the amount of calcite precipitated at $x = 0.98$ m equals 89% of the theoretical pore capacity, with initial porosity of 0.01, at the same time. The difference in behaviors of the two systems cannot be rationalized by invoking prograde versus retrograde variations of the solubility products with temperature, because both products decrease monotonically with decreasing temperature (see curves R1 and R2 in Figure 1).

In both systems, precipitation of solid occurs continuously with the passage of time because of advective transport of solutes, in equilibrium with solid at one temperature, to a region at a lower temperature where the solubility product is exceeded. The consequence is precipitation of enough solid to achieve equilibrium at the lower temperature, and the amount of solid deposited must be related directly to the extent of change of a key solute concentration from the higher to the lower temperature. The key solutes are silicic acid in the quartz-water system and calcium in the calcite-water system. In the case of quartz, the silicic acid concentration equals the solubility product. In the case of calcite, Figure 5 shows that the concentrations of calcium, bicarbonate, and hydroxide are roughly equal over the entire spatial domain, so the concentration of calcium can be approximated by the cube root of the calcite solubility product. Equation (1) can be rewritten to show the implicit dependence of the solubility product, K_{sp}, on distance, x, through the dependence of temperature, T, on x; thus

$$K_{sp}(x) = \exp\left\{\beta\left[A + \frac{C}{T(x)} + ET(x)\right] + D \ln T(x)\right\}, \qquad (2)$$

where $\beta = \ln 10$. Then

$$\frac{d}{dx}\left[K_{sp}(x)\right] = K_{sp}(x)\left\{\beta\left[-\frac{C}{T(x)^2} + E\right] + \frac{D}{T(x)}\right\}\frac{d}{dx}\left[T(x)\right]. \qquad (3)$$

For the calcite-water system,

$$\frac{d}{dx}\left[K_{sp}(x)^{1/3}\right] = \frac{1}{3}\left[K_{sp}(x)\right]^{-2/3}\frac{d}{dx}\left[K_{sp}(x)\right]. \qquad (4)$$

For both systems we have

$$T(x) = 363.15 - 60x, \quad dT(x)/dx = -60, \quad 0 \le x \le 1, \qquad (5)$$

where the units of x and $T(x)$ are meters and kelvins, respectively. Figure 6 shows values of $-dK_{sp}(x)/dx$ versus x for quartz and $-d[K_{sp}(x)^{1/3}]/dx$ versus x for calcite, calculated using Eqs. (2)–(5) and data in Table 1. The larger the value of the plotted quantity is, the higher the rate of deposition of solid is expected to be. The plotted quantity for quartz is largest near the inlet at $x = 0$ and decreases monotonically with increasing x. On the other hand, the plotted quantity for calcite is lowest near the inlet and increases monotonically with increasing x. These features are consistent with the modes of deposition in the numerical simulations. Over the entire domain, the plotted quantity for calcite is considerably smaller than that for quartz; this is consistent with the computational result that at the same simulated elapsed time (1×10^{10} s), precipitated quartz has filled up more than five times as much pore space as has precipitated calcite.

The interaction between the gradient of temperature and the temperature dependence of the solubility product, expressed mathematically in Eqs. (3) and (4) and illustrated in Figure 6, can provide a capability for predicting the mode of deposition of a mineral. In the cases of quartz and calcite, the modes are different and would not have been predicted solely through consideration of the temperature dependences of chemical equilibria.

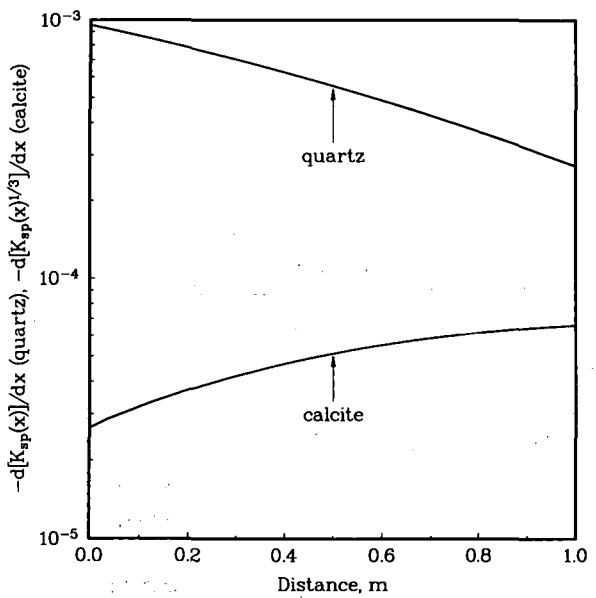

Figure 6. Variations with distance of negative gradients of solubility product of quartz and of cube root of solubility product of calcite under a constant gradient of temperature. [XBL 933-354]

REFERENCES

Carnahan, C.L., 1991. Numerical simulations of heterogeneous chemical reactions coupled to fluid flow in varying thermal fields. *In* C.G. Sombret (ed.), Scientific Basis for Nuclear Waste Management XV (Materials Research Society Symposium Proceedings, v. 257). Materials Research Society, Pittsburgh, Pennsylvania, p. 683–690 (LBL-31018).

Carnahan, C.L., 1992a. Numerical simulations of coupling among heterogeneous chemical reactions, temperature, and fluid flow. *In* Earth Sciences Division Annual Report 1991, Lawrence Berkeley Laboratory Report LBL-31500, p. 139–142.

Carnahan, C.L., 1992b. Numerical simulations of near-field effects on waste transport. Radioactive Waste Management and the Nuclear Fuel Cycle (in press).

Clarke, E.C.W., and Glew, D.W., 1966. Evaluation of thermodynamic functions from equilibrium constants. Trans. Faraday Soc., v. 62, p. 539–547.

Distribution of Radon Sources and Effects on Radon Emanation in Granitic Soil at Ben Lomond, California

*S. Flexser, H. A. Wollenberg, and A. R. Smith**

To better understand the sources of radon and its availability for transport through the soil, the distribution of uranium and radium in soil and bedrock were investigated at the site of the Small Structures project, Ben Lomond, California. In this project, the ingress of Rn into the basements of houses is being investigated by means of "mini-basement" structures installed in the shallow subsurface, which permit detailed examination of the movement of Rn from its sites in the soil, through the soil-pore system, and, by way of controlled entry slots, into the basements (Fisk et al., 1992).

For this study of Rn sources in the soil, samples were obtained mainly from core and auger holes, with additional samples from outcrops and soil rock fragments. Radioelement contents and radon emanation rates of bulk samples were determined by gamma spectrometry, and this was complemented by microscopic examination of fission-track radiographs of grain mounts and polished thin sections and by electron microscopy (SEM) with x-ray spectroscopy (EDS) to obtain compositional data. Clay mineral contents were also characterized by x-ray diffraction, and soil solutions of 1:1 soil:water mixtures were obtained and analyzed by ICP-atomic emission spectroscopy.

SITE AND SOIL CHARACTERISTICS

The Small Structures site is located at an altitude of 790 m on a broad-topped ridge (Figure 1), with high seasonal rainfall (~ 150 cm per year). There is occasionally light snowfall, but the ground does not freeze. The topography and climate have encouraged deep weathering of the granitic bedrock, forming a well-developed saprolite to > 5 m. At the surface, a brown sandy loam is present to a depth of 1.4 to 2.4 m overlying the saprolite across an irregular and partly transitional boundary. Roots and burrow

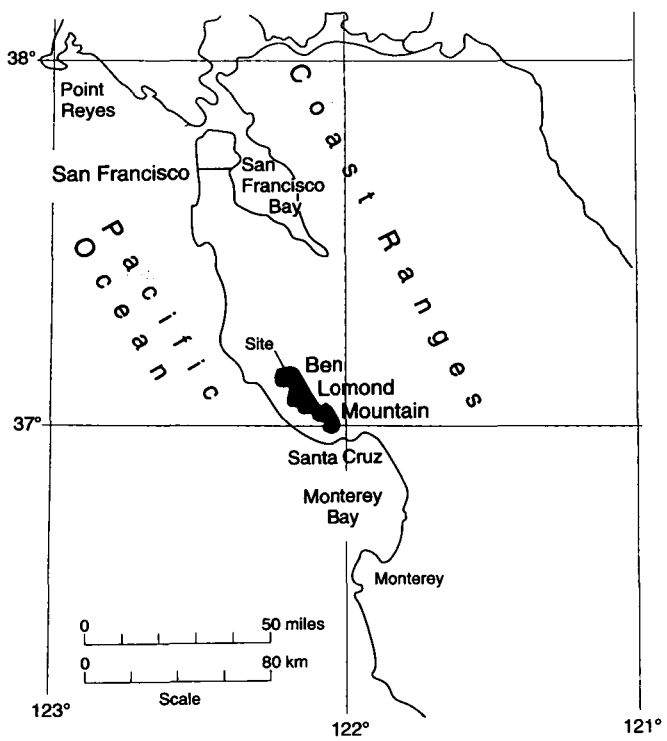

Figure 1. Regional map showing location of Small Structures site on Ben Lomond Mountain, north of Santa Cruz, California. [XBL 898-7697a]

* Engineering Division, Lawrence Berkeley Laboratory.

holes are very abundant to depths of > 3 m. The soil parent rock, or protolith, is weathered quartz diorite of the Ben Lomond pluton (Leo, 1967; Bowman and Estrada, 1980), a medium-grained granitic rock containing abundant finer- and coarser-grained inclusions and dikes. The main mineral constituents of the quartz diorite are plagioclase, quartz, potassium feldspar, biotite, and hornblende; accessory minerals include sphene, zircon, ilmenite, epidote, apatite, and minor monazite and allanite. Most minerals, particularly biotite and plagioclase, show significant effects of weathering, with quartz and zircon the only minerals consistently clear and unweathered. Clay-size gibbsite and either kaolinite or halloysite occur as weathering products.

Mineralogically, the main difference between the soil and weathered protolith is the abundance of gibbsite in the soil from the surface through the upper saprolite (to ~ 2.5–3 m depth). Smectite, by contrast, is abundant in the soil only below the upper saprolite. The deeper saprolite is distinctly more competent than the upper saprolite and preserves protolith igneous textures largely intact. It also maintains abundant narrow, near-vertical fractures consisting of zones ~ 5 mm wide, darkly stained and coated by Fe-oxyhydroxide (Fe-OOH) and possibly organic matter and bordered by deformed and fragmented mineral grains. Fine root casts are present in the fracture zones to depths of at least 5 m.

RADIOELEMENT DISTRIBUTION

The abundance and distribution of radioelements were determined on bulk and microscopic scales. Bulk-scale analyses employed gamma spectrometry for analyses of radium (direct precursor of radon), thorium, and potassium and for determination of radon emanation rates. Results of analyses of bulk soil and rock samples are shown in Figure 2, which combines data from soil samples from a core hole (C) and an auger hole (A), as well as grab samples from the two structure excavations and rock samples from soil and outcrop. Soil samples vary between 0.61 and 1.33 pCi/g Ra content, corresponding to 1.71 and 3.76 ppm equivalent U (U content based on U-series secular equilibrium and corrected for Rn emanation). Most of the variation in radioelement concentrations (Figure 2B to D) is attributable to heterogeneities inherited from the parent granitic rock rather than to secondary radioelement re-

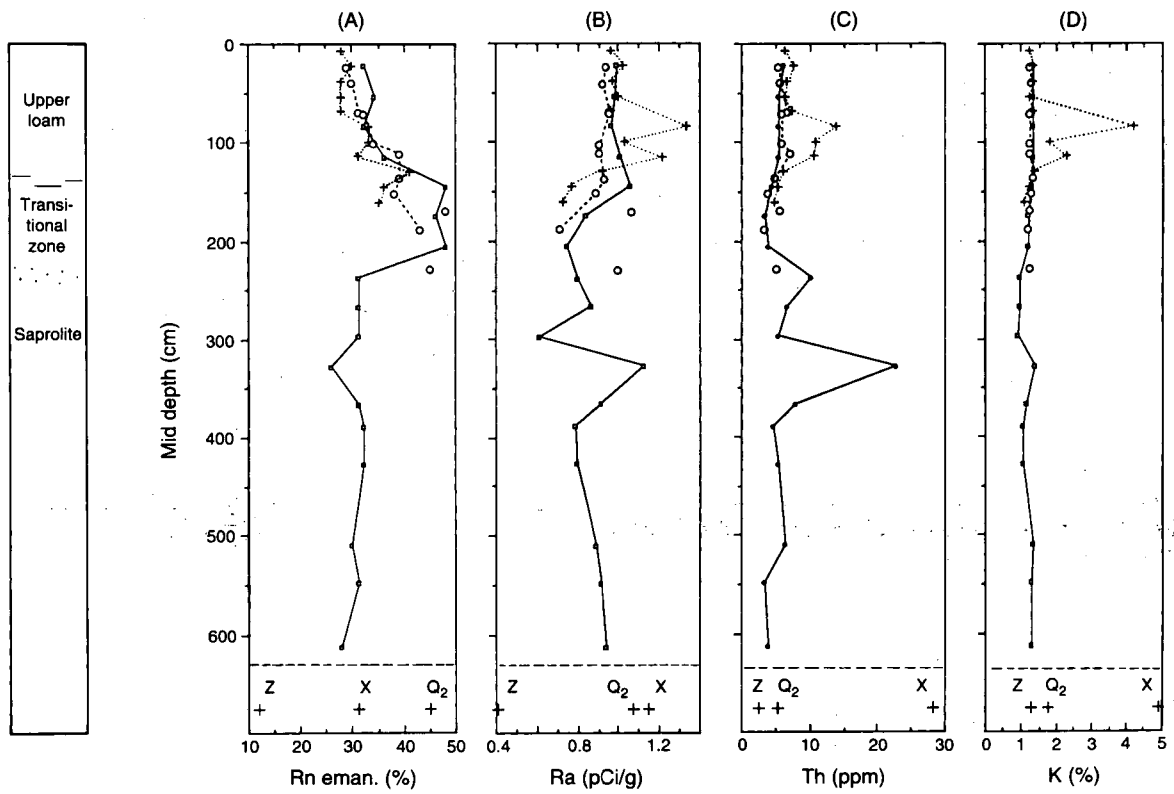

Figure 2. Radioelement abundances and radon emanation rates of soil samples from core hole C (solid line), auger hole A (crosses), and structure excavations (circles; dashed for east excavation). Bottom of each plot shows data for intact rock samples Q_2 (weathered quartz diorite), X (coarse-grained dike fragment), and Z (fine-grained dark inclusion). Soil zonation shown at left. [XBL 9210-5817]

distribution by pedogenic processes. This is suggested by the contrasting radioelement contents of rock samples X and Z— texturally and mineralogically distinct phases of the parent rock—compared with the main phase of weathered quartz diorite (Q_2). It is also indicated in the anomalously high radioelement contents of the auger (A) samples between 80 and 120 cm depth, which contain abundant rock fragments very similar to sample X. Aside from this anomalous interval (and that at 330 cm in core C, also likely due to parent rock heterogeneity), the auger and core samples' radioelement contents match reasonably well, as do those from the east excavation; a poorer match is observed with the samples from the west excavation.

Radon emanation rates (Figure 2A) show a pattern of variation apparently independent of that of the radioelement concentrations, being related instead to soil zonation (Figure 2, left side): emanation increases with depth through the upper loam, peaks in the transitional soil zone and upper saprolite, and returns to a rather constant lower level in underlying saprolite. The variation shown by Rn emanation also is similar to the variation observed in the abundance of fine pedogenic phases, notably gibbsite, in the soil, as discussed below. The large differences in emanation rates of the three rock samples analyzed reflects different degrees of weathering and redistribution of U (and Ra) on accessible grain boundaries and secondary minerals.

On the microscopic scale, the distribution of U in soil and parent rock was investigated by fission-track radiography to provide a guide to Ra distribution. U in the soil is located in (1) small granitic accessory minerals, predominantly zircon; (2) primary igneous minerals weathered partly or completely, most frequently sphene; (3) margins and cracks in mineral grains; and (4) fracture zones in the saprolite. Secondary sites (2, 3, 4), which show prior mobilization of U in the soil or parent rock, are the main focus here, as U and Ra tend to concentrate on grain boundaries and pore walls at these sites, enabling recoiling Rn atoms to emanate much more readily than from primary minerals. Table 1 summarizes the sites of elevated U concentration in the soil and rock samples. Sphene is the most common

Table 1: Summary of U-bearing sites in soil and parent rock. U concentrations determined by fission-track radiography of thin sections and grain mounts. Minimum U concentrations given where high fission-track density, small grain size, or linear site geometry impede estimation of U content.

Mineral or other site	Sample type	Mean U (ppm)	(±s. d.)	#	Range (ppm)
Sphene	soil	≥ 193	(±138)	73	30 – > 700
	qtz dior*	≥ 157	(±186)	10	40 – > 630
	other	302	(±166)	25	40 – 620
Grain boundaries	soil	≥ 133	(±172)	15	20 – > 660
	qtz dior	134		1	
	other	> 87		2	45 – > 130
Altered biotite	soil	75	(±46)	6	20 – 150
Altered plagioclase	soil	76	(±81)	3	17 – 160
	other	48	(±17)	3	37 – 68
Epidote	soil	119	(±113)	3	51 – 250
	qtz dior	≥ 50		2	35 – > 60
	other	50		2	38 – 60
Altered allanite	other	≥ 195	(±130)	7	82 – > 440
Apatite	qtz dior	253	(±324)	3	64 – 630
Fractures in saprolite	soil				
Fe-rich coatings		46	(±24)	7	20 – 90
phosphate coatings		≥ 290	(±140)	7	180 – > 580

*Rock samples: "qtz dior" = main phase quartz diorite parent rock, outcrops; "other" = dike or other granitic samples, soil clasts.

site, containing widely varying U concentrations usually ranging between 100 and 400 ppm, but with both lower and higher concentrations (to ≥ 700 ppm) also common. Figure 3 shows examples of typical sphene from a soil sample and of more-uraniferous sphene (with U concentrated in weathered parts) from a granitic rock fragment. Mineral grain-boundary coatings also commonly contain U, with more-uraniferous sites ranging between 20 and 200 ppm U and in some cases to ≥ 700 ppm (Table 1). Less commonly, significant U is associated with weathered plagioclase or biotite, or occasionally with epidote, allanite, or apatite. Also, minute highly uraniferous grains of uraninite and monazite are sometimes observed, usually enclosed within primary biotite or feldspar crystals.

Compositional data for the main types of U-bearing sites in the soil and parent rock show that U enrichment in secondary sites generally corresponds with very high Ti concentrations (to ≥ 70% TiO_2), along with elevated Al, Fe, and P contents, with more-mobile elements like Ca and K removed by solution. Weathering in primary minerals, especially sphene and biotite, is characterized by a porous, skeletal or mesh-like framework on which Ti is concentrated, with recesses in the framework containing high concentrations of Al. U-bearing grain-boundary coatings contain minute (submicron) grains of rutile or anatase, as well as Th- and REE-bearing phases. In samples of parent rock, large differences in U concentration were observed between weathered and unweathered sphene; similar differences were not noted in soil samples, suggesting that U is fixed temporarily in residual weathered sphene in the soil protolith and later remobilized during further weathering in the soil.

In the saprolite, U is consistently present at elevated levels in the high-angle fracture zones, where it is associated with Fe-OOH and, locally, with a secondary REE-phosphate mineral. Figure 4 illustrates textural features and U associations of the fracture zones examined in intact polished sections. U concentrations in the dense Fe-rich fracture coatings generally vary between ~ 20 and 90 ppm U, averaging 30–50 ppm (Table 1), whereas in the phosphate mineral they average 5 to 10 times higher (200 to > 580 ppm).

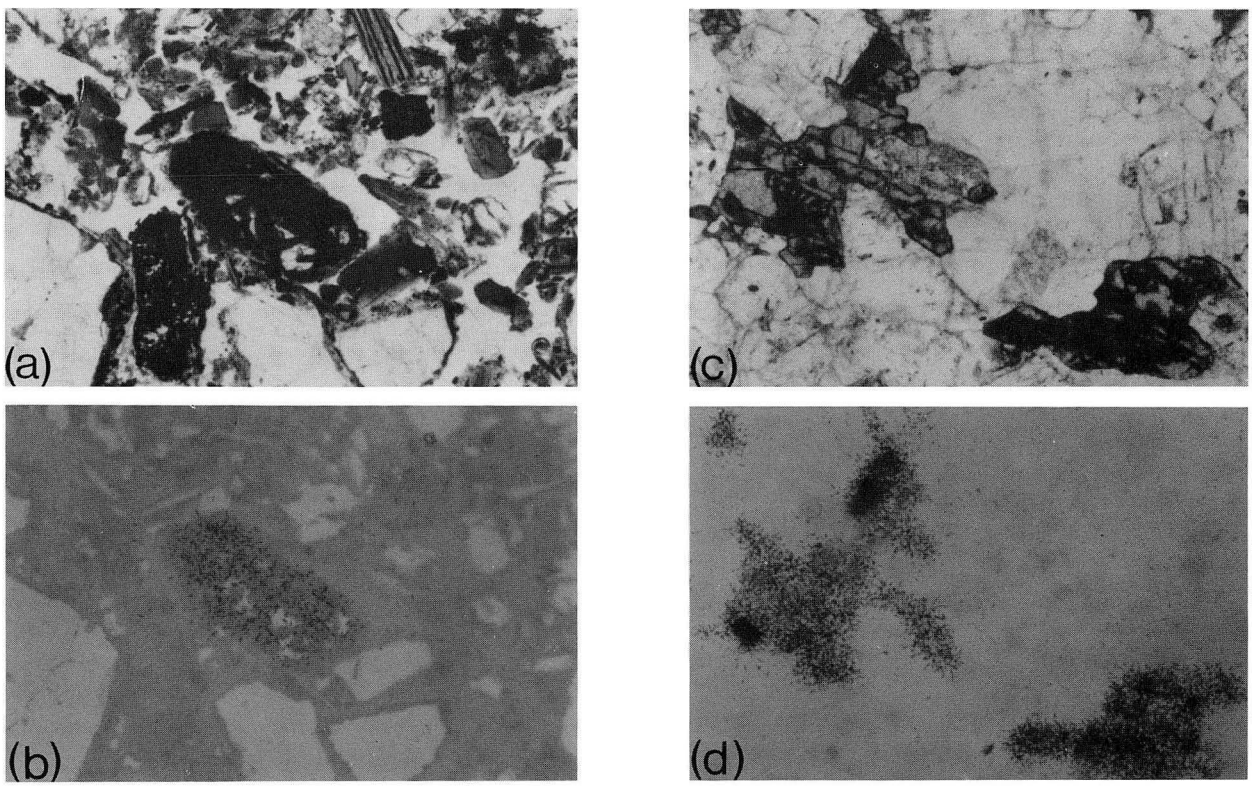

Figure 3. Examples of U-bearing sphene and associated fission tracks. Weathered portion (dark) of sphene grain from soil at 1.3 m depth (**A**) contains ~ 190 ppm U, determined from track density shown in (**B**). (Grain outlines in B due to neutron irradiation.) U in sphene from intact rock fragment (**C**) is strongly influenced by degree of weathering, with concentrations in weathered parts far greater (**D**) than those (~ 430 ppm U) in unweathered parts. Photo widths are 1.8 mm, plane-polarized light. [CBB 920-8047]

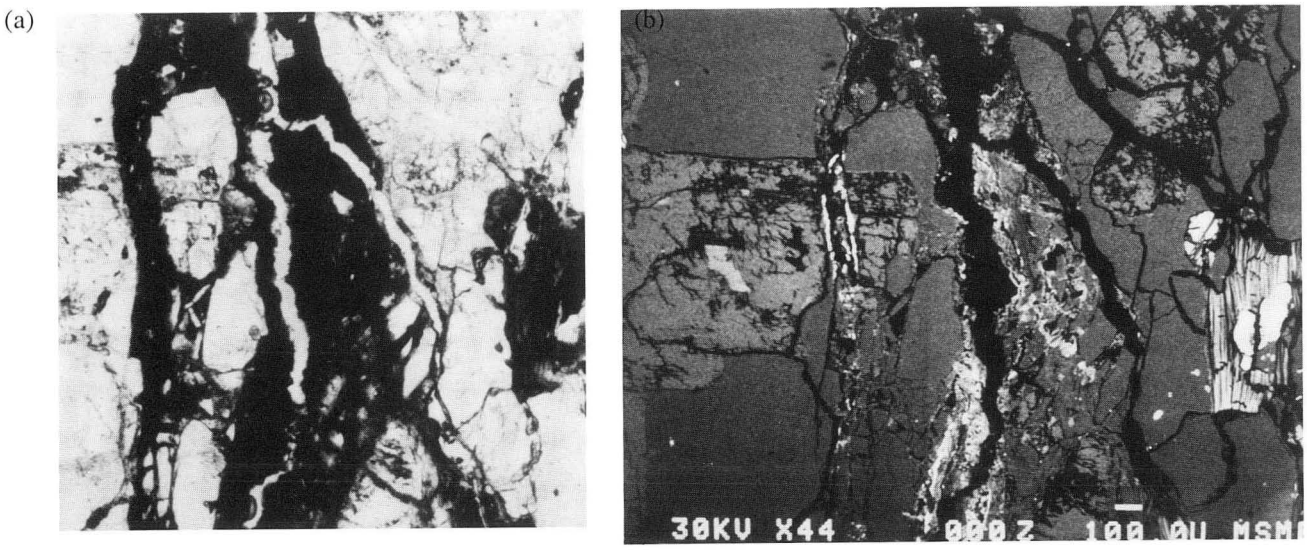

Figure 4. Segment of narrow fracture zone in saprolite shown in plane-polarized light (**A**) and back-scattered electron image (**B**). Dark areas in (A) are Fe-rich fracture fillings cutting plagioclase grain at left (note displacement) and porous zone in center. Open cracks are white in (A), black in (B). Dense Fe-rich fillings average 20–30 ppm U. Narrow bright bands—cutting plagioclase grain and at bottom center in (B)—contain ≥ 200 ppm U due to presence of REE-phosphate mineral. Scale bar in (B) represents 100 μm. [CBB 920-8102]

DISCUSSION

The observed preferential distribution of U (and, by inference, Ra) on secondary sites—grain boundaries, fractures, and relatively porous weathered minerals—is reflected in the high Rn emanation rates (between ~ 30% and 50%) of the Ben Lomond soil. However, the detailed variation in Rn emanation with depth is not readily explained by variation in U distribution. Highest emanation rates occur between 1.3 and 2.3 m depth (Figure 2A), and in this interval soil clay fractions show a maximum in the relative abundance of gibbsite, the main crystalline pedogenic phase, as well as abundant amorphous silica and Fe-OOH. This suggests that enhanced emanation is related to the occurrence of these pedogenic phases.

Further insight into pedogenic processes was provided by chemical analyses of soil solutions, which served as guides to which elements are most readily released to solution in the soil and saprolite. Compositional data on the soil solutions are plotted in Figure 5, and show that numerous elements are relatively abundant in the shallow soil but decline sharply below. Most notable are Al, Ti, and Fe, which figure prominently in secondary U-bearing sites and which follow very similar patterns with depth in the soil solutions. The presence in solution of these elements—particularly Al and Ti, which are highly immobile in most geochemical environments—in the upper 1–1.5 m of the soil indicates that shallow soil fluids are quite acidic due to abundant rainfall and vegetation and are possible locally reducing. These elements (as well as others soluble only in the topmost soil; Figure 5B) probably precipitate in this shallow soil or at adjacent depths as hydroxides or hydrous oxides; the concentration of gibbsite, silica, and Fe-OOH observed between 1.3 and ≥ 2 m depth indicates that some portion of these precipitated phases is then transported by suspension in soil fluids and accumulates in this depth interval. Sorption of radionuclides by these colloidal phases (and possibly also by colloidal organic matter) probably explains the high Rn emanation rates observed in this interval. This conclusion is broadly consistent with modeling of Semkow (1990) of Rn emanation rates from particulate matter on which Ra is distributed preferentially on surficial coatings. The high emanation rates in this soil interval could readily result, by this model, from sorption of Ra onto colloidal particles in the size range observed in soil clay suspensions (abundant at ≥ 0.3 μm), given their likely formation by aggregation of finer precipitates.

Another factor that may influence Rn production and emanation is the degree of separation of Ra from U (U-series disequilibrium) in the soil. Significant differences in Ra vs. U sorption efficiencies of a number of phases present in the soil, mainly Fe-, Ti-, or Mn-OOH, amorphous silica, clays, and organic material—as well as suppression of Ra sorption by competing alkaline-earth cations in solution—indicate that some separation of Ra from U is probable. The association of U in secondary sites with Ti, Al, and other elements readily mobilized in the shallow soil suggests that U and its daughter elements are mobilized and redistributed, perhaps repeatedly, from these sites, increasing the likelihood of disequilibrium by differential sorption.

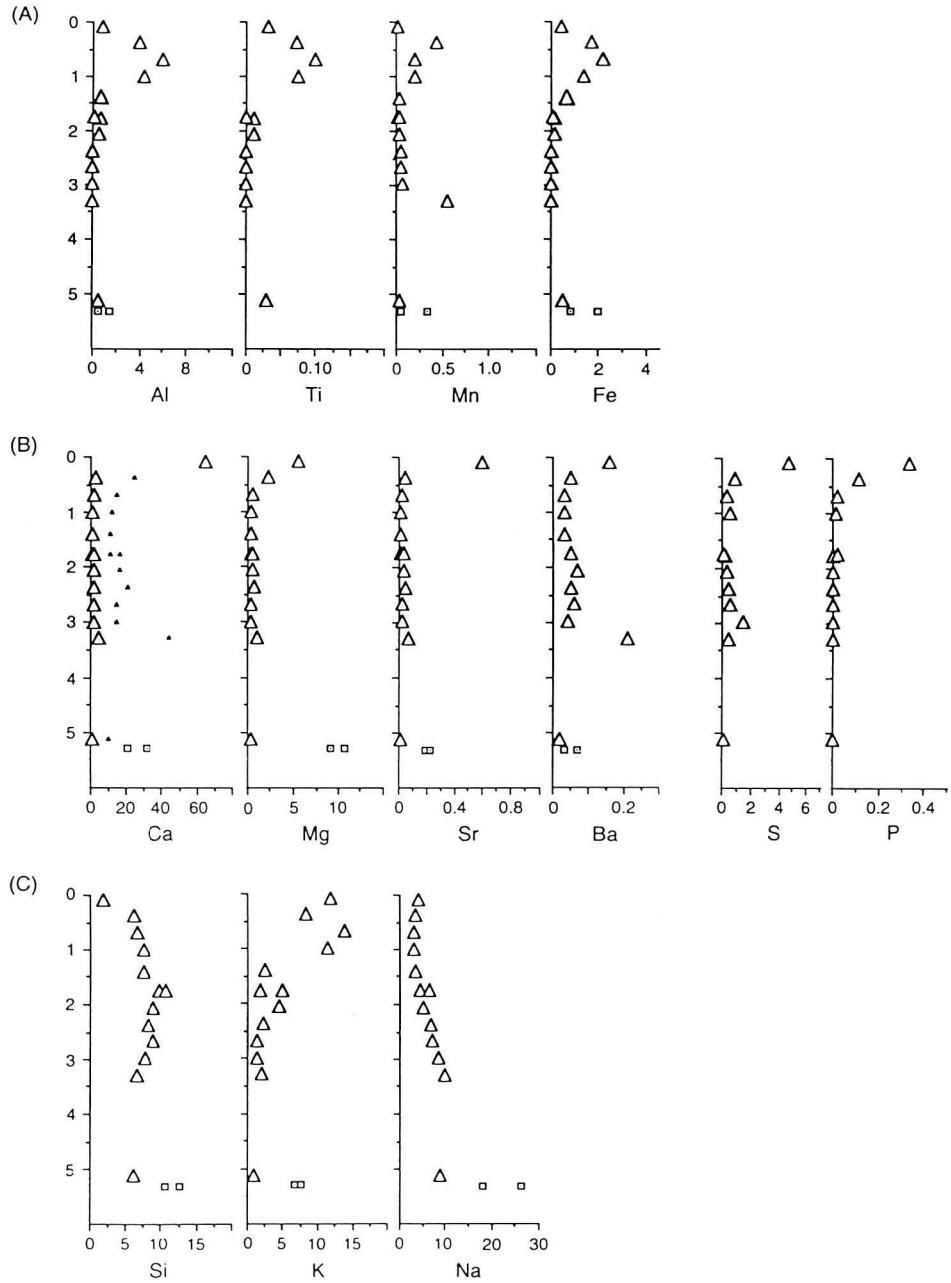

Figure 5. Elemental concentrations (ppm) in soil solutions obtained from 15-cm soil intervals (mean depths in m) in the hole C core. Elements grouped in **(A)** and **(B)** based on similarity in concentration patterns with depth; remaining elements included in **(C)**. (Small squares near base of plots are two well-water samplings from 15 to 16 m depth.) Small solid triangles in Ca plot are 10× concentration, to show detail. Analyses by A. Yee. [XBL 9210-5815]

The fracture zones in the saprolite, which contain elevated U concentrations along near-vertical permeable flow paths, may be important in the overall balance of Rn in the soil. Although relatively deep (> 2 m), they could serve as conduits for Rn transport to shallower levels. The presence of several phases in the fracture zones—particularly the uraniferous phosphate mineral, crystalline Fe-OOH (lepidocrocite), and cryptomelane or a similar Ba-Mn mineral—suggests that separation of Ra from U may be as much or more of a factor there as it is higher in the soil column. Considerable variation in CO_2 partial pressure and redox conditions may also occur in the fracture zones, with additional implications for radioelement distributions.

In future we hope to resolve questions of U-series disequilibrium and separation of Ra from U by means of high-resolution gamma spectrometry. Determination of the distribution and character of soil organic matter and dissolved carbonate species is also a high priority, as these are vital to an understanding of radioelement sorption and Rn emanation.

ACKNOWLEDGMENTS

Andy Yee provided analyses of soil solution samples, and Ron Wilson of the Department of Material Science and Mineral Engineering, U.C. Berkeley, assisted with electron microscopy. Thermal neutron irradiations were provided by the Oregon State University Radiation Center. We also thank Harold Wells and his staff at the California Division of Forestry Ben Lomond Nursery for their cooperation and support at the field site.

REFERENCES

Bowman, R.H., and Estrada, D.C., 1980. Soil survey of Santa Cruz County, California. U.S. Department of Agriculture, Soil Conservation Service.

Fisk, W.J., Modera, M.P., Sextro, R.G., Garbesi, K., Wollenberg, H.A., Narasimhan, T.N., Nuzum, T., and Tsang, Y.W., 1992. Radon entry into basements: Approach, experimental structures, and instrumentation of the Small Structures research project. Submitted to Environmental Science and Technology.

Leo, G.W., 1967. The plutonic and metamorphic rocks of the Ben Lomond Mountain area, Santa Cruz county, California. Calif. Div. Mines Geol. Spec. Rept. 91, p. 27–43.

Semkow, T.M., 1990. Recoil-emanation theory applied to radon release from mineral grains. Geochim. Cosmochim. Acta, v. 54, p. 425–440.

Interpretation of Sr Isotope Data from Yucca Mountain: Modeling the Effects of Water-Rock Interaction

T. M. Johnson and D. J. DePaolo

The paleohydrologic record is of great concern at Yucca Mountain, because the proposed nuclear waste repository depends on the existence over many thousands of years of a thick unsaturated zone where groundwater transport should be very slow. Investigations of present and past groundwater conditions in the Yucca Mountain area have been aided by isotope measurements on groundwater samples and on minerals precipitated by groundwater. Strontium isotope ratios in calcite deposits at the land surface and calcite vein fillings at depth may contain information relating to changes in water table elevation over the last few million years. The Sr isotope ratios in secondary minerals such as calcite are easily interpreted because they are equal to the isotope ratios in the groundwater at the time the minerals precipitated. The isotope ratios of the groundwater may in turn reflect its source, but only if the source signature has not been altered by reaction with nearby rock. The purpose of this study was to explore the influence that water-rock interaction exerts on Sr isotope ratios of groundwaters.

Sr isotope measurements on the calcites from Yucca Mountain reveal a clear pattern (Marshall et al., 1992) (Figure 1). Calcites from levels higher than 100 m above the modern water table have distinctly higher Sr isotope ratios than both the groundwater samples and the calcites from the saturated zone. This pattern fits a model in which calcites in the unsaturated zone would be produced by downward percolating waters that obtained their Sr isotope signature near the surface. The rocks near the surface have a relatively high Sr isotope ratio (Peterman et al., 1991a) (Figure 2), and both the groundwater and groundwater-pre-

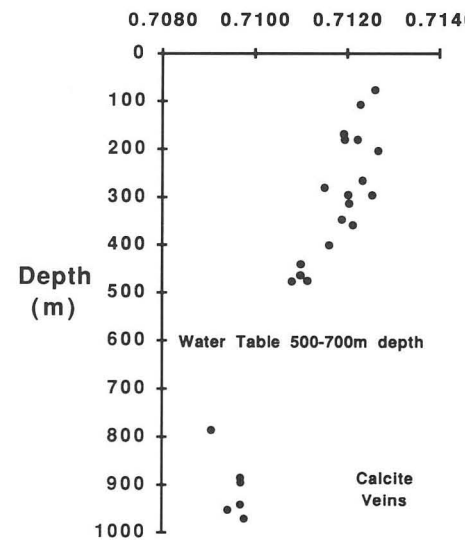

Figure 1. $^{87}Sr/^{86}Sr$ measured on calcite from vein fillings at Yucca Mountain, plotted versus depth (data from Marshall et al., 1992). Calcite samples from above the present-day water table have higher $^{87}Sr/^{86}Sr$ than those below it. [XBL 933-355]

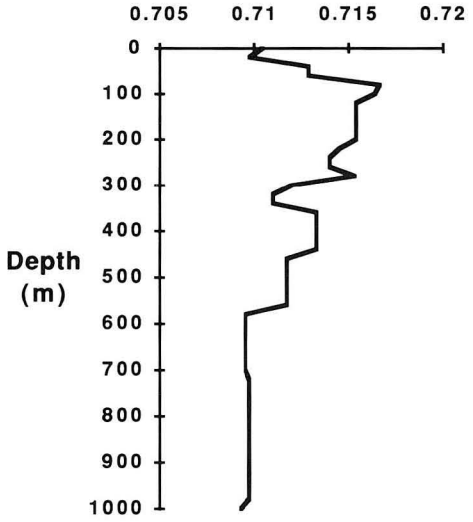

Figure 2. Whole-rock $^{87}Sr/^{86}Sr$ for silicic tuffs at Yucca Mountain, plotted versus depth (data from Peterman et al., 1991a). Groundwaters may have acquired their $^{87}Sr/^{86}Sr$ ratios partially from nearby rocks, so multiple interpretations for the data in Figure 1 are possible. [XBL 933-356]

cipitated minerals would inherit this signature. This model is plausible and, if proven accurate, would strengthen the case for building the proposed waste repository.

However, scenarios of upwelling groundwater, which could jeopardize the safety of the proposed facility, have been proposed (National Research Council, 1992), and it is critical to determine whether these models are consistent with the vein calcite data. The simplest case can be ruled out; groundwater of present-day composition ($^{87}Sr/^{86}Sr$ = 0.7100 to 0.7115; Peterman et al., 1991b) rising *without any reaction with the rock* could not have produced the calcite vein fillings in the unsaturated zone, because their Sr isotope ratios are different. However, the groundwater does react slowly with the rock, and it is necessary to include the likely effects of this water-rock interaction on the Sr isotope ratio as scenarios of past groundwater flow are evaluated. If groundwater were to flow upward as it passed into the rocks of the present-day unsaturated zone, it would react with the rocks and its Sr isotope ratio would increase, perhaps enough to produce the pattern seen in the calcite data. Despite the slow rate at which the reactions occur, strontium concentrations in the groundwater are about 10,000 times smaller than those in the rock and, accordingly, a small reaction flux from the rock has a magnified effect on the Sr isotope ratio of the water.

The focus of this work was to quantify the water-rock interaction effect and to construct a model capable of verifying whether upward-flowing groundwater scenarios that include this effect are consistent with the Sr isotope data from the calcites. This model is part of a broader effort to provide a framework that can be used to interpret isotope data in hydrologic systems.

MODELING OF STRONTIUM ISOTOPE RATIOS IN GROUNDWATER

The model constructed for this study is one dimensional. It describes the Sr isotope ratio in the groundwater as a function of depth, given values for the vertical velocity of the groundwater, the rate of reaction of the rock, the rock/water mass ratio, and the rock/water distribution coefficient for Sr. Several simplifying assumptions were made, and the transport parameters were assigned order-of-magnitude estimates so that a first-order evaluation of the upward-groundwater-flow scenario could be carried out. As a rough approximation, the rock dissolution and secondary phase precipitation rates were set equal to each other. Moreover, the rock was assumed to react as a single homogeneous phase; no allowance was made for differing reaction rates among the various minerals present. The system was treated as a homogeneous, saturated, porous continuum.

The differential equation that describes the concentration of Sr in the groundwater is

$$\frac{dc_f}{dt} = D\frac{\partial^2 c_f}{\partial x^2} - v\frac{dc_f}{dx} - RM\left(c_s - kc_f\right), \qquad (1)$$

where c_f and c_s are the concentration of Sr in the fluid and in the solid, v is the groundwater velocity, D is the dispersion coefficient, R is the reaction rate (fraction of solid dissolved per unit time), k is the equilibrium distribution coefficient for the element in the precipitated solid, and M is the solid/fluid mass ratio. The appropriate differential equation for the isotope ratio is

$$\frac{\partial r_f}{\partial t} = D\frac{\partial^2 r_f}{\partial x^2} - 2D\frac{\partial \ln c_f}{\partial x}\frac{\partial r_f}{\partial x} - v\frac{\partial r_f}{\partial x} + RM\frac{c_s}{c_f}\left[r_s - r_f\right], \qquad (2)$$

where r_f and r_s are the Sr isotope ratios in the fluid and in the solid, respectively. Equations (1) and (2) were solved numerically, using a finite difference approach, for chosen values of v, D, R, M and k, with values of $c_s(x)$ and $r_s(x)$ taken from recently published whole-rock data (Peterman et al., 1991a) (Figure 2).

RESULTS

The following values were chosen as estimates for the model parameters: v = 1 m/year, upward, $D = 10^{-2}$ m^2/year, $R = 10^{-8}$ /year (1% of the rock reacts per million years), M = 100 (corresponds to about 3% effective porosity), and k = 10,000 (based on reported Sr concentrations for rock and groundwater).

The results of the model based on the above parameters are shown in Figure 3. Also plotted are the vein calcite data for comparison.

DISCUSSION

The upward-flow scenario modeled here is consistent with the vein calcite data. Groundwater would initially have a low Sr isotope ratio, but as it flowed upward, it would react with the upper rock units and the ratio would increase, giving the pattern reflected in the calcites. Although the uncertainties in the model parameters are very large, the upward flow model is plausible for reasonable values of the parameters. Accordingly, at this stage in the investigation it appears that the Sr isotope pattern could be produced by either upward or downward flow of groundwater, and the Sr isotope data appear to give an equivocal indication of past groundwater flow conditions. Several other lines of evidence are available that may be used to understand the paleohydrology of the Yucca Mountain area, and further work with the Sr systematics may provide additional insights.

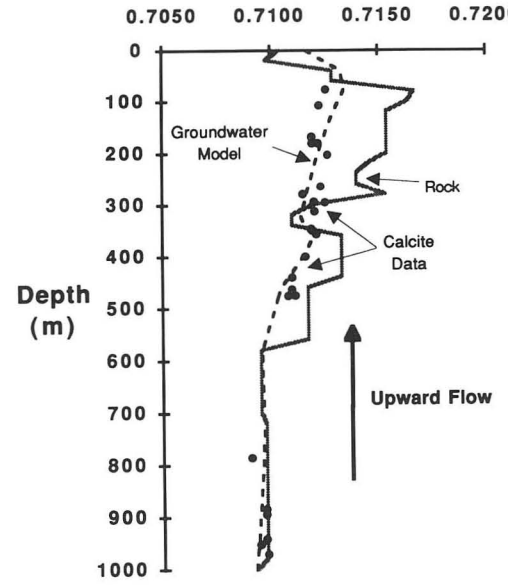

Figure 3. $^{87}Sr/^{86}Sr$ calculated from the model for ascending groundwater with water-rock interaction. $^{87}Sr/^{86}Sr$ is plotted versus depth (broken line), and data from vein-filling calcites and bulk rock are shown for comparison. [XBL 933-377]

REFERENCES

Marshall, B.D., Whelan, J.F., Peterman, Z.E., Futa, K., Mahan, S.A., and Stuckless, J.S., 1992. Isotopic studies of fracture coatings at Yucca Mountain, Nevada, USA. *In* Proceedings, Seventh Water-Rock Interaction Conference, Park City, July 12–17, 1992, p. 737–740.

National Research Council, 1992. Ground Water at Yucca Mountain: How High Can It Rise? National Academy Press, Washington, D.C.

Peterman, Z.E., Spengler, R.W., Futa, K., Marshall, B.D., and Mahan, S.A., 1991a. Assessing the natural performance of felsictuffusing the Rb-Sr and Sm-Nd systems—A study of the altered zone in the Topopah Spring Member, Paintbrush Tuff, Yucca Mountain, Nevada. *In* T. Abrajano, Jr., and L.H. Johnson (eds.), Scientific Basis for Nuclear Waste Management XIV (Materials Research Society Symposium Proceedings, v. 212). Materials Research Society, Pittsburgh, Pennsylvania, p. 687–694.

Peterman, Z.E., Stuckless, J.S., Spengler, R.W., Mahan, S.A., Gutentag, E.D., and Downey, J.S., 1991b. Strontium isotope characterization of groundwater flow systems in southern Nevada. Geol. Soc. Am. Abstracts with Programs, v. 23, p. A117.

Radionuclide Solubility and Speciation Studies for the Yucca Mountain Site Characterization Project

H. Nitsche, K. Roberts, T. Prussin, D. Keeney, S. A. Carpenter, K. Becraft, and R. C. Gatti

Yucca Mountain, Nevada, has been designated by the U.S. Department of Energy (DOE) for characterization as a potential site for a geologic high-level nuclear waste repository. As a worst case scenario, intrusion of water into the repository must be considered when preparing the risk assessment. Water moving through the emplacement area toward the accessible environment can transport radionuclides in two ways, either as dissolved species in the water or as particulate material carried by the water. The Site Characterization Plan requires "Studies to Provide the Information Required on Radionuclide Retardation by Precipitation Processes along Flow Paths to the Accessible Environment" before licensing and construction of the repository (U.S. DOE, 1988).

The purpose of our solubility and speciation studies is to supply data for calculating radionuclide transport along potential pathways from the repository to the accessible environment. Data derived from solubility studies are important for validating the geochemical codes that are part of transport models, and such codes should be capable of predicting the results of solubility experiments. Furthermore, agreement between geochemical calculations and experimental results can validate the thermodynamic database used with the modeling calculation.

In addition, results of solubility experiments also provide the source terms and starting concentrations used for studies of sorption in the absence of precipitation processes.

Neptunium, plutonium, and americium are expected to be sparingly soluble with solubility-limited dissolution rates. Water samples with compositions that bracket the range of waters expected in the vicinity of Yucca Mountain were chosen for solubility measurements (Kerrisk, 1984). These samples come from two sources: well J-13 taps the tuff aquifer, and samples from it may be representative of the water composition of the unsaturated zone near the proposed emplacement area; well UE-25p #1 taps the carbonate aquifer that underlies the emplacement horizon.

Table 1 shows the chemical composition obtained from the analysis of both groundwaters (Ogard and Kerrisk, 1984). The UE-25p #1 water has an ionic strength and total carbonate content higher by approximately a factor of 5 than well J-13 water. Well J-13 water represents natural water with the highest concentrations of dissolved species expected in the vicinity of Yucca Mountain. The water from both wells is oxidizing. Generally, radionuclide solubility studies under oxidizing conditions lead to higher solubilities for a number of radionuclides than would occur under mildly or strongly reducing conditions. These experiments will therefore provide conservative upper limits; in this article, we compare the results of solubility studies of neptunium, plutonium, and americium in waters from wells J-13 and UE-25p #1 at 25° and 60°C.

Table 1. Analyzed chemical composition of J-13 and UE-25p #1 well waters.

Species	Well J-13 concentration (mM)	Well UE-25p #1 concentration (mM)
Na^+	1.96	7.43
K^+	0.14	0.34
Ca^{2+}	0.29	2.19
Mg^{2+}	0.07	1.31
SiO_2 (aq)	1.07	0.62
Cl^-	0.18	1.04
SO_4^{2-}	0.19	1.34
F^-	0.11	0.18
Total carbonate	2.81	15.31
Ionic strength	~3	~20
pH	7.0	6.7
Total alkalinity	2.34 meq/L	11.44 meq/L
Eh	700 mV	360 mV

Source: Ogard and Kerrisk, 1984.

EXPERIMENTAL APPROACH

We followed the principles for complete and reliable solubility experiments described earlier (Nitsche, 1991). We studied the solubilities of $^{237}NpO_2^+$, $^{239}Pu^{4+}$, and $^{241}Am^{3+}/Nd^{3+}$ in two different groundwaters from the Yucca Mountain region at 25° and 60°C and respective pH values of 6.0, 7.0, and 8.5. The solubilities were studied from oversaturation by injecting a small amount, usually between 0.5 and 1 mL, of actinide stock solution into 80 mL of groundwater obtained from well J-13 or well UE-25p #1. The well waters' total dissolved carbonate was preserved at each individual pH and temperature by equilibrating the solution with mixtures of CO_2 in argon at one atmosphere. The concentrations of the equilibration gas mixtures are given in Table 2. Because the solubilities are highly sensitive to pH and temperature changes, close control of these parameters is necessary. We controlled the solutions' pH within 0.1 unit and the temperature within 1°C. Achievement of steady-state conditions for the solubility measurements was monitored by sampling aliquots of the solution phases and analyzing for the respective radioisotope as a function of time. Depending on the radionuclide and temperature, the solubility experiments were monitored for 55 to 308 days. Concentration measurements of the supernatants were made by counting liquid aliquots with a germanium low-energy counting system.

Table 2. Concentrations (in percent) of CO_2 gas in argon to maintain a total dissolved carbonate concentration of 1.531×10^{-2} M in UE-25p #1 and 2.81×10^{-3} M in J-13 water at 1 atm and at different pH and temperatures.

	J-13		UE-25p #1	
	25° C	60° C	25° C	60° C
pH 6	6.06	9.67	28.44	52.03
pH 7	1.57	2.35	6.555	11.22
pH 8.5	0.0573	0.0877	0.2353	0.3909

RESULTS AND DISCUSSION

Neptunium

Results of the neptunium solubility studies are given in Table 3. The neptunium solubility in each groundwater decreased with increasing pH. At each individual pH, the neptunium was less soluble in UE-25p #1 water than in J-13 water. In J-13 well water, neptunium solubility increased with temperature at all three pH values. The opposite trend was found in UE-25p #1 well water except at pH 8.5, where the neptunium solubility also increased with temperature. All solids formed in both waters were identified by x-ray powder diffraction as sodium neptunium carbonates, $NaNpO_2CO_3 \cdot xH_2O$. With this study, we established that the solubility-controlling solids in these two Yucca Mountain groundwaters are ternary sodium neptunium carbonates, and not binary compounds such as amorphous NpO_2OH or crystalline NpO_2, as was assumed in modeling exercises (Wilson and Bruton, 1989). The neptunium species in solution were free neptunium(V) and neptunium(V) hydrolysis products at pH 6, with increasing amount of carbonate complexes forming at pH 7 and 8.5. Because of the much higher concentration of free carbonate, the UE-25p #1 solution at pH 8.5 contained no uncomplexed neptunium; all the neptunium was present in the form of hydrolysis products and carbonate complexes.

Plutonium

Results for plutonium steady-state concentrations are listed in Table 4. No clear trend of changing solubility with pH was observed. The solubility decreased significantly with increasing temperature. At corresponding pH values, plutonium solubility was slightly lower in J-13 water than in UE-25p #1 water except at pH 6 and 25°C, where the solubility was lower in UE-25p #1. The precipitates in both groundwaters had a dark green appearance, and they are mainly made from Pu(IV) polymer, which contains increasing amounts of carbonate with increasing pH. The predominance of Pu(IV) polymer explains why the plutonium solution concentrations are relatively unaffected by changes in groundwater composition and pH in the near-neutral region.

The plutonium oxidation state distribution was determined by a combination of solvent extractions and coprecipitation (Nitsche et al., 1988). The plutonium exists in both groundwaters predominantly as Pu(V) and Pu(VI), although it was initially added to the solutions as Pu(IV).

Americium

Steady-state solubility concentrations are listed in Table 5. The americium solubility difference between the two waters is significant. At 25 C°, the solubility in UE-

Table 3. Results for NpO_2^+ solubility experiments in J-13 and UE-25p #1 groundwaters at 25° and 60° C.

pH	Concentration (M)			
	J-13		UE-25p #1	
	25° C	60° C	25° C	60° C
6	$(5.3 \pm 0.3) \times 10^{-3}$	$(6.4 \pm 0.4) \times 10^{-3}$	$(2.9 \pm 0.6) \times 10^{-3}$	$(2.5 \pm 0.2) \times 10^{-3}$
7	$(1.3 \pm 0.2) \times 10^{-4}$	$(9.8 \pm 1.0) \times 10^{-4}$	$(4.7 \pm 1.1) \times 10^{-5}$	$(3.4 \pm 1.0) \times 10^{-5}$
8.5	$(4.4 \pm 0.7) \times 10^{-5}$	$(1.0 \pm 0.1) \times 10^{-4}$	$(7.0 \pm 0.6) \times 10^{-6}$	$(1.4 \pm 0.6) \times 10^{-5}$

Table 4. Results for Pu^{4+} solubility experiments in J-13 and UE-25p #1 groundwaters at 25° and 60° C.

pH	Concentration (M)			
	J-13		UE-25p #1	
	25° C	60° C	25° C	60° C
6	$(1.1 \pm 0.4) \times 10^{-6}$	$(2.7 \pm 1.1) \times 10^{-8}$	$(8.3 \pm 0.4) \times 10^{-7}$	$(8.9 \pm 1.4) \times 10^{-8}$
7	$(2.3 \pm 1.4) \times 10^{-7}$	$(3.7 \pm 0.9) \times 10^{-8}$	$(4.5 \pm 0.4) \times 10^{-7}$	$(9.1 \pm 1.2) \times 10^{-8}$
8.5	$(2.9 \pm 0.8) \times 10^{-7}$	$(1.2 \pm 0.1) \times 10^{-7}$	$(1.0 \pm 0.1) \times 10^{-6}$	$(9.3 \pm 6.0) \times 10^{-7}$

Table 5. Results for $Nd^{3+}/^{241}Am^{3+}$ solubility experiments in J-13 and UE-25p #1 groundwaters at 25° and 60° C.

pH	Concentration (M)			
	J-13		UE-25p #1	
		25° C	60° C	25° C 60° C
6	$(1.8 \pm 0.6) \times 10^{-9}$	$(2.5 \pm 0.7) \times 10^{-6}$	$(3.1 \pm 1.1) \times 10^{-7}$	$(2.7 \pm 0.4) \times 10^{-9}$
7	$(1.2 \pm 0.3) \times 10^{-9}$	$(9.9 \pm 9.2) \times 10^{-9}$	$(3.2 \pm 1.6) \times 10^{-7}$	$(7.1 \pm 0.5) \times 10^{-10}$
8.5	$(2.4 \pm 1.9) \times 10^{-9}$	$(1.2 \pm 1.3) \times 10^{-8}$	$(3.1 \pm 0.8) \times 10^{-6}$	$(7.8 \pm 4.3) \times 10^{-9}$

25p #1 water was about two to three orders of magnitude higher than in J-13 water. This trend was reversed for the 60 C° experiments, and not quite as pronounced for the pH 7 solutions. The solids in both waters are crystalline americium hydroxycarbonates, $AmOHCO_3$. We established that the trivalent americium did not change its oxidation state during the experiment.

CONCLUSION

Neptunium and americium showed different solubilities in J-13 groundwater compared with UE-25p #1 groundwater. Neptunium solubilities were lower and americium solubilities were higher in UE-25p #1 than in J-13 water. We believe these solubility effects result from the different carbonate contents of the waters. Plutonium solubilities did not significantly change with changing water composition. We are currently measuring the solubilities of these radionuclides in a noncomplexing sodium perchlorate electrolyte with ionic strengths and carbonate contents similar to those of J-13 and UE-25p #1 well waters. These experiments will help to establish whether the solubility changes are only due to the different carbonate contents of the waters or whether the other chemical groundwater components also influence the solubility significantly. We are also assembling a thermodynamic data set, including solubility product and complex equilibrium constants, that will allow us to compare our experimental results with modeling calculations. Agreement between the experimental results and the modeling calculations will validate the data base and the chemical module of the transport model.

ACKNOWLEDGMENTS

This work was prepared by Yucca Mountain Site Characterization Project (YMP) participants as part of the U.S. Civilian Radioactive Waste Management Program. The Yucca Mountain Site Characterization Project (YMP) is managed by the U.S. Department of Energy, Yucca Mountain Project. This work was performed at the Lawrence Berkeley Laboratory (LBL) for the Los Alamos National Laboratory (LANL). The Lawrence Berkeley Laboratory is operated by the University of California for the U.S. Department of Energy under Contract DE-AC-03-76SF00098. The Yucca Mountain Project Automated Technical Data Tracking Number is LA000000000033.001.

REFERENCES

Kerrisk, J.F., 1984. An assessment of the important radionuclides in nuclear waste. Report LA-10414-MS, Los Alamos National Laboratory, New Mexico.

Nitsche, H., Lee, S.C., and Gatti, R.C., 1988. Determination of plutonium oxidation states at trace levels pertinent to nuclear waste disposal. J. Radioanal. Nucl. Chem. v. 124, no. 1, p. 171–185.

Nitsche, H., 1991. Solubility studies of transuranium elements for nuclear waste disposal: Principles and overview. Radiochim. Acta, v. 52, no. 53, p. 3–8.

U.S. DOE, 1988. Nuclear Waste Policy Act (Section 113), Site characterization plan, Yucca Mountain Site, Nevada Research and Development Area, Nevada. U.S. Department of Energy, Office of Civilian Radioactive Waste Management, Washington, D.C.

Ogard, A.E., and Kerrisk, J.F., 1984. Groundwater chemistry along the flow path between a proposed repository site and the accessible environment. Report LA-10188-MS, Los Alamos National Laboratory, New Mexico.

Wilson, C.N., and Bruton, C.J., 1989. Studies on spent fuel dissolution behavior under Yucca Mountain Repository Conditions. Report PNL-SA-16832 (or UCRL-10023), Pacific Northwest Laboratory, Richland, Washington.

Vibrational Studies of Toxic Heavy-Metal-Organic Co-Contaminant Systems

D. L. Perry, L. A. Feliu, and J. A. Centeno†*

Much attention in recent years has been focused on heavy metals and organic compounds that are found at toxic waste sites on Departments of Energy and Defense reservations. The heavy metals that are found at these sites range from transition metals such as chromium, nickel, and cobalt to radioactive uranium, thorium, and plutonium. In addition to the heavy metals, many of the waste sites also contain hazardous organic compounds ranging from unsubstituted hydrocarbons to chlorinated solvents and aromatic hydrocarbons.

In the present study, work was conducted on the vibrational studies of the heavy-metal-organic complex bis(2,2′-bipyridyl) copper(II) nitrate hydrate, the central coordination sphere being shown in Figure 1. This molecule was chosen for study because it contains several chemical aspects of interest in the field of co-contaminant waste chemistry. First, the central metal ion is copper, a heavy metal that is present in some Department of Energy waste sites. Second, the nitrate counterion is present in huge quantities at one of the waste sites due to the dumping of thousands of gallons of concentrated nitric acid. Third, the 2,2′-bipyridine is actually a dimer of pyridine, an organic found in some of the toxic waste mixtures.

The complex pictured in Figure 1 consists of a central coordination sphere in which the two bidentate 2,2′-bipyridine molecules are attached to the central copper(II) ion; additionally, one of the nitrate oxygen atoms is definitely coordinated to the copper atom, whereas the other oxygen atom in the "bidentate" nitrate group is at a greater bond distance from the copper than is the first oxygen atom. The vibrational study of a structurally documented species such as the one discussed here is important, since it provides one more experimental approach for the identification, analysis, and monitoring of the complex in the remediation of such toxic compounds from the environment.

Figure 2 illustrates the vibrational Raman spectrum of bis(2,2′-bipyridyl) copper(II) nitrate hydrate, along with that of the uncomplexed 2,2′-bipyridine itself. Although infrared studies have been conducted (Inskeep, 1962; Sinha, 1964) on this co-contaminant pair, none has been reported for Raman spectroscopy. The Raman spectrum of the free 2,2′-bipyridine molecule exhibits vibrational bands at 1592, 1575, 1485, and 1449 cm^{-1}. The first two peaks are due to the ring stretching of the pyridine; those at 1485 and 1449 cm^{-1} can be assigned to carbon-hydrogen ring bending modes. These four lines undergo quite marked intensity changes upon complexation with the copper(II)

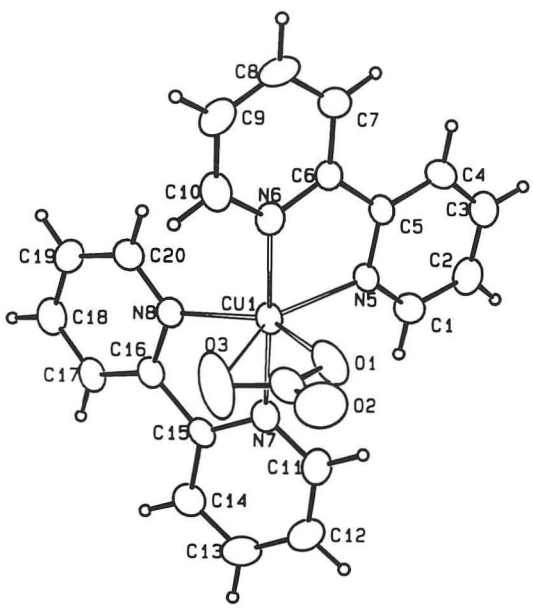

Figure 1. The central coordination sphere of the complex $[Cu(bipy)_2NO_3]^+$ NOS(–,3) · H_2O. The bipy molecule in the formula refers to 2,2′-bipyridine. [XBL 921-107]

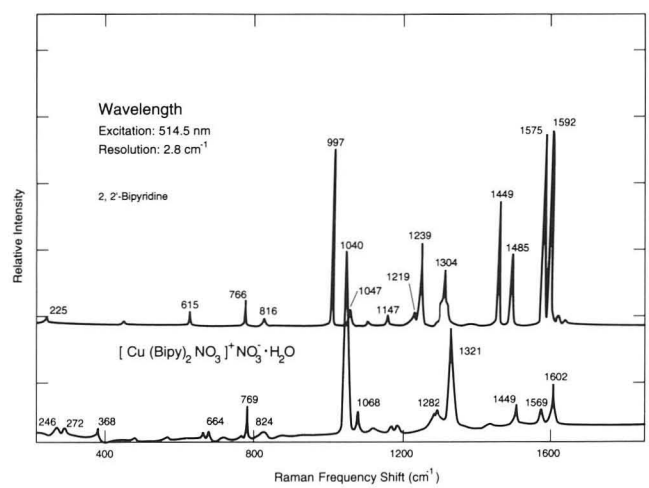

Figure 2. The Raman spectrum of $[Cu(bipy)_2\ BI_3]^+$ NOS(–,3) · H_2O. [XBL 922-4647]

* AGM University System, Rio Piedras, PR 00928,

†Armed Forces Institute of Pathology, Department of the Army, Washington, D.C. 20306.

nitrate. The pyridyl bending motion at 997 cm^{-1} shifts to a higher 1040 cm^{-1} frequency upon binding to the copper, presumably due to the donation of electrons from the nitrogen atoms to the copper(II) ion. The band at 1282 cm^{-1} in the spectrum of the complex is in good agreement with its assignment of a bidentate nitrate anion in other complexes; the bands at 1282 and 1321 cm^{-1} also can be attributed to the coordinated nitrate anion. The complex bands at 246 and 272 cm^{-1} may be tentatively assigned to metal-nitrogen stretches; these two bands, along with the one at 368 cm^{-1}, are also in the range previously assigned to metal-oxygen stretching frequencies in metal nitrates.

REFERENCES

Inskeep, R.G., 1962. Metal complexes of 2,2′-bipyridine. J. Inorg. Nucl. Chem., v. 24, p. 763–776.

Sinha, S.P., 1964. Vibrational studies of transition metal ion complexes of 2,2′-bipyridine. Spectrochim. Acta, v. 20, p. 879–886.

Thermodynamics of Thorium Chloride in Aqueous Acidic Solution

K. S. Pitzer, A. R. Felmy, and R. N. Roy†*

Thorium is an important element in various geological and practical processes; in addition, it is of theoretical interest as a quadruply charged, simple aqueous ion. This investigation involved a three-centered collaboration involving experimental measurements with electrochemical cells of solutions of a mixed $ThCl_4$-HCl solution at Drury College, together with theory and calculations at both Battelle Northwest and Lawrence Berkeley Laboratory.

The general pattern of this investigation followed that of earlier work on similar systems with singly, doubly, and triply charged ions. Examples are studies on KCl-HCl by Macaskill and Bates (1978), on $BaCl_2$-HCl by Roy et al. (1990), and on $LaCl_3$-HCl by Roy et al. (1983). The study on $ThCl_4$ was more complex because of the stronger tendency of the Th^{4+} ion to hydrolyze or to form chloride complexes as compared with La^{3+} or ions of still smaller charge. Indeed, the very recent work of Felmy et al. (1991) on the solubility of $Th(OH)_4$ in chloride solutions of defined pH was critical for the interpretation of the new results.

The experiments were measurements of the potential of the cell

$$Pt, H_2(g) | HCl(m_A), ThCl_4(m_B) | AgCl, Ag,$$

which yields the activity of HCl by the Nernst equation

$$E = E^\circ - (RT/F) \ln a_{HCl}$$

and the activity coefficient by the relationship

$$a_{HCl} = \gamma_A^2 (m_A)(m_A + 4m_B) .$$

The results, which are being published in detail by Roy et al. (submitted), cover the range 0.006 to 3.0 $mol \cdot kg^{-1}$ in ionic strength I, 0.0 to 0.9 in ionic strength fraction y_B of $ThCl_4$, and 5 to 55°C in temperature.

Two treatments are given of the results. The first is that of Harned equation

$$\log \gamma_A = \log \gamma_A^\circ - \alpha_{AB} y_B - \beta_{AB} y_B^2 ,$$

where $\gamma S(\circ,A)$ is the activity coefficient of pure HCl and α_{AB} and β_{AB} are Harned parameters. For electrolytes with only singly charged ions, β_{AB} is usually not needed and α_{AB} is small. As the ion charge increases, both parameters are needed and they increase in magnitude. For the present system, satisfactory fits are obtained for ionic strengths up to I = 2.0, but at 3.0 the Harned equation is clearly inadequate for the full range of y_B. However, by excluding the single point at y_B = 0.9, I = 3.0, a satisfactory fit was obtained. The interpretation of this situation is given below.

The second theoretical treatment is that with the ion-interaction equations (Pitzer, 1975, 1991). The complete equation for ln γ_A is

* Battelle Northwest Laboratories, Richland, Washington 99352.

† Department of Chemistry, Drury College, Springfield, Missouri 65802.

$$\ln \gamma_A = -A_\phi \left[\frac{I^{1/2}}{1+bI^{1/2}} + \frac{2}{b} \ln\left(1+bI^{1/2}\right) \right]$$

$$+ I\left\{ \left(2 - \frac{8}{5}y\right)\left[\beta^{(0)}_{HCl} + \beta^{(1)}_{HCl}\, g\left(\alpha_1 I^{1/2}\right)\right] \right.$$

$$+ \frac{1}{10}y\left[\beta^{(0)}_{ThCl} + {}^{s}\theta_{Th,H} + {}^{E}\theta_{4,1}(I) \right.$$

$$\left. + \beta^{(1)}_{ThCl} \exp\left(-\alpha_1 I^{1/2}\right) + \beta^{(2)}_{ThCl} \exp\left(-\alpha_2 I^{1/2}\right)\right]$$

$$+ (1-y)\left(1 - \frac{3}{5}y\right)\beta^{(1)}_{HCl} g'\left(\alpha_1 I^{1/2}\right)$$

$$\left. + \frac{3}{50}y^2\left[\beta^{(1)}_{ThCl} g'\left(\alpha_1 I^{1/2}\right) + \beta^{(2)}_{ThCl}\, g'\left(\alpha_2 I^{1/2}\right)\right]\right\}$$

$$+ I^2\left\{ \left(3 - \frac{13}{5}y\right)\left(1 - \frac{3}{5}y\right) C_{HCl} \right.$$

$$+ \frac{1}{10}y\left[2\left(1 - \frac{3}{5}y\right) C_{ThCl} \right.$$

$$\left.\left. + \left(1 - \frac{4}{5}y\right)\psi_{Th,H,Cl} + (1-y)\, {}^{E}\theta'_{4,1}(I)\right]\right\},$$

with

$$g(x) = 2\left[1 - (1+x)\exp(-x)\right]/x^2\,,$$

$$g'(x) = -2\left[1 - (1 + x + x^2/2)\exp(-x)\right]/x^2\,.$$

Four types of parameters are included. The first term involves the Debye-Hückel effect, which applies to all ionic systems. Next are the parameters $\beta^{(0)}_{HCl}$, $\beta^{(1)}_{HCl}$, and C_{HCl}, which relate to pure HCl and are well known. Third are the corresponding parameters for pure $ThCl_4$, which come primarily from Felmy et al. (1991) but were refined in the present calculation. Finally, there are the Th^{4+}-H^+ mixing parameters of two types. First are those for long-range electrostatic forces ${}^{E}\theta_{4,1}$ and ${}^{E}\theta'_{4,1}$ for +4, +1 mixing, whose values are known theoretically (Pitzer, 1975), whereas $\theta_{Th,H}$ and $\psi_{Th,H,Cl}$ relate to short-range interactions and are evaluated empirically from the present data and recent measurements of Felmy and Rai (1992). Table 1 gives for 25°C all of the parameters specific to HCl, to $ThCl_4$, and to Th^{4+}-H^+ mixing. Pitzer (1991) gives values of the general parameters and other details.

Although the ion-interaction equation contains many parameters, all were known in advance, at least approximately, from other systems for 25°C. Some adjustments in thallium parameters were required, after which good agreement was obtained with all of the present data except for the same one point at $I = 3.0$, $y_B = 0.9$, which deviated from the Harned equation treatment. That one point deviated from the ion-interaction equation by 6.4 mV, whereas the average deviation for the other 79 points was only 0.6 mV. The presently reported data are more precise than earlier results for thallium systems and yield parameters of much higher accuracy.

Table 2 compares the accuracy of fit σ and the magnitude of certain mixing terms for otherwise similar systems of different cation charge. Note the very rapid increase in ${}^{E}\theta$, the theoretical electrostatic term for unsymmetrical mixing. The three-particle mixing term ψ is much smaller but also increases rapidly with increase in charge. Although the standard deviation of fit also increases significantly with charge, it is still quite satisfactory for the 4-1 case.

It remains, finally, to discuss the cause of the deviation at $I = 3.0$, $y_B = 0.9$. Here the observed value of E is higher than that calculated, which indicates a lower than expected activity of HCl. This decrease in HCl activity must arise from chloride complexation effects in addition to the effect implied by the $\beta^{(2)}_{ThCl}$ term, which concerns the formation of the species $ThCl^{+3}$. If this additional complexation appears suddenly at high I, it must involve a large number of chloride ions. Thus $ThCl_6^{2-}$ is a prime candidate; it is known in solids such as K_2ThCl_6, but there is little independent evidence of its occurrence in solution. The aqueous species $ThCl_4$ has been reported, however. The conversion of about 13% of the thorium to $ThCl_6^{2-}$ would account for the deviation in E at I = 3, y_B = 0.9. If $ThCl_4$ were the species formed, about 20% conversion would be needed. Moreover, there is information about $Th_2(OH)_2Cl_2^{4+}$, but such hydrolyzed species would not

Table 1. Ion-interaction equation parameters.

	H,Cl	Th,Cl
$\beta^{(0)}$/kg·mol^{-1}	0.1775	1.092
$\beta^{(1)}$/kg·mol^{-1}	0.2945	13.7
$\beta^{(2)}$/kg·mol^{-1}	—	–160.
C^{ϕ}/kg^2·mol^{-2}	0.0008	–0.112

$C_{HCl} = C^{\phi}_{HCl}/2$, $C_{ThCl} = C^{\phi}_{ThCl}/4$

${}^{S}\theta_{Th,H} = 0.60$, $\psi_{Th,H,Cl} = 0.37$

Table 2. Comparison of MCl_n–HCl–H_2O systems for various charges on M^{n+} at 25°C.

System	θ or $^{S}\theta$	$^{E}\theta$ (I = 1.0)	ψ	σ/mV
KCl-HCl	-0.009_6	—	—	0.20
$BaCl_2$-HCl	0.069	0.145	0.002	0.44
$LaCl_3$-HCl	0.278	0.87	0.009	0.41
$ThCl_4$-HCl	0.60	2.63	0.37	0.64

explain the present results, since their formation would produce additional H^+ and increase, not decrease, the activity of HCl.

In summary, by bringing together results from several separate investigations, a satisfactory ion-interaction-equation treatment was obtained for the very demanding system $ThCl_4$-HCl over almost all of its composition range.

REFERENCES

Felmy, A.R., and Rai, D.J., 1992. An aqueous thermodynamic model for a high valence 4:2 electrolyte Th^{4+}-SO_4^{2-} in the system Na^+-K^+-Li^+-NH_4^+-Th^{4+}-SO_4^{2-}-HSO_4^--H_2O to high concentration. J. Solution Chem., v. 2l, p. 407–423.

Felmy, A.R., Rai, D., and Mason, M.J., 1991. The solubility of hydrous thorium(IV) oxide in chloride media: Development of an aqueous ion-interaction model. Radiochimica Acta, v. 55, p. l77–185.

Macaskill, J.B., and Bates, R.G., 1978. Activity coefficient of hydrochloric acid in the system HCl-KCl-H_2O at 25°C and ionic strengths from 0.1 to 3 moles-kg^{-1}. J. Solution Chem., v. 7, p. 433–442.

Pitzer, K.S., 1975. Thermodynamics of electrolytes. V. Effects of higher order electrostatic terms. J. Solution Chem., v. 4, p. 249–265.

Pitzer, K.S., 1991. Ion interaction approach: Theory and data correlation. *In* K.S. Pitzer (ed.), Activity Coefficients in Electrolyte Solutions, 2nd edition (CRC Press: Boca Raton, FL), Chapter 3, p. 75–153.

Roy, R.N., Gibbons, J.J., Peiper, J.C., and Pitzer, K.S., 1983. Thermodynamics of the unsymmetrical mixed electrolyte HCl-$LaCl_3$. J. Phys. Chem., v. 87, p. 2365–2369.

Roy, R.N., Rice, S.A., Vogel, K.M., Roy, L.N., and Millero, F.J., 1990. Activity coefficients for HCl + $BaCl_2$ + H_2O at different temperatures and effects of higher order electrostatic terms. J. Phys. Chem., v. 94, p. 7706–7710.

Application of Airborne Gamma Spectrometric Survey Data to Estimating Terrestrial Gamma-Ray Dose Rates: An Example in California

H. A. Wollenberg, K. L. Revzan, and A. R. Smith†*

The terrestrial component of the natural gamma environmental radiation depends on the abundance of U and Th, their decay products, and ^{40}K in rock and soil. An extensive database that may be used to determine these abundances over broad regions was developed by the U.S. Department of Energy's National Aerial Radiometric Reconnaissance (NARR) for uranium resources, conducted by gamma spectrometric surveys from helicopter and fixed-wing aircraft in the 1970s and early 1980s. In these surveys, flight lines were spaced ~ 5 km apart; flight altitude was ~ 125 m above the ground surface. Uranium concentrations were calculated from ^{214}Bi radioactivity and Th from ^{208}Tl radioactivity, assuming radioactive equilibrium in the U and Th decay series; K concentrations were calculated from ^{40}K radioactivity. In this article we test the efficacy of these data for estimating terrestrial gamma-ray dose rates (expressed in nanoGrays per hour (nGy/h)) by comparing dose rates calculated from aeroradiometric surveys with dose rates calculated from a radiogeologic database and lithologic information covering California. (These terrestrially derived dose rates are superimposed on a background from cosmic radiation of ~ 3 nGy/h at sea level, which approximately doubles with every 1500-m increase in altitude.)

The geology of California is varied enough so that most of the lithologies of the continents are represented, including those of bedrock areas in mountains and upland

* Energy and Environment Division, Lawrence Berkeley Laboratory.

† Engineering Division, Lawrence Berkeley Laboratory.

regions and those of large alluvial-filled basins. In this regard, we are fortunate in having an extensive database on radioelement concentrations of California rocks and soils to compare with radioelement concentrations measured by the NARR aeroradiometric surveys.

COMPILATION AND RESULTS

We compare the geographic distribution of gamma-ray absorbed dose rates of soils and rocks of California with their lithologic settings. The aeroradiometric data (Revzan, 1988) and the database at Lawrence Berkeley Laboratory on U, Th, and K concentrations (Table 1) provided dose rates when the equations of Beck and dePlanque (1968) were applied to the radioelement data. These equations were used to calculate gamma-ray absorbed dose rates in air, at a height of 1 m above ground surface, for uniformly distributed sources in a homogeneous semi-infinite medium. The dose rates were applied to the fractions of total area occupied by specific lithologic units as initially

Table 1. Average radioelement concentrations and gamma dose rates in major lithologic units.

Description (number of entries)	U (ppm)	Th (ppm)	K (%)	Dose rate (nGy h^{-1})
Quaternary and Tertiary sediments, southern Sacramento Valley (16)	2.2	5.7	1.1	43
Quaternary sediments, northern San Joaquin Valley (12)	2.5	10.2	1.4	61
Soils, east side San Joaquin Valley (8)	2.2	10.1	2.7	78
Soils, San Francisco Bay Area (27)	1.9	5.8	1.4	50
Tertiary volcanic and sedimentary rocks, Berkeley Hills (6)	1.3	4.6	0.9	35
Tertiary volcanic rocks north of San Francisco Bay (10)	3.7	8.1	1.5	64
Tertiary marine sedimentary rocks, central and south coast (6)	3.1	5.2	1.2	54
Eocene sedimentary rocks bordering the Great Valley (46)	3.7	13.1	0.7	66
Predominantly sandstone of the Great Valley series (20)	1.1	3.5	0.9	47
Graywacke of the Franciscan Formation and its Coastal Belt (81)	2.1	7.2	1.4	51
Granitic rocks of Central Coast Ranges (63)	2.5	9.3	2.2	86
Mesozoic sedimentary and volcanic rocks of Sierra Nevada foothills (15)	1.5	5.2	1.1	38
Paleozoic sedimentary and volcanic rocks of Sierra Nevada foothills (19)	1.3	4.5	0.96	33
Mesozoic pendants of Sierra Nevada (7)	2.9	8.1	2.2	69
Paleozoic pendants of Sierra Nevada (20)	3.5	5.1	1.2	51
Paleozoic rocks, Inyo and White Mts. (39)	2.1	8.2	1.4	54
Precambrian of Death Valley area (10)	1.9	8.9	1.8	61
Ultrabasic rocks of the Sierra Nevada, Klamath Mts., and Coast Ranges (26)	0.11	0.07	0.001	0.8
Basic intrusive rocks, Klamath Mts. (26)	0.26	0.64	0.19	5.9
Basic intrusive rocks of northern Sierra Nevada (12)	0.18	0.34	0.31	6.3
Cretaceous plutons of central Sierra Nevada (169)	5.6	19.6	3.2	160
Jurassic or Cretaceous plutons of central Sierra Nevada (91)	3.4	12.8	1.95	92
Triassic or Jurassic plutons of eastern Sierra Nevada (10)	4.3	18.6	3.8	128
Plutons of western Sierra Nevada (25)	1.3	3.7	1.3	41
Rhyolite of eastern Sierra Nevada (12)	5.4	16.4	3.7	127
Rhyolite (general) (124)	5.7	22.4	3.7	150
Andesite (general) (57)	2.1	6.7	2	56
Basalt (general) (77)	0.9	2.5	0.7	22
Plutonic rocks of Southern California batholith (39)	2.3	7.9	1.7	67
Plutonic rocks, southeastern California (18)	2.7	10.6	2.1	84
Precambrian metamorphic rocks of southeastern California (43)	4.6	15.5	2.5	118

estimated from the 1:2,500,000-scale geologic map of California (CDMG, USGS 1966) in $1 \times 2°$ quadrangles covering the state. Larger-scale (1:250,000) geologic maps of individual $1 \times 2°$ quadrangles published by the California Division of Mines and Geology provided more detail, as did printouts of the NARR data, which indicate the rock types and corresponding radioelement concentrations under segments of the flight lines. (*Note:* An appendix containing estimates of percentages of rock types and of lithologically weighted absorbed dose rates in each of the $1 \times 2°$ quadrangles, along with references for Table 1, may be obtained by contacting the authors.) The aeroradiometrically and lithologically determined dose rates are compared, and their geographic distribution is shown in Figure 1.

DISCUSSION

A general north-to-south increase in terrestrial gamma-ray dose rates is evident between 42° and 36°N, but dose rates remain generally high farther to the south (Figure 1). This pattern is explained primarily by (1) the preponderance of basalt in northeastern California and the relatively large abundance of basic to ultrabasic intrusive rocks, generally low in radioelements, that make up the bedrock and soils of northwestern California; (2) the predominance in north-central and central California of clastic sedimentary rocks and basic volcanics of the Franciscan Formation in the Coast Ranges and metamorphic rocks of the northern Sierra Nevada, all of intermediate radioactivity; (3) an increasing contribution to central and south-central California soils by higher-radioactivity rocks of the Sierra Nevada batholith, whose exposure begins at about 40°N and increases to the south, and by Tertiary marine sedimentary rocks, intermediate to acidic volcanic rocks, and Mesozoic granitic plutons of the central Coast Ranges; and (4) the preponderance, south of 36°N, of relatively high-radioactivity granitic rocks of the southern Sierra Nevada, Transverse Ranges, and Southern California

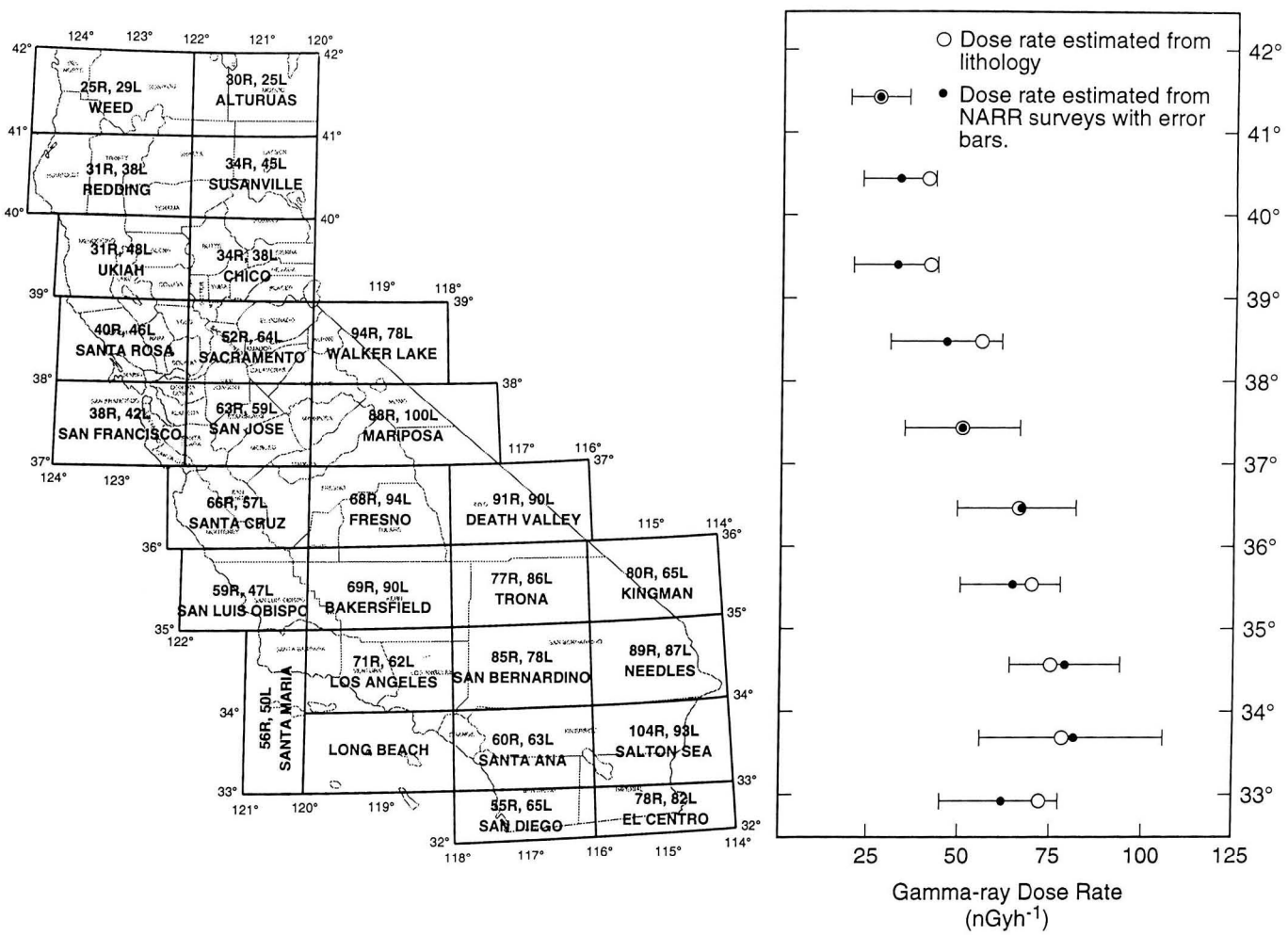

Figure 1. **(Left)** Terrestrial gamma dose rates (in nGy h^{-1}) from NARR data (R) and lithologic estimates (L) in California quadrangles. Lithologic estimates in Walker Lake and Kingman quadrangles are for California portions only. **(Right)** Plots of data at left in a band 4° of longitude in width along the Pacific coast. [XBL 933-358]

batholith, and Precambrian and pre-Cenozoic metamorphic and plutonic rocks of southeastern California.

The trend in mean dose rates estimated lithologically matches that from aeroradiometric data. In most cases, there is good agreement in individual quadrangles between lithologically weighted and aeroradiometrically determined dose rates (Table 2). Exceptions to this are the Ukiah, Fresno, and Bakersfield quadrangles, where lithologically weighted dose rates are 30 to 40% greater than those from aeroradiometric surveys. In the Ukiah quadrangle, rocks of the Franciscan Formation and its coastal belt predominate, and their radioelement concentrations were assumed to be representative of graywacke, the predominant rock type in the Franciscan of the north Coast Ranges, with a dose rate of 51 nGy/h. However, the Franciscan rocks also contain a significant proportion of chert and metabasalt, both of lower radioelement concentration than the graywacke, thus perhaps causing the lower radioelement concentrations measured by the aeroradiometric surveys. Franciscan rocks also make up a large proportion of the bedrock of the neighboring Santa Rosa quadrangle, but the discrepancy between lithologically and aeroradiometrically based dose rates is not as great there as in the Ukiah quadrangle. In the Bakersfield and Fresno quadrangles, alluvium of the San Joaquin Valley makes up a large portion of the surface area, 50 and 35%, respectively. The dose rates associated with the alluvium, 85 to 90 nGy/h, were calculated from the weighted composite of dose rates of the rocks bordering the San Joaquin Valley, which have relatively high radioelement concentrations. The actual radioelement concentrations of the alluvium in the Fresno and Bakersfield quadrangles might be more similar to those measured in Quaternary sediments of the northern San Joaquin Valley, whose associated dose rate is 61 nGy/h. If this were the case, the lithologically based dose rates would be more in keeping with those from aeroradiometric data. We also note that the aeroradiometric flight lines over the alluvium in the San Joaquin Valley covered extensive areas of irrigated soil, where near-surface moisture contents were high, causing lower apparent radioelement concentrations than those estimated from lithologic data, where moisture content was not considered. In general, this effect of the presence of soil moisture may account for the elevated y-intercept (~ 9 nGy/h) of the regression line relating aeroradiometrically and lithologically based dose rates in Figure 2.

All told, however, in the other quadrangles and throughout California, mean dose rates determined by lithology or aeroradiometric surveys are similar (Figure 2), with statewide means of 63 and 60 nGy/h, respectively. As shown in Table 2, these are somewhat higher than a population-weighted global average of 51 nGy/h, but well within the range of 37 to 94 nGy/h reported by the United Nations Scientific Committee on the Effects of Atomic Radiation (UNSCEAR 1982) and a mean of 46 nGy/h for non-coastal plain regions of the United States, reported by Oakley and Moeller (1972). The latter value was substantiated by a compilation of aeroradiometric data from 65 reactor sites surveyed by the Aerial Measurements Operations of EG&G (Wollenberg and Smith 1984). The aeroradiometrically and lithologically weighted California means are similar to the weighted continental average based on the global distribution of rock types, 70 nGy/h, reported by Wollenberg and Smith (1990). This similarity reflects the abundance of bedrock exposure in California and the predominance of bedrock lithologies in the composition of California soils, in contrast to mid-continental regions of less varied terrain and more widespread and deep

Table 2. Comparison of terrestrial gamma-ray dose rates.

Description	Dose rate (nGy/hr)	Source
Population-weighted global average	51 (range 37 to 94)	UNSCEAR, 1982
Non-coastal plain regions of U.S. (1972)	46 (range 13 to 100)	Oakley and Moeller
65 reactor sites in U.S.	46 (s.d. 18)	Wollenberg and Smith (1984)
Continental average, weighted by lithology	70	Wollenberg and Smith (1990)
California, airborne surveys	60 (s.d. 22)	This report
California, lithologic estimates	63 (s.d. 22	This report

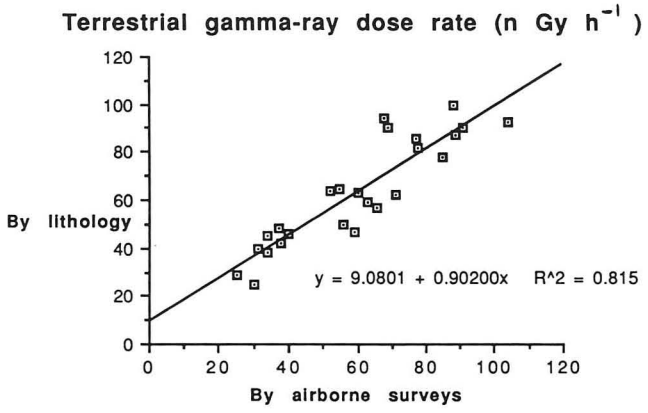

Figure 2. Comparison of terrestrial gamma-ray dose rates in California 1 × 2° quadrangles, estimated from lithology and measured by aeroradiometric surveys. [XBL 933-359]

development of soils, which are generally lower in radioelements than their bedrock predecessors.

CONCLUSIONS

Though standard deviations of mean gamma-ray dose rates are large, and outcrop-area percentages are estimated, it is clear that the north-to-south regional variation of dose rates in California is attributable to lithology. The general concurrence of lithologically and aeroradiometrically determined dose rates in California, with its varied terrain and geology, indicates that the NARR aeroradiometric data make sense geologically and are therefore quite applicable to estimates of terrestrial dose rates from natural gamma emitters.

ACKNOWLEDGMENT

We thank Joseph Duval, U.S. Geological Survey, for providing the most recent compilation of aeroradiometric data for the Ukiah quadrangle.

REFERENCES

Beck, H., and dePlanque, G., 1968. The radiation field in air due to distributed gamma-ray sources in the ground. U.S. Atomic Energy Commission, Health and Safety Laboratory Report HASL-195.

CDMG/USGS, 1966. Geologic Map of California, compiled by the U.S. Geological Survey and the California Division of Mines and Geology.

Oakley, D.T., and Moeller, D.W., 1972. Estimate of terrestrial radiation exposure based on aerial surveys, *In* J.A.S. Adams, W.M. Lowder, and T.F. Gesell (eds.), The Natural Radiation Environment II. U.S.E.R.D.A. Conf. 72805-P2, p. 441–456.

Revzan, K.L., 1988. Supplemental information on the National Aerial Radiometric Reconnaissance (NARR) database. Lawrence Berkeley Laboratory Report LBID-1453.

UNSCEAR, 1982. Ionizing radiation, 1982: Sources and biological effects. United Nations Scientific Committee on the Effects of Atomic Radiation Report to the General Assembly. New York, United Nations.

Wollenberg, H.A., and Smith, A.R., 1984. Naturally occurring radioelements and terrestrial gamma-ray exposure rates: An assessment based on recent geochemical data. Lawrence Berkeley Laboratory Report LBL-18714.

Wollenberg, H.A., and Smith, A.R., 1990. A geochemical assessment of terrestrial gamma-ray absorbed dose rates. Health Phys., v. 58, p. 183–189.

Thermal Effects on Water Exclusion from a Cavity in Unsaturated Tuff

W. Zhou, P. L. Chambré, T. H. Pigford, and W. W.-L. Lee

For an unsaturated, fractured porous medium subject to uniform infiltration, we analyze thermal effects on water exclusion from cavities. This is of practical interest in a nuclear waste repository. A crucial question is: How much infiltration will cause the heated tunnel walls to become saturated, so that water can enter a cavity?

Water exclusion from cavities in unsaturated rock was analyzed by Philip et al. (1989). We extend the analysis to include thermal effects. The Darcy velocity with temperature-corrected hydraulic conductivity is (see inset of Figure 1)

$$\mathbf{v} = -K(\psi)f(T)(\nabla\psi - \mathbf{e_z}), \tag{1}$$

where $\mathbf{v}$ is Darcy velocity, $K(\psi)$ is hydraulic conductivity, ψ is moisture potential ($-\infty < \psi \leq 0$), T is temperature, ∇ is the gradient operator, and $\mathbf{e_z}$ is the unit vector in the z direction.

The analysis is applicable when the temperature near the cavity is below boiling but above the ambient temperature. The thermal field is calculated using conduction only, and is independent of flow, whereas the flow is influenced by the thermal field (Eq. 1). The dimensionless function of temperature modifying the hydraulic conductivity $f(T)$ is assumed to be

$$f(T) = e^{b(T-T_0)}, \tag{2}$$

where b is an experimentally determined constant [1/K] and T_0 is the ambient temperature; b can be positive or negative.

The steady-state flow continuity equation about a cylindrical cavity is solved together with boundary conditions to determine the moisture potential distribution near the cavity (Zhou, 1992). The ambient moisture potential is ψ_0, and for water exclusion the Darcy velocity at the cavity-rock interface is zero. Given the infiltration rate, material properties, and cavity size, there are three possible cases. Assuming that ψ_w is the moisture potential at the cavity interface, then

1. $\psi_w < 0$, the cavity surface is undersaturated and water is excluded from the cavity.
2. $\psi_w = 0$, the cavity surface is saturated and water is ready to flow into the cavity.
3. $\psi_w > 0$, the boundary condition of zero velocity at the cavity surface is violated, since the moisture potential ψ cannot be greater than zero. Thus the normal velocity component at the cavity surface is not zero: water enters the cavity.

We study the critical case ($\psi_w = 0$) and apply the model to Topopah Springs welded tuff (the potential repository medium at Yucca Mountain, Nevada) using material properties from Barnard and Dockery (1991). Figure 1 shows the combination of cavity size, dimensionless temperature difference, and infiltration rate that will lead to the critical condition at the cavity apex A (see inset, Figure 1 for diagram). The dimensionless temperature difference is $\Delta\tau = b\,(T_w - T_0)$, where T_w is the temperature at the cavity surface. An effective continuum is used in the calculation (Pruess et al., 1988). The general declining pattern of the curves indicates that the critical infiltration rate decreases with an increasing cavity radius. The temperature effect is that if $f(T)$ increases with T ($b > 0$), water flows more easily in the unsaturated rock around the cavity, requiring more infiltrated liquid to saturate the interface.

Figure 2 shows the combination of cavity size, dimensionless temperature difference, and infiltration rate that will lead to the critical condition at the cavity apex; this calculation considers the tuff *matrix* only. Here the large projection area of the cavity intercepts large amounts of infiltration, requiring a lesser critical infiltration rate to saturate the cavity apex. This figure shows that in the tight tuff matrix, water can only enter into very big cavities. In contrast to Figure 2, Figure 1 shows the critical infiltration rates vs. cavity radii for an effective continuum tuff where the presence of fractures makes it easy for water to enter a cavity. Therefore, the cavity radii corresponding to the critical infiltration rates are much smaller than those shown in Figure 2.

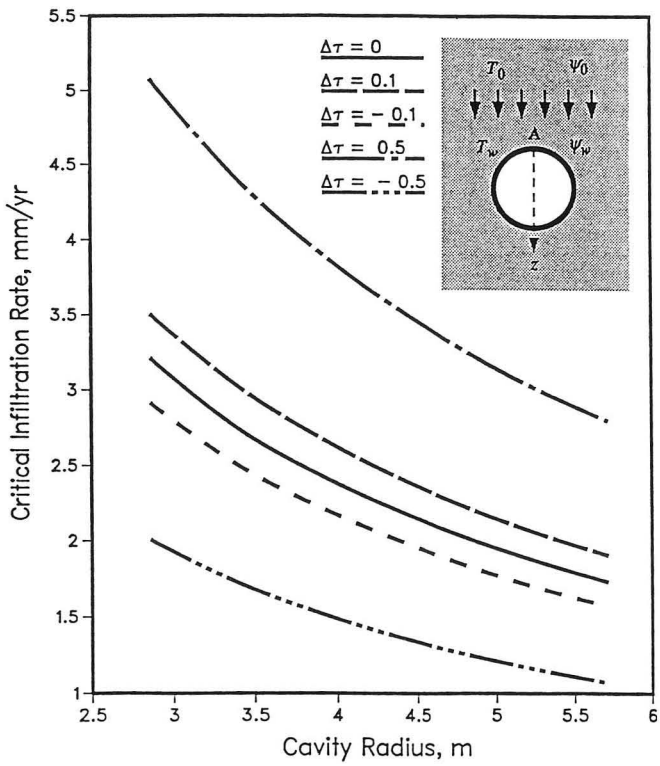

Figure 1. Critical infiltration rate as a function of cavity radius for different values of the dimensionless temperature difference $\Delta\tau = b(T_w - T_0)$ for fracture flow in effective continuum tuff (material properties from Peters et al., 1984). [XBL 933-360]

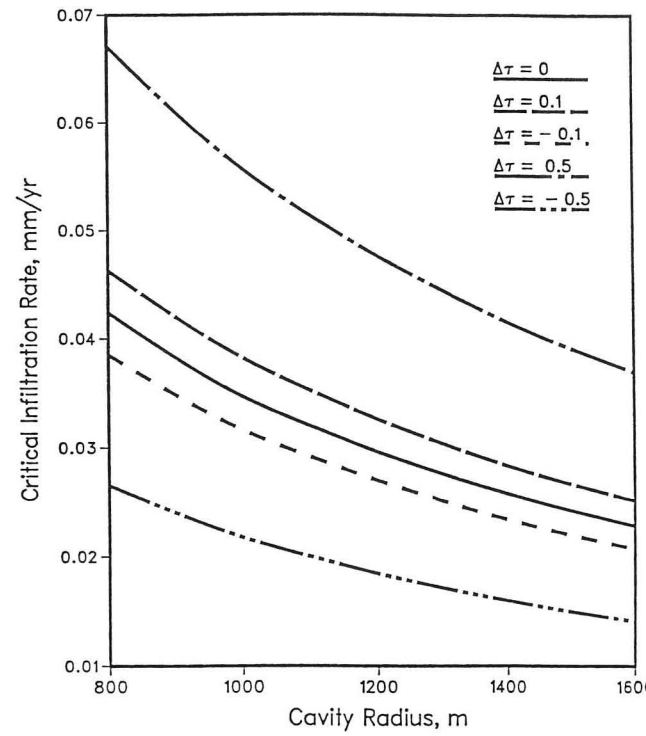

Figure 2. Critical infiltration rate as a function of cavity radius for different values of the dimensionless temperature difference $\Delta\tau = b(T_w - T_0)$ for a medium consisting of tuff matrix only and neglecting fractures (material properties from Peters et al., 1984). [XBL 933-361]

REFERENCES

Barnard, R.W., and Dockery, H.A., (eds.), 1991. Technical summaries of the performance assessment calculational exercises for 1990 (PACE-90), Volume 1: "Nominal Configuration" Hydrogeologic Parameters and Calculational Results, Sandia National Laboratories Report SAND90-2726.

Peters, R.R., Klavetter, R.R., Hall, I.J., Blair, S.C., Heller, P.R., and Gee, G.W., 1984. Fracture and matrix hydrologic characteristics of tuffaceous materials from Yucca Mountain, Nye County, Nevada, Sandia National Laboratories Report SAND84-1471.

Philip, J.R., Knight, J.H., and Waechter, R.T., 1989. Unsaturated seepage and subterranean holes: Conspectus, and exclusion problem for circular cylindrical cavities. Water Resour. Res. v. 25, no. 1, p. 16–28.

Pruess, K., Wang, J.S., and Tsang, Y.W., 1988. Effective continuum approximation for modeling fluid and heat flow in fractured porous tuff. Sandia National Laboratories Report SAND86-7000.

Zhou, W., 1992. Mass transfer induced by thermal effects in unsaturated porous media (Ph.D. thesis), University of California at Berkeley, 1992.

GEOPHYSICS AND GEOMECHANICS

The Geophysics and Geomechanics group conducts basic and applied research relevant to the nation's energy development programs and helps train the next generation of scientists and engineers in the geosciences. The research utilizes unique facilities at Lawrence Berkeley Laboratory and is directed toward the solution of problems related to the disposal of nuclear and toxic wastes, the exploration for and recovery of fossil fuels, the definition of fundamental properties and processes in the earth's crust, and the development of geothermal energy. The aim is to address not only today's needs but also needs that will arise from the ever-increasing pressures placed upon the earth's resources. The group has focused, and will continue to focus, on a collaborative approach, not only between geophysical and geomechanical disciplines, but with other disciplines in government and industry as well. The thrust is for a strong theoretical foundation coupled with laboratory, numerical, and field-based studies. We are unique in that this group has a strong emphasis in all three areas. The overall philosophy is to address broad research bases rather than individual program areas. The group draws upon the unique resources within other divisions at the Laboratory and the various earth sciences departments on the U.C. Berkeley campus. Current emphasis is on the development of techniques for characterizing and monitoring processes in heterogeneous rock and soils using high-resolution seismic and electrical imaging. Applications are in environmental remediation, hazard assessment, evaluation of geothermal and petroleum resources, and storage and disposal of high-level nuclear waste. Future growth will come about only through a coordinated and balanced program based on solid research principles—one that can respond to changing needs in the earth sciences and new objectives of DOE programs in a timely and efficient manner.

Marine Seismic Investigations of the Geometry and Evolution of the San Francisco Bay Area Faults

E. D. Karageorgi, J. Weber Band, P. L. Williams, T. V. McEvilly, and K.H. Williams

The investigation of the crustal structure and complex fault geometries of the Bay Area has been the main focus of the CALCRUST-North consortium. Under this research program, approximately 172 miles of high-quality industry data have been purchased for interpretation and integration with the marine seismic reflection profiling known as BASIX (Bay Area Seismic Imaging eXperiment) and other geological data.

BASIX MULTICHANNEL REFLECTION PROFILING

The BASIX reflection survey—conducted in September 1991—provides valuable coverage across the Coast Ranges from the Sacramento River Delta into the San Francisco Bay region and through the Golden Gate. The BASIX data were collected by deploying daily a complex survey geometry of up to 100 buoyed receivers and two non-coincident 15-km-long passes of the shooting ship through the line. Land receiver arrays were also deployed to complement the marine data.

Processing

We have processed data from the northeastern section of the profile—from the Sacramento River Delta westward to San Pablo Bay (Figure 1). The processing steps for the generation of the initial stacked sections of the BASIX line involve trace editing, sorting to Common Depth Point (CDP) gathers, and preliminary velocity analysis. The

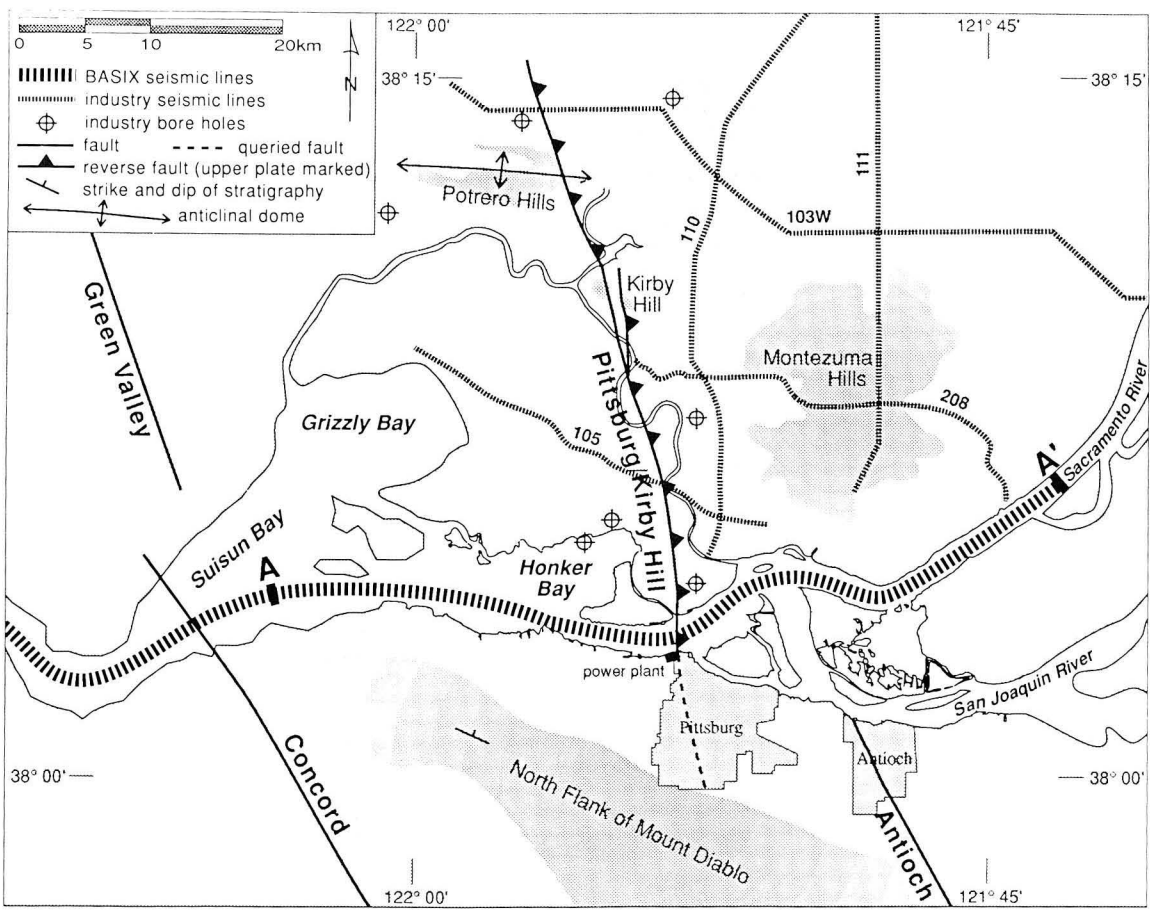

Figure 1. Map showing the processed lines 101, 102, and part of 103 of the BASIX reflection survey (indicated by A, A′), four of the CALCRUST-North lines, surface trace of the Pittsburg/Kirby Hills fault, and geomorphic features. [XBL 933-400]

complexity of the source-receiver geometry and editing of traces contaminated by the current-generated noise have been challenging aspects of the data processing, especially in view of the need to combine overlapping data from successive nights in order to obtain the maximum possible CDP fold. The resulting data quality on preliminary stacks is very good in the Delta and Suisun Bay waters at the east end of the survey, which corresponds to BASIX lines 101, 102, and part of 103 (Figure 2a). However, the high CDP fold due to the unique geometry of the survey, coupled with further velocity analysis and application of static corrections, is expected to yield usable sections for the remaining part of the survey.

Interpretation

Geologic interpretation, guided by well log analysis, is an attempt to determine shallow-to-mid-crustal structure in the eastern Coast Ranges. This region is crucial to understanding the nature, style, and relative activity of tectonism at the broad plate boundary system that encompasses the Bay Area. The study area lies at the junction of three large terranes: the Elder Creek (EC), the Del Puerto (DP), and the Central Valley (CV, part of the Sierran Block). South of the Sacramento River, CV abuts the DP terrane. The junction of DP with EC and CV terranes appears to be under the river between Pittsburg and the west end of Suisun Bay. The fault zone identified on BASIX lines 101 and 102 has been interpreted as a 1-km-wide zone of closely spaced thrust slivers that cuts all but the youngest river deposits at Pittsburg (Figure 2b). We identified the same fault on industry lines 105, 208, and 103W north of the river, where it lines up with the Kirby Hills fault as mapped at the surface (Figure 1). At the western end of line 103W, the thrust appears to displace Tertiary deposits at the surface, indicating a recently active (Quaternary) thrust fault (Figure 3). Time-to-depth conversion of reflections seen in the industry lines enabled us to correlate with horizons in well logs corresponding to the top of the Cretaceous, top of the Paleocene, and top of the Eocene (Figure 3).

The "Pittsburg/Kirby Hills fault," which was unknown before the BASIX experiment, changes from a steeply east-dipping multipole-splaying thrust zone in the river to a west-verging thrust that dips 30 degrees where it crosses line 103W; the thrust appears to join a detachment fault interpreted at 2.5 to 3 sec. The geometry of this thrust and the position of the detachment fault describe a tectonic wedge similar to wedges found at the Dunnigan Hills to the north and the Kettleman Hills to the south. Therefore, we are considering the Pittsburg/Kirby Hills fault as the active bounding structure that separates the eastern Coast Ranges from the Central Valley.

Future work will extend our interpretations to the west in order to tie in major faults that cross the river—namely, the Concord, Franklin, Pinole, and Hayward.

BASIX HIGH-RESOLUTION PROFILING

Three high-resolution sounding systems were applied in the BASIX experiment and its follow-on. Use of these systems, each with distinctive acoustic properties and source-receiver geometry, allowed us to make a critical comparison of these systems and to characterize formerly undetected shallow structure. BASIX led to three key findings in the San Pablo Bay area: (1) a broad area of Pleistocene(?) extensional warping in the southeastern portion of the Bay, which indicates that extensional tectonics have prevailed for a long period in the step-over zone between the Hayward and Rogers Creek faults, (2) a broad zone of distributed faulting in southern San Pablo Bay between the Hayward and Rogers Creek faults, and (3) a throughgoing and active fault connection between the Pinole and Rogers Creek faults. The clear evidence for multiple late Holocene ruptures of the Pinole fault indicates independent tectonic hazard from this structure. The broad and distributed Hayward fault zone in southern San Pablo Bay indicates that the Hayward fault probably breaks up into many small splays close to its on-land terminus at Point Pinole. This section presents evidence for the Pinole-Rogers Creek fault connection.

DATA ACQUISITION

The initial BASIX high-resolution data were recorded on the *S.P. Lee*, the 210-ft oceanographic research vessel of the U.S. Geological Survey, using a four-plate UNIBOOM system (Williams et al., 1992). A second high-resolution BASIX cruise, funded by NSF and CALTRANS, was conducted by the 40-ft USGS research vessel *David Johnston,* which provided access to shallower water (2-ft draft), allowing a substantial increase in the area of high-resolution track coverage. A single-plate GEOPULSE system was deployed on the second cruise (Williams and others, 1992). In a third survey a simple hull-mounted system was deployed from the CALTRANS vessel *Marsh*. This Japanese-manufactured very high resolution (VHR) instrument was loaned to us by Japanese colleagues.[1] The VHR instrument produces a source pulse with a center frequency of approximately 5 kHz. Return energy is captured in an unconventional inverted-cone receiver. Analog recording is accomplished by a standard paper recorder. The fidelity of this equipment proved to be excellent in soft sediment

[1]Kunihiko Shimazaki, Noboru Chida, Makoto Okamura, Takashi Nakata, and Takashi Kumamoto.

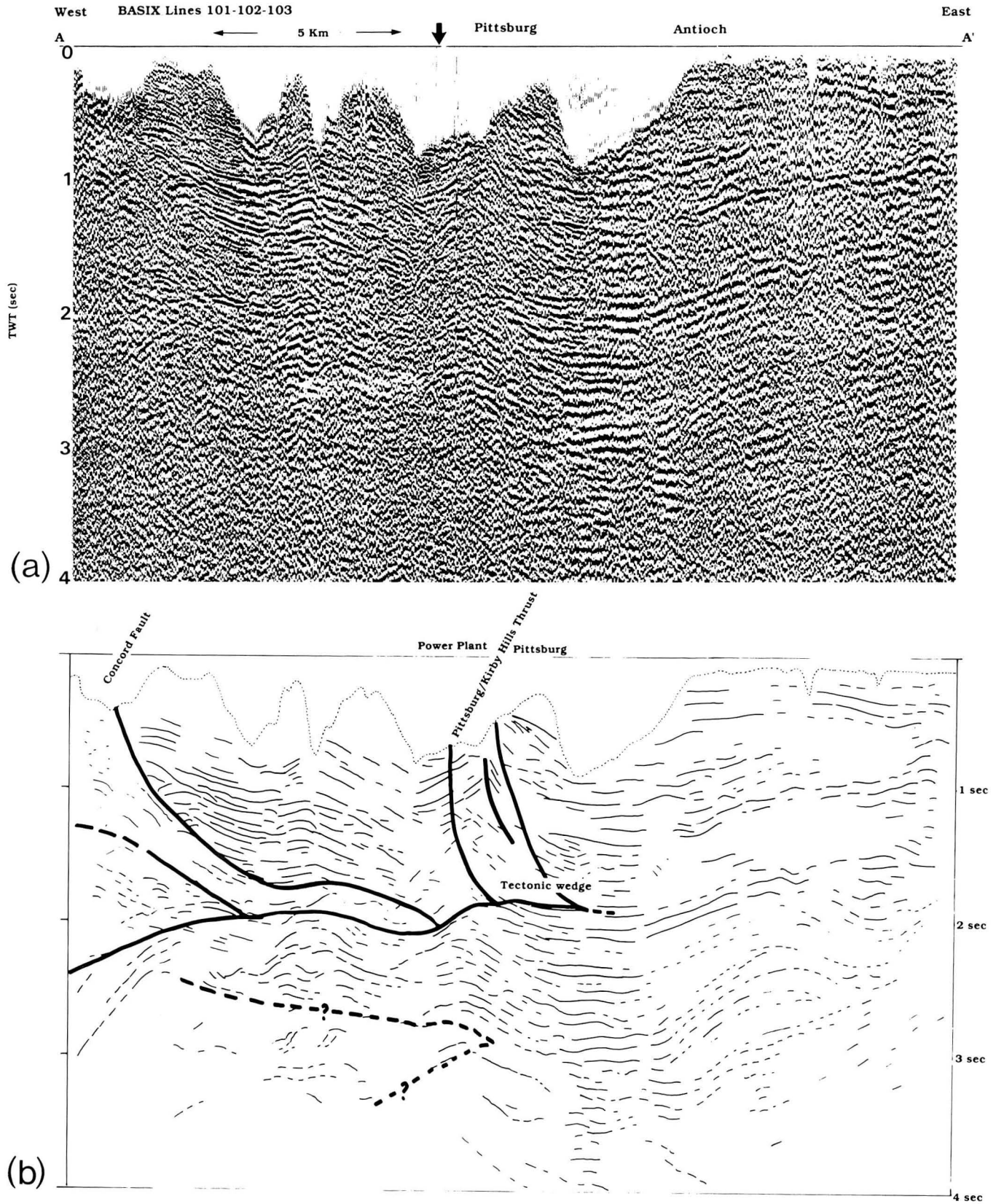

Figure 2. **(a)** Brute stack profile of BASIX lines 101, 102, and part of 103; the Pittsburg/Kirby Hills fault is imaged in the disturbed reflections between 1 and 2 sec at the arrow. **(b)** Preliminary interpretation of the BASIX profile. [XBL 931-152]

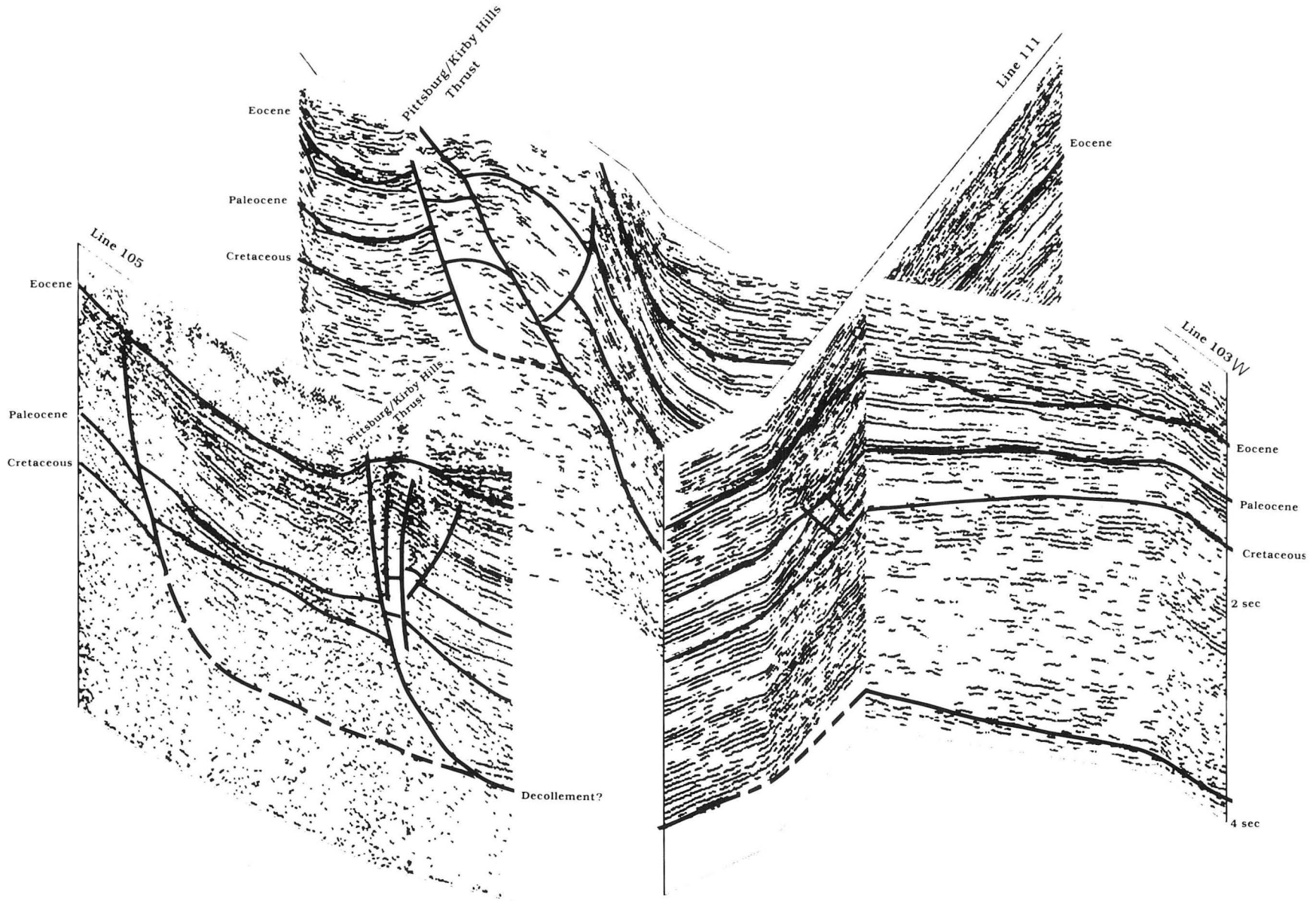

Figure 3. Fence diagram with structural and stratigraphic interpretation of industry reflection lines 103W, 105, and 111. West is to the left. [XBL 931-153]

areas with minor bottom roughness. Maximum recording depth was 18 m with the VHR system, but the majority of records produced high-quality data to a depth of 10 to 12 m.

RESULTS

A fault in the general vicinity of a projected Pinole-Rogers Creek fault intersection was located by Williams and others (1992). New data collected with the VHR equipment greatly improves our understanding of the geometry of the Pinole-Rogers Creek fault connection (Figure 4). The Pinole fault extends more than 10 km to the north of the San Pablo Bay shoreline near the town of Pinole, striking N18°W. Its trend is about 26 degrees oblique to the southeastward projection of the Rogers Creek fault. A fault aligned and parallel to the Rogers Creek fault was found 2 km to the southeast of the junction of the Pinole and Rogers Creek faults. This appears to be the southeasternmost extension of the Rogers Creek fault.

Maximum vertical displacement of the Holocene bay sediments is 3 m down to the west. Separate vertical offsets can be detected by distinguishing sedimentary packages that were laid down over a fault scarp from those that were deposited on a flat-lying surface. Wedges of sediment over the down-dropped side of the fault are interpreted to post-date earthquakes. All the recorded earthquakes offset what was an essentially flat-lying surface. Three earthquakes are recorded in the sediments profiled in Figure 5. The earliest offset was 0.7 m; the penultimate offset, 0.6 m; and the latest offset, 1.2 m. The latest offset is capped by 1.5 m of sediment. Small mismatches of the sedimentary sequence across the fault also indicate the occurrence of additional minor strike-slip displacement across the Pinole fault.

We conclude that the Pinole and southernmost Rogers Creek faults are active and participate in the stepping of dextral slip between the Hayward and Rogers Creek faults. Evidence of a contemporary extensional environment in this right-stepping transfer zone includes the drape of Pleistocene(?) deposits across the southeastern portion of the Bay and a broad zone of distributed small fractures near and to the east of the Hayward fault beneath San Pablo Bay.

The application of several high-resolution seismic reflection technologies has allowed us to investigate fine de-

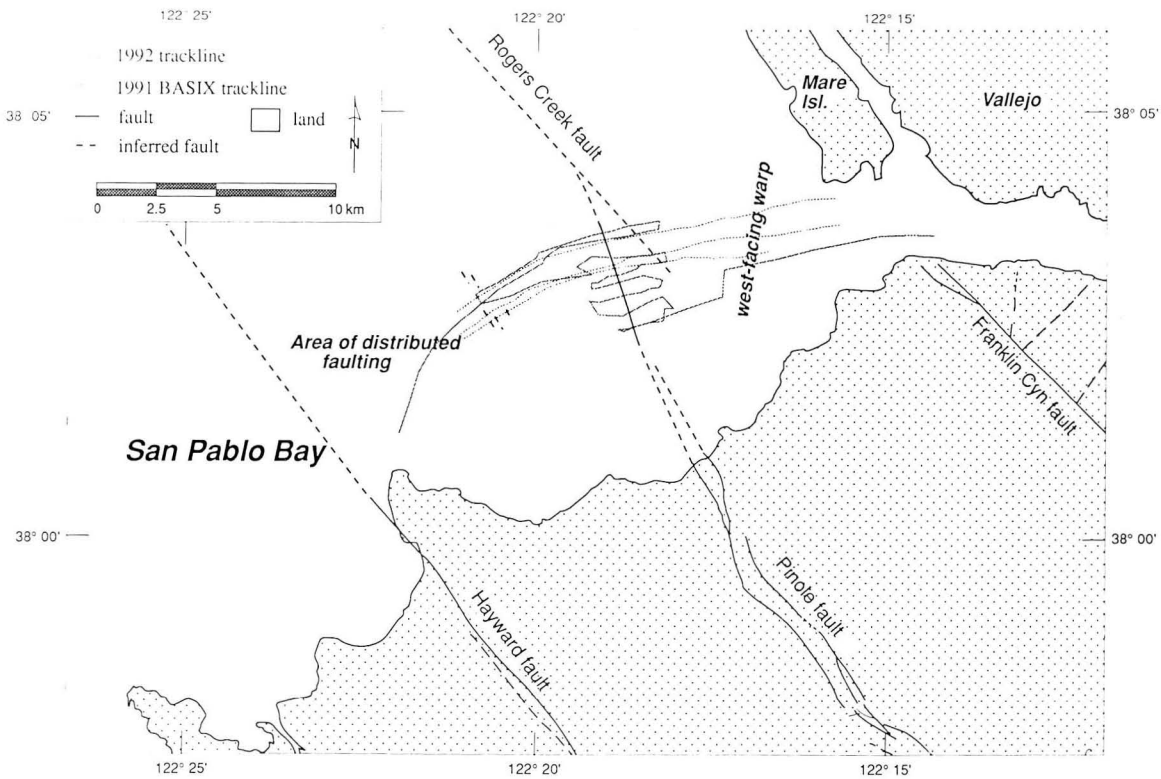

Figure 4. Map of the southern San Pablo Bay area. Shown are ship tracks and faulting in the vicinity of the Pinole fault-Rogers Creek fault junction. The profile shown in Figure 5 was obtained at the southernmost crossing of the Pinole fault beneath San Pablo Bay. [XBL 933-401]

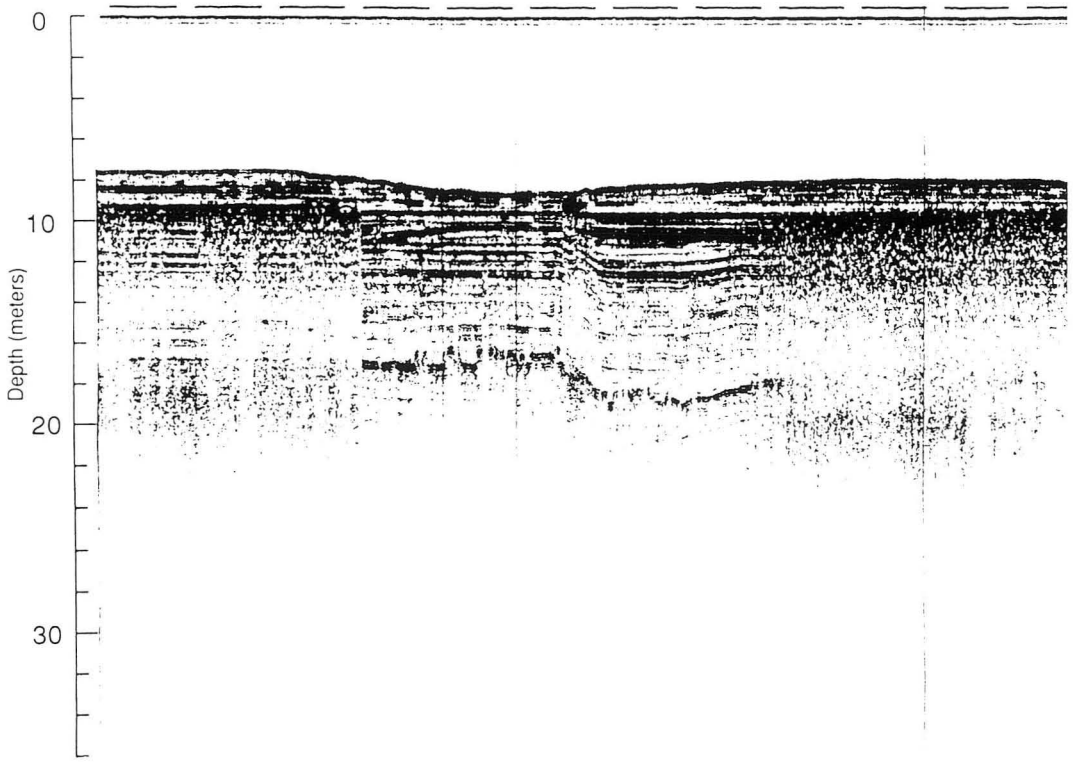

Figure 5. Very high resolution seismic profile across the Pinole fault. East is to the left. Vertical exaggeration is about 15:1. Water extends to a depth of 8 m. Total sediment penetration is 12 m. [XBL 9212-2568]

tails of faulting in San Pablo Bay. The use of a very high resolution seismic reflection system can provide results that compare well with direct observation and trenching on land. The success of this study suggests the start of a revitalized and exciting period in the use of high-resolution seismic reflection technology for investigation of the nature of tectonic hazard.

REFERENCE

Williams, P.L., McEvilly, T.V., Clymer, R.W., Karageorgi, E., and Holland, P., 1992. Marine seismic investigations of the East Bay faults. *In* Earth Sciences Division Annual Report 1991. Lawrence Berkeley Laboratory Report LBL-31500, p. 32–38.

Shear-Wave Monitoring with Vibroseis at Parkfield, California

E. D. Karageorgi, R. Clymer, and T. V. McEvilly

Our ongoing program of seismic-wave analysis continues to focus on the San Andreas fault at Parkfield in Central California. We routinely record both earthquakes and waves generated with a controlled source, using the Parkfield high-resolution seismic network (HRSN). This article concentrates on the controlled-source part of the experiment. Our goal is an evaluation, at the highest possible resolution, of the premise that controlled-source monitoring can detect variations premonitory to earthquakes in those parameters expected to be the most sensitive indicators of changes in material properties associated with fault-zone failure, namely shear-wave velocity, amplitude, frequency content, and anisotropy.

The HRSN (Figure 1) consists of ten 3-component, borehole seismometers surrounding the epicenter of the 1966 Parkfield M6 earthquake. Data-acquisition features

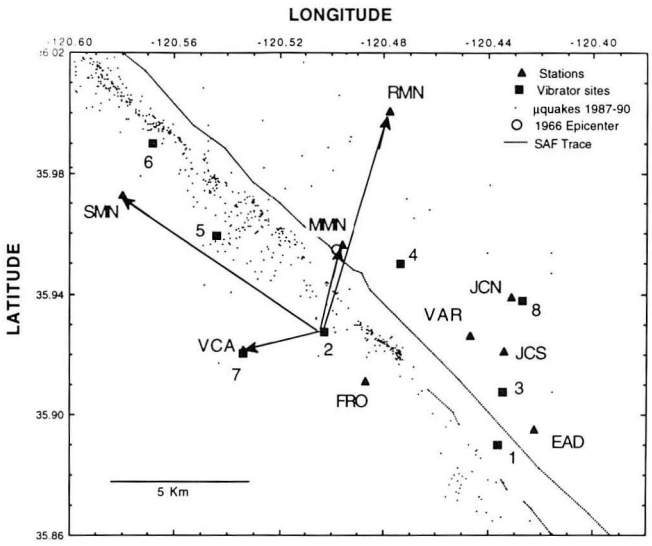

Figure 1. Location map showing the borehole seismometer network, vibrator positions (VPs), and microearthquake seismicity for 1987–1990; the arrows indicate the four paths from VP2 used in Figure 4. [XBL 933-402]

digital telemetry with 125-Hz bandwidth and 16-bit resolution and can operate in external-trigger (i.e., controlled-source) or event-trigger (earthquake) modes. Network characteristics are summarized in Karageorgi et al. (1992). Under present funding levels, 4–6 vibrator data sets are collected each year. Data reduction and analysis are accomplished at the Center for Computational Seismology (CCS) in the Earth Sciences Division of the Lawrence Berkeley Laboratory.

ANALYSIS AND RESULTS

From June 1987 through December 1992, the HRSN has been illuminated 43 times with *S*-waves of three polarizations at seven (originally eight) vibrator positions (VPs), shown in Figure 1, using a shear-wave Vibroseis source (a truck-mounted, hydraulically driven vibrator). The final working data sets for analysis are "time gathers" of seismograms (Figure 2): one source orientation into one receiver gathered across calendar time, producing 720 files (3 source polarizations at 8 VPs into ten 3-component seismometers), each containing, at present, up to 42 highly

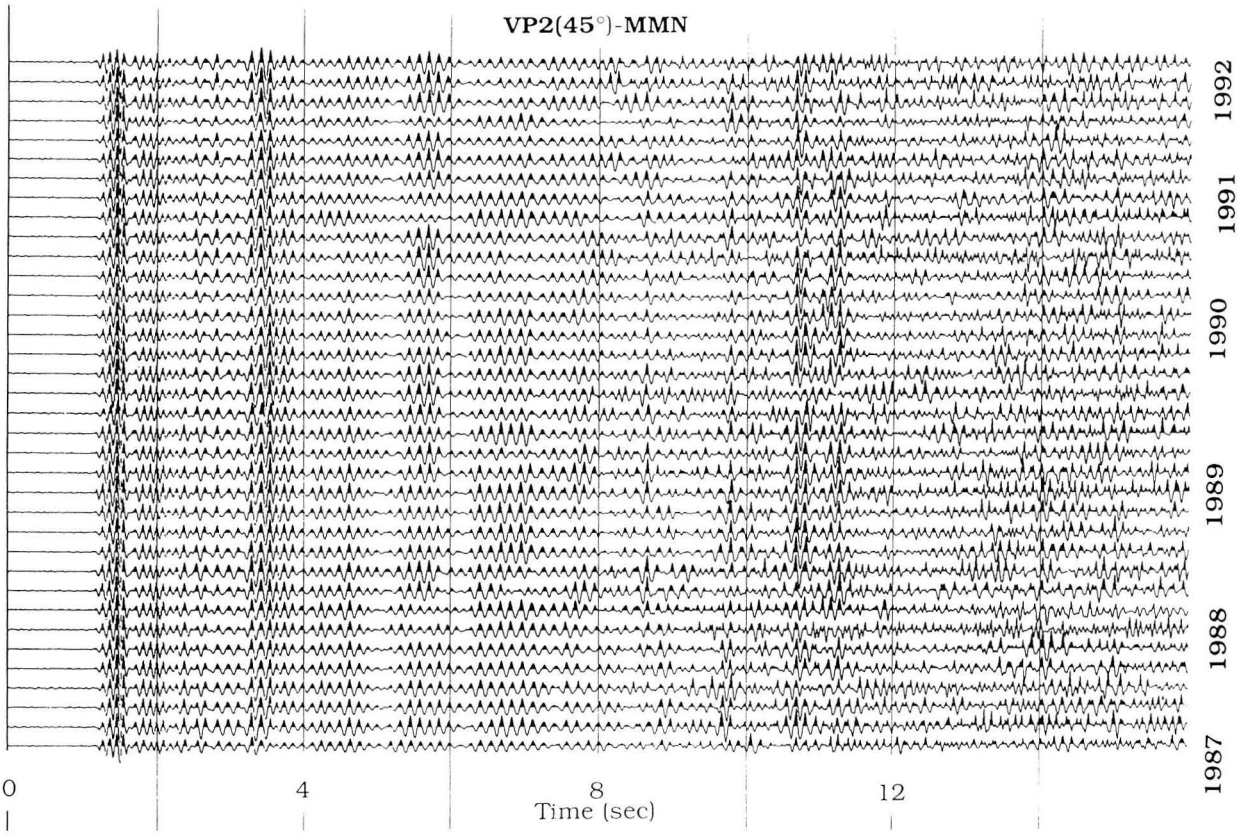

Figure 2. Example of a gather across calendar time for the path from VP2 (45° source orientation) to MMN (H2 component). [XBL 933-403]

similar traces (four unprocessed data sets remain from late 1987 for specific VPs). The time gathers are then examined for temporal variations in waveform parameters.

We now have an extensive baseline—nearly five years of high quality data—adequate for meaningful analysis. Over the past several years, analysis tools have been developed to display waveform properties of windowed phases, of whole traces, and of entire time gathers. We have developed color-graphics displays of trace amplitude, frequency content, travel-time changes, and particle-motion parameters. An application of these methods to a subset of travel paths through the expected nucleation zone of the next M6 Parkfield earthquake is presented in Karageorgi et al. (1992). Some paths showed only seasonal variations in various properties. Seasonal variations are due to very near surface moisture changes under the vibrator (Clymer and McEvilly, 1981). However, this preliminary effort also identified a potentially significant and progressive travel-time decrease in the expected nucleation region. In particular, the paths from VP2 to MMN (NNW) and to VCA (ESE), show advances in travel time of 30–60 msec for a band of late phases relative to an arbitrarily chosen reference trace. In the past year, with the automation of the steps for data reduction editing and processing, we have extended the analysis to the *entire* data set in order to better localize the anomaly and investigate possible causes. A comprehensive study of the travel-time anomaly revealed a travel-time advance in the coda of the *S*-wave, localized southeast of Middle Mountain. The results are shown in map form in Figure 3. Figure 4 shows travel-time variations on four paths from VP2 (paths shown in Figure 1), updated through late October 1992. Displayed is travel-time change (correlation lag) relative to an arbitrarily chosen reference trace measured across the time gather in a window that is stepped along the travel-time axis. The anomalies appear as dark zones, indicating that those phases are arriving early with respect to the same time window on the reference trace.

We investigated the possible causes of the changes in travel time in order to determine if the anomaly is source- or receiver-related or if it is a result of surface effects to the phases involved (ground roll, surface waves).

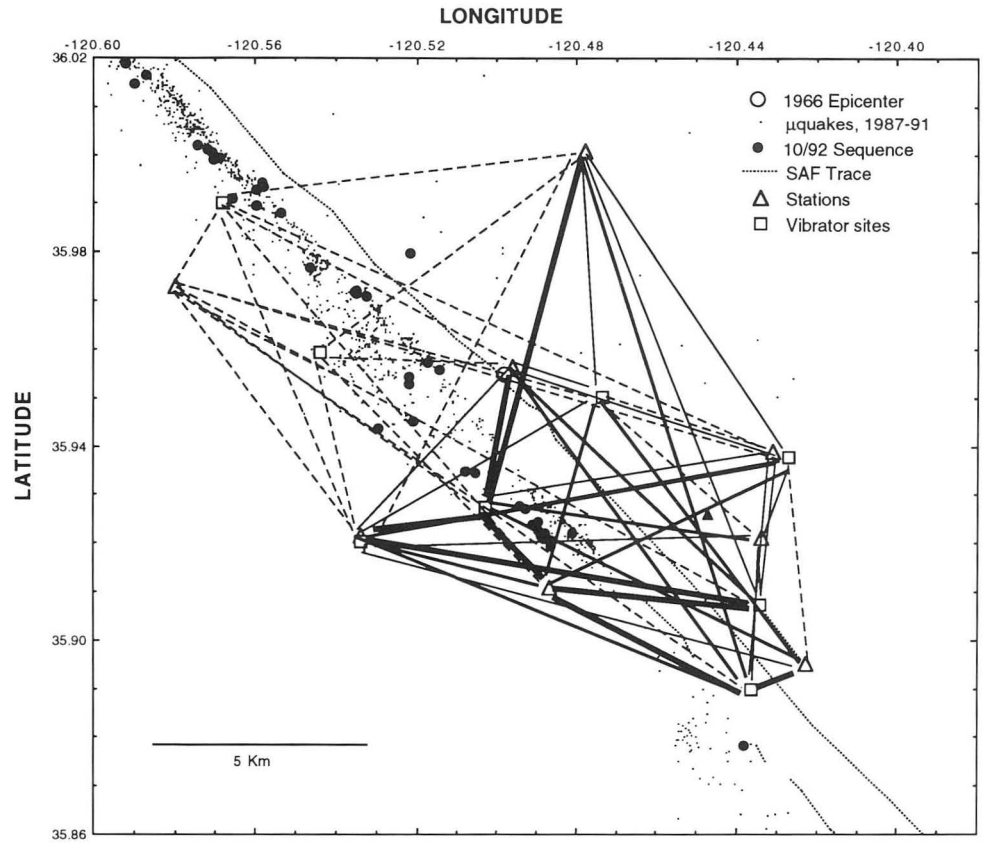

Figure 3. Paths showing velocity variations. Heavy solid lines represent paths with strong travel-time advance in the *S*-wave coda (concentrated primarily SE of Middle Mountain); broken lines represent stable paths; and light solid lines represent paths that indicate marginal anomalies. [XBL 933-404]

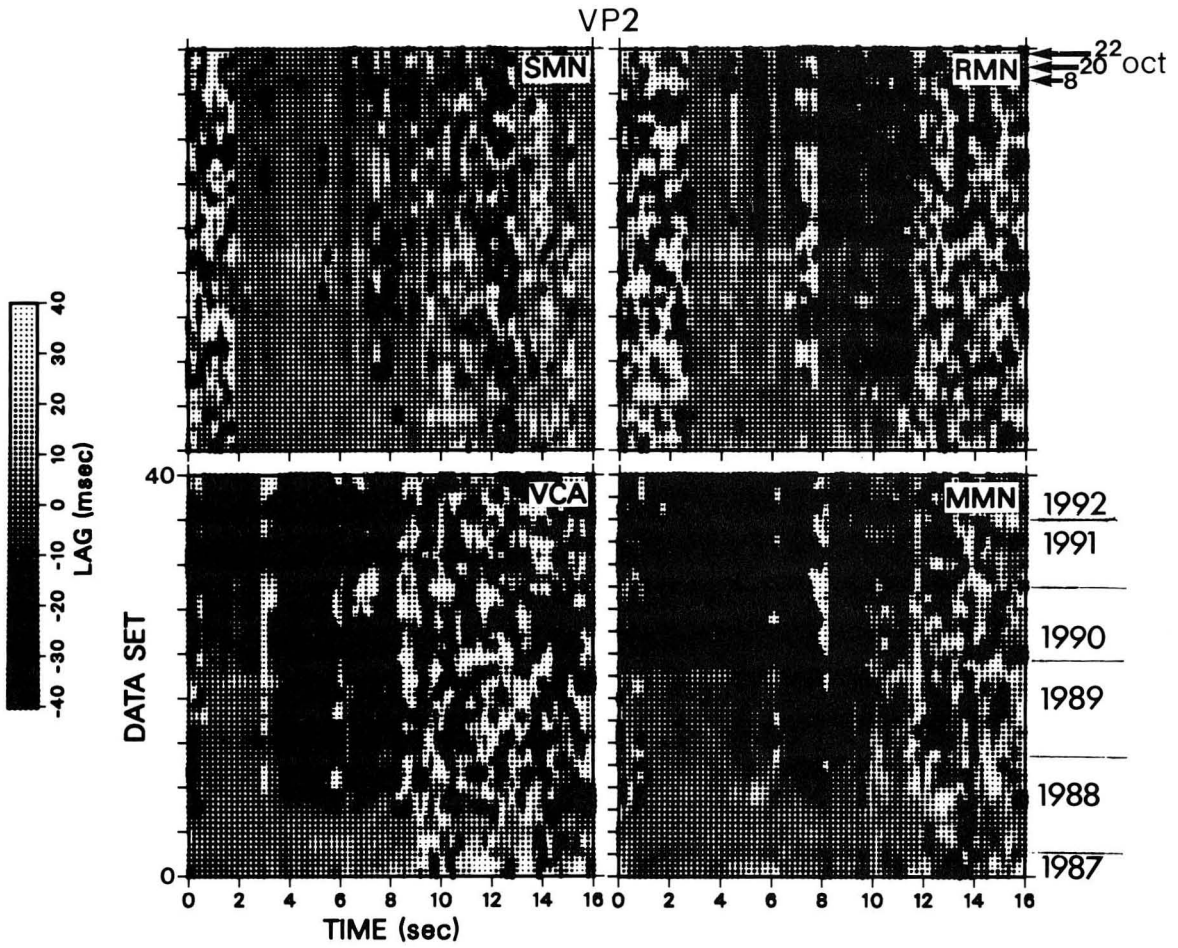

Figure 4. Travel-time variations relative to a reference trace (data shown here arbitrarily chosen for mid-1988) measured across the repeated 16-sec seismograms in a moving window for four paths from VP2. [XBL 933-405]

The anomalous decrease in the travel time is not seen in all the paths from VP2; in particular, there is a conspicuous stability of travel time on the path to the northwest to SMN (Figure 4), implying that the effect is not source induced. In contrast, paths from VP2 in various azimuths, clockwise from north to west, show the anomaly at late times. Similarly, we examined the possibility of a receiver-related cause by viewing travel-time changes for all sources into each receiver. Again, the travel-time decrease at each receiver is seen only from certain sources and only on late arrivals. Such results are seen on all such receiver "fans," indicating that the anomalies observed are not receiver related.

The group velocity of the later arrivals appears to be too large for these phases to be surface waves, and the sensors are too deep to be sensitive to surface waves at the expected wavelengths. Moreover, the paths showing the anomaly are not influenced by the valley sediments. Finally, we question that the effect could somehow be due to the prolonged drought in central California. In fact, time-gathers from source sites with strong seasonal variations show a *slowing* of all arrivals in the dry season, whereas the observed prolonged anomaly is an *increase* in velocity of late phases during the several-year dry period.

We have recently carried out a small two-dimensional profile at VP2, moving the vibrator in small increments. This data set may help distinguish between shallow and deeply propagating waves.

REFERENCES

Clymer, R.W., and McEvilly, T.V., 1981. Travel time monitoring with Vibroseis. Bull. Seismol. Soc. Am., v. 71, p. 1902–1927.

Karageorgi, E.D., Clymer, R.W., and McEvilly, T.V., 1992a. Shear-wave propagation in the San Andreas fault zone monitored with Vibroseis. Seismol. Res. Lett., v. 63, p. 75 (abstr.).

Karageorgi, E., Clymer, R.W., and McEvilly, T.V., 1992b. Seismological studies at Parkfield. II. Search for temporal variations in wave propagation using Vibroseis. Bull. Seismol. Soc. Am., v. 82, p. 1388–1415.

Joint Inversion of VSP and Microearthquake Data for Shallow Fault Zone Structure

T. M. Daley and T. V. McEvilly

Past research at Lawrence Berkeley Laboratory's Center for Computational Seismology (CCS) has included studies of microearthquake (natural source) and seismic exploration (controlled source) data sets. Typically these two types of data are treated separately and for different purposes. Recent work near Parkfield, California, however, provided us with an opportunity to combine these data in a joint inversion scheme with hopes of obtaining a higher-resolution image of the shallow structure of the San Andreas fault zone. This work included a multi-offset shear-wave vertical seismic profile (VSP) recorded in the Varian well and microearthquake studies conducted within the Parkfield earthquake prediction experiment.

During VSP studies in the Varian well (initially reported in Daley and McEvilly, 1990), which were conducted as part of the Parkfield experiment, we observed a remarkable difference in *Vp/Vs* ratio between equally offset source points southwest of Varian (with rays crossing the fault zone) and northeast of Varian (with rays crossing a sedimentary section) (Daley and McEvilly, 1992). Figure 1 shows data that demonstrate this *Vp/Vs* ratio variation. Because we were convinced that the San Andreas fault zone was creating an anomalously high *Vp/Vs* ratio, we wanted to locate this zone of anomalously high *Vp/Vs* ratio and image its lateral and depth extent.

Figure 2 shows the geologic cross section perpendicular to the San Andreas fault through the Varian well (John Sims, 1991, personal communication). The VSP data used in this study is from a string of permanently emplaced sensors in the Varian well and 6 source locations from 100 m to 2500 m offset. The well is instrumented with eighteen 3-component sensors between 25 and 1000 m in depth. Both strong-motion (overdamped) and high-gain seismometers were used.

A 3-D *P* and *S* velocity structure for the Parkfield area has been developed by Michelini and McEvilly (1991), including locations for about 1200 microearthquakes. Using the same inversion algorithm, we created a smaller 3-D inversion volume around the Varian well. The volume is 6 km across the fault zone, 3 km along the fault, and 4 km deep. The inversion used *P*- and *S*-wave travel times from the 6 VSP

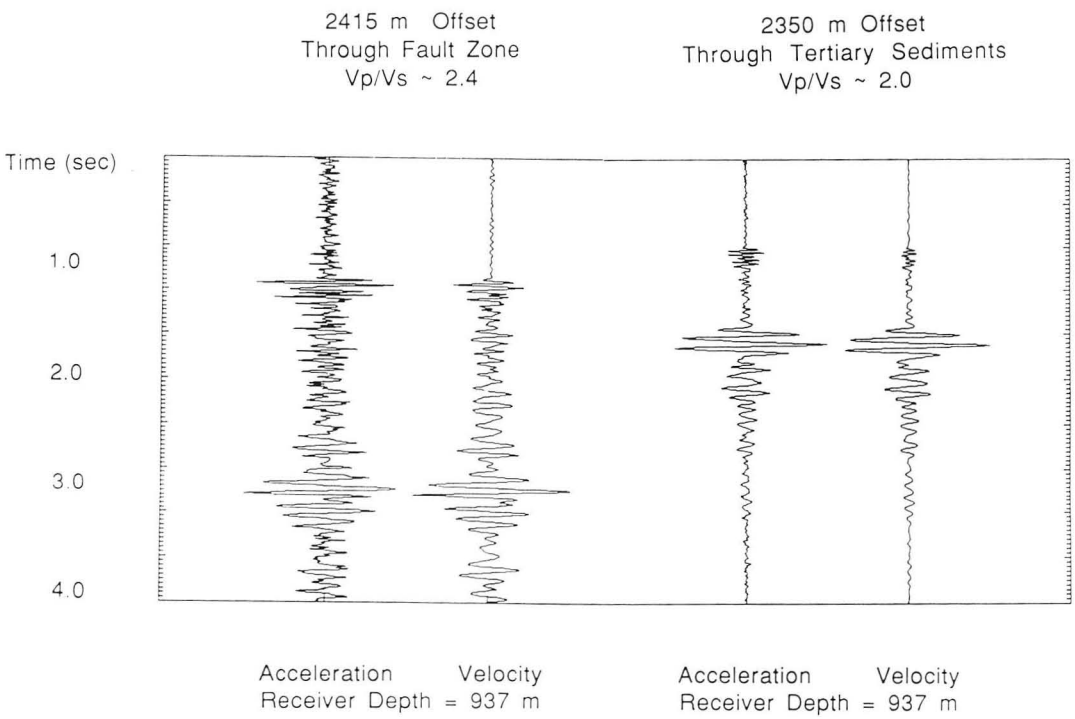

Figure 1. Two pair of seismograms from the Varian well VSP. The left-hand pair propagated through the fault zone; the right-hand pair propagated northeast of the fault zone. Each pair has an acceleration (left) and velocity (right) receiver at a depth of 937 m. The *P*-wave (near 1 sec) and *S*-wave (largest amplitude arrival) are seen to arrive at very different times despite the nearly identical source-receiver distances (2400 m). [XBL 933–393]

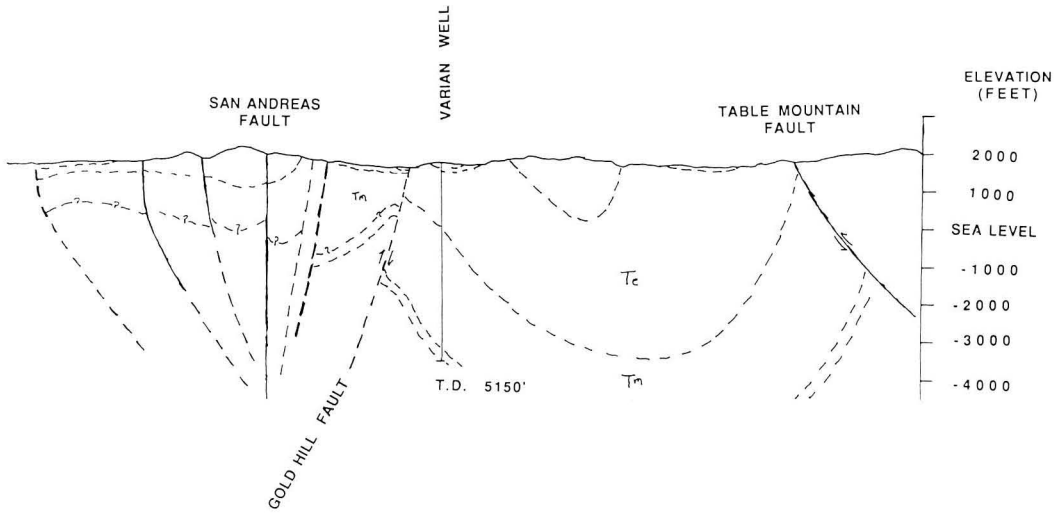

Figure 2. Geologic cross section perpendicular to the San Andreas fault zone. The data from Figure 1 were recorded on opposite sides of the Varian well along this cross section. [XBL 933–394]

source points, and we chose 18 microearthquake events located at shallow depth (< 5 km) and near the Varian well. The inversion began with the Michelini/McEvilly model and solved separately for *P* and *S* velocities at 60 grid points within the volume. We interpolated with cubic splines to 500-m grid points for the velocity cross sections.

Figure 3 shows results of the *P*- and *S*-velocity inversions displayed as *Vp/Vs* ratios for a cross section through the Varian well perpendicular to the fault zone. The *P* raypaths within 500 m of the cross section are also plotted. A *Vp/Vs* anomaly does appear in the joint inversion results, with values around *Vp/Vs* = 3.0 near the surface. We do see a zone of *Vp/Vs* > 2.2 about 2 km wide and 2 km deep, centered slightly southwest of the San Andreas fault trace. Figure 4 shows a horizontal slice of the *Vp/Vs* ratio at 0.5 km depth. We can infer that the anomaly extends farther to the south-

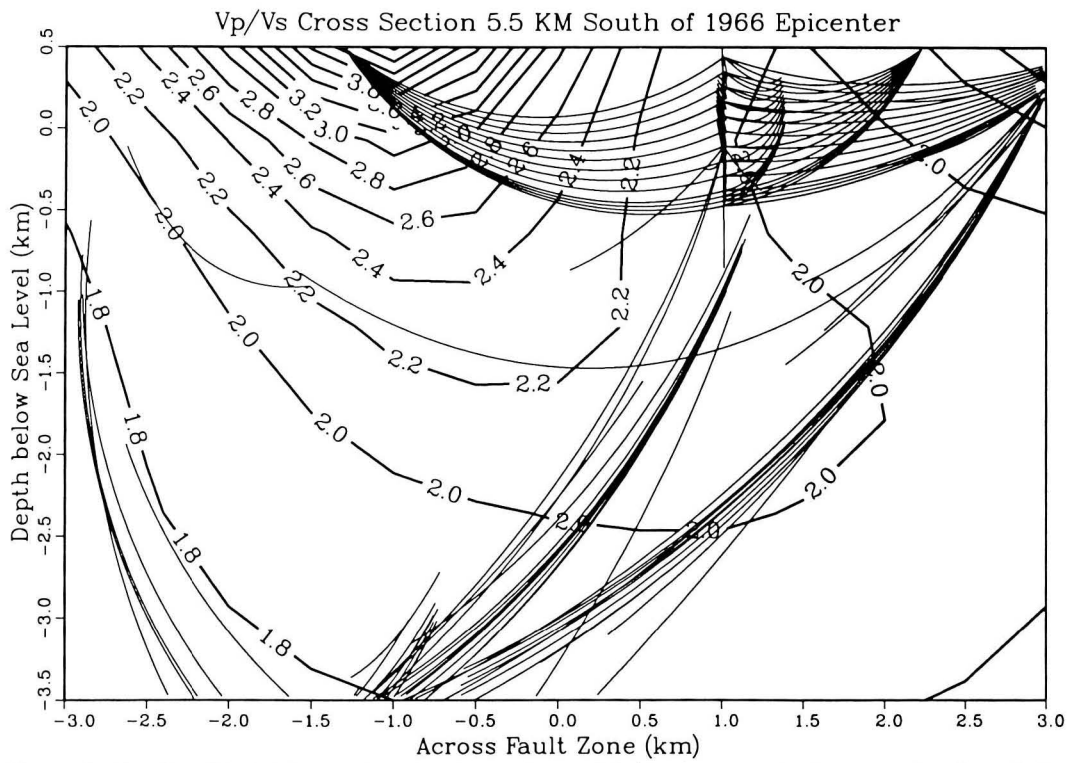

Figure 3. Results of the joint inversion, showing contours of *Vp/Vs* along a vertical cross section through the Varian well, with the *P*-wave raypaths near this cross section. [XBL 933–395]

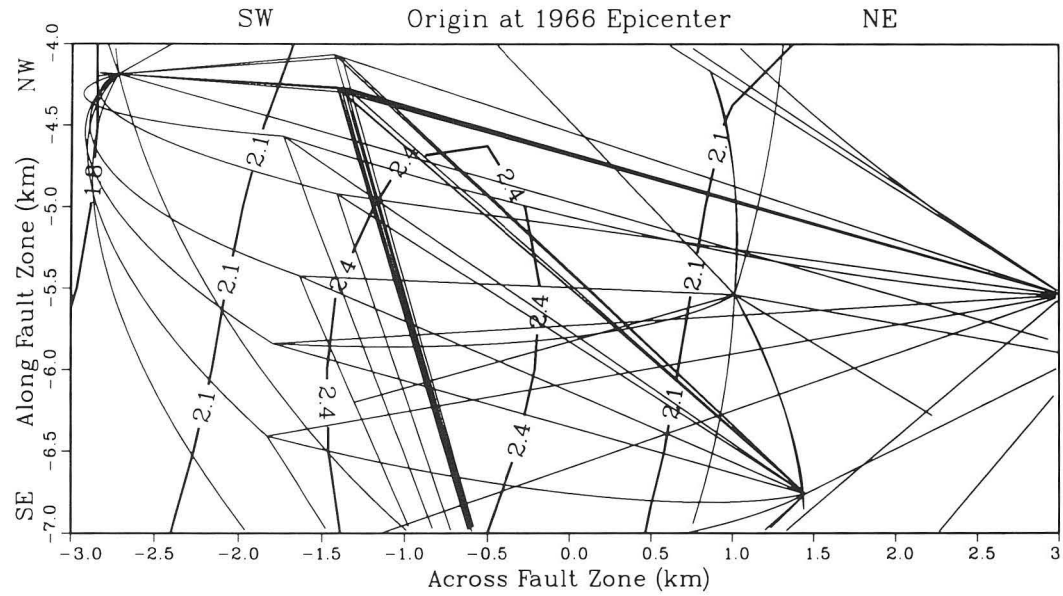

Figure 4. Results of the joint inversion, showing contours of *Vp/Vs* along a horizontal cross section at 0.5 km depth, with the *P*-wave raypaths projected onto the cross section. [XBL 933-396]

east, while seeming to decline in magnitude to the northwest. We feel that this anomaly represents the volumetric extent of the shallow fault zone. A more accurate delineation of the anomaly could be obtained with more VSP source points, especially southwest of the Varian Well.

REFERENCES

Daley, T.M., and McEvilly, T.V., 1990. Shear-wave anisotropy in the Parkfield Varian well VSP. Bull. Seismol. Soc. Am., v. 80, p. 857–869.

Daley, T.M., and McEvilly, T.V., 1992. Joint VSP and microearthquake tomography for fault-zone structure. Seismol. Res. Lett. v. 63, no. 1, p. 62.

Michelini, A., and McEvilly, T.V., 1991. Seismological studies at Parkfield. I. Simultaneous inversion for velocity structure and hypocenters using cubic B-splines parameterization. Bull. Seismol. Soc. Am., v. 81, p. 524–552.

Application of 4-Component Shear-Wave VSP Rotation for Determination of Fracture-Induced Anisotropy

*T. M. Daley, E. L. Majer, and J. H. Queen**

Previous studies of vertical seismic profiles (VSP) have attempted to use shear-wave anisotropy to determine the dominant fracture orientation (Majer et al., 1988; Daley et al., 1988). Unfortunately, these studies often provided unconfirmable results because the fracture orientation was not well determined. Recent cooperative work with Conoco Inc. has provided a data set acquired in a location whose fracture properties are fairly well understood. Moreover, the analysis of shear-wave VSP data for transversely isotropic media with a vertical axis of symmetry has been improved by the development of a 4-component rotation technique. We have performed this VSP analysis on the Conoco data as a confirmation of the previously determined fracture orientation.

Conoco conducted a 9-component VSP (three source polarizations, *P*, *SV*, and *SH*, and three receiver orientations at each depth) in well 33-5 at their borehole test facility. This facility has a number of wells and a previously studied fracture property. We analyzed Conoco's 9-component VSP data from well 33-5 for indications of seismic anisotropy as indicated by shear-wave splitting. We began with stacked and edited data from each source. We used our own rotation algorithm to determine the orientation of the horizontal receiver

* Conoco Inc., Exploration Research and Services, Ponca City, OK.

components at each depth (they are recorded with random orientation due to downhole tool rotation while moving between depth locations). This provided a data set with vertical, horizontal-radial, and horizontal-transverse receiver components for each source. Initial interpretation of the data was made using the travel-time difference between arrivals for the *SV* radial data and the *SH* transverse data. Figure 1 shows these travel-time differences for each depth. These travel-time differences provide a depth-dependent measure of the shear-wave splitting caused by anisotropic propagation. However, the travel times only give a magnitude of anisotropic effects for the particular azimuthal orientation of the sources.

To improve the interpretation, we performed a 4-component rotation into the "best fit" coordinate system for transversely isotropic media (Alford rotation, Alford, 1986). The 4-component rotation can give an azimuthal orientation of the vertical axis of symmetry of anisotropy (and by implication, the fractures). This method of 4-component rotation was originally proposed by Alford (1986), with further development by Thomsen (1988), and was recently demonstrated in field experiments by Winterstein and Meadows (1991). Thomsen shows that for a set of orthogonal VSP shear-wave sources and receivers, $s_{(i,j)}$ $i,j = 1,2$, where i is a source and j is a receiver and 1 is an in-line orientation and 2 is a cross-line orientation, which are oriented at an angle θ to the symmetry azimuth of anisotropy, we can determine θ and construct the "principal time series." These are the time series $s_{(parallel)}$ and $s_{(perpendicular)}$ that would be recorded if the sources and receivers were oriented along θ. Winterstein and Meadows apply this 4-component rotation method and extend it by proposing a layer-stripping scheme that allows more accurate measurement of anisotropy azimuth at depth and measurement of changes in θ as a function of depth.

Figure 2 shows the calculated 4-component rotation angles for the Conoco data set. These angles are measured from the azimuth of the in-line shear-wave source, and they agree well with the previously inferred fracture orientation (Queen and Rizer, 1990). After the shallowest four depths, the angles are fairly well clustered around 70 degrees. The average angle for data from 1000 to 3000 ft is 70 degrees, with a standard deviation of 5.2 degrees. Figure 3 shows the travel-time difference using the in-line and cross-line traces from the 4-component rotation. The travel-time difference has been increased from the original recordings (Figure 1) because the new rotation gives the orientation with the most travel-time splitting. The results indicate three zones of anisotropy: a shallow zone (above the shallowest receiver at 500 ft), an intermediate zone above 1400 ft, and a deeper zone ranging from 1600 ft to about 2300 ft. The maximum travel-time difference of about 0.02 sec in a total travel time of 0.6 sec is 3.3% average anisotropy in shear-wave propagation.

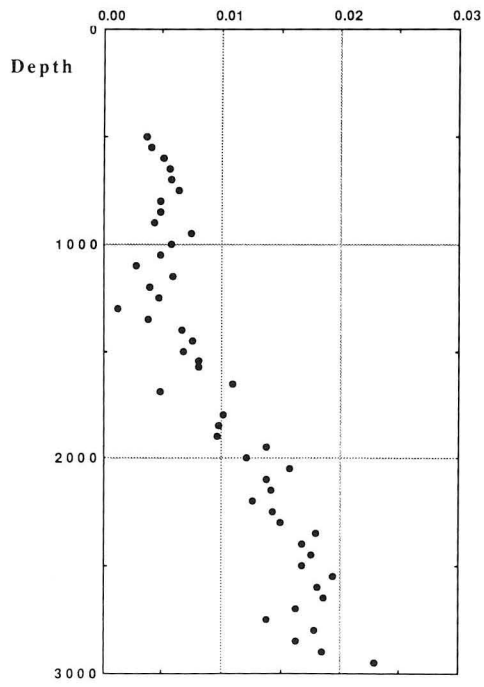

Figure 1. Shear-wave travel-time difference (in seconds) between *SV* (in-line) and *SH* (cross-line) sources before 4-component rotation. Note that the shear-wave has already been split at the shallowest recording (500 ft). [XBL 933-397]

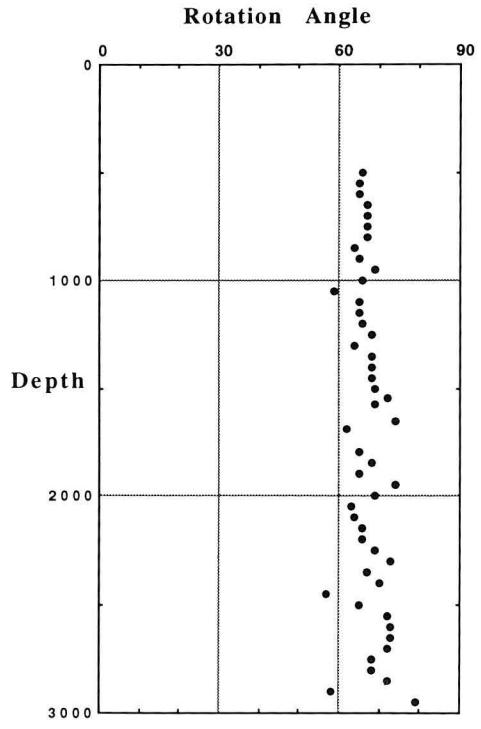

Figure 2. Calculated angles for 4-component (Alford) rotation. The angle is measured from the azimuth of the in-line shear-wave source. The average angle of 70 degrees agrees well with the previously inferred fracture orientation at this site. [XBL 933-398]

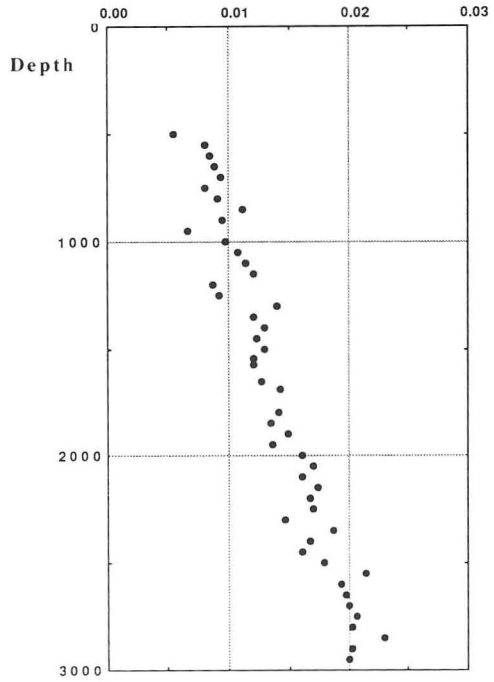

Figure 3. Shear-wave travel-time difference (in seconds) between in-line and cross-line components after 4-component (Alford) rotation. Note that there is less scatter and greater time difference compared with the data in Figure 1. [XBL 933-399]

REFERENCES

Alford, R.M., 1986. Shear data in the presence of azimuthal anisotropy. 56th Annual International Meeting, Society of Exploration Geophysicists, Expanded Abstracts, p. 476–479.

Daley, T.M., McEvilly, T.V., and Majer, E.L., 1988. Analysis of *P* and *S* wave vertical seismic profile data from the Salton Sea Scientific Drilling Project. J. Geophys. Res., v. 93, no. B11, p. 13025–13036 (LBL-22246).

Majer, E.L., McEvilly, T.V., Eastwood, F., and Myer, L., 1988. Fracture detection using *P*- and *S*-wave VSPs at The Geysers geothermal field. Geophysics, v. 53, p. 76–84 (LBL-20100).

Queen, J.H., and Rizer, W.D., 1990. An integrated study of seismic anisotropy and the natural fracture system at the Conoco Borehole Test Facility, Kay County, Oklahoma. J. Geophys. Res., v. 95, p. 11255–11273.

Thomsen, L., 1988. Reflection seismology over azimuthally anisotropic media. Geophysics, v. 53, p. 304–313.

Winterstein, D.F., and Meadows, M.A., 1991. Shear-wave polarizations and subsurface stress directions at Lost Hills field. Geophysics, v. 56, p. 1331–1348.

Applications of the LBL High-Frequency Seismic Imaging System

T. M. Daley, E. L. Majer, J. H. Queen, and P. Buller**

During 1992 a number of field experiments were completed using the Lawrence Berkeley Laboratory (LBL) high-frequency piezoelectric seismic imaging system. These experiments were conducted in a variety of geologic and hydrologic settings to test and demonstrate the utility of high-frequency imaging. Standard seismic imaging, such as surface reflection surveys or borehole vertical seismic profiles (VSP), use frequencies of 10 to 200 Hz, providing resolution of 10 to 100 m. We are demonstrating the uses of a system that can provide 200- to 10,000-Hz signals at distances of 100 m or more in rock types ranging from volcanic tuffs to carbonaceous sediments to granite, providing resolutions of 1 m or less to 10 m or more.

The system has been developed over the past 4 years for the Department of Energy, principally for nuclear and environmental programs, but with assistance from the Office of Fossil Energy research budget. Additional support was received from Amoco, BP, and Conoco, and engineering assistance was received from the High Energy Physics and Accelerator and Fusion Research Divisions of LBL. The seismic source is a high-voltage piezoelectric transducer that can be operated in a pulse mode or in a controlled signal-sweep mode. In pulse mode, we use pulse widths from 10 μsec to 100 msec with up to 20,000 V at about 0.5 A of current. The pulse rise time, which has proved to be a critical parameter, is controllable down to 1 μsec. In sweep mode, the source can produce a chirp signal analogous to radar signals. The sweep frequencies range from 200 to 20,000 Hz, but a typical sweep would be between 500 and 5000 Hz. In this mode, the source is driven by 5 to 6 A at 6000 V from a state-of-the-art high-voltage linear transformer. This power is delivered down an armored coaxial borehole cable, which can be up to 10,000 feet long. Sweeps are fully programmable, and we

* Conoco Inc., Ponca City, Oklahoma

are investigating the uses of digital sweeps with +1's and –1's produced by phase reversals of a carrier frequency. One such sweep, called a Barker code, has autocorrelation functions as good as conventional sweeps. A piezoelectric source, unlike a mechanical vibrator, is fast enough to follow a Barker code's phase reversals, and the source can then operate near its resonance peak. The resonance peak of the source is 4000 Hz for the longitudinal (vertical) component and 11,000 Hz for the radial (transverse) component. The data-recording system has a 16-bit analog-to-digital converter designed for up to 400,000 samples per second. The current system has 12 channels but is expandable to 48 or more by adding boards. The acquisition boards are made by Aerial using a 25 Mflop AT&T 32-bit digital signal-processing chip with 2 channels per board.

Two experiments were conducted using this system at the Conoco borehole test facility near Newkirk, Oklahoma (Figure 1). This site has been previously studied and characterized, so that parameters such as fracture orientation are fairly well known (Queen and Rizer, 1990; Lines et al., 1992). The first survey was between wells 33-5 and 33-6, a cross-well distance of 400 ft, at depths of 1500 to 2400 ft. The geology consists of layered sediments with a dominant fracture orientation approximately normal to the survey azimuth. The initial attempt at data acquisition was not successful because of problems inherent in our use of active accelerometers for a receiver sensor. Fortunately, a set of hydrophone receivers borrowed from Stanford University by Conoco Inc. was on site for testing with the LBL source. The

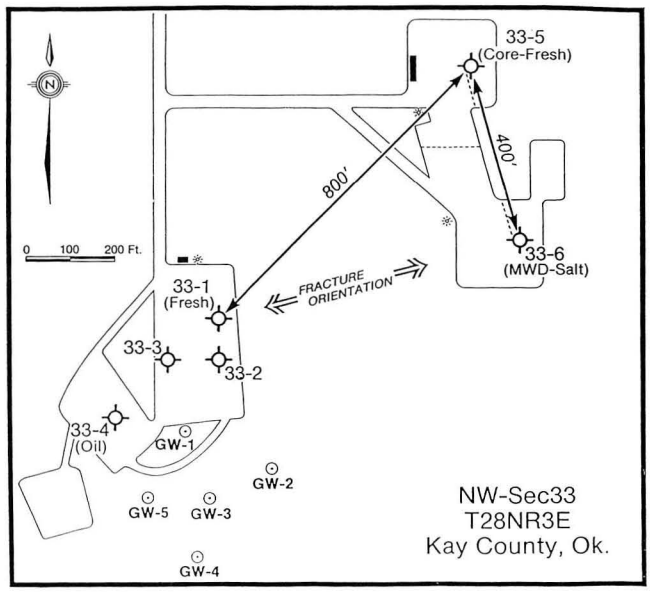

Figure 1. Layout map of the Conoco Borehole Test Facility. Cross-hole seismic surveys were conducted between wells 33-5 and 33-6 at greater depths (down to 2400 feet) and between the GW wells at shallow depths (less than 120 ft). [XBL 934-489]

data acquired with these hydrophones was quite good. Figure 2 shows data acquired with this setup at 5-ft intervals from 1400 to 1645 ft for a receiver at 1450 ft. We were able to acquire high-frequency data with source-receiver separations of up to 500 ft. The data in Figure 2a were produced by

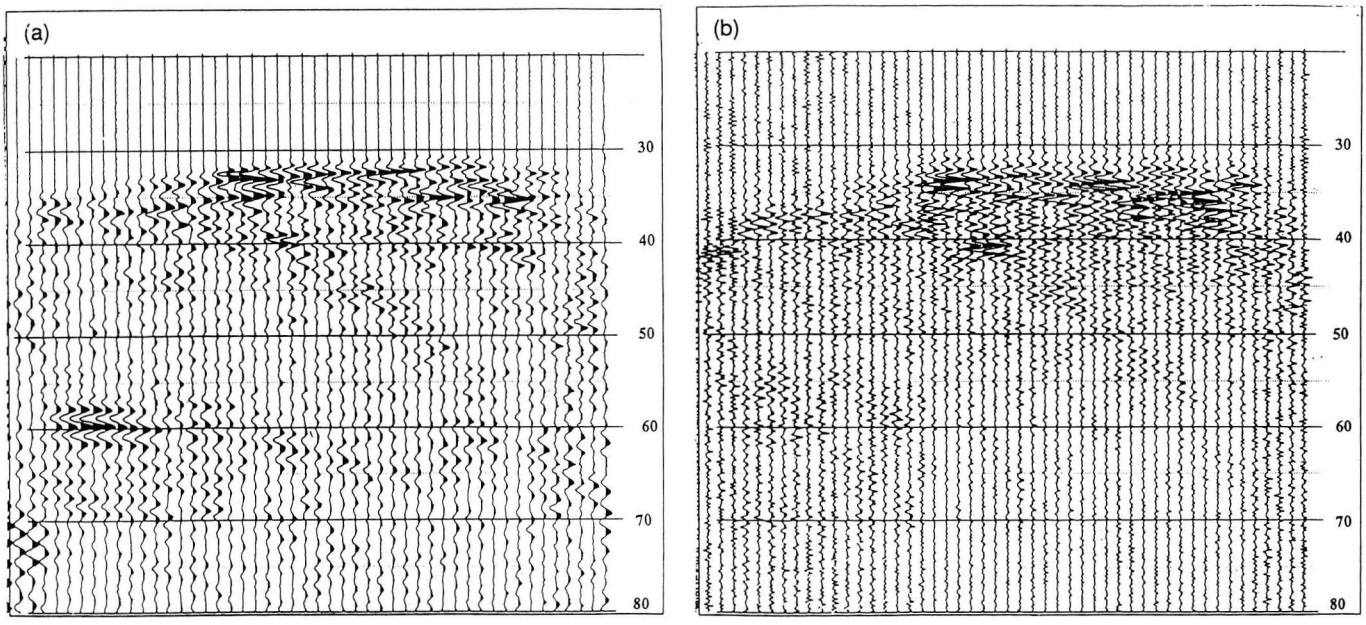

Figure 2. (**a**) A receiver gather of cross-hole seismic traces from the Conoco test site. The receiver was fixed at 1450 ft in well 33-6, and the source was fired at 5-ft intervals between 1400 ft and 1640 ft in well 33-5. The time scale on the right side is in milliseconds. (**b**) Same geometry as in part (a), but the source was swept and the data correlated with a 500- to 4000-Hz linear sweep. The time scale on the right side is in milliseconds. [XBL 934-490]

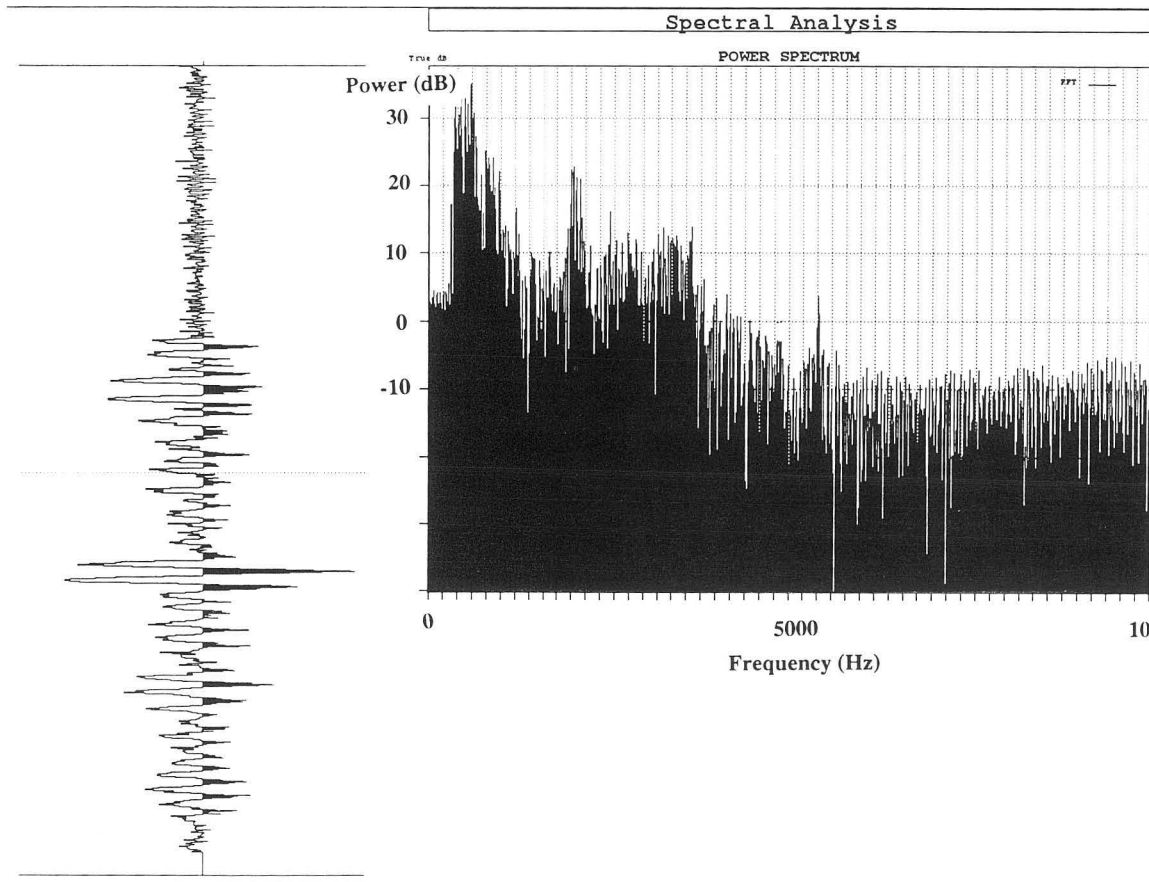

Figure 3. Power spectra of a cross-hole seismic trace from the deep Conoco wells for a pulsed source. The background noise level is about –10 dB; signal levels above +10 dB are seen from about 500 to 3600 Hz. [XBL 934-491]

pulsing the source, whereas the data in Figure 2b were produced using a swept-frequency signal that was correlated to produce the displayed section. The pulsed source gives a higher signal level, especially at the longer source-receiver separations. However, the swept source gives higher frequencies and better resolution. Figure 3 shows a sample trace from the pulse data and a Fourier transform of the trace demonstrating signal content up to 5000 Hz. These data show the potential uses of the LBL imaging system at depths and separations used in petroleum reservoir studies.

In a separate experiment conducted at the Conoco facility, 5 cross-well surveys were recorded in the shallow groundwater wells (GW-1 through GW-5 in Figure 1). These data, reported upon in another article in this volume (Daley et al., 1992), demonstrate the use of the LBL imaging system at depths and separations used for groundwater and contamination studies.

A third data set, acquired in layered volcanic tuffs in the C-hole complex at Yucca Mountain, Nevada, is part of a full cross-well tomography survey conducted to verify the usefulness of seismic imaging in the geologic setting of the proposed nuclear waste disposal site. Planned uses include characterizing fracture content and orientation for incorporation in hydrologic modeling. This survey included over 22,000 individual seismograms recorded within a 1700-ft interval between 2 wells about 100 ft apart. Figure 4 shows a typical set of seismic traces for one receiver position. The frequency content of this data set is above 5000 Hz, as shown in Figure 5. The C-hole survey was conducted over 3 weeks, including 8 to 10 consecutive days of more than 10-hour operation at this relatively remote and harsh environment on the edge of the Nevada Test Site. This work effectively demonstrates the high quality of data that can be acquired by the LBL seismic imaging system.

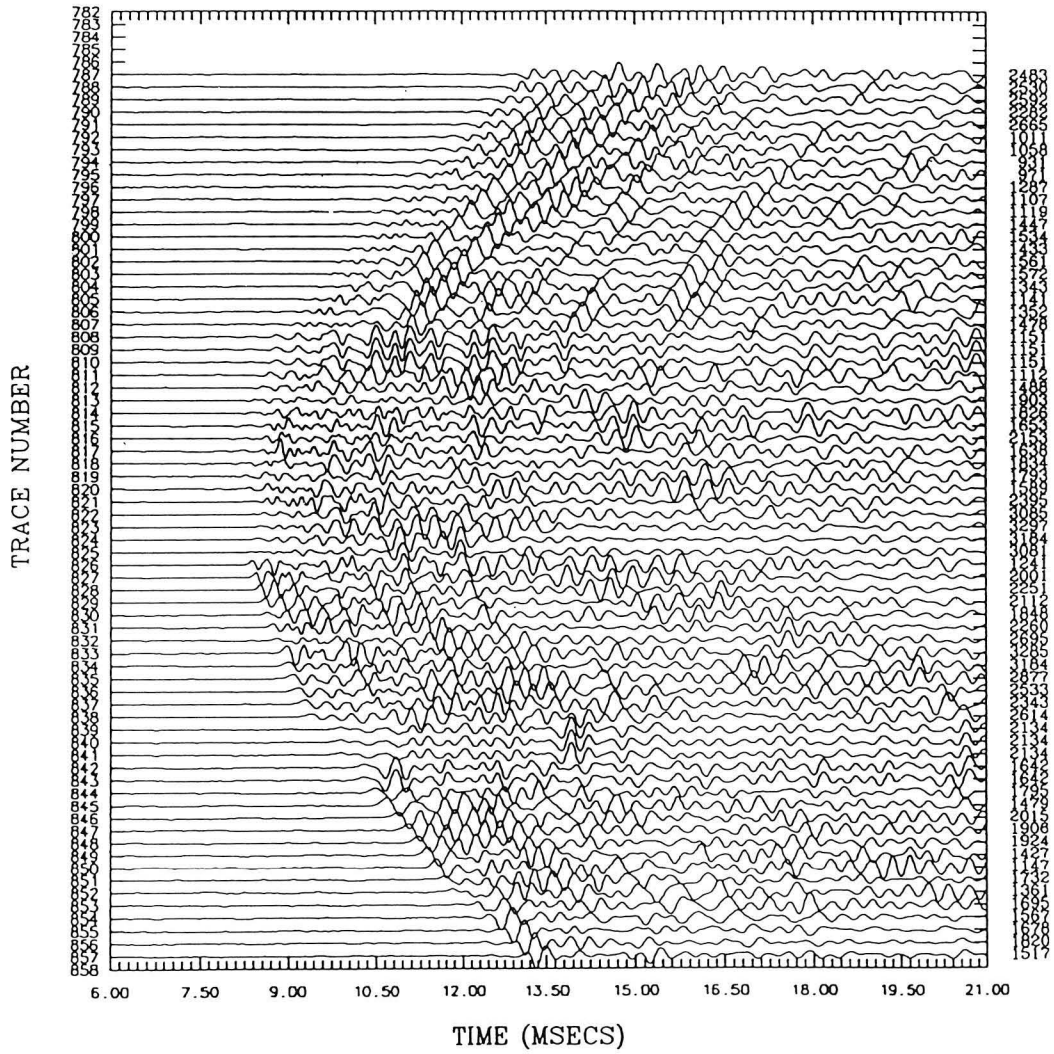

Figure 4. A receiver gather of cross-hole seismic traces from the Yucca Mountain C-holes. The receiver is at 817 m depth in well C-2. The source was fired every 1 m from 787 m to 857 m. Multiple arrivals can be seen, as well as depth zones that have high-amplitude later arrivals. The maximum amplitude of each trace is plotted on the right and source depth on the left. [XBL 934-492]

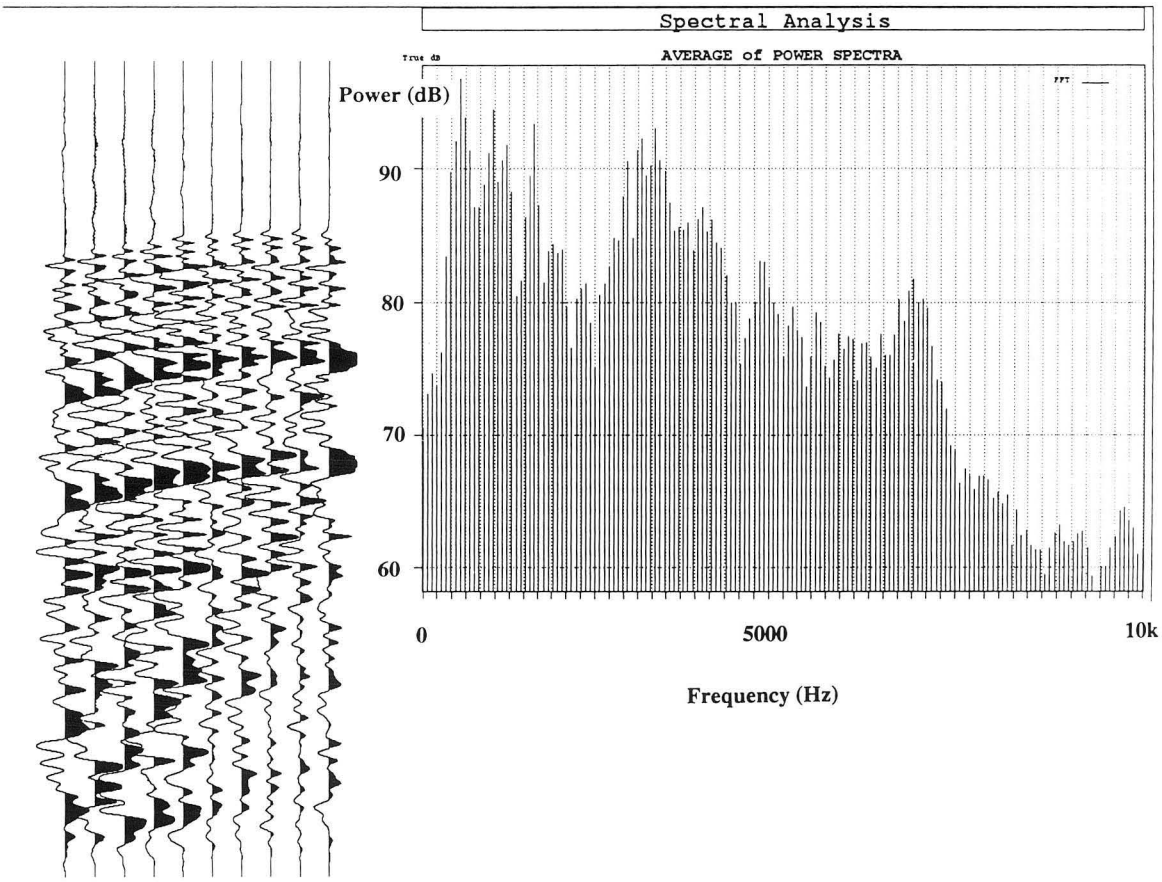

Figure 5. A power spectrum for a suite of 10 traces from the Yucca Mountain data set. The traces are plotted on the left. The background noise level is about 65 dB. Signal levels of 80 dB and above are seen between 400 and 7000 Hz. [XBL 934-493]

REFERENCES

Daley, T.M., Majer, E.L., Long, J.C.S., Hestir, K., D'Onfro, P.D., Rizer, W.D., and Queen, J.H., 1992. LBL/Industry heterogeneous reservoir performance definition project: The Conoco site. *In this Annual Report.*

Lines, L.R., Kelly, K.R., and Queen, J.H., 1992. Channel waves in cross-borehole data. Geophysics, v. 5, p. 1–9.

Queen, J.H., and Rizer, W.D., 1990. An integrated study of seismic anisotropy and the natural fracture system at the Conoco borehole test facility, Kay County, Oklahoma. J. of Geophys. Res., v. 95, p. 11255–11273.

A Search for Production-Induced Changes in Seismicity or Seismic Velocities at the Northwest Geysers Geothermal Field, California

A. E. Romero Jr., T. V. McEvilly, E. L. Majer, J. E. Peterson Jr., and T. M. Daley

Temporal changes in the velocity structure and seismicity patterns in response to geothermal activity were investigated in the Central California Power Assoc. (CCPA) operating area at the Northwest Geysers geothermal field. Particular attention was focused on the changes in the *Vp/Vs* structure because of its sensitivity to fluid saturation changes expected in a geothermal region. Two time periods were analyzed separately: January to June 1988, when the CCPA field was being tested; and July to December 1988, when the field was in sustained production. The average production rates for the two periods were 570 and 740 kph, respectively (A. Nunez, personal communication, 1992).

The data set consists of carefully picked *P*- and *S*-wave arrival times recorded by a 16-element borehole net-

work. From the 5000 events recorded during the year, 300 high-quality events were selected for each of the time periods for the joint hypocenter-velocity inversion. The region was parametrized into a 3-D rectangular grid with velocities assigned to each nodal point. The grid contains 294 nodes spaced at 3 km (×7 nodes) horizontally, and 1 km (×6 nodes) vertically. The joint problem for 3-D velocity structure and hypocenter locations is solved using the progressive inversion scheme proposed by Thurber (1983) with cubic spline interpolation (Michelini, 1991).

Several previous studies have concluded that the high seismicity in The Geysers region is related to geothermal development (Eberhart-Phillips and Oppenheimer, 1984; Stark, 1990; Romero, et al., 1992). Results of the present study indicate further that seismicity rate is related to production and injection and that changes in reservoir properties due to exploitation may be detected. Figure 1 shows the relocated hypocenters of the events around the CCPA area. Microearthquake hypocenters are concentrated within the CCPA field and extend south and east into the older sections of the producing field. Seismicity is low to the north and west in the direction where the field is undeveloped. Seismicity occurs at two zones: a broad, shallow zone between 1 and 3 km depth, presumably related to the production zone, and a deeper cluster between 3.5 and 5 km depth just beyond the southeast edge of the field. A cluster of microearthquakes with focal depths between 2 and 3 km is located beneath the injector well Prati-8, as shown in Figure 2. The microearthquake distribution seems to define a vertical planar structure striking roughly north-south.

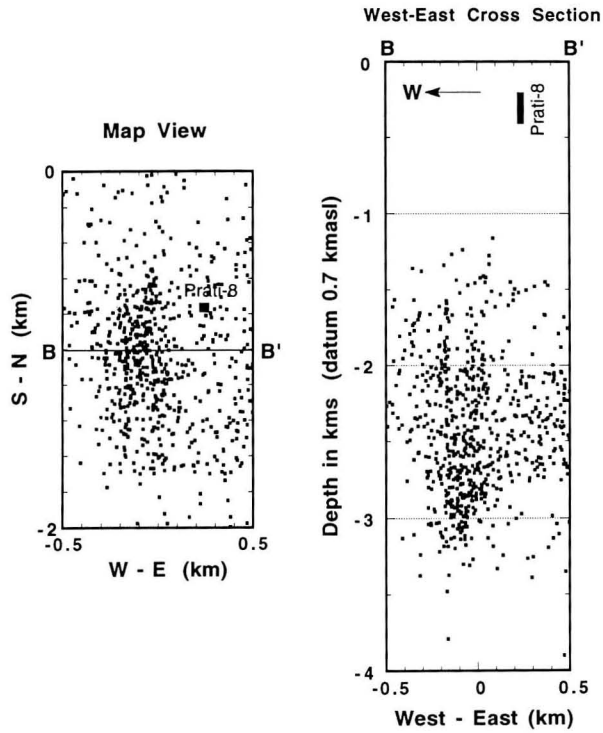

Figure 2. Map view and W-E cross section showing the locations of microearthquakes around the injector Prati-8. The microearthquake distribution seems to define a vertical plane striking N-S. Datum plane is 0.7 kmasl. [XBL 933-407]

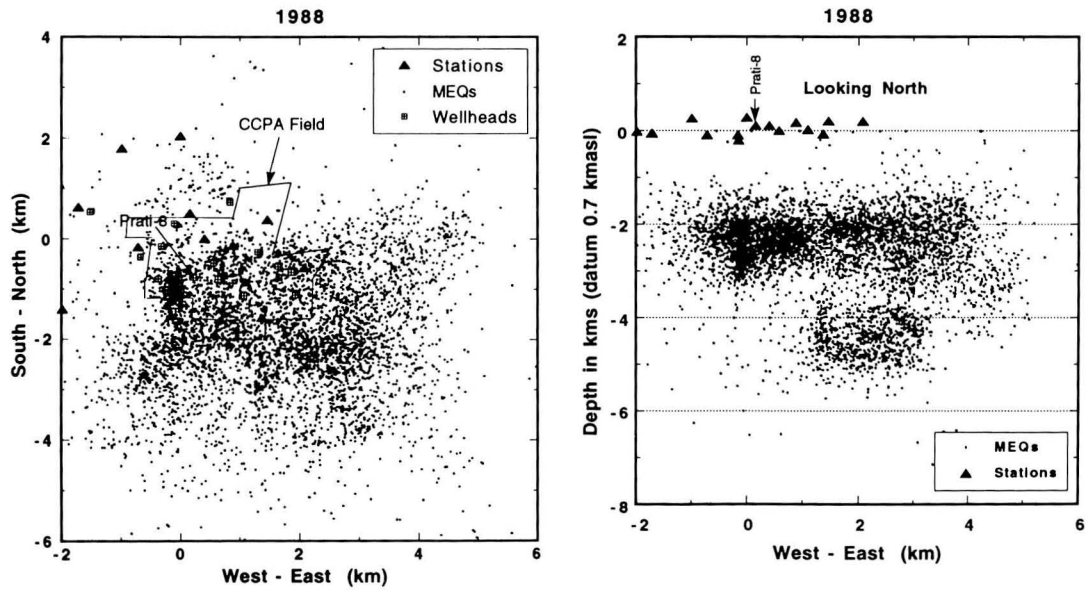

Figure 1. Map view and W-E cross section showing the locations of microearthquakes during the study period around the CCPA geothermal field. Microearthquake hypocenters are concentrated within the central part of the field and extend south and east. Seismicity is low to the north where the field is not being produced. Note the clustering of events beneath the injector Prati-8. Datum plane is 0.7 kmasl. [XBL 933-406]

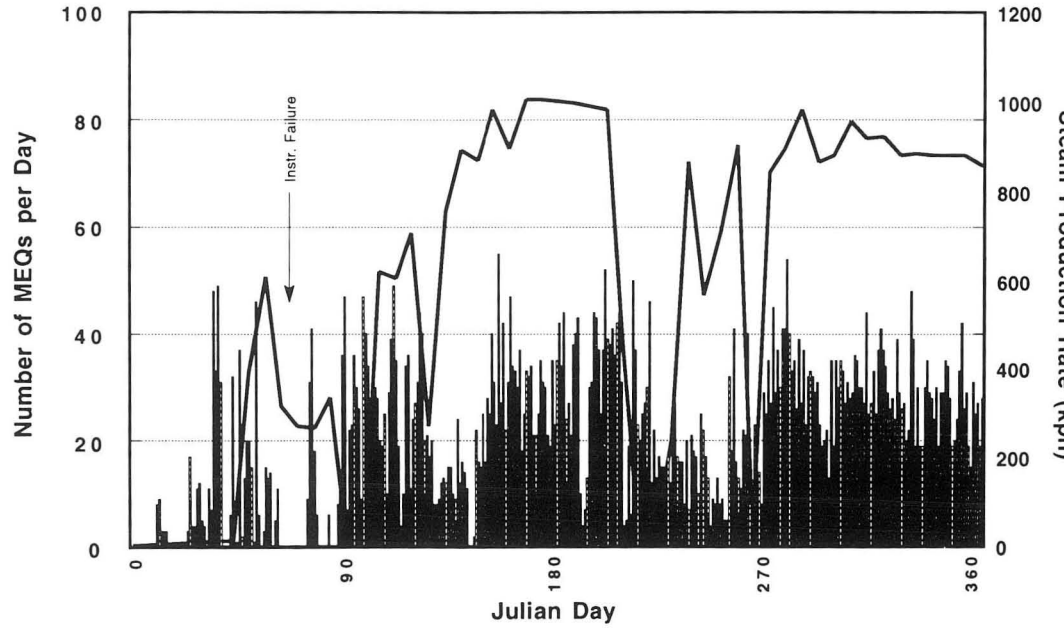

Figure 3. Comparison between the seismicity rate within the CCPA area and field-wide steam production rate. Seismicity more than doubled with the start of sustained production. [XBL 933-408]

Figure 3 compares the seismicity rate within the CCPA area and the field-wide steam production rate. Beginning at Julian day 90, 1988, seismicity increased significantly to approximately 20 events per day, more than double the pre-production seismicity rate. High seismicity was sustained during the course of steam production except during a short lull between Julian days 225 and 270, when production rate decreased temporarily. Figure 4 compares

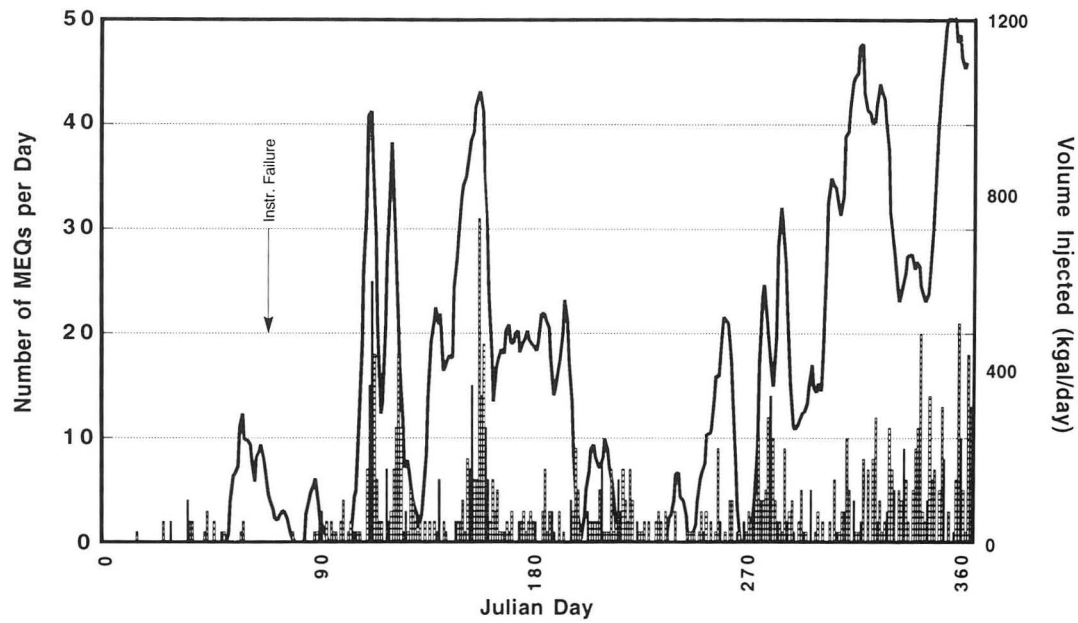

Figure 4. Comparison between injection history of Prati-8 and seismicity rate nearby. Note the good correlation between peaks in seismic activity and injection rate. [XBL 933-409]

Prati-8's injection history and the seismicity rate nearby. Note the good correlation between peaks in seismic activity and injection rate. Seismicity increased with the start of sustained injection, and peaks in seismicity occurred during periods of maximum injection. Spatial and temporal correlation between injection activity and seismicity provide compelling evidence for induced seismicity around Prati-8.

Despite the differences in the production rate, no substantial change in the *Vp/Vs* structure was evident between the two time periods (January to June and July to December 1988). One possible reason is that six months may not be sufficient time to detect appreciable changes in reservoir properties. The production zone is marked by a low *Vp/Vs* ratio between depths of 1 and 3 km, suggesting undersaturation of the reservoir rocks. Although poorly resolved, the region with high *Vp/Vs* ratio located east of the field at 1 km depth suggests the possibility of increased fluid saturation, the presence of more fractures, or a region of higher permeability. The temporal change in the *Vp/Vs* structure from early to late 1988 is shown in Figure 5. *Vp/Vs* decreased slightly within the central part of the producing horizon between 1 and 3 km depth. This observation may indicate further undersaturation of the reservoir rocks in response to continued steam withdrawal.

The results of this study have shown that the velocity structure and the seismicity pattern in the Northwest Geysers area seem to be related to geothermal exploitation. Although tentative, the slight decrease in *Vp/Vs* ratio within the producing zone is consistent with continued depletion of reservoir rocks as the field is produced. Ongoing monitoring of *Vp/Vs* may be useful in tracking the expansion of the steam zone with time. Spatial and temporal correlation between seismicity and geothermal activity provide compelling evidence for induced seismicity. High-resolution

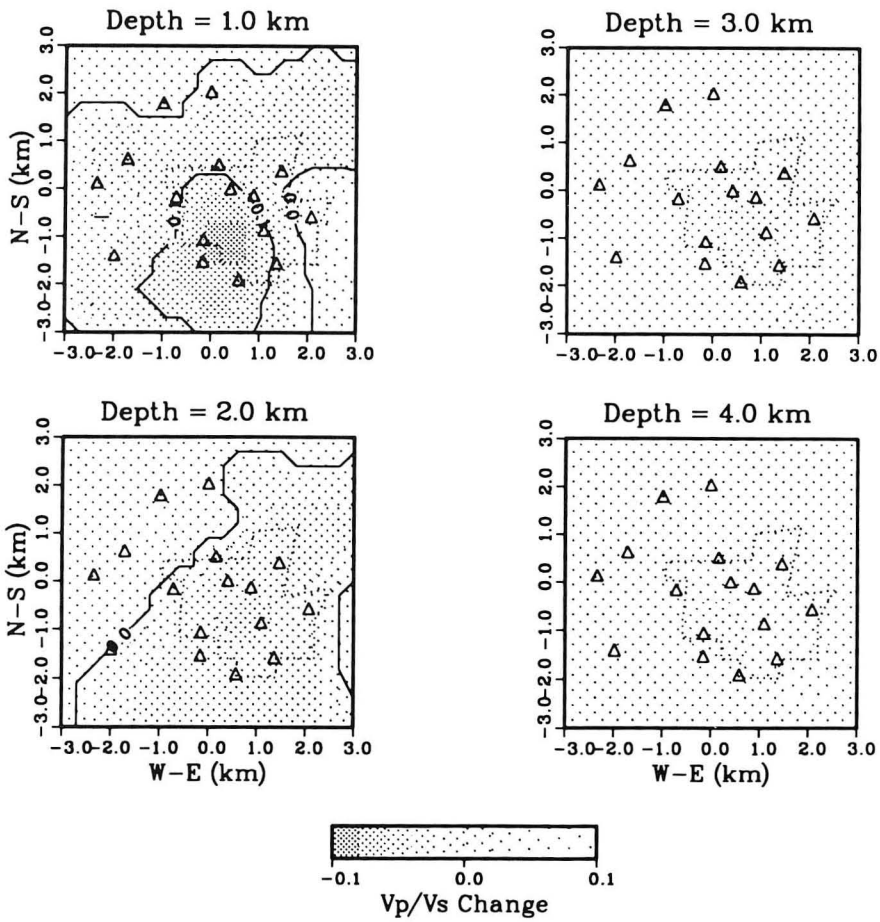

Figure 5. The temporal changes in the *Vp/Vs* structure between the first and second half of 1988. *Vp/Vs* decreased slightly within the central part of the producing zone between 1 and 3 km depth, indicating further undersaturation of the reservoir rocks in response to continued steam withdrawal. Triangles denote seismometer locations. Outline of CCPA field is shown for reference. [XBL 933-410]

microearthquake locations hold promise for inferring fluid flow paths, especially in tracking injectate. This work was conducted as part of the Department of Energy's Geothermal Reservoir Technology Program.

REFERENCES

Eberhart-Phillips, D., and Oppenheimer, D.H., 1984. Induced seismicity in The Geysers geothermal area, California. J. Geophys. Res., v. 89, p. 1191–1207.

Michelini, A., 1991. Fault zone structure determined through the analysis of earthquake arrival times. Ph.D. Thesis, University of California at Berkeley. Lawrence Berkeley Laboratory Report LBL-31534.

Romero, A.E., McEvilly, T.V., Majer, E.L., Peterson, J.E., and Daley, T.M, 1992. Initial results of the microseismic monitoring at The Geysers. *In* Lawrence Berkeley Laboratory Annual Report 1991 (LBL-31500).

Stark, M.A., 1990. Imaging injected water in The Geysers reservoir using microearthquake data. Geoth. Resour. Counc. Trans., v. 14, p. 1697–1704.

Thurber, C.H., 1983. Earthquake locations and three-dimensional crustal structure in the Coyote Lake area, Central California. J. Geophys. Res., v. 88, p. 8226–8236.

Nonlinear Interaction of Plane Elastic Waves

V. A. Korneev, L. R. Myer, and T. V. McEvilly

Nonlinearity is ordinarily not included in studies of elastic-wave propagation phenomena. It is well known that under sufficiently large stresses, solids deform by plastic flow or by strain hardening, etc. However, as shown by the results of measurements and numerical experiments in solid-state physics (Zarembo and Krasil'nikov, 1970), even for regular strain values there could be clearly pronounced nonlinear effects, such as generation of secondary harmonics, scattering of one wave by another, or nonlinear resonance. According to the nonlinear theory of elasticity (Murnaghan, 1951), macroscopic nonlinear elastic properties of solids are determined by the nonlinear relation between the components of the strain tensor and the derivatives of the displacements with respect to the coordinates. This feature of finite strain does not depend on the physical properties of the deformed body and is usually called geometrical nonlinearity. The physical nonlinearity is due to the fact that the internal energy of the deformed solid is not only a quadratic function of the invariants of the strain tensor but also a cubic one. The physical nonlinearity is determined by the elastic moduli of third, fourth, and higher orders. The existence of both geometrical and physical nonlinearity makes the generalized Hook's law (the connection between the stresses and the strains) also nonlinear, and its nonlinearities are determined by the geometrical and physical nonlinearities simultaneously.

INTERACTION OF TWO WAVES

To study the interaction of two elastic waves in a nonlinear elastic medium, we retain terms of cubic degree in the strain energy function to derive an equation of motion in the form

$$\rho\frac{\partial^2 U_i}{\partial t^2}-\mu\frac{\partial^2 u_i}{\partial x_k^2}-(\lambda+\mu)\frac{\partial^2 u_k}{\partial x_k\partial x_i}=F_i\ , \tag{1}$$

where F_i is given by

$$F_i = C_1\left(\frac{\partial^2 u_s}{\partial x_k^2}\frac{\partial u_s}{\partial x_i}+\frac{\partial^2 u_s}{\partial x_k^2}\frac{\partial u_i}{\partial x_s}+2\frac{\partial^2 u_i}{\partial x_s\partial x_k}\frac{\partial u_s}{\partial x_k}\right)$$

$$+C_2\left(\frac{\partial^2 u_s}{\partial x_i\partial x_k}\frac{\partial u_s}{\partial x_k}+\frac{\partial^2 u_k}{\partial x_s\partial x_k}\frac{\partial u_i}{\partial x_s}\right)$$

$$+C_3\frac{\partial^2 u_i}{\partial x_k^2}\frac{\partial u_s}{\partial x_s}+C_4\left(\frac{\partial^2 u_k}{\partial x_s\partial x_k}\frac{\partial u_s}{\partial x_i}+\frac{\partial^2 u_s}{\partial x_i\partial x_k}\frac{\partial u_k}{\partial x_s}\right)$$

$$+C_5\frac{\partial^2 u_k}{\partial x_i\partial x_k}\frac{\partial u_s}{\partial x_s}\ .$$

The scattered field due to interaction of two beams in a volume V (Figure 1),

$$\mathbf{u}_0 = \mathbf{A}_0 \cos(\omega_1 t - \mathbf{k}_1 \mathbf{r}) + \mathbf{B}_0 \cos(\omega_2 t - \mathbf{k}_2 \mathbf{r}) \,, \tag{2}$$

is given by (Jones and Kobett, 1963):

$$\mathbf{u}_1(\mathbf{r},t) = \frac{(\mathbf{I}^+\hat{\mathbf{r}})\hat{\mathbf{r}}}{4\pi v_p^2 \rho r} \int_V \sin\left[\left(\frac{\omega_1+\omega_2}{v_p}\hat{\mathbf{r}} - \mathbf{k}_1 - \mathbf{k}_2\right)\cdot \mathbf{r}' - (\omega_1+\omega_2)\left(\frac{r}{v_p} - t\right)\right] dV$$

$$+ \frac{(\mathbf{I}^-\hat{\mathbf{r}})\hat{\mathbf{r}}}{4\pi v_p^2 \rho r} \int_V \sin\left[\left(\frac{\omega_1-\omega_2}{v_p}\hat{\mathbf{r}} - \mathbf{k}_1 - \mathbf{k}_2\right)\cdot \mathbf{r}' - (\omega_1-\omega_2)\left(\frac{r}{v_p} - t\right)\right] dV$$

$$+ \frac{\mathbf{I}^+ - (\mathbf{I}^+\hat{\mathbf{r}})\hat{\mathbf{r}}}{4\pi v_s^2 \rho r} \int_V \sin\left[\left(\frac{\omega_1+\omega_2}{v_s}\hat{\mathbf{r}} - \mathbf{k}_1 - \mathbf{k}_2\right)\cdot \mathbf{r}' - (\omega_1+\omega_2)\left(\frac{r}{v_s} - t\right)\right] dV$$

$$+ \frac{\mathbf{I}^- - (\mathbf{I}^-\hat{\mathbf{r}})\hat{\mathbf{r}}}{4\pi v_s^2 \rho r} \int_V \sin\left[\left(\frac{\omega_1-\omega_2}{v_s}\hat{\mathbf{r}} - \mathbf{k}_1 - \mathbf{k}_2\right)\cdot \mathbf{r}' - (\omega_1-\omega_2)\left(\frac{r}{v_s} - t\right)\right] dV \,, \tag{3}$$

where

$$\mathbf{I}^{\pm} = -\frac{1}{2}C_1\left[(\mathbf{A}_0\mathbf{B}_0)(\mathbf{k}_2\mathbf{k}_2)\mathbf{k}_1 \pm (\mathbf{A}_0\mathbf{B}_0)(\mathbf{k}_1\mathbf{k}_1)\mathbf{k}_2 + (\mathbf{B}_0\mathbf{k}_1)(\mathbf{k}_2\mathbf{k}_2)\mathbf{A}_0 + (\mathbf{A}_0\mathbf{k}_2)(\mathbf{k}_1\mathbf{k}_1)\mathbf{B}_0 + \right.$$

$$\left. 2(\mathbf{A}_0\mathbf{k}_2)(\mathbf{k}_1\mathbf{k}_2)\mathbf{B}_0 \pm 2(\mathbf{B}_0\mathbf{k}_1)(\mathbf{k}_1\mathbf{k}_2)\mathbf{A}_0\right]$$

$$-\frac{1}{2}C_2\left[(\mathbf{A}_0\mathbf{B}_0)(\mathbf{k}_1\mathbf{k}_2)\mathbf{k}_2 \pm (\mathbf{A}_0\mathbf{B}_0)(\mathbf{k}_1\mathbf{k}_2)\mathbf{k}_1 + (\mathbf{B}_0\mathbf{k}_2)(\mathbf{k}_1\mathbf{k}_2)\mathbf{A}_0 + (\mathbf{A}_0\mathbf{k}_1)(\mathbf{k}_1\mathbf{k}_2)\mathbf{B}_0\right]$$

$$-\frac{1}{2}C_3\left[(\mathbf{A}_0\mathbf{k}_2)(\mathbf{B}_0\mathbf{k}_2)\mathbf{k}_1 \pm (\mathbf{A}_0\mathbf{k}_1)(\mathbf{B}_0\mathbf{k}_1)\mathbf{k}_2 + (\mathbf{A}_0\mathbf{k}_2)(\mathbf{B}_0\mathbf{k}_1)\mathbf{k}_2 \pm (\mathbf{A}_0\mathbf{k}_2)(\mathbf{B}_0\mathbf{k}_1)\mathbf{k}_1\right]$$

$$-\frac{1}{2}C_4\left[(\mathbf{A}_0\mathbf{k}_1)(\mathbf{B}_0\mathbf{k}_2)\mathbf{k}_2 \pm (\mathbf{A}_0\mathbf{k}_1)(\mathbf{B}_0\mathbf{k}_2)\mathbf{k}_1\right] - \frac{1}{2}C_5\left[(\mathbf{A}_0\mathbf{k}_1)(\mathbf{k}_2\mathbf{k}_2)\mathbf{B}_0 \pm (\mathbf{B}_0\mathbf{k}_2)(\mathbf{k}_1\mathbf{k}_1)\mathbf{A}_0\right]$$

and

$$C_1 = \mu + \frac{A}{4}, \quad C_2 = \lambda + \mu + \frac{A}{4} + B, \quad C_3 = \frac{A}{4} + B,$$

$$C_4 = B + 2C, \quad C_5 = \lambda + B.$$

Parameters μ and λ are Lamé constants, and A, B, and C are the third-order constants of Landau and Lifshits (1953). Vector $\mathbf{r} = r\hat{\mathbf{r}}$; $|\hat{\mathbf{r}}| = 1$ is the radius vector from the center point of the interaction region and observation point; and $\mathbf{r}'$ is the radius vector of integration inside the volume V (geometry shown in Figure 1).

The first and second terms in (3) are compressional waves, with the sum frequency represented by $\omega_1 + \omega_2$ and the difference frequency by $\omega_1 + \omega_2$, respectively. The third and fourth terms are shear waves, with the same sum and difference frequencies. As we integrate over $\mathbf{r}¢$, all the integrands in (3) oscillate with frequencies determined by the coefficients of $\mathbf{r}¢$, and the results of any integration will depend on just how the waves fit into the region V. Scattered waves have natural polarization: parallel to $\mathbf{r}$ for P-waves and orthogonal to $\mathbf{r}$ for S-waves. The integrals in (3) are so-called volume factors.

If we satisfy resonant conditions,

$$\omega_r = \omega_1 \pm \omega_2 \,, \tag{4'}$$

$$\mathbf{k}_r = \mathbf{k}_1 \pm \mathbf{k}_2 \,. \tag{4''}$$

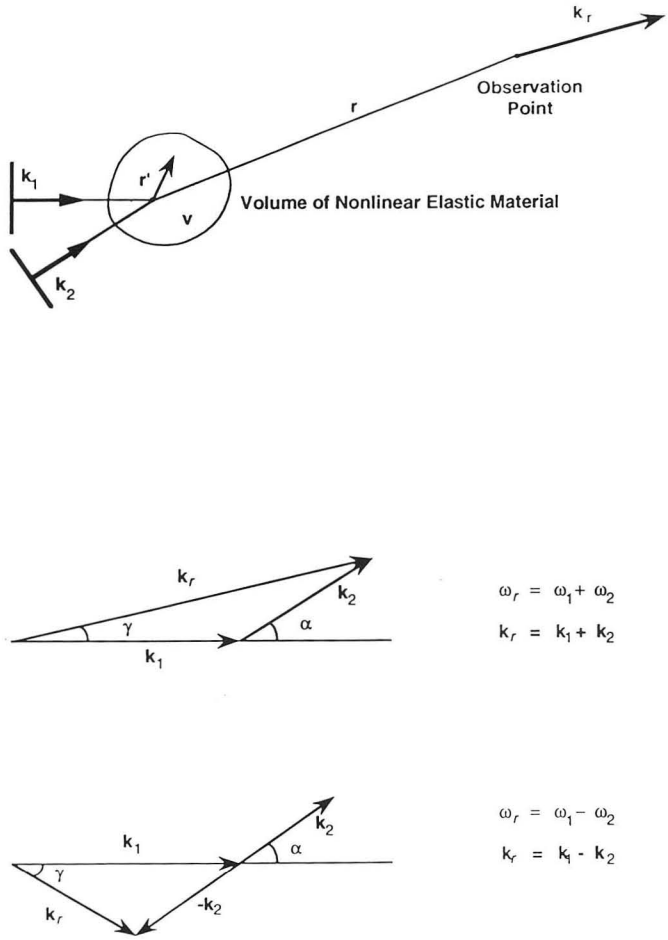

Figure 1. Interaction and resonant conditions for two plane waves in a volume V of elastic material. [XBL 933-411]

If appropriate directions of wave vectors are chosen, the scattered waves become proportional to the volume V of integration. The upper plus sign in (4) corresponds to the case of the sum resonant frequency, and the minus sign corresponds to the case of the difference resonant frequency.

From (3) it also follows that amplitudes of the scattered waves are proportional to their projections on the natural unit vector of polarization. This means that the resonant scattering amplitude may be zero even if resonant conditions (4) are satisfied. Zero scattering amplitude due to polarization are referred to as polarization restriction.

All types of elastic-wave resonant interactions are shown in Table 1, where the symbol × means that interaction is possible and the symbol → means that interaction is possible only when interacting waves are collinear. All other types of interactions are forbidden. The letter O indicates interactions that are forbidden because of polarization restrictions; all others are forbidden because the resonant conditions (4) for them cannot be satisfied. As one can see, only 10 of 54 interactions are possible. Sum frequency resonance may exist for compressional scattered waves only.

The ratio of the amplitudes of the scattered waves to the amplitudes of the primary waves can be found by using the values of W shown in Figure 2 for the interaction $P(\omega_1) + SV(\omega_2) = P(\omega_1 + \omega_2)$. If the amplitudes of the primary waves are assumed to be equal and given by U_0, the ratio of the scattered wave amplitude, U_{sc} to U, is proportional to

$$\frac{U_{sc}}{U_0} = WU_0 \frac{V}{r} \omega_1^3 \cdot 10^{-16} \quad \text{(CGS)} .$$

Table 1. Forbidden and allowed scattering processes for an isotropic solid.

No.	Interaction waves		Scattered waves					
				$\omega_1 + \omega_2$			$\omega_1 - \omega_2$	
			P	*SV*	*SH*	*P*	*SV*	*SH*
1	$P(\omega_1)$	$P(\omega_2)$	→			→	×	O
2	$P(\omega_1)$	$SV(\omega_2)$	×			×	×	O
3	$SV(\omega_1)$	$P(\omega_2)$	×					
4	$SV(\omega_1)$	$SV(\omega_2)$	×	O	O		O	O
5	$SH(\omega_1)$	$SH(\omega_2)$	×	O	O		O	O
6	$P(\omega_1)$	$SH(\omega_2)$	O			O	O	×
7	$SH(\omega_1)$	$P(\omega_2)$	O					
8	$SH(\omega_1)$	$SV(\omega_2)$	O	O	O		O	O
9	$SV(\omega_1)$	$SH(\omega_2)$	O	O	O		O	O

Explanation of symbols: → = possible only when waves propagate in one direction; × = scattering possible; O = polarization restriction; blank space = interaction restriction.

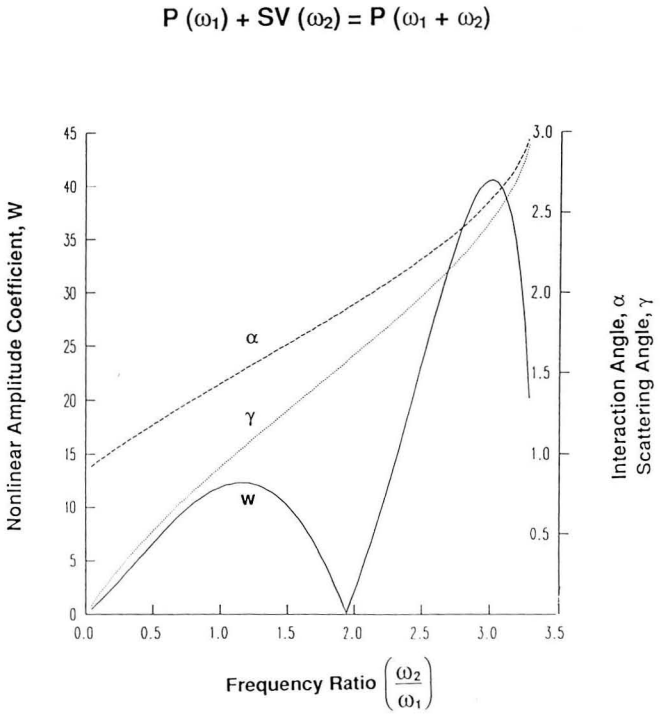

Figure 2. Nonlinear amplitude coefficient W versus frequency ratio ω_2/ω_1 for interaction $P(\omega_1) + SV(\omega_2) = P(\omega_1 + \omega_2)$. Angles α and γ are introduced in Figure 1. [XBL 933-412]

For example, for the values $V = 100$ m, r = 100 m, and $\omega_1 = 100$ rad/sec, and assuming strains on the order of 10 in sandstone, this ratio can be 10% or larger.

CONCLUSIONS

1. Out of 54 possible combinations of intersecting beams, in only 10 cases will resonant scattering occur.
2. Amplitudes of scattered waves, except for interactions of *SH* waves, are directly proportional to nonlinear elastic constants.
3. The results suggest that scattered waves with amplitudes that are a significant proportion of the primary wave amplitudes may arise due to nonlinear elastic properties of rocks.
4. The results also suggest that, for the interaction of two waves at different frequencies, scattered waves at sum frequencies will be of greater amplitude than those at difference frequencies.

REFERENCES

Jones, G.L., and Kobett, D.R., 1963. Interaction of elastic waves in an isotropic solid. J. Acoust. Soc. Am., v. 35, no. 1, p. 5–10.

Landau, L.D., and Lifshits, E.M., 1953. Theory of Elasticity. John Wiley, New York.

Murnaghan, F.D., 1951. Finite Deformation of Elastic Solids. John Wiley, New York.

Zarembo, L.K., and Krasil'nikov, V.A., 1971. Nonlinear phenomena in the propagation of elastic waves in solids. Soviet Physics Uspekhi, v. 13, no. 6, p. 778–797.

Wave-Path Travel-Time Tomography

D. W. Vasco and E. L. Majer

The elastic-wave equation is used to construct sensitivity kernels relating perturbations in elastic parameters to travel-time deviations. Computation of the functions requires a correlation of the forward-propagating seismic wave field with a backward propagation of the residual wave field. The computation of the wave fields may be accomplished using a finite difference algorithm and is efficiently executed on a parallel processor. The source and receiver locations have maximum sensitivity to velocity structure. The sensitivity kernels, or wave paths, are well suited for cross-borehole travel-time inversions. Conventional ray tomography and wave-path tomography are applied to a set of *P*-wave arrival times from a cross-borehole experiment at Kesterson, California. Because the wave paths have increased sensitivity near the source and receiver, there are differences in resolution of the velocity structure. Both techniques recover the same relative variations in velocity where the coverage is adequate. The ray approach places the maximum anomaly farther from the boreholes than does the wave-path inversion. This possibly reflects a smearing along ray paths.

A basic objective of this work is to derive wave paths for travel-time tomography. By wave paths we mean sensitivity kernels relating deviations in elastic structure to perturbations in travel-time, much as ray paths may be used to relate travel-time deviations to changes in wave speed

along the ray. However, the approach taken here proceeds directly from the elastic-wave equation and generalizes the derivation of Luo (1991), which was based on the acoustic-wave equation.

The travel time, T, of a seismic wave from a source to a given receiver is a functional of the elastic parameters $c^{ijkl}(x)$ of a body V,

$$T = \int_V \mathcal{F}\left\{x_s, x_r, c^{ijkl}(x)\right\} dV .$$

For small deviations, $\delta c^{ijkl}(x)$, from an initial model, $c_0{}^{ijkl}(x)$, the functional may be expanded in terms of the initial structure,

$$\mathcal{F}\left\{x_s, x_r, c^{ijkl}(x) + \delta c^{ijkl}(x)\right\} = \mathcal{F}\left\{x_s, x_r, c^{ijkl}{}_0(x)\right\}$$
$$+ \nabla_{ijkl}\mathcal{F}\left\{x_s, x_r, c^{ijkl}{}_0(x)\right\}\delta c^{ijkl}(x) + \ldots .$$

The summation convention is assumed in all equations that follow. $\nabla_{ijkl}\mathcal{F}\left\{x_s, x_r, c^{ijkl}{}_0(x)\right\}$, the Frechet derivative, is defined over all space and represents the change in travel time due to a perturbation in the elastic structure,

$$\frac{\partial T}{\partial c^{ijkl}(x)} .$$

It is equivalent to

$$-\frac{\partial \delta T}{\partial c^{ijkl}(x)} ,$$

where δT is the travel-time residual, i.e., the difference between the observed travel time, T_0, and the computed travel time. Neglecting terms of order $\delta^2 c^{ijkl}(x)$ and higher gives

$$\delta T = T - \int_V \mathcal{F}\left\{x_s, x_r, c^{ijkl}{}_0(x)\right\} dV$$
$$= \int_V \nabla_{ijkl}\mathcal{F}\left\{x_s, x_r, c^{ijkl}{}_0(x)\right\}\delta c^{ijkl}(x)\, dV .$$

This quantity depends on which method is used to determine travel-time residuals. It is increasingly common to estimate travel-time residuals by cross-correlating two waveforms, say the ith component of an observed seismogram, $u^i_{obs}(x_s, x_r, t)$, and a corresponding synthetic seismogram, $u^i(x_s, x_r, t)$,

$$C(\tau) = \int u^i_{obs}(x_s, x_r, t+\tau) u^i(x_s, x_r, t)\, dt ,$$

where $u^i_{obs}(x_s, x_r, t)$ is normalized to have a maximum amplitude identical to $u^i(x_s, x_r, t)$. Then the travel-time residual, δT, is the time shift τ that maximizes the cross-correlation function. For high-frequency impulsive waveforms, the shift will be nearly equivalent to the difference between picked first arrivals and calculated ray-theoretical travel times. Following Luo and Schuster (1991), the change in a travel-time residual due to a perturbation in elastic parameters is obtained using implicit differentiation to calculate the Frechet derivatives,

$$\frac{\partial \delta T}{\partial c^{ijkl}(x)} = \left[\frac{\partial C(\tau)}{\partial c^{ijkl}(x)}\right]\left[\frac{\partial C(\tau)}{\partial \delta T}\right]^{-1} .$$

Then

$$\delta(\delta T) = \int_V \frac{1}{E}\int_t \dot{u}^i_{obs}(x_s, x_r, t+\delta T)$$
$$\times \frac{\partial \dot{u}^i(x_s, x_r, t)}{\partial c^{ijkl}(x)}\delta c^{ijkl}(x) dt dV ,$$

where

$$E = \int_t \dot{u}^i_{obs}(x_s, x_r, t+\delta T)\dot{u}^i(x_s, x_r, t)\, dt .$$

It remains to compute the Frechet derivatives of the displacements with respect to the model parameter perturbations. Consider an isotropic medium, i.e., a medium described by Lamé's parameters $\lambda_0(x)$ and $\mu_0(x)$,

$$c^{ijkl}{}_0(x) = \lambda_0(x)\delta^{ij}\delta^{kl} + \mu_0(x)\left(\delta^{ik}\delta^{jl} + \delta^{il}\delta^{jk}\right) ,$$

and density $\rho_0(x)$, subject only to perturbations in these parameters, with no perturbations in surface tractions or body forces. Because the medium is completely represented by $\lambda(x)$, $\mu(x)$, and density $\rho(x)$, the expansion of the perturbed field is, to first order

$$\delta(\delta T) = \int_V \nabla_\lambda \mathcal{F}(x)\delta\lambda(x) dV + \int_V \nabla_\mu \mathcal{F}(x)\delta\mu(x) dV$$
$$+ \int_V \nabla_\rho \mathcal{F}(x)\delta\rho(x) dV .$$

The form of the wave-path kernels follows directly from Tarantola (1984),

$$\nabla_\lambda \mathcal{F}(x) = \left[\int_t \left(-G_{li,l}(x',t;x,0) * \dot{u}^i_{obs}(x_s,x_r,t)\right) u_{j,j}(x,t)dt\right] \times \left[\int_t \dot{u}^i_{obs}(x_s,x_r,t)\dot{u}^i(x_s,x_r,t)dt\right]^{-1},$$

$$\nabla_\mu \mathcal{F}(x) = \left[\int_t \left(-G_{ll,i}(x',t;x,0) * \dot{u}^i_{obs}(x_s,x_r,t)\right) u_{j,j}(x,t)dt\right] \times \left[\int_t \dot{u}^i_{obs}(x_s,x_r,t)\dot{u}^i(x_s,x_r,t)dt\right]^{-1},$$

$$\nabla_\rho \mathcal{F}(x) = \left[\int_t \left(-\dot{G}_{ij}(x',t;x,0) * \dot{u}^i_{obs}(x_s,x_r,t)\right) \dot{u}_j(x,t)dt\right] \times \left[\int_t \dot{u}^i_{obs}(x_s,x_r,t)\dot{u}^i(x_s,x_r,t)dt\right]^{-1}.$$

These are the desired integral forms relating the additional shift in the waveforms to deviations in medium parameters. Thus, by solving the wave equation in the reference medium twice, once to obtain the calculated displacement at the receivers and again to obtain the impulse response for a source at the receivers, it is possible to obtain the Frechet derivatives of displacement. These derivatives are expressed entirely in terms of observed and computable quantities.

If the shear modulus is assumed to vanish, the medium becomes acoustic and the pressure variations, $p(x)$, obey the scalar wave equation. The medium is now characterized by the bulk modulus, $K_0(x)$, as well as the density. For the acoustic-wave equation, the computation of the wave paths has been described by Luo (1991).

KESTERSON CROSS-HOLE EXPERIMENT

A series of cross-borehole seismic and hydrological experiments were conducted at Kesterson in the San Joaquin Valley of California. This was part of the Department of Energy's Subsurface Science Program to examine the relationship between seismic and hydrologic properties that might control fluid transport. A detailed description of the experiment is presented in Majer et al. (1991). Seven shallow (less than 15 m) wells were drilled through porous sands and gravels underlying a surface clay layer. A hydrological tracer test was conducted to determine the variation of permeability with depth. About halfway through the sand layer, a high-permeability zone was observed. Cross-hole experiments were subsequently undertaken to determine if the variations in permeability could be observed in seismic data. A piezoelectric system was used to transmit pulses containing frequencies up to 10 kHz between the boreholes. The transmitted energy was recorded by a string of unclamped accelerometers lowered into an adjacent water-filled borehole. The geometry of a subset of the data used in this work—230 source-receiver pairs from two wells, LBL-11 and LBL-5, less than 3 m apart—is shown in Figure 1. The *P* travel times, determined from the waveforms, were corrected for anisotropy (Majer et al., 1991). The resulting arrival times deviate only a few percent from those calculated using a homogeneous medium with a *P* velocity of 1.74 km/s. Thus a linearized approach is acceptable, and a homogeneous velocity model is an appropriate choice for a background. Because of interference from later phases, including modes within the borehole, the *S*-wave arrival times could not be picked. Therefore, only the *P* arrivals were considered, and the acoustic-wave equation was used to compute the wave paths. First arrivals were picked from the synthetic seismograms, and it was assumed that the predicted pulses were just time-shifted versions of the observed first pulses. Because of the high

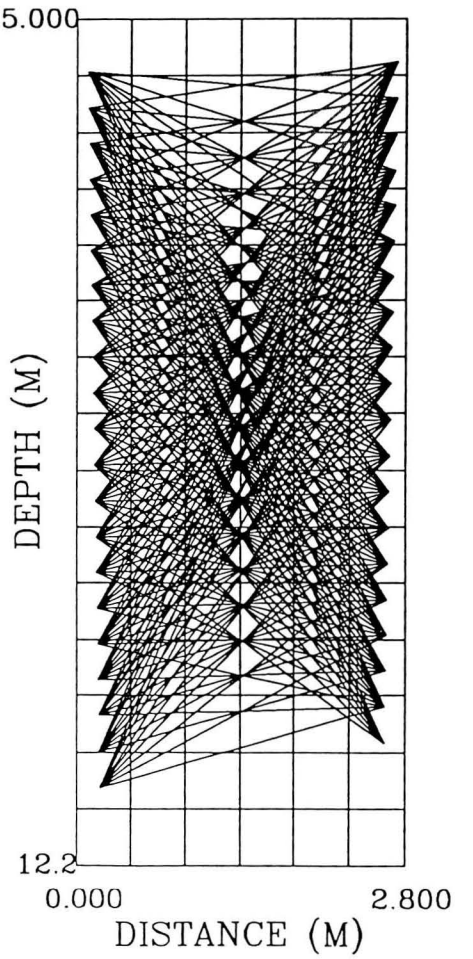

Figure 1. The geometry and straight ray paths for the subset of the Kesterson cross-hole data obtained from two wells less than 3 m apart. [XBL 933-413].

frequencies, node spacings of 2 cm were required, and the resulting grid was 550 nodes on a side and 750 nodes vertically. Some 230 wave paths were computed on the CM-2 at the Advanced Computing Laboratory of Los Alamos National Laboratory. The two wave paths shown in Figure 2 display a maximum in sensitivity at the source and receiver locations.

The area between the two boreholes was divided into a grid of cells, 6 on a side and 15 vertically. The integrated ray lengths and wave-path areas in each of the cells are shown in Figure 3. The upper and lower ends of the area are poorly sampled by both ray paths and wave paths. The sampling is reflected in the resolution of the velocity in each cell (Figure 4). Note the increased resolution near the sources and receivers in the wave-path resolution. This is very different from the ray-theoretical resolution and indicates that the near-source and receiver structure may be very important.

A singular value decomposition was used to determine the velocity deviations from the uniform background that agree with the travel-time observations in a least-squares sense. The resulting velocity variations are shown in Figure 5. The poorly sampled areas are not well determined and are not presented (white areas). Visible in both the ray-path and wave-path tomograms is a region of low velocity bounded above and below by higher velocities. The location of this feature is in agreement with the high-permeability zone determined by the tracer test. The wave-path velocity structure is generally smoother and more horizontally continuous than the ray-path result. The ray-path solution contains lateral variations between positive and negative anomalies over the length of a single block dimension. This is surprising for this layered sedimentary region, and these features are most likely artifacts of the inversion procedure.

DISCUSSION AND CONCLUSIONS

It is now possible to compute wave-path sensitivity kernels for band-limited seismograms. Wave-path-based inversion is well suited for cross-borehole data sets in which the waveform following the first arrival is a complex combination of oscillations due to the borehole. The wave-path kernels may be easily incorporated into current tomographic inversion algorithms. The wave-equation-based approach gives physical meaning to quantities used to assess the solution such as spatial averaging and correlation lengths. Moreover,

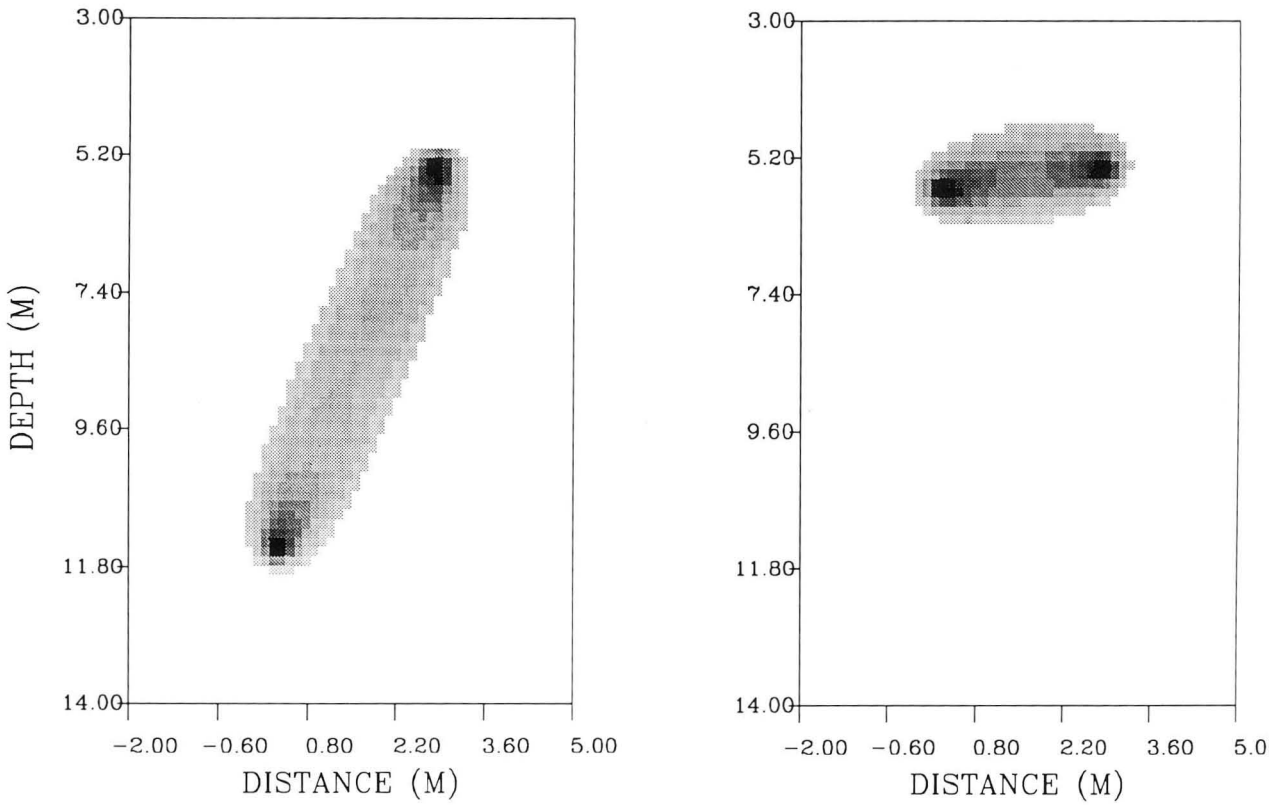

Figure 2. Two wave paths, displaying the maximum sensitivity at the source and receiver. The kernels have been normalized such that the shading varies from 0 (white) to 1 (black). [XBL 933-414]

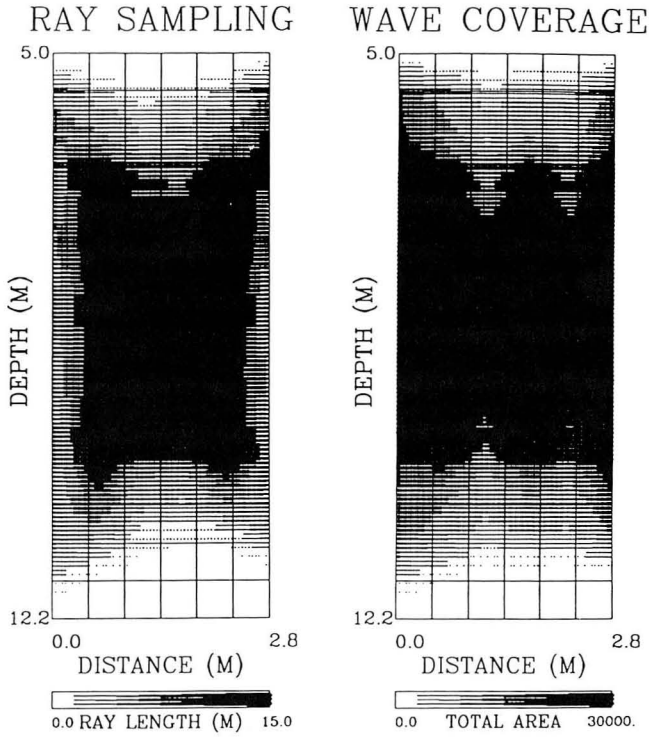

Figure 3. The area between the two boreholes was divided into a grid of cells, 6 on a side and 15 vertically. Shown here are the integrated ray lengths and wave-path areas in the cells. The ends of the boreholes are poorly sampled in both cases. [XBL 933-415]

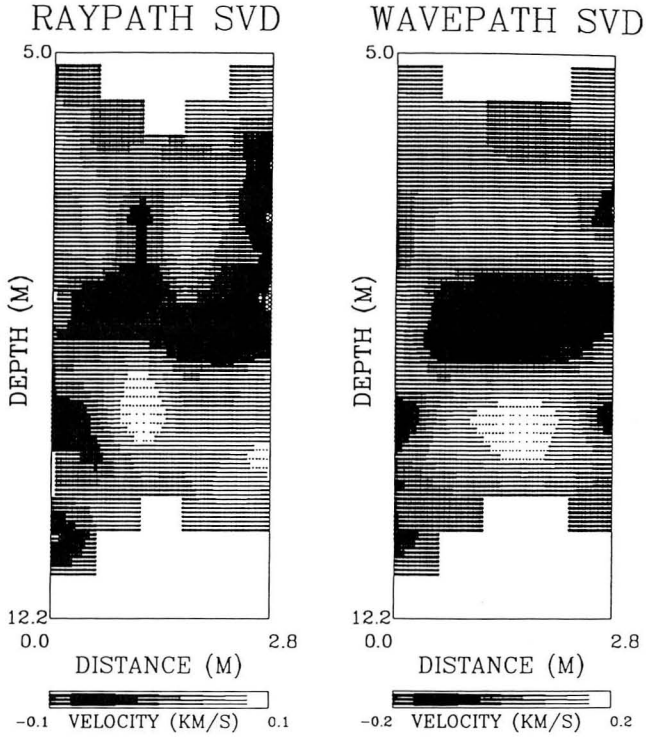

Figure 5. A singular-value decomposition was used to determine the velocity deviations from the uniform background that satisfy the travel-time observations in a least-squares sense. [XBL 933-417]

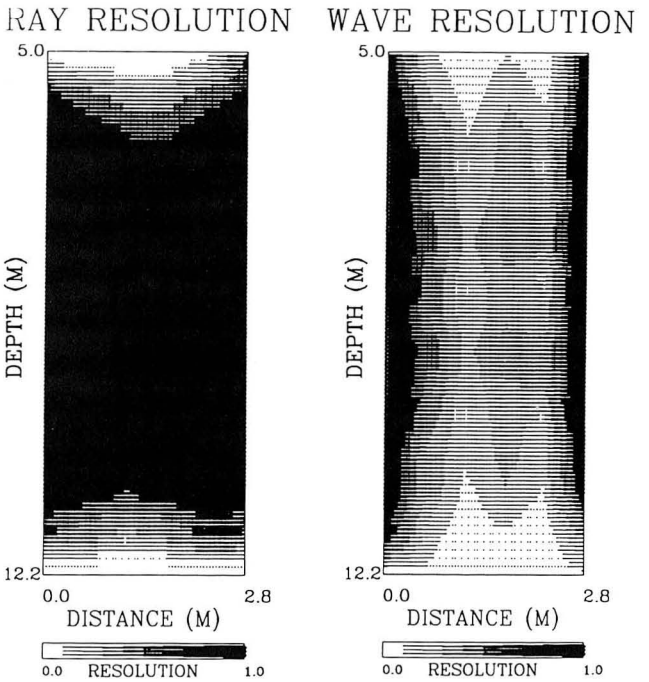

Figure 4. The sampling is reflected in the resolution of the velocity in each cell. Shown here are the diagonal elements of the resolution matrix for the ray-path and wave-path sensitivity functions. Note also the increased resolution near the sources and receivers in the wave-path resolution. [XBL 933-416]

it may be seen from the example that using wave paths as sensitivity kernels can produce fewer artifacts in velocity estimates. Though linearization about a uniform medium was adequate in the example presented here, the wave-path technique should prove more stable in treating the nonlinear inverse problem, in which iteration is necessary.

The computation of wave path is currently feasible for high-frequency cross-hole travel-time data sets like those presented here. The sensitivity kernels may even be computed for complicated anisotropic media, eliminating the need for ray tracing. Given further improvements in parallel computation, one of the most rapidly developing technologies, it should soon be practical to apply the method to three-dimensional data sets. As demonstrated above, the wave paths may be used as a basis for representing the velocity structure (Michelena and Harris, 1991). This provides a physically based representation and results in a system of equations that has a unique solution.

ACKNOWLEDGMENTS

We wish to thank John Peterson for supplying the very high quality Kesterson travel-time data. Essential to this work was the generosity of the Advanced Computing Laboratory of Los Alamos National Laboratory in providing time on its Connection Machine 2.

REFERENCES

Luo, Y., 1991a. Calculation of wavepaths for band-limited seismic waves, 61st Annual Meeting Soc. Explor. Geophys., Expanded Abstracts, 1509–1512.

Luo, Y., and Schuster, G.T., 1991. Wave-equation traveltime inversion, Geophysics, v. 56, p. 645–653.

Majer, E.L., Peterson, J.E., Benson, S.M., and Long, J.C.S., 1991. High-frequency seismic tomographic imaging for hydrologic properties of near-surface materials. *In* Earth Sciences Division Annual Report 1990. Lawrence Berkeley Laboratory, Report LBL-29700, p. 171–175.

Michelena, R.J., and Harris, J.M., 1991. Tomographic traveltime inversion using natural pixels. Geophysics, v. 56, p. 635–644.

Tarantola, A., 1984. The seismic reflection inverse problem. F. Santosa, Y. Pao, W.W. Symes, and C. Holland (eds.), *In* Inverse Problems of Acoustic and Elastic Waves. Society of Industrial and Applied Mathematics, Philadelphia, Pennsylvania.

Definition of Physical Heterogeneity in Soils from High-Resolution Seismic Measurements

E. L. Majer and J. T. Geller

As part of the DOE Office of Health and Environmental Research Subsurface Science Program, Lawrence Berkeley Laboratory has been using high-resolution seismic field and laboratory experiments to image physical heterogeneity controlling fluid transport properties. The field experiments have been carried out at controlled sites at scales of several meters between boreholes at depths of as much as 15 m. Detailed geologic tests (lithology, grain size, clay content) and hydrologic tests (tracer, single, and multiple-hole pump) have also been carried out at these sites. The results of the field geophysical tests show a predictable correlation between seismic velocity and amplitude to grain size/clay content. The results also indicate that the physical heterogeneity mapped by the seismic imaging of the subsurface is a good indication of hydrologic heterogeneity as well.

The potential benefit of using geophysical methods to characterize aquifer heterogeneities that control contaminant transport has motivated a laboratory investigation of the relationship between seismic response and hydraulic conductivity in unconsolidated aquifer materials. Hydraulic conductivity and seismic-wave propagation are measured simultaneously in a triaxial test cell (shown in Figure 1), so that the relationship between the measured parameters is valid despite any discrepancy between field and laboratory measurements that results from sample disturbance and the change in sample orientation from the field to the laboratory. High-quality aquifer samples were obtained using a piston sampler with 7-cm-diameter, thin-walled, stainless steel Shelby tubes. The samples were taken from a site where field hydrological and seismic mea-

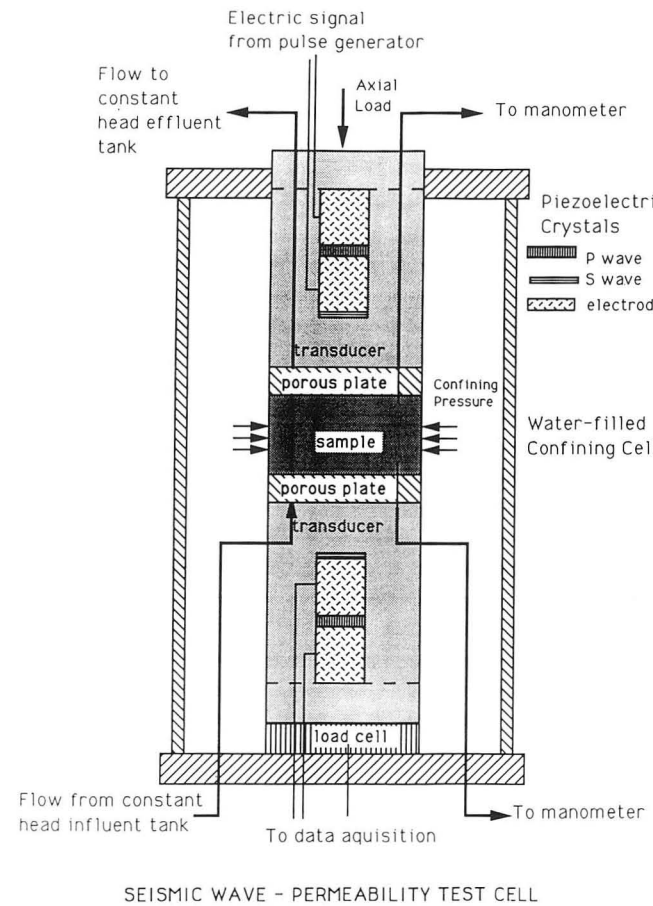

Figure 1. The triaxial test cell used for the simultaneous measurement of hydraulic conductivity and seismic-wave propagation through unconsolidated aquifer materials. [XBL 933-418]

surements were made previously, allowing a comparison between laboratory and field results. A 4-cm length of sample is extruded from the Shelby tube into a latex membrane and held between porous plates to ensure an even flow distribution over the sample cross section. The applied confining and axial stresses represent *in situ* conditions. Manometers connected to both sample ends indicate the head loss that occurs for a constant flow rate of degassed, *in situ* water. *P*- or *S*-waves are transmitted through the sample by applying a voltage pulse across the respective piezoelectric crystal.

Figure 2 compares the field and preliminary laboratory measurements. The lines point to the location of the samples in the plane of the seismic tomograms. The top sample is from a layer of high hydraulic conductivity, as indicated by the tracer velocity, and low *P*-wave velocity and high attenuation, as indicated by the anomolies in the seismic tomograms. The second sample is from a layer of lower hydraulic conductivity, higher *P*-wave velocity, and lower attenuation. The results of the laboratory measurements listed are the permeability, *k*; the *P*-wave velocity, *Vp;* and the amplitude, *A*, of the first *P*-wave arriving at the receiver. A higher value of *A* indicates that the sample attenuates seismic energy to a lesser degree. The laboratory measurements are consistent with the correlation between hydraulic conductivity, *P*-wave velocity, and attenuation observed in the field data. These results indicate the potential of laboratory measurements to obtain a quantitative correlation between hydraulic and seismic properties of unconsolidated media that could be used to interpret crosshole seismic measurements for characterizing the distribution of hydraulic conductivities in heterogeneous aquifers.

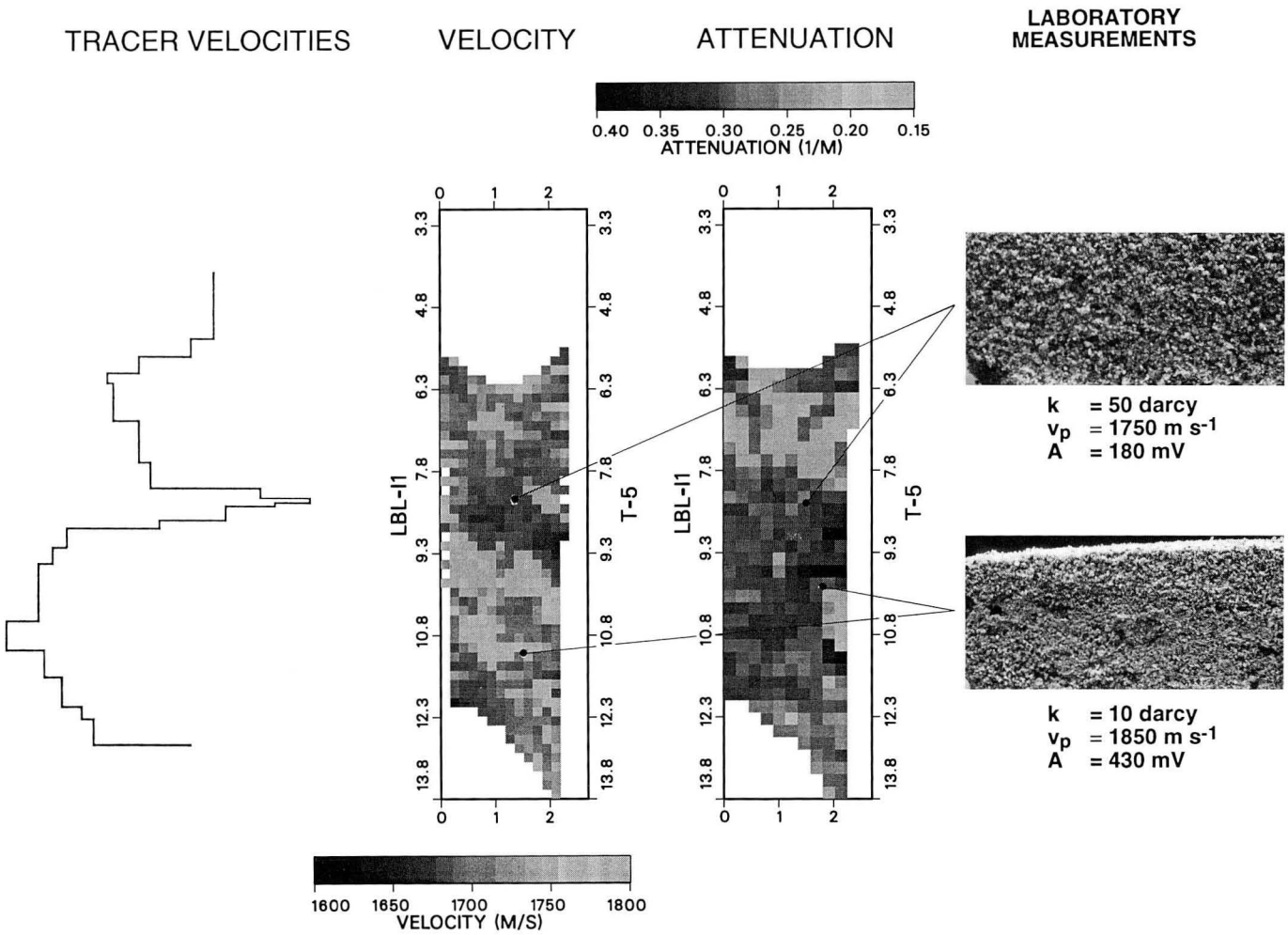

Figure 2. Comparison of field and laboratory measurements. **(a)** Tracer velocity. **(b)** Seismic tomograms of *P*-wave velocity and attenuation. **(c)** Laboratory measurements, including a photograph of the sample cross section (3 in. dia. × 1.5 in. high), the measured values of permeability, *k*; *P*-wave velocity, *Vp*; and the amplitude of the first *P*-wave arrival, *A*. The lines indicate the location of the sample in the plane of the seismic tomograms; note the difference in the grain size of the two samples. [XBB 936-3686]

Saltwater Injection Monitoring with Cross-Hole EM: A Report of 1992 Field Activities at the UC Richmond Field Station

*D. L. Alumbaugh, A. Becker, H. F. Morrison, K. H. Lee, and M. J. Wilt**

Beginning in 1988, a series of saltwater injection experiments were conducted at the University of California Richmond Field Station test site to evaluate the use of different geophysical methods for monitoring the injection process and for determining the geometry of the resulting plume. The first set of experiments involved surface-to-borehole resistivity measurements and were conducted in February of 1988 and 1989 (Bevc and Morrison, 1991). Approximately 25,000 gallons of 1.0-ohm-m salt water was pumped into a 3-m-thick, 30-m-deep, flat-lying aquifer. Resistivity measurements were made both before and after injection with current electrodes above, in, and below the aquifer with the potential electrodes at the surface spaced at 5-m intervals along lines radiating outward from the injection well (INJ in Figure 1). These experiments were useful in determining the migration path of the salt water, but no inversion of the data was attempted to determine the geometry of the injected plume.

In the spring of 1991, cross-borehole electromagnetic (EM) measurements were made by Lawrence Berkeley Laboratory (LBL) and Lawrence Livermore Laboratory personnel to track a similar volume of injected salt water. About 36,000 gallons of water was used in this experiment, and cross-borehole EM data were collected both before and after the injection. The test employed two observation boreholes, EMNE and EMSW (Figure 1), which are approximately equidistant from well INJ. The EM data were collected at a frequency of 18,800 Hz using a nearly continuous transmitter tool spacing

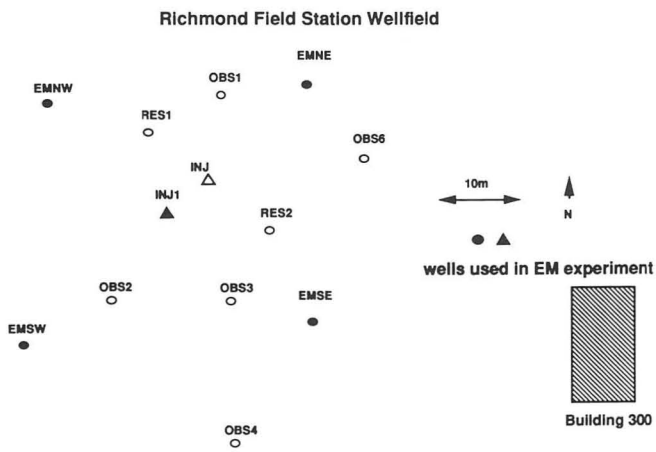

Figure 1. Location map for the Building 300 wellfield at the Richmond Field Station. [XBL 933-419]

* Lawrence Livermore National Laboratory, Livermore, California

of 0.2 m from the surface to a depth of 85 m in the EMSW well. The receiver station spacing was 5 m, starting at the surface and extending to a depth of 85 m. Significant findings from that field experiment are summarized below:

1. The saltwater slug provided a good imaging target. The maximum difference in magnetic field amplitudes between measurements made before and after injection was more than 10% and was easily detectable with our system. The anomaly was evident in a large number of the EM measurements.
2. At an operating frequency of 18.8 kHz in a noisy industrial environment, our data profile repeatability was approximately 3.0% in amplitude and 1.5 degrees in phase. This measurement accuracy was considerably worse than was achieved during a cross-hole EM survey in Devine, Texas (Wilt et al., 1991).
3. We could decipher a clear EM field anomaly due to the salt water injection, but we were not successful in fitting the field data with any numerical modeling code. Attempts were made using a 2.5-D inversion code (Zhou, 1989) and with a 3-D "block" model in a layered host (Tripp, 1991, personal communication). These efforts were not successful, primarily because the surrounding medium is not one-dimensional and the saltwater body was neither a two-dimensional object nor a tabular block. The saltwater plume appeared to be an irregular three-dimensional zone of varying salt concentration that followed the existing high-permeability network around the injection zone.

Although the 1991 experiment at the Richmond field station was a technical success, our mission was incomplete because we did not obtain a cross-hole EM data set that was suitable for conductivity imaging with existing codes. Our "proven" code uses an assumption of two-dimensional geometry with a cylindrical symmetry (Alumbaugh and Morrison, 1992). To make proper use of this code, we needed to acquire a data set with appropriate geometry, and this was the primary goal for the field experiment in 1992.

THE 1992 RICHMOND FIELD STATION EXPERIMENT

The 1992 saltwater injection experiment at Richmond was considerably more ambitious in scope than the 1991 effort. The experiment included the drilling of three new wells, each to a depth of 70 m, as well as an expanded set of field measurements. Well INJ1 (Figure 1) is a new

injection borehole located 5 m southwest of the older injection hole (INJ). It has a plastic well casing perforated in a gravel aquifer at a depth of 26–30 m. It was necessary to drill this well because we wished to use it for imaging as well as for fluid injection. Hole INJ is unsuitable for use in EM imaging, as it is only 35 m deep and has three segments of steel screening or casing that were previously used as resistivity current electrodes (Bevc and Morrison, 1991). The new observation wells (EMNW and EMSE) were drilled along a NW–SE diagonal that passes through the new injection well, with the result that the observation wells form the corners of a polygon centered on the new injector (Figure 1).

The 1992 experiment proceeded in much the same manner as the previous experiments. That is, cross-hole EM data were collected before the saline fluid was injected and after the injection was completed. After an initial system setup and debugging session, a baseline cross-hole EM data set was collected in May 1992. It consisted of four cross-hole profiles with the transmitter in the central well (INJ1) and the receiver tool deployed in each of the four EM observation holes. This arrangement ensured a "first-order" cylindrical symmetry required by the imaging code. Data were collected at a frequency of 18,500 Hz using a transmitter tool spacing of 0.5 m from the surface to a depth of 60 m for each receiver position. Receiver stations were spaced 5 m apart from 5 m to 55 m in each of the four observation holes. Next, a volume of water was pumped into a 100,000-gallon holding pond and mixed with salt until the water conductivity was raised to 1 S/m. The fluid was then injected into borehole INJ1 at a rate of 10 gallons per minute for about 4 days. The total injected volume was approximately 50,000 gallons, which is approximately 50% greater than that used in the 1991 experiment. With an assumed porosity of 30%, the injected water would sweep a cylindrical space 3 m high and 8 m in radius. We collected a second set of cross-hole EM and induction logging data during a four-week period in June following the injection.

After the June measurements were made, fluid was pumped out of well INJ1 until the water conductivity was restored to the background value it had before the experiment began (60 mS/m). The total volume pumped out was 300,000 gallons, about 6 times the amount injected. The pumping began on July 6 at a rate of 20 gallons per minute and lasted 12 days. Water levels in the wells open to the aquifer were monitored during this period to better understand the hydrology of the site. The water was pumped into a drain that flows into San Francisco Bay. Finally, after a two-week period, which allowed the water level to recover its original position, we attempted to repeat the baseline EM measurements in the EMNE well. Unfortunately, instrument problems caused the data quality to be much poorer than in May, hence those data were not retained. In all, the experiment was conducted over a period of three months.

The overall system deployment was very similar to that described by Wilt et al. (1991), with the exception that an audio power amplifier (Crown model 610) was used for signal power amplification instead of the Zonge GGT-20 transmitter. The Crown amplifier has a high-frequency limit in excess of 20,000 Hz, whereas the Zonge transmitter was limited to 8000 Hz. This higher-frequency capability is essential at Richmond because the boreholes are closely spaced and the background resistivity is relatively high ($\approx$ 20 ohm-m). Other changes included the use of lightweight portable winches, short segments of logging cable, and the use of a special transmitter cable capable of carrying a current of 10 A.

In general, we found that the data repeatability and reciprocity errors for the Richmond 1992 experiment were 2 to 3 times worse than those at Devine, Texas (Wilt et al., 1991) and similar to those observed in the 1991 data set. We feel that the noise level is higher at Richmond because the frequencies used are higher and the source and receiver vans are closer together. Both of these factors allow for variable surficial coupling of the high-level transmitter signal to the receiver. Although considerable time was spent removing "ground loops" from our system before either the Devine or the Richmond tests were conducted, additional errors (and ground loops) were evident in the Richmond data, primarily as the result of these more difficult operating conditions. Secondly, because Richmond is located in an industrial area, external noise (from grounded power lines, BART, etc.) is more of a problem and constitutes an unknown source of error.

CROSS-HOLE EM PROFILES

Ten sets of cross-well data were collected with the transmitter in INJ1 and the receiver in each of the four surrounding EM wells. Four of these data sets were collected before injection and six after injection. In order to present all the data in any one cross-well set simultaneously, they were first normalized to a source strength of unit dipole moment. Then the amplitude and phase were plotted in a gray-scale format as a function of transmitter and receiver position. Plotting the data in this manner allows us to check for data continuity between profiles and also to determine any changes that take place due to the injection.

Though the changes caused by the introduction of the salt water are observable in the raw data, they are fairly small in comparison and appear as small perturbations in the total field amplitude and phase. To better demonstrate the effects of the injection, we have calculated the secondary or scattered fields resulting from the plume. This is a simple process involving the subtraction of the fields measured before the injection from those measured after injection. The resulting anomaly for the EMNW data shown in Figure 2 clearly indicate large changes that are not readily

apparent in the raw data. The fact that the anomalies are several times larger than the noise estimates suggests that the EMNW data are of sufficient quality to be used in various imaging schemes.

Calculations of the scattered field for the EMNE cross-well data sets yielded an anomaly similar to the one shown in Figure 2. However, the data collected in the wells to the south do not exhibit this same character. Although the preinjection and postinjection data for EMSE and EMSW appear to be fairly consistent, the scattered fields due to the salt water are smaller in magnitude, do not demonstrate the same pattern as in Figure 2, and in general are noisier. This may be due in part to lower-quality data but is more likely the result of the plume moving northward away from INJ1, as suggested by earlier experiments (Bevc and Morrison, 1991), rather than spreading symmetrically about the injection well.

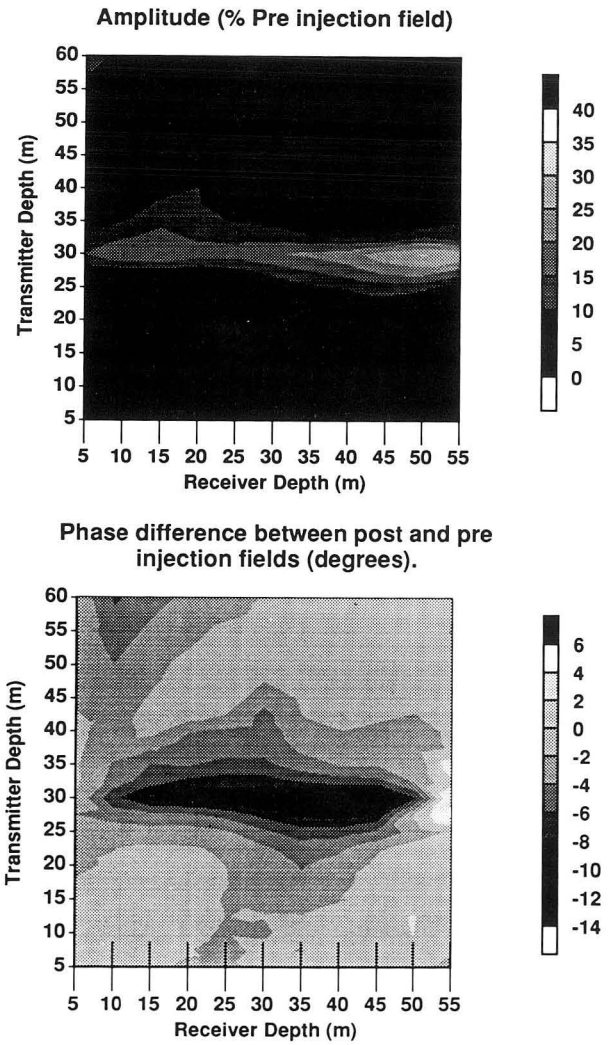

Figure 2. EMNW secondary fields calculated by subtracting the preinjection data from the postinjection data. Each line on the receiver axis represents an individual profile of continuous data in transmitter depth. [XBL 933-420]

INTERPRETATION OF DATA

One of the prime considerations of the Richmond 1992 experiment was to produce a data set in which the geology, to a first order, exhibits a geometry suitable for our 2-D inversion routine. This routine assumes a cylindrical symmetry of the conductivity distribution about the transmitter borehole in an otherwise homogenous half-space. It uses an iterative Born scheme to linearize the problem and regularized least squares to invert for the conductivity distribution (Alumbaugh and Morrison, 1992).

Because the Richmond geology consists of interbedded conductive shales and sands overlying a more resistive basement, the plume cannot be interpreted as being injected into a homogenous half-space. Thus, rather than inverting only for changes in conductivity resulting from the injection, the entire conductivity structure between the two wells was imaged both before and after injection and the results compared. The background conductivity used in the process was chosen by minimizing the magnitude of the secondary field.

Figure 3 shows the images obtained by inverting the pre- and postinjection data collected in the EMNW well. Though it does not indicate flat-lying layers, the preinjection image does show conductive shales and sands overlying a more resistive basement. The postinjection image clearly shows a high conductivity anomaly that corresponds to the injection zone. This strongly suggests that the salt water has migrated to the northwest, which agrees very well with the results published by Bevc and Morrison (1991). Inversions of the other data support this conclusion. Images of the EMNE data (Figure 4) indicate some migration to the

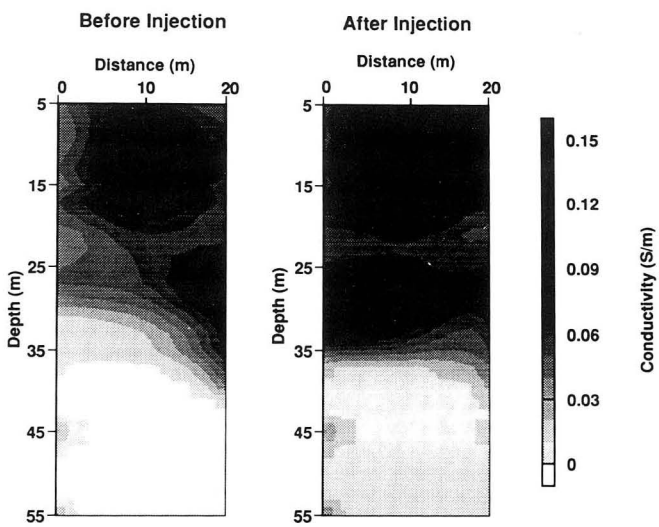

Figure 3. Iterative Born inversion of EMNW data. [XBL 933-421]

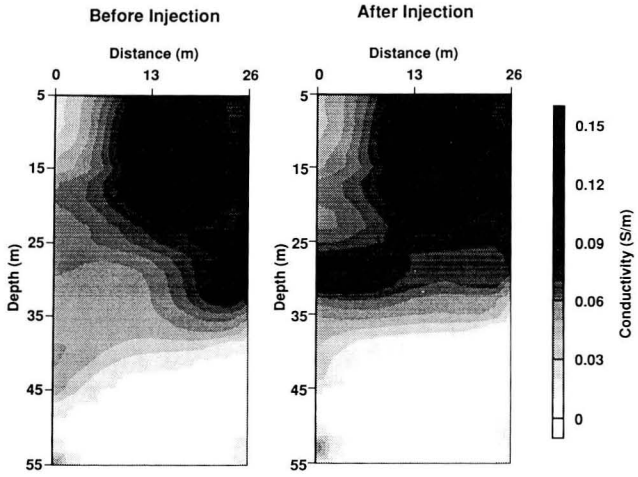

Figure 4. Iterative Born inversion of EMNE data. [XBL 933-422]

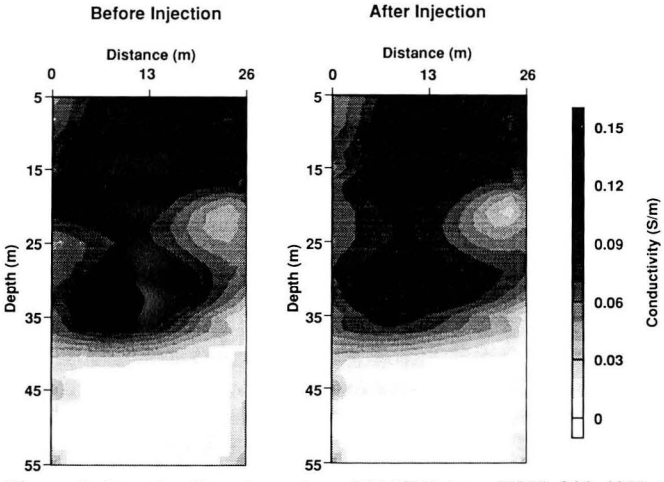

Figure 5. Iterative Born inversion of EMSW data. [XBL 933-423]

northeast, whereas the EMSW inversions (Figure 5) indicate almost no migration to the southwest. The direction of plume migration becomes even more apparent if we plot the change in conductivity between the "before" and "after" images, as shown in Figure 6.

Notice that the inversions from EMSE have not been included here. The reason is that the misfits to these data averaged more than 20% compared with 10% or less for data collected in the other three wells. This large misfit may be due to extreme 3-D geology between the two wells, poor data quality, or a combination of both.

CONCLUSIONS

The 1992 Richmond field experiment showed that a saltwater injection process can be monitored using cross-well electromagnetics. Although the cross-well EM system worked fairly well, there is definite room for improvement, as there were significant drift problems and repeatability errors. However, even with these problems, the data are in most cases of sufficient quality not only to detect the presence of the body but also to allow for simple imaging schemes to be applied. Results from this imaging process correlate well with previous experiments, which show the plume to be moving off to the northwest. Additional 3-D modeling needs to be done both to verify this and to test the limits of the 2-D inversion code.

ACKNOWLEDGMENT

The field personnel consisted of Dave Alumbaugh, Maryla Deszcz-Pan, and H.W. Tseng of the University of California at Berkeley and Mike Wilt from Lawrence Livermore National Laboratory. Technicians Jim Doherty and

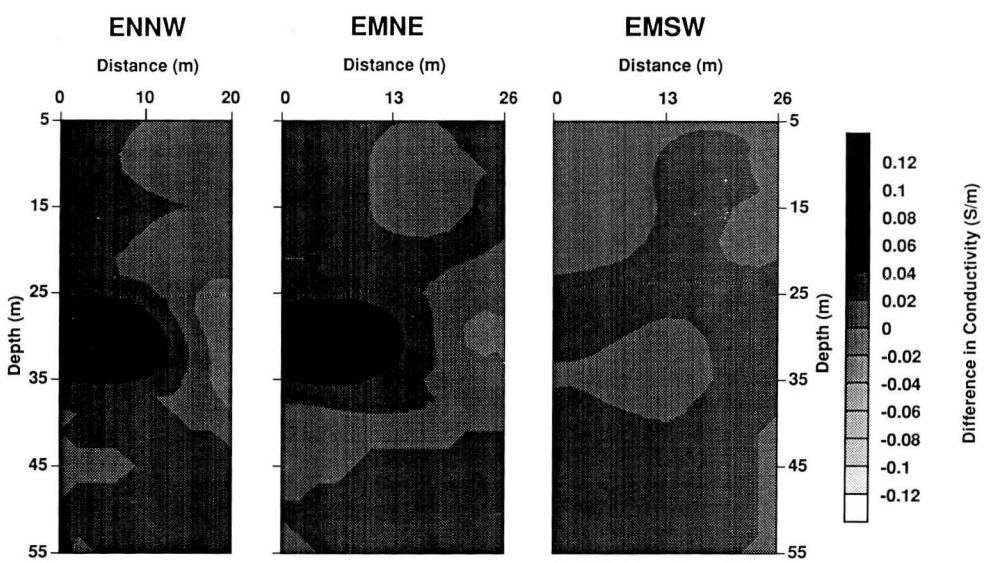

Figure 6. Difference in conductivity between the postinjection and preinjection images in Figures 3 to 5. [XBL 933-424]

Don Lippert from LBL reworked the plumbing system for the saltwater injection and extraction and provided technical support for the project. Peter Persoff from LBL was in charge of the water-level measurements made during the saltwater extraction. This work was done under the sponsorship of the U.S. Department of Energy Research and Fossil Energy programs. Principal funding for the field experiment was provided by an industrial research consortium that included Mobil, Schlumberger, Shell, Noranda, Exxon, NMC, British Petroleum, Texaco, and Amoco.

REFERENCES

Alumbaugh D.L., and Morrison, H.F., 1992. Tomographic imaging of cross well EM data. Extended abstracts from the Society of Exploration Geophysicists 1992 Annual Meeting, New Orleans, Louisiana.

Bevc, D., and Morrison, H.F, 1991. Borehole-to-surface electrical conductivity monitoring of a salt water injection experiment. Geophysics, v. 56, no. 6, p. 769–777.

Wilt, M.J., Morrison, H.F., Becker, A., and Lee K.H., 1991. Cross-borehole and surface-to-borehole electromagnetic induction for reservoir characterization. U.S. Department of Energy Report DOE/BC/91002253.

Zhou, Q., 1989. Audio-frequency electromagnetic tomography for reservoir evaluation. Ph.D. Thesis, Department of Engineering Geosciences, University of California at Berkeley (LBL-28171).

The Effects of State of Stress on the Static and Dynamic Properties of Berea Sandstone

S. Ita, N. G. W. Cook, L. R. Myer, and K. Nihei

Laboratory experiments have been conducted over the past year to study the effects of state of stress on static drained-pore compressibility, dynamic drained-pore compressibility, seismic velocity, and seismic amplitude. These experiments are part of an effort to improve seismic techniques for imaging and characterization of reservoir rocks and processes. The pore-compressibility measurements are important because they can be used to infer changes in the geometry of the intergranular pore space as grain microstructure is deformed under stress. The concurrent seismic-wave measurements allow us to deduce the effect of changing pore geometry, specifically grain contact areas, on the seismic properties of the sedimentary rocks.

LABORATORY PROCEDURES

Experiments were performed on three cylindrical samples of Berea sandstone taken from the same block. They measured 2 inches in diameter and 1.69 inches in length. Before testing, each sample was placed in a brass inner jacket and a rubber outer jacket to isolate the pore space from the confining fluid. The jacketed sample was placed in a confining cell, then the assembly was placed in a load frame. The axial and confining stresses were controlled independently by separate pumps. This allowed us to impose uniaxial, biaxial, and hydrostatic stress states on the sample. Stresses ranged from 0 to 25 MPa. Measurements were plotted as a function of the mean stress on the sample, defined as the average of the three principal stresses.

DRAINED-PORE COMPRESSIBILITIES

The static drained-pore compressibility was measured by monitoring the volume of fluid expelled from the specimen into a vertical capillary tube. These measurements were converted to compressibilities using the definition

$$\beta_p^s = \frac{\Delta V / V_0}{\Delta P}, \tag{1}$$

where β_p^s is the static drained-pore compressibility, ΔV is the change in pore volume, V_0 is the initial pore volume, and ΔP is the change in stress. Static pore-compressibility measurements were made on water- and brine-saturated samples.

The dynamic (low-frequency) drained-pore compressibility, β_p^d, was calculated by means of the following formula, derived from a consideration of a continuum with pores, using the reciprocal relation:

$$\left(\frac{1}{K_u} - \frac{1}{K_{in}}\right) = \phi\, \beta_p^d \left[1 - \frac{\beta_p^d}{\beta_p^d + \frac{1}{K_{fl}} - \frac{1}{K_{in}}}\right], \tag{2}$$

where K_u is the dynamic undrained bulk modulus, K_{in} is the intrinsic bulk modulus (40×10^9 Pa for quartz), ϕ is the

porosity (0.22 for Berea sandstone), and K_{fl} is the pore fluid bulk modulus (2×10^9 Pa for water). The undrained dynamic bulk modulus, K_u, was calculated from the measured P- and *S*-wave velocities:

$$K_u = \rho\left[V_p{}^2 - \frac{4}{3}V_s{}^2\right], \tag{3}$$

where ρ is the density of Berea sandstone (2.10 g/cc), V_p is the measured *P*-wave velocity, and V_s is the measured *S*-wave velocity. Dynamic pore-compressibility measurements were computed for water-saturated, brine-saturated, and oven-dry samples.

Measured, static drained-pore compressibilities for the three specimens are shown in Figure 1a. It can be seen that for all stress states, compressibilities decrease with increasing mean stress, as expected. However, the biaxial and uniaxial compressibilities are lower than the hydrostatic compressibility at a given mean stress. This is direct evidence that the pore geometry changes between the different states of stress.

Calculated, dynamic drained-pore compressibilities for the same three specimens are shown in Figure 1b. As with the static data, the hydrostatic and uniaxial dynamic compressibilities decrease with increasing mean stress. In contrast to the static data, the biaxial dynamic compressibilities increase with increasing mean stress and also have higher magnitudes than the corresponding hydrostatic values. Since biaxial dynamic compressibilities were measured by wave propagation in the direction perpendicular to the applied stress, this behavior is attributed to dilation at the grain contacts in the minimum stress direction, offsetting compression in the maximum stress direction.

Figure 2 shows a comparison between fluid-saturated and oven-dry compressibilities for one sample. It can be seen that for all three states of stress the dry compressibilities are larger than the fluid-saturated compressibilities. Because the calculation of the dynamic drained-pore compressibilities accounts for the elastic bulk modulus stiffening effect of the pore fluid, these differences suggest that fluid in the grain contacts may introduce an additional stiffening effect that depends on the fluid viscosity.

The static measurements reported here are three to four times larger than the dynamic measurements. This is in contrast to values reported by King (1969), who found close agreement between the static and dynamic measurements. However, he noted that his velocity measurements were anomalously low, leading to greater calculated dynamic compressibilities (p. 335). The difference between the static and dynamic measurements can be attributed to frictional lockup in the short duration dynamic measurements.

Both the static and dynamic compressibility data show that compressibility and thus bulk modulus are not just functions of mean stress. The state of stress, in addition to the magnitude of the mean stress, affects the compressibility and bulk modulus of Berea sandstone and influences the microgeometry.

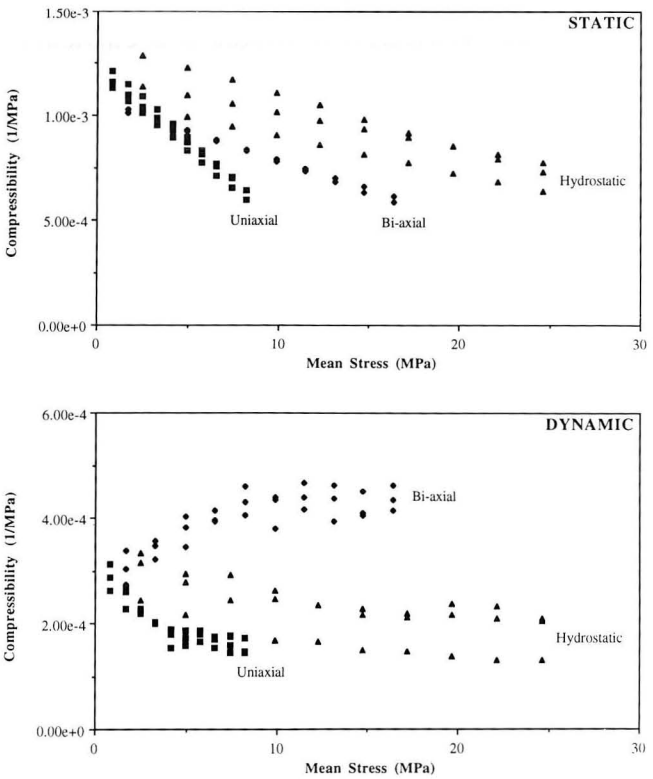

Figure 1. Static (**a**) and dynamic (**b**) drained-pore compressibilities for three Berea sandstone cores. [XBL 934-494]

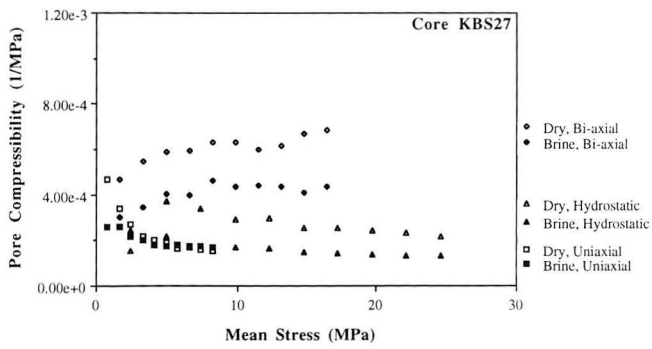

Figure 2. Dynamic drained-core compressibilities for Berea sandstone core KBS27, dry and brine saturated. [XBL 934-495]

SEISMIC PROPERTIES

Seismic velocities and attenuation were measured using an ultrasonic pulse-transmission system. The ultrasonic measurements, performed in conjunction with the compressibility measurements, were conducted on water-saturated, brine-saturated, and oven dry samples.

The seismic velocities were calculated from the first break arrival times. The *S*- and *P*-wave velocities increase from 1700 to 2200 m/sec and from 2600 to 4000 m/sec, respectively, with increasing mean stress. Both types of waves appeared to be independent of the state of stress. However, the *P*-wave velocities were dependent on the presence of fluid. The presence of fluid increased the velocity at a given mean stress. This results from the stiffening effect of fluid at grain contacts. Fluids that do not support shear deformation, such as water, do not affect the rigidity of the granular framework and thus do not have an effect on *S*-wave velocities.

Peak-to-peak amplitude changes were used as a measure of seismic-wave attenuation. The *S*-wave and *P*-wave peak-to-peak amplitudes for the different states of stress are given in Figure 3. The dry amplitudes are consistently higher than the fluid-saturated amplitudes for both wave types and for all states of stress. This indicates that fluids introduce a loss mechanism into seismic-wave propagation.

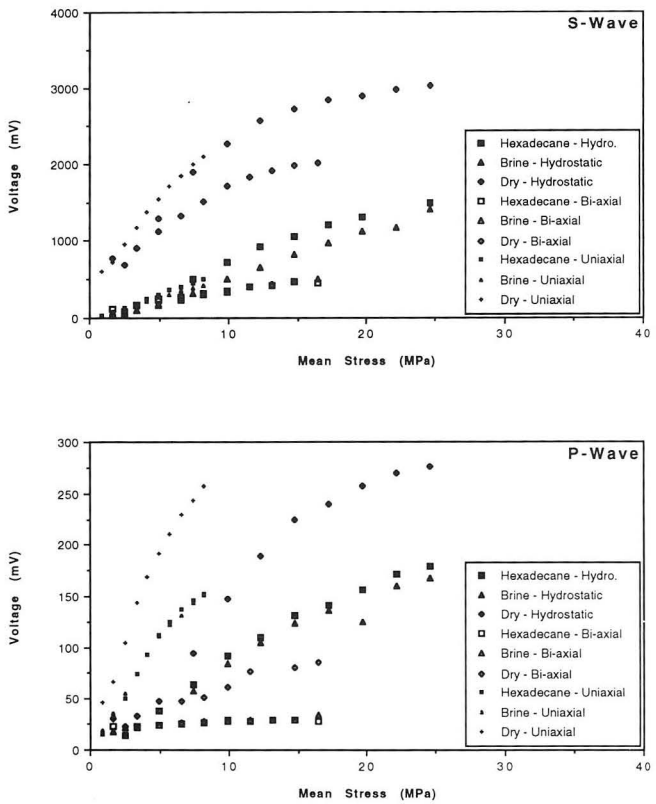

Figure 3. *S*-wave (**a**) and *P*-wave (**b**) peak-to-peak amplitudes for Berea sandstone core KBS27 with different fluid types and for three states of stress. [XBL 934-496]

For a given mean stress, the uniaxial and hydrostatic *S*-wave peak-to-peak amplitudes are similar in magnitude. The biaxial amplitudes are slightly lower. This may be partially a result of incomplete coupling between the transducers and samples under biaxial loading. The similarity in amplitudes for the three states of stress suggests that *S*-wave propagation is primarily influenced by the mean stress.

For a given mean stress, the uniaxial *P*-wave peak-to-peak amplitudes were highest, followed next by the hydrostatic and then by the biaxial amplitudes, respectively. For the uniaxial tests, the grain contacts in the direction of propagation experience a stress roughly three times that produced in a hydrostatic test. If plotted as a function of the axial stress, the uniaxial amplitudes are in the same range as the hydrostatic amplitudes. The biaxial *P*-wave amplitudes are lower than either the uniaxial or hydrostatic values and appear to be insensitive to the magnitude of stress. The biaxial stress was applied orthogonal to the direction of propagation. Therefore, grain contacts in the direction of propagation were subjected to very low stresses. These results indicate that *P*-wave propagation is primarily influenced by stress applied perpendicular to the direction of propagation. This suggests that, like seismic velocities, attenuation may be controlled by grain contacts in addition to scattering off the pores.

Figure 4 presents plots of peak-to-peak amplitudes versus corresponding velocities for both *S*-waves and

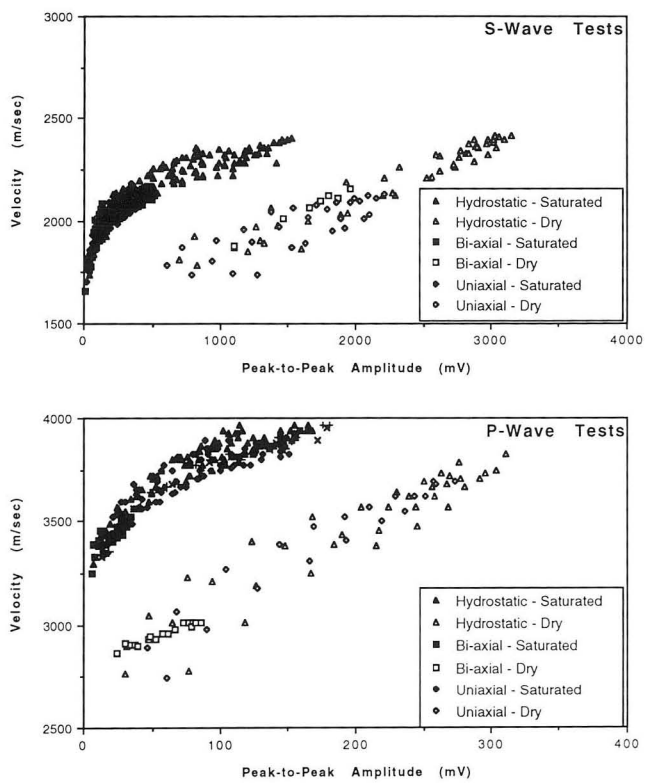

Figure 4. Peak-to-peak amplitude versus velocity for *S*-waves (**a**) and *P*-waves (**b**) with different fluids and for three states of stress. [XBL 934-497]

P-waves. For each type of wave, the data separate into two distinct curves for dry and fluid-saturated conditions. The fact that data from different stress states and with different fluid types lie along the same curve suggests that seismic wave velocity and attenuation are controlled by the same mechanism. The smaller amplitudes for the fluid-saturated data compared with the dry amplitudes at the same velocity indicates that pore fluids introduce a loss mechanism into seismic wave propagation.

CONCLUSIONS

Laboratory experiments have been conducted to investigate the static drained-pore compressibility, dynamic drained-pore compressibility, seismic velocities, and seismic amplitudes in Berea sandstone samples under three different states of stress: hydrostatic, biaxial, and uniaxial. Measurements of static and dynamic drained-pore compressibilities displayed a dependence on the state of stress in addition to the magnitude of the stress. The data suggested that grain contacts may dilate in the minimum principle stress direction under differential compression. A comparison of the dynamic compressibilities of fluid-saturated and oven-dry samples indicated that fluids may introduce a viscous stiffening in addition to an elastic stiffening of the grain contacts.

The *S*-wave and *P*-wave velocities showed no stress-state dependence. The *P*-wave velocities were increased by the presence of pore fluids. This can be related to fluid stiffening the grain contacts. Both *S*-wave and *P*-wave peak-to-peak amplitudes were reduced by the presence of pore fluids, suggesting that fluids introduce a loss mechanism into seismic wave propagation. *S*-wave amplitudes were dependent on the mean stress, and *P*-wave amplitudes were dependent on the state of the applied stress in addition to the magnitude. Plots of peak-to-peak amplitude versus velocity indicate that both velocities and attenuation are controlled by the same mechanism(s). We propose that the mechanism(s) takes place within the grain contacts and that *S*-waves are affected by the contacts in all three directions whereas *P*-waves are primarily affected by the grain contacts in the direction of propagation.

REFERENCE

King, M.S., 1969. Static and dynamic moduli of rocks under pressure. *In* Rock Mechanics—Theory and Practice: Proceedings of the Eleventh U.S. Symposium on Rock Mechanics. Society of Mining Engineers, New York, p. 329–351.

Computer Simulation of Macroscopic Properties of Clastic Rocks in Terms of Microscopic Processes

Z. Liu, L. R. Myer, and N. G. W. Cook

The study of granular materials, especially quasi-brittle materials, under compression; the stress-strain relationships; and the generation and propagation of microcracks in relation to the loading conditions are all essential for understanding the process of fracturing in these materials. Granular materials are typically composed of a great number of particles or grains, and such a system exhibits a corresponding large degree of freedom. As a result, the microfeatures of these materials are extremely complex. Nevertheless, at the macro scale, the entire system exhibits well-defined deformation under uniform external loading. This type of behavior is idealized in the notion of stress-strain relations in continuum theories. From a physical point of view, the stress-strain relation under uniform external conditions is a statistical average related to an almost independent behavior of different large parts of a large system in which significantly separated particles do not affect each other directly or, in other words, the macro behavior is the statistics of microscopic characters of the granular materials.

Our previous SEM experiments (Cook, 1979; Jaeger and Cook, 1979; Zheng et al., 1989) have shown that local stresses in individual grains are important in the overall response of granular materials. At the microscopic level, local stresses are related to (1) tensile strength of grains, (2) geometry, (3) pores, and (4) grain contacts. How can we quantify microstructure and the distribution of stresses? Once quantified, how should these parameters be related to the macromechanical behavior? Which parameter is the most important? That is, which parameter dominates the macromechanical properties?

Some micromechanical models have been used to study macroscopic properties in terms of microscopic processes. Some of these models are based on a continuum containing microcracks, whereas others are based on a granular or discrete element approach. In this article we develop a two-dimensional numerical model based on the elastic interaction and tensile fracture of grains and grain bonds to study the effects of heterogeneity in grain macroscopic strain-hardening and strain-softening deformation

under compressive stress. Stress distributions within grains are calculated using the Boundary Element Method (BEM).

METHODOLOGY

We have mentioned that local stresses in individual grains are important in the overall response of granular materials and crack propagation, so we need some detailed information about stress distribution within grains in granular materials. BEM is used to calculate the stress distribution within every grain. In BEM, boundary stresses and displacements are chosen as variables. For every grain in the system, the boundary is divided into n segments, so there are $2n$ unknowns:

$$\overset{j}{\sigma}_s,\ \overset{j}{\sigma}_n,\ \overset{j}{u}_s,\ \overset{j}{u}_n \quad \text{with} \quad j=1,2,\cdots,n\ .$$

where $\overset{j}{\sigma}_n$, $\overset{j}{u}_n$ are the normal stress and displacement of segment j and $\overset{j}{\sigma}_s$, $\overset{j}{u}_s$ are the tangential stress and displacement of segment j.

Using the reciprocal theorem gives

$$\oint_c(\sigma_s u_s' + \sigma_n u_n')ds = \oint_c(\sigma_s' u_s + \sigma_n' u_n)ds\ , \tag{1}$$

and by choosing $2n$ test solutions (Crouch and Starfield, 1983), we can derive the relation

$$B\{\sigma_B\} = A\{u_B\}\ , \tag{2}$$

which can be used to calculate the unknown stresses and displacements along the boundary. B and A in Eq. (2) are matrices of influence coefficients:

$$B = \begin{pmatrix} \overset{11}{B}_{ss} & \overset{11}{B}_{sn} & \overset{12}{B}_{ss} & \overset{12}{B}_{sn} & \cdots & \cdots & \overset{1n}{B}_{ss} & \overset{1n}{B}_{sn} \\ \overset{21}{B}_{ss} & \overset{21}{B}_{sn} & \overset{22}{B}_{ss} & \overset{22}{B}_{sn} & \cdots & \cdots & \overset{2n}{B}_{ss} & \overset{2n}{B}_{sn} \\ \cdots & \cdots & \cdots & \cdots & \cdots & \cdots & \cdots & \cdots \\ \overset{n1}{B}_{ss} & \overset{n1}{B}_{sn} & \overset{n2}{B}_{ss} & \overset{n2}{B}_{sn} & \cdots & \cdots & \overset{nn}{B}_{ss} & \overset{nn}{B}_{sn} \\ \overset{11}{B}_{ns} & \overset{11}{B}_{nn} & \overset{12}{B}_{ns} & \overset{12}{B}_{nn} & \cdots & \cdots & \overset{1n}{B}_{ns} & \overset{1n}{B}_{nn} \\ \cdots & \cdots & \cdots & \cdots & \cdots & \cdots & \cdots & \cdots \\ \overset{n1}{B}_{ns} & \overset{n1}{B}_{nn} & \overset{n2}{B}_{ns} & \overset{n2}{B}_{nn} & \cdots & \cdots & \overset{nn}{B}_{ns} & \overset{nn}{B}_{nn} \end{pmatrix},$$

$$A = \begin{pmatrix} \overset{11}{A}_{ss} & \overset{11}{A}_{sn} & \overset{12}{A}_{ss} & \overset{12}{A}_{sn} & \cdots & \cdots & \overset{1n}{A}_{ss} & \overset{1n}{A}_{sn} \\ \overset{21}{A}_{ss} & \overset{21}{A}_{sn} & \overset{22}{A}_{ss} & \overset{22}{A}_{sn} & \cdots & \cdots & \overset{2n}{A}_{ss} & \overset{2n}{A}_{sn} \\ \cdots & \cdots & \cdots & \cdots & \cdots & \cdots & \cdots & \cdots \\ \overset{n1}{A}_{ss} & \overset{n1}{A}_{sn} & \overset{n2}{A}_{ss} & \overset{n2}{A}_{sn} & \cdots & \cdots & \overset{nn}{A}_{ss} & \overset{nn}{A}_{sn} \\ \overset{11}{A}_{ns} & \overset{11}{A}_{nn} & \overset{12}{A}_{ns} & \overset{12}{A}_{nn} & \cdots & \cdots & \overset{1n}{A}_{ns} & \overset{1n}{A}_{nn} \\ \cdots & \cdots & \cdots & \cdots & \cdots & \cdots & \cdots & \cdots \\ \overset{n1}{A}_{ns} & \overset{n1}{A}_{nn} & \overset{n2}{A}_{ns} & \overset{n2}{A}_{nn} & \cdots & \cdots & \overset{nn}{A}_{ns} & \overset{nn}{A}_{nn} \end{pmatrix}.$$

Matrices B and A are dependent only on the geometry of the element boundary. If two elements have the same shape with different boundary stresses and displacements, there is no change for either matrix. $\{\sigma_B\}$ is a stress vector along the boundary, and $\{u_B\}$ is a displacement vector along the boundary:

$$\{\sigma_B\} = \begin{pmatrix} \overset{1}{\sigma}_s \\ \overset{1}{\sigma}_n \\ \overset{2}{\sigma}_s \\ \overset{2}{\sigma}_n \\ \vdots\downarrow \\ \overset{i}{\sigma}_s \\ \overset{i}{\sigma}_n \\ \vdots\downarrow \\ \overset{n}{\sigma}_s \\ \overset{n}{\sigma}_n \end{pmatrix}, \qquad \{u_B\} = \begin{pmatrix} \overset{1}{u}_s \\ \overset{1}{u}_n \\ \overset{2}{u}_s \\ \overset{2}{u}_n \\ \vdots\downarrow \\ \overset{i}{u}_s \\ \overset{i}{u}_n \\ \vdots\downarrow \\ \overset{n}{u}_s \\ \overset{n}{u}_n \end{pmatrix}.$$

For granular materials, the detailed stress distribution within grains needs to be computed to investigate the mechanisms of nonelastic behavior and microfracture. Granular materials are typically composed of a great number of grains. Every grain is divided into hundreds of seg-

ments. Such systems have hundreds of thousands of variables. We cannot directly use BEM to solve our problem. The number of variables must be reduced.

In systems of granular materials, external energy is input into grains through contacts. Stress distribution within grains can be described in terms of contact stresses and displacements along the boundary. Thus, for every grain, only contact stresses and contact displacements are chosen as variables. Assuming there are m contact points in a grain, because the stresses of all free elements along the boundary are zero, $\{\sigma_B\}$ in Eq. (2) can be expressed as:

$$\{\sigma_B\}' = \begin{pmatrix} \overset{1c}{\sigma_s} \\ \vdots\downarrow \\ \overset{mc}{\sigma_n} \\ 0 \\ \vdots\downarrow \\ 0 \end{pmatrix} .$$

Then $\{\sigma_B\}'$ can be divided into two subvectors: contact stresses $\{\sigma_{BC}\}$ and $\{0\}$, where

$$\{\sigma_{BC}\}_{1x2m} = \begin{pmatrix} \overset{1c}{\sigma_s} \\ \overset{1c}{\sigma_n} \\ \vdots\downarrow \\ \overset{mc}{\sigma_n} \end{pmatrix} \qquad \{0\}_{1x(2n-2m)} = \begin{pmatrix} 0 \\ \vdots\downarrow \\ 0 \end{pmatrix} .$$

Corresponding to the order of vector $\{\sigma_B\}$, the displacement vector $\{u_B\}$ is rearranged as two subvectors: contact-displacement vector $\{u_{BC}\}$ and free-stress-element vector $\{u_{BF}\}$. Matrices A and B in Eq. (2) can also be rearranged as

$$A' = \begin{pmatrix} \overset{11}{A}_{2mx2m} & \overset{12}{A}_{2mx2(n-m)} \\ \overset{21}{A}_{2(n-m)x2m} & \overset{22}{A}_{2(n-m)x2(n-m)} \end{pmatrix} ,$$

$$B' = \begin{pmatrix} \overset{11}{B}_{2mx2m} & \overset{12}{B}_{2mx2(n-m)} \\ \overset{21}{B}_{2(n-m)x2m} & \overset{22}{B}_{2(n-m)x2(n-m)} \end{pmatrix} . \tag{3}$$

From Eqs. (2) and (3), we get

$$\overset{11}{B}\{\sigma_{BC}\} = \overset{11}{A}\{u_{BC}\} + \overset{12}{A}\{u_{BF}\} ,$$

$$\overset{21}{B}\{\sigma_{BC}\} = \overset{21}{A}\{u_{BC}\} + \overset{22}{A}\{u_{BF}\} . \tag{4}$$

Equation (4) yields

$$\{u_{BF}\} = \left(\overset{22}{A}\right)^{-1} \overset{21}{B}\{\sigma_{BC}\} - \left(\overset{22}{A}\right)^{-1} \overset{21}{A}\{u_{BC}\} ,$$

$$B_C\{\sigma_{BC}\} = A_C\{u_{BC}\} , \tag{5}$$

where

$$B_C = \left(\overset{11}{B}\right) - \overset{12}{A}\left(\overset{22}{A}\right)^{-1} \overset{21}{B}$$

and

$$A_C = \left(\overset{11}{A}\right) - \overset{12}{A}\left(\overset{22}{A}\right)^{-1} \overset{22}{A} .$$

By using the principle of minimum energy and Eq. (4), the stress distribution within the grains of granular materials can be calculated.

SOME RESULTS

Some calculations have been obtained by using the above equations. We have used rectangular and hexagonal packings of cylindrical grains of the same size to study the effects of stochastic distributions of grain strength, uniform debonding strengths, and confining stresses on the ultimate strength and macroscopic deformation. The system consists of about 300 grains. The boundary of each grain is divided into 100 elements. For each grain, stresses of 50 points are calculated to find the maximum stress within the grain. As the load increases, the maximum stress point is searched throughout the whole system. When the maximum stresses reach the tensile strengths of grains, these grains are broken, and their Young's moduli are reduced for the next step in the calculation. If contact forces at interfaces reach debonding strengths, these interfaces are open. If two grains contact each other during the loading,

the matrices A_c and B_c of these two grains must be recalculated because the contact situation is changed.

Our calculations demonstrate that, as each grain or bond fractures, the effective macroscopic elastic modulus of the materials decreases and the stress at which the next fracture occurs changes. The effective Young's moduli and limiting stresses are shown in Figures 1 and 2 for homogeneous and heterogeneous grain strength distributions.

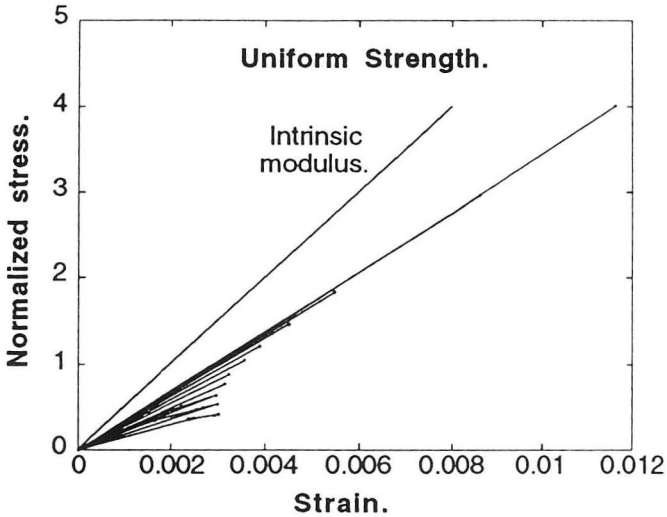

Figure 1. Stress-strain curves show decreasing effective Young's moduli with increasing grain and bond damage and strain-softening for homogeneous strength distributions. [XBL 934-498]

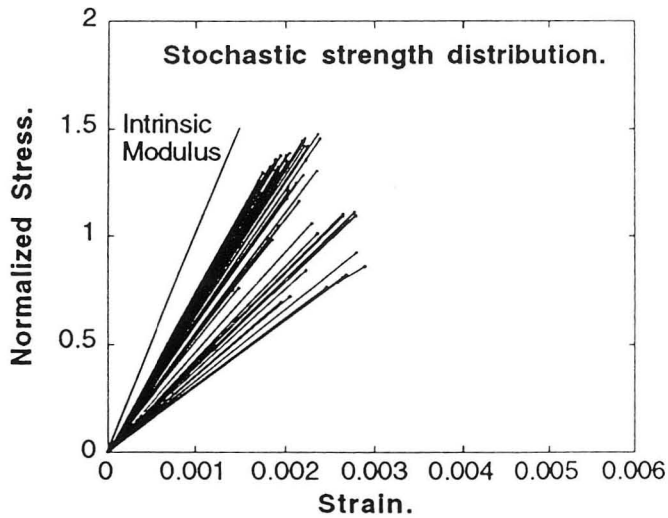

Figure 2. Stress-strain curves show both strain-hardening and strain-softening for stochastic strength distributions. [XBL 934-499]

Stresses are normalized with respect to tensile strength of the grains, and a hexagonal grain packing is assumed. The envelopes of these lines constitute the stress-strain curves. From Figure 1 it is clear that a homogeneous strength distribution results in only macroscopic strain-softening. Heterogeneous grain strength distributions result in both macroscopic strain-hardening and strain-softening, as shown in Figure 2.

For uniform grain and bond strengths, the deformation is extremely brittle, and failure occurs by localization and propagation of grain fractures along a diagonal spanning the whole network, as shown in Figure 3. Because of the stochastic strength distribution in the system, low confining stresses cause grain failures to be distributed throughout the sample, and grain fractures tend to be propagated along the direction of loading, as shown in Figure 4.

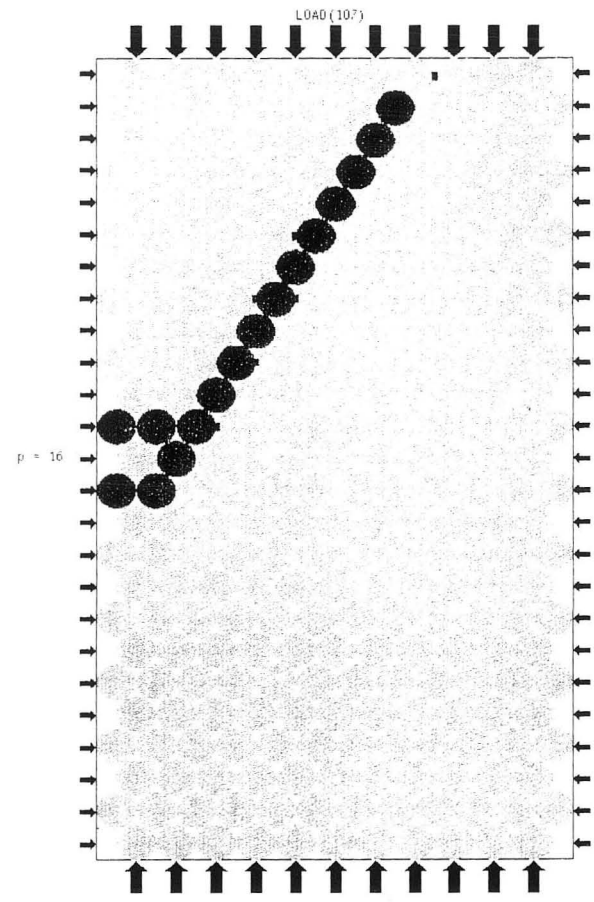

Figure 3. Interaction between failed grains results in propagation of a macroscopic fracture and strain-softening deformation. [XBL 934-500]

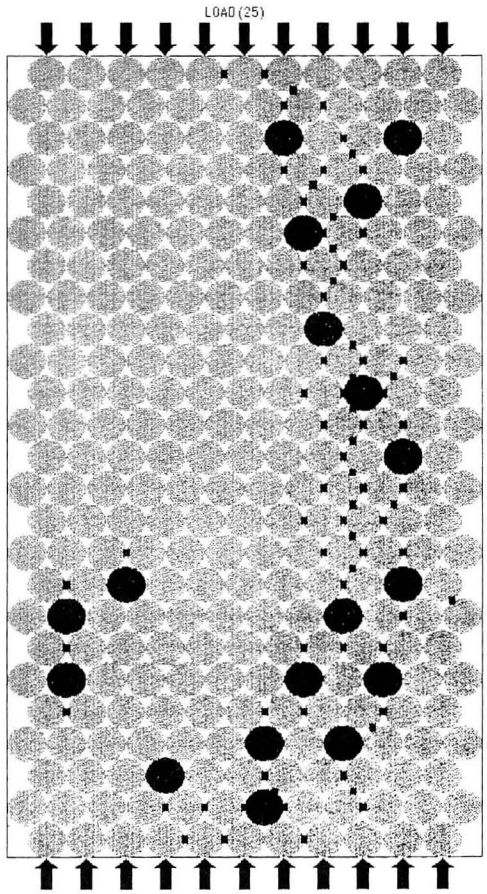

Figure 4. Initial failures of grains with a stochastic distribution of strengths produce strain-hardening deformation. [XBL 934-501]

REFERENCES

Cook, N.G.W., 1979. Rock fracture: Observations and interpretations. *In* Proceedings, 4th Tewksbury Symposium, Melbourne, Australia, Feb. 12–14, 1979.

Crouch, S.L., and Starfield, A.M., 1983. Boundary Element Methods in Solid Mechanics. Unwin Hyman, Cambridge, Massachusetts.

Jaeger, J.C., and Cook, N.G.W., 1979. Fundamentals of Rock Mechanics. Routledge, Chapman & Hall, New York.

Zheng, Z., Myer, L.R., and Cook, N.G.W., 1989. Stress induced microcrack geometry at failure in unconfined and confined axial compressive tests. *In* Proceedings, 30th U.S. Symposium on Rock Mechanics, Morgantown, West Virginia, June 19–22, 1989 (LBL-26595).

Formation Factor and the Microscopic Distribution of Wetting Phase in Pore Space of Berea Sandstone

E. M. Schlueter, L. R. Myer, N. G. W. Cook, and P. A. Witherspoon

Transport properties of porous rocks, such as hydraulic and electrical conductivity, are determined by pore geometry, topology, and the physics and chemistry of mineral-fluid and fluid-fluid interactions. A primary focus of our research is to understand, through analysis and experiment, how these factors affect the macroscopic property under consideration. In our experimental electrical conductivity studies, we have employed a wetting fluid that can be frozen in place: (1) to allow measurement of effective properties with an electrolyte solution in the rock pore spaces not occupied by a wetting fluid, (2) to allow direct observation and analysis of the wetting-fluid distribution at each fluid-saturation regime, and (3) to understand how the wetting-fluid invasion process is controlled by rock pore structure and topology with the aid of a complete pore cast. In addition, disseminated clay, often in the form of aggregates, may line rock pores or be distributed between matrix grains. Clay minerals are the solid phases that primarily exhibit surface reactivity in rocks and soils (Sposito, 1984). In our investigation, we have isolated the effect of clay minerals on formation factor and assessed their surface conductance contribution. The formation factor of a fully saturated rock is the ratio of the resistivity of an electrolyte-saturated core sample to the resistivity of the electrolyte solution. When more than one fluid is present in the rock pore space, e.g., oil/water, the empirically determined Archie saturation is often found to vary according to (Archie, 1942)

$$F = \phi^{-m} S_w^{-n} ,$$

where F is the effective formation factor, ϕ is porosity, m and n are dimensionless empirically determined constants, and S_w is the electrolyte saturation. The value of m varies with the degree of rock cementation, from about 1.3 to 2.3 (Wyllie, 1963). The value of n depends to a large degree on the wettability of a reservoir rock (Anderson, 1986). In rocks that are wholly oil-wet, i.e., rocks in which water is the nonwetting phase, $3.0 < n < 4.0$, whereas if the rock surface is entirely water-wet, $1.8 < n < 2.0$ (Wyllie, 1963). The Archie saturation equation assumes that the saturation/resistivity relation is unique, n is constant for a given porous medium, and all the saline solution contributes to the flow of electric current. To verify these assumptions, we have analyzed the experimental electrical conductivity data in light of the role of pore structure in the wetting-fluid invasion process with the aid of fluid distributions at each saturation regime, a complete pore cast, and its associated rock section.

APPARATUS AND PROCEDURE

The apparatus used in this study was designed to measure simultaneously both hydraulic and electrical conductivity (Schlueter et al., 1992). The rock core (5 cm in diameter and 5 cm in length) is encased in its rubber jacket and placed in the test cell. The test cell base is connected directly to the bottom of the sample, and a centrally located orifice is attached to allow fluids to flow through the mounted core. The electrodes are connected to the top and bottom of the core sample so that any current flow between them will necessarily pass through the core. A confining pressure of 50 psi (3.4 atm) is applied using nitrogen gas. Fluid flow through the core is controlled by a syringe pump providing a constant flow rate of 200 ml/hr. The basic procedure used for measuring the formation factor in a 100% electrolyte-saturated sample is first to vacuum saturate each core completely with distilled water. An aqueous zinc nitrate solution of known resistivity is then pumped through the core, and flow is continued for a sufficient time to establish constant pressure and resistance readings. It was found that about four pore volumes of electrolyte is required to achieve steady state. In our experiments, we used samples of Berea sandstone, a homogeneous sedimentary rock of Mississippian age, found in Berea, Ohio, often used as a reference rock in the petroleum industry. The intrinsic permeability and porosity of a Berea sandstone core are about 600 md (600×10^{-15} m^2) and 22%, respectively.

EFFECT OF HYDROCARBON SATURATION

Pore system conductivity can be varied either by altering pore water salinity or by changing the quantity of water of a particular salinity by introducing another solid/fluid phase into the pore space. To determine the effect of partial fluid saturation on formation factor, we utilized Berea sandstone samples that had been permeated with a sequence of triple-distilled water (to measure the hydraulic conductivity) followed by a 0.5-M zinc nitrate solution and again flushed with distilled water. This procedure was applied to each sample to discern the formation factor before paraffin application. Samples were then oven dried. After measuring formation factor, samples were partially filled with paraffin wax at predetermined saturations of 20%,

40%, 50%, 60%, and 69%. Hydrocarbon paraffin is a wetting phase with a density of 0.76 g/cm^3 and a melting point of 56°C. It is applied in the rock at temperatures higher than its melting point until uniform saturation is achieved throughout the sample. The paraffin is then solidified in place at ambient temperature conditions. After the hydrocarbon paraffin application, rock grain surfaces became hydrophobic. To measure effective formation factor, rock samples partially saturated with paraffin were permeated with a 0.5-M zinc nitrate solution at pH ~ 4. The effective formation factor vs. paraffin saturation is presented in Figure 1 (case A). Experiments in which formation factor had not been measured prior to paraffin impregnation were carried out on virgin samples. The result is shown in Figure 1 (case B). In summary, good agreement within experimental error was found between empirical sets A and B.

EFFECT OF CLAY

X-ray diffraction studies by Khilar and Fogler (1984), in conjunction with scanning electron microscopy and energy-dispersive x-ray analysis, indicate that Berea sandstone contains ~ 8% by weight of dispersible and swelling clays (mainly kaolinite with some illite and smectite), 80% quartz, and 12% feldspar. To reduce the tendency for the clays to disperse, zinc, a bivalent cation, was used. For solutions with cations of valence > 1, at pH = 7, no critical salt concentration has been found below which clay is released from Berea sandstone pore walls (Khilar and Fogler, 1984). It is important to recognize that clay minerals present in the rock have been immobilized by coating pores with hydrocarbon paraffin. Therefore, formation factor extrapolated to an electrolyte saturation of unity (i.e., no hydrocarbon paraffin) corresponds to that of clean rock without clays and without surface conduction effects caused by the pressure of surface reactive minerals. Formation factor at a paraffin saturation of zero, F = 18 (Figure 1), has been extrapolated from a plot of the multiplicative inverse of the residual formation factor vs. paraffin saturation. This hypothesis was verified by partially removing clays in a Berea sandstone core by acid treatment with a mixture of 6% hydrochloric and 1.5% hydrofluoric acids (Suarez-Rivera, personal communication, 1991). After the core was treated and clays flushed out, formation factor was found to be 16.4, larger than the average formation factor of 15.7, measured for samples containing clay.

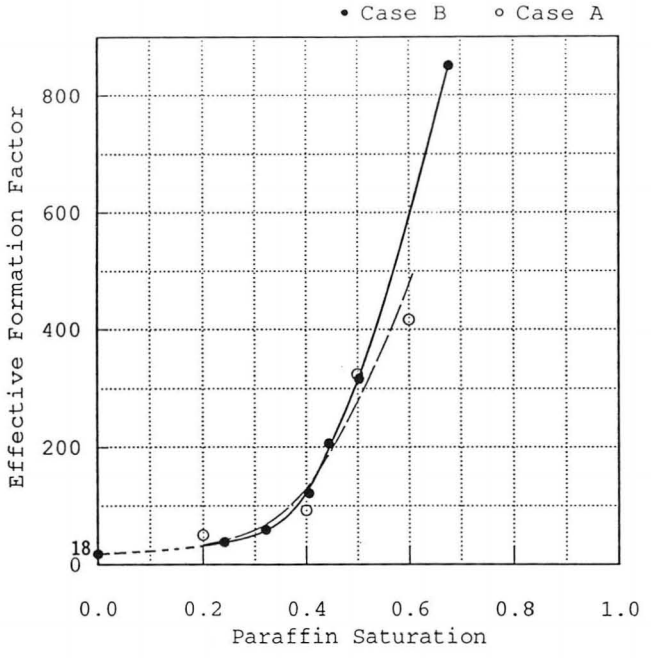

Figure 1. Effective formation factor vs. paraffin saturation for Berea sandstone. The pore space was partially saturated with hydrocarbon paraffin. The remaining portion of the pore space was filled with a 0.5-M zinc nitrate solution. Cases A and B correspond to experimental data on samples subjected or not subjected to a formation-factor measurement before paraffin application, respectively. [XBL 934-429]

EFFECT OF SURFACE CONDUCTANCE

To study the magnitude of surface conductance contribution due to clays on formation factor, we investigated the influence of solution concentration on rock electrical conductivity. Resistivity experiments were performed on Berea sandstone cores. Rock specimens were permeated with solutions of zinc nitrate at increasing concentrations from 0.005 M to 0.5 M while resistivity measurements were taken (Table 1). After equilibrium had been reached with one solution, another zinc nitrate solution of lower resistivity was flowed through the core, and a constant resistance reading was again obtained. The data thus obtained permitted the formation factor of the rock to be computed and also confirmed the ability of an invading fluid to displace interstitial water from a rock core. The trend of change in rock electrical conductivity at low electrolyte

Table 1. Resistivity data for Berea Sandstone with zinc nitrate solution saturating the sample.

M[a]	pH (effluent)	ρ_w (ohm-m)[b]	ρ_r (ohm-m)[c]
0.5	—	0.19	3.35
0.1	—	0.68	10.4
0.05	—	1.24	20.1
0.01	4.0	5.08	73.9
0.005	4.5	9.01	101.3

[a]Solution molarity.
[b]Solution resistivity.
[c]Rock resistivity.

concentrations reflects the contribution to surface conduction of clays. However, experimental results show that for Berea sandstone, the surface conduction component due to clays is a minor contribution to overall electrical conductivity and therefore can be ignored for most applications.

EFFECT OF PORE STRUCTURE

To understand how pore structure and topology control the transport property under consideration, electrical conductivity data (Figure 1) have been studied in light of the wetting-fluid distributions at each saturation regime (Figures 2 to 4) with the aid of a complete rock pore cast and its associated rock section (Figure 5). The rock pore cast was obtained from a rock specimen that had been fully impregnated with Wood's metal alloy and the quartz grains removed by hydrofluoric acid. The rock pore cast and its associated rock section clearly reveal that the pore space is composed of grain-contact porosity (thin sheets and micropores) and intergranular porosity. Figure 2 shows a scanning electron microscope (SEM) photomicrograph collage of a section of Berea sandstone that has been partially saturated with approximately 20–30% paraffin. The gray phase corresponds to quartz grains, the white phase corresponds to pores that have been impregnated with paraffin, and the black phase corresponds to the remaining pore space, which was filled with blue epoxy for imaging purposes. Paraffin has invaded grain-contact pore space (i.e.,

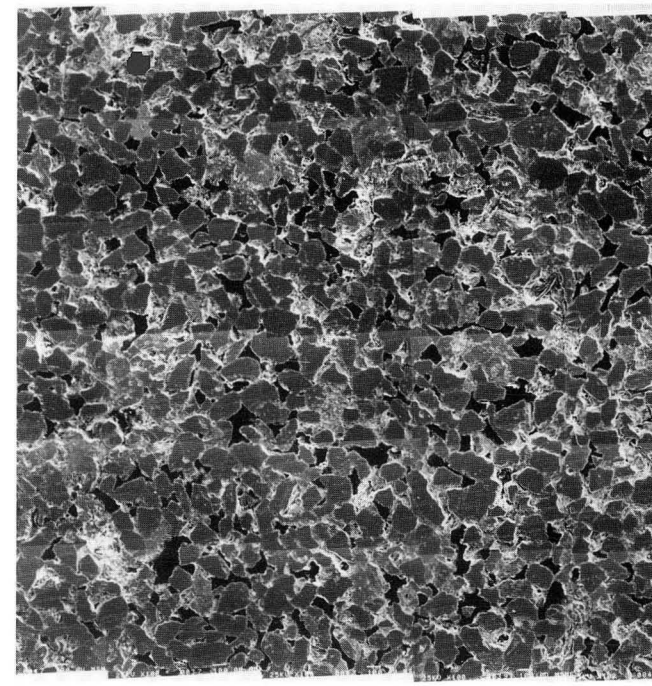

Figure 3. SEM photomicrograph collage of a Berea sandstone specimen impregnated with approximately 40–50% paraffin. The actual width of field is about 4.5 mm. The gray phase is quartz grains, the white phase is pores saturated with paraffin, and the black phase is remaining pores filled with blue epoxy for imaging purposes. [XBB 925-3164]

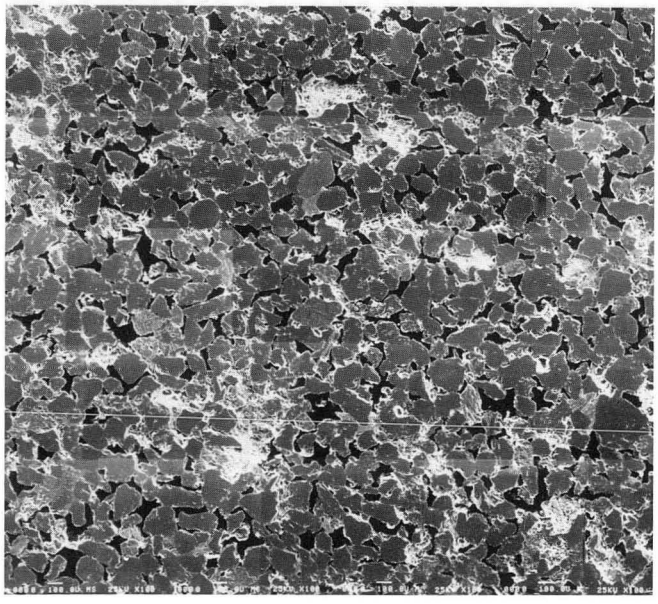

Figure 2. SEM photomicrograph collage of a Berea sandstone specimen impregnated with approximately 20–30% paraffin. The actual width of field is about 4.5 mm. The gray phase is quartz grains, the white phase is pores saturated with paraffin, and the black phase is remaining pores filled with blue epoxy for imaging purposes. [XBB 926-4990]

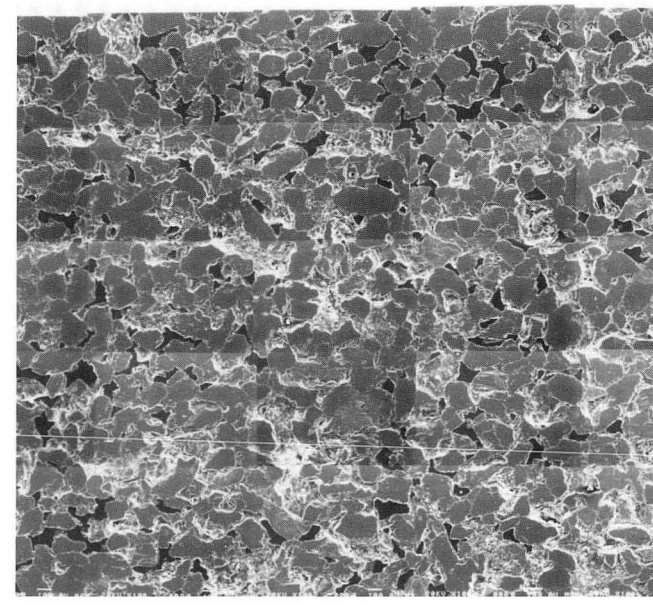

Figure 4. SEM photomicrograph collage of a Berea sandstone specimen impregnated with approximately 60–70% paraffin. The actual width of field is about 4.5 mm. The gray phase is quartz grains, the white phase is pores saturated with paraffin, and the black phase is remaining pores filled with blue epoxy for imaging purposes. [XBB 924-2700]

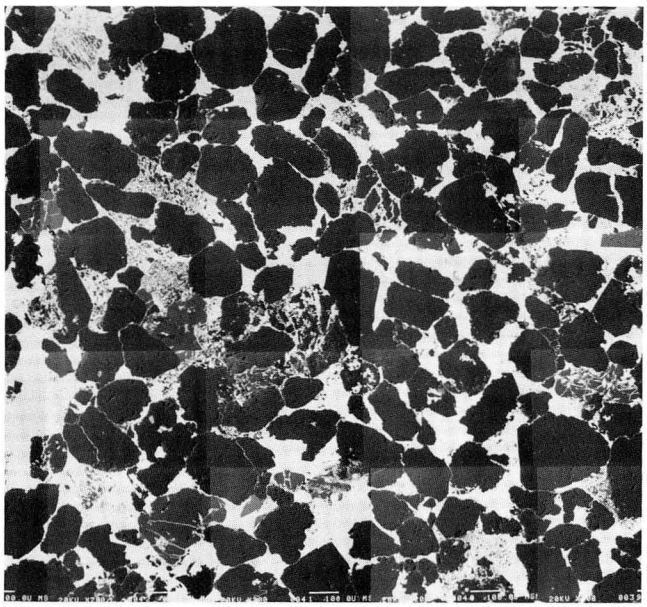

Figure 5. SEM photomicrograph collage of a Berea sandstone rock specimen fully impregnated with Wood's metal alloy. The actual width of field is about 2.3 mm. The gray phase is quartz grains, the white phase is pores saturated with the alloy. The section reveals that the pore space is composed of grain-contact porosity (i.e., thin sheets and micropores) and intergranular porosity. [XBB 932-1806]

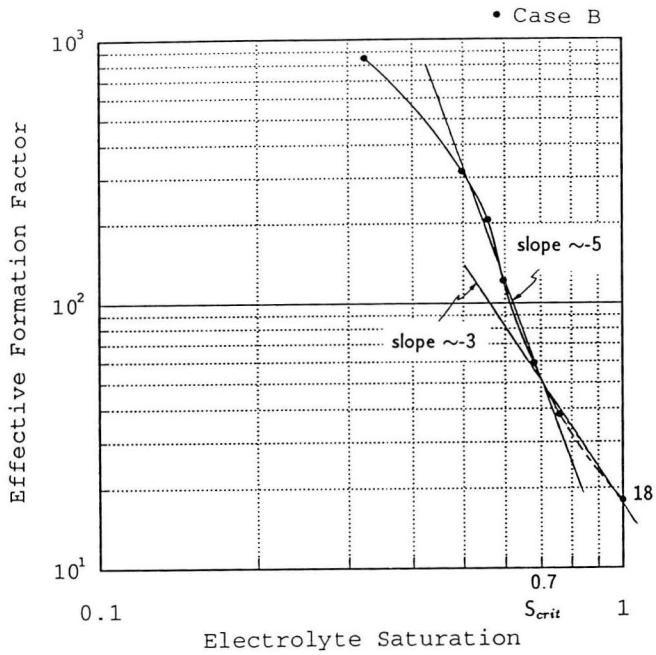

Figure 6. Effective formation factor vs. electrolyte saturation for Berea sandstone (case B). The pore space was partially saturated with hydrocarbon paraffin, with the remainder of the pore space filled with a 0.5-M zinc nitrate solution. [XBL 934-430]

thin sheets and micropores) and intergranular pore space connected by smaller throats but has only coated the available intergranular channels connected by larger throats. A strong effect on effective formation factor is observed. Therefore, the fraction of the pore structure connected by smaller constrictions provides the ions with important alternative routes to intergranular conduits connected by larger throats. Figure 3 shows an SEM photomicrograph collage of a rock section partially saturated with approximately 40–50% paraffin. At this stage, we are filling intergranular conduits connected by the larger throats, and a portion of the electrolyte has apparently lost continuity as the paraffin saturation is increased over about 30%, so that the resistivity increases at a faster rate. A still larger effect on effective formation factor is observed. Figure 4 shows an SEM photomicrograph collage of a rock section partially saturated with approximately 60–70% paraffin. We have filled almost all intergranular conduits connected by larger throats. A few intergranular pores not well connected still remain unfilled. When paraffin saturation is ~ 70%, the whole pore structure behaves as though disconnected.

THE ARCHIE SATURATION EXPONENT

Electrical conductivity data presented in Figure 1 (case B) have been replotted on a logarithmic scale for the effective formation factor vs. electrolyte saturation (Figure 6). To understand their physical significance, we have divided the plot into three zones: zone I, a linear zone of electrolyte saturations between about 0.7 (S_{crit}) and 1, with an Archie exponent of $n \sim 3$; zone II, a linear zone of electrolyte saturations between about 0.5 and 0.7, with an Archie exponent of $n \sim 5$; and zone III, a zone of electrolyte saturations less than 0.5. Zone I, with an Archie saturation exponent of approximately 3, reflects the fact that grain-contact pore space (e.g., thin sheets and micropores) and intergranular pore space connected by the smaller throats provide the ions with important alternate paths to intergranular conduits connected by larger throats. Zone II, with an Archie saturation exponent of approximately 5, reflects the fact that as the electrolyte saturation is lowered below S_{crit}, part of the rock structure composed of pores connected by the smaller throats becomes inactive. In addition, intergranular conduits connected by larger throats start being filled and partially filled with paraffin. Thus part of the electrolyte available for the transport of ions loses continuity and the resistivity is increased at a faster rate.

RECAPITULATION

Formation factor of a partially saturated rock with a wetting phase is controlled by the rock structure and topology as well as the physics and chemistry of mineral-fluid interactions. To understand the relationships, we have measured the effective formation factor with an electrolyte

in the pore spaces not occupied by a wetting fluid (paraffin wax) after solidifying the fluid in place. It is important to recognize that when the rock is partially saturated with hydrocarbon paraffin, clay minerals present in rock pore space are immobilized. Thus formation factor extrapolated to an electrolyte saturation of unity (and paraffin saturation of zero), $F = 18$, corresponds to that of "clean" rock (without clay). Even though the change in the trend of rock electrical conductivity at low electrolyte concentrations represents the contribution to surface conduction due to clays, this component is negligible. Effective formation factor data have been studied in light of the wetting-phase distribution observed at different saturations with the aid of a complete pore cast and its associated rock section. Our analysis shows that (1) ~ 30% of the pore space consists of grain-contact pores (i.e., thin sheets and micropores) and intergranular pores connected by smaller throats, (2) ~ 40% of the pore space consists of intergranular conduits composed of pores connected by larger throats, and (3) ~ 30% of the intergranular pore space remains disconnected. The grain-contact pore space of large surface areas (thin sheets), micropores, and intergranular pores connected by smaller throats provide the ions with important alternative paths to the intergranular conduits connected by larger throats. Therefore, for a consolidated rock such as Berea sandstone, we find no unique relationship between effective formation factor and electrolyte saturation, nor do we find a unique definition of the Archie saturation exponent, n, for the full range of saturation. Finally, the Archie saturation exponent n is found to vary from approximately 3 when connected grain-contact pore space (i.e., thin sheets and micropores) and intergranular pores connected by smaller throats are filled with hydrocarbon paraffin to approximately 5 when intergranular conduits connected by larger throats are filled with hydrocarbon paraffin, with a critical saturation (S_{crit}) of 0.7.

REFERENCES

Anderson, W.G., 1986. Wettability literature survey—Part 3: The effects of wettability on the electrical properties of porous media. J. Pet. Technol., v. 12, p. 1371–1378.

Archie, G.E., 1942. The electrical resistivity log as an aid in determining some reservoir characteristics. Trans. AIME, v. 146, p. 55–62.

Khilar, K.C., and Fogler, H.S., 1984. The existence of a critical salt concentration for particle release. J. Coll. Int. Sci., v. 101, p. 214–224.

Schlueter, E.M., Myer, L.R., Cook, N.G.W., and Witherspoon, P.A., 1992. Formation factor and the microscopic distribution of wetting phase in pore space of Berea sandstone. Lawrence Berkeley Laboratory Report LBL-33207.

Sposito, G., 1984. The Surface Chemistry of Soils. Oxford University Press, New York.

Wyllie, M.R.J., 1963. The Fundamentals of Electric Log Interpretation. Academic Press, Inc., New York.

Predicting the Capillary Pressure of Berea Sandstone from Microgeometry

E. M. Schlueter, R. W. Zimmerman, L. R. Myer, N. G. W. Cook, and P. A. Witherspoon

The macroscopic transport properties of porous (and fractured) media depend sensitively upon processes at the pore level, which are controlled principally by the geometry and connectivity of the pore space. In addition, the microphysical, microchemical, and microbiological processes at the pore level affect both the hydraulic and the electric properties of porous materials. Consequently, there is a need for a basic understanding of how pore morphology and other related factors can be used to predict single and multiphase physical properties of porous media, such as intrinsic permeability, relative permeability, and capillary pressure. Visual observation and analysis of Berea sandstone complete pore structure by means of pore casts reveal that the rock pore space is composed of grain-contact pore space (i.e., thin sheets and micropores) connected to larger intergranular pore segments and pore throats, with the whole structure arranged in a three-dimensional irregular network of irregularly shaped pores (Schlueter et al., 1992a).

In our study, we have attempted to understand, through analysis and experiment, how the relationship between capillary pressure and saturation is controlled by the rock pore structure and the distribution of wetting and nonwetting phases in the pore space. For this purpose, we have made analytical calculations of capillary pressure on the basis of pore microgeometry. As a zero-order approximation, we have idealized the porous medium as consisting of an assembly of parallel capillaries of arbitrary cross sections. The mathematical expression for capillary pressure as a function of saturation depends on the distribution of pore hydraulic radii and the area-perimeter power-law relationship of pores (Schlueter et al., 1992b). Two-dimensional scanning electron

microscope (SEM) photomicrographs of rock cross sections have been employed to measure directly the areas, perimeters, and hydraulic radii of the individual pores. Account is taken of the fact that the cross sections are randomly oriented with respect to the channel axes. The predictions of our model are compared with laboratory capillary pressure curves obtained with a technique using Wood's metal alloy as the nonwetting phase instead of the conventional mercury porosimetry. This technique allows for direct examination and analysis of the fluid distributions in the rock pore space (obtained at fixed pore pressures and saturation levels) after the experiment.

THE MODEL

In two-phase conditions, the capillary pressure between wetting and nonwetting phases in a circular tube of radius r is given by Laplace's equation (Scheidegger, 1974)

$$P_c = \frac{2\varsigma \cos\alpha}{r}, \tag{1}$$

where ς is the surface tension between wetting and nonwetting phases and α the contact angle between the wetting phase meniscus and the tube wall.

If the capillaries are not circular, the equation for the capillary pressure has to be generalized by replacing $2/r$ by $(1/r_1) + (1/r_2)$:

$$P_c = \varsigma\left(\frac{1}{r_1} + \frac{1}{r_2}\right), \tag{2}$$

where r_1 and r_2 are the principal radii of curvature of the meniscus.

If the pore openings are not of a simple geometric form, Eq. (2) is still a valid expression for the capillary pressure. To obtain a theoretical relationship between the saturation and capillary pressure for a porous medium, an analytical expression for the average interfacial curvature as a function of saturation is required. This is a very difficult task.

Schultze (1925a,b) has shown experimentally that the capillary pressures for such capillaries under the assumption of zero contact angle are given approximately by the equation

$$P_c = \frac{\varsigma}{R_H}, \tag{3}$$

where R_H is the ratio of area to perimeter of the capillary. A list of comparative values for testing Eq. (3) is given in Table 1 (Carman, 1941). Since Eq. (3) gives a reasonably accurate prediction of capillary pressure in noncircular capillaries, it can be assumed to be applicable to the capillary channels in a porous medium (Scheidegger, 1974).

In our model, it is assumed that there is no accessibility problem; i.e., regardless of the spatial arrangement of pores, the pores are occupied by the nonwetting phase in the order of largest pores first. Similarly, for the wetting phase, the pores are occupied by the wetting phase in the order of smallest pores first. Therefore, given a hydraulic radius distribution of intergranular pore space $\beta(R_H)$, and assuming that the pores are filled by the wetting phase in ascending order up to a cutoff radius R'_H, we may write the saturation of the wetting phase $S_w(R'_H)$ as (cf. Pruess and Tsang, 1989; Schlueter and Pruess, 1990)

$$S_w(R'_H) = \frac{\int_0^{R'_H} A(R_H)\beta(R_H)dR_H}{\int_0^{\infty} A(R_H)\beta(R_H)dR_H}, \tag{4}$$

where the pore hydraulic radius is defined as the ratio of the pore area A to the pore perimeter P.

Measurements of hydraulic radius of intergranular pore space obtained from two-dimensional SEM photomicrographs of Berea sandstone rock sections have been found to follow a skewed distribution that is well approximated by a log-normal distribution. The log-normal distribution is given by the following expression (hydraulic radius $R_H \geq 0$):

$$\beta(R_H) = \frac{1}{\sqrt{2\pi}\sigma \ln 10}\frac{1}{R_H}\exp\left(\frac{-\left[\log R_H - \log R_{H_0}\right]^2}{2\sigma^2}\right), \tag{5}$$

Table 1. List of comparative values to show equivalence of the reciprocal hydraulic radius $(1/R_H)$ and the reciprocal mean radius of curvature $(1/r_1) + (1/r_2)$ in a capillary (r_i is the radius of the inscribed circle).

Cross section	$1/r_1 + 1/r_2$	$1/R_H$
Circle	$2/r$	$2/r$
Parallel plates	$1/b$	$1/b$
Rectangle	$1/a + 1/b$	$1/a + 1/b$
Equilateral triangle	$2/r_i$	$2/r_i$
Square	$2/r_i$	$2/r_i$
Ellipse $a:b = 2:1$	$1.50/b$	$1.20/b$
Ellipse $a:b = 5:1$	$1.10/b$	$1.54/b$
Ellipse $a:b = 10:1$	$1.34/b$	$1.30/b$

Source: After Carman, 1941.

where R_{H_0} is the most probable hydraulic radius and σ the variance. The corresponding mean hydraulic radius R_{H_m} is larger than the most probable hydraulic radius; it is

$$R_{H_m} = R_{H_0} \exp\left(\frac{(\sigma \ln 10)^2}{2}\right) . \tag{6}$$

Invoking the perimeter-area power-law relationship (Schlueter et al., 1992b) gives

$$A = mP^{\gamma} , \tag{7}$$

where log m is the intercept on the log A axis and γ the noninteger slope of the log A – log P plot. The area can be expressed in terms of the hydraulic radius as follows:

$$A(R_H) = m^{1/(1-\gamma)} R_H^{\gamma/(\gamma-1)} . \tag{8}$$

Expressed in terms of the cutoff hydraulic radius, Eq. (4) becomes

$$S_w(R'_H) = \frac{\int_0^{R'_H} R_H^{\gamma/(\gamma-1)} \beta(R_H) dR_H}{\int_0^{\infty} R_H^{\gamma/(\gamma-1)} \beta(R_H) dR_H} . \tag{9}$$

Integrating Eq. (9) yields

$$S_w(R'_H) = \frac{1}{2}\left(1 \pm erf\left[\frac{(\log R'_H - \delta)}{\sqrt{2\sigma^2}}\right]\right) , \tag{10}$$

where the cutoff hydraulic radius is given by

$$R'_H = 10^{\delta - \sqrt{2\sigma^2}\, erfi(1-2S_w)} , \tag{11}$$

where $\delta = \sigma^2 \ln 10 \left[\gamma/(\gamma-1)\right] + \log R_{H_0}$, σ is the variance of log R_H, and *erf* and *erfi* are the error and the inverse error function, respectively. The capillary pressure is then given by

$$P_c = \frac{\varsigma}{R'_H} = \varsigma 10^{\sqrt{2\sigma^2}\, erfi[1-2S_w(R'_H)] - \delta} . \tag{12}$$

Capillary pressure is specific to the nature of the two fluids involved. If no specification is made, it is understood that the displaced fluid is a vacuum. If the displaced fluid is a vacuum, and the external pressure P_c is applied in a nonwetting fluid, then all capillaries with a radius larger than R'_H will be totally filled.

CORRECTION FOR PORE ORIENTATION

In the two-dimensional sections under consideration, however, the pore cross sections are randomly oriented with respect to the directions of the channel axes. The orientation effect has been corrected by means of the following geometrical and stereological considerations (cf. Underwood, 1970), which are exact for the case of circular cross sections.

For the hydraulic radius,

$$(R_H)_{actual} = \frac{\sqrt{2}}{2}\left\langle \frac{1}{\sqrt{1+\cos^2\theta}} \right\rangle^{-1} (R_H)_{measured} , \tag{13}$$

where the brackets denote a spherical average for pores of random orientation; i.e.,

$$\left\langle \frac{1}{\sqrt{1+\cos^2\theta}} \right\rangle = \frac{\int_0^{\pi}\int_0^{\theta_{\max}} \frac{\sin\theta}{\sqrt{1+\cos^2\theta}} d\theta d\phi}{\int_0^{\pi}\int_0^{\theta_{\max}} \sin\theta d\theta d\phi} , \tag{14}$$

with $\theta_{max} = \arctan(L/D)$, where (L/D) is the maximum ratio of pore length to diameter. Using an average value of $L/D = 5$, as estimated from the micrographs, we find that

$$(R_H)_{actual} = 0.85(R_H)_{measured} . \tag{15}$$

EXPERIMENTAL APPROACH

In this experimental investigation, we have sought to examine the relationship between the microscopic pore occupancy by means of the nonwetting fluid and its effect on capillary pressure. We have used three-dimensional imbibition of a nonwetting Wood's metal alloy instead of the conventional mercury porosimetry (Schlueter et al., 1992c). This technique offers the advantage of allowing analysis of the occupied pore space after the experiment. Wood's metal is an alloy of about 43% Bi, 38% Pb, 11% Sn, and 9% Cd, with a specific gravity of 9.6, a viscosity of about 1.3×10^{-3} Pa·s at 75°C, and a surface tension of about 400 mN/m (Yadav et al., 1987). The setup for the three-dimensional imbibition experiments consists of a metallic container of Wood's metal placed in a metal vacuum chamber provided with a lucite window and surrounded by a heating element to keep the metal molten (melting point varies from about 50 to 70°C, depending on its composition). A micrometer is attached to the metallic container to determine the pressure at which the Wood's metal first enters the specimen. The 50-mm-long and 50-mm-diameter

Berea sandstone sample is first oven-dried and then immersed in the molten Wood's metal in the metallic container and placed in the metal vacuum chamber. Then the sample is de-aired by applying a full vacuum for about 60 min, until no air bubbles are observed through the lucite window. A subatmospheric pressure is applied by drawing a partial vacuum, which is maintained at the desired value by a regulating valve until capillary equilibrium is achieved. Each sample was allowed to imbibe for approximately 90 min at a fixed equilibrium pressure and until no movement of Wood's metal was noticed through the lucite window. At a pressure of about 5 to 6 psia, the micrometer signaled the first indication of Wood's metal entering the pore space (probably an edge effect on the sample sides). The capillary pressure experiment was repeated on several samples by applying pressure in the range of approximately 6 to 14 psia. The imbibed samples were cut into four axial quarters, each of which had a different saturation. To minimize the effect of gravity (hydrostatic) gradient, we took the top quarter of each imbibed specimen at a particular equilibrium pressure and measured its saturation. Figure 1 shows the experimental capillary pressure curve obtained when partially saturating the rock with the nonwetting fluid. Fluid saturation increases rather sharply with a corresponding small increase in capillary pressure in the saturation range from about 10 to 50%. Our result is consistent with typical capillary pressure curves based on conventional mercury porosimetry saturation for Berea (BE-1) sandstone (Chatzis and Dullien, 1977). Berea (BE-1) sandstone has almost the same macroscopic properties as the Berea sandstone we used in our experiments (e.g., porosity of 22%, permeability to N_2 of 400 md, and a formation factor of 15.5). Berea sandstone is a homogeneous sedimentary rock used as a reference rock in the petroleum industry. It contains about 80% quartz, 12% feldspar, and 8% by weight of dispersible and swelling clays (mainly kaolinite, with some illite and smectite). It is estimated to be of Mississippian age and is found in Berea, Ohio.

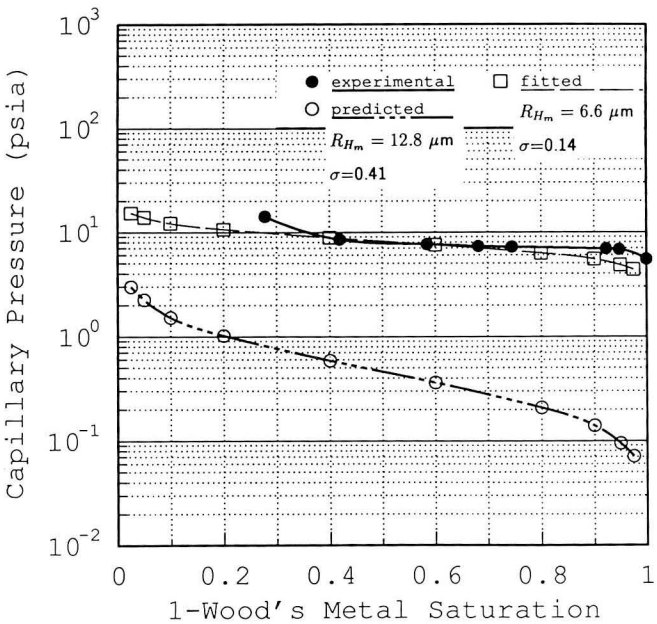

Figure 1. Experimental vs. predicted capillary pressure function for Berea sandstone. To obtain the experimental capillary pressure function, the rock has been impregnated with a nonwetting fluid (Wood's metal) at different equilibrium pressures and solidified in place. The procedure allows for direct observation and analysis of the fluid distribution at a fixed pore pressure and saturation level. [XBL 934-502]

PORE STRUCTURE AND TOPOLOGY

To understand how pore structure and topology control the physical property under consideration, we have studied the capillary pressure data in light of the nonwetting fluid distributions observed at each equilibrium pressure. For this purpose, optical and scanning electron microscopic examinations of the tops of samples (after cutting off 3 mm) have provided valuable insights into the pore-level complexity of the natural porous media. Figure 2 shows an optical photograph of the fluid distributions obtained in top axial quarters (top and bottom) in the pressure range 6.8 psia to 7.7 psia. It is observed that the nonwetting fluid flow network is composed of a set of imbibing clusters correlated in space. At every pressure step, the nonwetting fluid resides in the pores accessible through throats with a radius larger than that corresponding to the current equilibrium capillary pressure. As the pressure increases, the nonwetting phase saturation increases and the nonwetting fluid invades successively smaller pores and becomes connected to regions that were separated from this phase by small throats. Optical photographs of enlarged fluid distributions in top axial quarters obtained by partially saturating the rock with Wood's metal at equilibrium pressures of 6.8, 6.9, and 7.2 psia are presented in Figures 3, 4, and 5, respectively. At 6.8 psia (Figure 3), the fluid has preferentially penetrated the sample sides. The saturation is greatest near the perimeter of the sample and least at the center. This observation suggests that pores near the cylindrical surface of the sample are better connected than those toward the center. This interconnection could arise from exposure of pores where they intersect the surface or from damage adjacent to this surface. At 6.9 psia (Figure 4), a saturation gradation is observed in the direction of flow (preferentially horizontal). The longer flow paths are connected by smaller constrictions, so fewer flow channels are going to the sample center starting from all available channels at the sample surface. At pressures of 7.2 psia (Figure 5) and greater, the nonwetting fluid invades smaller and smaller pores, becoming connected to regions that were separated from this phase by smaller pores, and the clusters of nonwetting phase become larger and larger.

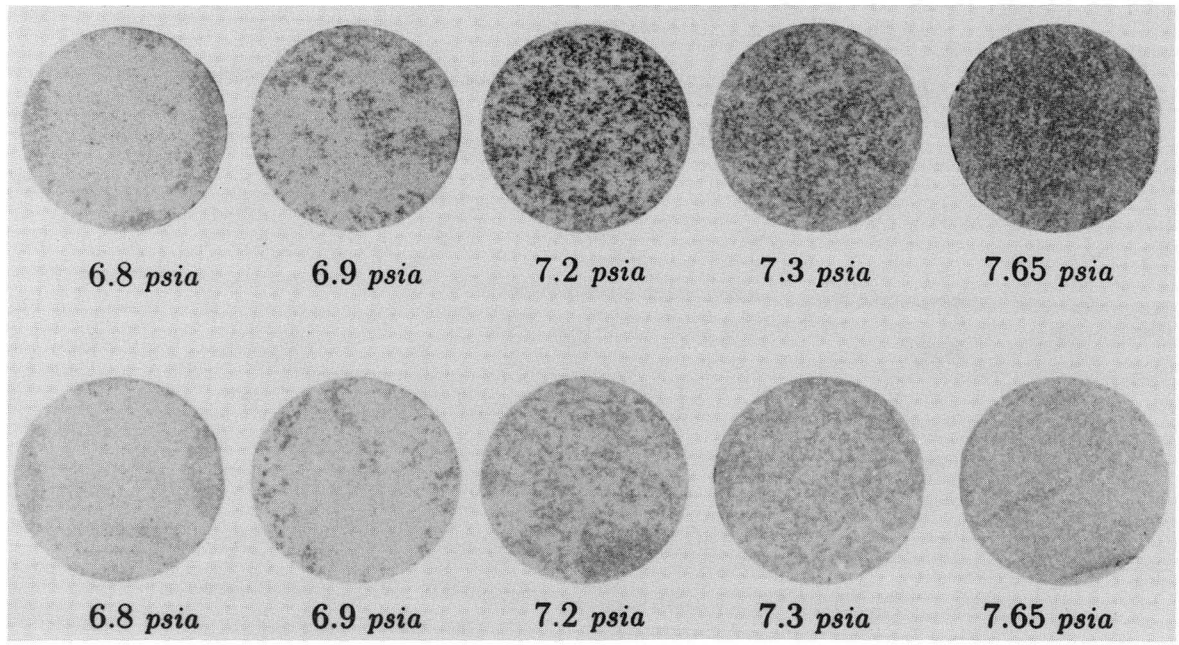

Figure 2. Top and bottom axial quarter sections of Berea sandstone core partially saturated with a nonwetting fluid (Wood's metal) at different equilibrium pressures and solidified in place. The sections reveal that the fluid distributions are composed of a set of imbibing clusters correlated in space. [CBB 919-7555]

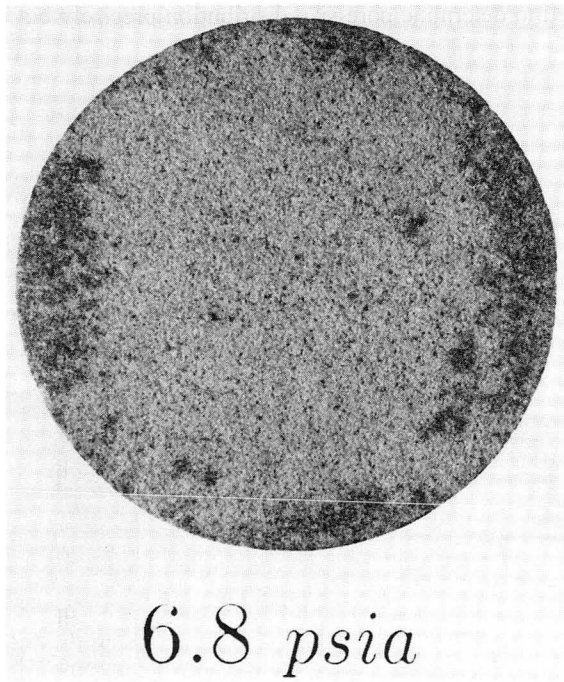

Figure 3. Top section of Berea sandstone core partially saturated with a nonwetting fluid (Wood's metal) at an equilibrium pressure of 6.8 psia and solidified in place. [CBB 910-8272]

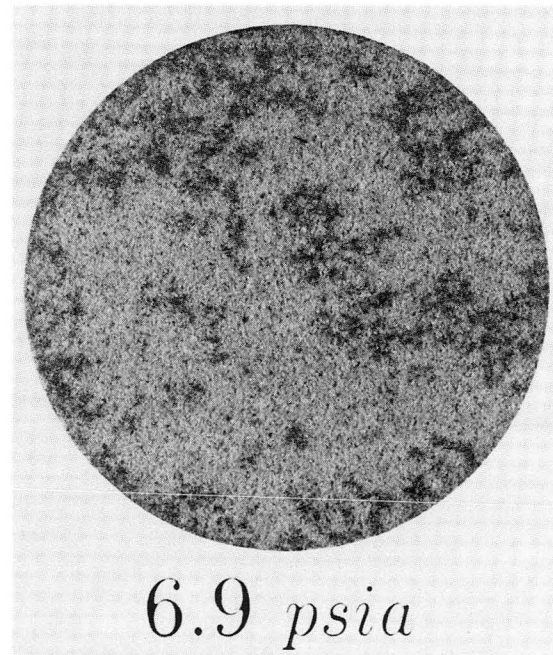

Figure 4. Top section of Berea sandstone core partially saturated with a nonwetting fluid (Wood's metal) at an equilibrium pressure of 6.9 psia and solidified in place. [CBB 910-8274]

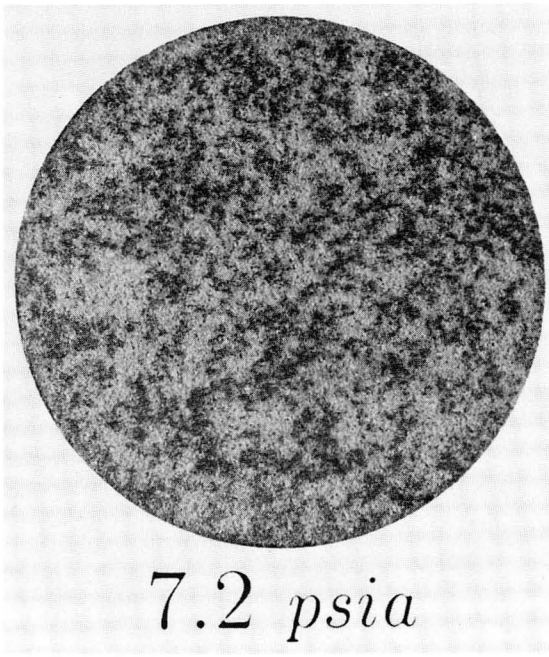

Figure 5. Top section of Berea sandstone core partially saturated with a nonwetting fluid (Wood's metal) at an equilibrium pressure of 7.2 psia and solidified in place. [CBB 910-8276]

APPLICATIONS

In this section, we calculate the predicted capillary pressure function for Berea sandstone for comparison with our experimental data. The analytical capillary pressure function for Berea sandstone has been computed using $\varsigma = 0.40$ N/m (surface tension), $\gamma = 1.49$ (perimeter-area power-law noninteger slope), $R_{H_m} = 12.8$ μm (mean hydraulic radius), $\sigma = 0.41$ (standard deviation), and $(R_H)_{actual} / (R_H)_{measured} = 0.85$ (stereological correction). It is worth noting that the contours of intergranular pore space used to obtain the perimeter-area power-law relationship of pores and the distribution of pore hydraulic radii are the same contours from which the transport properties (hydraulic and electric) have been previously calculated (Schlueter et al., 1991, 1992b). Preliminary results are presented in Figure 1. As expected, the predicted capillary pressure function from such a hydraulic radius distribution does not fit the experimental capillary pressure. The photomicrographic pore-size distribution gives a good measure of the larger pore bodies, but the smaller pore throats usually remain undetected. In addition, it is generally understood that pore-size distribution determined by mercury (or Wood's metal) porosimetry does not reveal the presence of larger pore bodies and assigns their volume to pore throats. To fit the analytical to the experimental function at approximately 50% fluid saturation, a distribution represented by $R_{H_m} = 6.6$ μm and $\sigma = 0.14$ is needed. An SEM photomicrograph collage of a rock specimen saturated with about 50% Wood's metal at 8.5 psia equilibrium pressure is presented in Figure 6. Simple statistical analysis of pore contour areas obtained from Figure 6 has shown that there are many intergranular pores connected by small intergranular throats that do not contribute to the flow of the nonwetting phase in the rock. In addition, the grain-contact pore space (i.e., thin sheets and micropores) does not contribute either. Therefore, a relatively small number of conduits connected by large intergranular throats carry a large fraction of the nonwetting fluid in the porous media under consideration, producing a clustered structure.

Thus our preliminary analyses show that the experimental capillary vs. saturation function (in the saturation range up to about 50%) is controlled primarily by large intergranular pore throats of narrow size distribution, represented by a mean hydraulic radius of about 6.6 μm, and a standard deviation of 0.14. This information is important because the resistance offered by the pore structure to various transport phenomena, i.e., permeability, is controlled by the pore throats.

CONCLUSIONS

Pore-size distributions and pore sizes of rocks have been measured by many researchers using a variety of methods (Dullien and Dhawan, 1974; Chatzis and Dullien, 1982; Chatzis et al., 1983; Yanuka et al., 1986; Jerauld and Salter, 1990). Most methods require a model of the pore space and simplifying assumptions. Because of these difficulties and the simplified model we use, we have not attempted to determine pore-size distribution precisely but use

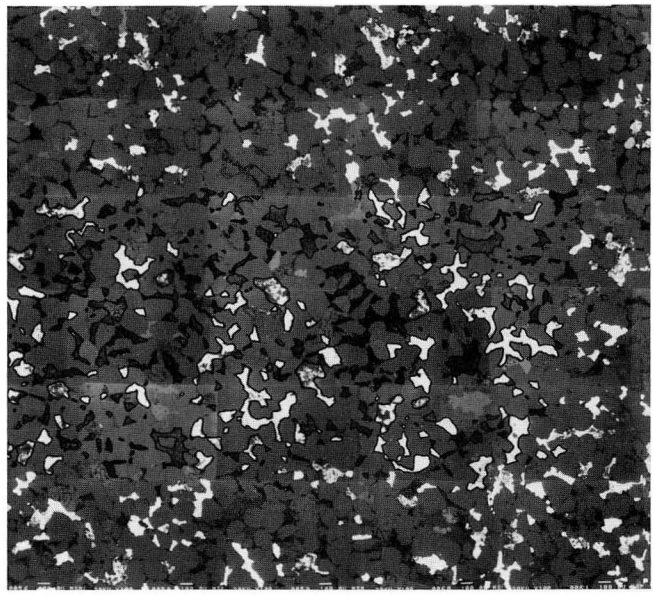

Figure 6. Scanning electron microscope photomicrograph collage of an enlarged partial section obtained from a Berea sandstone sample partially saturated with approximately 50% Wood's metal (white phase) at 8.5 psia equilibrium pressure. Actual width of the field is about 4.5 mm. [CBB 925-3596]

a simple functional form to determine average pore and throat sizes controlling capillary pressure. Our result, assuming a lognormal distribution of pore sizes, is consistent with the one obtained by Jerauld and Salter (1990), which uses an exponential pore-size distribution for Berea sandstone, and is similar to that used by Chatzis and Dullien (1982). For example, Jerauld and Salter (1990) found that pore throats are smaller than pore bodies; $r_{t_m} = 11\,\mu$m and $r_{b_m} = 38\,\mu$m. It should be noted that the simple concept leading to Eq. (12) has several limitations, so the result is only a first approximation. For example, we have ignored possible effects due to the wetting phase being held by small-scale roughness and adsorptive forces in the pore walls, and we have neglected the effect of clay minerals, which complicates phase occupancy. Finally, the model does not account for hysteresis effects that originate from different pore accessibilities during drying and wetting cycles.

On the basis of our experimental observations of the relationship between microscopic nonwetting fluid occupancy and the fluid distributions and of their effect on capillary pressure of Berea sandstone, we have found that relatively small number of channels connected by large intergranular throats of narrow size distribution are responsible for conducting a relatively large amount of the nonwetting fluid through the medium (at least in the saturation range up to approximately 50%). In fact, we have also found that a large percentage of the permeability of the medium is contributed by a relatively small number of conduits connected by large intergranular throats of narrow size distribution and high hydraulic conductance (Schlueter et al., 1992d).

REFERENCES

Carman, P.C., 1941. Capillary rise and capillary movement of moisture in fine sands. Soil Sci., v. 52, p. 1–14.

Chatzis, I., and Dullien, F.A.L., 1977. Modelling pore structure by 2-D and 3-D networks with application to sandstones. J. Can. Pet. Technol., v. 16, p. 97–108.

Chatzis, I., and Dullien, F.A.L., 1982. Application of the theory of percolation for a model of drainage in porous media and relative permeability of injected nonwetting liquid. Rev. l'Institut Francais du Petrole, v. 37, p. 183–205.

Chatzis, I., Morrow, N.R., and Lim, H.T., 1983. Magnitude and detailed structure of residual oil saturation. Soc. Pet. Eng. J., April, p. 311–326.

Dullien, F.A.L., and Dhawan, G.K., 1974. Characterization of pore structure by a combination of quantitative photomicrography and mercury porosimetry. J. Coll. Int. Sci., v. 47, p. 337–349.

Jerauld, G.R., and Salter, S.J., 1990. The effect of pore structure on hysteresis in relative permeability and capillary pressure: Pore-level modeling. Transport in Porous Media, v. 5, p. 103–151.

Pruess, K., and Tsang, Y.W., 1989. On relative permeability of rough-walled fractures. Lawrence Berkeley Laboratory Report LBL-26509.

Scheidegger, A.E., 1974. The Physics of Flow through Porous Media. University of Toronto Press.

Schlueter, E., and Pruess, K., 1990. Sensitivity studies on parameters affecting gas release from an underground rock cavern. Lawrence Laboratory Report LBL-28818.

Schlueter, E., Zimmerman, R.W., Cook, N.G.W., and Witherspoon, P.A., 1991. Predicting permeability and electrical conductivity of sedimentary rocks from microgeometry. *In* Proceedings, 32nd U.S. Symposium on Rock Mechanics, A.A. Balkema, Rotterdam, p. 355–364.

Schlueter, E., Myer, L.R., Cook, N.G.W., and Witherspoon, P.A., 1992a. Formation factor and the microscopic distribution of wetting phase in pore space of Berea sandstone. Lawrence Berkeley Laboratory Report LBL-33207.

Schlueter, E., Zimmerman, R.W., Cook, N.G.W., and Witherspoon, P.A., 1992b. Perimeter-area power-law relationship of pores in sedimentary rocks and implications for permeability. *In* Earth Sciences Division Annual Report 1991. Lawrence Berkeley Laboratory Report LBL-31500.

Schlueter, E., Zimmerman, R.W., Myer, L.R., Cook, N.G.W., and Witherspoon, P.A., 1992c. Predicting the capillary pressure of sedimentary rocks from microgeometry. Lawrence Berkeley Laboratory Report LBL-33830.

Schlueter, E., Myer, L.R., Cook, N.G.W., and Witherspoon, P.A., 1992d. Residual permeability and the distribution of wetting and non-wetting phases in pore space of Berea sandstone. Abstract presented at the 29th Annual Technical Meeting of the Society of Engineering Science, La Jolla, California. Lawrence Berkeley Laboratory Report LBL-32564A.

Schultze, K., 1925a. Kapillarität, Verdunstung, und Auswitterung. Kolloid Ztschr., v. 36, p. 65–78.

Schultze, K., 1925b. Kapillarität und Benetzung. Kolloid Ztschr., v. 37, p. 10–17.

Underwood, E.E., 1970. Quantitative Stereology. Addison-Wesley, Reading, Massachusetts.

Yadav, G.D., Dullien, F.A.L., Chatzis, I., and Macdonald, I.F., 1987. Microscopic distribution of wetting and nonwetting phases in sandstones during immiscible displacements. SPE Res. Eng., May, p. 137–147.

Yanuka, M., Dullien, F.A.L., and Elrick, D.E., 1986. Percolation processes and porous media: I. Geometrical and topological model of porous media using a three-dimensional joint pore size distribution. J. Coll. Int. Sci., v. 112, p. 24–41.

Application of Graph Theory to the Simulation of Percolation and Unsaturated Flows in Reservoir Rocks and Heterogeneous Vadose Zones

G. Yang, N. G. W. Cook, and L. R. Myer

The underground migration of contaminants is determined directly by the porosity and permeability of rock matrix to water and air. In principle, the necessary constitutive relationships can be obtained from laboratory measurements of capillary pressure and relative permeability data, both as a function of saturation, for each lithologic unit. Such an empirical approach is impracticable and uneconomic. Furthermore, such constitutive relationships are, in fact, only averages of these properties at the scale of the measurements. Heterogeneity, at all scales from pores to aquifers, frequently renders calculations based on homogeneous average properties inexact and inadequate. An understanding of the relationships between these properties and the microgeometry and topology at the pore level would go far toward alleviating these problems.

A variety of conceptual models ranging from bundles of capillary tubes to percolation theory, have been invoked to analyze and understand these complex relationships. Although the contributions of these models cannot be overemphasized, their weaknesses should not be ignored. We have recently conducted one-dimensional, nonwetting-phase invasion experiments on cores of Berea sandstone using Wood's metal. These experiments revealed the surprising result that "preferred paths" of best-interconnected pores and throats dominate breakthrough, relative permeability, and electrical resistivity. The concept of "preferred paths" on a different scale has become topical in hydrology of vadose zone, which is the major concerning zone in groundwater pollution.

The objectives of this study are to obtain a much better understanding than currently existing micronetwork models provide of unsaturated flow through heterogeneous porous materials and of the relationship between the material properties and the geometry or topology of the pore space. These objectives can be attained through numerical experiments on irregular networks, with different stochastic and spatially correlated properties, representing the geometry and interconnectedness of the pore space using the techniques of network analysis and graph theory. We expect that this will lead to a fundamentally different and more useful understanding of two-phase flow in porous media. Such an understanding is needed to improve our ability to determine those characteristics of such media important to contaminant migrations from a variety of different measurements. These concepts can also enable us to provide more realistic models for the analysis of two-phase flow; i.e., models that recognize the intrinsically heterogeneous and stochastic nature of the pore space.

To analyze the "preferred path" phenomenon and its relationship to pore geometry and interconnectedness, we have developed a numerical simulation program based on an irregular, two-dimensional, stochastic, and spatially correlated network. We analyze the behavior of this network using network techniques and graph theories. The analyses have revealed (1) the effects of stochastic and spatially correlated properties of the pore space on wetting or nonwetting-phase breakthrough, invasion, imbibition, draining, and trapping and (2) the influence of viscous, capillary, and gravity forces and micropermeability. A hierarchical method is used to find the path with largest minimum throat diameter or largest "bottleneck." Individual elements are placed into the network in decreasing order of throat diameter until a percolating path is formed. This is the critical path along which the first breakthrough takes place with the minimum capillary pressure. Although it is highly conductive, it is not necessarily the most conductive path. To find the preferred path of greatest conductance, several "priority first search" (Sedgewick, 1990) techniques have been used. To simulate the imbibition and drainage process, we used a priority queue structure according to which all connected neighbors are queued in the order of their diameters. The searching methods are employed to identify preferred paths for irregular networks with both near-uniform and highly skewed distributions of throat diameters, with or without spatial correlation. The results show that preferred paths become increasingly dominant as the throat diameters become more spatially correlated.

We compared the strongly spatially correlated networks with homogeneous ones in various probabilistic distributions. The simulation results show that the preferential pattern is the dominating feature in the spatially correlated network (Figure 1). For the homogeneous network, the patterns of preferred path might be seen if the throat diameters are distributed over a wide range. If the diameter distribution is narrowed down to a small range, the invasion will have basically a uniform front. For the invasion simulation, it can be seen that the computer results resemble the basic features of the lab experiment by Agrawal et al. (1991). For the imbibition and drainage simulation, the results can also be verified by Schlueter's experiments using wax as wetting fluid (Schlueter et al., 1992). Schlueter discovered that, under a microscope, most of the small voids are seen to be filled with wax, but some large voids are coated with wax. It is evident that the wax flows through the large diameters as preferred paths but is sucked into smaller diameters because smaller throats have larger

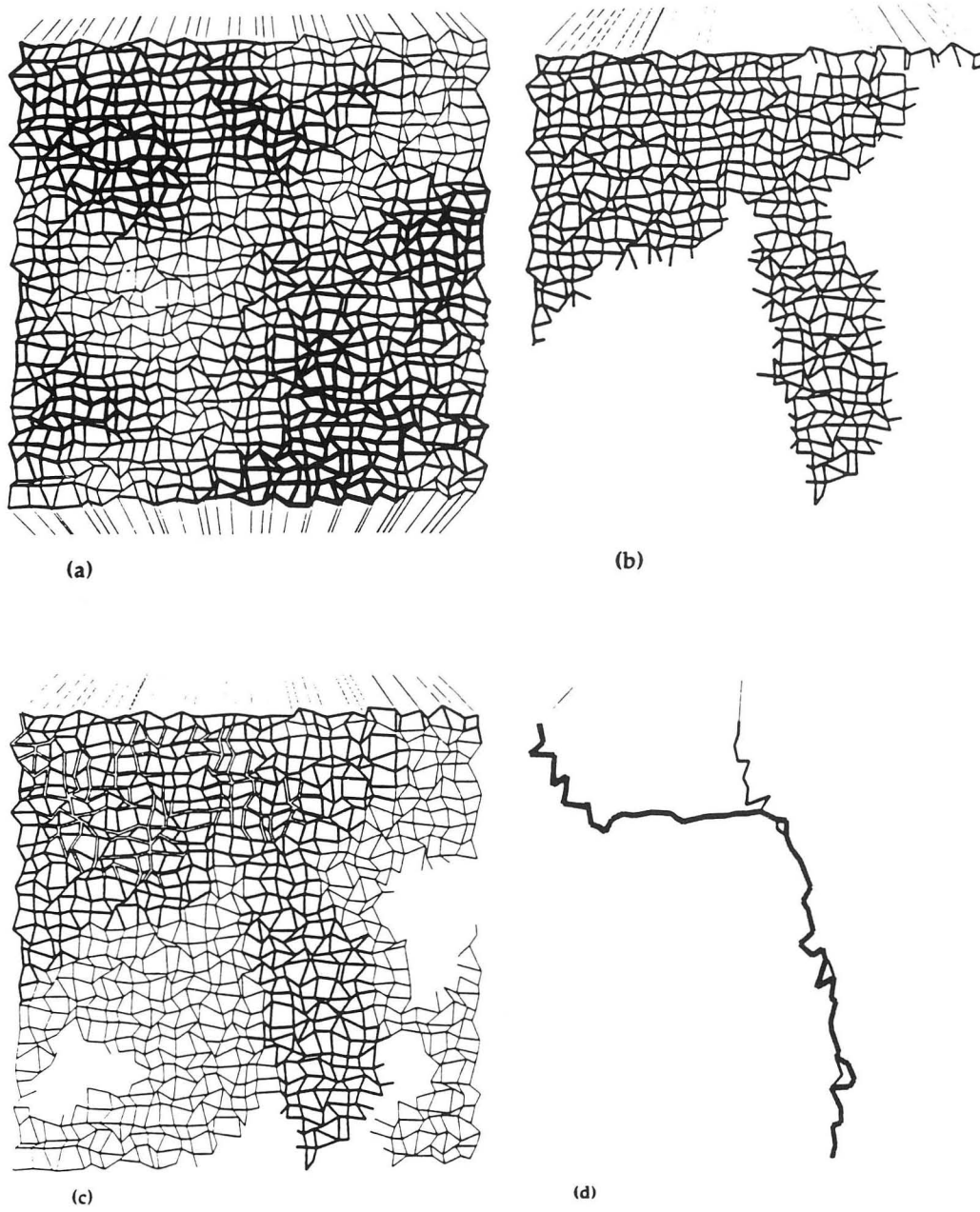

Figure 1. (**a**) Randomly generated network. (**b**) The invasion process. (**c**) The imbibition and drainage process. (**d**) Critical path (heavy line) and preferred path (light line) for spatially correlated distribution. [XBL 934-503]

capillary force. The simulation results show that the preferential trend of a medium is a strong function of spatial correlation, whether the fluid is wetting or nonwetting. For the random distributions without spatial correlation, the preferential trend is not very clear. Especially when the range of the distribution is narrow and uniform, the medium shows little possibility of forming any preferred path. The explanation for this is that connectivity rather than conductivity is the major factor in a heterogeneous flow field; high conductivity at local sites may contribute little to the global flow. Spatial correlation makes it possible for clusters of highly conductive elements to form bundles of channels that become the major contributors to the global flow.

REFERENCES

Agrawal, D.L., Cook, N.G.W., and Myer, L.R., 1991. The effect of percolating structures on the petrophysical properties of Berea sandstone. *In* Proceedings, 32nd U.S. Symposium on Rock Mechanics, Norman, Oklahoma, p. 345–354.

Schlueter, E.M., Cook, N.G.W., Witherspoon, P.A., and Myer, L.R., 1992. Relative permeability and microscopic distribution of wetting and non-wetting phases in pore space of Berea sandstone. Abstract presented at the American Geophysical Union Fall Meeting, San Francisco, California, December 7–11, 1992 (LBL-34109A).

Sedgewick, R., 1990. Algorithms in C. Addison-Wesley Publishing Company, Inc., New York.

RESERVOIR ENGINEERING AND HYDROGEOLOGY

The scientists and engineers of the Reservoir Engineering and Hydrogeology group are primarily concerned with the fundamental problem of the movement of mass and energy through heterogeneous porous or fractured-porous geologic formations. Several approaches—including modeling studies, laboratory measurements, and field experimentation—are used to unravel the complex processes that control such systems.

The group has contributed significantly to the understanding of fluid flow and tracer transport through single fractures and fracture networks in rocks. There is substantial activity in the area of multiphase and multicomponent nonisothermal flow through fractured porous media. A major effort is being applied to the development and field application of quantitative techniques for monitoring and predicting the movement of inorganic solutes and organic liquids in the subsurface. Another area of the group's diverse research program concerns the rather difficult problem of coupled effects relating thermal transfer, fluid flow, and mechanical stress changes in rocks.

Results of these different studies have found application in environmental evaluation and remediation projects, nuclear waste geologic disposal, and geothermal reservoir engineering. Other projects in which the group is active include petroleum reservoir engineering and advanced borehole testing techniques.

Numerical Study of the Effects of Brine Injection on the CP1 Production Area of Cerro Prieto

E. Antúnez and M. J. Lippmann

The present study is being conducted, under a cooperative agreement between the United States Department of Energy (DOE) and Mexico's Comisión Federal de Electricidad (CFE), to analyze how brine injection could affect the shallow (α) and deep (β) reservoirs of the CP1 production area of the Cerro Prieto geothermal field, Baja California, Mexico. Since the beginning of the exploitation of Cerro Prieto in 1973, one of the most important operational problems that CFE has had to face was the handling of the waste brine (Hiriart and Gutiérrez Puente, 1992). To date, most of the brine is discarded by means of evaporation ponds that cover an area of 18.6 km^2 (4600 acres) (Figure 1). An infiltration area west of the ponds is used during the winter, when the evaporation rate is significantly lower. Recently, CFE started a series of cold brine (approximately at 20°C) injection tests, using brine from the evaporation ponds. The objectives of these tests were to monitor the reservoir's response to injection and to test the injectivity of different areas of CP1 in the western part of the field. CFE's eventual goal is to inject all the separated brine back into the system, to eliminate its surface disposal, and, at the same time, maintain pressure in the reservoir.

The main objective of the present study is to use numerical simulation to help CFE define the possible location(s) for injection, minimizing possible negative effects and maximizing reservoir pressure. Of special interest is determining how brine injection will affect the CP1 zone in which wells are currently producing a steam and brine mixture. A numerical model of CP1 was built using data provided by CFE. The computational grid was defined on the basis of the geological model of the field (faults and structural features of the gray shale and the basement, as provided by CFE), the location and completion of the production and injection wells (see Figure 2), and interpretation of geochemical data (Truesdell et al., 1989). Figure 1 shows the location of the simulation grid with respect to the different Cerro Prieto production areas. In the vertical direction the model extends from the surface to 5000 m depth and is divided into six layers. All the layers have the same areal distribution and have 235 grid elements (Figure 3), except layer 5, which has 47 additional blocks in the northeast, simulating the volume of the CP2, CP3, and CP4 areas. The numerical model has a total of 1457 elements and was developed as a single-porosity model. The simulation

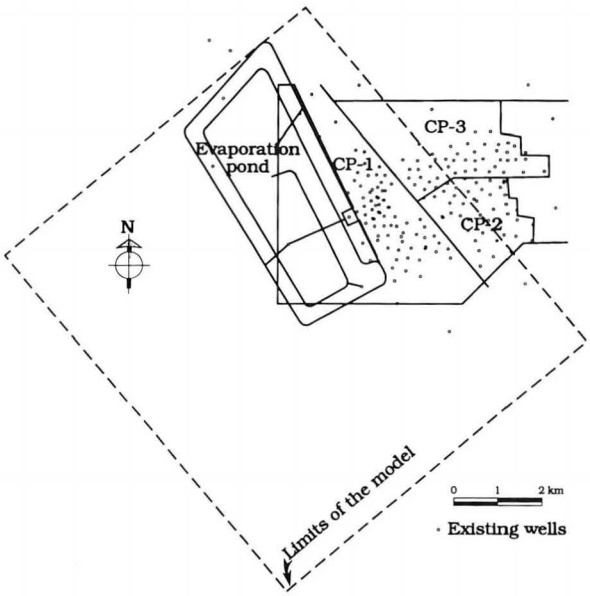

Figure 1. Location of the limits of the model with respect to the Cerro Prieto production areas. [XBL 935-801]

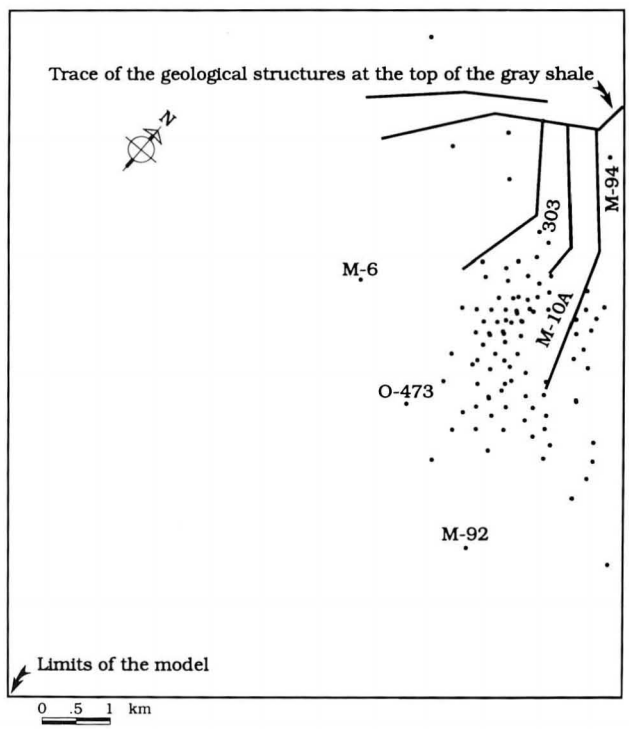

Figure 2. Well locations and geological structures within the modeled area. [XBL 935-802]

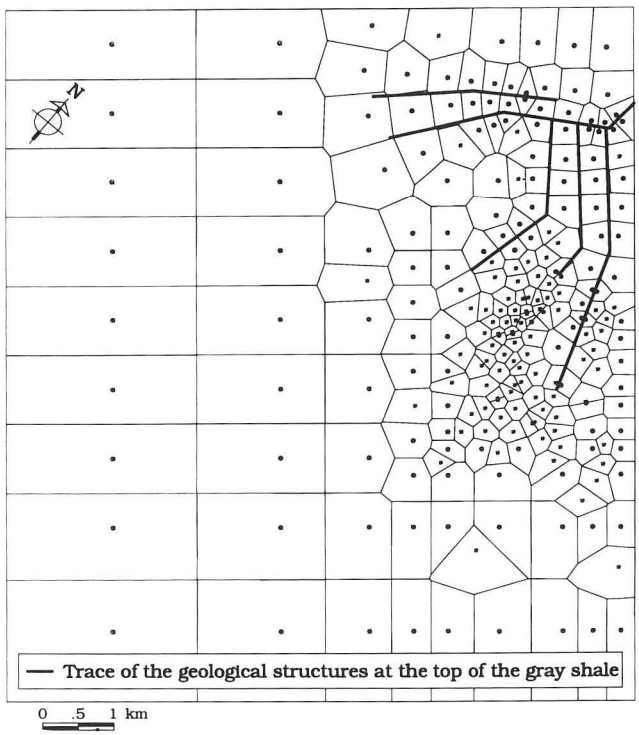

Figure 3. Areal distribution of the grid used in the numerical model to study the effects of brine injection in CP1. [XBL 935-803]

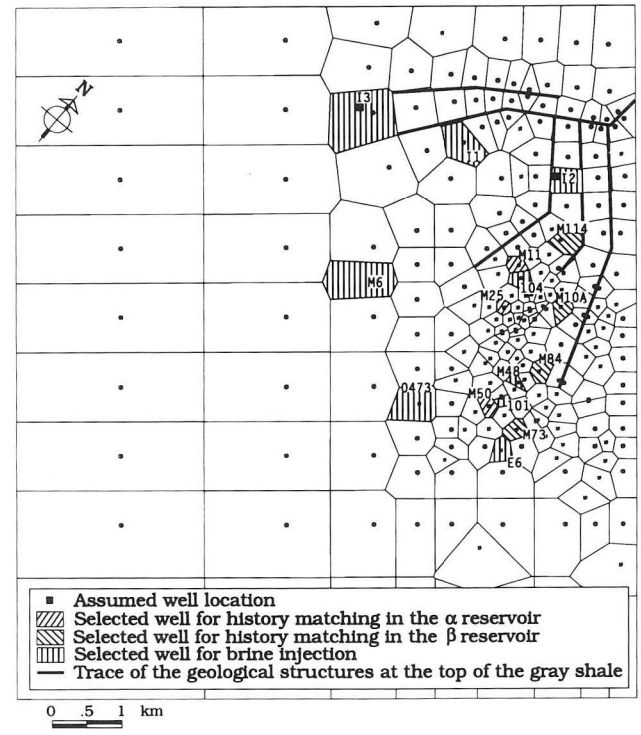

Figure 4. Location of the wells selected for production-history matching and to study brine injection. [XBL 935-804]

runs are being done with the TOUGH2 simulator developed at LBL (Pruess, 1991) and an improved matrix solver implemented by Bullivant et al. (1991).

The calibration of the model is being conducted in three stages. The first stage consists of the reproduction, with the model, of the undisturbed (initial-state) temperatures and pressures. The second stage will be achieved when the model matches (1) the production enthalpy history from April of 1973 to the end of 1985 and (2) the 1985 downhole measured pressures. The third stage will include the matching of the production data from 1986 (year that CP2 and CP3 started operating) to the end of 1991. Not all the active wells in CP1 were used for the history match; instead, seven wells with typical production behavior from the different CP1 zones were chosen. The selected wells with completions in the shallow reservoir (α) are M-11, M-25, and M-50; those completed in the deep reservoir (β) are M-10A, M-73, M-84, and M-114. Figure 4 shows the location of these wells in the computational grid. After the third calibration stage is accomplished, the model is used as a prediction tool to determine the behavior of the CP1 area under various assumed production/injection scenarios.

Personnel of CFE and LBL defined four scenarios to analyze the CP1 area response to 5 years of brine injection, starting on January 1, 1992.

Scenario I. Base case. Wells will continue producing at a rate equal to that measured at the end of 1991, when the average field production was 5459 t/h of steam and 6394 t/h of separated brine. No injection will be considered.

Scenario II. Inject 3500 t/h of 20°C brine evenly distributed between injection wells M-48, 101, 104, E-6, O-473, and M-6. Production is the same as for Scenario I. Injection well locations are shown in Figure 4.

Scenario III. Inject 3500 t/h of 20°C brine using six wells. Wells I-1, I-2, and I-3 will be receiving 800 t/h each, and the rest will be evenly distributed between wells E-6, O-473, and M-6. Production is the same as for Scenario I.

Scenario IV. Inject 3500 t/h of brine evenly distributed between wells M-48, 101, 104, E-6, O-473, and M-6. The first four wells will be injecting brine at 150°C and the other two at 20°C. Production is the same as for Scenario I.

To date, all stages of calibration and prediction are partially completed. At this point, these different stages are carried out sequentially from initial state to the end of the scenarios, changing the fitting parameters for the different simulation runs according to the results of previous runs.

The matching procedure is finished when the "best" match to the measured data is achieved. Preliminary results obtained from the prediction runs show that after injecting 3500 t/h of brine for 5 years, the temperature and pressure changes around the injection areas are not significant.

RECOMMENDATIONS

If a program of brine injection similar to those proposed in Scenarios II to IV is carried out in CP1, it is recommended that a temperature and pressure monitoring program be established using observation wells around the injection areas. Data collected from the observation wells should be used as feedback to the simulation model. The model could be a useful tool to detect and/or to predict trouble zones in the field. We consider that the analyses of the data from the observation wells and the simulation model will be a very useful in the design of the large-scale brine injection operations planned for Cerro Prieto.

REFERENCES

Bullivant, D.P., O'Sullivan, M.J., and Zyvoloski, G.A., 1991. Enhancements of the MULKOM geothermal simulator. *In* Proceedings, Thirteenth New Zealand Workshop, p. 175–182.

Hiriart, G.L., and Gutiérrez, H.P., 1992. An update of Cerro Prieto geothermal field—Twenty years of commercial power. Geoth. Resour. Counc. Bull., Sept/Oct, p. 289–294.

Pruess, K., 1991. TOUGH2—A general-purpose numerical simulator for multiphase fluid and heat flow. Lawrence Berkeley Laboratory Report LBL-29400.

Truesdell, A.H., Terrazas, B., Hernández, L., Janik, C., Quijano, L., and Tovar, R., 1989. The response of the Cerro Prieto reservoir to exploitation as indicated by fluid geochemistry. *In* Proceedings, Symposium on the Field of Geothermal Energy. U.S. DOE and CFE of Mexico Agreement, April 4 and 5, 1989, San Diego, California, p. 123–132.

Slit-Island Fractal Analysis of Single Fracture Aperture Patterns

B. L. Cox and J. S. Y. Wang

The character of fracture openings (apertures) is often one of the primary factors controlling fluid flow in the fracture. In particular, the shape, distribution, and connectivity of contact areas and flow channels can affect the relative permeability of wetting and nonwetting fluid phases in unsaturated systems. We used three methods of fractal analysis (the slit-island, the divider, and the variogram) as well as statistical and geostatistical analysis to characterize the geometry of measured fracture apertures obtained from two fractured rock specimens (Cox and Wang, 1993). One of these is a fracture in a granitic rock of homogeneous lithology; the other is a fracture in a specimen obtained from a highly altered fault zone containing striations and slickensides.

FRACTURE APERTURE DATA

Fracture aperture measurements of a fractured rock specimen sampled from a fault near Dixie Valley, Nevada, were obtained by three nondestructive fracture measurement techniques. The fracture aperture pattern was measured by profilometry (Power, 1989), by light transmission through translucent silicone casts (Cox et al., 1990), and by light transmission through dyed fluid in epoxy replicas of the rock (Persoff and Pruess, 1993). We examined the Dixie Valley fracture aperture as measured by the dyed-fluid method (Persoff and Pruess, 1993) and compared its aperture topography with that of a fracture in a specimen of Stripa granite (Persoff et al., 1991) measured by the same technique. Using this same approach, we compared the variability of the three Dixie Valley data sets measured by different techniques with the aim of distinguishing intrinsic features from experimental artifacts.

FRACTAL ANALYSIS BY THE SLIT-ISLAND METHOD

Fractal geometry offers an approach to geometric description of irregular geometric patterns (Mandelbrot, 1982). The fractal dimension of topographic surfaces measures the rate of change in the total length of contours or profiles as a function of the rate of change of a measurement interval. The fractal analysis of surfaces can be approached by at least seven different measurement methods (Cox and Wang, 1992), including the divider, variogram, and slit-island methods.

The slit-island method was first introduced by Mandelbrot et al. (1984), who used it to determine the fractal dimension of steel fractures. We applied this technique numerically to topographic surfaces (Figure 1) of

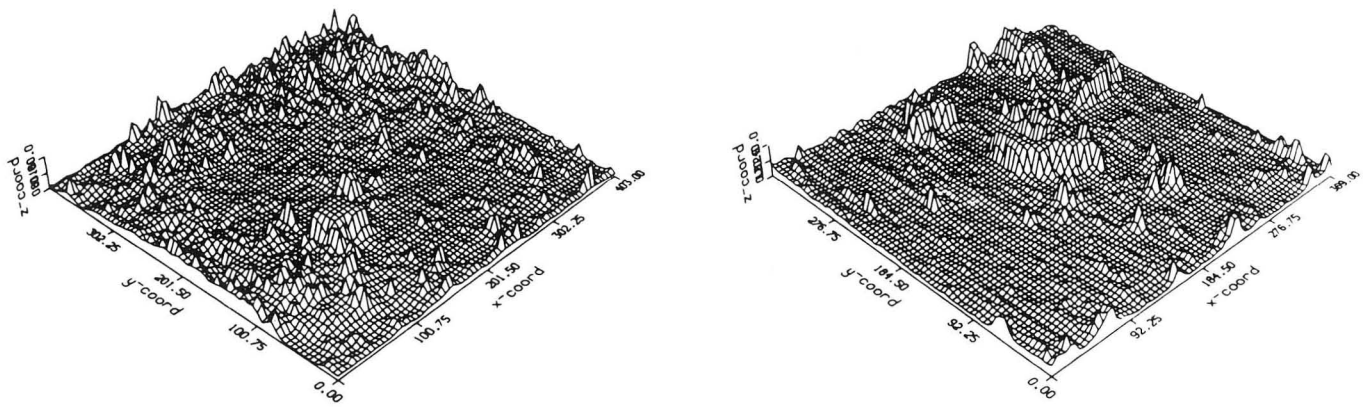

STRIPA FRACTURE

Min = 0.0 μm
Max = 110.06 μm
Mean = 37.00 μm
Standard Deviation = 21.28 μm
Covariance = 0.58
Skewness = 1.01
Kurtosis = 0.95
N = 152,943

DIXIE VALLEY FRACTURE

Min = 0.0 μm
Max = 152.90 μm
Mean = 41.95 μm
Standard Deviation = 20.92 μm
Covariance = 0.50
Skewness = 1.84
Kurtosis = 5.05
N = 128,014

Figure 1. Surface plots of Stripa and Dixie Valley fractures. [XBL 935-805]

data measurements (aperture thickness) by selecting several cutoffs, thereby creating surface contours that divided the surface into two kinds of shapes, positive (islands) and negative (water). We measured both the perimeter and the area of each island and made a log-log plot of the measurements, with the perimeter on the x axis and the area on the y axis. If the measurements form a straight line, this implies a self-similarity to the scaling of the population, and the slope can be used to determine the fractal dimension D, where $D = 2/\text{slope}$.

The log-log plots of the cutoffs of the two fractures all form straight lines, with least-squares correlation coefficients greater than 0.9. Cutoffs for each fracture are displayed in Figure 2, where the white areas represent aperture openings larger than the cutoffs and the dark areas represent aperture openings smaller than the cutoffs. (These cutoffs are referred to as "indicator maps" in the geostatistics literature; Isaaks and Srivastava, 1989.) The results of the fractal analyses for the cutoffs are shown in Table 1.

DISCUSSION

Both the fractal analyses and the statistics of the two fractures show that they have similar means, standard deviations, and fractal dimensions (Figure 1). The variograms show that there is evident anisotropy in the Dixie Valley fracture (Cox and Wang, 1993). However, the cutoff patterns for the two fractures look very different (Figure 2). The Stripa fracture shows a somewhat radial pattern of shapes, whereas the Dixie Valley fracture shows shapes that are extended in the sliding direction. These two very different patterns might have very different consequences for fluid flow. We could test the hypothesis that these patterns have significantly different effects on fluid flow by both numerical and physical experiments.

The concept of a cutoff pattern can be applied to aperture distributions to determine the possibility of different phase occupancy (Cox et al., 1990; Pruess and Tsang, 1990). A coarse average of a region of one of the fracture aperture distributions for the Dixie Valley rock specimen was previously analyzed for relative permeability (Cox et al., 1990). The analysis suggested that in small fractures with numerous asperity contacts, contiguous liquid flow paths exist even at small values of liquid saturation with strong capillary suction conditions. Cutoff patterns obtained from these two fractures could be used to test models (both computer and laboratory) for faulted versus radial patterns. If variability in the geometry of these otherwise similar fracture patterns does not result in a very different fluid flow regime, then a stochastic model might be adequate.

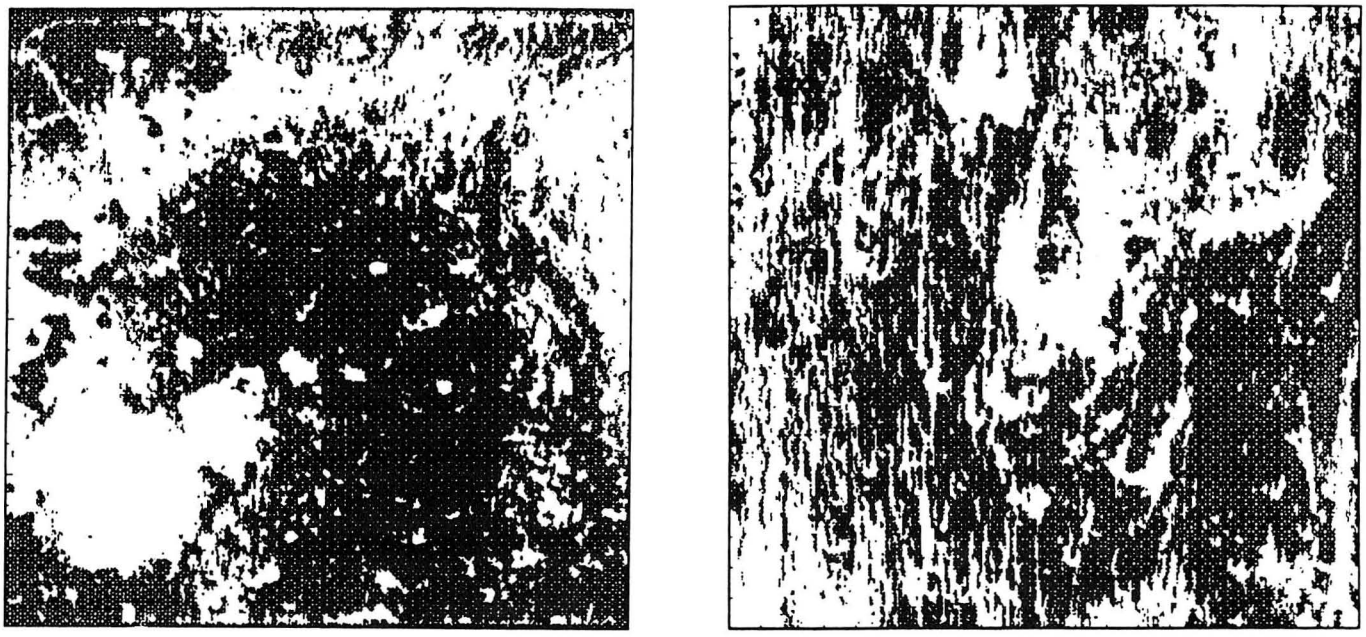

Figure 2. Cutoffs (indicator maps) for Stripa and Dixie Valley fractures. Apertures greater than 50 μm are shown in white. [XBL 935-806]

CONCLUSIONS

1. The fractal dimensions, means, and standard deviations for the Stripa and Dixie Valley apertures measured with the dyed-fluid technique are very similar. The slit-island and profile fractal dimensions were practically identical, whereas the variogram fractal dimensions were much higher (Cox and Wang, 1993). High variogram fractal dimensions were also observed in a literature review of fractal surface measurement techniques (Cox and Wang, 1992).
2. The cutoff patterns were distinctly different and were not similar to typical stochastic patterns. The Stripa cutoffs showed a radial pattern, and the Dixie Valley cutoffs showed patterns elongated in the sliding direction.
3. The cutoff patterns (or "indicator maps") could be used in flow models (Cox et al., 1990; Pruess and Tsang, 1990) to determine if the pattern would make a difference in the fluid flow characteristics. These predictions could then be tested by comparing flow visualization laboratory experiments in the two different fracture replicas (Persoff and Pruess, 1993).

Table 1. Slit-island analyses.

Name	Cutoff	No.Is.	Area%	Totalperimeter		Slope	*D*
Stripa	27.	536	36	25,890	1.52	1.31	
Stripa	37.	791	55	27,790	1.54	1.30	
Stripa	50.	919	72	26,470	1.51	1.33	
Stripa	(37.)	(653)	(45)	(27,790)	(1.49)	(1.34)	
Dix Val	30.	383	28	29,970	1.44	1.39	
Dix Val	40.	698	53	33,280	1.43	1.40	
Dix Val	50.	897	71	26,040	1.47	1.36	
Dix Val	(40.)	(598)	(47)	(33,280)	(1.44)	(1.39)	

Notes: Cutoff is in micrometers. No.Is. are islands greater than cutoffs (except for those in parentheses). Percent area is area with apertures greater than cutoff. Total perimeter is in grid units (grid spacing approximately 0.2 micrometers). Slope is from plot of log-log area versus perimeter. *D* is the fractal dimension from the slit-island slope. Cutoffs in parentheses are for the inverse analysis (i.e., islands are apertures less than the cutoff).

4. The slit-island fractal analysis indicates a higher fractal dimension and a higher total perimeter for the Dixie Valley fracture. In the absence of information about anisotropy or connectedness, the higher fractal dimension might indicate greater resistance to flow. However, visual inspection of the cutoff patterns suggests that the anisotropy of the Dixie Valley fracture patterns would be more important for flow properties than the fractal dimension of the total perimeter of the contacts. The fractal dimension is only one piece of information about the pattern geometry and does not indicate connectedness or anisotropy.

ACKNOWLEDGMENT

We wish to thank Dr. Peter Persoff for the aperture data sets.

REFERENCES

Cox, B.L., and Wang, J.S.Y., 1992. Fractal surfaces: Measurement and applications in the earth sciences. Accepted by Fractals (LBL-31737).

Cox, B.L., and Wang, J.S.Y., 1993. Single fracture aperture patterns: Characterization by slit-island fractal analysis. Presented at the International High Level Radioactive Waste Management Conference, Las Vegas, Nevada, April 26–30, 1993 (LBL-33660).

Cox, B.L., Pruess, K., and Persoff, P., 1990. A casting and imaging technique for determining void geometry and relative permeability behavior of a single fracture specimen. *In* Proceedings, 15th Workshop on Geothermal Reservoir Engineering, Stanford University, p. 173–178.

Isaaks, E.H., and Srivastava, R.M., 1989. An Introduction to Applied Geostatistics. Oxford University Press, New York, p. 80–89.

Mandelbrot, B.B., 1982. The Fractal Geometry of Nature. W.H. Freeman, New York.

Mandelbrot, B.B., Passoja, D.E., and Paullay, A.J., 1984. Fractal character of fracture surfaces of metals. Nature, v. 308, p. 721–722.

Persoff, P., and Pruess, K., 1993. Flow visualization and relative permeability measurement in a rough-walled fracture. Presented at the International High-Level Radioactive Waste Management Conference, Las Vegas, Nevada, April 26–30, 1993 (LBL-33447).

Persoff, P., Pruess, K., and Myer, L., 1991. Two-phase flow visualization and relative permeability measurement in transparent replicas of rough-walled rock fractures. Presented at the 16th Workshop on Geothermal Reservoir Engineering, Stanford, California, January 23–25, 1991 (LBL-30161).

Power, W.L., 1989. Roughness of natural fault surfaces: Implications for friction and deformation in fault zones. Ph.D. dissertation, Brown University, U.M.I. # 9002277, p. 101–141.

Pruess, K., and Tsang, Y.W., 1990. On two-phase relative permeability and capillary pressure in rough-walled rock fractures. Water Resour. Res., v. 26, no. 9, p. 1915–1926 (LBL–27449).

LBL/Industry Heterogeneous Reservoir Performance Definition Project: The Conoco Site

T. M. Daley, E. L. Majer, J. C. S. Long, K. Hestir, P. D'Onfro, W. D. Rizer,* and J. H. Queen**

The Earth Sciences Division at Lawrence Berkeley Laboratory (LBL) is conducting interdisciplinary projects for characterizing heterogeneous reservoirs. As part of this work, a number of hydrologic and seismic field experiments were performed during 1992. With these experiments, we hope to develop equipment, field techniques, and interpretational methods that will improve geophysical imaging and hydrologic definition of reservoir rock. Our experiment at a Conoco Inc. test facility is one of two experiments being conducted to apply this approach to a fractured reservoir. Further information on the background of the interdisciplinary approach and a description of work in a porous reservoir site is given in Doughty et al. (1992).

We are currently in the initial stages of studies at the Conoco well test site in Kay County, Oklahoma, which penetrates a fractured groundwater reservoir consisting of limestones and shales. This site has been previously studied, and many of the hydrologic and seismic properties are

* Conoco Inc., Exploration Research and Services, Ponca City, Oklahoma.

understood (e.g., Queen and Rizer, 1990, Lines et al., 1992). Because of these previous studies, we can test new concepts while developing a more refined understanding of this site. To improve and refine our field techniques, test current analysis methods, and work toward an improved description of reservoir properties, separate hydrologic and seismic field experiments have been carried out at this site. The results of these separate experiments will eventually be integrated.

In the initial seismic experiment, five cross-well surveys were recorded in the shallow groundwater wells (GW-1 through GW-5 in Figure 1). The surveys were done with fairly coarse sampling of the subsurface because of field problems. A lightning strike was apparently responsible for the breakdown of two out of six recording channels, and the remaining four channels were found to be out of calibration upon our return to LBL. Nonetheless, we feel the acquired data represent the frequency response and signal-to-noise ratios that we can expect upon returning for more detailed surveys in 1993.

Each of the five seismic cross-hole surveys used a separate pair of wells, with the seismic source in one well and a string of seismic receivers in the second well. The data were acquired at depths between 50 and 110 feet, covering the Fort Riley formation, a limestone with thin interbedded shales. The seismic data were acquired with LBL's high-frequency seismic imaging system (Daley and Majer, 1992). The eight seismic receivers were recorded

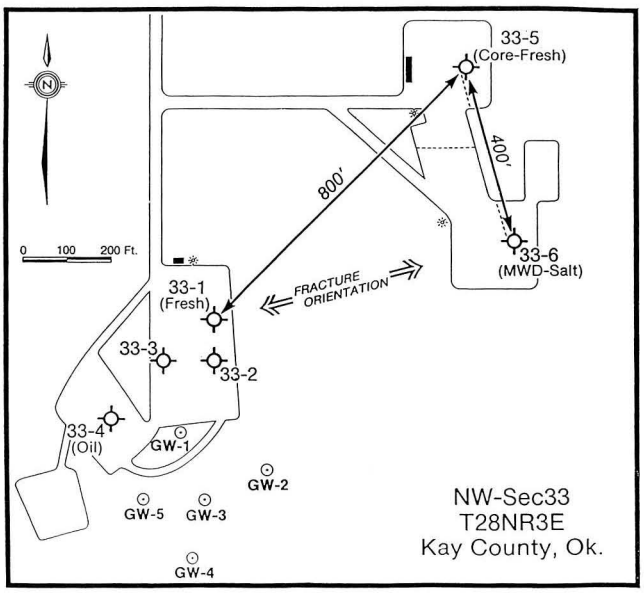

Figure 1. Layout map of Conoco Inc. borehole test facility. The field tests were conducted in wells GW-1 through GW-5. [XBL 934-489]

four at a time at 6-ft spacing for each of 60 source points spaced 2 ft apart. The distance between wells was approximately 150 ft. Figure 2 shows an example of the data acquired in the groundwater wells. A Fourier transform of these shallow data (Figure 3) shows that energy above 10,000 Hz is being transmitted between wells. Since the velocities are above 10,000 ft/sec, we can potentially expect a resolution of one foot, although the data acquisition was not designed to take advantage of this resolution. Now that the potential resolution is known, future work will use smaller spacing between source locations and receiver locations.

The seismic data can be analyzed for velocity, velocity anisotropy, attenuation, and other attributes that can characterize the fracture content. However, we feel that many wave-propagation effects may be caused by the thin bedding of sedimentary layers. Among the observed effects in the seismic recordings are oscillatory channel waves, apparently caused by the thin high-velocity layers. These channel waves, which were previously reported at this site (Lines et al., 1992) could prove a valuable tool for understanding the details of seismic propagation, including separating the effects of fractures from the effects of thin layering.

In the hydrologic experiments, a series of interference tests were conducted in the GW holes. The interference data will be used in fiscal 1993 as a basis for developing a hydrologic model of the site. Hydrologic inversion methods will be used to identify fracture flow paths. Several techniques are under investigation. In each of these a conceptual model will be optimized such that the well tests simulated by the model will match the observations taken in the field. Two methods are under consideration at this time. The first method is based on representing the fracture network as an "attractor." The attractor is determined using a simple iterative mathematical process called iterated function systems (ifs), which can be used to determine a complex heterogeneous field of permeability (Doughty et al., 1992). The parameters of the ifs are optimized until a case is found that matches the well test data. Such a process results in the determination of a fractal model for the reservoir. The second method is based on using the outcrop information to infer the genetic history of the rock. Then a heuristic process is defined that will "grow" fractures the same way. A series of these generated fracture systems are examined until one is found that matches the well test data. Either of these techniques can be conditioned with geophysical information. To the extent that geophysics indicates the orientation or density of the fractures, the inversion can be constrained to produce models that also have these properties. The second step in the inversion process will be to design and accomplish conditioning with geophysical information.

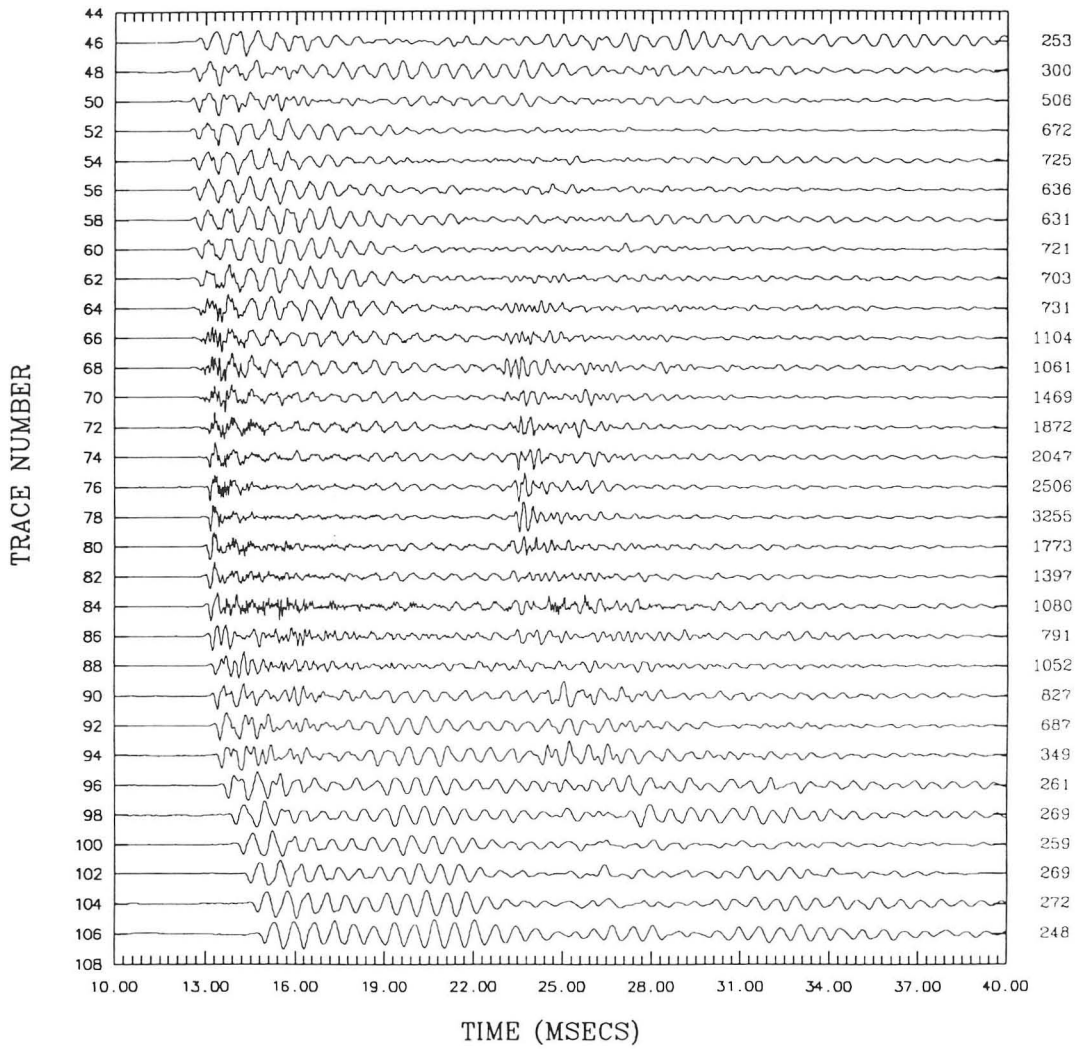

Figure 2. Cross-borehole seismic data. Each trace is a single source-receiver pair. The source was in well GW-3 from depths of 45 through 106 feet. The receiver was fixed at 72 feet in well GW-2. The first *P*-wave arrival is seen at about 13 msec. A later arrival at about 24 msec is probably a shear wave. The oscillatory arrivals (e.g., traces 96–106) are probably channel waves. [XBL 935-607]

The first well tests were carried out in July and August of 1992. Simple pumping tests were designed that would perturb each well in succession and monitor the other four. Thus each test would produce five records of drawdown. Testing conditions were extremely difficult. The tests were planned for this time period because it is usually a period of dry weather. Unfortunately, this turned out to be one of the wettest years in recent history. Consequently, the water levels in the wells were fluctuating over many centimeters within periods of hours. The horizontal permeability of the formation was low enough that these fluctuations completely masked the signal from the pumping well. In addition, the pumping rates had to be maintained at a very low level (0.5 gal/min) in order to avoid drawing the wells down below the formation. This constraint effectively reduced the size of the signal such that it was impossible to conduct controlled tests until the rain stopped.

During some eight weeks in the field, the rain held off for two periods long enough to obtain two good interference tests, one from well GW-5 and one from well GW-2. The first test was conducted at a relatively constant pumping rate. It was not possible to hold the rate constant for the second test, but the pumping rate was measured regularly. Plans for fiscal 1993 include analysis of our data as described above, collection of more detailed seismic data, and beginning to integrate the hydrologic and geophysical data.

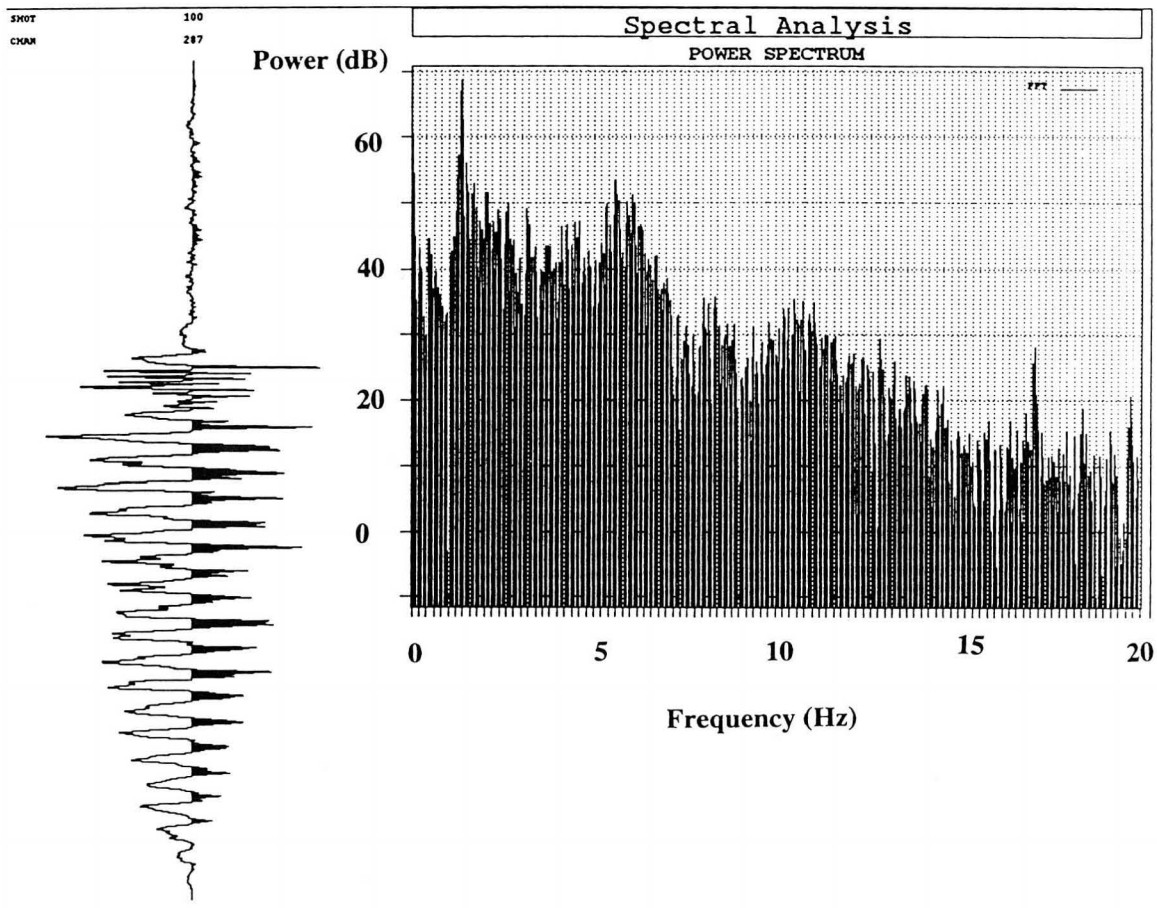

Figure 3. Frequency content of one representative seismic data trace. The trace is shown on the left. The background noise level is about 10 dB. The signal level is seen to exceed 30 dB for most frequencies up to 10,000 Hz. [XBL 935-808]

REFERENCES

Daley, T.M., and Majer, E.L., 1992. Applications of the LBL high-frequency seismic imaging system. *In this Annual Report.*

Doughty, C., Daley, T.M., Long, J.C.S., and Majer, E.L., 1992. LBL/Industry heterogeneous reservoir performance definition project: The BP Gypsy Site. *In this Annual Report.*

Lines, L.R., Kelly, K.R., and Queen, J.H., 1992. Channel waves in cross-borehole data. Geophysics, v. 5, p. 1–9.

Queen, J.H., and Rizer, W.D., 1990. An integrated study of seismic anisotropy and the natural fracture system at the Conoco Borehole Test Facility, Kay County, Oklahoma. J. Geophys. Res., v. 95, p. 11255–11273.

LBL/Industry Heterogeneous Reservoir Performance Definition Project: The BP Gypsy Site

C. Doughty, T. M. Daley, J. C. S. Long, and E. L. Majer

The goal of this work is to demonstrate the combined use of state-of-the-art technology in fluid flow modeling and geophysical imaging in an interdisciplinary approach for characterizing heterogeneous petroleum reservoirs. The product of this work will be improved interpretational and predictive methods, which the petroleum industry will use to enhance production from existing and new reservoirs. This project focuses on porous reservoirs and is being done in conjunction with British Petroleum (BP). A related project focusing on fractured reservoirs is being done in conjunction with Conoco (Daley et al., 1992).

The purpose of characterizing the behavior of a petroleum reservoir is to create a model that will be a useful tool for planning the development of the reservoir. In highly heterogeneous and fractured reservoirs, the characterization process is both difficult and critical to efficient recovery. Its success depends on the ability to successfully interpolate and extrapolate *in situ* point measurements made from the surface and wells to the volumetric properties affecting the production of the resource.

Fundamentally there are two ways to create a model of a heterogeneous system: the forward approach and the inverse approach. In the forward approach, one takes measurements of the relevant physical parameters (permeability, porosity, etc.) and develops a technique to assign these values to areas of the reservoir where the parameters have not been measured. Forward calculations of the reservoir behavior can then be made. The advantage of the forward approach is that it is based on physical laws relating parameters to behavior. The disadvantage is that there may not be enough data available to adequately specify the model. In the inverse approach, the behavior of the reservoir during some testing phase is used to infer the physical properties throughout the field. The advantage of the inverse approach is that the model focuses directly on the behavior of the system that we want to predict. The disadvantages are that the technique may be computationally intensive, as it essentially requires performing forward calculations repeatedly, and the results may be non-unique.

No matter which of these techniques is used, there is rarely enough fluid flow information to adequately characterize the reservoir flow parameters. One of the most promising approaches to this problem is to use geophysical imaging to infer the pattern of heterogeneities that exist between wells. For example, the propagation of seismic or electromagnetic waves may be studied to infer mechanical or electrical properties of the subsurface, using inverse techniques. Learning how to properly use this information in the development of a flow model (i.e., how to relate mechanical and electrical properties to flow properties) is a key factor in reservoir definition. In this first year of the project, independent hydrologic and seismic analyses are being carried out; in future work an integrated analysis will be done.

THE GYPSY SITE

The BP Gypsy site consists of two suites of boreholes and an outcrop in a mixed-load meander belt formation in northeast Oklahoma. The Gypsy outcrop is a 1000 ft long, 50 ft high road cut that reveals six fluvial sandstone channels, as well as lower-permeability formations (see Figure 1). Over 1100 permeability and porosity measurements have been obtained, along with detailed geologic mapping. Three-dimensional information has been obtained by coring 20 shallow boreholes near the outcrop. At the subsurface pilot site, located about 20 miles away, six wells have been drilled into the Gypsy formation (located at a depth of 1000 ft). The data collected by BP include an extensive set of well logs, core information, pressure transient well tests, and 3-D surface seismic and cross-well seismic tests.

HYDROLOGIC INVESTIGATIONS

The first order of business was to evaluate existing data and begin to develop an understanding of the Gypsy site. Efforts to date have concentrated on the subsurface pilot site and involve reviewing the well-test data and evaluating its potential for inclusion in a hydrologic inversion to characterize heterogeneities at the pilot site. Sixteen well tests were conducted, using multiple observation intervals in six wells. A matrix display of well-test results provides a concise way to assess the consistency, precision, and coverage of a large number of well tests. Each entry in the matrix describes the response between a pair of pumping and observation well intervals. Each of the wells has two or three screened intervals, making a total of 16 intervals altogether, leading to a matrix with 256 entries. According to the principle of reciprocity (Barker, 1991), the response at well A during a test in which well B is pumped should be the same as the response at well B during a test in which well A is pumped, if the same pumping rates are

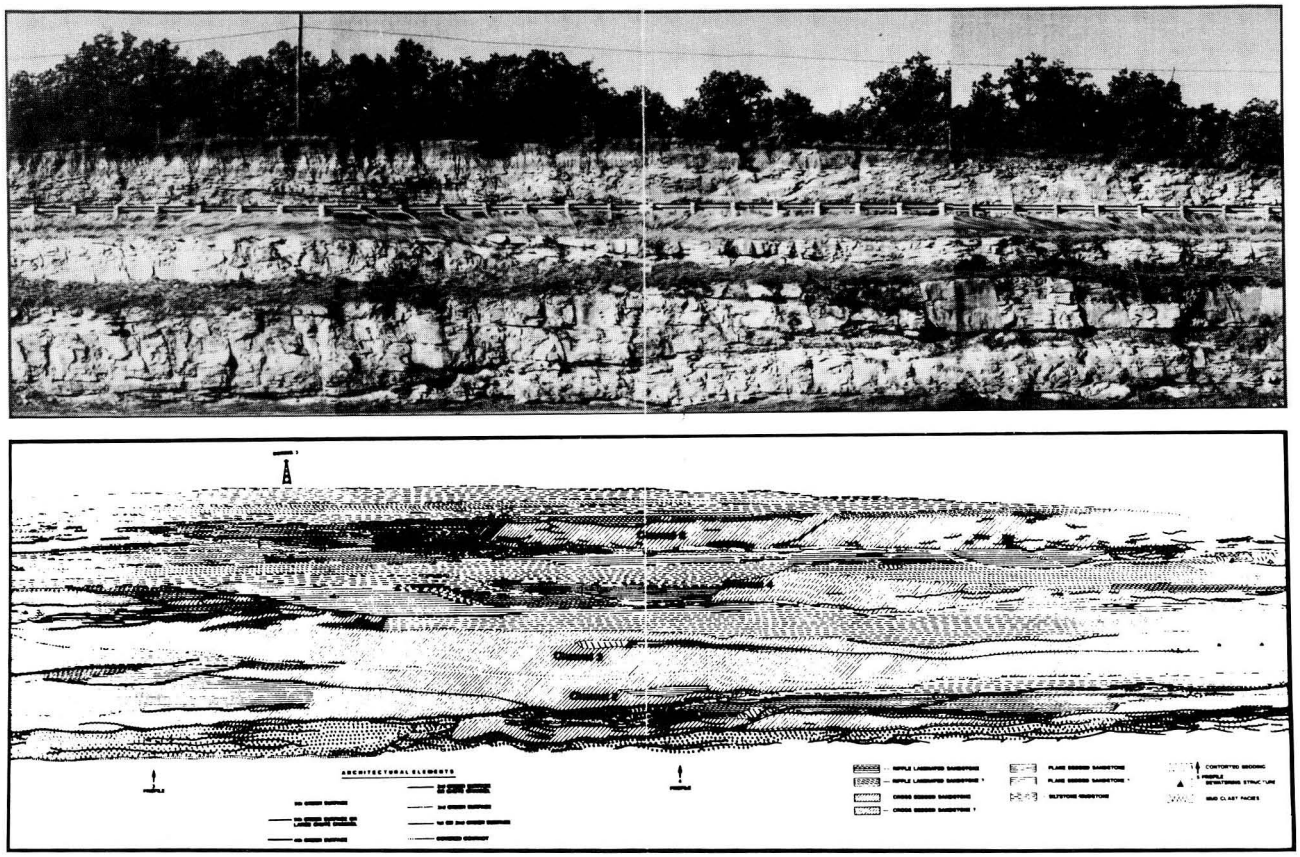

Figure 1. An orthophotograph of the central portion of the Gypsy outcrop and a geologic facies map inferred from geologic mapping. [CBB 927-5725]

used in both tests. This relationship even holds when different flow rates are used, if each drawdown response is normalized by the flow rate used. We have located several entries in the matrix that qualitatively contradict the reciprocity principle (i.e., no response at well A when well B is pumped but a large response at well B when well A is pumped). This is an indication of instrument or operational failure (e.g., packer failure, electrical power outage). We have also found reciprocal entries in the matrix that are qualitatively the same but differ quantitatively; these will be used to assess the precision of the pressure measurements and flow rate control. Finally, the matrix has been used to identify gaps in coverage; that is, combinations of wells that have not been tested together but which would be useful locations for future well tests.

Based on the internal BP reports describing the pilot-site well tests, we expected to have 130 pressure transients from 16 well tests to use for our hydrologic inversions. Our evaluation of the data has indicated that 90 pressure transients from a total of 13 tests will be directly usable in the inversion method. The remaining 40 pressure transients fall into one of five categories:

- 13 pressure transients that qualitatively satisfy the reciprocity principle or involve duplicate tests; these will be useful for checking the precision of the data.
- 6 pressure transients that qualitatively contradict the reciprocity principle; these have been used to identify three occurrences of instrument failure.
- 10 pressure transients that were measured during one of the tests with instrument failure; these are not usable.
- 8 pressure transients for which the data were missing or garbled; these are not usable.
- 3 pressure transients from tests that were designed in such a way as to make the results uninterpretable with our inverse method; these are not usable.

Overall, we will be able to use 103 out of 130 pressure transients, either directly in the inversions or indirectly to check the precision of the data.

Our evaluation of the data indicates that the well-test data as a whole support the conceptual geological model of the pilot site presented in the BP reports. This model consists of three sand channels (denoted the lower, middle, and upper channels) separated vertically by two clay layers. The lower clay layer (the dense red clay) is inferred to be continuous and the upper clay layer discontinuous. We have developed a tentative strategy for doing hydrological inversions, which will be carried out during fiscal 1993.

SEISMIC INVESTIGATIONS

The goal for seismic field work in fiscal 1992 was to do a set of mini cross-hole seismic surveys at the Gypsy outcrop site, using boreholes located near the outcrop. In this setting the results of the seismic survey can be related to the geology with some confidence because the outcrop reveals an extensive 2-D picture of the formation. The resulting relations can then be used to interpret seismic surveys done at other locations in the Gypsy formation, such as at the subsurface pilot site, where only 1-D geological observations are available via boreholes. These interpretations can then be used in conjunction with the hydrologic characterization of the subsurface pilot site.

Three wells were drilled to a depth of 75 ft around well 5, which is located about 10 ft from the outcrop. The new wells, identified as wells A, B, and C, are all 25 ft from well 5 (Figure 2). When we arrived at the outcrop site to perform the surveys, we found that the well A water level was 58 ft below the surface, the well B water level was 68 ft below the surface, and that well C was dry and blocked at a depth of 45 ft. We attempted to fill each well with water, but none would hold water for enough time to allow a reliable survey to be performed (the cross-hole source and receivers need to be in water to function properly). It is notable that well 5 maintained a water level of about 5 ft below the surface throughout our attempts to fill the other wells, supporting the notion that fluid flow paths are highly heterogeneous.

The limited data obtained indicate that good data could be collected if the wells were sealed. Further field work will be conducted in fiscal 1993 by first sealing the wells so that they will hold water and then conducting the cross-hole survey.

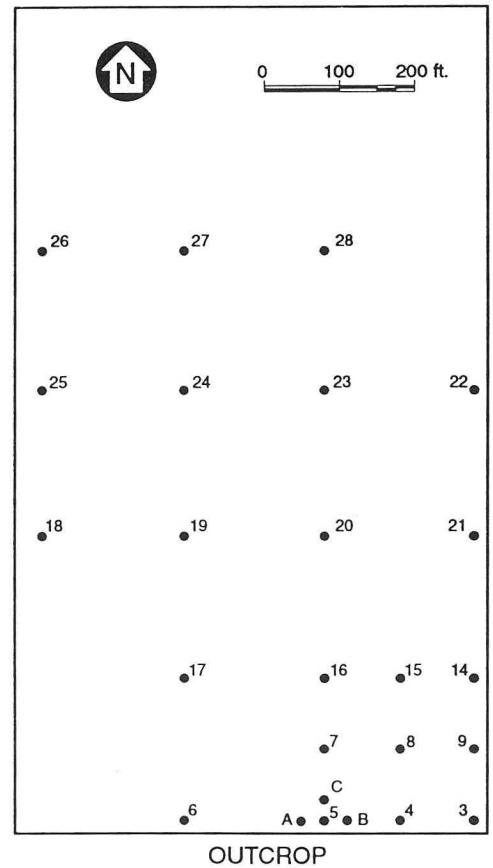

Figure 2. A plan view of the boreholes adjacent to the outcrop. The wells labeled A, B, and C were drilled for the mini cross-hole seismic survey. [XBL 935-809]

REFERENCES

Barker, J.A., 1991. The reciprocity principle and an analytical solution for Darcian flow in a network. Water Resour. Res., v. 27, no. 5, p. 743–746.

Daley, T.M., Majer, E.L., Long, J.C.S, Hestir, K., D'Onfro, P., Rizer, W., and Queen, J., 1992. LBL/Industry Heterogeneous Reservoir Performance Definition Project: The Conoco Site. *In this Annual Report.*

Fracture Characterization Study at the Raymond Quarry Site

K. Karasaki and B. Freifeld

The U.S. Department of Energy (DOE) and the Atomic Energy of Canada (AECL) have entered into a bilateral agreement for cooperative research and development in the area of high-level nuclear waste management. Under the currently implemented Subsidiary Agreement No. 2, there are eight technical tasks that DOE and AECL agreed to conduct cooperatively. LBL's responsibility is to co-lead with the USGS a task entitled "Development of Multiple-Well Hydraulic Test and Field Tracer Test Methods." The purpose of the task is to develop and test a multidisciplinary approach to the characterization of groundwater flow in heterogeneous and complexly fractured rocks. More specifically, the objectives of the task are (1) to test and improve the field procedures, equipment, and analysis method to be used at multiwell test sites at Yucca Mountain; (2) to improve understanding of the fundamental processes that govern flow and transport in heterogeneous systems; (3) to improve subsurface imaging techniques; (4) to improve understanding of coupled hydromechanical processes that may be significant in the Yucca Mountain site-scale groundwater flow system; and (5) to exchange technology and comparison of approaches to the modeling of groundwater flow in fractured rocks with the AECL. As the first activity of the task, we have established a dedicated field prototype site in Raymond, California. In the following sections, the present status and future plans of the tests planned at the site are described with a focus on hydraulic and tracer-testing activity.

RAYMOND QUARRY SITE

The Raymond Quarry Site is located in the Sierra Nevada foothills, approximately 3.2 km east of Raymond, California, and 100 km north of the city of Fresno (Figure 1). The principal rock type at the site is the so-called granodiorite of Knowles, which is light gray, of uniform grain size, and widely used for a building material in California (Bateman and Sawka, 1981). The property of the site is owned by the Coldspring Granite Company, which operates a quarry nearby. A cluster of nine boreholes have been drilled so far. The wells are laid out in an inverted V pattern with radially increasing spacing between boreholes (Figure 2). The spacing of 25, 50, 100, and 200 ft from the central well was chosen to allow the study of scale effects on the flow and transport parameters. The angle between the southwest and southeast legs is approximately 60 degrees. Two of the wells, SW2 and SE2, are drilled to a diameter of 10 in., with the remaining wells drilled to 6 in. The wells are cased to approximately 30 ft and vary in depth between 250 and 300 ft. The water level is normally between 6 and 11 ft below the casing head.

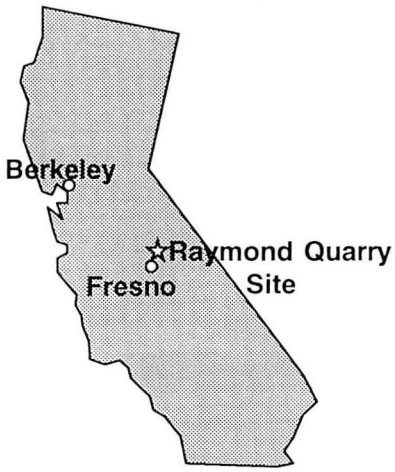

Figure 1. Location of the Raymond Quarry Site. [XBL 935-770]

PRELIMINARY INVESTIGATIONS

Geophysical logs obtained for the nine boreholes include natural gamma, resistivity, acoustic televiewer, caliper, and deviation. An intra-borehole flow survey was also conducted using a heat-pulse flow meter (Paillet, personal communication, 1992). Fish-eye television camera logs were run in all nine holes. In addition two visual-band borehole scanner surveys were conducted using different systems in well 0-0. The preliminary information is being

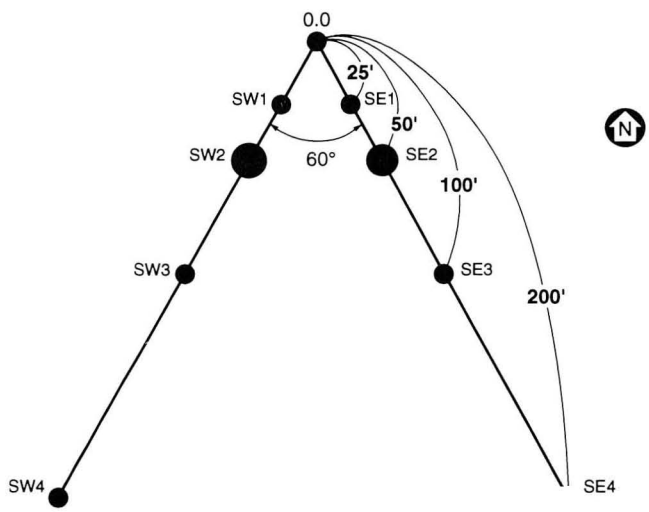

Figure 2. Layout of the wellfield at the Raymond Quarry Site. [XBL 935-771]

used to determine the hydraulic tests to be conducted and the locations for setting packers. In particular, the heat-pulse flow survey has been very useful in pinpointing in-flow locations within the well. It appears that there are two major conductive zones: one at a depth of about 100 ft and the other between 180 and 200 ft. These conductive zones are associated with a few highly fractured zones intersecting each wellbore.

For reconnaissance purposes, interference tests have been conducted by pumping in an open well, 0-0, with the observation wells being divided into upper and lower zones using a pneumatic packer. The objectives of the tests were to see if the wells are hydraulically connected to each other and to see if there are conductive zones in the deeper parts of the wells that are not surficial features, such as weathered zones. Figure 3 shows the data for an interference test using the SE well array. Because the x-axis scale is normalized to a square of the radial distance, the curves that connect the pumping period data points should fall on top of each other if the aquifer is homogeneous. However, as can be seen from the figure, the curves don't entirely fall on top of each other. It seems that there is a moderate degree of heterogeneity of up to a factor of 3. Another observation is that the larger the time or the distance from the pumping well, the closer the pressure responses in the upper and lower zone in the same well. This indicates that the features in the upper and lower zone identified by the geophysical logs are hydraulically connected to one another.

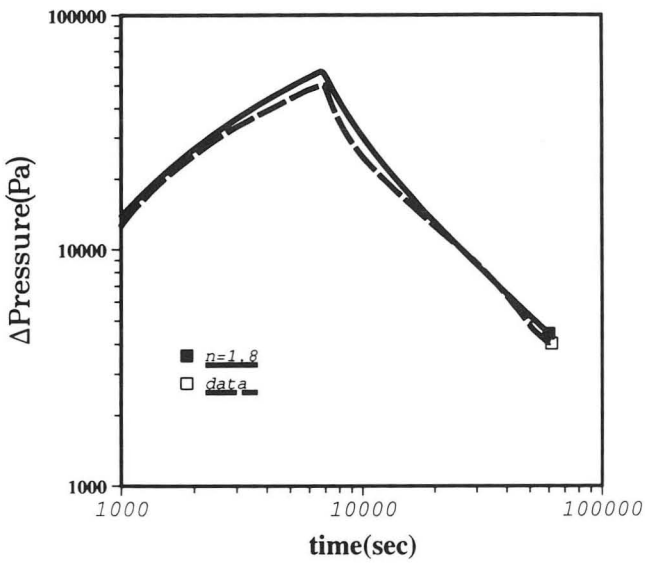

Figure 3. Interference test data with time normalized with respect to the square of radial distance from the pumping well. [XBL 935-772]

FRACTAL DIMENSION ANALYSIS

The problem of scaling up is an essential element in the site characterization effort. Field tests cannot be designed to stress a large enough volume of rock, nor can enough boreholes be drilled to sample and test every aspect of the site. Scaling up is extremely difficult in a highly heterogeneous system, and one needs to make some assumptions regarding the structure of the heterogeneity at the larger scale. One appealing assumption is that the heterogeneity has a fractal structure.

Barker (1988) solved the equation of flow to a well in fractional dimension space (as opposed to integral dimension space, i.e., two- or three-dimensional space) and presented type curves for various dimensions. The solution to the generalized radial flow equation in Laplace space is

$$\bar{h}(r,p)=\frac{Q_0 r^{\nu} K_{\nu}(\lambda r)}{pK_f b^{3-n}\alpha_n K_{\nu-1}(\lambda r_w)(\lambda r_w)^{1-\nu}\lambda^{\nu}}\,, \tag{1}$$

where

$$\nu = 1 - n/2\,, \tag{2}$$

$$\lambda^2 = p\frac{S_{sf}}{K_f}\,, \tag{3}$$

and where p is the Laplace variable, Q_0 is the pump rate, r the distance to the pump well, r_w the well radius, α_n the area of a unit sphere in n-dimensional space, b the extent of the flow region, and K_ν the modified Bessel function; K_f and S_{sf} are the standard hydraulic conductivity and specific storage, respectively. One can intuitively draw an association between a fracture system and a fractal. Simply put, a fractal implies that the space is fragmented or irregular, which is the very characteristic of fracture systems. Polek (1990) showed through numerical studies that a flow system with a fractal structure displays a characteristic signature in the well-test response curve as predicted by Barker.

Some of the interference test data was analyzed by evaluating Eq. (1) using the numerical inversion algorithm of Stehfest. The superposition principle was used to analyze a multi-rate pump test and a pump-and-recover test. A sample test and simulation are shown in Figure 4. The dimension had been chosen by examining the slope of the late-time pump data plotted on a log-log graph. It has been estimated that the dimension of the particular case is 1.5.

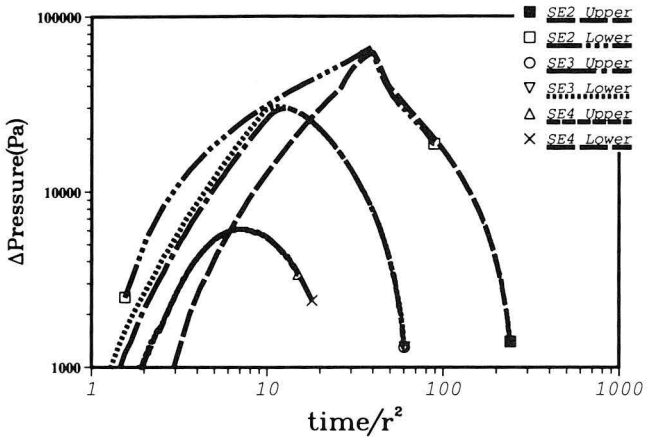

Figure 4. Data and a simulation using a fractional dimensional flow model for an interference test between 0-0, the pump well, and SW1, the observation well. [XBL 935-773]

HYDRAULIC AND TRACER TEST EQUIPMENT

During field testing many variables need to be monitored continuously. These include pressures of both water and air, flow rates, temperatures, and chemical concentration for tracer tests. The quality of data is based upon the accuracy of the sensor and the precision with which it is transmitted and converted into numerical information. All equipment must be integrated and the accuracy of each measurement known so that total error bounds for all calculations can be assessed.

The equipment used at the Raymond Quarry Site includes multipacker strings of Roctest packers with feed throughs for electrical and hydraulic communication between test zones. Differential pressures up to 150 psi can be maintained between adjacent zones. Pressure measurement is obtained with Paroscientific DigiQuartz transducers with an accuracy of 0.01% or with Druck Depth Sensors with an accuracy of 0.1%. Flow rates are controlled with a Kates Flow Controller to 1.5% of its set point. Data are transferred over RS-232 connections using intelligent transmitters or sent to a Keithley Model 2001 Digital Multimeter through a Keithley Model 7001 Multiplexer operating on an IEEE488.2 bus. All controlled parameters and data are logged on a 486 PC running data-acquisition software called "Labview for Windows." Figure 5 is a schematic diagram of the field equipment.

FUTURE PLANS

Multizone, cross-borehole hydraulic and conservative tracer tests are being designed so that the heterogeneous and discontinuous flow and transport pathways can be characterized. By alternately stressing different intervals in various holes and recording pressure transients in all the intervals in a crude tomographic fashion, it is expected that the hydraulic structure between the holes can be estimated. The results of different tests will be compared to see what benefit is gained by using complicated multipacker tests as opposed to the various open-hole tests commonly used. The data from single well tests should provide information

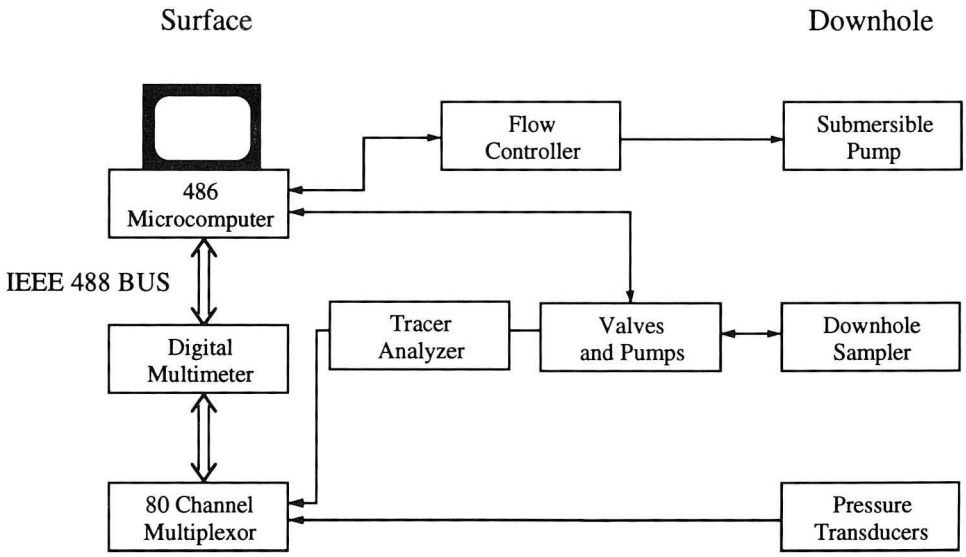

Figure 5. Schematic diagram of data acquisition system used at the Raymond Quarry Site. [XBL 935-774]

on local horizontal and vertical spatial variability of hydraulic properties. Long-term pumping tests are planned to assess the existence of a scale-dependent permeability structure, taking advantage of the well arrays with radially increasing spacing.

Conservative tracer tests will be carried out in much the same way by creating a convergent flow field into an interval and releasing various tracers from other intervals. Groundwater flow paths will be estimated by analyzing the tracer arrivals from the various release points. Both organic and inorganic tracers are planned for use, and the sampling and measurement methods are currently under development. The data from various tests will be used to construct a coherent hydrologic model of the site. Optimization algorithms such as simulated annealing will be used to invert both hydraulic and tracer-test data. Further experiments will then be conducted to test the accuracy and applicability of the model.

ACKNOWLEDGMENTS

Credits are due to the following people for participating in the project at various stages and capacities: Sally Benson, Wes Bethel, Preston Holland, Chris Kim, Ernie Majer, Steve Martel, Don Lippert, Ray Solbau, and Peter Zawislanski.

REFERENCES

Barker, J., 1988. A generalized radial flow model for hydraulic tests in fractured rock. Water Resour. Res., v. 24, no. 10, p. 1796–1804.

Bateman, P.C., and Sawka, W.N., 1981. Raymond Quadrangle, Madera and Mariposa Counties, California—Analytic data. USGS Professional Paper 1214.

Polek, J., 1990. Studies of the hydraulic behavior of hierarchically fractured rock geometries. M.S. Thesis, Lawrence Berkeley Laboratory Report LBL-28612.

A Tool for Studying Two-Phase Flow in Fracture Networks

K. Karasaki, S. Segan, and K. Pruess

Problems concerning two-phase flow in fractured media are commonly encountered in oil fields, geothermal fields, groundwater reservoirs, and other geologic media of engineering interest. In recent years, considerable attention has been focused on the storage of radioactive wastes in fractured rock. In the United States, the site for the potential high-level nuclear waste repository is in the unsaturated, fractured welded tuff at Yucca Mountain, Nevada. One possible scenario by which radionuclides could reach the accessible environment is transport by groundwater through the unsaturated zone to the water table and then into the saturated zone. Therefore, accurate characterization of the two-phase flow behavior of the fractured rock mass is vital to the safety of such an operation. The most direct information regarding the two-phase flow characteristics can be obtained by conducting *in situ* cross-hole pneumatic tests. However, analysis of the test results is extremely difficult, because the two-phase flow phenomena in a fractured rock are not well understood and the initial saturation condition and the intrinsic rock properties, such as fracture and matrix permeability, are not known *a priori*.

A numerical model is an essential tool for assessing the performance of the potential repository for tens of thousands of years, during which the spent fuel remains highly radioactive. To model the volume of rock within the 5-km distance from the potential repository perimeter, given the current computational capability, a node would have to be as large as 200 m × 200 m × 20 m in order to be feasible. For each nodal volume the two-phase flow parameters, such as relative permeability and capillary pressure, are necessary inputs for a two-phase flow simulator. It is very important, therefore, to develop an understanding of how water and air flow in fractures and to accurately represent a volume of rock that contains a network of fractures for field test interpretation and reliable performance assessment modeling. Persoff et al. (1991) carried out a laboratory investigation of two-phase flow in transparent replicas of rock fractures. Pruess and Tsang (1990) and Kwicklis and Healy (1992) numerically studied two-phase flow in a single fracture. Kwicklis and Healy constructed a simple network using the parameters obtained from their single fracture simulation. In the present report, we outline a tool for studying two-phase flow in numerically generated networks, showing how networks are generated randomly and how the flow path for each phase is tracked rigorously using accessibility criteria based on the connection to the boundary and the different rules at the intersections. We then describe the assumptions involved, how the networks are generated, how the two-phase flow is simulated in them, and provide some sample results.

ASSUMPTIONS

For the particular case of air and water flowing through a fracture network embedded in an impermeable rock matrix, certain reasonable assumptions can be made that will allow this system to be studied systematically with computer-generated fracture networks. It is assumed that capillary pressure is the dominant driving force causing movement of the phases but that these pressures are in a range in which volume compressibility and changes of state can be ignored. The rock is assumed to be water-wet, which means that water preferentially occupies thinner fractures. With capillary pressure being the predominant force, one of the criteria for a given fracture element to be occupied by either fluid is established by the relationship between capillary pressure, P_c, and aperture size, b, given by

$$P_c = \frac{2\gamma}{b}, \tag{1}$$

where γ is the surface tension between water and air. It is assumed that the contact angle between water and air is zero. This capillary pressure criterion is called "allowability." The no-compressibility assumption, combined with the allowability criterion, implies that each element has only one phase in it and that this phase is present until a sufficient change in capillary pressure allows the other phase to occupy the element, at which point the initially present phase is considered to flow out smoothly.

Two assumptions are made regarding interaction of fluids at an intersection (Figure 1). In the first assumption, it is assumed that fluids do not "see" each other (no-blocking case); that is, the remainder of a water-filled fracture cut by a second fracture is considered accessible to water, even if the second fracture is filled with air (Figure 1a). In the second assumption, the remainder of a fracture cut by an air-filled fracture may be considered inaccessible until the latter gets filled with water (blocking case, Figure 1b); this assumption is probably more rigorous in a strictly two-dimensional geometry. However, the first assumption essentially makes the two-dimensional network pseudo-three-dimensional, which may be a better representation of the real situation, which is three-dimensional. Nonetheless, these two assumptions are believed to be the limiting cases.

Another mechanism examined is the effect of trapping of one phase by the other. In one case, it is assumed that a phase can replace the other in any element as long as the element is accessible and allowable for the replacing phase (no-trapping case). In the other case, a phase is not permitted to replace the other unless there is a continuous exit path by which the replaced phase can reach the outflow boundary (trapping case, Figure 2); this assumption leads to a somewhat more rigorous treatment of the actual phenomena but does not fully account for the dynamics of the transient imbibition/drainage process. That process is treated as a succession of steady states with incremental change in capillary pressure. In total, four combinations of assumptions were examined: (1) no blocking and no trapping, (2) blocking and no trapping, (3) no blocking and trapping, and (4) blocking and trapping.

In this study, simple rules were applied to stochastically generated fracture networks of varying density. It is assumed throughout that the distribution of apertures is uniform and that the same holds true for length and orientation. Values for these quantities were chosen arbitrarily on the basis of intuitive arguments. For example, the average length of an element should be small compared with the length of the study region, and, in the absence of experimental data, distributions should be kept simple because they will probably be easier to analyze.

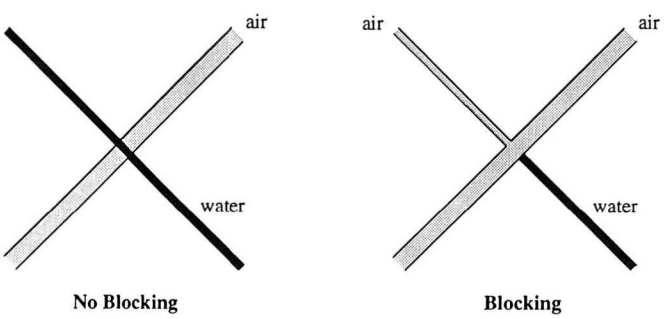

Figure 1. No-blocking and blocking assumption at a fracture intersection. [XBL 935-778]

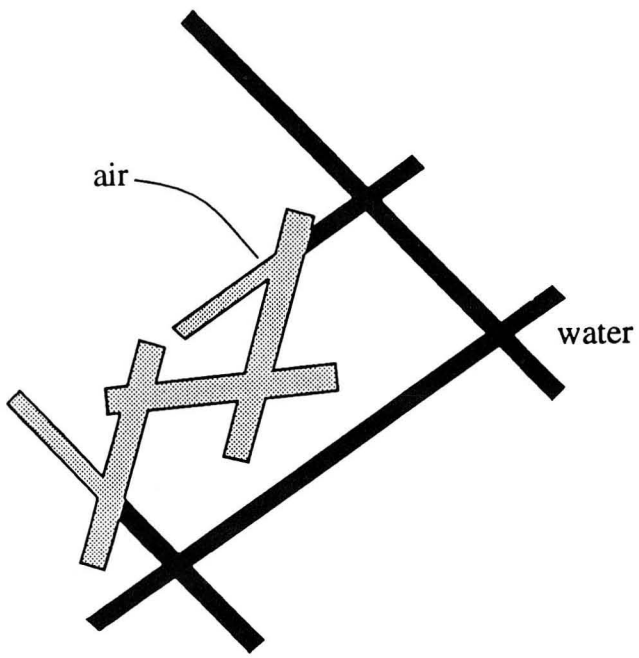

Figure 2. Trapping assumption. Air is trapped because there is no exit path for it. [XBL 935-779]

Our model ensures that flow takes place only along pathways that are geometrically connected to the inflow boundary. Among the important mechanisms represented are the blocking of a water-flow pathway by an air-filled path and the effect of trapping of either phase, leading to the phenomenon of irreducible residual saturation. In this regard, the present work goes significantly beyond previous work using percolation models that turn elements on and off without regard to physical connections while retaining the important feature of a percolation model, which is the ability to discuss a fracture network as a system of discrete objects and not as a continuum.

APPROACH

The random fracture network is generated using the fracture network generation program FMG (Billaux et al., 1989a,b). A path-tracking program, RENUM (Billaux et al., 1989a,b), is then used to trace flow paths for each phase from the boundary. RENUM was originally written to renumber the nodes of the random fracture network to minimize the bandwidth of the matrix for flow calculation and to identify and eliminate isolated clusters and dead-ends that do not contribute to flow. In the present study, some modifications were made to RENUM so that the original network can be divided into two subnetworks, one representing the elements that contribute to water permeability and water saturation and the other representing those elements that contribute to air permeability and air saturation. The assumption that only one phase may occupy a given element at a time guarantees that each element of the original fracture network is uniquely placed in one or the other of the two subnetworks. This implies that the combined saturation of the two subnetworks are exactly equal to the saturation of the original fracture network.

The capillary pressure criterion discussed previously is employed to determine which elements are eligible to belong in which subnetwork. For a given aperture size distribution, there exists a range of corresponding capillary pressure, which may be divided into a specified number of intervals (e.g., 32). For a given interval, each element with a corresponding capillary pressure that falls below the maximum capillary pressure is allowable to the air phase and any element with a capillary pressure larger than the maximum of the interval is allowable to the water phase. This implies that air will preferentially occupy the larger-aperture elements and water the smaller, which is consistent with the assumption that water is the wetting fluid in this configuration. As stated previously, allowability is not the only criterion that determines phase occupancy. Also considered is the accessibility criterion, which is determined by path connections using different assumptions regarding blocking and trapping as well as the direction of flow in the sense of imbibition and drainage. At each capillary pressure interval, two subnetworks are constructed on the basis of the above criteria. The total flow across each network is calculated using a single-phase fracture flow and transport code, TRINET (Karasaki, 1987). The corresponding saturation for either phase at each capillary pressure is calculated by summing the volume of elements occupied by the phase and dividing that by the volume of the total network. Relative permeability and capillary pressure curves are calculated by stepping through a range of capillary pressure in either the imbibition or the drainage direction. Resaturation and redrainage processes can also be simulated.

SAMPLE RESULTS

Using the computational tools described above, a detailed study of two-phase flow in fracture networks can be made. The effect of blocking and trapping on relative permeability and saturation can be examined. Figure 3 shows a sample of simulation results. The example shown is the case of blocking with no trapping under an imbibition process. It is interesting to note that the saturation changes

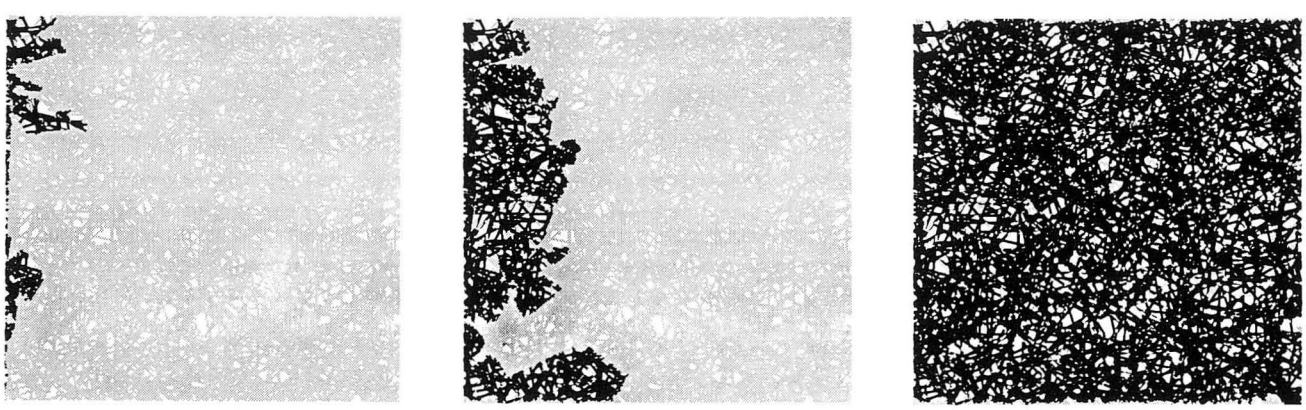

Figure 3. Imbibition from left-hand side with blocking and no-trapping assumption. [**a**, XBL 935-775; **b**, XBL 935-776; **c**, XBL 935-777]

dramatically between parts b and c of Figure 3, although there is only a very small capillary pressure increment. The relative permeability for water changes almost like a step-function, and for a wide range of saturation the relative permeability for both phases is zero (not shown). This is the result of a few bottleneck fractures with large apertures that obstruct the advancement of the imbibition front due to the blocking assumption.

REFERENCES

Billaux, D., Bodea, S., and Long, J., 1989a. FMG, RENUM, LINEL, ELLFMG, ELLP, and DIMES: Chain of programs for calculating and analyzing fluid flow through two-dimensional fracture networks. Theory and design. Lawrence Berkeley Laboratory Report LBL-24914.

Billaux, D., Peterson, J., Bodea, S., and Long, J., 1989b. FMG, RENUM, LINEL, ELLFMG, ELLP, and DIMES: Chain of programs for calculating and analyzing fluid flow through two-dimensional fracture networks. Users manual and listings. Lawrence Berkeley Laboratory Report LBL-24915.

Karasaki, K., 1987. A new advection dispersion code for calculating transport in fracture networks. Earth Sciences Division Annual Report 1986. Lawrence Berkeley Laboratory Report LBL-22090, p. 55–58.

Kwicklis, E.M., and Healy, R.W., 1992. Numerical investigation of steady liquid water flow in a variably saturated fracture network. Paper submitted to Water Resour. Res.

Persoff, P., Pruess, K., and Myer, L., 1991. Two phase flow visualization and relative permeability measurement in transparent replicas of rough-walled rock fractures. *In* Proceedings, 16th Workshop on Geothermal Reservoir Engineering, Stanford, California, January 23–25, 1991 (LBL-30161).

Pruess, K., and Tsang, Y., 1990. On two-phase relative permeability and capillary pressure of rough-walled rock fractures. Water Resour. Res., v. 26, no. 9, p. 1915–1926 (LBL-27449).

Wilkinson, D., and Willemsen, J.F., 1983. Invasion percolation: A new form of percolation theory. J. Phys. A: Math. Gen. 16, p. 3365–3376.

A Numerical Study of the Structure of Two-Phase Geothermal Reservoirs

C. H. Lai and G. S. Bodvarsson

Major two-phase vapor-dominated geothermal reservoirs have been exploited at The Geysers, California; Larderello, Italy; Matsukawa, Japan; and Kamojang, Indonesia. These reservoirs produce only steam and have nearly vapor-static pressure gradients at corresponding saturation temperatures. High observed upward heat transport in these reservoirs results from counterflows of vapor and liquid.

White et al. (1971) proposed a model involving counterflow of ascending steam and descending condensate that was elaborated upon by many investigators. In these models, boiling at a deep brine "water table" was assumed, with steam moving upward in large fractures along the pressure gradient produced by boiling and then condensing at the top of the reservoir because of conductive heat loss to the surface. The condensate flowed downward by gravity in the rock matrix and small fractures. However, recent discoveries in the northern part of The Geysers and some evidence from Larderello suggest that dry high-temperature rock underlies the vapor-dominated reservoir. Some wells in the Coldwater Creek field of The Geysers encounter a high-temperature zone (up to 347°C) only 200 m below the 245°C vapor-dominated reservoir. At Larderello, a number of deep wells show temperatures above 350°C.

The objectives of the present study are (1) to characterize possible thermodynamic states as well as flow structures and heat-transfer processes in typical vapor-dominated geothermal reservoirs and (2) to explain the thermodynamic conditions encountered in the high-temperature reservoirs observed in The Geysers and Larderello.

DESCRIPTION OF THE PROBLEM

A numerical study of steady-state two-phase geothermal reservoirs was performed using a two-dimensional vertical cross section of porous medium. The cross section is heated locally from below, reflecting situations where localized magmatic intrusion occurs beneath the reservoir. Figure 1 shows a schematic representation of the right half of the physical problem considered in the study. The cross

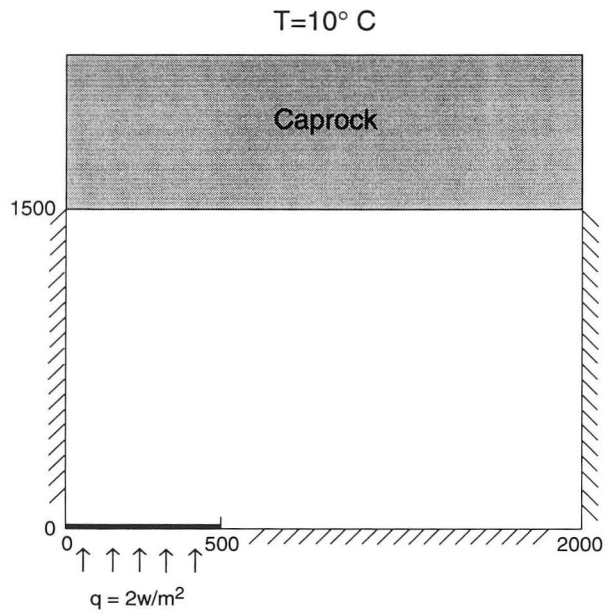

Figure 1. A schematic representation of the physical problem. [XBL 9112-7097]

section is overlain by an impermeable caprock, which is maintained at a constant temperature of 10°C at its top, representing the ground surface. Heat transfer in the caprock occurs only by conduction.

The numerical simulator TOUGH2 (Pruess, 1991a) was used with a uniform grid spacing of 100 m in both the x and z directions forming a 20×15 mesh. The parameters used in the simulations are considered to be appropriate for The Geysers and Larderello. The main parameters varied in the simulations were initial mass of *in situ* fluid and permeability.

Base Case: 25% Initial Steam Saturation

The phase structure may depend on the initial mass of *in situ* fluid (i.e., initial steam saturation). To test this hypothesis, numerical studies are performed to examine the effects of initial steam saturations on the phase and flow structures as well as on the heat-transfer process at steady-state conditions. In the numerical simulations, four cases with initial steam saturations of 25, 50, 70, and 75% and with a high permeability of 10^{-13} m^2 are designed to investigate the basic thermodynamic structures of the two-phase geothermal reservoirs. Cases 1, 2, 3, and 4 have steam saturations of 25, 50, 70, and 75%, respectively.

In case 1, the base case, we consider an initial steam saturation of 25% and a relatively high permeability of 10^{-13} m^2; under these conditions, the liquid tends to drain to the lower portion of the reservoir and the vapor to rise to the upper portion of the reservoir because of the large density difference between liquid and vapor, with the result that phase segregation occurs in the system. Figure 2a shows the steam saturation and mass flux distributions. Note that the mass flux shown in Figure 2 is generated by summing the mass flux in the liquid and steam phases. Examination of the figure reveals that two distinct zones with different steam saturations are developed in the reservoirs. In the upper two-phase vapor-dominated zone ($z > -500$ m), counterflow with an equal mass flux of steam (up) and liquid water (down) (i.e., a heat pipe) develops; the net mass flux in the two-phase zone is negligible compared with that in the underlying liquid zone ($z < -500$ m).

Figure 2b shows the temperature and mass flux distributions in the reservoir. The heat transfer in the liquid zone occurs by both conduction and convection. The adiabatic lateral boundary conditions and the constant heat flux imposed at the bottom surface serve to induce and sustain a buoyancy-driven flow in the vicinity of the heat source. As a result, a strong unicellular convective flow develops in the entire liquid zone, and the conduction-temperature field in the zone is greatly perturbed. Above the constant heat flux ($0 < x < 500$ m), the high-temperature isotherms shift toward the upper liquid zone ($-620 < z < -500$ m), resulting in a highly stratified region around $z = -560$ m.

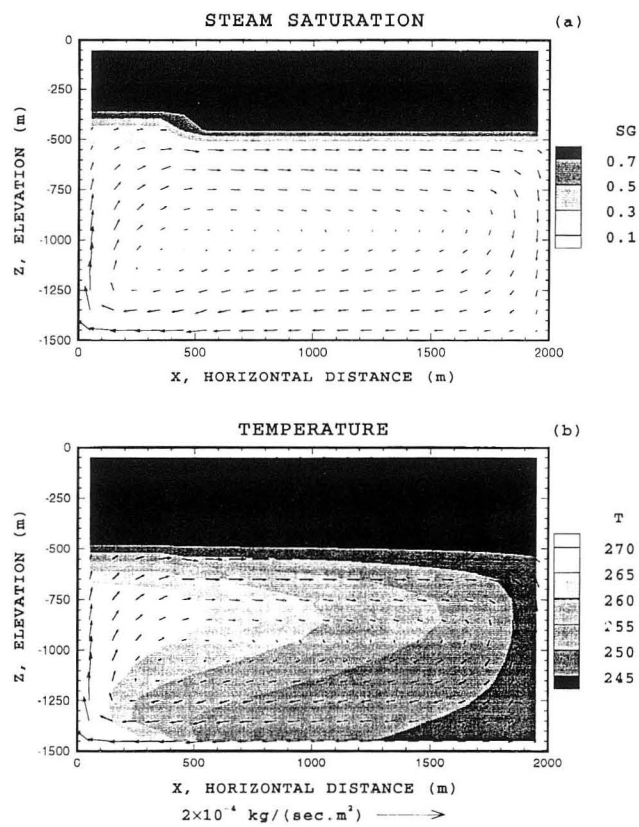

Figure 2. Distribution of (**a**) steam saturation (S) and mass flux and (**b**) temperature (T) and mass flux for case 1 with initial steam saturation of 25% and permeability of 10^{-13} m^2. [XBL 935-792]

Effect of Initial Steam Saturation

As the initial steam saturation increases to 50% (case 2), the initial mass of *in situ* fluid is decreased and the amount of mobile liquid water is reduced. Figure 3 shows the phase structure and distributions of temperature and mass flux. The interface between the liquid and two-phase zones is located at a depth of approximately 1050 m, and the thickness of the liquid zone is 450 m. Because the aspect ratio of the liquid zone (width over thickness) is larger than that derived from case 1, the convective cell is smaller and extends only over the left half of the zone. Consequently, the lateral extent of thermal activities is reduced and thus heat-transfer rates are decreased.

When the initial steam saturation is increased to 70% (case 3), a balanced liquid-vapor counterflow prevails in the entire reservoir. A small temperature variation of 240 to 245°C is observed in the system, indicating that the heat pipe efficiently dissipates the heat released from the heat source. However, when the steam saturation is increased to 75% (case 4), the amount of mobile liquid is further decreased and is not sufficient to produce a balanced liquid-vapor counterflow everywhere in the system. Figure 4 shows phase structure and distributions of the temperature and mass flux. Examination of these figures shows that a conduction-dominated zone develops in a region near the heat source; although a vapor convective flow field is observed, it is not as efficient as liquid convective flow to dissipate heat. Thus, a superheated vapor zone develops in the region near the heat source. This may reflect the situation where a superheated vapor zone underlies a two-phase zone in the Northern Geysers. The heat transfer in the two-phase zone overlying the superheated vapor zone is again by heat pipe.

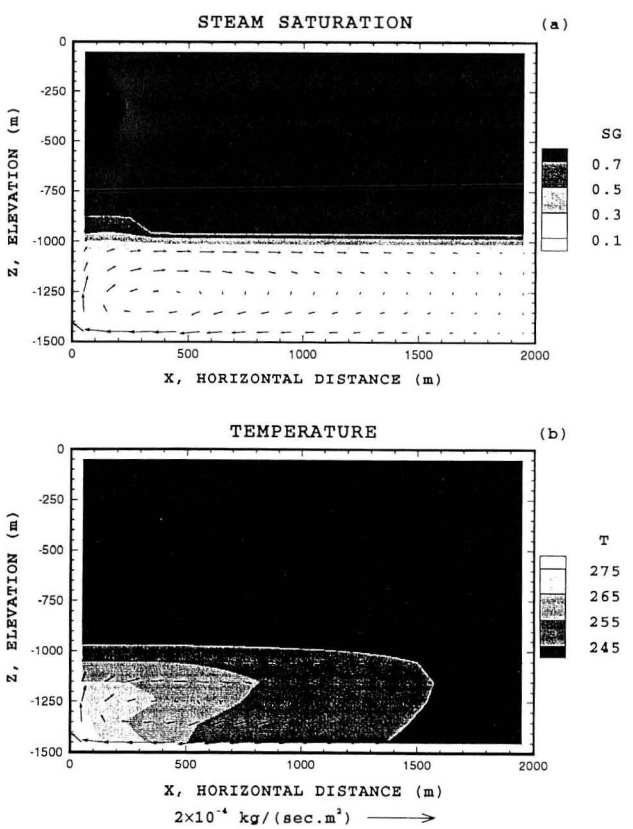

Figure 3. Distribution of (**a**) steam saturation (S) and mass flux and (**b**) temperature (T) and mass flux for case 2 with initial steam saturation of 50% and permeability of 10^{-13} m^2. [XBL 935-793]

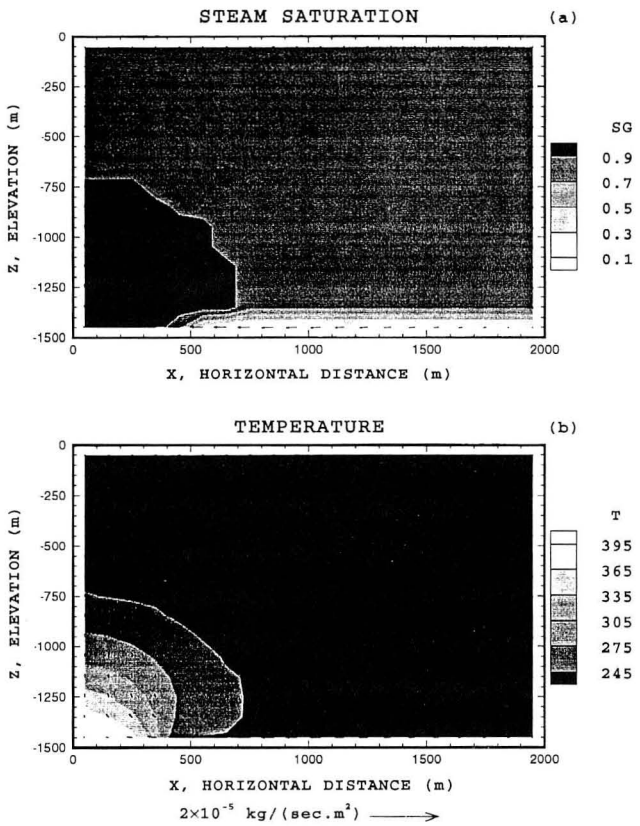

Figure 4. Distribution of (**a**) steam saturation (S) and mass flux and (**b**) temperature (T) and mass flux for case 4 with initial steam saturation of 75% and permeability of 10^{-13} m^2. [XBL 935-794]

Effect of Permeability

To investigate the effects of permeability on flow and heat-transfer processes, simulations are carried out with a permeability of 10^{-15} m^2 (case 5). An initial steam saturation of 25% is considered, with the rest of the physical parameters remaining the same as those used in case 1. In case 5, a conduction-dominated zone is developed in the region surrounding the heat source. Because heat conduction cannot efficiently dissipate the heat released from the heat source, a high-temperature zone of approximately 375°C occurs immediately above the heat source. This

results in the development of a boiling zone in a region above the heat source, as shown in Figure 5. The temperature and pressure profiles along the vertical cross section with $0 < x < 300$ m may reflect the situation observed in Olkaria, Kenya, where permeabilities are low and on the order of millidarcies (Bodvarsson et al., 1987). Contrary to the situation in cases 1 to 4, the temperature in the two-phase zone decreases with distance away from $x = 0$, resulting in a higher heat flow near the surface immediately above the heat source.

Effect of Grid Orientation

Experience with simulations of multiphase flow through porous media using the conventional five-point differencing scheme shows that in the vertical plane, the effect of grid orientation may be significant on predicted simultaneous movement of two fluids with a large density contrast (Pruess, 1991b; Lai and Bodvarsson, 1993). The lighter fluid tends to move along the vertical grid lines aligned with gravity, and the heavier one tends to sink down along the gravitational direction.

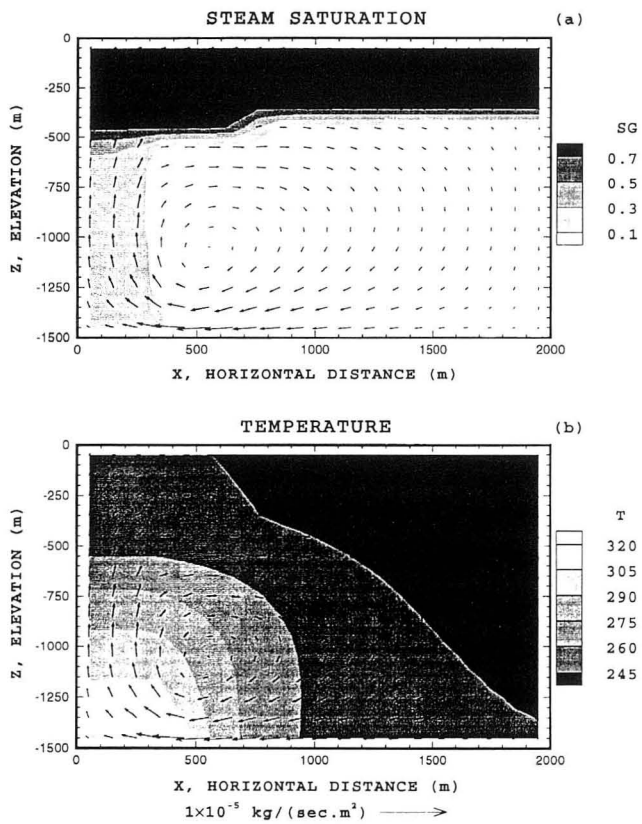

Figure 5. Distribution of (**a**) steam saturation (S) and mass flux and (**b**) temperature (T) and mass flux for case 5 with initial steam saturation of 25% and permeability of 10^{-15} m^2. [XBL 935-795]

To investigate the effects of grid orientation on our numerical simulation results, two different grid discretizations are used with so-called parallel and diagonal grids. For a parallel grid, the interface between the grid cells is either parallel or perpendicular to the gravitational direction. For a diagonal grid, the interface between the grid cells is oblique to the gravitational direction at 45 or 135 degree angles. We expect that the results calculated from case 5 possess a potential for grid orientation errors, because the vapor flow of the boiling zone immediately above the heat source tends to move vertically upward. As Figure 5 shows, this results in a zone with a relatively uniform width calculated with a parallel grid. However, the results derived from case 6 using a diagonal grid show that distribution of the temperature and saturation, and the shape of the boiling zone are only slightly different from those predicted from a parallel grid. Therefore, grid orientation effects for the present problem are probably insignificant.

CONCLUSIONS

The purpose of this work has been (1) to conduct a numerical study of flow, phase structure, and heat-transfer processes in natural-state two-phase geothermal reservoirs using a two-dimensional porous cross section with a localized heat flux from below as an idealized model for a geothermal system and (2) to analyze the effects of the mass of *in situ* fluid (i.e., initial steam saturation) and permeability on features of phase structure and heat-transfer processes.

The results show that when an initial steam saturation of 25% and a rather high permeability of 10^{-13} m^2 are employed, a two-phase vapor-dominated zone overlying a liquid zone develops. In the two-phase zone, a balanced liquid-vapor counterflow develops. The vapor rises to the top of the reservoir, where it condenses and releases latent heat, which is transferred through the caprock by conduction. The condensate either remains *in situ* or returns to the liquid zone. In the liquid zone, a convective flow field extends over the entire reservoir. The strength of the convective flow strongly depends on the mass of *in situ* fluid and the permeability of the reservoir. With an increase in initial steam saturation from 25 to 50%, the convective flow field extends only over the left half of the reservoir, resulting in lower heat-transfer rates. As the steam saturation is increased to 70%, a vapor-dominated heat pipe prevails in the entire system. When the steam saturation is increased to 75%, the amount of mobile liquid is reduced. Under such a circumstance, although a vapor convective flow develops, it is not as efficient as liquid convective flow in dissipating heat, resulting in a high-temperature superheated vapor zone underlying a two-phase vapor-dominated zone.

In general, the smaller the permeability considered in the model, the smaller the portion of the liquid zone affected by convective flow, leading to reduction of the rates of heat transfer. When a low permeability of 10^{-15} m^2 and an initial steam saturation of 25% are employed, conduction is the dominant heat-transfer mode in the liquid zone. Because heat released from the source cannot be efficiently dissipated by conduction, a two-phase liquid-dominated boiling zone develops immediately above it.

REFERENCES

Bodvarsson, G.S., Pruess, K., Stefansson, V., Bjornsson, S., and Ojiambo, S.B., 1987. East Olkaria geothermal field, Kenya: 1. History match with production and pressure decline data. J. Geophys. Res., v. 92, no. B1, p. 521–539 (LBL-20098).

Lai, C.H., and Bodvarsson, G.S., 1993. Numerical studies of cold water injection into vapor-dominated geothermal systems (to be published).

Pruess, K., 1991a. TOUGH2—A general-purpose numerical simulator for multiphase fluid and heat flow. Lawrence Berkeley Laboratory Report LBL-29400.

Pruess, K., 1991b. Grid orientation and capillary pressure effects in the simulation of cold water injection into depleted vapor zones. Geothermics, v. 20, p. 257–277, 1991 (LBL-30562).

White, D.E., Muffler, L.J.P., and Truesdell, A.H., 1971. Vapor-dominated hydrothermal systems compared with hot-water systems. Economic Geology, v. 66, p. 424–457.

Modeling Flow and Transport for Stripa Phase III: What Did We Learn?

J. C. S. Long

The Stripa Project represents a major milestone in the development of technology for the characterization of fractured rock for the purpose of predicting fluid flow and transport. There is probably no other *in situ* block of rock of similar scale that has been probed in so many ways with such intensity in such a brief period of time. An examination of what was learned at Stripa is nearly equivalent to an examination of what is currently knowable about flow and transport in crystalline rock.

This article reviews a few of the key findings that involved fluid flow and transport modeling. The analyses are based on the conceptual model described in Olsson et al. (1989), Black (1991), and Olsson (1992). This model included the definition of the major fracture zones in the Site Characterization and Validation (SCV) rock block. In particular, the conceptual model identified the H-zone as a subvertical zone that was the only major fracture zone to intersect the Validation Drift (VD).

This discussion of model predictions will refer to three hydraulic experiments. The first is the set of cross-hole interference tests (Black, 1991) that took place between packed-off intervals of the SCV boreholes. In particular, we concentrate on the C1-2 test, whose source was confined to interval 2 in borehole C1, which intersected fracture zone H. The second experiment was the Simulated Drift Experiment (SDE) (Black et al., 1991), which was meant to mimic the behavior of a drift from the hydrologic point of view by placing six parallel boreholes within a ring. The third is the VD inflow experiment (Olsson, 1992), which was conducted from a drift excavated through one-half the length of the SDE boreholes. The SDE provided a unique study of the effects of excavation on hydrology.

The discussion will also refer to three sets of tracer experiments. The radar-saline experiments (Olsson, 1991a,b) consisted of combining a saline tracer test with radar tomography. In the first test, 30 l/min of saline was injected into the C1-2 interval and collected at a sink formed by opening the D-holes in the vicinity of the H-zone. The second test was a repeat of the first but took place after the excavation of the VD. The third set of tests consisted of tracer tests conducted after the excavation of the VD, where a variety of tracers were injected at very low rates from a variety of borehole intervals intersecting the H-zone and collected at the VD (Birgersson et al., 1992)

These experiments were used in the following ways. The C1-2 test was used to develop a model of fracture flow in the SDE based on the conceptual model of Black et al. (1991). The modeling approach used by LBL was to create hierarchical fracture systems through an iterative optimization procedure, or inverse method (Long et al., 1991, 1992a). In this approach, the fracture network is optimized so that it matches certain observations—for example, interference test results such as those from the C1-2 test. In

particular, this method obviates the need to measure the conductance distribution of individual fractures in the field. Simulated annealing is used as the optimization technique because the inversion problem is highly nonlinear and simulated annealing allows the optimization process to escape from local minima (Davey-Mauldon et al., 1993). A model annealed to the C1-2 test is first used to predict the SDE inflow results. The model is then annealed to both the C1-2 and the SDE results and used to predict the VD inflow. Finally, the ratio of flux to velocity in both of these models is calibrated such that the models will best predict the breakthrough curve for the first radar-saline test. These calibrated models are used to predict the second radar-saline test and the subsequent tracer tests.

THE IMPORTANCE OF THE CONCEPTUAL MODEL

A conceptual model is an interpretation of all the observations of a fracture system; it describes how flow and transport occurs and is the basis of numerical models that can quantify flow and transport. The conceptual model is built on the basis of interpretation of laboratory studies, field mapping, geophysical measurements, and *in situ* hydrologic tests. Building the conceptual model is the most important part of fracture characterization because the conceptual model is critical to making predictions. For example, suppose we have *in situ* measurement of transmissivity. The transport velocity we predict for this system will vary by many orders of magnitude, depending on whether we use a 3-D porous media approximation, a 2-D parallel-plate model for the fracture, or a 1-D channel model. The error associated with choosing the wrong conceptual model in this case is much more significant than the measurement error or the numerical errors.

Understanding the geometry of the fracture system and how that geometry controls flow is central to conceptual modeling. There are two types of fracture patterns that result in important flow paths: one is a well-connected cluster of open fractures, or a fracture zone. The other is an extension feature of significant extent. The former is apparently the case at Stripa. Nearly 100% of the flow is observed to occur in fracture zones.

Geophysics was extensively used to detect these fracture zones. Well testing can provide the proof that a geophysically identified feature is hydrologically important because a well can be drilled into the feature and used to test the flow and transport properties directly. Some success in identifying important fracture zones from borehole data was achieved at Stripa by using a variety of measurements together, each of which might be expected to be related to hydrologically important fracture features: e.g., transmissivity, fracture density, electrical conductivity, low acoustic velocity. A variable that was shown to be a good indicator for important fracture features was the first eigenvector of the correlation matrix for these parameters (Black et al., 1991). Used together, these data provide a very good understanding of the likely location of major flow paths within major fracture zones.

The process of taking all of this information and turning it into a conceptual model is a process of abstraction. The analyst shapes the panoply of data using theoretical constructs and observational analogies to make a working description of the fluid flow system. The process should be fluid and interactive. As questions arise, further data collection is required to address these questions. It is very difficult to continue to make progress on understanding an earth science system when access to the field is cut off. This process was applied successfully at Stripa, particularly with respect to geophysics. In this sense, Stripa serves as an exemplar to those concerned with flow and transport in fractured rock.

The choice of an appropriate conceptual model also depends on the phenomena of interest. A simple prediction of flow rate as a function of time is not highly dependent on having a physically realistic conceptual model. Thus the prediction of inflow was insensitive to detailed conceptual modeling. If, however, one needs know where waste will migrate, a more complete understanding is critical. The purpose of the detailed conceptual modeling and development of sophisticated flow models was primarily to set the stage for the more complex transport modeling.

Some salient features of the conceptual model for the Stripa SCV can be briefly summarized as follows: The fluid flow is largely confined to fracture zones. There are approximately seven fracture zones in the block, including major zones whose location, orientation, and extent have been determined. The fracture zones are not uniformly permeable.

PREDICTION OF THE SIMULATED DRIFT EXPERIMENT

The conceptual model formed the basis of a series of numerical models for flow and transport. These models were formed by creating a lattice of conductors on each of the planes representing the fracture zones identified in the conceptual modeling exercise. Simulated annealing was used to conduct a random search through the elements of the lattice to find a configuration of elements that matches the hydraulic test data (Long et al., 1992a). Simulated annealing results in a solution that is constrained to agree with the hydrologic observations. The process can be repeated many times to get a series of models that all agree with the hydrologic observations. Although this was not done for the Stripa data, it is possible in this way to determine what constraints are placed on the model by the data.

Two kinds of models were created. One looked at the H-zone alone as though it were the only fracture zone to intersect the VD. The other represented all seven fracture zones (Figure 1). Each of these was annealed to the C1-2 data. Figure 2 shows the 2-D H-zone model annealed to the C1-2 data. Each of these annealed models was used to predict the inflow to the D-holes. The 2-D model predicted an inflow of 0.77 l/min, and the 3-D model predicted 0.95 l/min. The measured inflow was 0.77 l/min. These are highly encouraging results. The models are constrained by the conceptual modeling and a single interference test, and they predict a second test extremely well.

ISSUES THAT AROSE IN MODELING THE VALIDATION DRIFT

The next stage of the SCV project was to excavate the VD through the holes of the SDE. Prediction of inflow to the drift was to be accomplished with the models developed using the data from the SDE. The inflow measurement was meant to be used to test the predictive abilities of the models. Below we examine the reasons why this inflow measurement was inappropriate for this purpose but valuable as a measure of excavation effects.

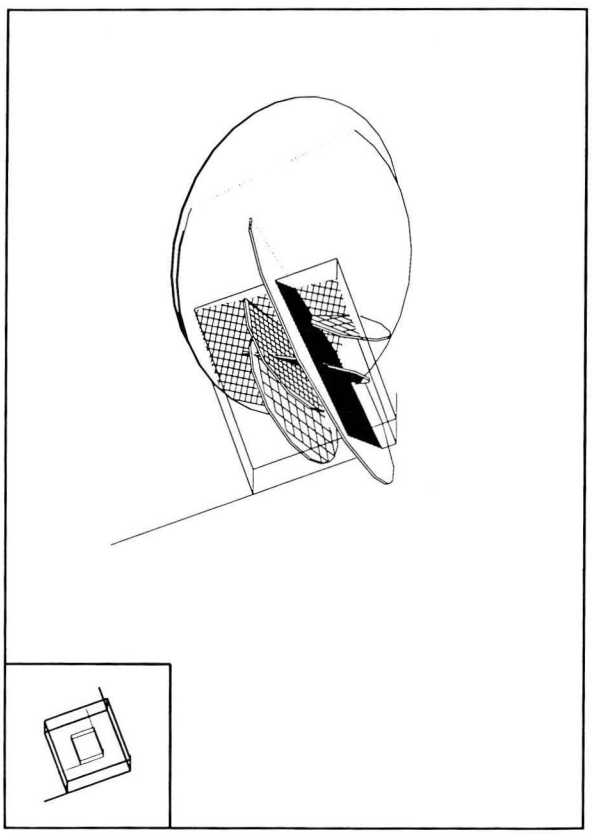

Figure 1. The 3-D model of the SCV, showing seven fracture zones represented by seven lattice structures. [XBL 921-5543]

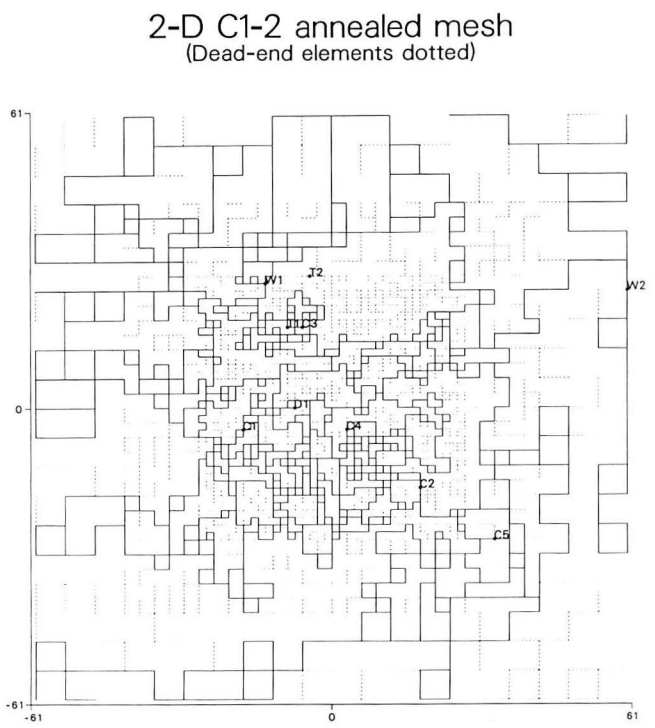

Figure 2. The configuration of the 2-D H-zone model that resulted from annealing to the C1-2 data. [XBL 9110-2207]

The SDE was conducted by lowering the pressure head in the boreholes in three separate steps. Lowering the head in the boreholes increases the gradient into the holes and increases the flow rate. In each step, the head was maintained for several weeks to develop steady-state conditions. Figure 3 shows the flow rate measured at the end of each step as a function of pressure head. During the last step, the pressure head in the boreholes was lowered to approximately 17 m above the elevation of the boreholes.

The shape of the isopotential boundary conditions imposed by the D-holes was almost identical to that imposed by the excavation (Black et al., 1991). Thus extrapolating the flow rates observed during the three steps of the SDE to the case for atmospheric pressure gives an estimate of the VD inflow, discounting any other effects due to excavation.

The total inflow to the D-holes consists of flow to the first 50-m sections of the boreholes, which were later excavated, plus the second 50-m sections, which were not excavated. Between the second and third steps, flow was redistributed among the boreholes as evidenced by the nonlinear flow plots shown in Figure 3 for each of these two borehole sections. However, the total flow is linear with pressure decrease, as expected. Extrapolating the flow rate from each of the three steps indicates that flow into the first 50 m of the boreholes was about 0.88 l/min (880 ml/min) at atmospheric pressure.

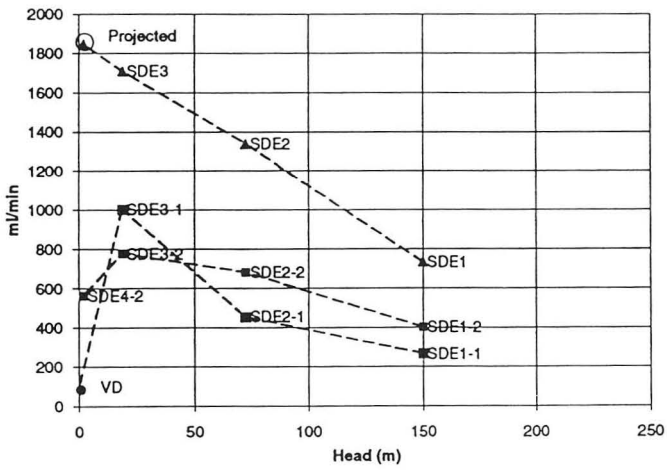

Figure 3. Inflow to the D-holes as a function of pressure head. SDEx = total flow, SDEx-1 = flow to 0 to 50 m, SDEx-2 = flow to 50–100 m, + = flow to "average rock," i.e., rock not in the H-zone. (The x denotes the steps of the SDE.) Validation Drift inflow is shown by a • symbol. [XBL 936-953]

The excavation of the VD reduced the pressure in the drift to atmospheric. Thus the flow into the excavation area should have increased and the pressures in the surrounding rock should have decreased. Pressures in the surrounding rock began to rise shortly after excavation commenced and continued to rise steadily during excavation. This means that inflow must have been decreasing. After excavation, the total measured inflow was approximately 0.1 l/min, roughly a factor of 9 lower than the SDE measurement.

A series of numerical analyses were conducted, first to simulate the SDE experiment and then, after the simulations were modified, to predict the VD inflow (Herbert et al., 1992; Dershowitz et al., 1991; Long et al., 1991, 1992a,b). Herbert et al. used an analysis of elastic, continuum stress changes due to excavation (McKinnon and Carr, 1990) to modify a discrete fracture model of the SDE to predict drift inflow. Herbert et al. used the computed change in normal stress acting on each fracture in the model and a relationship between stress and permeability derived from laboratory measurements (Gale et al., 1990) to change the permeability of the affected fractures. The net result was a small increase in inflow over that calculated for the SDE, contrary to what was observed. Dershowitz performed similar analyses in a stochastic mode and found increases in flow for some realizations and decreases in others.

Long et al. (1992a) used the equivalent-discontinuum models for the SDE described above, which included flow only in the fracture zones in the vicinity of the D-holes. Data on pressure distribution around a drift a few hundred meters to the west of the VD (the Macropermeability Drift) were used to infer the magnitude of permeability decrease in a 5-m-wide zone around the drift. These data indicate that the permeability in the first 5 m is decreased on average by a factor of four (Wilson et al., 1981). When this permeability reduction was used in predictions of the inflow to the VD, the predicted inflows were high by a factor of about 5. To match the drift inflow, the permeability in the first 5 m had to be decreased by a factor of 40. Evidently the rock around the VD experiences a significantly less permeable skin than that observed during the Macropermeability Experiment (Wilson et al., 1981). The maximum reduction in permeability that can be inferred from the Macropermeability Experiment is a factor of 20. So the factor of 40 for the VD may not be unreasonable. The remainder of this section summarizes the possible causes examined by Long et al. (1992b) for this dramatic decrease in permeability in the vicinity of the VD. These are summarized below.

The effect of additional sinks drawing off an increasing proportion of the flow after excavation was examined numerically and shown to be unlikely to explain the decrease in Validation Drift inflow.

Drifts can significantly perturb the stress field and hence the fracture conductivity within a few diameters of the drift walls. The stress perturbation caused by the excavation of the VD was analyzed to examine the possible effect of VD inflow along the H-zone (Long et al., 1992a). The orientations of the VD and the most compressive far-field horizontal stress differ by only 4 ft. The stress state and the relevant geometries thus indicate that the change in stress on fractures perpendicular to the drift axis will be minimal. Therefore a 2-D plane-strain analysis is useful for analyzing the stress effects on the H-zone due to excavation. This analysis, based on the most recent stress measurements for the VD area, indicates that the maximum increase in normal stress will occur for fractures radiating from the drift. The compressive normal stress tangential to the drift wall should increase between 50% (at the drift walls) and 133% (at the roof and floor of the drift); these effects decay to less than 10% within a few meters from the drift. Experimental work on laboratory core samples suggests that the ratio of the change in fracture hydraulic conductivity to the change in normal stress varies as σN^{α}, where α most likely is in the range –0.2 to –1 (Gale et al., 1990, Makurat et al., 1990). Accordingly, the hydraulic conductivity along fractures oriented radially to the drift should decrease by no more than 40% at the drift perimeter and by no more than 7% as appropriately averaged over a 5-m distance from the drift. Changes in the absolute magnitude of the normal stress parallel to the drift are small (< 15%), averaging to zero around the perimeter of the drift. There should be little direct effect on the inflow along drift-perpendicular fractures (i.e., the longest H-zone fractures).

A 3-D simulation of the stress field around the drift was made by Tinucci and Israelsson (1991) using the discrete fracture code 3-DEC. The result of their work essentially confirms the conclusions based on the 2-D plane strain analysis presented above. In a two-dimensional simulation with a fully coupled model, Monsen et al. (1991) show no significant differences with the continuum model results. It is difficult to see how changes in normal stress across fractures could decrease the overall permeability of the first 5 m of rock by a factor of 40. On the other hand, shear displacements may result from excavation. These may lead either to increases or to decreases in permeability, depending on the amount of shear and the accompanying normal stress acting on the fracture. Although shear deformation cannot be ruled out as a contributor to flow reduction, the fact that pressure heads began to rise before the main conductor was excavated does not support this theory.

Two-phase flow caused by differential drying during ventilation has been suggested as a possible reason for a decrease in flow (K. Pruess, personal communication, 1991). Drying could be caused by the ventilation procedure. As the ventilation rate is increased, either by raising the temperature in the drift or increasing the air flow rate, the measured inflow of water will change. At first, an increased ventilation rate will increase the measured flow as more water is essentially sucked out of the rock. The rock will then start to dry out, and air invasion could decrease the effective permeability of the rock near the wall. During one stage of the drift inflow measurements, the plastic sheets were removed, thus effectively increasing the ventilation rate. When the sheets were removed, the measured flow rate increased. This indicates that the ventilation was not producing any significant two-phase flow effects.

Blasting can damage the rock through the creation of new fractures (i.e., increase permeability) or cause gas to be intruded into the rock mass and shake loose fine particles, which then block flow paths (i.e., decrease permeability). The effect of fracture formation may explain some of the difference between the Macropermeability Drift (MD) and the VD because the MD was excavated with a smooth blasting technique and the VD was excavated with a pilot and slash technique that caused very little blast damage to the rock. It may be that the careful blasting in the VD did not increase the permeability near the drift as much as blasting did in the MD.

The near-surface waters at Stripa are rich in carbonates, and the deeper waters are rich in sodium. Mixing of these waters occurs when both waters flow toward the same sink, i.e., the VD, resulting in a water that is oversaturated in calcite. Precipitation of calcite in the fractures would decrease the permeability, but this precipitation should be independent of whether the drain consists of a borehole or a drift. In addition, if calcite precipitation were significant, a permeability reduction would be expected during the SDE, but this was not observed.

During the last step of the SDE, gas bubbles were observed in the outflow tubing. Gas bubbles that are constantly released as water approaches atmospheric pressure could have a very significant effect by causing two-phase flow and a significant decrease in relative permeability if the gas bubbles remain in the rock mass. Samples of the inflow water show that as much as 5 or 6% by volume of the water is nitrogen that comes out of solution at atmospheric pressure (Laaksoharju, 1990). Application of Henry's law to the measured gas content of the inflow water shows that much smaller amounts of gas should come out of solution at the 17-m pressure head used in the last step of the SDE. Thus the scenario whereby degassing causes two-phase flow is consistent with a significant flow drop between the SDE and the VD. Degassing is also consistent with the observation that pressures began to increase immediately following the start of excavation. Finsterle and Vomvoris (1991) attempted to numerically simulate degassing for the VD and found no effect on inflow rate, but they might have obtained a different result if the simulations had used different parameters or geometry, more like those of the true flow system.

In conclusion, the most plausible cause for a significant decrease in the permeability of the skin surrounding the VD is degassing as the pressure of the water is dropped to atmospheric on inflow. Excavation method, stress effects, and dynamic loading may also have some importance. It should be noted that the orientation of this tunnel with respect to the maximum principal stress and the dominant fracture orientation and its small size (< 3 m diameter) may be largely responsible for the fact that stress changes appear to be relatively unimportant. An important consequence of these observations is that hydrologic measurements in tunnels cannot be used straightforwardly for characterizing the flow system because of the unknown magnitude and cause of the skin. It is certainly inappropriate to consider inflow measurements to drifts as indicative of the undisturbed hydrologic regime. In the case of the SCV modeling effort, the VD measurements were dominated by physical effects that were not part of the modeling exercise. Hence, the VD inflow was not useful for examining the appropriateness of the modeling efforts. The combination of the SDE and VD experiments were, however, very valuable for understanding excavation effects. The process of gas dissolution is eventually reversible, and if a low-permeability skin is caused by two-phase flow effects, refilling the tunnel is likely to cause permeability to increase. This is of importance for the storage of nuclear waste in underground repositories, for water transport tunnels, and for other cases where inflow to an underground excavation needs to be understood. This phenomenon may create an

opportunity to study two-phase flow effects in fractured rock by controlling the pressure in boreholes drilled from an underground facility.

WHAT WAS LEARNED FROM MODELING THE TRACER TESTS

A series of tracer simulations were compared with results of *in situ* tracer tests. The simulations were based on two 2-D equivalent discontinuum models of the H-zone. The first, mentioned above in the section on the conceptual model, was annealed to the C1-2 test and is called the "C1 model." The second, called the co-annealed case, was simultaneously annealed to the C1-2 test and the observations made at the end of the SDE.

Both models were used to simulate the first Radar/ Saline (RSI) experiment, i.e., injection of tracer in C1-2 and collection of tracer in a sink caused by opening the D-holes in the vicinity of the H-zone. The actual breakthrough curve was used to calibrate the model by changing the ratio of flow to velocity in the conductive elements of the model to match the breakthrough curve. Only advective dispersion of tracer was allowed. This calibrated model was then modified to include the low-permeability skin around the drift and used to predict the second Radar/ Saline experiment (RSII), this time from C1-2 to the VD. Figure 4 shows the predicted and measured breakthrough curves for RSI and RSII, respectively, in the C1-2 configuration. Then a series of tracer tests from a variety of borehole intervals within the H-zone to the drift were simulated.

In the models, the change in boundary conditions from RSI to RSII had the effect of increasing the maximum C/Co. In the experiment, excavation left the maximum C/Co relatively unchanged. The increase in C/Co from the RSI simulation to the RSII simulation is explainable because the injected water is a greater proportion of the inflow to the drift than the inflow to the D-holes. However, the lack of a similar trend in the observed data may be due to (1) the effects of excavation and the resulting two-phase flow near the drift, (2) the influence of the remaining open D-holes in pulling tracer away from the drift, or (3) an increase in local dispersion phenomena caused by the higher injection pressures of RSII. Thus lack of knowledge of the boundary conditions prevents a

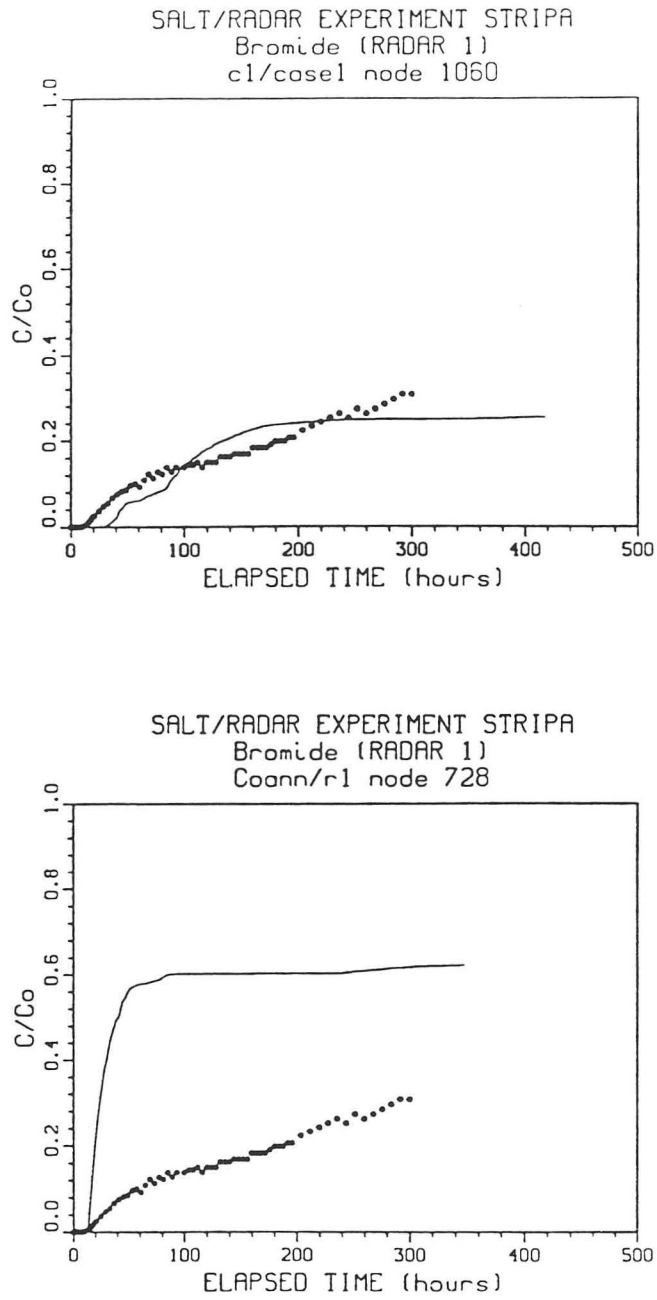

Figure 4. Predicted and measured breakthrough curves for RSI (**top**) and RSII (**bottom**). [XBL 935-796]

Table 1. Estimates of first arrival and maximum concentration for the tracer tests.

		First arrival (hr)		Maximum C/Co	
Case	Source	Predicted	Data	Predicted	Data
1	T1:2	800 to 2800	400	0.0001 to 0.0005	
2	T2:1	200 to 1400	200	0.0001 to 0.0004	0.002
3	C2	200 to never	300	0 to 0.002	0.002

good estimate of the maximum concentration. Both the C1 and the co-annealed configurations match the arrival time of the RSII data fairly well.

The tracer tests were simulated twice: once with the C1-2 configuration and once with the co-annealed configuration as described above. No dispersion coefficient was used. The breakthrough curves are all much steeper than that observed. As can be seen in Table 1, the models do extremely well in predicting the breakthrough times. It seems as if these hydraulically based models do reasonably well in predicting arrival times. However, more physical reality, e.g., more channel conductance variability, may be needed to capture more of the transport behavior. Knowledge of boundary conditions is critical to predicting tracer transport in a way that prediction of flow is not anywhere near as sensitive to.

CONCLUSIONS

Some of what was gained from the Stripa Project was not planned: as in most earth science research, the results may not exactly match the original goals. Nevertheless, the actual results are significant. The stated aims of the project included "validation" of fluid flow and transport codes. I would argue that this is not a possible achievement in a strict sense. Simply changing the definition of validation in such a way that validation somehow becomes achievable trivializes and obfuscates an accurate assessment of the modeling effort. What we have learned is that the codes are a mathematical formalization of the exceedingly more important effort of "conceptual modeling." Stripa is by far the best example of conceptual modeling done to date.

Although only the modeling efforts done by LBL are discussed here, all of the modeling efforts that have been done show that the key to good modeling is good characterization. Each of the codes has advantages and disadvantages, and each could be applied with flexibility in meeting the challenge of predicting behavior. None of the codes would have come anywhere near making good predictions without a good understanding of the fracture system.

A recommendation for future work is that future studies of tracer transport in fracture networks should not be confounded with excavation effects. There are many things that we do not fully understand about the physics of the transport phenomenon in fractures. It may be possible to match breakthrough curves, but we do not yet know the best way to build predictive models. The SCV project has shown clearly that we do not understand the hydrology of excavations. Coupling these two problems makes it very difficult to interpret the experiments.

It may be very productive to conduct a series of interference tests as the basis for an iterative model development process. The idea would be to optimize the model to one test and predict the second, then optimize the model to the first two tests and predict the third, etc. In this way it may be possible to see how the ability to predict improves with additional data. It will be very important to study the effects of excavation in such a way that the various physical phenomena can be deconvolved. Much of the inferences about a rock mass being considered for a nuclear waste repository will be made from observations in underground excavations. We will consequently need to know how to condition our inferences to reflect the excavation effects. Finally, in formations rich in dissolved gases, underground excavations in otherwise saturated rock may provide an excellent opportunity to perform controlled studies of two-phase flow in fractures.

REFERENCES

Birgersson, L., Widen, H., Agren, T., Neretnieks, I., and Moreno, L., 1992. Characterization and validation. Tracer migration experiment in the Validation Drift. Report 2, Part 1: Performed experiments, results and evaluation. Stripa Project TR 92-03, SKB, Stockholm, Sweden.

Black, J., Olsson, O., Gale, J., and Holmes, D., 1991. Site characterization and validation, stage IV-Preliminary assessment and detail predictions. Stripa Project TR 91-08, SKB, Stockholm, Sweden.

Davey-Mauldon, A., Karasaki, K., Martel, S.J., Long, J.C.S., Landsfeld, M., and Mensch, A., 1993. An inverse technique for developing models for fluid flow in fracture systems using simulated annealing. Water Resour. Res., in press (LBL-31379).

Dershowitz, W., Wallman, P., and Kindred, S., 1991. Discrete fracture modeling for the Stripa site characterization and validation drift inflow predictions. Stripa Project TR 91-16, SKB, Stockholm, Sweden.

Finsterle, S., and Vomvoris, S., 1991. Inflow to Stripa Validation Drift under two-phase conditions: Scoping calculations. NAGRA Report 91-40, Baden, Switzerland.

Gale, J., MacLeod, R., and LeMessurier, P., 1990. Site characterization and validation—Measurement of flowrate, solute velocities and aperture variation in natural fractures as a function of normal and shear stress, stage III. Stripa Project TR 90-11, SKB, Stockholm, Sweden.

Herbert, A.W., Gale, J.E., Lanyon, G.W., and MacLeod, B., 1992. Modeling for the Stripa site characterization and Validation Drift inflow prediction of flow through fractured rock. Stripa Project TR 91-35, SKB, Stockholm, Sweden.

Laaksoharju, M., 1990. Site Characterization and Validation—Hydrochemical Investigations in Stage 3. Stripa Project TR 90-08, SKB, Stockholm, Sweden.

Long, J., Karasaki, K., Davey, A., Peterson, J., Landsfeld, M., Kemeny, J., and Martel, S., 1991. An inverse approach to the construction of fracture hydrology models conditioned by geophysical data—An example from the validations exercises at the Stripa Mine. Int. J. Rock Mech. Min. Sci. & Geomech. Abstr., v. 28, no. 2/3, p. 121–142.

Long, J.C.S., Mauldon, A.D., Nelson, K., Martel, S., Fuller, P., and Karasaki, K., 1992a. Prediction of flow and draw-down for the site characterization and validation site in the Stripa mine. Lawrence Berkeley Laboratory Report LBL-31761 (SKB 92-05).

Long, J.C.S., Olsson, O., Martel, S., and Black, J., 1992b. Effects of excavation on water inflow to a drift. I.S.R.M Symposium on Fractured Rock Masses, Tahoe City, California, June 1992.

Makurat, A., Barton, N., and Tunbridge, L., 1992. Site characterization and validation—Coupled stress-flow testing of mineralized joints of 200 mm and 140 mm length in the laboratory and in situ, stage III. Stripa Project TR 90-07, SKB, Stockholm, Sweden.

McKinnon, S., and Carr, P., 1990. Site characterization and validation—Stress field in the SCV block and around the Validation Drift, stage III. Stripa Project TR 90-09, SKB, Stockholm, Sweden.

Monsen, K., Makurat, A., and Barton, N., 1991. Disturbed zone modelling of SCV Validation Drift using UDEC-BB, models 1 to 8—Stripa phase 3.

Olsson, O., Black, J.H., Gale, J., and Holmes, D., 1989. Site characterization and validation stage II-Preliminary predictions. Stripa Project TR 89-03, SKB, Stockholm, Sweden.

Olsson, O., Andersson, P., and Gustafsson, E., 1991a. Site characterization and validation—Monitoring of saline tracer transport by borehole radar measurements—Phase 1, Swedish Nuclear Fuel and Waste Management Co., Stockholm, Sweden. Stripa Project TR 91-09, SKB, Stockholm, Sweden.

Olsson, O., Andersson, P., and Gustafsson, E., 1991b. Site characterization and validation—Monitoring of saline tracer transport by borehole radar measurements—Final report. Swedish Nuclear Fuel and Waste Management Co., Stockholm, Sweden. Stripa Project TR 91-18, SKB, Stockholm, Sweden.

Olsson, O. (editor), 1992. Site characterization and validation—Final report. Stripa Project TR 92-22, SKB, Stockholm, Sweden.

Tinucci, J.P., and Israelsson, J., 1991. Site characterization and validation, Excavation stress effects around the Validation Drift. Stripa Project TR 91-20, SKB, Stockholm, Sweden.

Wilson, C.R., Long, J., Galbraith, R.M., Karasaki, K., Endo, H.K., DuBois, A.O., McPherson, M.J., and Ramqvist, G., 1981. Geohydrological data from the macropermeability experiment at Stripa, Sweden. Lawrence Berkeley Laboratory Report LBL-12520 (SAC -37).

Evaluating the Degradation of Chlorinated Hydrocarbons in Contaminated Groundwater

W. W. McNab, Jr., and T. N. Narasimhan

Since 1983, it has become known that groundwater beneath the site of the Lawrence Livermore National Laboratory (LLNL) has been contaminated with volatile organic compounds (VOCs), notably PCE, TCE, 1,1- and 1,2-DCE, 1,1,1-TCA, and 1,1- and 1,2-DCA. The Environmental Restoration Division (ERD) of LLNL is exploring many alternatives to remove the VOCs from groundwater so as to comply with the regulations of the Environmental Protection Agency (EPA). In evaluating the relative merits of these strategies, an important issue concerns whether the dissolved organic compounds undergo degradation into daughter products and, if so, determining the half-lives of such degradation reactions.

The purpose of this study is to analyze the water quality data already collected from the site by the ERD for evidence of degradation. This work is based on the premise that dissolved organic compounds may follow a variety of degradation pathways, determined largely by the overall groundwater geochemistry, notably redox conditions. Therefore, it is rational to commence the evaluation effort with a study of the thermodynamic state of groundwater at the site. A detailed report of this study is presented in McNab and Narasimhan (1992).

THERMODYNAMIC CONSTRAINTS ON DEGRADATION REACTIONS IN GROUNDWATER

Highly halogenated VOCs, such as those found at LLNL, primarily tend to degrade through reduction reactions (reductive dehalogenation), whereas their less chlorinated counterparts tend to be more susceptible to oxidation. The contaminants of greatest concern at LLNL—PCE and TCE—are highly chlorinated and hence would be expected to degrade primarily through reduction. One way to quantify the susceptibility of VOCs in LLNL groundwater to reductive dehalogenation is to follow the lead of Vogel et al. (1987) and calculate the equilibrium pE value at which a particular degradation path will be favored. Such values, relevant to the chlorinated ethanes and ethenes at the site, are given in Table 1. These estimates assume a mean pH of 7.6 and a mean Cl^- concentration of 2.8×10^{-3} mol/l, approximately representative of conditions in LLNL groundwater. Potential reductive dehalogenation pathways involving VOCs found in LLNL groundwater are shown in Figure 1. Clearly, whether degradation by reductive dehalogenation does or does not occur at the site depends on redox conditions in local groundwater.

LOCAL HYDROGEOCHEMISTRY

Geochemical evidence strongly suggests that the local subsurface environment at LLNL is highly oxidizing in nature and hence is highly unfavorable for the reductive dehalogenations shown in Figure 1. The prevalent oxidizing state is manifested in (a) the presence of dissolved oxygen up to 8 mg/l in a large number of groundwater samples, (b) the presence of iron oxide stains in Holocene alluvium, (c) the presence of solid phase MnO_2 and low Mn^{2+} concentrations in the aqueous state, and (d) the dominance of Cr^{6+} over Cr^{3+}. On the basis of the mean pH value and the speciation of Mn and Cr, it has been estimated that effective pE values in groundwater are at least 9.0 or 10.0.

Table 1. Redox constraints on common reductive VOC-degradation reactions in LLNL groundwater.

Reaction[1]	Maximum pE	Remarks
PCE → TCE	9.3	
TCE → 1,2-DCE	8.6	
1,2-DCE → VC	6.1	
1,1,1-TCA → 1,1-DCA	9.0	
1,1-DCA → CA	8.3	Product not observed[2]
1,1-DCE → VC	6.3	Product not observed

[1]CA = chloroethane; VC = vinyl chloride.
[2]Chloroethane has been detected only twice out of 2019 samples.

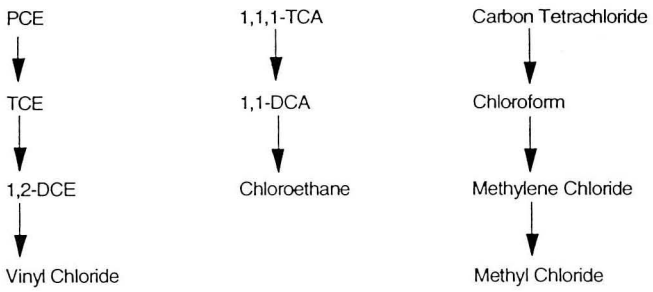

Figure 1. Reductive dehalogenation pathways for VOCs in LLNL groundwater. [XBL 935-797]

NONREDOX PROCESSES

Apart from redox-dependent reactions, many other degradation reactions are known that do not involve electron transfer (i.e., nonredox reactions). These reactions need not depend on the presence of microbial agents to proceed at measurable rates. Such reactions would therefore not be as strongly system-dependent as redox degradation reactions. As a result, abiotic degradation rates measured in the laboratory might sometimes be qualitatively extended to actual field conditions. Studies of hydrolysis rates for a variety of compounds of environmental concern were conducted by Mabey and Mill (1978), Vogel et al., (1987), and Jeffers et al. (1989). These studies indicate that chlorinated ethenes generally do not hydrolyze at significant rates. Estimated hydrolysis half-lives for chlorinated ethenes found in LLNL groundwater (PCE, TCE, 1,1-DCE and 1,2-DCE) range from millions to hundreds of millions of years and are thus insignificant. Halogenated ethanes, as a group, appear to be more susceptible to hydrolysis. 1,1,1-TCA is the most reactive of the group, with an effective half-life on the order of 0.5 to 2.5 years under neutral pH conditions, with 1,1-DCE and acetic acid noted as possible daughter products. Because 1,1,1-TCA is among the VOCs present in LLNL groundwater, its degradation is perhaps the most likely to be detected.

DATA ANALYSIS

The most intuitive approach for ascertaining whether a given chemical is degrading is to measure the change in its total mass as a function of time. However, the existing spatial and temporal resolution of the LLNL groundwater chemistry database does not readily permit accurate estimates of such changes. The error associated with integrating under inferred concentration contour intervals may be greater than the degradation effects being measured. A more suitable method for searching for field evidence for degradation reactions is to qualitatively compare the behavior of suspected parent compound-daughter compound pairs. Such an evaluation may include examining spatial

and temporal trends in the ratio of concentrations of the daughter and parent compounds.

To test the various degradation hypotheses, two scenarios were considered. The first was the degradation of 1,1,1-TCA to 1,1-DCE, perhaps the most likely degradation reaction in LLNL groundwater. For comparative purposes, the second considered the reductive degradation of PCE to TCE. From thermodynamic considerations, we concluded that for the redox conditions prevalent at the site, the most plausible dehalogenation path would be that of PCE transforming to TCE.

1,1,1-TCA AND 1,1-DCE

The abiotic transformation of 1,1,1-TCA into 1,1-DCE through dehydrohalogenation may be expressed as

$$Cl_3CCH_3(1,1,1-\mathrm{TCA}) \rightarrow Cl_2CCH_2(1,1-\mathrm{DCE}) + H^+ + Cl^- \quad (1)$$

If 1,1,1-TCA does indeed transform into 1,1-DCE at some measurable rate, it should be expected that the ratio of the concentration of 1,1-DCE to that of 1,1,1-TCA would tend to increase over time wherever both chemicals are detected. However, 1,1,1-TCA is more hydrophobic than 1,1-DCE (Mercer et al., 1990) and thus is likely to be less mobile in groundwater. Retardation effects alone should therefore result in a decrease in the [1,1-DCE] to [1,1,1-TCA][1] ratio over time in regions where 1,1,1-TCA is detectable (as 1,1-DCE would tend to escape such regions at a faster rate). Thus the superimposed effects of both degradation and adsorption may influence the [1,1-DCE] to [1,1,1-TCA] ratio in a complex manner. To qualitatively evaluate the expected variation in the [1,1-DCE] to [1,1,1-TCA] ratio influenced by both degradation and sorption, a numerical solute transport model was used to compare two possible scenarios: chemical degradation effects combined with retardation, and retardation alone. Both scenarios are based upon hydrologic data collected from the LLNL facility. Modeling results indicate that the primary difference between the two scenarios is an increase in the [1,1-DCE] to [1,1,1-TCA] ratio associated with degradation contrasted by a decrease in the ratio in the absence of degradation. Figure 2 shows measured temporal trends in the [1,1-DCE] to [1,1,1-TCA] ratio for a number of wells located on the major longitudinal axis of the 1,1,1-TCA plume along Arroyo Seco on the LLNL site. An increase in this ratio in the data is clearly evident. This is qualitatively consistent with the degradation scenario and entirely inconsistent with the nonreactive scenario.

[1] Square brackets, [ ], refer to chemical concentration.

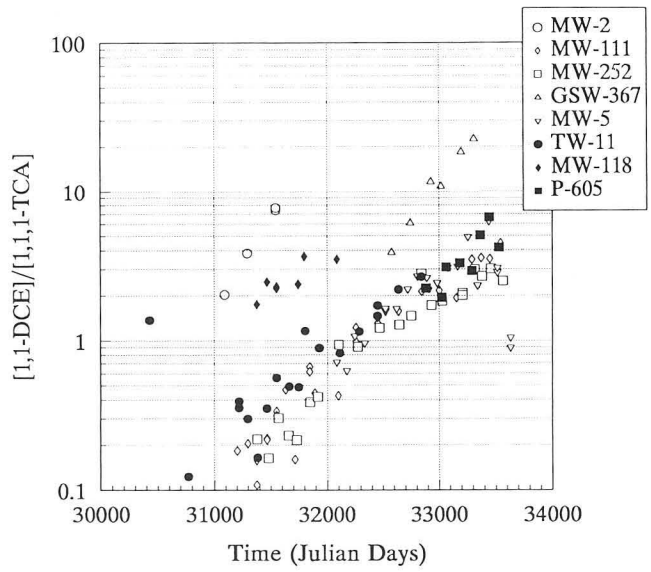

Figure 2. Temporal variation of the [1,1-DCE] to [1,1,1-TCA] ratio (mol/l) with distance in select Arroyo Seco area wells. [XBL 935-798]

Semiquantitative evidence for the degradation of 1,1,1-TCA to 1,1-DCE was also obtained by examining apparent changes in their respective total masses in a given area over time. Although this calculation was not feasible over the entire LLNL site, the relatively well-defined plumes in the Arroyo Seco area allowed such a calculation on a local level. The relative total masses of dissolved 1,1,1-TCA and 1,1-DCE along the Arroyo Seco Creek for each year were calculated by integrating the spatial distribution of the concentrations. The implied variation of the relative total masses of 1,1,1-TCA and 1,1-DCE shows a pronounced decline in 1,1,1-TCA concentrations compared with 1,1-DCE (Figure 3). It is unlikely that this relative decrease in the total mass of 1,1,1-TCA compared with 1,1-DCE is due to preferential transport of 1,1,1-TCA, as it is likely less mobile than 1,1-DCE (based upon hydrophobicity). The decline in the concentration of 1,1,1-TCA is equivalent to an effective half-life of approximately 2 yr, which agrees very well with published values ranging from 0.5 yr to 2.5 yr (Vogel et al., 1987, Jeffers et al., 1989). However, the degree to which other mechanisms, such as advection and dispersion, influence the observed decline is difficult to establish. Unfortunately, it is not possible to establish a direct mass-balance relationship between the observed relative masses of 1,1,1-TCA and 1,1-DCE. This is not just due to transport effects, because other degradation products, particularly acetic acid, may also be produced from 1,1,1-TCA.

To gain further insight into the behavior of 1,1-DCE with respect to 1,1,1-TCA across the entire LLNL facility, temporal trends in the [1,1-DCE] to [1,1,1-TCA] ratio were

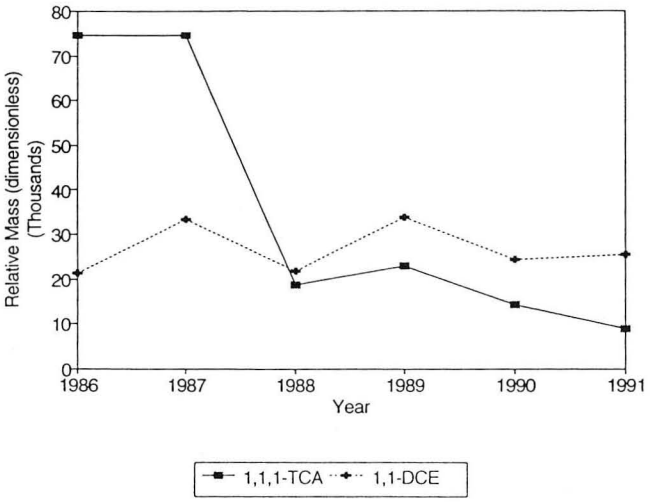

Figure 3. Relative total masses of 1,1,1-TCA and 1,1-DCE in the Arroyo Seco area over time. [XBL 935-799]

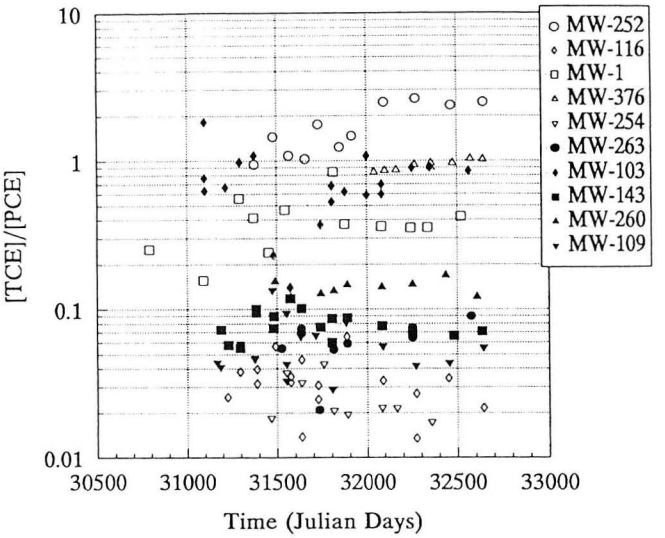

Figure 4. Temporal variation of the [TCE] to [PCE] ratio (mol/l) with distance in select Arroyo Seco area wells. [XBL 935-800]

studied in 64 individual wells located in different areas and screened in different water-bearing zones. These results also corroborated the inference that 1,1,1-TCA is indeed degrading to 1,1-DCE.

PCE AND TCE

The evidence presented for the 1,1,1-TCA degradation illustrates how observations of patterns in correlated concentration data for suspected reaction pairs may be used to assess possible degradation. The same general methodology was also used to search for evidence of the transformation of PCE to TCE, a reaction that is probably unlikely to occur in LLNL groundwater for thermodynamic reasons. The reductive dehalogenation of PCE to TCE may be expressed as

$$Cl_2CCCl_2\ (PCE) + H^+ + 2e^- \rightarrow Cl_2CCHCl\,(TCE) + Cl^- \quad (2)$$

The ratio of the concentration of TCE to PCE (mol/l) over time for a number of wells in the Arroyo Seco area is illustrated in Figure 4. This information is equivalent to that in Figure 2 for 1,1-DCE and 1,1,1-TCA in that the data points represent sampling locations along the major axis of a presumed localized plume. Unlike the same graph for 1,1-DCE and 1,1,1-TCA, however, no apparent overall increase in the daughter-to-parent product ratio over time is observable. We conclude that field evidence at the LLNL site does not support the degradation of PCE to TCE.

As with 1,1-DCE and 1,1,1-TCA, temporal trends in the concentration ratio of 1,1-DCE to 1,1,1-TCA were evaluated in wells across the LLNL facility in an effort to establish an overall behavior in the ratio (i.e., increasing or decreasing with time). This analysis also corroborated the inference that PCE is not degrading to TCE at the site.

A final comparison with the 1,1-DCE/1,1,1-TCA case was based on the overall association of the suspected daughter and parent compounds by well. Out of approximately 400 individual groundwater samples collected from the Arroyo Seco area and included in our evaluation, approximately 18% contained detectable concentrations of PCE but no detectable concentrations of TCE. In contrast, out of approximately 5600 individual samples evaluated for 1,1,1-TCA and 1,1-DCE across the entire LLNL facility, less than 3% of the samples contained detectable 1,1,1-TCA concentrations but no detectable 1,1-DCE concentrations. A strong correlation between detections of two given chemicals does not necessarily imply degradation, as the two may have been introduced into the groundwater environment as co-contaminants. However, a significant number of samples containing detectable amounts of the suspected parent compound without the daughter compound calls into question the suspected degradation relationship. This appears to be the case with respect to PCE and TCE.

SUMMARY

Careful cross-correlation of aqueous VOC concentrations at the LLNL facility indicates evidence for the degradation of 1,1,1-TCA to 1,1-DCE with a half-life of about 2 yr. No such evidence has been found for the degradation of PCE to TCE. These findings are consistent with the highly oxidizing state of the local groundwater and the paucity of anaerobic organisms in the aquifer environment. Both of these factors do not favor the reductive dehalogenation of chlorine-rich PCE.

REFERENCES

Jeffers, P.M., Ward, L.M., Woytowitch, L.M., and Wolfe, N.L., 1989. Homogeneous hydrolysis rate constants for selected chlorinated methanes, ethanes, ethenes, and propanes. Environmental Sci. & Technol., v. 23, p. 965–969.

Mabey, W., and Mill, T., 1978. Critical review of hydrolysis of organic compounds in water under environmental conditions. J. Phys. & Chem. Ref. Data, v. 7, no. 2, p. 383–415.

McNab, W.W., and Narasimhan, T.N., 1992. Groundwater geochemistry and VOC degradation patterns at Lawrence Livermore National Laboratory. Lawrence Berkeley Laboratory Report LBL-32586, 47 p.

Mercer, J.W., Skipp, D.C., and Giffin, D., 1990. Basics of pump-and-treat ground-water remediation technology. U.S. Environmental Protection Agency Report 600/8-90/003, 31 p.

Vogel, T.M., Criddle, C.S., and McCarty, P.L., 1987. Transformation of halogenated aliphatic compounds. Environmental Sci. & Technol., v. 21, no. 8, p. 722–736.

Multiple-Peak Response to Tracer Injection Tests in Single Fractures: A Numerical Study

L. Moreno and C.F. Tsang*

In experimental tracer tests carried out in a single fracture zone in crystalline rock, the breakthrough curves obtained using pulse tracer injection have multiple peaks in some situations (Steffen and Steiger, 1988; J. Hadermann, Paul Scherrer Inst., Switzerland, private communication, 1989; Hoehn et al., 1989). In some cases, it is observed that the shape of these breakthrough curves changes when the injection flow rate is varied. Moreover, the behavior of these multi-peaked curves is observed only for a limited range of injection flow rates.

This article presents some recent simulations of tracer tests in a single fracture with variable apertures. The aim of the work is to study the conditions under which the breakthrough curve may present multiple peaks and to determine how the injection flow rate modifies the shape of the curves in different situations. Although the study focuses on multiple peaks observed during tracer tests with pulse injection, the results can be applied to the case of continuous injection. The breakthrough curve for the latter case would show multiple steps, where each step corresponds to the arrival of a pulse in the pulse test.

DESCRIPTION OF THE MODEL

The apertures of a fracture are not constant in magnitude but vary spatially in the fracture plane. Fluid flowing through the fracture seeks out the least resistive pathways. The main flow is expected to occur through a few channels in the fracture plane (Abelin et al., 1985; Neretnieks, 1987). In defining channels, we mean preferred flow paths in the fracture. If the direction of the pressure gradient is changed, then a new pattern of channel networks would emerge, depending on pressure gradients. Tsang and Tsang (1989) demonstrated that they can be characterized stochastically by the same set of parameters as long as the anisotropy of the spatial correlation of the apertures remains relatively small.

Let us assume that we have a fracture with an overall flow under a "regional" pressure gradient. A solution containing the solute is then injected with a given flow rate at a point in the fracture plane. The injection pressure increases the local pressure profile and hence modifies the original flow pattern around the injection point. For a given distribution of the variable apertures, the injection feeds the solute into flow paths that are in the neighborhood of the injection point. The larger the injection flow, the larger the local pressure profile and the larger the number of paths that may be reached by the solute. However, the pattern of these flow paths depends strongly on the variable apertures near the injection point.

More specifically, the spatial distribution of fracture apertures is obtained by using a grid to partition the fracture and assigning a different aperture to each node enclosed by grid lines. The aperture values used are defined by an aperture density distribution (mean aperture $b = 80\ \mu m$ and spread $\sigma_{inb} = 0.5$) and a spatial correlation length (λ/L). A lognormal distribution for these apertures and an exponential fraction for the spatial covariance of the apertures were chosen. Details may be found in Moreno et al. (1988). For the

*Department of Chemical Engineering, Royal Institute of Technology, S-100 44 Stockholm, Sweden.

present study the grid is 40×40 nodes. An example of the generated variable-aperture fracture is shown in Figure 1.

Now let us locate a production well with pumping flow rate Q at the upper-right corner of the square shown in Figure 1. We may assume that this represents a quarter of the fracture plane with a production well at its center. Then, by symmetry, the upper and right boundaries are closed boundaries and left and lower boundaries are constant-pressure boundaries. The model is an approximation of a case of convergent tracer test in a fracture where the production well may be a drift in which tracer is collected, such as the MI experiment carried out at Grimsel, Switzerland (Hoehn et al., 1989). The location of a tracer injection well, with injection rate q, may be chosen at different points in the fracture plane; and in Figure 1, it is defined by the index (n_x,n_y) of the respective node, where n_x and n_y are between 1 and 40. Typically, q is much less than Q. Fluid flow is then calculated on the assumption that it is proportional to the cube of the aperture at each node. We assumed the apertures to be much smaller than the flow distance in the nodes, so that the influence on pressure drop by the diverging or converging parts of the flow path is negligible. The pressure at each node is calculated from the fluid balance in each node.

The solute transport is simulated using a particle-tracking technique (Schwartz et al., 1983; Robinson, 1984; Moreno et al., 1988, 1990). Six thousand particles are introduced in the flow field at the injection node. Each particle is then followed along its path from the injection point to the collection point through the intersections. The particle-tracking method used considers no mixing at these intersections. However, within each branch between adjacent intersections, perfect mixing is assumed (see Moreno et al., 1990). Note that the method includes an intrinsic transverse dispersivity equal to grid size due to numerical dispersion. The residence time of an individual particle over the whole path in the fracture plane is determined as the sum of residence times in all the steps that the particle has traversed. The residence time distribution is then obtained from the residence times of a multitude of individual particle runs.

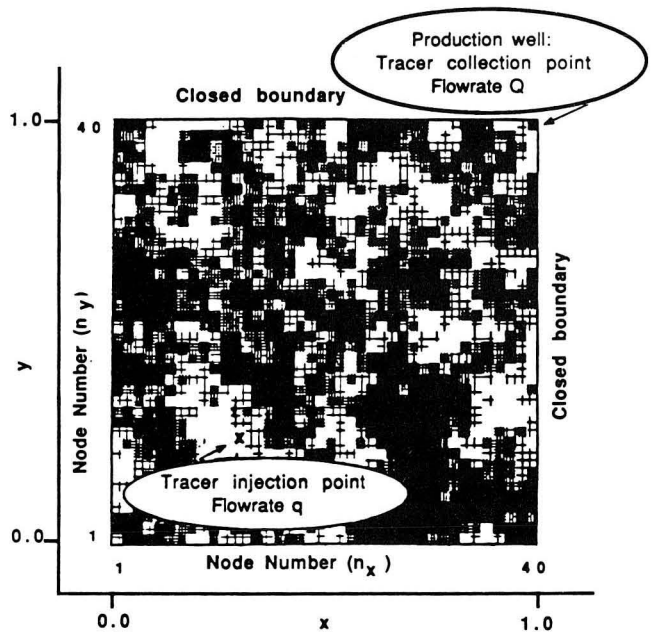

Figure 1. One realization of variable-aperture fracture. A typical tracer injection point (with injection flow rate q) is marked by "x." The top and right hand-side boundaries are closed, and the bottom and left hand-side boundaries are maintained at a constant pressure relative to the production well. [XBL 935-780]

RESULTS OF THE SIMULATIONS

Flow and solute transport for these different fractures were calculated using the same fracture aperture probability density function and spatial correlation length. Thus they are actually different realizations of the same statistical input parameters. With the production well (see Figure 1) maintained a flow rate Q, tracer injection in a single fracture is simulated for different injection locations and flow rates. For each case, flow paths, solute paths, and breakthrough curves are calculated and plotted. The injection flow rate q is first varied over a wide range (0 to 3% of Q) to determine the interval within which the shape of the breakthrough curves is sensitive to this value. When this interval is found, additional calculations are performed using flow rates within this interval to study in detail the breakthrough curves as a function of flow rates.

In preliminary simulations, we also studied the tracer breakthrough curves as a composite of several partial breakthrough curves, each of which is due to transport of tracer particles through different specified areas in the fracture plane between the injection and collection points. We have computed a number of such partial breakthrough curves. In most cases, when the total breakthrough curve is observed to possess multiple peaks at the collection hole, the partial curves are also found to display multiple peaks. We also noticed that the shape of the curves is predominantly influenced by the condition around the injection point.

The characteristics of the area around the injection point that require further investigation would be (1) the nearby fracture apertures, (2) the existence (or nonexistence) of paths with a large flow rate close to the injection point, and (3) the pressure distribution around the injection point. Large fracture apertures around the injection point may imply large residence times at this location. Conversely, small apertures may cause the injected tracer to be dispersed round the injection point. The existence of paths of large flow close to the injection point would permit a

greater proportion of the tracer flow into these paths. On the other hand, if there are no paths of large flow close to the injection point, the solute has to seek some small and slow paths to flow to the collection hole. The travel times may then be very different from each other, resulting in multiple peaks on the breakthrough curves. The pressure distribution around the injection hole is a function of the injection flow rate and determines the major directions in which the solute would start to flow from the injection point. For small injection flow rates, the solute follows the flow pattern that was established prior to injection. As the injection flow rate increases, however, the solute tends to flow radially from the injection point, and, in particular, may even flow away from the collection point.

As an example, we would like to show some detailed results of one of the generated fractures. The water flow paths with a negligible injection flow rate are shown in Figure 2. For this fracture, simulations were performed at three injection locations (n_x, n_y), given by (15,15), (11,11), and (8,8), respectively.

For injection at (15,15), the breakthrough curves show only one peak for the range of injection flow rates used in the simulations ($0.003Q$ to $0.03Q$). The tails of the breakthrough curves increase with increasing injection flow rates. This could be explained as follows. Original flow at the injection point is small, but the injection point is located close to a path with enough good connections to the collection hole. Thus, as flow rate increases, more and more solute feeds into this channel, giving rise to the longer tail.

The breakthrough curves for injection at (11,11) show one peak over the whole range of injection flow rates used (from $0.001Q$ to $0.03Q$). The fracture apertures around the injection point are large, and the flow rate in the injection point is also large. The patterns for the solute transport are then similar for all cases having different injection flow rates.

For injection at (8,8), the breakthrough curve for tracer concentration shows one peak for flow rates smaller than $0.003Q$. When the flow rate is increased beyond this value, a new peak starts to build up at a shorter residence time and the previous peak is reduced. For an injection flow rate of $0.03Q$, the peak at the short residence time is larger than the peak at the longer residence time. This variation of the relative sizes of the peaks is shown in Figure 3. The patterns of solute transport are shown in Figure 4. For an injection flow rate of $0.01Q$, new transport paths are created near the injection point, but the solute paths farther away are similar to those at lower flow rates. When the flow rate is increased even more, new paths are formed and new areas away from the injection point are involved in solute transport (Figure 4).

SUMMARY OF THE RESULTS

From the results of our many simulations, we distinguish the following causes of injection tracer tests:

- If injection occurs on a main flow channel in the fracture plane, the breakthrough curve would possess a single peak. This peak is almost independent of the injection flow rate.

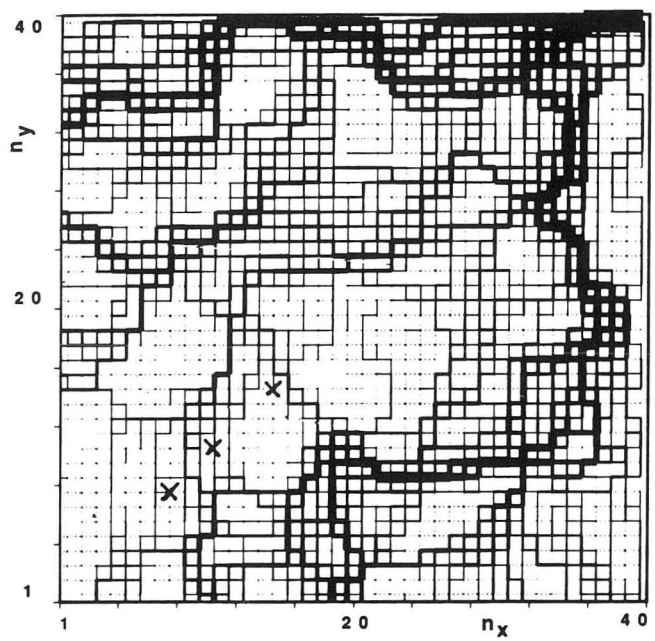

Figure 2. Flow paths in fracture 3 for a negligible injection flow rate. The injection points ("x") are (15,15), (11,11), and (8,8). [XBL 935-781]

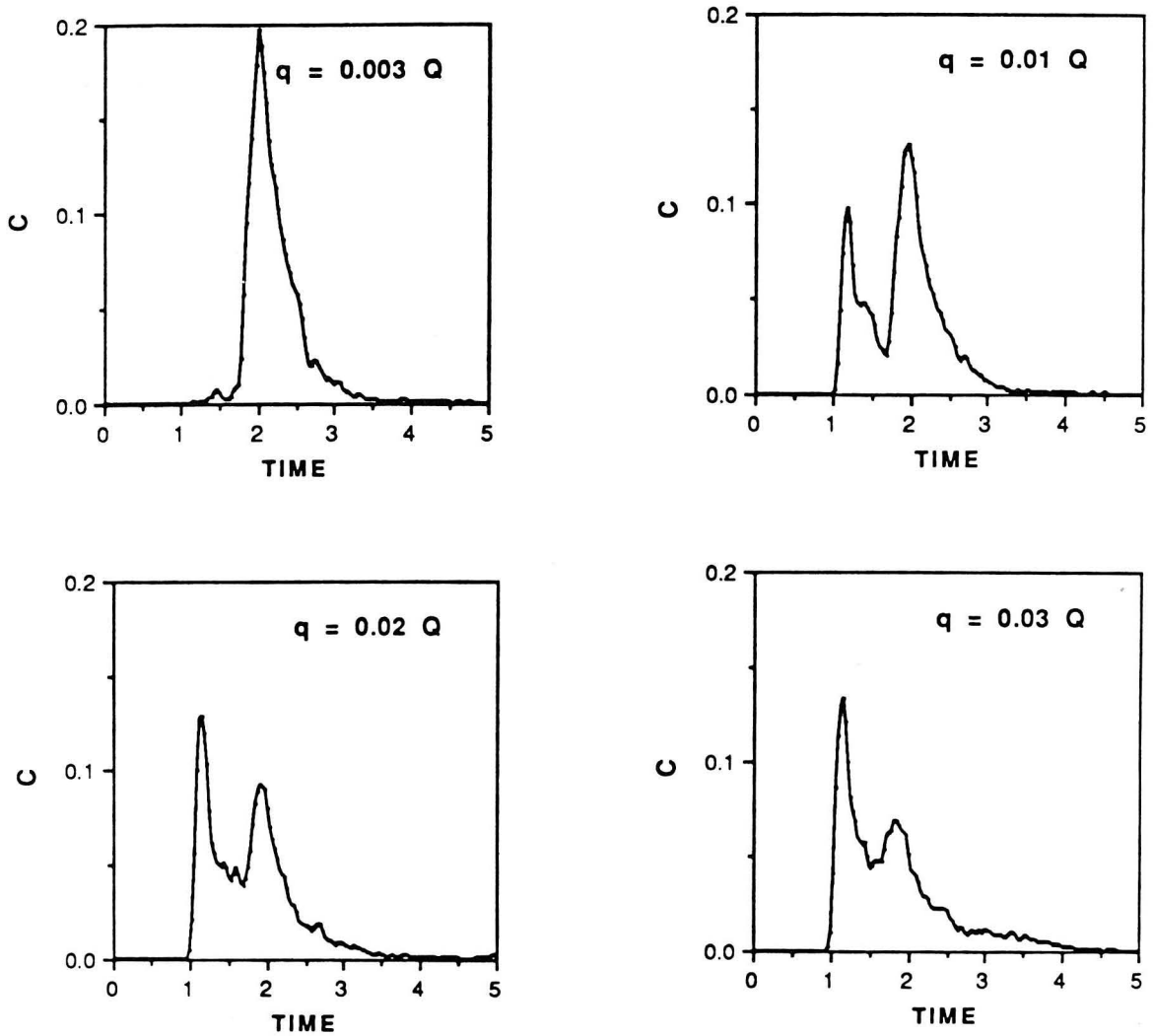

Figure 3. Breakthrough curves for fracture 3, for injection flow rates of $0.003Q$, $0.01Q$, $0.02Q$, and $0.03Q$. Injection at (8,8). [XBL 935-782]

- If injection does not occur on a main flow channel, multiple peaks may be observed.
- Dispersion depends on the number of possible paths near injection point.

In the case where injection does not occur on a main flow channel, we distinguish three possible alternative cases:

- A time shift of the first peak with a variation of the injection flow rate: the residence time decreases with an increase of the injection flow rate.
- When the injection flow rate is increased, the magnitude of the first peak decreases and the second peak builds up. Additional small peaks for long residence times may also emerge.
- Alternatively, when the injection flow rate is increased, the magnitude of the first peak increases.

The discussion and results given here may equally apply to tracer tests in a two-dimensional strongly heterogeneous medium. Although there are differences in permeability-porosity relationships between fractured and porous media, we expect that qualitatively the multiple-peak tracer transport behavior as discussed here should also be expected in such heterogeneous porous medium systems.

ACKNOWLEDGMENTS

The main impetus that motivated this work came from a number of discussions on recent field data on tracer transport in a single fracture with Jörg Hadermann, to whom we are most grateful. We would also like to acknowledge continued discussion and cooperation with Y.W. Tsang and I. Neretnieks.

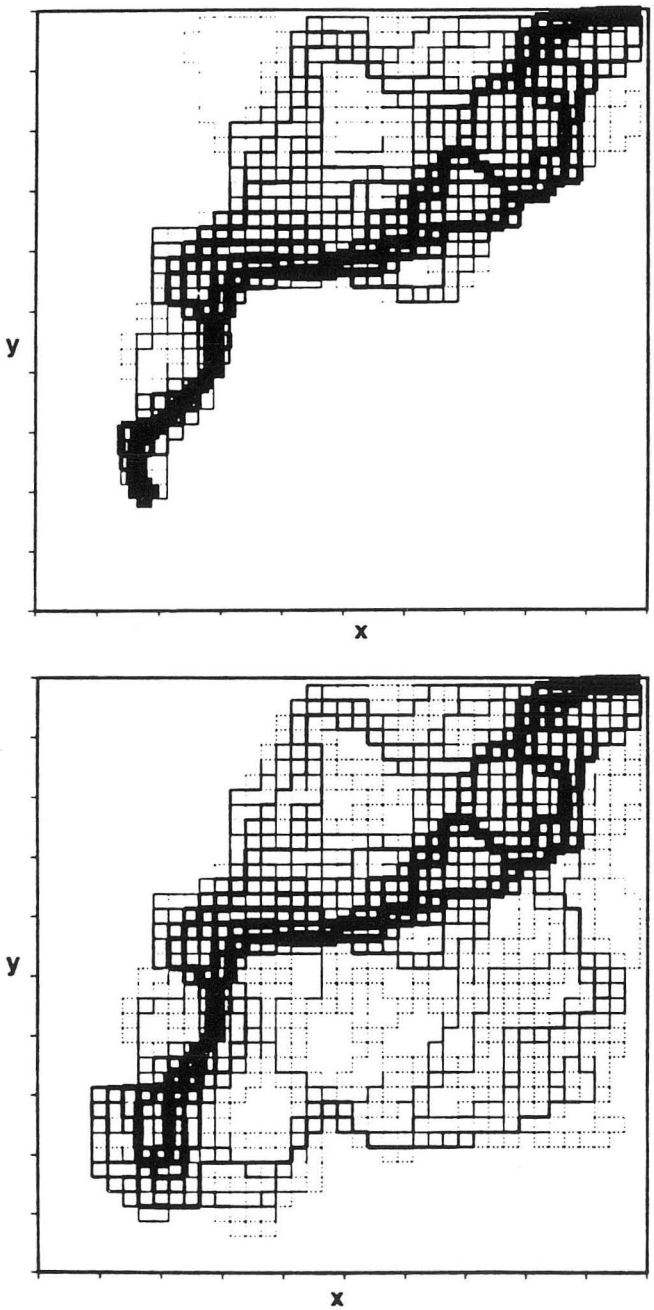

Figure 4. Tracer paths in fracture 3 for an injection flow rate of $0.003Q$ and $0.03Q$. Injection at (8,8). [XBL 935-783]

REFERENCES

Abelin, H., Neretnieks, I., Tunbrant, S., Moreno, L., 1985. Final report of the migration in a single fracture, experimental results and evaluation. Stripa Project TR 85-03, Nuclear Fueled Safety Project, Stockholm, Sweden.

Hoehn, E., Frick, U., and Hadermann, J., 1989. A radionuclide migration experiment in fractured granitic rock. *In* Proceedings, International Symposium on Processes Governing the Movement and Fate of Contaminants in the Subsurface Environment, Stanford, California, July 24–26.

Moreno, L., Tsang, Y.W., Tsang, C.F., Hale, F.V., and Neretnieks, I., 1988. Flow and tracer transport in a single fracture: A stochastic model and its relation to some field observations. Water Resour. Res., v. 24, no. 12, p. 2033-2048 (LBL-25049).

Moreno, L., Tsang, C.F., Tsang, Y., and Neretnieks, I., 1990. Some anomalous features of flow and solute transport arising from fracture aperture variability. Water Resour. Res., v. 26, no. 10, p. 2377–2391.

Neretnieks, I., 1987. Channeling effects in flow and transport in fractured rocks—Some recent observations and models. Swedish Nuclear Power Inspectorate, Proceedings of GEOVAL-87, Stockholm, Sweden.

Robinson, P.C., 1984. Connectivity, flow and transport in network models of fractured media. Ph.D. Thesis, Oxford University, Oxford.

Schwartz, F.W., Smith, L., and Crowe, A.S., 1983. A stochastic analysis of macroscopic dispersion in fractured media. Water Resour. Res., v. 19, no. 5, p. 1253–1265.

Steffen, P., and Steiger, H., 1988. NAGRA Felslabor Grimsel, Migration, Traceruntersuchungen, Vorversuche 1–4, GEMAG (Aktiengesellschaft für Geologisch-Physikalische Messungen), Alberswil, Switzerland.

Tsang, Y.W., and Tsang, C.F., 1989. Flow channeling in a single fracture as a two-dimensional strongly heterogeneous permeable media. Water Resour. Res., v. 25, no. 9, p. 2076–2080 (LBL-26595).

TOUGH Simulations of Updegraff's Set of Fluid and Heat Flow Problems

G. J. Moridis and K. Pruess

Under the sponsorship of the U.S. Nuclear Regulatory Commission, Sandia National Laboratories (SNL) is developing a performance assessment methodology for the analysis of long-term disposal of High-level Radioactive Waste (HRW) in unsaturated welded tuff (the only potential host rock presently under consideration by the U.S. Department of Energy). As part of this effort, a comparison study of three simulation codes modeling strongly coupled mass and heat flow in unsaturated porous media was conducted (Updegraff, 1989).

The three codes evaluated were (1) TOUGH, developed by Pruess (1987) at Lawrence Berkeley Laboratory (LBL); (2) NORIA, developed by Bixler (1985) at SNL; and (3) PETROS, developed by Hadley (1985) at SNL. The capabilities of these codes were tested using 1-D and 2-D problems selected to represent a wide variety of flow systems of different levels of complexity and numerical difficulty, ranging from simple, uncoupled processes (such as 1-D infiltration) to strongly coupled processes (such as 2-D heat-driven flow and vaporization).

The SNL report (Updegraff, 1989) stated that all three codes had serious weaknesses and recommended that a new code be developed. The performance review of TOUGH ranked it as the best of the three codes and concluded that it was capable of solving most of the problems. However, Updegraff (1989) concluded that TOUGH exhibited significant limitations, the most severe of which were difficulty or inability to converge in certain problems, significant numerical dispersion in heat transport problems, and large core storage and execution time requirements.

The purpose of this study was to address the issues raised by Updegraff (1989) in the SNL Report. All the test problems examined in the SNL study were reinvestigated. These included five verification problems (for which either analytical or numerical solutions exist) and three validation problems (for which experimental results are available). In our approach, we first attempted to reproduce Updegraff's (1989) results using the original input data for the eight problems. We then corrected and modified the input data and run TOUGH using the modified inputs. Finally, the new simulation results were discussed.

We demonstrated that (1) the difficulties encountered by Updegraff (1989) can be overcome by careful consideration of the physical processes modeled, (2) TOUGH is capable of handling all the test problems and obtaining correct answers by suitable preparation of input data, without any code modification, and (3) in all test problems TOUGH produces very efficient runs that cover the entire desired simulation periods. A detailed presentation of this study can be found in Moridis and Pruess (1992). In this summary, we discuss two of the test problems: a validation problem of radial heat transport, and a verification problem of a heat convection cell. By analyzing the difficulties encountered by Updegraff (1989), we hope to demonstrate a set of sound simulation principles and practices to be used in the application of TOUGH.

RADIAL HEAT TRANSPORT

The verification test problem of radial heat transport was originally solved analytically by Avdonin (1964), and was later described by Ross et al. (1982). Cold water is injected into a semi-infinite, high-temperature aquifer. The overburden and underburden are impermeable to mass and heat flow, acting as no-flow and adiabatic boundaries. The TOUGH predictions of the temperature distribution were sought after $t = t_{max} = 10^9$ sec (i.e., 32 years) of cold water injection.

Updegraff's Approach and Results

Updegraff (1989) discretized the space domain in 252 unequally sized gridblocks, which included two boundary gridblocks. A very large volume was assigned to the boundary gridblocks, thus ensuring constant boundary pressures and temperatures throughout the simulation. The boundary gridblocks were assigned constant pressures and temperatures. The initial pressure distribution was determined using a logarithmic pressure function (Updegraff, 1989). Instead of a direct injection, the prescribed pressure differential on the boundaries created an influx that resulted in an equivalent system.

Constraining the computation to $\leq$ 3000 time steps, Updegraff (1989) could only simulate the first 1.5×10^6 sec of this problem. He concluded from this that TOUGH was unlikely to simulate the required period of $t_{max} = 10^9$ sec within a reasonable time, and compared the numerical and the analytical solutions at $t = 10^6$ sec. His comparison indicated that the TOUGH solution showed limited numerical dispersion and lagged behind the analytical solution, a discrepancy he assigned to the temperature dependence of the water viscosity and density in TOUGH (unaccounted for in the analytical solution).

Examination of the report and input file revealed the following problems: (1) The correct analytical solution at $t = 10^6$ sec bore no resemblance to the analytical solution shown by Updegraff (1989); (2) incorrect water properties

had been used for the computation of the analytical solution, thus producing an incorrect analytical solution and causing conflict with the correct water property data "hardwired" in TOUGH; and (3) an excessively fine discretization had been used immediately next to the well bore. Such a fine discretization can produce severe loss of accuracy when calculating interblock flows from small differences in the pressure of adjacent gridblocks, and it increases the size of the system of linear equations to be solved without resolving additional physics. The inability to reach the desired observation time of $t_{max} = 10^9$ sec was traced to the exceedingly fine space discretization.

Modification and Results

We reduced the number of gridblocks from 252 to 127, which considerably decreased the execution time. In our data set, cold water was injected at the prescribed rate directly into the gridblock next to the wellbore. This approach was more physically correct and significantly reduced the size of the input file. We evaluated the ability of TOUGH to yield an accurate solution at $t = 10^6$ sec (used for comparisons by Updegraff) and $t = t_{max} = 10^9$ sec (specified by the problem). Both upstream and midpoint weighting schemes were considered, for a total of four input files. These produced very efficient runs, which did not suffer from any of the shortcomings reported by Updegraff (1989).

This problem has a "similarity solution" in terms of the variable r^2/t (Doughty and Pruess, 1990; 1992). In Figure 1 we plot the analytical solution, the two TOUGH solutions at $t = 10^6$ sec (with the fine time discretization), and the two TOUGH solutions at $t = 10^9$ sec versus the similarity variable r^2/t. An examination of the results reveals that

1. TOUGH efficiently simulated the radial heat transport problem. The number of time steps to reach 10^6 and 10^9 sec was 27 and 1031.
2. The TOUGH results are consistent with the r^2/t invariance that is known to exist in this problem. At $t_{max} = 10^9$ sec, the two TOUGH solutions virtually coincide with the analytical solution. The midpoint-weighted solution is slightly more accurate, but the difference from the upstream-weighted solution is imperceptible. Similar observations are made for the solutions at $t = 10^6$ sec.

THE CONVECTION CELL EXPERIMENT

The second validation problem is a laboratory convection cell Reda (1984). A porous medium consisting of glass beads with an average diameter of d =0.65 mm fills the annular region between the two vertical concentric cylinders. Application of heat generates a thermal buoyancy force, giving rise to the development of convection cells.

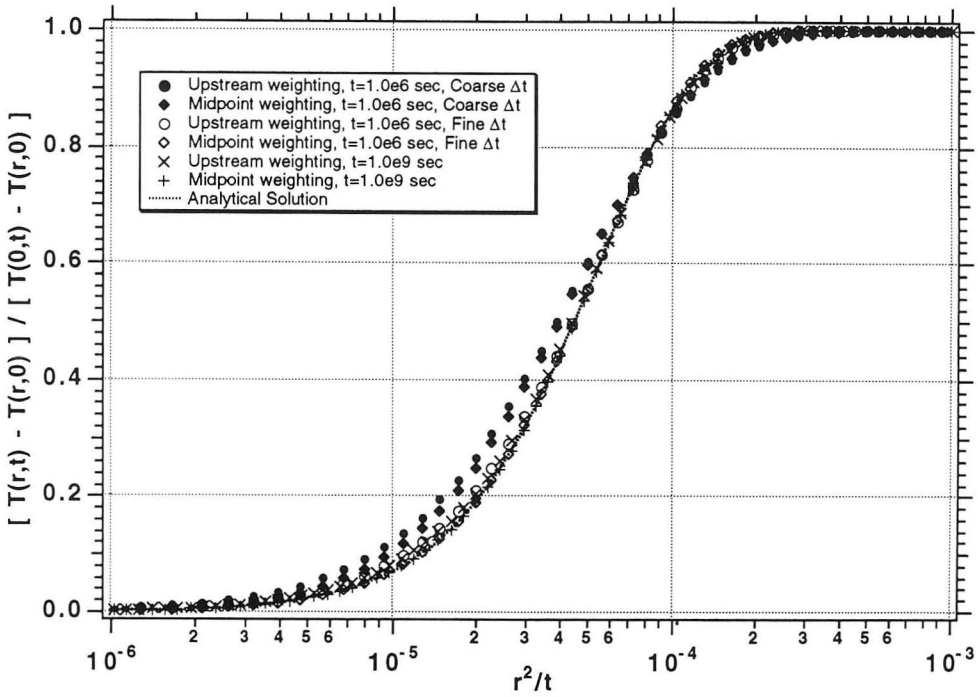

Figure 1. The analytical and numerical similarity solutions to the radial heat flow problem. [XBL 935-784]

Numerical predictions are compared with temperature measurements at the bottom and top of the heating element at a time $t = 10^5$ sec.

Updegraff's Approach and Results

Updegraff's (1989) simulation assigned a very large volume to the gridblocks at the top boundary to maintain a constant temperature and pressure. The outer cylinder boundary gridblocks were assigned a very small volume and a very large specific heat in order to model zero mass flux and constant temperature boundary conditions. Zero mass and heat flux boundaries were assigned along the bottom and the left side of the grid.

Updegraff was unable to simulate this experiment, obtaining results that significantly overpredicted temperatures (by 15 to 30°C) while not exhibiting sufficient temperature differentials between the top and the bottom of the heating elements (less than 10°C, when the observed difference was 30°C). The reasons for Updegraff's failure to successfully simulate this experiment were traced to inadequate and/or inappropriate data inputs. More specifically:

1. The discretization in the radial direction was excessively coarse. Because of cylindrical geometry, large temperature gradients are expected near the heater, and convective effects would be concentrated within a short distance from the heater. The original report on the experiment (Reda, 1984) supported this expectation. Moreover, Reda (1984) stated that the packing of the spherical particles against the heater surface led to important flow channeling effects due to porosity and permeability enhancement. These channeling effects were localized within $5d = 3.25$ mm. The radial increment Δr used by Updegraff in this region was 20.96 mm; i.e., 6.45 times larger, completely overwhelming its effects, introducing very large discretization errors, and causing the large discrepancies between Updegraff's TOUGH predictions and the experimental data.

2. The assignment of small volumes to the outer boundary gridblocks to approximate the "no-mass-flow" conditions resulted in a boundary with permeable connections to the flow domain, which may have a noticeable impact on predicted convection behavior.

3. Permeability enhancement in the immediate vicinity of the heater was not accounted for

4. The heater domain in Updegraff's simulation was assigned porous medium properties, with nonzero porosity, zero permeability in the r and z directions, and zero medium compressibility. This resulted in enormous pressures because, with the constraint of zero permeability, the gridblocks had no outlet and no compressibility other than that of water. This problem was further exacerbated by the poor selection of the location of the grid points at which the comparisons were made.

Modification and Results

For our simulation, we used a grid with a sufficiently fine discretization in the all-important region near the heater and created two new data sets: the first accounted for permeability-enhancement effects; the second neglected them. A very large volume and specific heat were assigned to the top permeable boundary of the model to maintain constant pressure and temperature. The gridblocks at the outer radial boundary had a very low porosity, zero permeability, and a very high specific heat to force strict "no mass-flow" boundaries while maintaining a constant temperature. The gridblocks assigned to the heater had a very low porosity, a large compressibility, zero permeability to impose a "no-mass-flow" boundary, and the properties of cast iron.

We evaluated the performance of TOUGH by comparing the simulation results (Figure 2) over time to the experimental measurements (Reda, 1984). The maximum simulation time was $t_{max} = 10^5$ sec. The following conclusions were drawn:

1. Both input files produced very efficient runs, covering the simulation period in less than 40 time steps.

2. A very good agreement between experiment and prediction was observed for the period of transient convection, as well as for the steady state. A very strong dependence of temperature on the radial distance was evident.

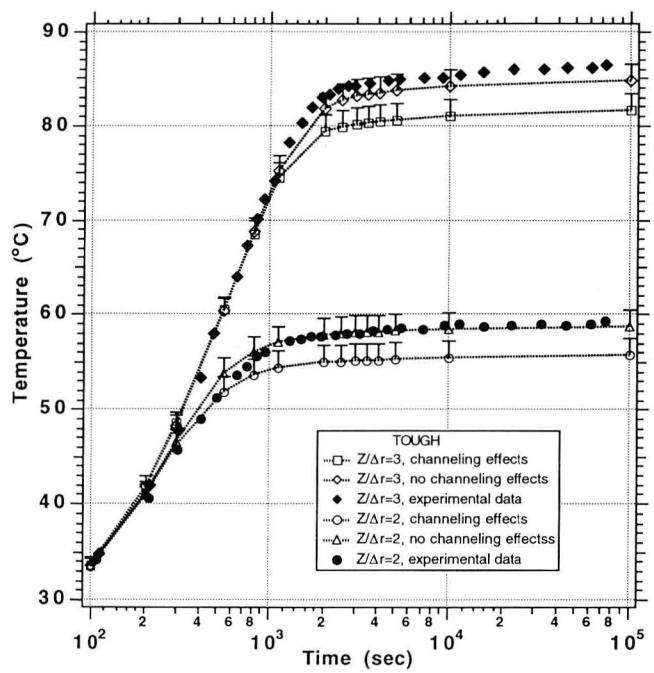

Figure 2. Comparison of TOUGH predictions with experimental data at the heater bottom ($z/\Delta r = 2$) and top ($z/\Delta r = 3$). The bars attached to the TOUGH curves indicate the predicted temperature in the first radial element (i.e., on the surface of the heating element). [XBL 935-785]

3. We found a significant difference between the runs with and without permeability enhancement. Temperatures predicted without permeability enhancement were consistently higher both at the bottom and the top of the heater. Without flow channeling, there was a somewhat slower initiation of convection and a weaker convection process at later times when steady state is approached.

4. Despite its apparent better agreement with measurements (at least near steady state), it is inappropriate to state that neglecting channeling effects produces more accurate results because of the extremely steep temperature gradients in the vicinity of the heater.

5. A significant dependence of temperature on the vertical distance z was noticed (more pronounced near the top than the bottom of the heater), where even minute (i.e., submillimeter) changes in the position of the measuring device can effect sizable temperature differentials. This observation adds further perspective on the comparison between experimental and numerical results.

CONCLUSIONS AND DISCUSSION

TOUGH has performed well on a series of fluid and heat flow problems that involved 1-D and 2-D dimensional flows, with varying degrees of nonlinearity, coupling between fluid and heat flows, and complexity of boundary conditions. These results substantiate the accuracy of the physics model employed in the code and of the mathematical and numerical approaches used. The two-phase two-component fluid and heat flow capability offered by TOUGH, and the flexibility of the space discretization by means of integral finite differences, make possible applications to a great diversity of flow problems on different space and time scales (Pruess, 1990)

Key to successful application of TOUGH is a careful consideration of the physical processes that are involved in a given flow problem. In particular, space discretization, time stepping, and interface weighting procedures need to be carefully selected so that accurate results may be obtained. Application of TOUGH (or, for that matter, of any other two-phase fluid and heat flow code) without due attention to these issues may result in poor (inefficient) performance, inaccurate results, or both. An important aspect of discretization is the interface and time-weighting procedure. TOUGH was designed for robustness and stability in difficult nonlinear problems with phase change and propagating phase fronts. The appropriate weighting procedures for such problems are fully upstream weighting in space and "fully implicit" first-order backward finite differences in time.

Some of the problems and limitations in TOUGH with regard to ease of use and description of physical processes that were noted by Updegraff (1989) were overcome with the recently released successor code, TOUGH2 (Pruess, 1991; ESTSC, 1992). TOUGH2 is upward compatible with TOUGH, with additional capabilities and user-friendly features; these include an internal version control system, more convenient facilities for specifying boundary conditions, and internal mesh processing and generating capabilities (used for mesh generation in Verification Problem 3 and Validation Problems 1 and 2). TOUGH2 offers a multiple interacting continua capability (MINC) for fractured media simulations, a simplified description of Knudsen diffusion by means of a Klinkenberg factor for permeability, and an ability to handle different fluid mixtures.

Further enhancements of process description, such as a capability for multicomponent dispersion and diffusion in multiphase flow, will be included in future releases of TOUGH2. We also expect to release a set of efficient conjugate gradient solvers for use with TOUGH2, which, compared with the presently employed direct solution technique, will drastically shorten execution times for large 3-D problems.

REFERENCES

Avdonin, N.A., 1964. Some formulas for calculating the temperature field of a stratum subject to thermal injection. Neft'i Gaz. v. 3, p. 37–41.

Bixler, N.E., 1985. NORIA—A finite element computer program for analyzing water, vapor, and energy transport in porous media. Sandia National Laboratories Report SAND84-2057.

Doughty, C., and Pruess, K., 1990. A similarity solution for two-phase fluid and heat flow near high-level nuclear waste packages emplaced in porous media. Int. J. Heat & Mass Transfer, v. 33, no. 6, p. 1205–1222 (LBL-26057).

Doughty, C., and Pruess, K., 1992. A similarity solution for two-phase water, air, and heat flow near a linear heat source in a porous medium. J. Geophy. Res., v. 97, no. B2, p. 1821–1838 (LBL-30051).

ESTSC, Energy Science and Technology Software Center, Software Listing, May 1992. Report ESTSC-2, Energy Science and Technology Software Center, Oak Ridge, Tennessee.

Hadley, G.R., 1985. PETROS—A program for calculating transport of heat, water, water vapor, and air through a porous material. Sandia National Laboratories Report SAND84-0878.

Moridis, G.J., and Pruess, K., 1992. TOUGH simulations of Updegraff's set of fluid and heat flow problems. Lawrence Berkeley Laboratory Report LBL-32611.

Pruess, K., 1987. TOUGH user's guide. Lawrence Berkeley Laboratory Report LBL-20700 (NUREG/CR-4645, SAND86-7104).

Pruess, K. (editor), 1990. Proceedings of the TOUGH workshop. Lawrence Berkeley Laboratory Report LBL-29710.

Pruess, K., 1991. TOUGH2—A general-purpose numerical simulator for multiphase fluid and heat flow. Lawrence Berkeley Laboratory Report LBL-29400.

Reda, D.C., 1984. Natural convection experiments about a finite-length cylindrical heat source in a liquid-saturated porous medium. Sandia National Laboratories, SAND83-2209C.

Ross, B., Mercer, J.W., Thomas, S.D., and Lester, B.H., 1982. Benchmark problems for repository siting models. NUREG/CR-3097, Geotrans, Inc., Reston, Virginia.

Updegraff, C.D., 1989. Comparison of strongly heat-driven flow codes for unsaturated media. Sandia National Laboratories Report SAND 88-7145.

The Laplace Transform MultiQuadrics (LTMQ) for the Solution of the Groundwater Flow Equation

*G. J. Moridis and E. J. Kansa**

MultiQuadrics (MQ) is a true scattered-data grid-free scheme for representing surfaces and bodies in an arbitrary number of dimensions by using approximations given by an expansion in terms of upper hyperboloids. It is continuously differentiable and integrable, and is capable of representing functions with steep gradients with very high accuracy. Hardy (1971) first derived MQ to approximate geographical surfaces and magnetic anomalies, but it was mostly ignored until Franke (1982) showed that MQ outperformed 29 other interpolation methods. Micchelli (1986) and Madych and Nelson (1988) provided the theoretical justification for the performance of MQ.

The extension of MQ to applications in the solution of Partial Differential Equations (PDE) in computational fluid dynamics is credited to Kansa (1990a,b), who employed MQ to solve the advection-diffusion equation, the von Neumann blast wave problem, and Poisson's equation. He showed that MQ (1) yields excellent results with a much coarser distribution of data points, (2) is an excellent estimator of partial derivatives, (3) does not need any special stabilizing treatment for instability and numerical dispersion, (4) is far more efficient and accurate than standard Finite Difference (FD) schemes, and (5) is considerably more flexible and robust than FD in the solution of the traditionally troublesome problem of steep moving fronts.

Laplace transforms are a powerful tool in the solution of PDEs, but their application was limited to simple one-dimensional problems with homogeneous properties. By combining traditional space discretization schemes with Laplace transforms, Moridis and Reddell (1990,1991a,b,c) developed a family of new numerical methods for the solution of parabolic and hyperbolic PDE's. These methods eliminate the need for time discretization of traditional numerical methods while maintaining their flexibility in the simulation of heterogeneous systems with irregular boundaries. The method of Laplace Transform MultiQuadrics (LTMQ) is based on the same concepts but uses MQ as the space approximation scheme.

THE LTMQ METHOD

The governing PDE of transient groundwater flow is

$$\nabla \cdot (K \nabla H) = S_0 \frac{\partial H}{\partial t} + Q \,, \tag{1}$$

where K is the hydraulic conductivity, H is the piezometric head, S_0 is the specific aquifer storativity, $Q = q\ \delta_c(x)\ \delta_c(y)\ \delta_c(z)$, q is the volumetric flow rate of a source or sink per unit volume, and δ_c is the Kronecker delta. The solution of Eq. (1) with the LTMQ method is accomplished in the four steps described in the following sections.

Step 1: The Laplace Transform of the PDE

For a homogeneous and anisotropic 2-D porous medium, the Laplace transform of Eq. (1) expanded in Cartesian coordinates yields

$$K_x \frac{\partial^2 \Psi}{\partial x^2} + K_y \frac{\partial^2 \Psi}{\partial y^2} = S_0 \lambda \Psi - S_0 H(0) + \frac{Q}{\lambda} \,, \tag{2}$$

* Earth Sciences Division, Lawrence Livermore National Laboratory, Livermore, California.

where λ is the Laplace space variable, $\Psi = L\{H\}$, and $L\{\}$ denotes the Laplace transform of the quantity in brackets. It should be noted that the analysis in cylindrical coordinates is entirely analogous.

Step 2: The MQ Scheme in the Laplace Space

Following Madych and Nelson (1986), we expand the continuous function Ψ in terms of MQ basis functions and an appended constant, i.e.,

$$\Psi(\mathbf{x}) = a_1 + \sum_{j=2}^{N} \hat{g}(\mathbf{x} - \mathbf{x}_j) a_j \,, \tag{3}$$

where

$$\hat{g}(\mathbf{x} - \mathbf{x}_j) = g(\mathbf{x} - \mathbf{x}_j) - g(\mathbf{x} - \mathbf{x}_1), \qquad j = 2, \ldots, N \,, \tag{4}$$

$$g(\mathbf{x} - \mathbf{x}_j) = \left[(x - x_j)^2 + (y - y_j)^2 + r_j^2 \right]^{1/2} , \tag{5}$$

$$r_j^2 = r_{min}^2 \left(\frac{r_{max}^2}{r_{min}^2} \right)^{(j-1)/(N-1)} , \qquad j = 1, \ldots, N \,, \tag{6}$$

N is the number of basis functions (i.e., data points in space), and r_{max}, r_{min} are input parameters (Kansa, 1990b). The set of linear equations relating the expansion coefficients a_j to the set of discretized values Ψ_i, $1 \le i \le N$ is

$$\Psi_i = \sum_{j=1}^{N} G_{ij} \, a_j \,, \tag{7}$$

where $G_{i1} = 1$ and $G_{ij} = \hat{g}(\mathbf{x}_i - \mathbf{x}_j)$ for $2 \le j \le N$. The terms G_{ij} represent the ith row of the coefficient matrix $\mathbf{G}$. The first and second partial derivatives of Ψ_i with respect to x are

$$\left(\frac{\partial \Psi}{\partial x} \right) i = \sum_{j=2}^{N} \left(\frac{\partial \hat{g}_{ij}}{\partial x} \right) a_j = \sum_{j=2}^{N} \left(\frac{\partial g_{ij}}{\partial x} - \frac{\partial g_{i1}}{\partial x} \right) a_j \,, \tag{8}$$

$$\left(\frac{\partial^2 \Psi}{\partial x^2} \right) i = \sum_{j=2}^{N} \left(\frac{\partial^2 \hat{g}_{ij}}{\partial x^2} \right) a_j = \sum_{j=2}^{N} \left(\frac{\partial^2 g_{ij}}{\partial x^2} - \frac{\partial^2 g_{i1}}{\partial x^2} \right) a_j \,, \tag{9}$$

where

$$\frac{\partial^2 g_{ij}}{\partial x} = (x_i - x_j) \left[(x_i - x_j)^2 + (y_i - y_j)^2 + r_j^2 \right]^{-1/2} , \tag{10}$$

and

$$\frac{\partial^2 g_{ij}}{\partial x^2} = \left\{ 1 - \frac{(x_i - x_j)^2}{\left[(x_i - x_j)^2 + (y_i - y_j)^2 + r_j^2 \right]} \right\} \times \left[(x_i - x_j)^2 + (y_i - y_j)^2 + r_j^2 \right]^{-1/2} . \tag{11}$$

The partial derivatives with respect to y are obtained in exactly the same manner. Substitution in Eq. (2) leads to the matrix equation

$$\mathbf{W} \, \vec{a} = \vec{b} \,, \tag{12}$$

where the elements of the fully populated coefficient matrix $\mathbf{W}$ and the vector $\vec{b}$ are

$$W_{i1} = -S_0 \lambda \,,$$

$$W_{ij} = K_x \frac{\partial^2 \hat{g}_{ij}}{\partial x^2} + K_y \frac{\partial^2 \hat{g}_{ij}}{\partial y^2} - S_0 \lambda \hat{g}_{ij}, \quad \text{for } 2 \le j \le N, \tag{13}$$

$$b_j = Q / \lambda - S_0 H(0)_{ij}, \quad \text{for } 1 \le j \le N \,.$$

Step 3: The Solution in the Laplace Space

The MQ approximation of the PDE in the Laplace space results in N simultaneous equations. Since the matrix $\mathbf{W}$ is nonsingular for distinct points, the vector of the MQ expansion coefficients $\vec{a}$ is given by

$$\vec{a} = \mathbf{W}^{-1} \vec{b} \,. \tag{14}$$

The computation of $\mathbf{W}$, $\mathbf{W}^{-1}$, and $\vec{b}$ necessitates values for the Laplace parameter λ. For a desired observation time t, λ is provided by the first part of the Stehfest (1970) algorithm as

$$\lambda_v = \frac{\ln 2}{t} v \,, \qquad v = 1, \ldots, N_S \,, \tag{15}$$

where N_S is the number of summation terms in the algorithm and N_S is an even number between 6 and 20. Solution of Eq. (15) returns a set of N_S vectors of the transformed pressures $\vec{a}_v$

$$\vec{a}_v = \left[\mathbf{W}(\lambda_v)\right]^{-1} \vec{b}_v(\lambda_v), \qquad v = 1,\ldots,N_S \,. \tag{16}$$

To obtain a solution at a time t, all vectors $\vec{a}_v$, $v = 1,\ldots, N_S$ are needed, i.e., the system of simultaneous equations has to be solved N_S times.

Step 4: The Laplace Domain Predictions

Once the $\vec{a}_v$ vectors are known, the Laplace space solutions $\bar{\Psi}_v$ at the original $\mathbf{x}_j$, $j = 1,\ldots, N$ points are obtained from Eq. (7). Then the transformed dependent variable at any point $\mathbf{x}_K$ in the domain of interest is computed by direct substitution in the MQ Eq. (7).

Step 5: The Numerical Inversion of the Laplace Solution

The vector of the unknown heads $\vec{H}$ at any time t is obtained by using the Stehfest (1970) algorithm to numerically invert the Laplace solutions $\bar{\Psi}_v$, yielding

$$\vec{H}(t) = \frac{\ln 2}{t} \sum_{v=1}^{N_S} V_v \, \bar{\Psi}_v \,, \tag{17}$$

where the terms V_v are constants. The vector $\bar{\Psi}_v$ may include solutions at the original $\mathbf{x}_j$, $j = 1,\ldots, N$ points, predictions at another set of points $\mathbf{x}_K$, $k = 1,\ldots, K$, or both.

Inverting known functions, Stehfest (1970) determined the optimum $N_S = 18$ for double precision variables. However, Moridis and Reddell (1991a) determined that the performance of Laplace transform based numerical methods is practically insensitive to N_S for $6 \le N_S \le 20$.

The solution in the Laplace space removes the need for time discretization and eliminates the stability and accuracy problems caused by the treatment of the time derivative. An unlimited time step size is thus possible without any loss of accuracy. Owing to the absence of a time truncation error, LTMQ offers a stable, nonincreasing roundoff error irrespective of the time of observation t_{obs}, because a single solution (involving N_S matrix inversions) is required, with a $\Delta t = t_{obs}$. On the other hand, in a standard MQ method or any other traditional numerical method, solutions must be obtained at all the intermediate times of the discretized time domain, requiring longer execution times and continuously accumulating roundoff error in the process.

VERIFICATION AND EVALUATION

The performance of the LTMQ method was evaluated in the solution of the problem of transient flow into a homogeneous and anisotropic aquifer with a fully penetrating well and constant discharge conditions. The LTMQ solution was verified through comparison with the analytical solution (Papadopulos, 1965), as well as the solution obtained from a standard implicit FD simulator. The origin of this 2-D, infinite-acting system is placed at the well. Assuming that the axes of the Cartesian system coincide with the principal axes of the permeability tensor, the piezometric head distribution at $t = 20$ days is predicted along the $x = y$ axis, i.e., at an angle of 45° from the x axis. Only one-quarter of the infinite domain (i.e., x in $[0,\infty)$, y in $[0,\infty)$) needs to be simulated in LTMQ and FD. For the LTMQ solution, $N = 35$ and $N_S = 8$. A total of 625 gridblocks was used in the FD simulation. Figure 1 presents (1) the analytical solution, (2) the LTMQ solution, (3) the FD solutions, as well as (4) relevant information on the parameters used in this simulation. It is obvious that the LTMQ method produces an accurate solution, a fact indicated by its virtual coincidence with the analytical solution and the FD solution for a large number of small Δt's.

SUMMARY AND DISCUSSION

A new numerical method, the Laplace Transform MultiQuadrics (LTMQ) method, has been developed for the solution of the diffusion-type parabolic Partial Differential Equation (PDE) of groundwater flow through porous media. LTMQ combines a MultiQuadrics (MQ) approximation scheme for the solution of the PDE with a Laplace transform formulation for the elimination of the need for time discretization. The use of MQ in the spatial approximations allows the accurate description of problems in complex porous media with a very limited number of gridded or scattered nodes. The Laplace transform formulation eliminates the time dependency of the problem and consequently the need for time discretization. An unlimited time step size is thus possible without any loss of accuracy. In a 2-D test problem for which an analytical solution exists, an excellent agreement between the LTMQ, the FD and analytical solutions was observed. Owing to its formulation, the LTMQ method requires solution of the simultaneous equations N_S times and a linear combination of the resulting N_S solutions. Compared with a standard FD method, LTMQ requires drastically fewer (at least one order of magnitude) gridded or scattered nodes for the same level of accuracy but produces fully populated matrices (as opposed to sparse banded matrices in FD). Execution times may be reduced by orders of magnitude because solutions in the LTMQ scheme are necessary only at the desired observation times, whereas in standard numerical and MQ schemes solutions are needed at all the intermediate times of the discretized time domain.

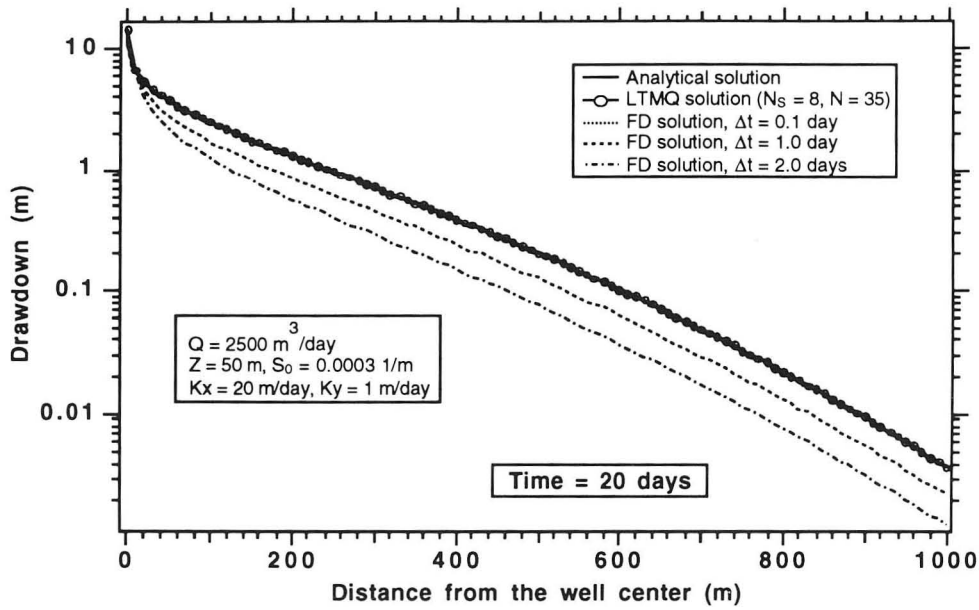

Figure 1. Comparison of the LTMQ solution to the analytical and the FD solutions along the $x = y$ axis in the test problem. [XBL 935-786]

REFERENCES

Franke, R., 1982. Scattered data interpolation: Test of some methods. Math. Comp., v. 38, p. 181–200.

Hardy, R.L., 1971. Multiquadric equations of topography and other irregular surfaces. J. Geophys. Res., v. 176, p. 1905–1915.

Kansa, E.J., 1990a. Multiquadrics—A scattered data approximation scheme with application to computational fluid dynamics—I. Computers Math. Applic., v. 19, no. 8/9, p. 127–145.

Kansa, E.J., 1990b. Multiquadrics—A scattered data approximation scheme with application to computational fluid dynamics—II. Computers Math. Applic., v. 19, no. 8/9, p. 147–161.

Micchelli, C.A., 1986. Interpolation of scattered data: Distance matrices and conditionally positive definite functions. Constr. Approx., v. 2, p. 11–22.

Madych, W.R., and Nelson, S.A., 1988. Multivariate interpolation and conditionally positive definite functions. J. Approx. Theory Applic., v. 4, p. 77–89.

Moridis, G.J., and Reddell, D.L., 1990. The Laplace Transform Finite Difference (LTFD) numerical method for the simulation of solute transport in groundwater. EOS: Trans. Am. Geophys. Union, v. 71, no. 43, p. 1336.

Moridis. G.J., and Reddell, D.L., 1991a. The Laplace Transform Finite Difference (LTFD) method for simulation of flow through porous media. Water Resour. Res., v. 27, no. 8, p. 1873–1884.

Moridis. G.J., and Reddell, D.L., 1991b. The Laplace Transform Finite Element (LTFE) numerical method for the solution of the groundwater equation. EOS: Trans. Am. Geophys. Union, v. 72, no. 17, p. 112.

Moridis. G.J., and Reddell, D.L., 1991c. The Laplace Transform Boundary Element (LTBE) numerical method for the solution of diffusion-type equations. Boundary Elements XIII, London: Computational Mechanics Publications and Elsevier Applied Sciences, p. 83–97.

Papadopulos, I.S., 1965. Nonsteady flow to a well in an infinite anisotropic aquifer. Presented at the 6th Symposium, International Association Sci. Hydrology, Dubrovnik.

Stehfest, H., 1970. Numerical inversion of Laplace transforms. Alg. 368, J. ACM, v. 13, no. 1, p. 47–49.

The Transformational Decomposition (TD) Method for Compressible Fluid Flow Simulations

*G. J. Moridis and D. A. McVay**

In transient flow through porous media, the Partial Differential Equation (PDE) to be solved is

$$\nabla \cdot (k \nabla p) = C_T \frac{\partial p}{\partial t} + q \,, \tag{1}$$

where p is the pressure, k is the permeability, q is the source or sink flow rate, t is the time, $C_T = \phi \mu C_L$, ϕ is the porosity, and μ and C_L are the fluid viscosity and compressibility, respectively. Equation (1) is solved numerically in all but the simplest problems. The basic concept of any numerical method is the substitution of a set of algebraic equations for the original PDE. Instead of solving for the continuous smooth function $p(x,y,z,t)$, the space domain (x,y,z) is subdivided into N_D subdomains, and the time t is discretized in N_T time steps; N_T sets of approximations $\tilde{p}$ of the solution are obtained at the N_D predetermined points in space.

Despite their power and flexibility, numerical solutions have some serious drawbacks. Minimization of the error introduced by the numerical approximation of the spatial derivatives in the PDEs dictates the discretization of the space domain into a large number of subdomains at all of which solutions must be obtained (whether desired or not). This increases the execution time requirements and requires a large amount of computer memory. Accuracy and stability considerations necessitate a large number of small time steps between observation times; solutions must be obtained at all these intermediate times, increasing the execution times and the roundoff errors.

The Transformational Decomposition (TD) method is a new method that addresses the shortcomings of traditional numerical techniques. The major advantage of the TD method is that it requires no time discretization and a very coarse space discretization to yield an accurate, stable solution that is semianalytical in time and analytical in space.

THE TD METHOD

There are two stages in the TD method, the Decomposition stage and the Reconstitution stage. In the Decomposition stage, the original PDE is decomposed by using successive levels of integral transforms. The first step in this stage involves the application of the Laplace transform to eliminate the time dependency of the original PDE. The resulting equation is then subjected to successive Finite Cosine Transforms (FCT).

Each level of FCT eliminates one active dimension until single-point equations remain. The original PDE is thus decomposed into much simpler point algebraic equations, for which solutions are obtained in the transformed space. In the Reconstitution stage, solutions in space and time are obtained by applying successive levels of inverse transforms. The development of the TD method in one dimension presented here neglects gravity and considers ϕ a constant. The application of the TD method to multidimensional systems with gravity and pressure-dependent ϕ's can be found in Moridis and McVay (1993).

Step 1: The Laplace Transform of the PDE

The boundary conditions in the 1-D problem depicted in Figure 1 are

$$\begin{aligned} &p'(x=0) = p'(x_1 = 0) = u_0 = 0, \\ &p'(x = X_{\max}) = p'(x_3 = X_3) = u_3 = 0, \end{aligned} \tag{2}$$

indicating no flow at the outermost boundaries, and

$$p_i'(x_1 = X_1) = u_1(t), \quad p_i'(x_2 = X_2) = u_2(t), \tag{3}$$

which describe internal boundaries that are unknown functions of time. The subscripted x_i ($i \equiv 1, 2, 3$) denote local coordinates; the global coordinates have no subscripts.

The Laplace transform of Eq. (1) in the ith ($i = 1, 2, 3$) locally homogeneous subdomain of the 1-D problem yields

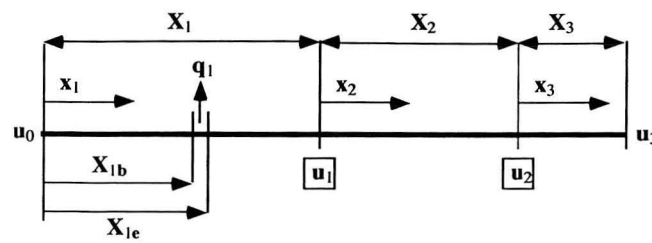

Figure 1. The TD method in one dimension. The quantities in the boxes indicate the unknown internal boundaries. [XBL 935-787]

* S.A. Holditch and Associates, College Station, Texas.

$$k_i \frac{d^2\Psi_i}{dx_i^2} - C_T s\Psi_i = -C_T p_i(0) + \ddot{q}_i, \tag{4}$$

where s is the Laplace parameter, $p(0)$ is the distribution of p at $t = 0$, $\Psi = L\{p\}$, $\ddot{q} = L\{q\}$, and $L\{\ \}$ denotes the Laplace transform of the quantity in the brackets. Equation (4) is subject to the boundary conditions

$$\Psi_1'(x_1 = 0) = U_0 = 0, \quad \Psi_3'(x_3 = X_3) = U_3 = 0, \tag{5}$$

$$\begin{aligned} &\Psi_1'(x_1 = X_1) = U_1, \quad \Psi_2'(x_2 = 0) = \varepsilon_1 U_1, \\ &\Psi_2'(x_2 = X_2) = U_2, \quad \Psi_3'(x_3 = 0) = \varepsilon_2 U_2, \end{aligned} \tag{6}$$

where $\Psi_i' = L\{p_i' = dp_i/dx_i\}$, $U_\ell = L\{u_\ell(t)\}$ $(\ell = 0,\ldots,3)$, and $\varepsilon_i = k_i/k_{i+1}$.. These boundary conditions incorporate the tangent law at the boundaries (continuity of fluxes).

Step 2: The Finite Integral Transform

The FCT of Eq. (4) yields

$$k_i\left[-\frac{n^2\pi^2}{X_i^2}\Theta_i + (-1)^n\Psi_{iX}' - \Psi_{i0}'\right] - C_T s\Theta_i = -C_T\hat{p}_i(0) + \hat{q}_i, \tag{7}$$

where

$$\Theta_i(s,n) = \mathcal{F}_c\{\Psi_i\} = \int_0^{x_i} \Psi_i \cos\left(\frac{n\pi x_i}{X_i}\right) dx_i, \tag{8}$$

$\hat{p}_i(0) = \mathcal{F}_c\{p_i(0)\}$, $\hat{q}_i = \mathcal{F}_c\{\ddot{q}_i\}$, $\Psi_{i0}' = \Psi_i'(x_i = 0)$, $\Psi_{iX}' = \Psi_i'(x_i = X_i)$, and $\mathcal{F}_c\{\}$ denotes the FCT of the quantity in brackets. Note that $p_i(0)$ need not be a constant; any known function of x_i for which an FCT exists is acceptable. As for the source/sink term $\hat{q}_i$, if $\tilde{q} \neq 0$ for $X_{ib} \le x_i \le X_{ie}$ (see Figure 1), then

$$\hat{q}_i = \begin{cases} \dfrac{\ddot{q}X_i}{n\pi}\left[\sin\left(\dfrac{n\pi X_{ie}}{X_i}\right) - \sin\left(\dfrac{n\pi X_{ib}}{X_i}\right)\right] & n > 0 \\ \ddot{q}(X_{ie} - X_{ib}) & n = 0, \end{cases} \tag{9}$$

The flexibility that Eq. (9) affords is obvious, as it allows the positioning of wells anywhere in the subdomains. Equation (7) then yields

$$\Theta_i = \alpha_i\Psi_{i,BO}' + b_i\Psi_{i,BX}' + c_i, \tag{10}$$

where

$$a_i(s,n) = \frac{-r_i^2}{n^2 + \omega_i^2}, \quad b_i(s,n) = (-1)^{n+1}a_i, \tag{11}$$

$$c_i = c_i(s,n) = \frac{\omega_i^2}{n^2 + \omega_i^2}\frac{\hat{r}_i(0)}{s} - \frac{\hat{q}_i}{\lambda_i}\frac{\tau_i^2}{n^2 + \omega_i^2}, \tag{12}$$

and

$$\tau_i = \frac{X_i}{\pi}, \quad \omega_i = \tau_i\sigma_i, \quad \sigma_i = \sqrt{\frac{C_T s}{\lambda_i}}. \tag{13}$$

Equation (10) is a simple, single-point algebraic equation, and represents the decomposed form of the original 1-D PDE. If both $\Psi_{i,B0}'$ and $\Psi_{i,BX}'$ are known (as in the case of a homogeneous system), the decomposition stage ends here.

Step 3: The Internal Boundary Conditions

In heterogeneous systems with multiple subdomains, the internal boundary conditions must be determined next. The pressures being equal on both sides of the boundary between subdomains 1 and 2 in Figure 1, $\Psi_1(x_1 = X_1) = \Psi_2(x_2 = 0)$. Applying the inverse FCT on the governing equations in the two subdomains gives

$$\begin{aligned} &\frac{1}{X_i}\Theta_1(s,0) + \frac{2}{X_1}\sum_{n=1}^{\infty}\Theta_1(s,n)\cos\left(\frac{n\pi X_1}{X_i}\right) \\ &= \frac{1}{X_i}\Theta_2(s,0) + \frac{2}{X_2}\sum_{n=1}^{\infty}\Theta_2(s,n)\cos\left(\frac{n\pi 0}{X_2}\right), \end{aligned} \tag{14}$$

from which we obtain the boundary equation

$$F_1U_0 + G_1U_1 + H_1U_2 = R_1.$$

Closed forms for F, G, H, and R are obtained as

$$F_1 = -\frac{1}{\sigma_1 \sinh(\pi\omega_1)},$$

$$G_1 = \frac{1}{\sigma_1 \tanh(\pi\omega_1)} + \frac{\varepsilon_1}{\sigma 2 \tanh(\pi\omega_2)},$$

$$H_1 = -\frac{1}{\sigma_2 \sinh(\pi\omega_2)},$$

$$R_1 = \frac{r_{2c} - r_{1c}}{s}$$

$$-\frac{\ddot{q}_2}{\lambda_2}\frac{1}{\sigma_2^2}\left[\frac{\sinh(\omega_2\pi - \sigma_2 X_{2b}) - \sinh(\omega_2\pi - \sigma_2 X_{2e})}{\sinh(\omega_2\pi)}\right]$$

$$+\frac{\ddot{q}_1}{\lambda_1}\frac{1}{\sigma_1^2}\left[\frac{\sinh(\sigma_1 X_{1e}) - \sinh(\sigma_1 X_{1b})}{\sinh(\omega_1\pi)}\right]. \qquad (19)$$

An analogous equation is obtained from subdomains 2 and 3. For any subdomain i other than the first, the numerator of F_i must be changed to ε_{i-1}. Since $U_0 = U_3 = 0$, the unknown U_1 and U_2 are readily obtained from the two boundary equations. In general, if there are N subdomains with locally homogeneous properties; these define $N + 1$ boundaries of which two (the outermost) are known, and the remaining $N_B = N - 1$ are the internal unknown boundaries. Writing the resulting N_B simultaneous equations in a matrix notation, we have

$$\mathbf{M}_v \vec{U}_v = \vec{R}v \quad \text{and} \quad \vec{U}_v = \mathbf{M}_v^{-1}\vec{R}_v, \qquad (20)$$

where $\mathbf{M}$ is the coefficient matrix, $\vec{R}$ is the "known" right-hand side vector, and $\vec{U}$ is the vector of the unknown conditions $U = L\{\Psi'\}$ at the internal boundaries. Values for the Laplace parameter s for an observation time t are provided by the Stehfest (1970) algorithm as $s_v = (\ln 2/t)v, v = 1,\ldots,N_S$. Optimum values for N_S were discussed by Moridis et al. (1991). Steps 1 through 3 represent the Decomposition stage. The Reconstitution stage is described in Steps 4 and 5.

Step 4: The Laplace Domain Solution

Once the $\vec{U}_v$ becomes known, then the Ψ_v at any point x_ℓ within a subdomain i with boundaries U_ξ and $U_{\xi+1}$ is given by the inverse FCT as

$$\Psi_i(s_v, x_\ell) = a_{iT}U_\xi(v) + b_{iT}U_{\xi+1}(v) + c_{iT}, \qquad (21)$$

where

$$a_{iT} = \varepsilon_{i-1}F_1 \cosh(\omega_i\pi - \sigma_i x_\ell), \qquad (22)$$

$$b_{iT} = -F_1 \cosh(\sigma_i x_\ell), \qquad (23)$$

$$c_{iT} = \frac{\ddot{q}_i}{2\lambda_i}\frac{1}{\sigma_i^2}\left\{\frac{\sinh[\omega_i\pi - \sigma_i(X_{ie} + x_\ell)]}{\sinh(\omega_i\pi)}\right.$$

$$+\frac{\sinh[\omega_i\pi - \sigma_i(X_{ie} + x_\ell)]}{\sinh(\omega_i\pi)}$$

$$-\frac{\sinh[\omega_i\pi - \sigma_i(X_{ib} + x_\ell)]}{\sinh(\omega_i\pi)}$$

$$\left.-\frac{\sinh[\omega_i\pi - \sigma_i(X_{ib} + x_\ell)]}{\sinh(\omega_i\pi)}\right\} + \frac{r_{ic}}{s}. \qquad (24)$$

Step 5: The Solution at Time t

To obtain a solution at a time t at a number of desired points x_ℓ, all vectors $\vec{\Psi}_v, v = 1,\ldots,N_S$ are needed. Using the Stehfest algorithm, the unknown vector $\vec{p}$ at time t is computed as

$$\vec{p}(t) = \frac{\ln 2}{t}\sum_{v=1}^{N_S} W_v \cdot \vec{\Psi}_v, \qquad (25)$$

where the terms W_v are constant. Because of its formulation, the TD method provides semianalytical solutions that are fully differentiable and integrable; continuous velocity fields are thus easily determined, and mass balance calculations over the subdomains are simple.

VERIFICATION

The test problem used for verification involves flow to a well located at a vertical fracture of length L (perpendicular to the x axis) and depth h in a rectangular (1-D) reservoir. The TD solution is compared with FD solutions, as well as with the analytical solution given by

$$p_D = L^{-1}\{\Psi_D\}, \quad \Psi_D = H_1 + H_2, \tag{26}$$

where

$$H_1 = \frac{\exp\left(-x_D\sqrt{s}\right)}{s^{1.5}\left[1-\exp\left(-2X_D\sqrt{s}\right)\right]}, \tag{27}$$

$$H_2 = \frac{\exp\left[\left(x_D - 2X_D\right)\sqrt{s}\right]}{s^{1.5}\left[1-\exp\left(-2X_D\sqrt{s}\right)\right]}, \tag{28}$$

$p_D = (p_i - p)\left(k\sqrt{A}/q\mu\right)$, $t_D = \left(kt/A\phi\mu C_L\right)$, and $x_D = \left(x/\sqrt{A}\right)$. Here X is the length of the reservoir, and $A = L \times h$.

Two subproblems are investigated. In Problem 1a we obtain the TD solution using the equation for a single homogeneous domain (as specified). In Problem 1b we test the performance of the TD concept by subdividing the domain (5000 ft) into two subdomains (300 and 4200 ft) and comparing the solution with the one from Problem 1a. The two TD solutions are virtually identical, differing in the 8th or 9th decimal place. This confirmed the validity of the concept. All results correspond to both subproblems and are presented together.

Figure 2 shows the TD solutions at a number of times. The measure of the accuracy of the TD method is given by Figure 3, which compares the TD results with the analytical solution. The observed deviations are extremely small, and the TD method is shown to be practically insensitive to the size of the time increment (thus allowing an unlimited time step).

Figure 4 compares the TD solution at $t_D = 1000$ (i.e., using a time step size of 533.35 days) with the FD solutions obtained for various space discretizations. To minimize the contribution of time-related truncation error to the FD solutions, a very fine time discretization is used, requiring 543 time steps and 1117 matrix inversions. With an increasingly fine space discretization, the FD solutions approach the TD solution. The superiority of the TD is obvious, as it is capable of delivering a more accurate solution with a single (or none at all) algebraic equation (which has to be solved N_S times) than an FD scheme, which needs to invert 1117 times a matrix of order 111. This reduces the computational effort by orders of magnitude.

In Figure 5 the TD method is compared with FD solutions with increasingly fine time discretizations. To minimize the effects of space-related truncation errors, a

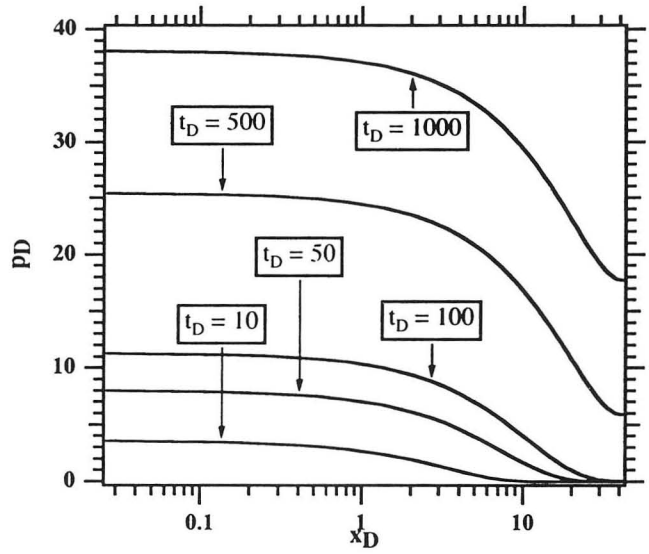

Figure 2. The TD solutions of p_D for various t_D's. [XBL 935-788]

fine space discretization (111 gridblocks) is used. A pattern similar to the one observed in Figure 4 is evident: with an increasingly fine time discretization, the FD solutions tend toward the analytical solutions and the TD solutions, further attesting to the power of the method. The TD solution exhibits a very small deviation from the analytical solution and is consistently superior to the FD solution. The superiority of TD persisted even when a very fine time discretization (263 time steps, and a total of 541 matrix

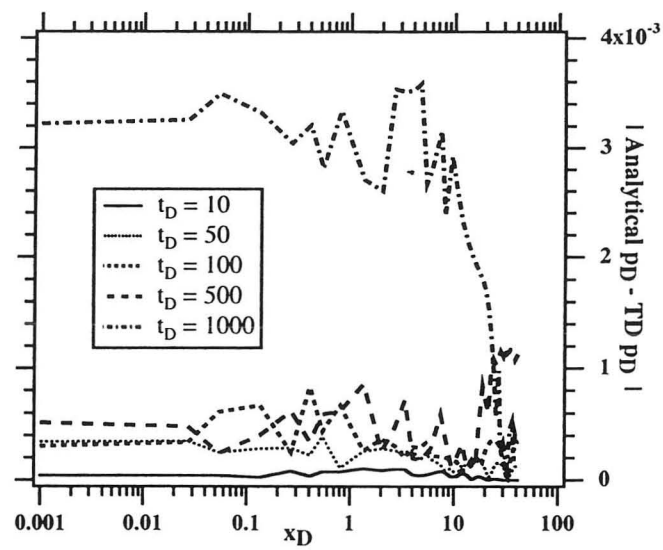

Figure 3. Absolute differences between the TD and the analytical solutions. [XBL 935-789]

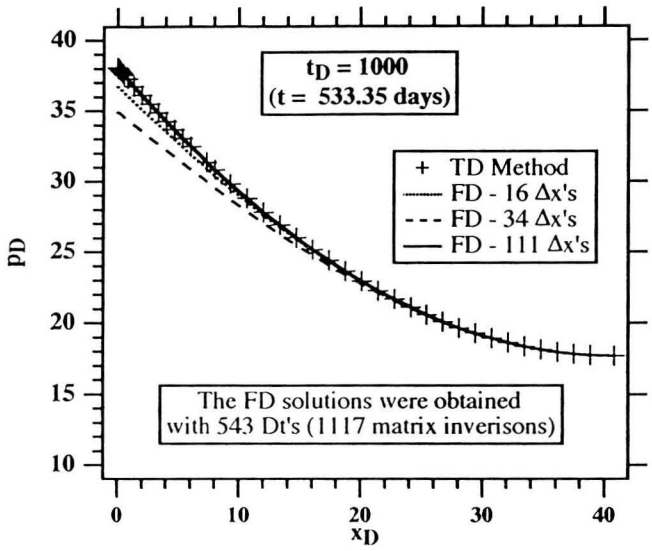

Figure 4. Comparison of the TD with the FD solution for various space discretizations. [XBL 935-790]

solutions) was used in the FD simulation. The corresponding TD computational effort to achieve this level of accuracy is essentially trivial: either direct substitution into Eqs. (22) through (24) at the desired time and location or (in the case of the two subdomains of subproblem 1b) solution of the single-point algebraic equation (20) N_S times, followed by the direct substitution.

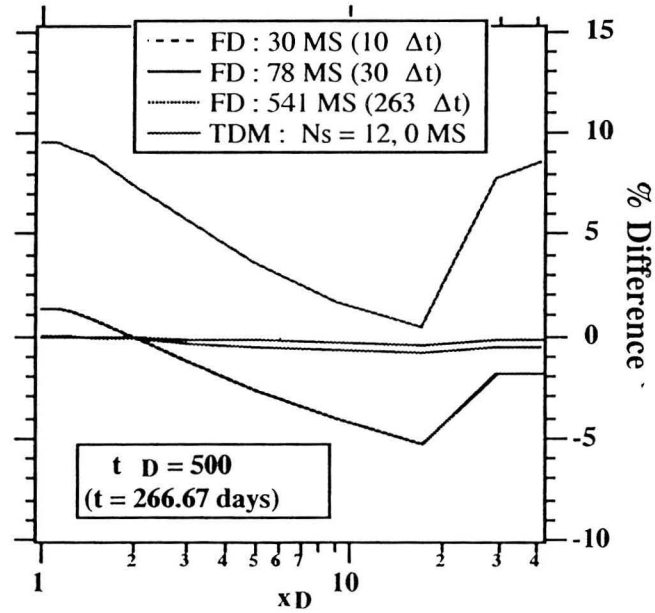

Figure 5. Comparison of the TD solution with the FD solutions for various time discretizations. [XBL 935-791]

CONCLUSIONS

A new numerical method, the Transformational Decomposition (TD) method, was developed for the solution of the nonlinear, parabolic Partial Differential Equation (PDE) of transient, slightly compressible, single-phase liquid flow through porous media. Because TD uses a Laplace transform formulation, it eliminates the need for time discretization and allows an unlimited time step size without loss of stability or accuracy. By using Finite Cosine Transforms, the method drastically reduces the need for space discretization, requiring only a small number of large subdomains for an accurate solution. The TD method provides semianalytical solutions in space and time by decomposing the original PDE into a small number of algebraic equations and by equating and solving for conditions at internal boundaries. These solutions are fully differentiable and integrable, allowing the determination of continuous velocity maps and easy mass balance calculations.

With finer space and time discretizations, the FD solutions tend to the TD solution. The TD method provides a solution generally more accurate than the FD solution. This was expected because the elimination of the traditional time and space discretizations limit the truncation error.

The TD method may significantly reduce the computer memory requirements because discretization in time is not needed and a very coarse grid suffices for the space discretization. Execution times may be substantially reduced because smaller matrices are inverted in the TD method, and solutions are obtained at the desired points in space and time only, whereas in standard numerical methods solutions are necessary at all of the points of the discretized time and space domains.

REFERENCES

Moridis, G.J., and McVay, D.A., 1993. The Transformational Decomposition (TD) method for compressible fluid flow simulations. Paper SPE 25264 presented at the SPE 12th Reservoir Simulation Symposium, New Orleans, Louisiana, February 28–March 3, 1993.

Moridis, G.J., McVay, D.A., Reddell, D.L., and Blasingame, T.A., 1991. The Laplace Transform Finite Difference (LTFD) numerical method for simulation of compressible fluid flow in reservoirs. Paper SPE 22888 presented at the 1991 66th Annual Technical Conference and Exhibition, Dallas, Texas, October 6–9, 1991.

Stehfest, H., 1970. Numerical inversion of Laplace transforms. Com. of the ACM, v. 13, no. 1, Algorithm 368, p. 47–49.

Solution of Bench-Mark and Test-Case Problems Proposed by the DECOVALEX International Project

J. Noorishad and C. F. Tsang

In 1990 an international cooperative project was formed, spearheaded by the Swedish Nuclear Power Inspectorate (SKI) and Lawrence Berkeley Laboratory (LBL), for the development of coupled models and their validation against experiments in nuclear waste isolation. This project, called DECOVALEX (DEvelopment of COupled models and their VALidation against EXperiments), was initiated by a proposal to the participating organizations that a number of bench-mark tests and a test case be approved for modeling. The LBL team decided on the modeling of the bench-mark test 2 and test-case 1 problems, which will be discussed here (for details, see Noorishad and Tsang, 1992).

THE SIMULATOR

The proposed modelings involve the solution of coupled thermal-hydraulic-mechanical phenomena in the conceptualized domain of the problems. The existence of nonlinearity features requires process linearization, often in the context of an incremental loading. Large differences in the time constants of the heat flow and fluid flow problems add to the complexity of the solution scheme. LBL's ROCMAS code, developed to cope with such requirements, is used in our simulation efforts.

Bench-Mark Test 2 (BMT2)

In this problem, the subject of analysis is the thermohydromechanical behavior of a 0.5 m × 0.75 m block of hard rock intersected by four fractures. Figure 1 demonstrates the geometry and the initial and boundary conditions of the problem. The block is heated at part of the left-hand face of the block by a source with a strength of 60 W/m^2.

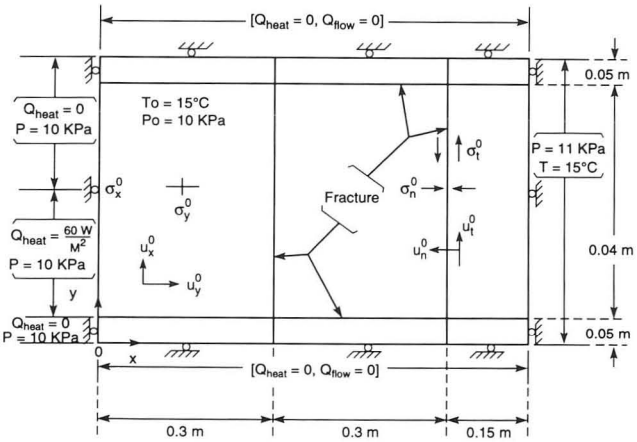

Figure 1. BMT2 model (geometry and initial and boundary conditions). [XBL 927-5735]

A linear elastic material model for the continuum and a trilinear compression and ideal elastoplastic model for the joint are used in the BMT2 model. We used two geometric discretizations for the solution. The first mesh included 252 elements and 285 nodes, and the second mesh included 1996 elements and 2091 nodes. The coarse mesh was used for the initial setup of the problem, and its very short solution turnaround time proved very useful. The refined mesh was strategically designed to reduce the truncation errors with regard to the diffusive aspects of fluid flow and heat flow. However, refinements of this order or higher cannot remedy the difficulties in solving problems that involve high Peclet and Courant numbers. Simple calculations for BMT2 showed fracture fluid velocities on the order of 10^{-2} m/sec, leading to very high grid Courant and Peclet numbers for both meshes. To overcome the expected solution difficulties of the BMT2 when flow in the fractures is considered, we employed the recent upwinding criteria suggested by Noorishad et al. (1992). The solution of the BMT2 on the refined mesh is used as the final result and as a measure of discretization sensitivity for the problem.

Solution Strategy

Another important aspect of the BMT2 solution attempt was in the selection of the solution strategy. An implicit solution of a Thermo-Hydro-Mechanical (THM) problem may require exuberant CPU times, from hours to days. However, by considering order-of-magnitude differences in the time constants of the fluid flow and heat flow evolutions, the thermal calculations (T) can be decoupled from the hydromechanical (HM) calculations. In this setup, transient calculations of the HM problem can be replaced with steady-state (snapshot) solutions at each step of the transient calculations of the heat equation. Thus the calculation load is reduced by using a fast time-marching approach to obtain the thermal solution. The solution of BMT2 began with 10^3 sec as the first time increment and was geometrically time-marched to the final total time of 10^7 sec.

Results

We obtained two alternative solutions for the BMT2. In the first solution, heat convection in the problem was neglected. The results provide a critical basis for cross-code verification. In this attempt, a maximum temperature of 21°C was obtained at the mid-point location of the source at 10^7 sec. The system was stabilized at this time as well. Figures 2 to 4 show the resulting temperatures at

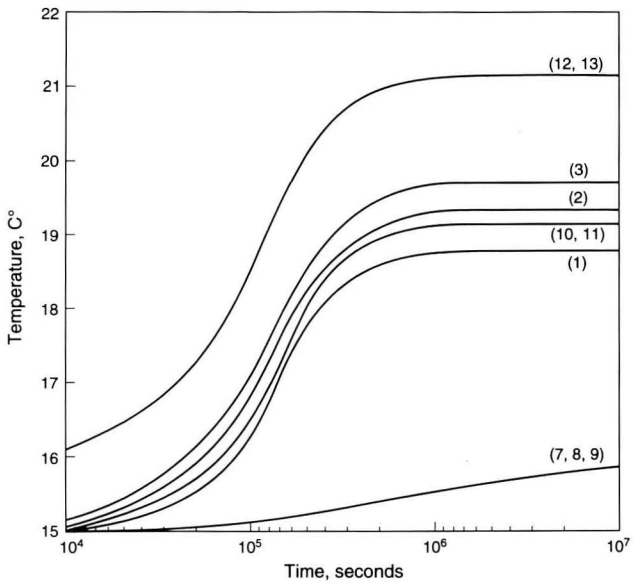

Figure 2. Temperature vs. time at various points in the mesh. [XBL 927-5744]

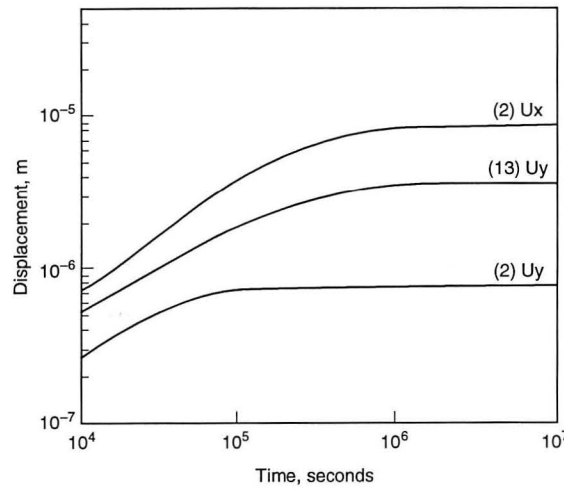

Figure 3. Displacement vs. time at various points. [XBL 927-5736]

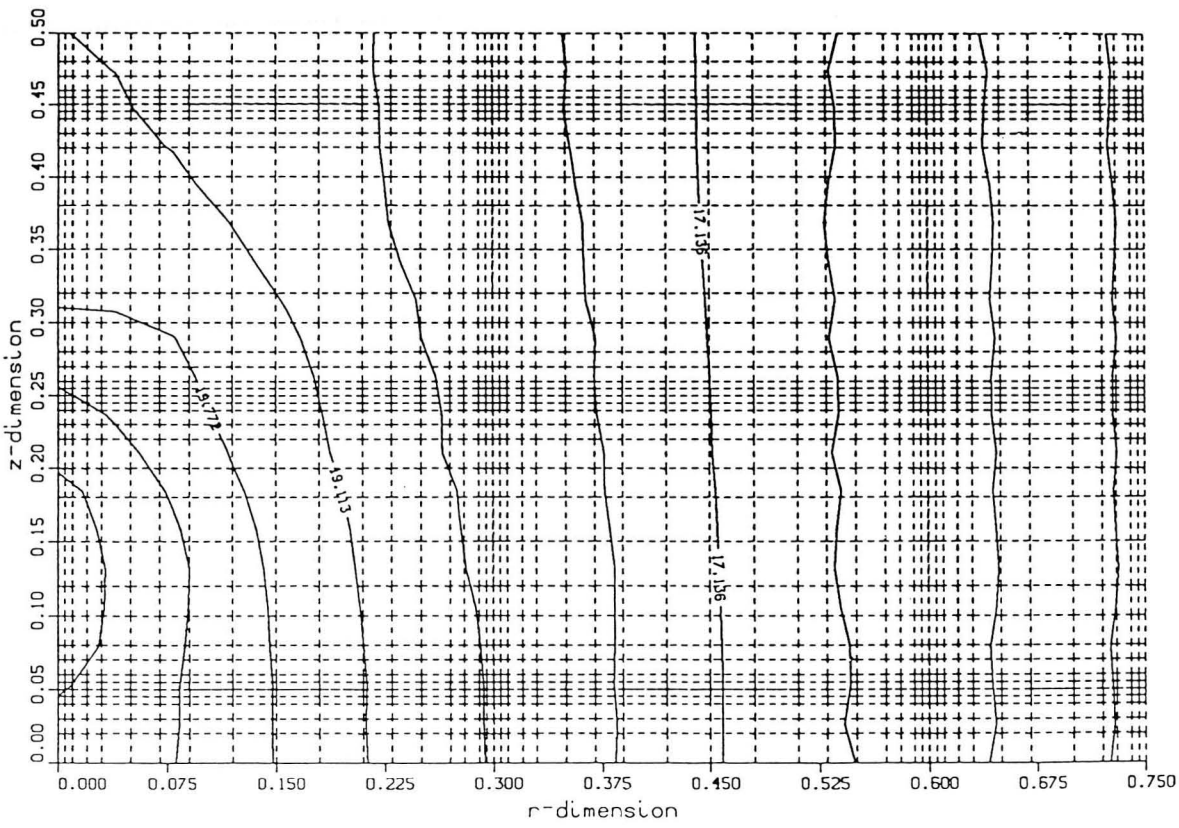

Figure 4. Temperature contours at 10^7 sec (no-convection case). [XBL 936-923]

discrete points in the mesh and provide temperature contours throughout the mesh. In the second solution, we allowed for convection in the domain. Because of the very low permeability of the continuum, fractures played the dominant role. As expected, special upstreaming (Noorishad et al., 1992) was required. With the exception of a small amount of oscillation (< 0.5°C) at 10^5 sec, the evolution of the temperature throughout the mesh was obtained as depicted in Figure 5. Comparison of the two solutions—one with and one without convection in the fractures—shows that the differences are dramatic. In the former, the cooling effect of the flow in the joints confined the heating of the rock to an area with a characteristic size almost equal to the source dimension. Using the coarse mesh, we also obtained a solution for the case with convection. Comparisons with the refined mesh results are fairly good for all of the output data.

TEST CASE 1 (TC1)

The TC1 is based on a conceptualization of the shear test in a fractured rock core, as reported in the SKB report 90-07 (Makurat et al., 1990). A fluid flow gradient is maintained during the test. Figure 6a depicts the problem configuration. Because of the low fracture fluid pressure in the test, the analysis essentially requires only mechanical simulation. However, the HM version of the ROCMAS code is utilized to do the mechanical analysis. The code also updates the fluid flow conditions in the joint as a result of the fracture closure during loading. Figure 6b shows the loading conceptualization of the test for the simulation.

Expecting various solution difficulties at the early stages of simulations of this nature, we decided to simplify the model by eliminating the steel bracket and hence the epoxy-steel contact at the boundary. Moreover, because of the complex geometry of the model, we used a nonstrategic design to generate a finite element mesh consisting of 530 four-nodal-point isoparametric elements and a total of 566 nodes. Figure 7 shows the mesh with material numbers in each element designating the epoxy (1), the rock (2), the rock joint (3), and the epoxy-epoxy contact (4). The joints are represented by a thin row of four-nodal-point joint elements that are not shown in the figure. The epoxy is assumed to be linear elastic and the epoxy-epoxy contact is a frictionless low-shear-resistant material with linear behavior in compression. The rock joint emulated a Barton-Bandis model.

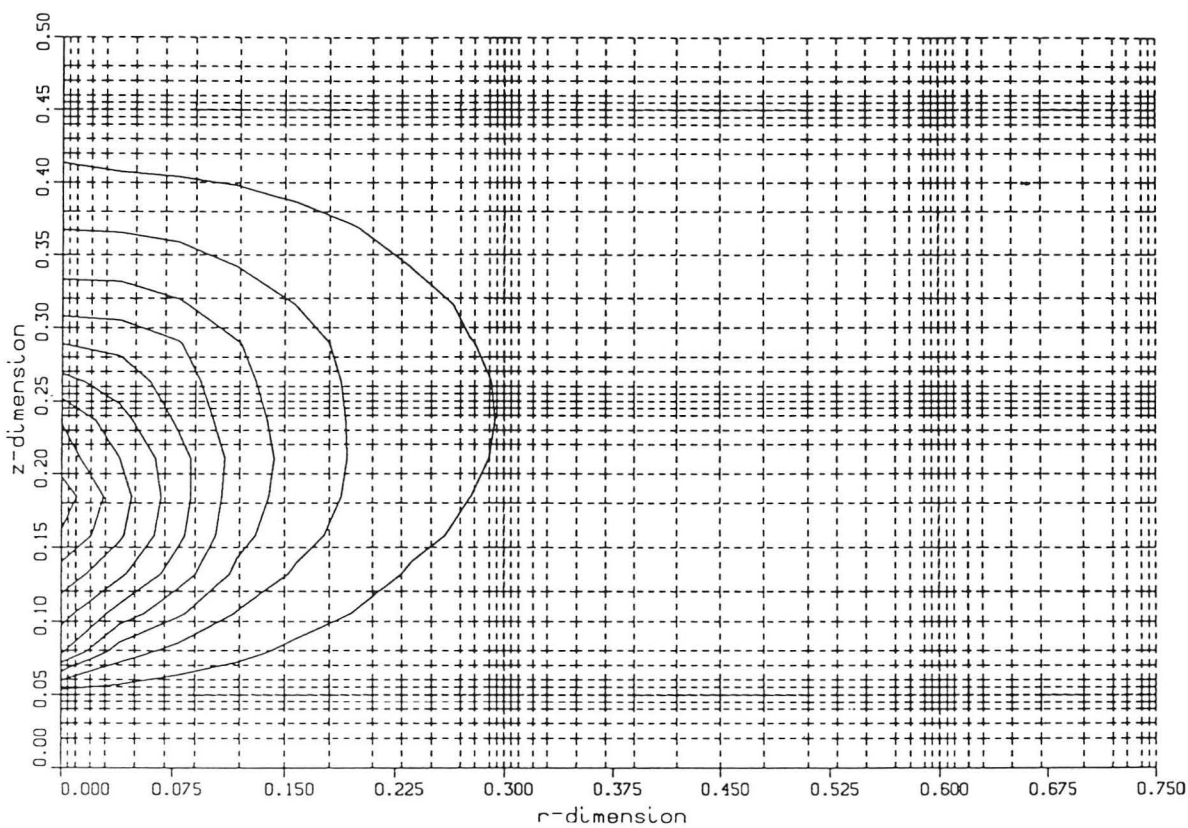

Figure 5. Temperature contours at 10^7 sec (convection case). [XBL 936-924]

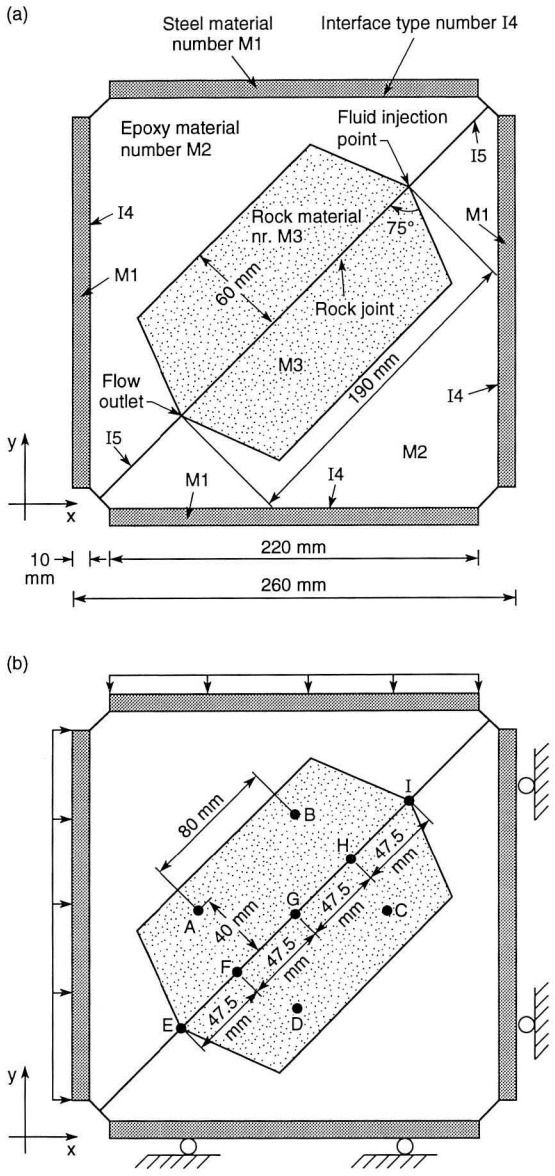

Figure 6. (**a**) TC1 model geometry and initial and boundary conditions. (**b**) TC1 loading scheme and observation points. [XBL 927-5737]

The two loading sequences—i.e., the hydrostatic loading sequence (A) and the constant displacement shear sequence (B)—were both simulated. Sequence A was performed by 5-MPa-step loading and unloading from 0 to 25 MPa and from 25 to 0 MPa. Sequence B was performed first by 5-MPa-step loading until a 25-MPa hydrostatic loading was achieved. Then, by assigning incremental displacements of +0.5, +0.3, +1.2, 2.0, –2.0, and –2.0 mm, along the fracture direction at the upper boundary (while the hydrostatic load was maintained), shearing was induced in pre- and post-failure modes at the fracture.

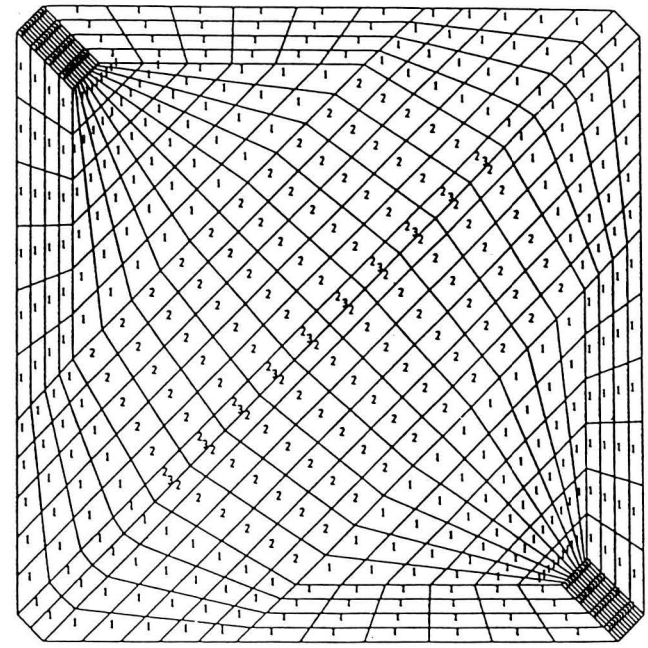

Figure 7. Finite element mesh for TC1. [XBL 936-925]

Results

Sequence A. The results of the analysis are presented in accord with the general format requested by DECOVALEX. Figure 8 shows the distribution of the average normal stress across the joint versus the average normal deformation between points A and D and B and C. As evidenced also by Figures 9 and 10, the behavior in sequence A (hydrostatic loading and unloading) is non-hysteretic, with the exception of some deviation for flow, which is expected as a result of cubic dependence on aperture.

Sequence B. The behavior in this sequence was affected markedly by two shortcomings of our model. First, the absence of the steel brackets, and hence the inability for forcing of a better distribution of the boundary loads, led to a very high concentration of stresses at the core edges. Second, this effect was further aggravated by the lack of strategic refinements of the mesh at locations on the core edges. Figure 11 demonstrates the very uneven normal stresses at the joint, which reaches a maximum at the edge. As a result, the ensuing high strength of the joint at these critical locations inhibited shear failure. The broken curve in Figure 12 exhibits the elastic behavior of the joint in forward and reverse loading.

Vivid demonstrations of the aforementioned reasons for the lack of proper performance of the model in the shear mode was attained by two small modifications of the model. In the first attempt, the epoxy was given the material property of rock while maintaining the weak epoxy-

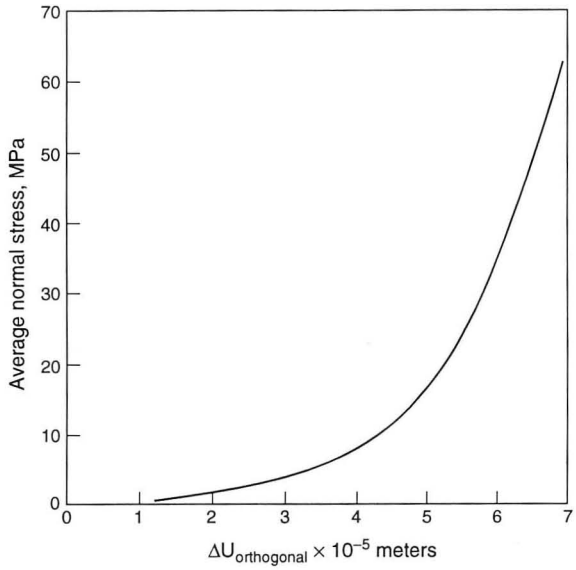

Figure 8. Average normal stress vs. average normal joint displacement. [XBL 927-5738]

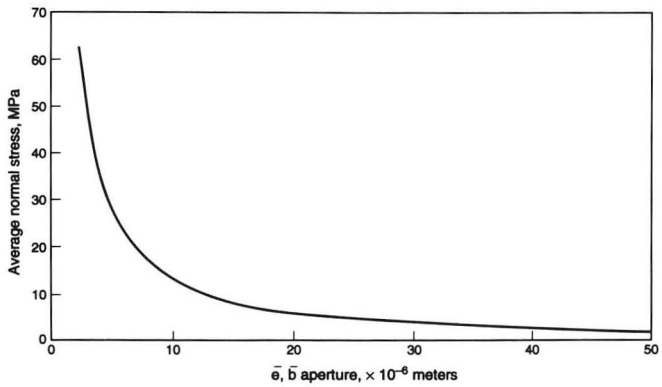

Figure 9. Average normal stress vs. average joint aperture. [XBL 927-5739]

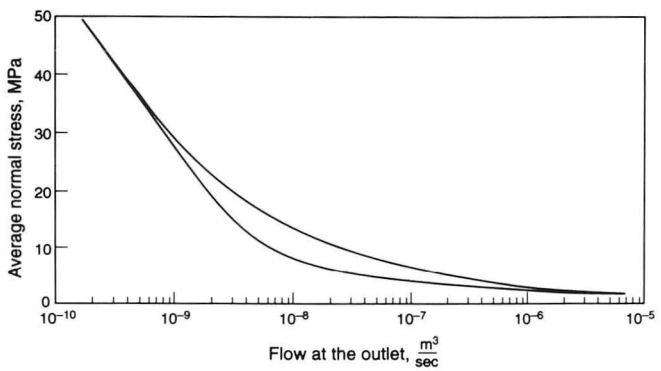

Figure 10. Average normal stress vs. outlet flow. [XBL 927-5740]

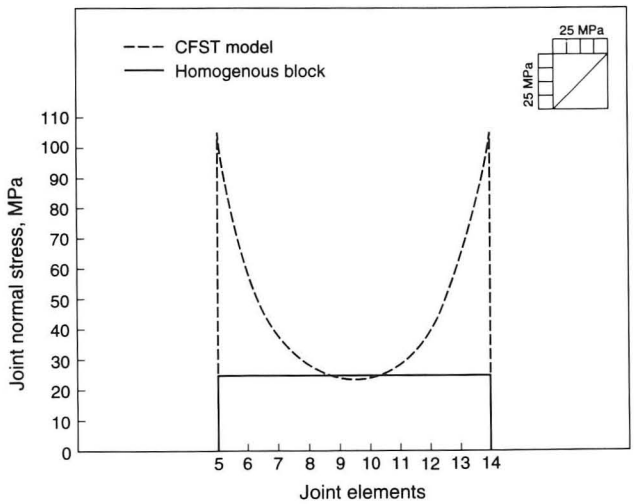

Figure 11. Joint normal stresses along the fracture. [XBL 927-5741]

epoxy contact as before. The results for this model in forward and reverse shearing are shown by the solid curve in Figure 12. The behavior is obviously more classic, with the exception of a measure of hardening caused by high stress concentration at the rock edge, where the rock joint meets the epoxy-epoxy joint. In the second attempt, the rock and the epoxy were given incompressible properties, thus eliminating the deficiencies resulting from load distribution and mesh configurations. The results of this run provide the perfect classic response shown in Figure 13.

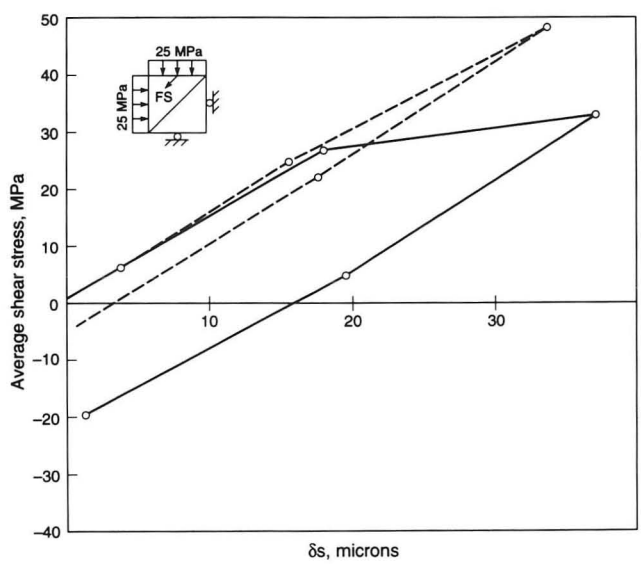

Figure 12. Average shear stress vs. average shear displacement along the joint—nonhomogeneous and homogeneous cases. [XBL 924-5745]

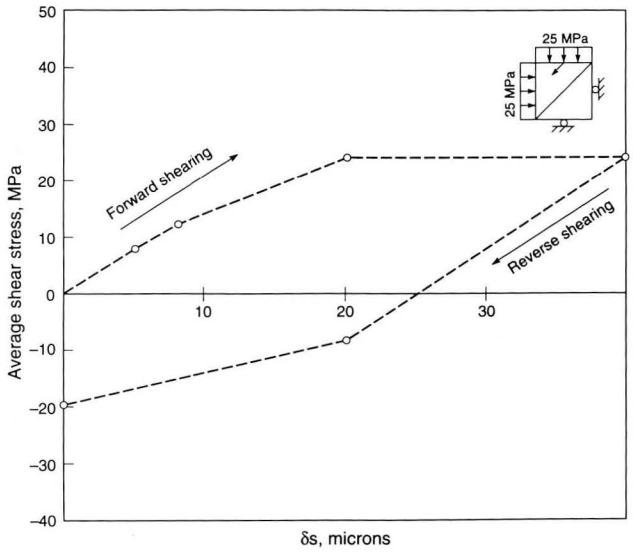

Figure 13. Average shear stress vs. average shear displacement along the joint—incompressible rock and epoxy. [XBL 924-5746]

DISCUSSION

BMT2 Problem. Because of the low strength of the heat source, only minimal HM effects on the fractures were observed. Dealing with the high-velocity heat convection proved to be the challenging part of the problem design. As a result of the cooling effects of the fracture fluid flow, heating was confined to a small part of the block. As a result, this problem served only to test the HT aspects of the THM capability.

TC1 Problem. Proper conceptualization of the test and strategically designed finite element idealization proved to be the main challenges posed by this problem. Elimination of the steel bracket from our model created very high concentrations of stress at the fracture edges. As a result, shearing became impossible. The underlying reasons became more clear when the model was altered. Prior thinking and discussion of the physics of the test should become part of the problem design for more realistic modeling.

REFERENCES

Makurat, A., Barton, N., Vik, G., and Tunbridge, L., 1990. Site characterization and validation-coupled stress-flow testing of mineralized joints of 200 mm and 1400 mm length in the laboratory and in situ, Stage 3. Swedish Nuclear Fuel and Waste Management Co., Stripa Project Report 90-07.

Noorishad, J., and Tsang, C.F., 1992. Coupled thermohydromechanical modeling bench mark Test 2 (BMT2) and Test Case 1 (TC1). DECOVALEX—Phase 1 report, 1992.

Noorishad, J., Tsang, C.F., Perrochet, P., and Musy, A., 1992. A perspective on the numerical solution of convection dominated transport problems. Water Resour. Res., v. 28, no. 2, p. 551–561.

Two-Dimensional Dispersion Model for TOUGH2

C. M. Oldenburg and K. Pruess

We have added a general model for Fickian solute dispersion to the multiphase porous media transport code TOUGH2 (Pruess, 1987; 1991). Used in conjunction with the equation of state module for water, brine, and air (EOS7), the TOUGH2 Dispersion Module (T2DM) models brine transport, including the effects of molecular diffusion and hydrodynamic dispersion in rectangular two-dimensional regions. Diffusion and dispersion of vapor and air in the gas phase are also modeled. This brief report consists of a discussion of the dispersion model and its implementation in TOUGH2, followed by results from one verification problem.

FORMULATION

The general conservation equations solved by the integral finite difference method (IFDM) in TOUGH2 consist of balances between mass accumulation and flux and source terms over the grid blocks into which the flow domain has been partitioned. The flux term has contributions from both the phase flux ($\mathbf{F}_\beta$) and from dispersion and can be written

$$\mathbf{F}^{(\kappa)} = \sum_{\beta=1}^{NPH} \left(X_\beta^{(\kappa)} \mathbf{F}_\beta - \rho_\beta \overline{\mathbf{D}}_\beta^{(\kappa)} \nabla X_\beta^{(\kappa)} \right), \qquad (1)$$

where *NPH* is the number of phases present, β is the phase index, κ is the component index, X is the species mass fraction, and ρ is density. The bold $\overline{\mathbf{D}}$ in Eq. (1) is the dispersion tensor, a second-order symmetric tensor with one principal direction in the average (Darcy) flow direction and the other normal to it. The dispersion model is written in terms of dispersion coefficients in the longitudinal (D_L) and transverse (D_T) directions relative to the flow direction as

$$D^{\kappa}_{L,\beta} = \phi \cdot S_\beta \cdot \tau \cdot d^{\kappa}_{\beta} + \alpha_L \, u_\beta \quad , \tag{2}$$

$$D^{\kappa}_{T,\beta} = \phi \cdot S_\beta \cdot \tau \cdot d^{\kappa}_{\beta} + \alpha_T \, u_\beta \quad , \tag{3}$$

where ϕ is the porosity, S_β is the saturation of phase β, τ is the tortuosity of the medium, d is the molecular diffusivity with indices for components κ in phase β, α_L is the intrinsic longitudinal dispersion coefficient (often called the longitudinal dispersivity, or longitudinal dispersion length), α_T is the intrinsic transverse dispersion coefficient, and u_β is the magnitude of the Darcy velocity of phase β (deMarsily, 1986). Thus the dispersion tensor of Eq. (1) can be written as

$$\overline{\mathbf{D}}^{\kappa}_{\beta} = D^{\kappa}_{T,\beta} \, \overline{\mathbf{I}} + \frac{\left(D^{\kappa}_{L,\beta} - D^{\kappa}_{T,\beta}\right)}{u^2_{\beta}} \mathbf{u}_\beta \, \mathbf{u}_\beta \quad . \tag{4}$$

Substituting Eq. (4) into Eq. (1) gives the corresponding mass flux of component κ due to molecular diffusion and hydrodynamic dispersion in phase β:

$$\mathbf{F}^{(\kappa)}_{\beta,d} = -\rho_\beta \, \overline{\mathbf{D}}^{(\kappa)}_{\beta} \nabla X = -\rho_\beta D^{\kappa}_{T,\beta} \nabla X^{(\kappa)}_{\beta}$$

$$- \rho_\beta \frac{\left(D^{\kappa}_{L,\beta} - D^{\kappa}_{T,\beta}\right)}{u^2_{\beta}} \mathbf{u}_\beta \left(\mathbf{u}_\beta \cdot \nabla X^{(\kappa)}_{\beta}\right) . \tag{5}$$

This expression is calculated in the present dispersion module and is added to the phase flux (first term in Eq. 1). Because the dispersion module simply augments the phase flux by the flux due to dispersion, none of the many capabilities of the standard TOUGH2 are taken away with the use of T2DM.

IMPLEMENTATION

The dispersive fluxes depend on the vector quantities of Darcy velocity and species concentration gradient at each interface. Because the IFDM uses a staggered grid (Patankar, 1980), interpolation is required to form the vector quantities at each interface. As shown in Figure 1, in two-dimensional flow, one of the vector components is perpendicular to the interface and is known directly from parameters of the adjacent grid blocks; the other component parallel to the interface must be interpolated from data at neighboring grid blocks. In order to perform this interpolation, some terminology must be adopted and a coordinate system referenced. Shown in Figure 2 is the terminology we use to interpolate the required interface quantities. In this terminology, grid block nodes are referred to by lower-case letters and vertices and interfaces are referred to by upper-case letters. For example, if grid block m is chosen as the reference grid block, the lower case grid blocks e, s, w, and n are the grid blocks to the east, south, west, and north, respectively. The uppercase E, S, W, and N are the interfaces to the east, south, west and north. Vertices are given by the upper-case letter pairs corresponding to their direction away from m.

In T2DM, the Darcy velocity vector and the gradient vector of the mass fraction of component κ are linearly interpolated from the interface centers onto the vertices of the intersecting grid lines (lines forming boundaries of grid blocks) and then directly onto the center of the interface where they will be needed to calculate the dispersive flux by Eq. (5). For example, with reference to Figure 3, the Y component (U) of the Darcy velocity vector at interface N is given by

$$U_N = \frac{D_{1E} U_{NW} + D_{1W} U_{NE}}{D_{1E} + D_{1W}} \quad , \tag{6}$$

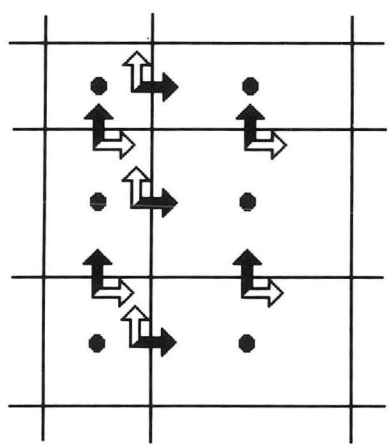

Figure 1. Velocity or concentration gradient vector components at grid block interfaces. Filled (black) components are known directly. Unfilled (white) components must be interpolated. [XBL 936-918]

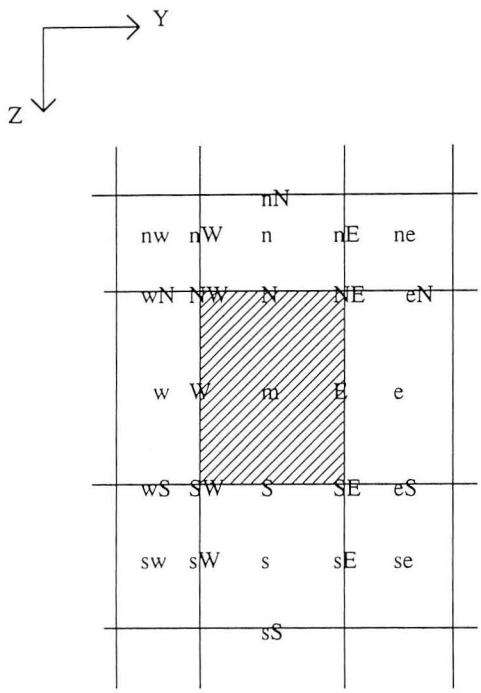

Figure 2. Terminology for the grid blocks and interfaces in the neighborhood of grid block *m* in the *Y-Z* coordinate plane. Lowercase letters refer to nodes, upper case letters to interfaces between grid blocks. [XBL 936-919]

where

$$U_{NW} = \frac{U_{nW}D_{1N} + U_{W}D_{2N}}{D_{1N} + D_{2N}}, \tag{7}$$

$$U_{NE} = \frac{U_{nE}D_{1N} + U_{E}D_{2N}}{D_{1N} + D_{2N}}. \tag{8}$$

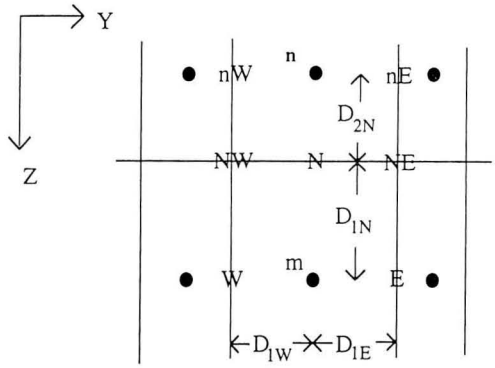

Figure 3. Interfacial distances relevant to the interpolation of velocity and gradient vectors onto interface N. [XBL 936-920]

Thus the *Y* component of velocity at interface N is dependent on thermodynamic conditions (primary variables) at all of the six grid blocks shown in Figure 3. The *Z* component of velocity is known explicitly at N from data given for grid blocks n and m, and no interpolation is required. Analogous interpolation is made at all other interfaces. The component of the solute concentration gradient vector perpendicular to the interface is calculated as a first-order finite difference by taking the difference of the nodal values divided by the connection distance. The direct values of the components of velocity and composition gradient vectors are used where they are available.

In the standard TOUGH2 methodology, the flow rate across the interface between two grid blocks depends only on the primary variables and properties of the two grid blocks involved. The flow thus gives rise to two submatrices of nonzero derivatives in the Jacobian matrix located in the off-diagonal locations corresponding to the two relevant grid blocks. The use of neighboring grid blocks for the interpolation of vectorial components involves the inclusion of additional nonzero submatrices in the Jacobian for all of the six grid blocks used in the interpolation onto each interface.

VERIFICATION PROBLEM

We present next a verification problem of transport and dispersion of a tracer introduced into the left-hand side of a homogeneous, isotropic, saturated porous medium with a steady-state flow field from left to right of 0.1 m/day pore velocity. The tracer is introduced along a line source of length $a = 0.5$ m on the upper part of the left-hand side of a 4×7 m domain. Transverse and longitudinal dispersivities are 0.025 and 0.1 m, respectively. An analytical solution for this problem is given in Javandel et al. (1984).

Global numerical results for the tracer concentration at $t = 20$ days are shown in Figure 4. For the purposes of

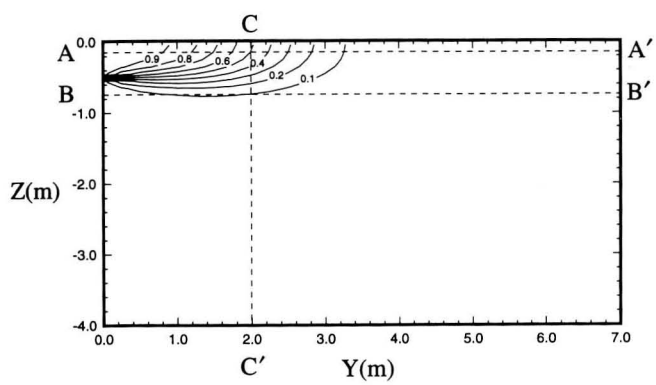

Figure 4. Two-dimensional results for the tracer concentration at $t = 20$ days along with the cross sections of Figure 5. [XBL 936-921]

rigorous comparison between analytical and numerical results, one-dimensional cross-sections through the two-dimensional field are shown in Figure 5 along with the same cross sections from the analytical solution. The agreement with the analytical result is good. Deviations from the analytical result arise from numerical dispersion due to the space and time discretization.

CONCLUSION

We have implemented a general dispersion model into TOUGH2. Interpolation is required to form the vector components necessary to calculate dispersive fluxes at each interface between grid blocks. Because of the interpolation, the dispersive flux at each interface is dependent on primary variables in six neighboring grid blocks, resulting in more nonzero terms in the Jacobian matrix than in the standard TOUGH2. T2DM calculates the flux due to dispersion and adds it to the phase flux. Thus none of the many capabilities of TOUGH2 are lost by the use of T2DM except for the current restriction to two dimensions and a rectangular domain. In particular, T2DM can handle variable density flow and unsaturated flow problems. Future work will focus on applying the model to strongly coupled flow problems such as the variable-density flow of concentrated brine solutions around salt domes (Oldenburg and Pruess, 1993).

REFERENCES

deMarsily, G., 1986. Quantitative Hydrogeology. Academic Press, New York, p. 230–247.

Javandel, I., Doughty, C., and Tsang, C.-F., 1984. Groundwater Transport, Handbook of Mathematical Models. American Geophysical Union, Washington, DC, p. 14–19.

Oldenburg, C.M., and Pruess, K., 1993. Dispersive transport dynamics in a strongly-coupled groundwater-brine flow system. Submitted to Water Resour. Res. (LBL-34487).

Patankar, S.V., 1980. Numerical heat transfer and fluid flow, Hemisphere, p. 118.

Pruess, K., 1987. TOUGH User's Guide. U.S. Nuclear Regulatory Commission Report NUREG/CR-4645 (Lawrence Berkeley Laboratory Report LBL-20700).

Pruess, K., 1991. TOUGH2—A general purpose numerical simulator for multiphase fluid and heat flow. Lawrence Berkeley Laboratory Report LBL-29400.

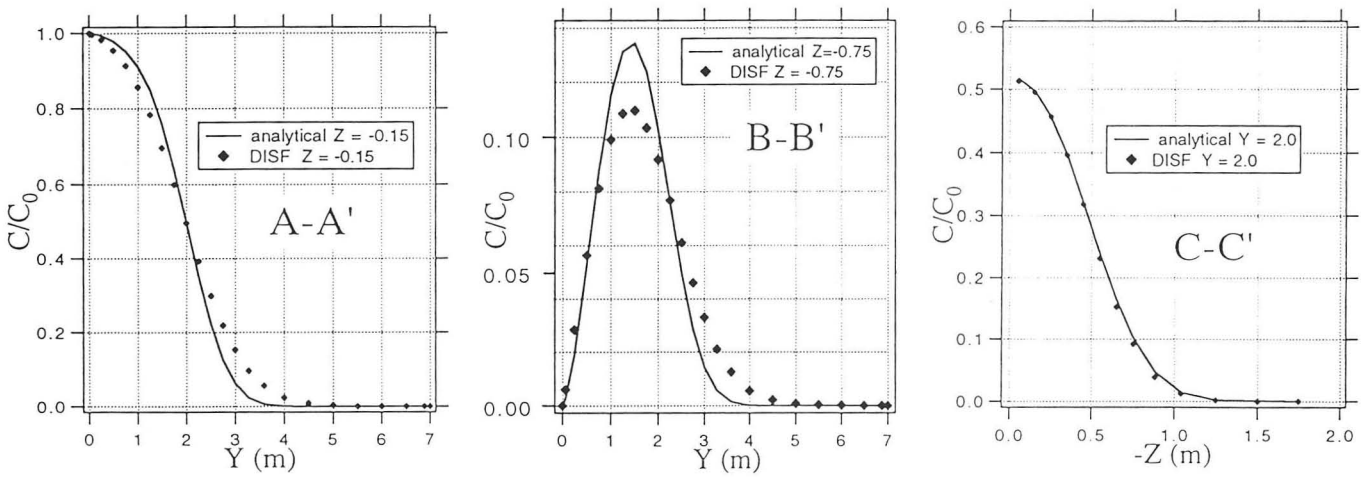

Figure 5. Tracer brine concentration profiles A-A′ ($Z = -0.15$ m), B-B′ ($Z = -0.75$ m), C-C′ ($Y = 2$ m) for analytical and numerical (DISF) calculations. [XBL 936-922]

Melting from Below in a Binary Eutectic System: Numerical Experiments on Magma Body Formation

*C. M. Oldenburg and F. J. Spera**

It has been estimated that 20 km^3 of basaltic magma is generated in the earth's crust each year, mostly along mid-ocean ridge spreading centers (Crisp, 1984). Associated with melting and partial melting is the accumulation of large volumes of magma into magma bodies. One scenario for melting and the formation of magma bodies involves the heating from below of lower crustal mafic gabbro by hot, refractory, partially molten rock generated in the mantle. We have performed numerical experiments on the melting from below of a silicate solid in the diopside-anorthite system to understand more fully the process of magma body formation. In particular, we are interested in (1) the possibility of forming compositional heterogeneity in the magma body during the time of formation of the body (*ab initio*) and (2) the convective dynamics of this strongly coupled flow system. We present in this report a numerical experiment and a discussion of the strong coupling that arises in this magma-generation problem. Although the primary aim of the study was to understand magma bodies, this work is relevant to current efforts aimed at melting contaminated regions of the ground—a method known as *in situ* vitrification (Jacobs et al., 1992).

MODEL FOR PHASE CHANGE AND CONVECTION

In order to investigate a wide range of magmatic convection problems involving phase change (solidification, melting, or both), we have developed a two-dimensional continuum numerical model for phase change and convection of silicate melt (Oldenburg and Spera, 1991,1992a). This model is an extension of the continuum model developed for phase change in metallurgical systems (Bennon and Incropera, 1987). In the continuum model, one set of equations is valid over the entire domain, regardless of whether the local region is entirely solid, entirely liquid, or a mushy mixture of both. In the experiments discussed here, we use the hybrid model (Oldenburg and Spera, 1992a) for the dependence of the form of the momentum equations on the fraction solid (*fs*) present in mushy regions. The model equations include expressions for conservation of mass, momentum, energy, and species for a binary eutectic system. These equations are solved by a control-volume finite difference method along with supplementary relations that relate enthalpy to temperature and *fs*. The iterative solution method handles the nonlinear couplings involved in phase change and convection. The model, its numerical solution, example calculations, and comparison with laboratory experiments have been presented previously (Oldenburg and Spera, 1990, 1991, 1992a,b).

The model system for the melting experiments is a two-dimensional rectangular domain with bulk composition 80% diopside and 20% anorthite (Di80). This composition models the behavior of mafic gabbro in the lower crust, with generation of basaltic magma upon melting. The phase diagram is shown in Figure 1. The initial temperature (T_0) of the solid body is uniform and 5°C below the eutectic temperature. The bottom of the body (T_b) is held 5°C above the liquidus temperature for Di80. Because our focus is on the bottom-heating scenario, the sidewalls were held insulated for simplicity.

The thermophysical properties of the system are given in Table 1. Because of the practical limits of the computational scheme arising from finite time and space discretizations, the domain is limited to regions of very small size relative to magma bodies. In particular, the domain studied here is 0.20 m in height (L). Nevertheless, the processes of melting and convection and the coupling between these processes are accounted for in the model. We expect the same strong coupling to occur in natural systems despite the different length and time scales.

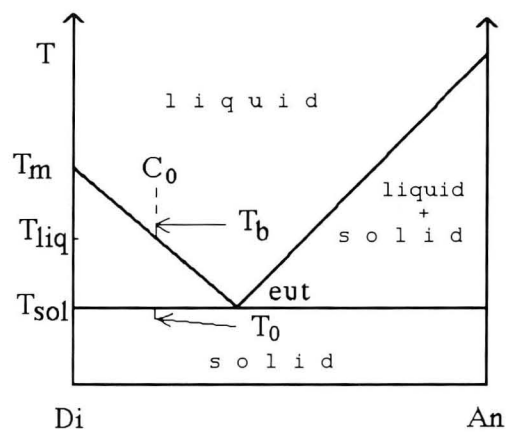

Figure 1. Phase diagram for the pure binary eutectic system diopside-anorthite (Di-An). Initial composition C_0 is Di80. The liquidus temperature (T_{liq}) is shown along with the solidus temperature (T_{sol}), the initial temperature, T_0, and the bottom temperature, T_b. [XBL 936-885]

* Department of Geological Sciences and Institute for Crustal Studies, University of California at Santa Barbara.

Table 1. Thermophysical parameters of Di80 melting problem.

Property	Name	Units	Value
T_{liq}	Liquidus temperature	K	1606
T_{sol}	Solidus temperature	K	1548
T_{bottom}	Temperature at bottom	K	1611
T_{top}	Temperature at top	K	1543
T_0	Initial temperature	K	1543
c_p	Heat capacity	J kg^{-1} K^{-1}	1006
ρ	Density	kg m^{-3}	2660
κ	Thermal diffusivity	m^2 s^{-1}	10^{-6}
D	Chemical diffusivity	m^2 s^{-1}	10^{-8}
μ	Viscosity	m kg^{-1} s^{-1}	3.6
α	Thermal expansivity	K^{-1}	10^{-5}
β	Compositional expansivity	—	10^{-2}
L	Height of the body	m	.20

RESULTS

In general, the behavior of this silicate binary eutectic system upon melting will involve the initial generation of eutectic-rich melt along the hot bottom boundary. As melting continues along with thermal and chemical diffusion, this zone of melt and mushy two-phase mixture will become thicker and the solid lid will become thinner. When the mushy fluid layer is sufficiently thick, it will become gravitationally unstable and begin to convect because of thermal and compositional buoyancy. Convection will transport heat and mass upward, resulting in more melting of the lid above the plume. The hot eutectic-rich plumes generated at the bottom boundary are a manifestation of the strong couplings between the flow field and the thermal and compositional fields.

Results from a numerical experiment are shown in Figures 2 and 3 as plots of velocity of the mixture and isopleths of the relevant fields. Figure 2 shows the *fs* and mixture velocity fields at four different times ($t = 0.05$, 0.10, 0.15, 0.20), where the time has been scaled by the thermal diffusion time. At $t = 0.05$, the layer of mushy mixture extends to about $Y = 0.35$ and convection has just begun in the lower right-hand corner of the body. Convection is weak in this system, as seen by the slight bowing of isopleths, because of the small height of the system. The region of convecting magma is limited to regions where *fs* is less than about 50%, above which the mixture is effectively locked (Arzi, 1978). Even values of *fs* in the range 0 to 0.5 strongly affect the viscosity and prevent vigorous convection. At $t = 0.10$, the convection becomes more vigorous, as seen by the plume that has formed near $X = 0.25$. The solid lid has melted more, and the original convection cell in the lower right-hand corner remains from earlier times. At $t = 0.15$ and $t = 0.20$, these basic features persist, with the convecting layer getting thicker and the solid lid thinner. The melting process proceeds from the bottom upward. Rather than separating into a liquid and a solid region during heating from below, the body becomes mostly a mushy two-phase mixture.

Shown in Figure 3 are the temperature and dimensionless composition fields for the same experiment at $t = 0.20$. The hot upward plumes and the colder downward plumes are shown by the isotherms. This coupling is the fundamental nonlinearity in pure thermal convection. However, in this binary eutectic system, there is coupling between composition and *fs* fields as well as temperature. In particular, the *fs* is lower in the hot upward plumes, and thus the viscosity is lower and the plume is more mobile than adjacent more *fs*-rich regions (see Figure 2). As for composition, the first melt to form is of eutectic composition, enriched in the light component (anorthite) and therefore less dense due to compositional buoyancy. In Figure 3, we show the normalized mixture composition field, C^*, where $C^* = (C - C_{min})/(C_{max} - C_{min})$ and $C_{max} = 0.23$ and $C_{min} = 0.20$. The C^* field shows a compositional heterogeneity associated with the upward plume near $X = 0.25$. Thus the effects of thermal buoyancy, compositional buoyancy, and *fs* are all contributing to the upward flow. The coupling of the temperature, composition, and *fs* fields leads to this preferential flow phenomena for the present melting scenario with bulk composition Di80.

CONCLUSIONS

The first-order observation is that most of the domain becomes a mushy solid-liquid region. This arises because temperature gradients tend to be rather gentle because of the thermal diffusivity of rock, and the system tends toward intermediate temperatures where both solid and liquid phases are stable. This is in fact what is observed in nature; natural magmas are mixtures of liquid and one or more solid phases. We also observe the *ab initio* formation of compositional heterogeneity from a homogeneous initial condition.

The other important observation is the strong coupling between the velocity, temperature, composition, and *fs* fields and the effect of this coupling on the convective dynamics. In particular, one sees in Figure 3 the strength of the plumes being reinforced by thermal buoyancy, compositional buoyancy, and the small *fs*. It is this sort of nonlinear dynamics that may be responsible for producing much of the natural volcanic activity we observe at the earth's surface. Even in a small and simplified system such as we have modeled, some fundamental nonlinear processes are observed.

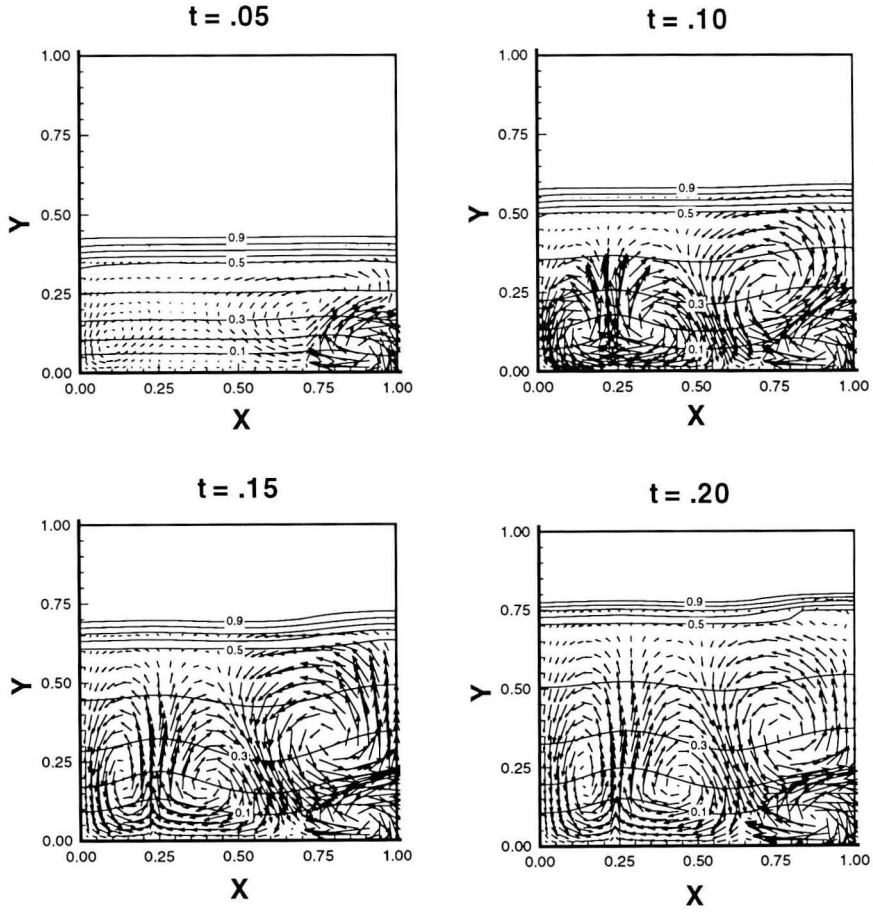

Figure 2. Evolution of the *fs* field. Plot shows vectors of mixture velocity and isopleths of *fs* at $t = 0.05$, 0.10, 0.15, and 0.20. Note the overall decrease in thickness of the solid lid with time and the increase in thickness of the melted mushy layer. Convection becomes more vigorous as the mushy layer thickens. [XBL 936-886]

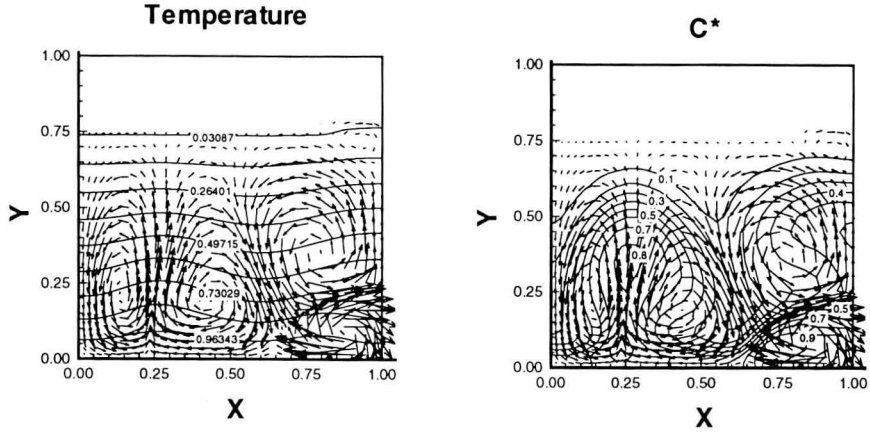

Figure 3. Temperature and normalized composition (C^*) at $t = 0.20$. The isotherms show the plume is hotter than adjacent mushy fluid. The C^* field shows the strong compositional anomaly associated with the plume near $X = 0.25$. The lower *fs* associated with the plume has already been shown in Figure 2. These fields show the strong coupling between velocity, temperature, composition and *fs* fields in this melting problem. [XBL 936-887]

REFERENCES

Arzi, A.A., 1978. Critical phenomena in the rheology of partially melted rocks. Tectonophysics, v. 44, p. 173–184.

Bennon, W.D., and Incropera, F.P., 1987. A continuum model for momentum, heat and species transport in binary solid-liquid phase change systems—I. Model formulation. Int. J. Heat & Mass Transfer, v. 10, p. 2161–2170.

Crisp, J.A., 1984. Rates of magma emplacement and volcanic output. J. Volcanol. & Geotherm. Res., v. 20, p. 177–211.

Jacobs, G.K., Dunbar, N.W., Naney, M.T., and Williams, R.T., 1992. Petrologic and geophysical studies of an artificial magma. Eos: Trans. Am. Geophys. Union, v. 73, p. 401, 411–412.

Oldenburg, C.M., and Spera, F.J., 1990. Simulation of phase change and convection in magma bodies. *In* C. Carrigan and T.Y. Chu (eds.), Heat Transfer in Earth Science Studies (ASME-HTD Vol. 149), p. 35–42.

Oldenburg, C.M., and Spera, F.J., 1991. Numerical modeling of solidification and convection in a viscous pure binary eutectic system. Int. J. Heat & Mass Transfer, v. 34, p. 2107–2121.

Oldenburg, C.M., and Spera, F.J., 1992a. Hybrid model for solidification and convection. Num. Heat Transfer B, v. 21, p. 217–229.

Oldenburg, C.M., and Spera, F.J., 1992b. Modeling transport processes in non-linear systems: The example of solidification and convection. *In* D.A. Yuen (ed.), Chaotic Processes in the Geological Sciences. IMA Volumes in Mathematics and Its Applications, v. 41, p. 205–224.

Effects of Capillarity and Vapor Adsorption in the Depletion of Vapor-Dominated Geothermal Reservoirs

*K. Pruess and M. O'Sullivan**

Vapor-dominated geothermal reservoirs in natural (undisturbed) conditions contain water as both vapor and liquid phases. In response to fluid production, the liquid phase will boil, with heat of vaporization supplied by the reservoir rocks. As reservoir temperatures decline, reservoir pressures will decline also. For depletion of "bulk" liquid, the pressure would decline along the saturated vapor pressure curve, whereas for liquid held by capillary and adsorptive forces inside porous media, "vapor pressure lowering (VPL)" will cause an additional decline.

We have examined experimental data on vapor adsorption and capillary pressures in an effort to identify constitutive relationships that would be applicable to the tight matrix rocks of vapor-dominated systems. Numerical simulations have been performed to evaluate the impact of these effects on the depletion of vapor-dominated reservoirs.

CAPILLARY SUCTION, VAPOR ADSORPTION, AND VAPOR PRESSURE LOWERING

Thermodynamic analysis shows that for pure single-component fluids such as water, coexistence of liquid and vapor phases at any given temperature T is possible only for a certain unique pressure, which is termed the saturated vapor pressure, or saturation pressure, $P_{sat}(T)$. The thermodynamic properties of liquid and vapor, and the conditions under which these phases can coexist, are altered inside porous media. Vapor pressure above a liquid held by capillary or adsorptive forces is reduced in comparison with vapor pressure above the flat surface of a bulk liquid. The reduction is expressed in terms of a vapor pressure lowering factor, or relative vapor pressure, β, defined by

$$\beta = P_v / P_{sat}(T) \ . \tag{1}$$

The relationship between β and the capillary pressure, or adsorption-induced suction pressure P_{suc}, is given by the Kelvin equation

$$\beta = \exp\left(\frac{M_{H_2O} P_{suc}}{\rho_l R(T + 273.15)}\right), \tag{2}$$

where M_{H_2O} is the molecular weight of water, ρ_l is liquid phase density, R is the universal gas constant, and T is the temperature measured in degrees Celsius. β depends chiefly

* Department of Engineering Science, University of Auckland, Auckland, New Zealand.

on suction pressure, which in turn is primarily a function of liquid saturation, S_l. At typical vapor-dominated conditions of T = 240°C, the suction pressures required for 1%, 10%, and 20% vapor pressure lowering (i.e., β equal to 0.99, 0.90, and 0.80) are, respectively, –19.4 bars, –203 bars, and –430 bars. Thus significant reduction in vapor pressure will occur only for very large suction pressures.

Several experimental techniques are available for measuring suction pressure and vapor adsorption characteristics of porous materials. Illustrative data from the literature are given in Figure 1 in the form of liquid saturation vs. suction pressure. Although the range of suction behavior is large, it is seen that significant reduction of vapor pressure, 10% say, will occur only for rather small liquid saturations on the order of 20% or less. Vapor pressure lowering effects will be unimportant for reservoir processes at higher liquid saturations.

NUMERICAL SIMULATIONS

We have performed numerical simulations to examine and evaluate the nature and strength of fluid retention from capillarity and adsorption. The calculations were performed with LBL's general-purpose simulator TOUGH2, which implements the general MULKOM architecture for coupled multiphase fluid and heat flows (Pruess, 1991). For the illustrative calculations discussed here, we have used the suction pressure relationship obtained by Peters et al. (1984) for their sample G4-6, employing a cutoff of $-P_{suc} \leq 5000$ bars. This is a tight welded tuff with a permeability of 1.9×10^{-18} m^2 (1.9 microdarcies), which may be representative of the tight reservoir rocks of The Geysers.

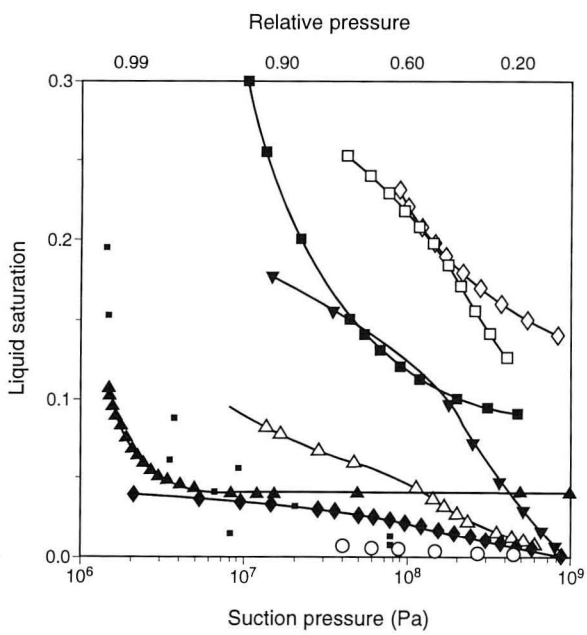

Figure 1. Liquid suction pressure characteristics for different geologic materials. [XBL 936-4335]

Our first simulation examines constant-rate production from a zero-dimensional "lumped-parameter" reservoir model (single gridblock) with an initial liquid saturation of 80% and a pressure of 33.44 bars, corresponding to a saturation temperature of 239.93°C. No permeability specifications are needed in this problem because the reservoir is modeled as a single gridblock. Production occurs at a constant rate of 34.37 kg/s, which at initial fluid reserves of 32.7×10^9 kg can be sustained for 30.16 years. The system is taken through 20 depletion steps of 1.5 years each, and simulated pressures, temperatures, and liquid saturations with and without VPL are given in Table 1. The reservoir with VPL effects starts off with a temperature that is slightly higher (0.44°C) than the reservoir without VPL, in order to attain the same vapor pressure as in the no-VPL system. Temperatures and liquid saturations for depletion with and without VPL are seen to remain very close at all times. Differences in reservoir pressures are small at early times, reaching 0.7 bar at 50% depletion (15 years), 2.7 bars at 75% depletion (22.5 years), and becoming very large as ultimate dry-out, with extremely strong suction pressures and VPL effects, is approached. Thus VPL effects are insignificant for most of the productive life of the system.

Depletion of Tight Matrix Blocks

Most of the fluid reserves in vapor-dominated systems are stored in tight matrix blocks with permeability of order 1 microdarcy (10^{-18} m^2). The fracture system is believed to contribute little to fluid storage but provides large-scale permeability. We have simulated fluid production from tight matrix blocks under conditions considered representative for the depletion of vapor-dominated systems such as The Geysers and Larderello.

The model system (see Figure 2) consists of a single block of rock matrix in the shape of a cube with side length $D = 50$ m, which is to be viewed as a subdomain of a large reservoir volume. Matrix permeability is of order 10^{-18} m^2, and matrix porosity is 5%. The block is surrounded by fractures assigned an arbitrary (small) fractional volume of 10^{-4}. Initial conditions are a pressure of 33.44 bars throughout and liquid saturations of 80% in the matrix block and 1% in the fractures, respectively.

Depletion is initiated by placing a "well" on deliverability in the fractures. Well specifications are a bottomhole pressure of 10 bars and a productivity index of 1.788×10^{-13} m^3. For the depletion simulation, the matrix block is discretized according to the MINC method (Pruess and Narasimhan, 1982, 1985). For matrix permeabilities of 1 and 5×10^{-18} m^2, three cases were simulated: case 1, including both suction pressure and VPL effects; case 2,

Table 1. Depletion of zero-dimensional reservoir.

Time Step	Time (yr)	Pressure (bars)		Temperature (°C)		Liquid Saturation (%)	
		VPL	No VPL	VPL	No VPL	VPL	No VPL
	0	33.44	33.44	240.37	239.93	80	80
1	1.5	32.69	32.73	239.15	238.72	75.76	75.77
2	3	31.95	32.04	237.94	237.15	71.55	71.56
3	4.5	31.21	31.34	236.71	236.28	67.36	67.37
4	6	30.48	30.66	235.48	235.05	63.19	63.20
5	7.5	29.74	29.98	234.24	233.81	59.04	59.05
6	9	29.01	29.32	233.00	232.57	54.91	54.92
7	10.5	28.28	28.66	231.74	231.31	50.80	50.81
8	12	27.54	28.00	230.48	230.05	46.72	46.73
9	13.5	26.80	27.36	229.21	228.78	42.65	42.66
10	15	26.03	26.72	227.94	227.51	38.61	38.61
11	16.5	25.24	26.09	226.66	226.23	34.59	34.58
12	18	24.40	25.47	225.37	224.94	30.59	30.58
13	19.5	23.47	24.86	224.07	223.64	26.62	26.59
14	21	22.36	24.25	222.77	222.34	22.68	22.62
15	22.5	20.90	23.66	221.46	221.03	18.77	18.66
16	24	18.49	23.07	220.15	219.71	14.95	14.73
17	25.5	12.71	22.49	218.87	218.38	11.33	10.81
18	27	1.62	21.92	217.64	217.05	8.00	6.92
19	28.5	1.57	21.35	216.23	215.71	4.13	3.04
20	30.0	1.53	7.66	214.82	214.56	0.28	0

including suction pressures but no VPL effects; and case 3, "conventional" approach, neglecting capillary- and adsorption-induced suction pressures (and consequently neglecting VPL effects as well).

The effect of vapor pressure lowering is to accelerate pressure decline as fluid discharge proceeds from the block, diminishing the driving force for vapor outflow from the block and consequently slowing depletion of fluid reserves.

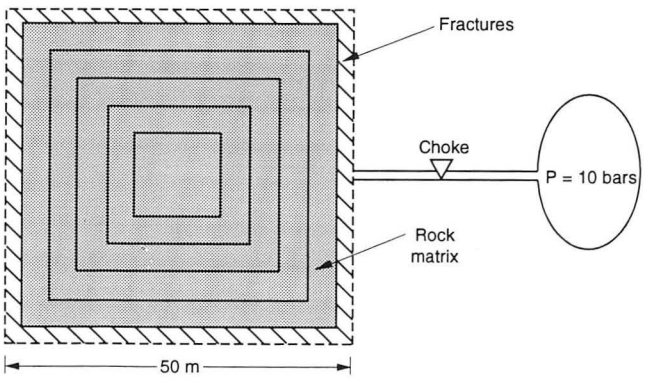

Figure 2. Schematic of matrix block depletion problem, with MINC discretization. [XBL 9112-7107]

For the parameters used here, this effect tends to approximately cancel the increase in depletion rate from suction pressure effects, so that the depletion behavior in case 1 is very similar to that in case 3. The effects from suction pressures and vapor pressure lowering are rather modest. Total produced mass in case 2 is approximately 20% larger at all times than cumulative production in case 3 (Figure 3).

DISCUSSION AND CONCLUSIONS

Capillarity, vapor adsorption on rock surfaces, and vapor pressure lowering are interrelated and strongly coupled effects. Different geologic media show a tremendous variety of capillary and adsorptive behavior. Although existing data are insufficient for a detailed quantitative description of vapor pressure lowering effects in vapor-dominated reservoirs such as The Geysers and Larderello, a survey of literature data indicates that VPL effects will become significant (reducing vapor pressure by 10% or more) only at low liquid saturations of 20% or less. Initial liquid saturations in vapor-dominated systems are believed to be large, in excess of 80% and most likely close to 100% (Pruess and Narasimhan, 1982; Pruess, 1985), so that VPL effects on production rates and pressures will be negligible

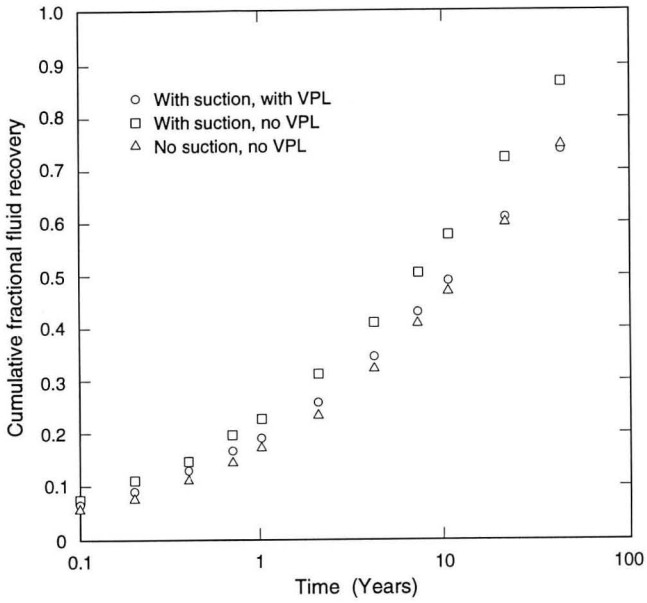

Figure 3. Cumulative fluid recovery in block depletion problem for matrix permeability of 10^{-18} m^2. [XBL 9112-7104]

for most of the productive life of vapor-dominated systems, playing a role only in the final stages of reservoir dry-out.

Depending on the relative permeability behavior of vapor-dominated systems, which has not yet been well characterized, it is possible that the suction effects from capillarity and vapor adsorption may significantly affect liquid flow in the matrix blocks. Although of minor importance for pressure and flow-rate behavior of vapor-dominated systems, the presence of adsorbed and capillary water at pressures below saturated values may play a crucial role in rock-fluid reactions and in the release and transport of noncondensable gases. A more detailed analysis of vapor pressure lowering effects has been given in Pruess and O'Sullivan (1992).

REFERENCES

Peters, R.R., Klavetter, E.A., Hall, I.J., Blair, S.C., Heller, P.R., and Gee, G.W., 1984. Fracture and matrix hydrologic characteristics of tuffaceous materials from Yucca Mountain, Nye County, Nevada. Sandia National Laboratories Report SAND84-1471.

Pruess, K., 1985. A quantitative model of vapor dominated geothermal reservoirs as heat pipes in fractured porous rock. Geothermal Resources Council, Trans., v. 9, Part II, p. 353–361.

Pruess, K., 1991. TOUGH2– A general-purpose numerical simulator for multiphase fluid and heat flow. Lawrence Berkeley Laboratory Report LBL-29400.

Pruess, K., and Narasimhan, T.N., 1982. On fluid reserves and the production of superheated steam from fractured, vapor-dominated geothermal reservoirs. J. Geophys. Res., v. 87, no. B11, p. 9329–9339.

Pruess, K., and Narasimhan, T.N., 1985. A practical method for modeling fluid and heat flow in fractured porous media. Soc. Petroleum Engineers Journal, v. 25, no. 1, p. 14–26.

Pruess, K., and O'Sullivan, M., 1992. Effects of capillarity and vapor adsorption in the depletion of vapor-dominated geothermal reservoirs. Presented at the Seventeenth Workshop on Geothermal Reservoir Engineering, Stanford, California, January 29–31, 1992 (LBL-31692).

Geochemical Studies of Reservoir Processes in the Southeast Geysers

A. H. Truesdell, S. Enedy,† J. L. Smith,† and M. J. Lippmann*

A nearly field-wide accelerated decline in pressure and steam production occurred at The Geysers in the late 1980s. As a result of this crisis, the U.S. Department of Energy has begun a program to examine the reservoir processes at The Geysers in greater detail, with particular attention to understanding the sources of steam and gas and predicting changes in pressure, steam flow, and gas content. The chemistry of steam has been used to indicate the distribution of liquid and gases in the reservoir and the sources of produced steam. These studies involve calculating temperature and fraction of steam in the feed to wells and tracing steam compositions that originate from partial condensation, evaporation of liquid, and mixing of steam sources. Steam sources now exploited include steam from the open fractures of the system, vaporized liquid from small fractures and the rock matrix, and fluids entering the reservoir from outside, including injected condensate and fluids from undrilled areas.

* Consultant, Menlo Park, California.
† No. California Power Agency, Middletown, California.

This study concentrated on the Northern California Power Agency (NCPA) field, located in the southeastern part of The Geysers (Figure 1). The field is bounded to the north by Unocal and Calpine leases, to the southwest by the Big Sulfur Creek fault zone, in which low permeability limits steam production, and partially to the south and east by liquid-saturated boundaries. Geochemical methods of tracing reservoir processes have been applied to steam analyses provided by NCPA.

GAS EQUILIBRIA

At equilibrium, concentrations of gases in reservoir steam and liquid differ because gases partition strongly into the steam. If reservoir liquid vaporizes during production and this steam mixes with original reservoir steam, gas concentrations in the mixture will not correspond to equilibrium in either liquid or steam. By combining gas solubilities and equilibria for two reactions, both reservoir temperature and steam fraction, "y," which is equal to the fraction of original reservoir steam in the produced mixture (also called effective reservoir steam saturation), can be calculated. Methods for this calculation were first described by Giggenbach (1980) and D'Amore et al. (1982).

Methane breakdown and pyrite-H_2S reactions were chosen for the calculation. These reactions are

$$CH_4 + 2H_2O = CO_2 + 4H_2$$

and

$$3FeS_2 + 4H_2O + 2H_2 = Fe_3O_4 + 6H_2S\ .$$

Equilibrium expressions for these reactions can be written as

$$4\log(H_2 / H_2O)WH + \log(CO_2 / CH_4)WH =$$

$$-15.35 - 3952 / T + 4.635\log T$$

$$+4\log AH_2 + \log(ACO_2 / ACH_4)$$

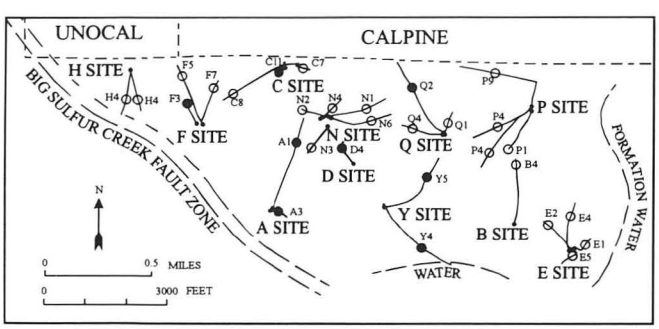

Figure 1. Map of the NCPA field showing locations of field boundaries, and selected well sites, well courses, mean steam entries, and mean injection points (solid circles). [XBL 936-888]

and

$$3\log(H_2S / H_2O)WH - \log(H_2 / H_2O)WH =$$

$$6.23 - 6222 / T - 0.412\log T$$

$$+3\log A_{H_2S} - \log A_{H_2}\ ,$$

where WH refers to wellhead analyses in molal units, T is in degrees kelvin, $A_i = y + (1 - y)/B_i$, and B_i is the gas distribution constant, C_{vapor}/C_{liquid} (given in Giggenbach, 1980).

On a grid drawn using these equations (Figure 2), the NCPA steam analyses indicate temperatures from about 210 to 265°C and steam fractions (y values) from about 0.005 to 0.25. Most steam analyses are between 225 and 250°C, and 0.05 and 0.2y. The indicated temperatures are reasonable. The original temperate at 2000 m depth was probably near 245°C (Truesdell and White, 1973), with somewhat lower temperatures expected as a result of exploitation. The calculated steam fraction values (5 to 20 wt% steam) indicate substantial liquid reserves.

GAS CONCENTRATIONS

Total gas concentrations (as mole fractions) are shown for a cross section of the NCPA field in Figure 3. These values vary with time and position in the field. Large increases occurred at the field margins after 1985, with smaller increases in the center of the field after 1987. These changes can be better seen in Figures 4 and 5, which show changes with time of the gas concentration of wells at the margins and center (except N wells) of the field. Gas concentrations in steam from N wells are lower and more variable as a result of intense nearby injection (Figure 6). (In-

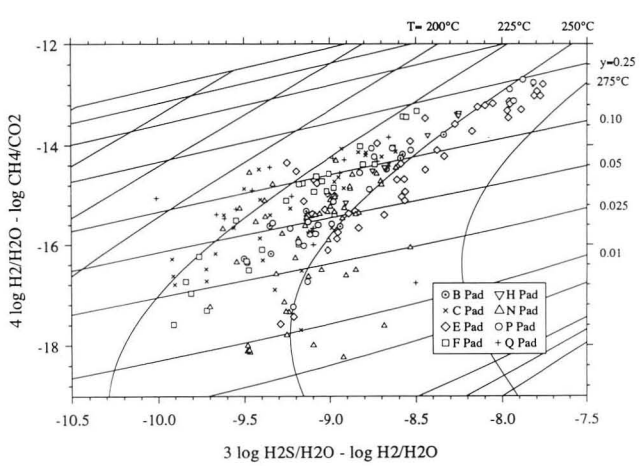

Figure 2. Part of the y-t "grid" diagram for CH_4-CO_2-H_2 and pyrite-magnetite-H_2S reactions showing effective vapor saturation, y, and temperature for selected NCPA steam samples collected from 1985 to 1990. [XBL 936-889]

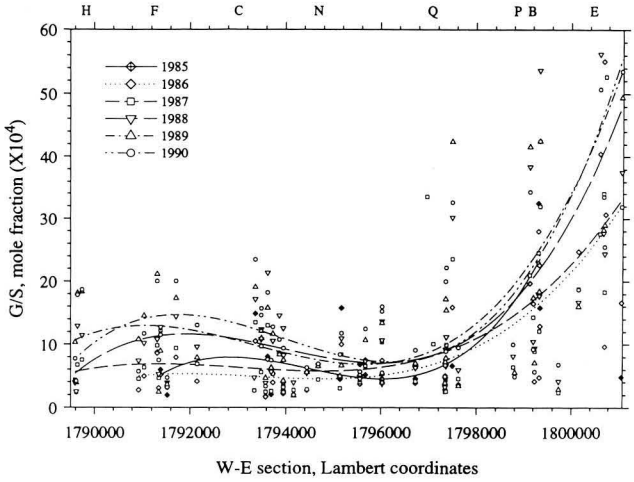

Figure 3. W-E cross section of the NCPA field showing gas to steam mole fractions for yearly steam samples and curves fitted to each year's data. [XBL 936-890]

jection well locations are shown as filled circles in Figure 1.) These figures show that gas concentrations in almost all steam analyses decreased or were constant until mid-1987 and increased markedly from 1987 to late 1989 or 1990.

Steam may exist in areas beyond the margins of the drilled field. These areas, initially rejected because of high gas or low productivity, eventually contribute to the total steam produced in neighboring wells. Steam at the reservoir margins is distinct chemically from steam in the center. In the Southeast Geysers and in several areas of Larderello, water-soluble salts are more concentrated in steam from the center of the field and water-insoluble gases more concentrated at the margins (D'Amore and Truesdell, 1979; Truesdell et al., 1987). Oxygen-18 is depleted in

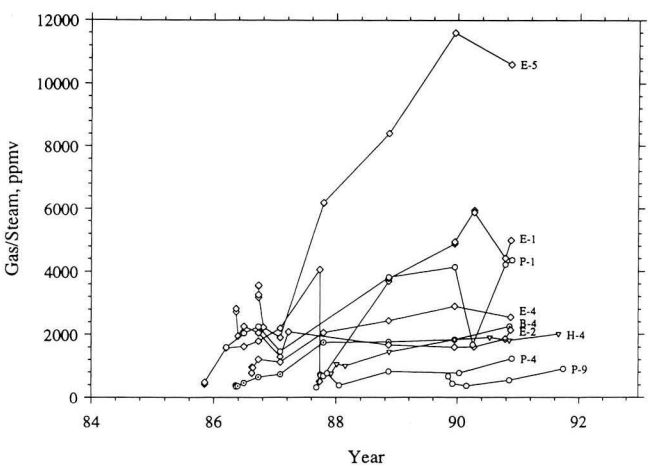

Figure 4. Changes with time of gas concentrations (in ppm by volume) for steam at the margins of the NCPA field (H, P, B, and E wells). [XBL 936-891]

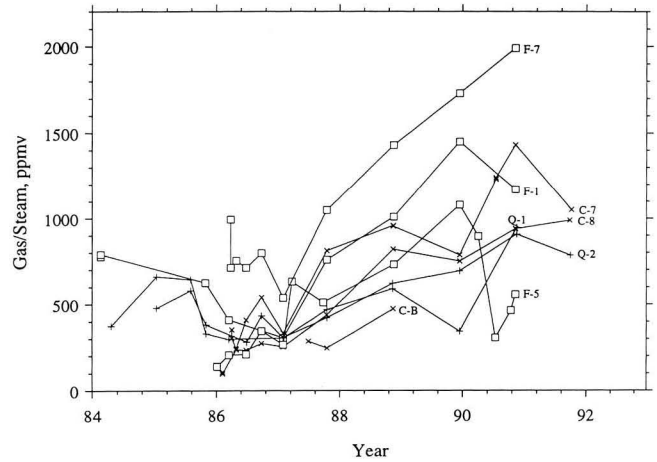

Figure 5. Changes in gas concentrations for steam from wells in the central NCPA field (except N wells). [XBL 936-892]

marginal steam. These patterns are produced by natural-state (pre-exploitation) lateral steam flow with partial condensation as heat is lost by conduction to the surface.

Steam from E and P wells clearly shows the effect of mixture with marginal steam (Figure 4). These wells generally produce the highest initial gas contents and have increased in gas with time starting in 1987. Wells E-5, E-1, and P-1 produce the highest gas of the field (to 12000 ppmv) and are nearest to the field margin. Steam from well H-4 on the western margin, which (along with E well steam) was originally low in ^{18}O, has moderately high gas relative to most wells but much lower than for E wells.

Steam from C, F, and Q wells (Figure 5) has somewhat higher gas contents than those from N wells and much lower gas than steam from field margins. This group shows a small decrease in gas before 1987 and a large increase in

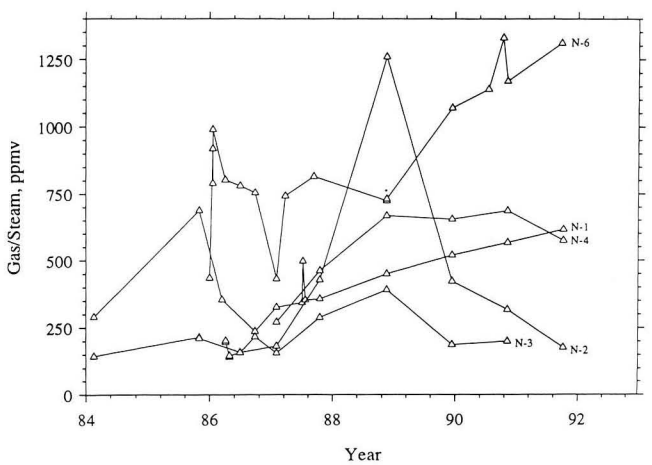

Figure 6. Changes in gas concentrations for steam from N wells. [XBL 936-893]

gas afterwards. The decrease in gas content before 1987 is due to dilution of reservoir steam by the continued vaporization of reservoir liquid. In 1987 this process stopped or slowed markedly and the gas contents of steam increased.

N well steam has the lowest gas of the NCPA field (Figure 6). This is probably due both to the position of N wells at the center of the field and to gas dilution from vaporization of injectate. Steam from wells N-1 through N-4 generally has gas contents below 750 ppmv and has not shown rapid increase in gas. These wells are evidently receiving enough injectate to stabilize gas contents of the produced steam.

ISOTOPES

Isotopes have been frequently used in tracing injection return in steam fields (Nuti et al., 1981; Beall and Box, 1992). Studies of injection in a low-pressure area (LPA) of the Southeast Geysers shared by NCPA, Calpine, and Unocal have demonstrated substantial increases in steam flow and reservoir pressure (Enedy et al., 1992). Isotopic data were used as tracers in this and other studies to estimate the quantity of steam generated from evaporation of injected condensate.

The effects of evaporation on the injected condensate and the results of mixing steam from vaporized condensate with reservoir steam are shown in Figures 7 and 8, in which steam isotope compositions for 1985–1986 are compared with those for 1990. In 1985–1986 some N and A wells were affected by condensate injection, whereas in 1990 this effect was felt strongly by F, C, and N wells, with some effect for most other wells. The effects of intense injection in the LPA near F and C wells is seen in Figure 8. In 1990 only wells far from injection wells (some E and H wells) retained their original isotope compositions.

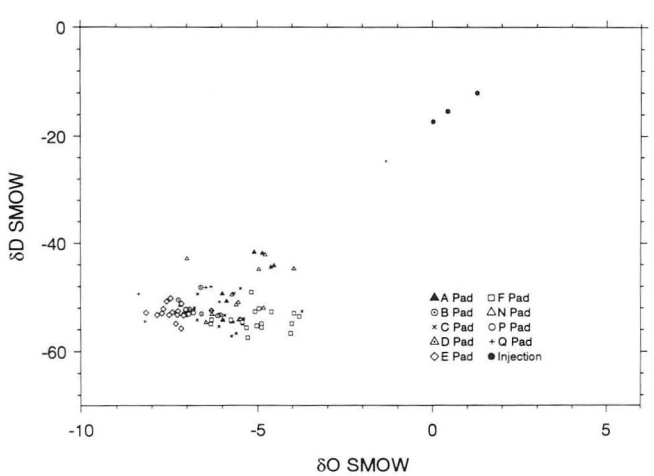

Figure 7. Isotope diagram showing values of $\delta^{18}O$ and δD (in permil SMOW) for 1985–1986 NCPA steam samples. [XBL 936-894]

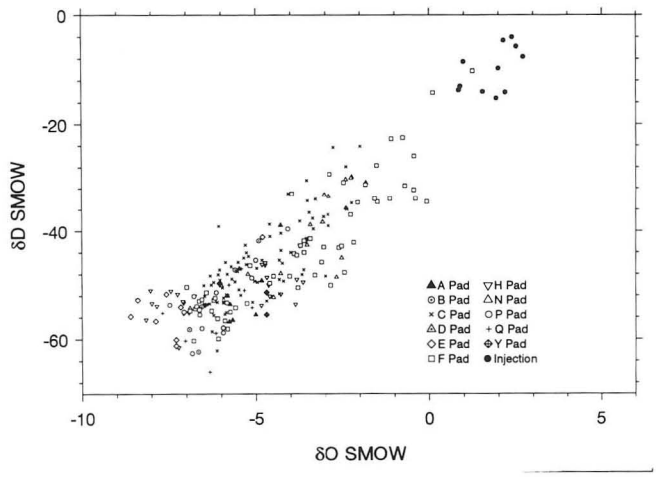

Figure 8. Isotope diagram (like Figure 7) for 1990 NCPA steam samples. [XBL 936-895]

DISCUSSION

The main influences on the gas and isotope compositions of steam from the NCPA field include: (1) original (pre-exploitation) gradients produced by the lateral movement of steam, resulting in the presence of high-gas steam at field margins; (2) injection of steam condensate, which vaporizes and mixes with reservoir steam to dilute gases and increase heavy isotope contents; and (3) a decrease in the availability of liquid in the reservoir, which has decreased pressures and flows and increased gas concentrations.

Natural-state gradients in gas and isotope chemistry result from lateral movement of steam from an upflow zone in the west-central part toward zones of condensation mainly to the south and east, with a smaller flow to the west. This movement was accompanied by partial condensation of steam along the flow path, causing the residual steam to be enriched in gas and depleted in ^{18}O. The resulting zones of condensation at the field margins contain subcommercial quantities of high-gas steam. As pressures decrease during production, the marginal steam is drawn into producing zones, causing an increase in gas concentrations. This effect may produce results similar to the general decrease of steam from vaporized liquid.

Injection of steam condensate has influenced steam compositions in the center of the field. Injection greatly increases heavy isotope (D and ^{18}O) contents of steam fed in part from vaporization of the injectate and lowers gas concentrations by dilution. Injection has affected the gas contents of some steam in the center of the field, but this effect has been overshadowed by the general change in steam origins discussed next.

The most important influence on steam compositions is the sudden decrease in 1987 of the amount of steam formed by vaporization of liquid water in the reservoir. This is clearly seen in the change in the gas concentration

of steam from individual wells (Figures 4 and 5). Before 1987 steam from most central wells contained less than 1000 ppmv, and wells at the eastern margin contained less than 3000 ppmv. In early 1987 gas contents increased rapidly from minimum values to maxima in 1990 (2 to 6 times greater). The decrease in vaporization of easily available liquid in the reservoir has caused rapid decreases in pressure and steam flow throughout most of The Geysers field. This has important consequences for the continued productivity of the entire field.

Numerous modeling studies of mass and heat transfer in vapor-dominated reservoirs have demonstrated steam-water counterflow, but only Pruess and Narasimhan (1982) indicate the location of liquid in the reservoir. These authors state that liquid is confined to matrix blocks because it will vaporize if it enters vertical fractures and cannot exist on fracture surfaces. This argument appears limited to very low permeability rocks in which conductive heat flow is as rapid as fluid flow. For a natural system at equilibrium, thermodynamic arguments indicate that water in rock pores, water on fracture surfaces, and steam can coexist.

It seems likely that the 1987 increase in gas and decline in pressure and flow was due to a decrease in the availability of liquid water in the reservoir. Pressure could be maintained by producing steam from a large volume of interconnected fractures with minimal vaporization of liquid in each unit volume or from a smaller production volume with extensive vaporization. Similarly, declining pressure could result from an increasing distance to the source of steam or from decreasing availability of nearby liquid.

The existence of well-defined chemical patterns inherited from the natural state in the long-exploited Larderello field (D'Amore and Truesdell, 1979) and in the geochemical results presented here suggest a local source of steam. In this view, rather than the exhaustion of a distant homogeneous source, the recent accelerated decline in pressure and flow at The Geysers resulted from the local disappearance of liquid held in easily accessible sites—liquid on surfaces of major fractures, in minor fractures opening upward, and perched liquid in structural traps. Continued production is from existing steam and vaporization of less-accessible reservoir liquid as well as from injected water and possibly from underexploited areas at the reservoir margins.

Before 1987 much of the steam produced from The Geysers probably originated from vaporization of easily accessible liquid. The field-wide pressure decline after 1987 indicated that the amount of easily accessible liquid had declined rapidly throughout the interconnected reservoir. Continued production is largely from existing steam and less-accessible liquid. This liquid is probably contained in limited matrix porosity (< 2% in Geysers graywacke; G.S. Bodvarsson, personal communication, 1992) and in small fractures of matrix blocks. The amount that this "matrix" liquid contributes to steam flow is indicated at least semiquantitatively by the gas equilibria calculations (Figure 2). At the NCPA field, vaporization of matrix liquid may still provide more than 75 or 80% of production from most wells. The rate at which the steam produced by vaporization of liquid within the matrix blocks can move to large fractures connecting to wells is limited by permeability. The Geysers cannot boil dry immediately (unlike a teakettle), but the rate of boiling may be limited. If the indication from gas geothermometry that most of present steam is from matrix blocks, then the amount of liquid water in the reservoir may be large but the production rate limited. This suggests that The Geysers will continue to be productive for a long time but at a lower rate.

REFERENCES

Beall, J.J., and Box, W.T., Jr., 1992. Recovery of injected condensate as steam in the south Geysers field. Geothermal Resources Council Special Report No. 17, p. 151–157.

D'Amore, F., and Truesdell, A.H., 1979. Models for steam chemistry at Larderello and The Geysers. *In* Proceedings, 5th Workshop on Geothermal Reservoir Engineering, Stanford, California, p. 283–297.

D'Amore, F., Celati, R., and Calore, C., 1982. Fluid geochemistry applications in reservoir engineering (vapor-dominated systems). *In* Proceedings, 8th Workshop on Geothermal Reservoir Engineering, Stanford, California, p. 295–308.

Enedy, S.L., Enedy, K.L., and Maney, J., 1992. Reservoir response to injection in the southeast Geysers. Geothermal Resources Council Special Report No. 17, p. 211–219.

Giggenbach, W.F., 1980. Geothermal gas equilibria. Geochim. Cosmochim. Acta, v. 44, p. 393–410.

Nuti, S., Calore, C., and Noto, P., 1981. Use of environmental isotopes as natural tracers in a reinjection experiment at Larderello. *In* Proceedings, 7th Workshop on Geothermal Reservoir Engineering, Stanford, California, p. 85–89.

Pruess, K., and Narasimhan, T.N., 1982. On fluid reserves and the production of superheated steam from fractured, vapor-dominated geothermal reservoirs. J. Geophys. Res., v. 87, p. 9329–9339 (LBL-12921).

Truesdell, A.H., and White, D.E., 1973. Production of superheated steam from vapor-dominated geothermal reservoirs. Geothermics, v. 2, no. 3-4, p. 154–173.

Truesdell, A.H., Haizlip, J.R., Box, W.T., and D'Amore, F., 1987. Fieldwide chemical and isotopic gradients in steam from The Geysers. *In* Proceedings, 12th Workshop on Geothermal Reservoir Engineering, Stanford, California, p. 241–246.

Effects of Periodic Atmospheric Pressure Variation on Radon Entry into Buildings

Y. W. Tsang and T. N. Narasimhan

Radon is produced within the soil by the radioactive decay of radium, which is present in all earth-crustal materials, and is transported within the soil both by diffusion and advective flow of soil gas. At the soil-basement interface, radon enters buildings through restricted openings (cracks, joints, and holes). Existing data (Nazaroff et al., 1988; Nazaroff and Nero, 1988) indicate that high concentrations of indoor radon are usually associated with elevated influx rates of radon that is advectively transported with the bulk soil gas inflow. Current reasoning is that the bulk soil gas entry into buildings is driven by small pressure differentials (on the order of a few pascals) between the basement and the outside atmosphere. The pressure differences are caused by indoor-outdoor temperature differences, interaction of wind with the building envelope, and operation of exhaust fans.

It is known that the transient barometric pressure fluctuations consist of periodic components with amplitudes ranging from a few pascals for periods of minutes to a few hundred pascals in diurnal variations. Since these transient pressure variations have magnitudes far larger than the pressure difference responsible for steady airflow, the question arises as to the effect of the atmospheric pressure pumping on radon entry rate into buildings. Here we report the results of our investigation (Tsang and Narasimhan, 1992) on the transport of radon by soil gas into building basements during periodic variations in barometric pressure.

MODELING STUDIES

To study the combined effects of barometric fluctuations and constant underpressure on soil gas inflow and radon entry at a basement, we define the problem as shown schematically in Figure 1. The water table lies 5 m below the land surface and 3 m below the 10-m-wide basement floor. In the absence of all driving forces except gravity, the soil air within the soil formation will be static if the gas

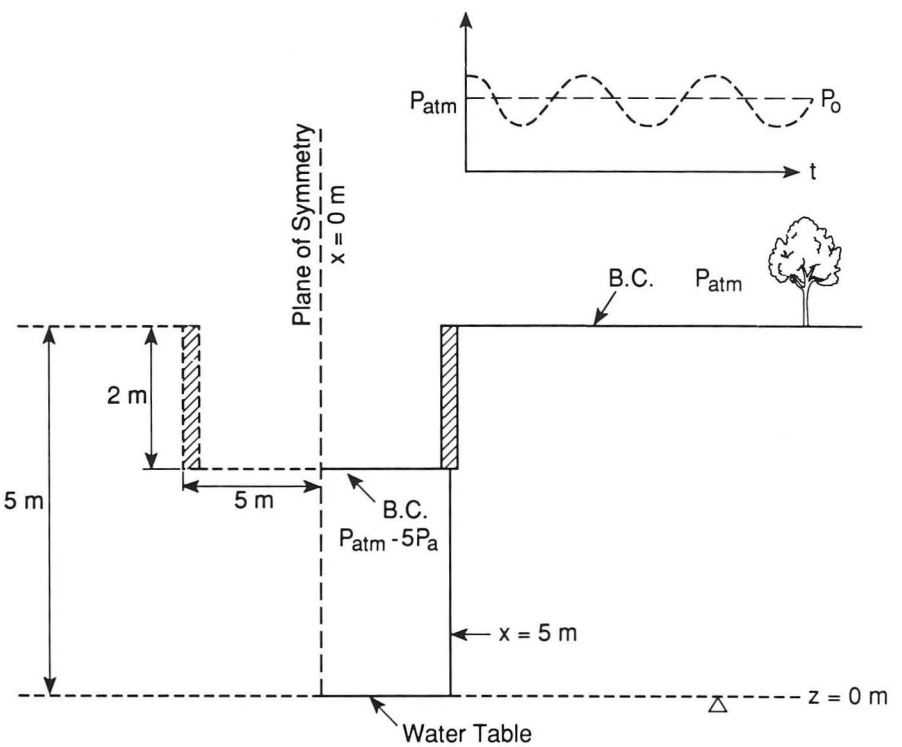

Figure 1. Schematic diagram for the basement configuration and pressure boundary conditions for modeling radon entry. [XBL 899-3439]

pressure at each elevation, z, above the water table is $P_0(z) = \overline{P}_{wt} - \rho g z$, where $\overline{P}_{wt}$ is the mean air pressure at the water table (assumed throughout this work to be 10^5 Pa), ρ is the density of air, and g is acceleration due to gravity. Pressure boundary conditions that would induce persistent air inflow into the basement were chosen as follows. The mean pressure $\overline{P}$ at the land surface is equal to P_0 (z = 5 m), and the mean pressure at the basement floor is assumed to be always 5 Pa below that corresponding to the pneumostatic state, P_0 (z = 3 m) – 5 Pa, thus ensuring a continuous Darcy flow of soil gas into the basement. The fluctuations in the atmospheric pressure are assumed to be felt at both the land surface and at the basement floor with no damping or phase lag. For our initial studies, the atmospheric pressure fluctuations are assumed to consist of a single sinusoidal component with a given amplitude and frequency, oscillating around the respective mean values of $\overline{P}$ at the outside land surface and the basement. Two frequencies with representative values of amplitudes (based on a Fourier decomposition of barometric pressure data) are chosen in this study to investigate the dependence of air flow and radon entry on barometric pressure pumping. They are (1) a short period of T = 0.5 hr with pressure amplitude A = 50 Pa and (2) a diurnal variation with a 24-hr period and the typical pressure amplitude of 250 Pa.

Two boundary conditions at the basement floor are implemented. One is an open boundary over the entire floor; this corresponds to a basement with no impermeable covering such as a concrete slab, referred hereafter to as the dirt floor basement. The other is a closed boundary, except for a 1-cm opening centered at x = 4.4 m (0.6 m from the basement edge); this corresponds to a basement covered by an "impermeable" concrete slab except for small penetrations (cracks, joints, holes) that extend between the indoors and the soil.

For our calculations we use an isothermal, multidimensional fluid flow and chemical transport model CHAMP (Narasimhan et al., 1985). We idealize the configuration shown in Figure 1 as a two-dimensional XZ planar region with a unit thickness in the third dimension Y. We consider a simplified system where the permeability is assumed not to vary with distance from the water table, and in most cases a homogeneous soil formation is assumed, where modeling studies are carried out with permeabilities ranging from 10^{-13} m^2 to 10^{-10} m^2 for both the dirt floor basement configuration as well as the impermeable basement floor with a 1-cm crack configuration. The only type of permeability heterogeneity considered in this study is the special case where a thin layer immediately below the basement floor has a permeability a few orders of magnitude larger than the rest of the soil formation. This corresponds to the physical situation where a porous sublayer of highly permeable aggregate is present below the basement floor. The permeability value chosen for this high-permeability layer of thickness Δz = 0.4 m is 10^{-10} m^2. For the radon source in soil, we assume a uniform production rate of 0.1836 Bq/m^3-s, per unit volume of soil gas, with a decay constant of 2.1×10^{-6}/s, which corresponds to the radon half-life of 3.8 days. The coefficient of diffusion of radon in soil, corrected for soil porosity and tortuosity effects, is chosen to be 1×10^{-6} m^2/s.

RESULTS—RADON ENTRY INTO A BASEMENT

Figure 2 shows (1) the time-varying oscillatory radon entry rate (the top four curves with reference to units on the left ordinate) for the basement with the 1-cm crack configuration when the forcing function has a period of 0.5 hr and (2) the sinusoidal time variation of the pumping pressure (bottom curve with reference to units on the right ordinate). Radon fluxes are shown for two cases: $k = 10^{-10}$ m^2 (solid curve) and $k = 10^{-11}$ m^2 (broken curve). The steady rates of radon entry into the basement in the absence of pressure pumping are represented by the two horizontal lines at –0.52 Bq/s (for $k = 10^{-10}$ m^2) and –0.075 Bq/s (for $k = 10^{-11}$ m^2). The negative sign attached to the radon fluxes simply indicates that the direction of radon flux is into the basement. The pressure increases in the first half of the 0.5-hr period, causing the air to flow from the basement back into the soil formation. In the modeling, we impose at the basement the boundary condition that the radon concentration is zero; this is based on the implicit assumption that the air in the basement is quickly mixed to dilute the influx of radon. Hence the air that is flowing back from the basement into the soil formation effectively carries no radon, thus forcing the advective

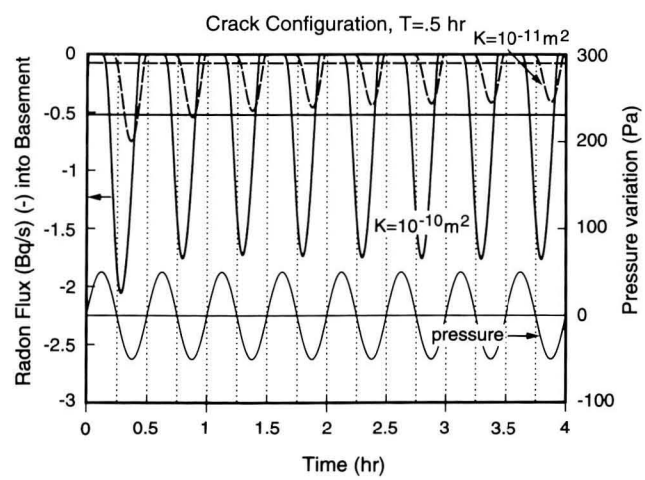

Figure 2. Radon inflow into a basement crack with and without pressure pumping of T = 0.5 hr for permeabilities 10^{-10} and 10^{-11} m^2 and pressure variation. [XBL 9110-6109]

radon flux to go to zero for the first part of the pumping period in Figure 2. Figure 2 displays the total radon flux, which includes both the advective and diffusive contributions; the fact that in the first part of the pumping cycle the total inflow practically reduces to zero indicates that the steady-state radon flow is dominated by advective flux and that there is negligible contribution from the diffusive radon flow. During the second part of the 0.5-hr pumping period, the pressure decreases below its mean value, hence the air flow from the soil column into the basement increases, carrying with it additional advective radon. If the radon flux is exactly in phase with the pumping pressure, then the radon entry will decrease for the first half and then increase for the second half of the pumping period. Note that, instead, there is a phase lag between the radon flow and the pressure variation. The total amount of radon entry into the basement for the cases with or without pressure pumping is compared by the estimated area enclosed by the radon flux curve and the axis $x = 0$ in each period. Let the area enclosed by the horizontal line of the steady-state radon flux and the axis $x = 0$ be A_1, and let the area enclosed by the oscillatory radon flux and the axis $x = 0$ be A_2. The percent increase in radon entry is defined as $[(A_2 - A_1)/A_1] \times 100$ and is given in Table 1.

The simulation results for the 1-cm crack configurations are summarized in Table 1. Table 1 is organized as follows. The first column specifies the absolute permeability, the second through fourth columns relate to soil gas flow, and the fifth through eighth columns relate to radon entry. In particular, the second column gives the steady-state soil air flow into the basement; that is, the air flux with only the –5 Pa of underpressure at the basement (in the absence of sinusoidal pressure pumping). With the sinusoidal pressure pumping, the air flux becomes oscillatory in time about the steady-state value. Columns 3 and 4 list the ratio of the amplitude of the oscillatory soil air flow to the steady-state value for the pumping periods of 0.5 and 24 hr, respectively. The fifth column lists the steady state total radon flux into the basement, including both the advective and diffusive contributions. The sixth column gives contributions from only the diffusive radon flow into the basement; that is, the influx of radon in the absence of all pressure differences. The diffusive flux is of course independent of the permeability. The seventh and eighth columns list, respectively, the percentage increase in radon entry (with reference to column 5) into the basement from sinusoidal pressure pumping with oscillatory periods of 0.5 and 24 hr and amplitudes of 50 and 250 Pa. Since the radon flux at the basement is oscillatory under the influence of pressure pumping, the percentage increase in radon entry over the constant steady-state value are time averages, as discussed earlier.

Columns 5 through 8 of Table 1 list the radon entry into the basement. In column 5, the steady-state radon flow is dominated by the diffusion process in the lowest-permeability case studied: (10^{-13} m^2); for the other cases, the steady radon inflow increases as permeability increases because of the advective process. We note that the increase of radon entry into the basement due to atmospheric pumping is not directly proportional to the soil permeability. With a high-permeability soil, there is large enhancement of radon inflow during that part of the cycle when the pumping pressure is decreasing, yet the radon inflow into the basement is forced to zero when the pressure is increasing. The steady-state radon inflow from the basement depressurization alone in the absence of pumping also increases with permeability. Consequently the relationship between permeability and increase in radon entry is complex. It is in the intermediate permeability range that the

Table 1. Air flow and radon entry at a basement crack with constant underpressure of 5 Pa in the absence or presence of barometric pumping.

Soil k (m^2)	Air flux (kg/s)			Radon entry (Bq/s)			
	Steady state	Ratio of oscillatory amplitude to steady state		Steady state		Percent increase of radon entry with pressure pumping	
		T = 0.5 hr A = 50 Pa	T = 24 hr A = 250 Pa	Diffusive + advective	Diffusive alone	T = 0.5 hr A = 50 Pa	T = 24 hr A = 250 Pa
10^{-10}	0.107×10^{-4}	2.9	0.3	0.520	0.011	10	0.5
10^{-11}	0.107×10^{-5}	12	3.1	0.075	0.011	38	6
10^{-12}	0.107×10^{-6}	15	28	0.015	0.011	31	120
10^{-12}*	0.259×10^{-6}	29	28	0.022	0.011	78	190
10^{-13}	0.107×10^{-7}	17	64	0.011	0.011	1	32
10^{-13}*	0.263×10^{-7}	41	131	0.012	0.011	31	198

*With a 0.4-m thick layer of aggregate ($k = 10^{-10}$ m^2) beneath the basement slab.

largest percentage increase in radon entry over time is found. This is the case when the steady-state radon inflow is not too large yet there is appreciable enhancement in advective radon inflow when the pressure is decreasing. The largest predicted increases (for uniform soil permeability) are for the cases $k = 10^{-11}$ m^2 and $T = 0.5$ hr in the dirt basement configuration and $k = 10^{-12}$ m^2 and $T = 24$ hr in the crack configuration. Table 1 shows that the increase in radon inflow is even greater if a high-permeability (10^{-10} m^2) layer is present beneath the concrete slab. This kind of permeability heterogeneity maximizes the effect of the "local" enhancement of the pumping advective radon transport at the basement opening, yet the effective permeability of the total soil mass remains small, since the high-permeability layer constitutes only a small fraction of the total volume; the small effective permeability ensures that steady-state radon inflow due to basement depressurization remains small if the soil permeability is $\leq 10^{-12}$ m^2.

SUMMARY AND CONCLUSION

Study results show that for a homogeneous soil medium, the largest increase in radon entry (over steady-state advective transport with a 5-Pa underpressure at the basement) occurs for $k = 10^{-12}$ m^2 with the barometric variation of period $T = 24$ hr and amplitude 250 Pa in the crack configuration. The increase is 120%. In the dirt floor configuration, the largest percentage increase is 68% over that of steady radon entry with 5 Pa underpressure at the basement for $k = 10^{-11}$ m^2 and a pumping period of 0.5 hr. The increase in radon entry with pumping is further enhanced when there is a heterogeneity in permeability arising from the physical situation of a high-permeability aggregate layer immediately below the basement floor.

The different configurations chosen (dirt floor basement and impermeable basement floor with crack) serve to demonstrate the relative importance of the different transport processes: diffusive, steady-state advective, and pressure-pumping advective. A significant result from this study is that the advective radon transport from pressure pumping may be an order of magnitude larger than the diffusive transport in the absence of a persistent underpressure at the basement, for $k = 10^{-10}$ m^2. This may help to explain indoor radon concentrations during periods of low steady-state driving force.

ACKNOWLEDGMENT

We would like to thank Mohsen Alavi of the Earth Sciences Division of LBL for help in modifying the computer code CHAMP.

REFERENCES

Narasimhan, T.N., Alavi, M., Liu, C.W., 1985. CHAMP—A computer code for modeling transient fluid flow and chemical transport with hydrodynamic dispersion in variably saturated systems. *In* Proceedings of the Symposium on Groundwater Flow and Transport Modeling for Performance Assessment of Deep Geologic Disposal of Radioactive Waste: A Critical Evaluation of the State of the Art. Albuquerque, New Mexico, May 20–21.

Nazaroff, W.W. and Nero, A.V., Jr. (eds.), 1988. Radon and Its Decay Products in Indoor Air. Wiley, New York, p. 57–111.

Nazaroff, W.W., Moed, B.A., and Sextro, R.G., 1988. Soil as a source of indoor radon: Generation, migration, and entry. *In* W.W. Nazaroff and A.V. Nero, Jr. (eds.), Radon and Its Decay Products in Indoor Air. Wiley, New York, p. 57–111.

Tsang, Y.W., and Narasimhan, T.N., 1992. Effects of periodic atmospheric pressure variation on radon entry into buildings. J. Geophys. Res., v. 97, no. B6, p. 9161–9170.

Studies of the Role of Fault Zones on Fluid Flow Using the Site-Scale Numerical Model of Yucca Mountain

C. S. Wittwer, G. Chen, and G. S. Bodvarsson

Lawrence Berkeley Laboratory (LBL) in cooperation with the United States Geological Survey (USGS) has developed a three-dimensional site-scale numerical model of the unsaturated zone at Yucca Mountain, Nevada. The hydrogeology of the site is controlled by fluid flow through heterogenous, unsaturated fractured and porous layers of volcanic tuffs in an arid environment. The site-scale model covers an area of about 30 km^2 around the potential repository area and is bounded by major fault zones to the north (Yucca Wash fault), east (Solitario Canyon fault), and west (Bow Ridge fault). The numerical grid was designed to account for the geological and hydrogeological mechanisms that have been described in the literature as being relevant to moisture flow at Yucca Mountain (Montazer

and Wilson, 1984). Additional data treatment reported in Wittwer et al. (1992) led to the development of a highly nonuniform three-dimensional numerical grid that reproduces both the complex geology of this fractured region and the spatial distribution of hydrogeological units and explicitly includes the offset of the hydrogeological units due to three major fault zones.

This article briefly summarizes results of steady-state simulations published in Wittwer et al. (1993) and performed with two NW to SE cross-sectional submodels extracted from the three-dimensional numerical grid of the site-scale model.

METHODOLOGY

The three-dimensional numerical grid consists of about 5000 elements and 20,000 connections. The horizontal grid for the site-scale model is shown in Figure 1. The vertical grid geometry consists of seventeen nonuniform layers that represent, as closely as possible, lithological variations within the main hydrogeological units; these include extremely massive vitrophyre layers at the border of the main ash flows, the occurrence of lithophysae cavities within the welded units, and the presence of zeolitic alteration. The computer-developed grid also allows one to readily modify and adapt the nonuniform numerical grid to new data or new problems.

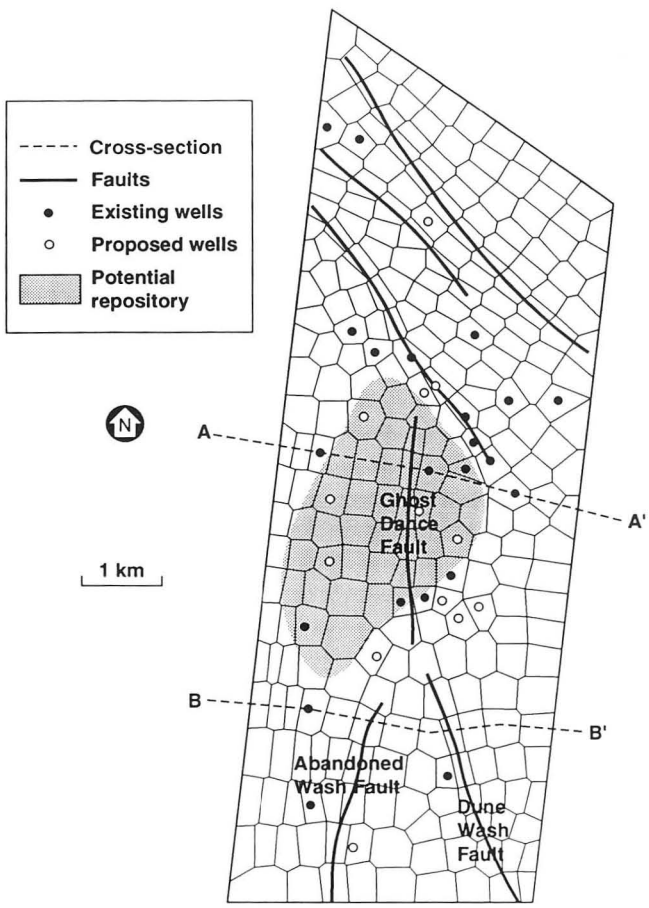

Figure 1. Horizontal grid for the site-scale model showing the two cross-sectional models. [XBL 936-879]

The simulations discussed here were performed with two-dimensional cross sections extracted from the three-dimensional grid. The northern cross section (A-A′) cuts the site-scale model area at the level of the potential repository and includes the Ghost Dance fault (see Figure 1). The second cross section (B-B′) is located about 3 km farther south and intersects the Abandoned Wash and Dune Wash faults.

Representative values shown in Table 1 for the parameters of the rock matrix were compiled from data found in the literature. The values used in the models were chosen on the basis of the distribution of the measured parameter values, the locations of the samples within the different units, and the lithological similarities within each of the hydrogeological layers.

The method developed by van Genuchten (1980) was used to represent the relationship between capillary pressure and liquid saturation, as well as between relative permeability and liquid saturation. New moisture-retention measurements performed on core and surface samples by Flint and Flint (personal communication, 1992) were used in this study, as these represent the best current available data sets.

As a high fracture density has been reported in the literature for the welded units, fracture flow representation was added to the rock matrix characteristic curves for the Tiva Canyon and Topopah Spring hydrogeological units. The equivalent continuum approximation developed by Klavetter and Peters (1986) on the basis of capillary equilibrium between the matrix and the fracture was used to integrate fracture flow to matrix flow.

Because no capillary functions have been reported in the literature for fracture flow, the approach used in the simulations is based on the assumption that the fractured medium has the same pore size distribution as the rock matrix for each rock type. The absolute fracture permeability was taken to be equal to 10^{-11} m^2 on the basis of values reported by Klavetter and Peters (1986). The air entry value is predicted from the saturated permeability value k_s by using the scaling relationship proposed in Wang (1992). The combined fracture and matrix characteristic curves were developed for the layers of the welded Tiva Canyon and Topopah Spring units. These curves show that fracture-dominated flow begins between 1000 and 3500 Pa for the various sublayers. The approach used therefore assumes only matrix flow until very high liquid saturations are reached.

Table 1. Rock matrix properties for the seventeen model layers.

Hydrogeological unit	Lithology	Sub-layer	Porosity Range (%)	Porosity Model (%)	Permeability Range (m^2)	Permeability Model (m^2)	$\alpha \times 10^{-5}$ (Pa)	n	m
Tiva Canyon	Caprock								
welded tuff	Upper cliff	1.1	6 – 24	17	2E-19 – 2E-14	1E-18	0.067	1.33	0.250
	Upper lithophysae								
	Clinkstone								
	Zone								
	Lower lithophysae	1.2	6 – 28	17	1E-20 – 2E-16	2E-18	0.067	1.33	0.250
	Hackly zone								
	Columnar zone								
	Vitrophyre	1.3	2 – 10	6	4E-17 – 1E-15	1E-18	0.067	1.33	0.250
Paintbrush	Shardy base	2.1	12 – 54	33	1E-17 – 5E-13	1E-13	1.67	1.20	0.167
nonwelded tuff	Nonwelded tuffs	2.2	18 – 57	37	5E-16 – 5E-12	5E-14	6.00	1.19	0.163
	Bedded tuffs								
	Nonwelded tuffs	2.3	10 – 55	32	4E-16 – 6E-13	1E-13	4.33	1.17	0.142
Topopah Spring	Vitrophyre	3.1	3 – 9	6		1E-18	0.067	1.41	0.290
welded tuff	Caprock	3.2	9 – 22	15	8E-17 – 4E-14	4E-16	0.125	1.22	0.180
	Rounded zone								
	Upper lithophysae	3.3	10 – 16	13	5E-20 – 3E-18	4E-18	0.20	1.28	0.220
	Middle non-lithophysae	3.4	6 – 22	14	4E-20 – 1E-17	5E-18	0.133	1.33	0.250
	Lower								
	Lithophysae								
	Lower non-lithophysae	3.5	6 – 18	12	4E-20 – 1E-17	5E-18	0.067	1.33	0.250
	Vitrophyre	3.6	1 – 10	5	5E-20 – 2E-17	1E-18	0.067	1.41	0.290
Calico Hills	Bedded tuffs	5.1	23 – 48	35	2E-13	2.0	1.15	0.130	
nonwelded tuff	Nonwelded vitric	5.2	8 – 48	28	1E-18 – 2E-15	3E-13	2.0	1.14	0.120
	Bedded tuffs								
	Nonwelded tuffs	5.3	30 – 48	39		3E-13	2.0	1.14	0.120
	Slightly zeolitized								
	Zeolitized,	5.4	14 – 36	25	5E-19 – 7E-17	1E-16	0.1	1.23	0.190
	Partly argillic	5.5							
	Zeolitized, devitrified								
	Zeolitized								

The three fault zones are represented in the numerical grid by columns of gridblocks about 200 to 350 m in width. In the present study, fault zones were treated as porous media with either very high or very low permeability compared with the neighboring rock matrix. The van Genuchten model was used to calculate the capillary pressure curves, as well as the relative permeability curves, of the fault zones for these two test cases.

RESULTS OF TWO-DIMENSIONAL NUMERICAL SIMULATIONS

Numerical simulations were performed with the computer code TOUGH2 (Pruess, 1990), which is based on the integral finite difference method and which accounts for the transport of moisture, air, and heat in unsaturated porous and fractured media. Capillary pressure and liquid saturation distributions for the two-dimensional vertical cross

sections were calculated for three spatially uniform infiltration rates of 10^{-1} to 10^{-3} mm y^{-1} .

Results for the set of simulations using the maximum infiltration rate of 10^{-1} mm y^{-1} used in this study, are shown in Figure 2a for capillary pressure and in Figure 2b for liquid saturation. The capillary pressure decreases in the Tiva Canyon, down to the middle of the Topopah, where high liquid saturations are reached in a low-permeability layer representing the upper lithophysae zone. The saturation distribution shows distinct features. The liquid saturation in the Tiva Canyon unit decreases with depth. A high-saturation zone occurs at the bottom of the Topopah Spring, just above the water table in the eastern part of the model, and propagates westward at the contact with the Calico Hills vitric layers slightly beyond the Ghost Dance fault. Liquid saturations of the different units vary within well-defined limits: for example, Tiva Canyon (0.97–0.91), Paintbrush (0.78–0.93), Topopah Spring (0.78–0.93), Calico Hills vitric (0.55–0.70), and Calico Hills zeolitic (0.90–0.99). Because of the chosen characteristic curves, low liquid saturations occur in the fault zone when it is modeled as a high-permeability zone. On the contrary, very high saturations occur in high-permeability fault zones.

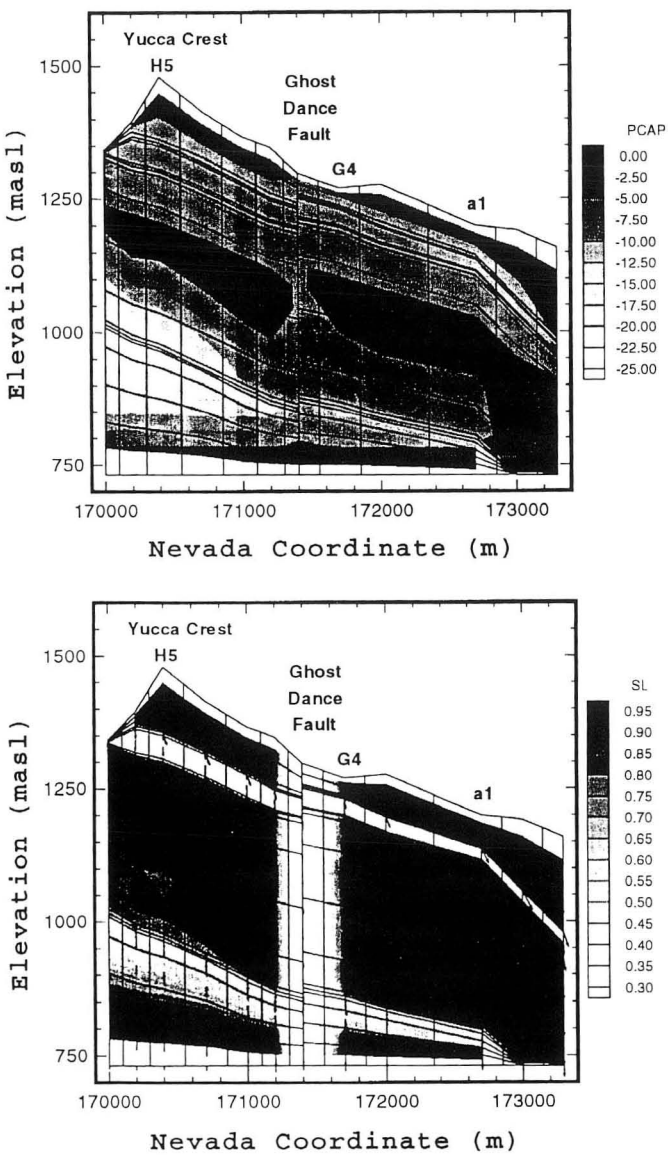

Figure 2. Capillary pressure distribution (**a**) and liquid saturation distributon (**b**) for cross section A-A′ with infiltration rate of 10^{-1} mm y^{-1} and a saturated permeability of 10^{-11} m^2 for the Ghost Dance fault. [XBL 936-880]

The saturation distribution for a decreased infiltration rate of 10^{-2} mm y^{-1} is similar to the previous simulations, but the liquid saturations have decreased to 0.84–0.80 in the Tiva Canyon, 0.40–0.53 in the Paintbrush, and 0.65–0.90 in the Topopah Spring. Numerical simulations were also run to reach steady state with an infiltration rate of 10^{-3} mm yr^{-1}. The capillary pressure distribution obtained for this very low rate does not deviate strongly from static conditions. The liquid saturations in the three upper units have now decreased even further to 0.77–0.67 in the Tiva Canyon, 0.35–0.45 in the Paintbrush, and 0.60–0.85 in the Topopah Spring.

Simulations with cross section B-B′ show the effects of two fault zones (the Abandoned Wash fault and the Dune Wash fault). Except for a few details, the distribution using high- and low-permeability fault zones do not differ significantly from the equivalent cases that include only the Ghost Dance fault.

Lateral flow occurs when the vertical flow is diverted because of the tilting of the layers, and may be enhanced by the permeability contrast. In our simulations, this lateral eastward flow is terminated by the fault zones, because of their assumed flow characteristics. As the intensity of lateral flow depends on the length of the flow path and the volume of the drainage zone, the flows calculated on the eastern side of the Abandoned Wash and Dune Wash faults are smaller than those defined at the Ghost Dance fault.

Vertical flow rates were also studied within the Ghost Dance fault zone. A general feature shows a strong decrease in vertical flow rate with depth in the fault zone, suggesting that water flows into the adjacent formation. This effect seems to be limited to the gridblocks close to the fault zone. The reason for this outflow from the fault zone is, again, the characteristic curves used. High flow within the fault zone results in relatively high capillary pressures, hence the moisture leaves the fault zone for the lower (more negative) capillary pressure of the surrounding rocks.

Outside of the fault zones, vertical flow is dominant, and eastward lateral flow remains about 100 times lower than vertical flow and is even lower in the vitrophyre lay-

ers, which have very low permeability. Increased lateral flow mainly occurs in the top of the Topopah, in the more permeable layer representing the rounded zone. Weaker lateral flow also occurs in the first layer of the Paintbrush unit, just below the very low permeable vitrophyre layer of the Tiva Canyon.

The various simulations show that perched water zones do not occur in the present set of simulations, because of the relatively low infiltration rates used. Potential zones are located in the base of the Topopah Spring, especially east of the Ghost Dance fault.

CONCLUSION

Two-dimensional simulations were carried out to investigate the role of major faults (Ghost Dance, Abandoned Wash, and Dune Wash) on fluid flow within the unsaturated zone of the site-scale model. As hydrological properties of these faults are not known at present, bounding calculations were performed in order to study the effect of the faults. The faults were assumed to have either very high permeability and low potential capillary pressure or very low permeability and high potential capillary pressure. The approach taken in the design of the numerical grid, together with the numerical capabilities of the TOUGH2 simulator, allows one to analyze the results in terms of preferential pathways, lateral flow, and capillary barriers. Future work will include higher infiltration rates and different representations of the fault zones.

Capillary pressure and liquid saturation distributions are obtained for cross sections with one or two fault zones with infiltration rates of 10^{-1} to 10^{-3} mm y^{-1} and high- and low-permeability fault zones. All results are strongly dependent on the characteristic curves chosen for the different rock types. For high infiltration rates, liquid saturations remain in well-defined limits for each of the hydrogeological units (Tiva Canyon, 0.97–0.91; Paintbrush, 0.78–0.93; Topopah Spring, 0.78–0.93; Calico Hills vitric, 0.55–0.70; and Calico Hills zeolitic, 0.90–0.99), and when less water flux is assumed to infiltrate, the range of liquid saturations decreases in the upper three units. Very different saturations are reached in the high- and low-permeabillity fault zones, depending on their characteristic curves. Vertical flow rate is dominant in all simulations, and lateral flow is generally lower than vertical flow. Increased lateral flow occurs in the upper part of the Topopah Spring and the Paintbrush. No perched water zones were created during the current set of simulations.

In the case of a permeable fault, the assumed characteristic curves result in relatively high (less negative) capillary pressures and very low liquid saturations at steady state. This in turn prevents the entry of flow from neighboring formations into the fault, and in fact some of the infiltration prescribed on the top of the fault is lost to those surrounding rocks. One would get significant vertical flow in a fault only if its properties are such that the characteristic curves are similar to those of the adjacent formations (i.e., not much lower air entry value) and the absolute saturated permeability is significantly larger.

ACKNOWLEDGMENT

The authors appreciate the contributions of M. Chornack, A. Flint, L. Flint, E. Kwiclis, and R. Spengler, U.S. Geological Survey, to this work.

REFERENCES

Klavetter, E.A., and Peters, R.R., 1986. Estimation of hydrologic properties of an unsaturated fractured rock mass. Sandia National Laboratories Report SAND84-2642.

Montazer, P., and Wilson, W.E., 1984. Conceptual hydrologic model of flow in the unsaturated zone at Yucca Mountain, Nevada. Water Resources Investigations Report 84-4355, U.S. Geological Survey.

Pruess, K., 1990. TOUGH2-A general-purpose numerical simulator for multiphase fluid and heat flow. Lawrence Berkeley Laboratory Report LBL-29400.

Pruess, K., Wang, J.S.Y., and Tsang, Y.W., 1990. On thermohydrological conditions near high-level nuclear wastes emplaced in partially saturated fractured tuff, Part 2. Effective continuum approximation. Water Resour. Res., v. 26, no. 6, p. 1249–1261.

van Genuchten, M.Th., 1980. A closed-form equation for predicting the hydraulic conductivity of unsaturated soils. Soil. Sci. Soc. Am. J., v. 44, p. 892–898 .

Wang, J.S.Y., 1992. Variations of hydrological parameters of tuff and soil. Proceedings, Third International Conference on High-Level Radioactive Waste Management, Las Vegas, Nevada, April 12–16, p. 727–731.

Wittwer, C.S., Bodvarsson, G.S., Chornack, M.P., Flint, A.L., Flint, L.E., Lewis, B.D., Spengler, R.W., and Rautman, C.A., 1992. Design of a three-dimensional site-scale model for the unsaturated zone at Yucca Mountain, Nevada. Proceedings, Third International High Level Radioactive Waste Management Conference, Las Vegas, Nevada, April 12–16, p. 263–271.

Wittwer, C.S., Chen, G., and Bodvarsson, G.S., 1993. Studies of the role of faults on fluid flow using the site-scale numerical model of Yucca Mountain. Submitted for publication in the Proceedings of the Fourth International High Level Radioactive Waste Management Conference, Las Vegas.

An Inverse Procedure for Estimating the Unsaturated Hydraulic Conductivities of Volcanic Tuffs

R. W. Zimmerman, G. S. Bodvarsson, A. L. Flint, and L. E. Flint**

Yucca Mountain, Nevada, is a potential site for a Department of Energy underground radioactive waste repository. The potential repository horizon is located above the water table in a formation consisting of volcanic tuffs. A key criterion in judging the suitability of the site is the rate, if any, at which precipitation percolates down to the water table. This flux of water could conceivably transport radionuclides to the saturated zone, so that they might eventually reach the groundwater supply. As water infiltrates down from the surface, it may at first flow mainly through the fracture network, but some of the water is imbibed from the fractures into the matrix blocks (Travis et al., 1984; Nitao and Buscheck, 1991). The rate at which this imbibition occurs is an important factor in determining whether water from a precipitation event is able to reach the water table or becomes absorbed into the matrix blocks and eventually evaporates out to the atmosphere. The parameters that determine this rate of matrix block imbibition include the size and shape of the matrix blocks, as well as the two characteristic functions of the tuff. These functions relate the water content of the tuff to its capillary pressure and its hydraulic conductivity. Because of the heterogeneity of the rocks at Yucca Mountain, it will be necessary to measure, or otherwise determine, these hydrologic properties at many locations. Because of the very small pore sizes of most of the tuffs found at Yucca Mountain, measurements of capillary pressure and hydraulic conductivity, as functions of water content, are very time-consuming, because these measurements require that either a steady state or an equilibrium state be reached. For this reason, it would be advantageous to be able to estimate the characteristic functions from other, more readily measurable properties.

One readily measurable property that is also of major importance to the overall hydrological behavior of Yucca Mountain is sorptivity (Philip, 1955), which quantifies the initial rate of imbibition during a one-dimensional imbibition process. The sorptivity is not a basic hydrological property of a rock, since it refers to a specific process. Nevertheless, it is related to, and is a function of, the above-mentioned characteristic functions. The advantage of measuring sorptivity is that because it intrinsically involves a transient process, measurements of sorptivity do not require that the sample reach equilibrium (or a steady state). We have developed an inverse procedure for using sorptivity measurements, along with measurements of the capillary pressure function, to find the hydraulic conductivity function. This method has the advantage, unlike many other inversion procedures (cf. Mishra and Parker, 1989), of not restricting us *a priori* to any specific mathematical form for the characteristic functions. This allows us to derive characteristic curves that, when substituted into a numerical model of the unsaturated zone at Yucca Mountain (Wittwer et al., 1992), will yield computed sorptivities that agree exactly with the values measured in the laboratory. Such agreement is not possible in general if the characteristic functions are restricted in advance to be of a certain mathematical form.

SORPTIVITY OF UNSATURATED ROCK

The governing equation for one-dimensional flow of liquid water in an unsaturated porous medium is the Richards equation (Hillel, 1980):

$$\frac{\partial}{\partial x}\left[\frac{k k_r(\theta)}{\mu\phi}\frac{\partial \psi}{\partial x}\right] = \frac{\partial \theta}{\partial t} \,. \tag{1a}$$

The parameter k, with dimensions of $[L^2]$, is the absolute permeability, which is the permeability of the medium when it is fully saturated with water. $k_r(\theta)$ is the dimensionless relative permeability function, which quantifies the extent to which partial saturation with air lowers the permeability of the liquid phase. μ is the viscosity of the water $[ML^{-1}T^{-1}]$, and ϕ is the porosity of the medium; in most treatments of absorption, both of these parameters are assumed to be constant. ψ is the capillary (matric) potential of the liquid in the porous medium, with dimensions of $[ML^{-1}T^{-2}]$, and θ is the degree of liquid saturation, which is defined as the water content divided by the porosity. The two functions $\psi(\theta)$ and $k_r(\theta)$ are often collectively referred to as the characteristic functions of the porous medium. In this form of the Richards equation, we ignore the gravitational term, since its effect is negligible during imbibition experiments conducted on small samples (Zimmerman et al., 1990).

Equation (1a) can be rewritten in a slightly different form that explicitly demonstrates that it is a nonlinear diffusion equation. Using the chain rule of differentiation gives

* Hydrologic Investigations Program, U.S. Geological Survey, Mercury, Nevada 89023.

$$\frac{\partial}{\partial x}\left[\frac{kk_r(\theta)}{\mu\phi}\frac{d\psi}{d\theta}\frac{\partial\theta}{\partial x}\right]\equiv\frac{\partial}{\partial x}\left[D(\theta)\frac{\partial\theta}{\partial x}\right]=\frac{\partial\theta}{\partial t}\ , \tag{1b}$$

in which the only independent variable that explicitly appears is θ. The diffusion coefficient $D(\theta)$ is given by $kk_r(\theta)\psi'(\theta)/\mu\phi$. The combination $kk_r\rho g/\mu$ is often referred to as the hydraulic conductivity, where ρ is the density of the fluid and g is the gravitational acceleration. Since ρ and μ are properties of the fluid, and not of the porous medium, we prefer to work with the combination $kk_r(\theta)$, which we will refer to as the permeability function of the medium.

The basic problem of one-dimensional absorption of water is specified by augmenting Eq. (1a) or (1b) with the following boundary/initial conditions:

$$\psi(x,t=0)=\psi_i\ , \tag{2}$$

$$\psi(x=0,t>0)=\psi_w\ . \tag{3}$$

The values ψ_i and ψ_w can be related to saturations θ_i and θ_w through the capillary pressure function $\psi(\theta)$. A commonly used boundary condition is $\theta_w = 0$, which is usually assumed to correspond to full liquid saturation; i.e., $\theta_w = 1$. The solution to Eq. (1) for the boundary/initial conditions given by Eqs. (2) and (3) can be expressed in terms of the Boltzmann variable, $\eta = x/\sqrt{t}$ (see Hillel, 1980). This in turn implies that the cumulative influx into the medium, $I(t)$, which has dimensions of volume of liquid [L^3], will be proportional to the cross-sectional area A and also proportional to $t^{1/2}$. The constant of proportionality was called the "sorptivity" by Philip (1955), and denoted by S, so that

$$I(t)=SAt^{1/2}\ . \tag{4}$$

The sorptivity, which has dimensions of [$LT^{-1/2}$], depends on the hydraulic properties of the porous medium, as well as on the initial saturation. If the hydraulic properties were known, the sorptivity could be found by solving the Richards equation using analytical or numerical methods. In practice, however, the sorptivity is much easier to measure than are either $\psi(\theta)$ or $kk_r(\theta)$. This suggests using measured values of the sorptivity to estimate the capillary pressure and/or permeability functions.

Two problems limit the possibility of finding a unique solution to estimating the characteristic functions from the sorptivity. First, since Eq. (1b) implies that $kk_r(\theta)$ and $\psi(\theta)$ affect S through the combination $kk_r(\theta)\psi'(\theta)$, it will not be possible to estimate $kk_r(\theta)$ and $\psi(\theta)$ separately. Furthermore, the sorptivity is generally not very sensitive to the diffusivity function. For example, the numerically computed sorptivity/saturation curves found by Zimmerman and Bodvarsson (1989,1991a) for media with van Genuchten (1980) and Brooks and Corey (1966) characteristic functions can be made to closely coincide over large ranges of initial saturations by proper choice of the parameters (see Zimmerman et al., 1993). Hence it would be difficult to distinguish between these two types of characteristic functions on the basis of their measured sorptivities.

INVERSION PROCEDURE

One feature of the sorptivity-saturation relationship that follows from both the van Genuchten and Brooks-Corey characteristic functions is that the $S(\theta_i)$ curve is concave downward and typically has a very steep (actually, infinite) slope at $\theta_i = 1$. In particular, for initial saturations that are close to 1, the sorptivity of a Brooks-Corey medium is proportional to $(1-\theta_i)^{1/2}$ (Zimmerman and Bodvarsson, 1991a), whereas the sorptivity of van Genuchten media varies as $(1-\theta_i)^{(n+1)/2n}$, where $n > 2$ is the van Genuchten parameter (Zimmerman and Bodvarsson, 1991b). No admissible choice of the van Genuchten or Brooks-Corey parameters will lead to sorptivities that are linear functions of the initial saturation. Some measured sorptivities of volcanic tuffs from Yucca Mountain, Nevada (Flint et al., 1993), however, have been found to be fairly well fitted with functions of the form $S(\theta_i) = S_{\max}(1-\theta_i)$, where $S_{\max}$ is a fitting parameter. To model these samples, we cannot use Brooks-Corey or van Genuchten characteristic functions but must find characteristic functions that lead to linear sorptivities.

To carry out our inversion procedure, we first note (Warrick and Broadbridge, 1992) that if the hydraulic diffusivity function $D(\theta)$ is a constant, say D_0, the sorptivity will have the form $S(\theta_i)=2\phi\sqrt{D_0/\pi}(1-\theta_i)$. A constant diffusivity is therefore consistent with the result $S = S_{\max}(1-\theta_i)$ if we make the identification

$$D_0=\frac{\pi S_{\max}^2}{4\phi^2}\ . \tag{5}$$

Some evidence that a linear sorptivity-saturation relationship corresponds *uniquely* to a constant hydraulic diffusivity is given by Zimmerman et al. (1993). Assuming therefore that the diffusivity is constant, the following relationship holds between $kk_r(\theta)$ and $\psi(\theta)$:

$$kk_r(\theta)=\frac{\mu\phi D_0}{\psi'(\theta)}\ , \tag{6}$$

which can be combined with Eq. (5) to yield

$$kk_r(\theta) = \frac{\pi\mu S_{\max}^2}{4\phi\psi'(\theta)} \,. \tag{7}$$

If we can determine $S_{\max}$ and $\psi(\theta)$ experimentally, Eq. (7) can then be used to predict the hydraulic permeability. Testing this method would require measurements of all three functions, $S(\theta_i)$, $kk_r(\theta)$, and $\psi(\theta)$. Currently, reliable data for all three of these functions are not available for many samples. As an example and test case for the method, consider sample 1UH, which is a vitrified tuff from the Calico Hills unit, with a porosity ϕ of about 0.39 (Flint and Flint, 1990). Figure 1 shows three measured values of the sorptivity as a function of initial saturation, which have been fitted with a curve of the form $S(\theta_i) = S_{\max}(1 - \theta_i)$. The value of $S_{\max}$ was found to be 9.44×10^{-5} m^2/s. Figure 2 shows the measured capillary pressures for this sample, fitted to a curve of the form $\psi(\theta) = \psi_a \theta^{-m}$, with $\psi_a = -1.50 \times 10^4$ Pa and $m = 5.45$. Since $\psi'(\theta) = -m\psi_a\theta^{-(m+1)}$, Eq. (7) yields

$$kk_r(\theta) = \frac{\pi\mu S_{\max}^2\,\theta^{m+1}}{4\phi(-m)\psi_a} = 2.19\times10^{-16}\;\theta^{6.45}\;m^2 \,, \tag{8}$$

in which the viscosity of water is taken to be 0.001 Pa·s. Figure 3 shows the permeabilities that were measured by Flint and Flint (1990) using the centrifuge method, along with those predicted by Eq. (8). The agreement is seen to

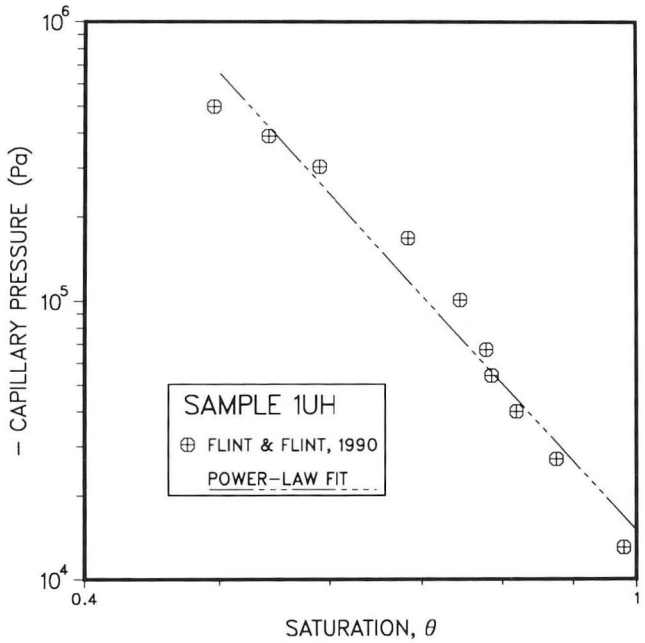

Figure 2. Capillary pressure of sample 1UH. The straight line was found by fitting $\psi(\theta)$ to a curve of the form $\psi = \psi_a\theta^{-m}$. The fitting parameters were found to be $\psi_a = -1.497 \times 10^4$ Pa and $m = 5.45$. [XBL 936-882]

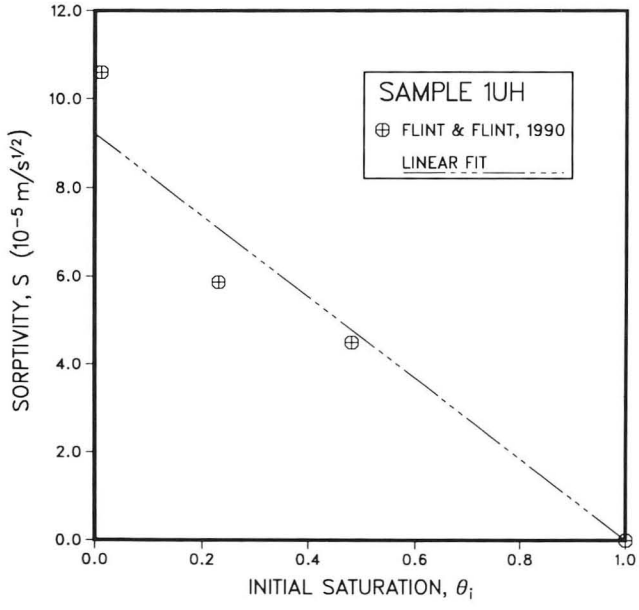

Figure 1. Sorptivity of sample 1UH, a vitrified tuff from the Calico Hills unit at Yucca Mountain, at several different initial saturations. The straight line was found by a least-squares fit to the function $S(\theta_i) = S_{\max}\,(1 - \theta_i)$. $S_{\max}$ was found to be 9.44×10^{-5} m/s$^{1/2}$. [XBL 936-881]

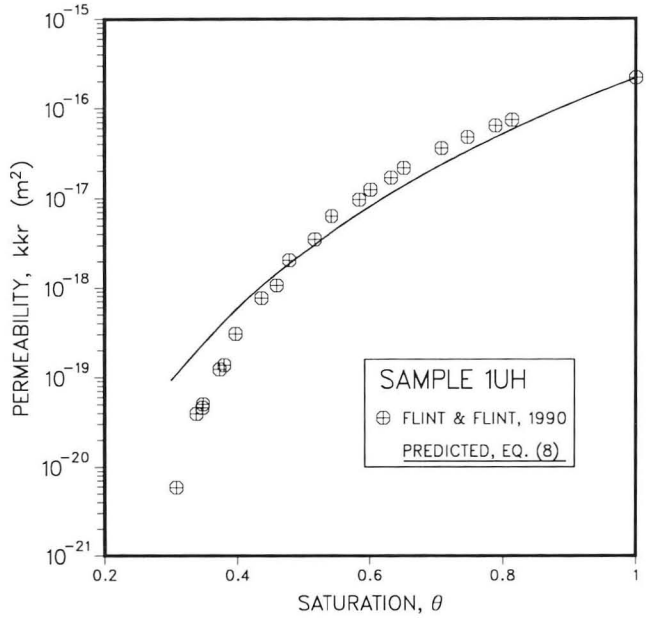

Figure 3. Hydraulic permeability of sample 1UH, as a function of saturation. The measured values are compared to the curve predicted by the inversion procedure: $kk_r(\theta) = 2.19 \times 10^{-16}\;\theta^{6.45}$ m^2. [XBL 936-883]

be fairly close, particularly when the saturation is greater than 0.40. For lower saturations, the curve in Figure 3 represents an extrapolation outside of the range where $\psi(\theta)$ data exist (see Figure 2).

SUMMARY AND CONCLUSIONS

Measurements made by Flint et al. (1993) showed that the sorptivities of some volcanic tuffs from Yucca Mountain were linear functions of the initial saturation. This is consistent with the hydraulic diffusivities of these tuffs being constant functions of the saturation. The assumption of constant diffusivity then leads to a one-to-one relationship between the capillary pressure function and the hydraulic permeability. Hence, we can use measurements of the sorptivity and capillary pressure, as functions of saturation, to find the permeability function. As an illustration of the inversion procedure, we applied this procedure to measurements on a sample of a vitrified tuff from the Calico Hills unit. The predicted permeability function was in reasonable agreement with the measured values. More data are needed to determine if this method can be reliably used to routinely predict permeabilities from the more readily measurable properties of sorptivity and capillary pressure.

REFERENCES

Brooks, R.H., and Corey, A.T., 1966. Properties of porous media affecting fluid flow. Proc. Am. Soc. Civil Eng., v. 92(IR2), p. 61–87.

Flint, A.L., and Flint, L.E., 1990. Preliminary permeability and water-retention data for nonwelded and bedded tuff samples, Yucca Mountain area, Nye County, Nevada. U.S. Geological Survey Open File Report 90-569.

Flint, A.L., Flint, L.E., and Richards, K.A., 1993. The influence of scale on calculated sorptivity values from imbibition experiments on welded and nonwelded tuff. Soil Sci. Soc. Am. J., in press.

Hillel, D., 1980. Applications of Soil Physics. Academic Press, New York.

Mishra, S., and Parker, J.C., 1989. Parameter estimation for coupled unsaturated flow and transport. Water Resour. Res., v. 25, p. 385–396.

Nitao, J.J., and Buscheck, T.A., 1991. Infiltration of a liquid front in an unsaturated, fractured porous medium. Water Resour. Res., v. 27, p. 2099–2112.

Philip. J.R., 1955. Numerical solution of equations of the diffusion type with diffusivity concentration-dependent. Trans. Faraday Soc., v. 51, p. 885–892.

Travis, B.J., Hodson, S.W., Nuttall, H.E., Cook, T.L., and Rundberg, R.S., 1984. Preliminary estimates of water flow and radionuclide transport in Yucca Mountain. Los Alamos National Laboratory Report LA-UR-84040.

van Genuchten, M.T., 1980. A closed-form equation for predicting the hydraulic conductivity of unsaturated soils. Soil Sci. Soc. Am. J., v. 44, p. 892–898.

Warrick, A.W., and Broadbridge, P., 1992. Sorptivity and macroscopic capillary length relationships. Water Resour. Res., v. 28, p. 427–431.

Wittwer, C.S., Bodvarsson, G.S., Chornack, M.P., Flint, A.L., Flint, L.E., Lewis, B.D., Spengler, R.W., and Rautman, C.A., 1992. Design of a three-dimensional site-scale model for the unsaturated zone at Yucca Mountain, Nevada. *In* Proceedings, Third International High-Level Radioactive Waste Management Conference, Las Vegas, Nevada, April 12–16, 1992, p. 263–271 (LBL-31799).

Zimmerman, R.W., and Bodvarsson, G.S., 1989. An approximate solution for one-dimensional absorption in unsaturated porous media. Water Resour. Res., v. 25, p. 1422–1428 (LBL-25629).

Zimmerman, R.W., and Bodvarsson, G.S., 1991a. A simple approximate solution for horizontal infiltration in a Brooks-Corey medium. Transport in Porous Media, v. 6, p. 195–205 (LBL-27674).

Zimmerman, R.W., and Bodvarsson, G.S., 1991b. Reply to Parlange et al. Water Resour. Res. v. 27, p. 2161–2162 (LBL-29912).

Zimmerman, R.W., Bodvarsson, G.S., and Kwicklis, E.M., 1990. Absorption of water into porous blocks of various shapes and sizes. Water Resour. Res., v. 26, p. 2797–2806 (LBL-27511).

Zimmerman, R.W., Bodvarsson, G.S., Flint, A.L., and Flint, L.E., 1993. An inverse procedure for estimating the unsaturated hydraulic conductivities of volcanic tuffs. *In* Proceedings, Fourth International High-Level Radioactive Waste Management Conference, Las Vegas, Nevada, April 26–30, 1993, p. 1052–1057 (LBL-33464).

Improved Dual-Porosity Models for Geothermal Reservoir Simulation

R. W. Zimmerman, G. Chen, T. Hadgu, and G. S. Bodvarsson

Since their introduction by Barenblatt et al. (1960), dual-porosity models have been widely used for simulating flow in fractured reservoirs. In a dual-porosity system, the matrix blocks provide most of the storage of the reservoir, whereas the fractures provide the global transmissivity. Initially, most work on dual-porosity models emphasized the development of analytical solutions for idealized reservoir problems. Increasingly, the dual-porosity approach is being implemented by numerical reservoir simulators. Accurate numerical simulation of a dual-porosity problem often requires a prohibitively large number of computational cells to resolve the transient pressure or saturation gradients in the matrix blocks. As part of our DOE-funded research on improved methods for geothermal reservoir simulation, we have been developing procedures for dual-porosity reservoir simulation that circumvent the need to discretize the matrix blocks. In our new approach, the mass and energy interactions between the fractures and matrix blocks are described by nonlinear ordinary differential equations. When implemented into a numerical simulator, this procedure eliminates the need to discretize the matrix blocks and thereby allows more efficient simulation of reservoir problems. This approach has been carried out for single-phase isothermal flow (Zimmerman et al., 1993a) and single-phase nonisothermal flow (Zimmerman et al., 1993b); it is currently being extended to two-phase (water/steam) flow of the type that occurs in geothermal reservoirs. In the following summary, we describe the application of this method to single-phase isothermal flow problems.

DUAL-POROSITY MODELS

When a single-phase, slightly compressible fluid flows isothermally through a macroscopically homogeneous fractured medium, the fluid pressure P_f in the fractures is governed by the equation

$$\phi_f c_f \frac{\partial P_f(x,t)}{\partial t} = \frac{k_f}{\mu} \nabla^2 P_f(x,t) + Q(x,t) \ , \tag{1}$$

where t is time, x is the position vector of a point in the fracture continuum, k_f is the effective permeability of the fracture continuum, ϕ_f is the total fracture porosity, and c_f is the total compressibility of the fractures and the fluid within them. Q is a volumetric source/sink term representing fluid flow from the matrix blocks to the fracture system per unit of total volume.

One commonly used type of dual-porosity model allows global flow only through the fracture network, with the matrix blocks serving as continuously distributed sources/sinks of fluid for the fractures. The matrix blocks at each location in the fracture continuum are represented by a single average pressure, $P_m(x,t)$. Conservation of mass for the matrix block leads to the following equation for P_m:

$$\phi_m c_m \frac{\partial P_m(x,t)}{\partial t} = -Q(x,t) \ . \tag{2}$$

To close the system of equations given by (1) and (2), an equation is needed to relate Q to P_f and P_m. Warren and Root (1963) assumed that Q is proportional to $P_f - P_m$:

$$Q(x,t) = -\frac{\alpha k_m}{\mu}\left(P_f - P_m\right) \ , \tag{3}$$

where α has dimensions of 1/area. Equation (3) is often referred to as the "quasi-steady-state" approximation (Chen, 1989). This terminology follows from consideration of the problem in which there is an instantaneous change in the fracture pressure P_f, which serves as the boundary condition for the matrix block, which we assume here to be a sphere of radius a_m. Differentiation of the most-slowly-decaying Fourier component in the expression for the average pressure, which is the dominant component at large times, leads to an equation of the same form as Eqs. (2) and (3), with $\alpha = \pi^2 / a_m^2$. Other matrix block shapes, such as slabs or cubes, lead to long-time behavior governed by similar equations, but with different expressions for α (see Zimmerman et al., 1993a).

NONLINEAR COUPLING EQUATION

An exact coupling term could be developed in terms of the step-function response of a single spherical matrix block by using the convolution principle. This would then require the calculation of convolution integrals for each fracture gridblock at each time step and would also require the storage of past values of the matrix pressure. Pruess and Wu (1989) and Dykhuizen (1990) improved upon the quasi-steady-state model by approximating flow in the matrix blocks with trial functions that satisfy the boundary conditions and global mass conservation. We have taken

the somewhat different approach of utilizing a nonlinear ordinary differential equation that, in some sense, approximates the linear partial differential equation that actually governs P_m. This equation, first proposed by Vermeulen (1953) in the context of ion-exchange chromatography, is:

$$\phi_m c_m \frac{\partial P_m}{\partial t} = \frac{\pi^2 k_m}{2\mu a_m^2} \frac{\left(P_f - P_i\right)^2 - \left(P_m - P_i\right)^2}{P_m - P_i} , \qquad (4)$$

where P_i is the initial pressure. When P_m is close to P_f, Eq. (4) reduces to Eq. (3) and is therefore accurate in the long-time regime. We have also proved that Eq. (4) is very accurate in the small-time limit for arbitrary fracture-pressure variations $P_f(t)$ (Zimmerman et al., 1993a).

Equation (4) has been tested under situations in which the fracture pressure, which serves as the boundary condition for the matrix block, is a known function of time, thereby isolating the matrix pressure response from that of the overall reservoir. Figure 1 shows the mean matrix block pressure for the case when the fracture pressure increases abruptly from P_i to P_0 at $t = 0$. The solution to Eq. (4) in this case very closely approximates the exact solution, whereas the prediction of the Warren-Root method, Eqs. (2) and (3), is not accurate until the process is nearly complete. The nonlinear Eq. (4) was also found to be more accurate than the Warren-Root method for ramp-function and other types of boundary conditions (Zimmerman et al., 1993a).

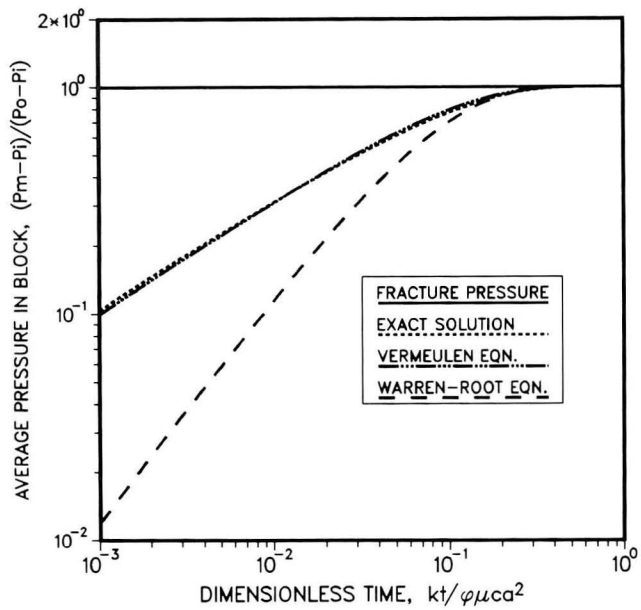

Figure 1. Average matrix pressure in a spherical block that is subjected to a step-function increase in pressure at its outer boundary. [XBL 927-1550]

DUAL-POROSITY SIMULATIONS

After verifying that Eq. (4) accurately predicts the mean matrix pressure under a wide variety of boundary conditions, we then incorporated it into the simulator TOUGH (Pruess, 1987) as a fracture/matrix coupling term. In this modification to TOUGH, Eqs. (2) and (4) are used in each fracture gridblock and at each time step to calculate the mass interaction term Q. The solution to the first-order ordinary differential equation (4) is carried out in a fully implicit manner, so as to be consistent with TOUGH and to avoid numerical instabilities. When performing reservoir simulations with this modified version of TOUGH, each computational gridblock represents an element of the fracture continuum, with the fracture/matrix flow interaction computed from Eqs. (2) and (4). We have verified the accuracy of this new approach by comparing its predictions against those of a MINC-type simulation (Pruess and Narasimhan, 1985), in which the matrix blocks are represented by nested concentric gridblocks. As an example of the use of the new method, consider flow from a boundary that is maintained at a constant pressure P_0, into a semi-infinite fractured formation that is initially at pressure P_i. The permeabilities are taken as $k_f = 10^{-15}$ m^2 and $k_m = 10^{-18}$ m^2, the porosities as $\phi_f = 0.001$ and $\phi_m = 0.1$, and the matrix block radii as $a_m = 1$ m. The temperature is 20°C, and the boundary and initial pressures are $P_i = 10$ MPa and $P_0 = 11$ MPa.

The flow rate into the formation is shown in Figure 2. In the case labeled "MINC-1 shell," each matrix block was represented by a single computational cell; this is a numerical implementation of the Warren-Root equation (3). In the case labeled "MINC-10 shells," each matrix block was discretized into 10 concentric shells. All three computations predict the correct pressure response in the short- and long-time limits, when $P_f \approx t^{-1/2}$. In the intermediate-time regime, when the matrix blocks near the inlet are being filled, the Warren-Root method incorrectly predicts $P_f \approx$ constant, whereas the new method correctly leads to the known (Nitao and Buscheck, 1991) $t^{-1/4}$ pressure dependence. The MINC solution becomes more accurate as the number of shells increases and eventually approaches the solution obtained using our new method. The agreement with the finely gridded MINC solution serves to validate the new method.

The computational time required for simulating a given problem with a code such as TOUGH grows linearly with the number of computational cells, since most of the computing effort consists in inverting a sparse matrix by Gaussian elimination. Since the nonlinear coupling equation removes the need for discretizing the matrix blocks, the number of computational gridblocks can be decreased by about a factor of N, where N is the number of MINC shells used in each gridblock. This would be expected to lead to a proportional decrease in CPU time. For example, in the simulations shown in Figure 2, 14 fracture gridblocks and 1 boundary gridblock were used to simulate flow into the

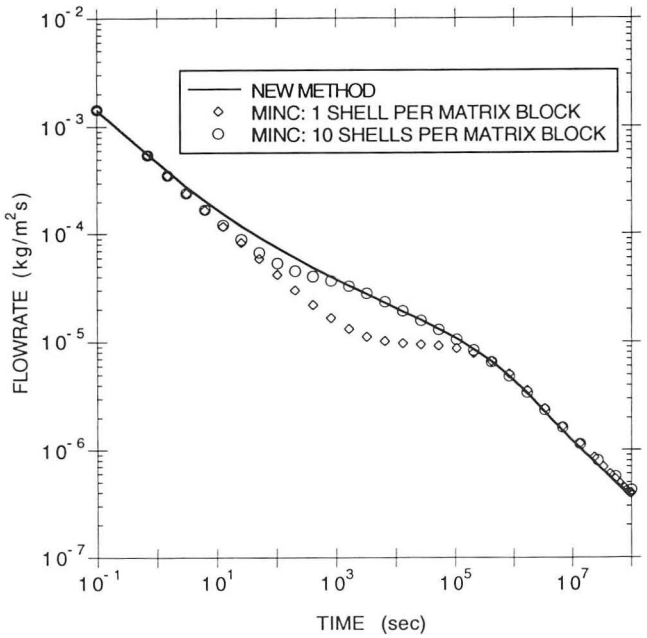

Figure 2. Flow rate into one-dimensional fractured formation under constant-pressure boundary conditions. Matrix and fracture properties are as described in text. [XBL 936-884]

semi-infinite formation when using the new method. The MINC-10 shell simulation therefore used 155 computational elements: 1 boundary element, 14 fracture elements, and $14 \times 10 = 140$ matrix elements. The decrease in the number of computational elements afforded by the new method was therefore 90%, and the savings in CPU time was in fact 88%. The slight difference is probably due to the small amount of computational work needed to solve Eq. (4).

DISCUSSION

The method described above for modeling the flow of a single-phase fluid between a matrix block and the surrounding fractures can also be used to model heat conduction, since both processes are governed by the diffusion equation. This analogy was pointed out by Pruess and Wu (1989), who used the integral-method approach to model both phenomena. We have extended our nonlinear coupling equation approach to heat conduction (Zimmerman et al., 1993b) and also to two-phase processes in which the liquid is immobile (Zimmerman, et al., 1993b). In the latter case, the fluid flow can be modeled by a single diffusion equation by introducing a "pseudo-compressibility" for the two-phase mixture (Grant and Sorey, 1979). We are currently working on extending this approach to two-phase flow processes in which both phases are mobile.

REFERENCES

Barenblatt, G.I., Zheltov, Y.P., and Kochina, I.N., 1960. Basic concepts in the theory of seepage of homogeneous liquids in fissured rocks. J. Appl. Math. Mech., v. 24, p. 1286–1303.

Chen, Z.-X., 1989. Transient flow of slightly compressible fluids through double-porosity, double-permeability systems—A state-of-the-art review. Transp. Porous Media, v. 4, p. 147–184.

Dykhuizen, R.C., 1990. A new coupling term for dual-porosity models. Water Resour. Res., v. 26, p. 351–356.

Grant, M.A., and Sorey, M.L., 1979. The compressibility and hydraulic diffusivity of a water-steam flow. Water Resour. Res., v. 15, p. 684–686.

Nitao, J.J., and Buscheck, T.A., 1991. Infiltration of a liquid front in an unsaturated, fractured porous medium. Water Resour. Res., v. 27, p. 2099–2112.

Pruess, K., 1987. TOUGH user's guide. Lawrence Berkeley Laboratory Report LBL-20700.

Pruess, K., and Narasimhan, T.N., 1985. A practical method for modeling heat and fluid flow in fractured porous media. Soc. Pet. Eng. J., v. 25, p. 14–26 (LBL-21274).

Pruess, K., and Wu, Y.-S., 1989. A new semi-analytical method for numerical simulation of fluid and heat flow in fractured reservoirs. Presented at the Tenth SPE Symposium on Reservoir Simulation, Houston, Texas, February 6–8, 1989 (LBL-26121).

Vermeulen, T., 1953. Theory of irreversible and constant-pattern solid diffusion. Ind. Eng. Chem., v. 45, p. 1664–1670.

Warren, J.E., and Root, P.J., 1963. The behavior of naturally fractured reservoirs. Soc. Petrol. Eng. J., v. 3, p. 245–255.

Zimmerman, R.W., Chen, G., Hadgu, T., and Bodvarsson, G.S., 1993a. A numerical dual-porosity model with semi-analytical treatment of fracture/matrix flow. Water Resour. Res., v. 29, p. 2127–2137 (LBL-34148).

Zimmerman, R.W., Hadgu, T., and Bodvarsson, G.S., 1993b. Development of a dual-porosity model for vapor-dominated fractured geothermal reservoirs using a semi-analytical fracture/matrix interaction term. Presented at the Eighteenth Workshop on Geothermal Reservoir Engineering, Stanford, California, January 26–28, 1993 (LBL-33727).

APPENDIXES

APPENDIX A: ABSTRACTS OF JOURNAL ARTICLES

Bergeron, V., and Radke, C.J., 1992. Equilibrium measurements of oscillatory disjoining pressures in aqueous foam films. Langmuir, v. 8, p. 3020–3026 (LBL-32983).

Disjoining pressure isotherms are measured for single, isolated foam films stabilized with sodium dodecyl sulfate above the critical micelle concentration (cmc). The measured isotherms exhibit an equilibrium oscillatory component that extends out to film thicknesses as large as 50 nm. The oscillations originate from surfactant structuring within the film and are responsible for the multiple black films extensively studied by Perrin in 1918. We find that as film thickness decreases, the slopes and peak heights of the oscillations increase for each subsequent black film encountered. The discrete changes in film thickness observed at each black film transition range from 6 to 10 nm and are a function of the ionic strength and surfactant concentration. Pressures required to rupture the multiple black films are several orders of magnitude lower than the final film-rupture pressure. Finally, the oscillatory form of the disjoining pressure permits quantitative interpretation of the stepwise thinning behavior observed in films containing surfactant above the cmc.

Bergeron, V., Jiménez-Laguna, A.I., and Radke, C.J., 1992. Hole formation and sheeting in the drainage of thin liquid films. Langmuir, v. 8, p. 3027–3032 (LBL-33125).

Foam, emulsion, and pseudoemulsion films stabilized by surfactants above the critical micelle concentration exhibit pronounced stepwise thinning or stratification. Dynamic removal of a layer is initiated by the formation and subsequent sheeting of a hole (or holes) at each step of the stratified thinning. We outline a nonlinear hydrodynamic stability analysis which successfully models the dynamics of hole formation and sheeting by accounting for an equilibrium oscillatory structural component in the disjoining pressure isotherm. Initiation of a hole is attributed to the nonlinear growth of a hydrodynamic instability during film thinning under the action of a constant capillary pressure and an oscillatory disjoining pressure. Subsequent growth or sheeting of the hole is explained by outward fluid flow within the inhomogeneous thin film as radial pressure gradients develop from curvature variations and viscous resistance to flow. Qualitative comparison is made between the proposed hydrodynamic theory and experimental observations of thinning events and rates.

Chou, I.-M., Sterner, S.M., and Pitzer, K.S., 1992. Phase relations in the system NaCl-KCl-H_2O. IV. Differential thermal analysis of the sylvite liquidus in the KCl-H_2O binary, the liquidus in the NaCl-KCl-H_2O ternary, and the solidus in the NaCl-KCl binary to 2 kb pressure, and a summary of experimental data for thermodynamic-*PTX* analysis of solid-liquid equilibria at elevated *P-T* conditions. Geochim. Cosmochim. Acta, v. 56, pp. 2281–2293 (LBL-31058).

The sylvite liquidus in the binary system KCl-H_2O and the liquidus in the ternary system NaCl-KCl-H_2O were determined by using isobaric differential thermal analysis (DTA) cooling scans at pressures up to 2 kbars. Sylvite solubilities along the three-phase curve in the binary system KCl-H_2O were obtained by the intersection of sylvite-liquidus isopleths with the three-phase curve in a *P-T* plot. These solubility data can be represented by the equation

$$\text{Wt.\% KCl } (\pm 0.2) = 12.19 + 0.1557T - 5.4071 \times 10^{-5}T^2,$$

where $400 \leq T \leq 770$°C. These data are consistent with previous experimental observations. The solidus in the binary system NaCl-KCl was determined by using isobaric DTA heating scans at pressures up to 2 kbars. Using these liquidus and solidus data and other published information, a thermodynamic-*PTX* analysis of solid-liquid equilibria at high pressures and temperatures for the ternary system has been performed and is presented in an accompanying paper (Part V of this series). However, all experimental liquidus, solidus, and solvus data used in this analysis are summarized in this report (Part IV) and they are compared with the calculated values based on the analysis.

Cook, N.G.W., 1992 Jaeger Memorial Dedication Lecture. Natural joints in rock: Mechanical, hydraulic and seismic behaviour and properties under stress. Int. J. Rock Mech. Min. Sci. & Geomech. Abstr., v. 29, no. 3, p. 198–223 (LBL-32201).

The mechanical and hydraulic properties of many rock masses are affected significantly by the additional mechanical compliance and fluid conductivity that result from joints, fractures or faults. The effects of these features, generally referred to as joints, can be so pronounced in many problems in geology or geophysics, mining or petroleum engineering, hydrogeology and waste management that it is important to be able to locate and characterize them remotely within a rock mass using geophysical methods. The effect of joints on seismic wave propagation, therefore, becomes important also. Experimental measurements of the deformation of natural joints are analyzed in terms of theories concerning the roughness of the two joint surfaces and their deformation under stress. For many rocks, the deformation of the surfaces is reversible after the first few cycles of loading and unloading and is, therefore, elastic. The highly non-linear stress-deformation curves for joints must be a result of changes in the geometry of the areas of contact between asperities brought about by the elastic deformation of adjacent voids in response to changes in the applied stress.

The flow of fluids between the surfaces of a joint must also depend upon the geometry of the void space between these surfaces. Measurements using liquid metal porosimetry, show that when the two surfaces of a natural joint are in contact with one another, this geometry becomes so complex that fluid through the joint cannot be approximated as laminar flow between parallel surfaces leading to a cubic relation between flux and aperture. At low stresses, fluid flow through a joint decreases much faster than the cube of the joint closure. This is shown to be a result of changes in contact area, tortuosity and hydraulic aperture brought about by deformation of the void space between the two surfaces of the joint. At high stresses, fluid flow through a joint asymptotes to an irreducible level, largely independent of joint closure and further changes in stress.

The slope of a tangent to the curve relating the average closure between the two surfaces of a joint to the stress across the joint defines a specific stiffness for the joint at that stress. The effect of joints on seismic waves can be analyzed by using this specific stiffness as a boundary condition in the seismic wave equation. Displacements across this boundary are discontinuous while stresses are continuous. Although the specific stiffness of the joint and the properties of the rock on each side of it are assumed to be completely elastic, the displacement discontinuity leads to frequency-dependent reflection and transmission coefficients for compressional and shear waves as well as frequency-dependent group time delay for the transmitted waves. This concept can be extended to include a velocity discontinuity across the joint, where the contained fluid or the properties of the rock provide viscous as well as elastic coupling across a joint. Theoretical predictions based on the displacement discontinuity and velocity discontinuity theories agree very well with the results of laboratory measurements of seismic pulses transmitted across natural joints with different specific stiffnesses.

Doughty, C., and Pruess, K., 1992. A similarity solution for two-phase water, air, and heat flow near a linear heat source in a porous medium. J. Geophys. Res., v. 97, no. B2, p. 1821–1838 (LBL-30051).

Placement of a heat source in a partially saturated geologic medium causes strongly coupled thermal and hydrologic behavior. To study this problem, a recently developed semianalytical solution for two-phase flow of water and heat in a porous medium has been extended to include an air component and to incorporate several physical effects that broaden its range of applicability. The problem considered is the placement of a constant-strength linear heat source in an infinite homogeneous medium with uniform initial conditions. Under these conditions the governing partial differential equations in radial distance r and time t reduce to ordinary differential equations through the introduction of a similarity variable $\eta = r/t^{1/2}$. The resulting equations are coupled and nonlinear, necessitating a numerical integration. The similarity solution developed here is used to investigate various physical phenomena related to partially saturated flow in low-permeability rock, such as vapor pressure lowering, pore level phase change effects, and an effective continuum representation of fractured/porous media. Application to several illustrative problems arising in the context of high-level nuclear waste disposal at Yucca Mountain, Nevada, indicates that fluid flow, phase changes, and latent heat transfer may have a significant impact on conditions at the repository.

Ettinger, R.A., and Radke, C.J., 1992. Influence of texture on steady foam flow in Berea sandstone. SPE Res. Eng., v. 7, no. 1, p. 83–90 (LBL-30922).

An understanding of texture, or bubble-size, evolution is paramount for modeling foam flow in porous media in that fine textures may impart large flow resistances. Bubble size, in turn, is determined by complicated lamella creation and decay processes. We study, for the first time, the quantitative role of bubble size in the steady flow of strong foam through a 0.8-μm^2 Berea sandstone. Inlet and outlet textures are determined from photomicrographs taken of bubbles flowing through specially designed visual cells. Concurrent measurements of pressure and liquid-saturation profiles by microwave attenuation are acquired for gas velocities from 1 to 3 m/d and foam qualities from 70% to 90%. A simple 1D foam population-balance model is outlined to quantify the observed flow and texture behavior. Agreement between the proposed model and the new bubble-size and flow data is adequate. The population-balance method proves to be a useful tool.

Falta, R.W., Pruess, K., Javandel, I., and Witherspoon, P.A., 1992. Numerical modeling of steam injection for the removal of nonaqueous phase liquids from the subsurface. 1. Numerical formulation. Water Resour. Res., v. 28, no. 2, p. 443–449 (LBL-29615).

A multidimensional integral finite difference numerical simulator is developed for modeling the steam displacement of nonaqueous phase liquid (NAPL) contaminants in shallow subsurface systems. This code, named STMVOC, considers three flowing phases, gas, aqueous, and NAPL; and three mass components, air, water, and an organic chemical. Interphase mass transfer of the components between any of the phases is calculated by assuming local chemical equilibrium between the phases, and adsorption of the chemical to the soil is included. Heat transfer occurs due to conduction and multiphase convection and includes latent heat effects. A general equation of state is implemented in the code for calculating the thermophysical properties of the NAPL/chemical. This equation of state is primarily based on corresponding states methods of property estimation using a chemical's critical constants. The necessary constants are readily available for several hundred hazardous organic liquid chemicals. In part 2 (Falta et al., this issue), the code is used to simulate two one-dimensional laboratory steam injection experiments and to examine the effect of NAPL properties on the steam displacement process.

Falta, R.W., Pruess, K., Javandel, I., and Witherspoon, P.A., 1992. Numerical modeling of steam injection for the removal of nonaqueous phase liquids from the subsurface. 2. Code validation and application. Water Resour. Res., v. 28, no. 2, p. 451–465 (LBL-29616).

The multiphase steam injection simulator developed in part 1 (Falta et al., this issue) is used to simulate two laboratory column steam displacement experiments. In the first simulation, steam is injected into a clean, water-saturated column, while in the second simulation, steam is injected into a column containing both water and separate phase trichloroethylene. In both cases, the numerical results are in good quantitative agreement with the experimental data. Based on the assumption of local chemical equilibrium between the phases, a simple criterion is derived for determining the major mechanism of nonaqueous phase liquid (NAPL)/chemical transport during the steam displacement process. Several one-dimensional simulations of the steam displacement of high-boiling-point NAPLs are discussed. These results are consistent with theoretical predictions and indicate that steam may efficiently displace organic liquids having boiling points substantially greater than that of water.

Hwang, Y., Pigford, T.H., Chambré, P.L., and Lee, W.W.-L., 1992. Analysis of mass transport in a nuclear waste repository in salt. Water Resour. Res., v. 28, no. 7, p. 1857–1868 (LBL-31849).

Salt is the proposed host rock for geologic repositories of nuclear waste in several nations because it is "dry" and probably "impermeable." To evaluate the safety of nuclear waste disposal in salt, it is necessary to calculate the rate of release of nuclides from solidified waste form and to predict the transport of released radionuclides. Our objective is to develop analytic methods for such prediction, based on mass transfer theory. First, we present an analysis of pressure-driven brine migration. After consolidation, brine migration analyzed by these equations and using the particular set of parameter values is of a small magnitude, with Darcy velocities of the order of micrometers per year. Brine migration in consolidated salt is very localized, within a few meters from the waste package, and highly transient. We have analyzed diffusion of radionuclides near waste packages in a salt repository, using analytic equations for low Peclet systems. According to this analysis it is unlikely that any low-solubility species will have difficulty meeting the U.S. Nuclear Regulatory Commission release rate requirement at the bare waste/salt interface. We have also analyzed the role that an interbed might play in being a preferential pathway for radionuclide migration. We calculate the diffusive mass fluxes from an infinitely long bare waste cylinder in salt, facing an interbed. The fractional release rates of solubility-limited species into the interbed are low for the parameter values used in the numerical illustrations.

Javandel, I., Falta, R.W., and Holman, H.-Y., 1990. Recent developments in transport and fate of nonaqueous phase liquids in the subsurface environment. Iranian J. Sci. & Technol., v. 14, nos. 2 & 3, pp. 269–287 (LBL-29373). [This publication did not actually appear in print until 1992.]

Deliberate and accidental releases of nonaqueous phase liquids (NAPLs) in the subsurface environment are responsible for a large number of groundwater contamination incidents. Restoration of these valuable water supply sources, if not impossible, requires hundreds of millions of dollars and years of continuous effort. During the last few years, tens of million dollars have been spent to develop a thorough understanding of the problem and to find methodologies for cost-effective cleanup of the subsurface environments contaminated by these chemicals. In this paper, we will briefly review the nature of the problem, mechanisms controlling the migration and fate of these NAPLs and some of the techniques that are used, or are being developed for cleaning the contaminated environments.

Karageorgi, E., Clymer, R., and McEvilly, T.V., 1992. Seismological studies at Parkfield. II. Search for temporal variations in wave propagation using Vibroseis. Bull. Seismol. Soc. Am., v. 82, no. 3, p. 1388–1415 (LBL-30875).

For more than 3 years the propagation characteristics of shear waves have been monitored for paths near the 1966 hypocenter at Parkfield, the presumed nucleation site for the expected next *M*6 earthquake there. Data have been collected repeatedly (33 sets as of April 1991) from eight *S*-wave Vibroseis source positions into the 10 borehole-installed three-component seismometers of the local high-sensitivity digital network. Twenty-second correlated records from a 6- to 24-Hz sweep are acquired, and the entire seismogram is viewed for analysis as the elastic response of the local crustal structure, which includes the San Andreas fault zone. Amplitudes, travel times, spectra, and particle motions of the *P* and *S* waves are monitored for indications of any changes in these properties that may be attributed to processes associated with nucleation. The horizontal vibrator at each source point is positioned at three surface-orientations to study anisotropy. Unorthodox methods have been developed to display the waveform properties in time in order to visualize the resulting massive data sets. The first-order variations seen in some of the parameters are attributed to changes from dry to wet conditions in the shallow subsurface due to the seasonal rainfall, which affects the source function of the vibrator. Corrections have been devised for these source-specific variations. Secular variations not obviously coupled to seasonal near-surface changes are also seen in some localized time intervals within the 20-sec records. The most striking of such changes is a progressive travel-time decrease at rates of 3 to 7 msec/year seen for late arrivals (7 to 11 sec travel time) on at least five paths into station VCA, which sample the region southeast of the anticipated epicenter at Middle Mountain. This anomaly appears to be genuine and is now the subject of intensified study. In the same general area, along the fault in the southwestern block, the direct *S* wave is clearly split, with the faster of the split phases polarized parallel to the fault zone, a result in agreement with that from the VSP survey in the Varian well on the northeast side of the fault.

Linn, A.M., DePaolo, D.J., and Ingersoll, R.V., 1992. Nd-Sr isotopic, geochemical, and petrographic stratigraphy and paleotectonic analysis: Mesozoic Great Valley forearc sedimentary rocks of California. Accepted for publication in Geol. Soc. Am. Bull., v. 104, p. 1264–1279 (LBL-30848).

Measurements of Nd-Sr isotopes, major and trace elements, and model mineralogy were made on Upper Jurassic and Cretaceous Great Valley forearc sedimentary rocks to test models for the temporal and spatial evolution of Sierra Nevada arc sources. Isotopes and major and trace elements are sensitive provenance indicators because of the large west-east isotopic, geochemical, and age gradients in the plutonic rocks of the Sierra Nevada batholith, and because petrographic models indicate that source areas moved east during the Cretaceous.

Isotopic and chemical variations are correlated in the forearc sandstone; as ϵ_{Nd} decreases, Th, U, La, Nb, Zr, Hf, Pb, Rb, SiO_2, and K_2O concentrations increase, and FeO, MgO, TiO_2, Ni, and Cr concentrations decrease. This relation is the same as that observed in the plutonic rocks and indicates that the arc was the primary source of sediment and that the sandstone chemistry was not disturbed by sedimentary processes. The ϵ_{Nd}–ϵ_{Sr} relation of San Joaquin Valley sandstone is the same as the plutonic rocks, but Sacramento Valley sandstone is elevated in ϵ_{Sr} because of seawater exchange, weathering, and diagenesis. Whole-rock sandstone decreases in ϵ_{Nd} from +7 to –5 and increases in $^{87}Sr/^{86}Sr$ from 0.7045 to 0.7073 with decreasing stratigraphic age. The Nd-Sr isotopic composition is correlative with the plagioclase to feldspar ratio and indicates that source areas moved inland during the Cretaceous. Upper Cretaceous San Joaquin Valley shale is similar in ϵ_{Nd} to the sandstone, indicating that sandstone and shale were derived from the same source and that the Nd isotopic composition is independent of grain size. The shale is higher in $^{87}Sr/^{86}Sr$ than the sandstone, possibly due to concentration of biotite in the fine fraction during transport and subsequent Rb loss during diagenesis.

Nd-Sr isotopes were used to construct models to locate source areas. Parameters include lithology, drainage basin geometry, and erosion rate. The age and isotopic compositions of the calculated igneous component of the sandstone correspond to the age and isotopic compositions of the plutonic rocks of the batholith; this correspondence indicates that (1) the isotopic composition of the plutonic rocks and the coeval volcanic cover were similar, (2) the volcanic front was denuded within a few million years, and (3) the sediment was derived from the head of the drainage basin, located at the migrating volcanic front.

Nir, A., Doughty, C., and Tsang, C.F., 1992. Validation of design procedure and performance modeling of a heat and fluid transport field experiment in the unsaturated zone. Adv. Water Resour., v. 15, p. 153–166 (LBL-31269).

Validation methods which developed in the context of deterministic concepts of past generations often cannot be directly applied to environmental problems, which may be characterized by limited reproducibility of results and highly complex models. Instead, validation is interpreted here as a series of activities, including both theoretical and experimental tests, designed to enhance our confidence in the capability of a proposed model to describe some aspect of reality. We examine the validation process applied to a project concerned with heat and fluid transport in porous media, in which mathematical modeling, simulation, and results of field experiments are evaluated in order to determine the feasibility of a system for seasonal thermal energy storage in shallow unsaturated soils. Technical details of the field experiments are not included, but appear in previous publications.

Validation activities are divided into three stages. The first stage, carried out prior to the field experiments, is concerned with modeling the relevant physical processes, optimization of the heat-exchanger configuration and the shape of the storage volume, and multi-year simulation. Subjects requiring further theoretical and experimental study are identified at this stage. The second stage encompasses the planning and evaluation of the initial field experiment. Simulations are made to determine the experimental time scale and optimal sensor locations. Soil thermal parameters and temperature boundary conditions are estimated using an inverse method. Then results of the experiment are compared with model predictions using different parameter values and modeling approximations. In the third stage, results of an experiment performed under different boundary conditions are compared to predictions made by the models developed in the second stage.

Various aspects of this theoretical and experimental field study are described as examples of the verification and validation procedure. There is no attempt to validate a specific model, but several models of increasing complexity are compared with experimental results. The outcome is interpreted as a demonstration of the paradigm proposed by van der Heijde, that different constituencies have different objectives for the validation process and therefore their acceptance criteria differ also.

Noorishad, J., Tsang, C.F., Perrochet, P., and Musy, A., 1992. A perspective on the numerical solution of convection-dominated transport problems: A price to pay for the easy way out. Water Resour. Res., v. 28, no. 2, p. 551–561 (LBL-31659).

In a brief but fundamental review of the evolution of the conventional numerical techniques used in the solution of convection-dominated transport problems, we explore the difficulties that have been remedied to various degrees by various workers. In the course of this review we obtain the performance characteristic of the Crank-Nicolson Galerkin finite element method in the form of a curve in Peclet number and Courant number space.

We show that the performance can be altered through a new upwind parameter that can easily be incorporated into many of the existing numerical solution methods. By providing an insight into the limitations of some of these methods we demonstrate, by means of numerical experiments, that the proposed upwinding procedure ensures acceptable solutions throughout the *Pe-Cr* space at a reasonable cost of the smearing effect.

Noorishad, J., Tsang, C.F., and Witherspoon, P.A., 1992. Theoretical and field studies of coupled hydromechanical behaviour of fractured rocks—1. Development and verification of a numerical simulator. Int. J. Rock Mech. Min. Sci. & Geomech. Abstr., v. 29, no. 4. p. 401–409 (LBL-32254).

Analysis of hydromechanical behaviour of fractured rocks requires the use of numerical methods, such as the ROCMAS code developed at LBL. We have developed a new version of this simulator which uses mixed Newton-Raphson linearization within an incremental configuration. This code, that is named ROCMAS II, was verified against: (1) a semi-analytic solution; and (2) against its predecessor ROCMAS which uses a direct iteration linearization scheme. This new coupled phenomenological model has been used successfully in a validation study of a field experiment which is reported in Part 2 [Int. J. Rock Mech. Min. Sci. & Geomech. Abstr. 29, 411-419 (1992)]. The verified ROCMAS II with its new feature such as an incremental set-up, the strain-softening and dilating shear, and hyperbolic closure joint model and the new linearization scheme, allows more realistic simulations of a host of rock mechanical problems in saturated rocks. Furthermore, the ROCMAS II set-up provides a basis upon which procedures for general treatment of various kinds of material non-linearity can be built.

Nordqvist, A.W., Tsang, Y.W., Tsang, C.F., Dverstorp, B., and Andersson, J., 1992. A variable aperture fracture network model for flow and transport in fractured rocks. Water Resour. Res., v. 28, no. 6, p. 1703–1713 (LBL-31554).

A three-dimensional variable aperture fracture network model for flow and transport in fractured rocks was developed. The model generates both the network of fractures and the variable aperture distribution of individual fractures in the network. Before solving for the flow and transport of the whole network, a library of single-fracture permeabilities and particle transport residence time spectra is first established. The spatially varying aperture field within an individual fracture plane is constructed by geostatistical methods. Then the flow pattern, the fracture transmissivity, and the residence times for transport of particles through each fracture are calculated. The library of transmissivities and frequency distributions of residence times is used for all fractures in the network by a random selection procedure. The solution of flow through the fracture network and the particle-tracking calculation of solute transport for the whole network are derived from one side of the network to the other. The model thus developed can handle flow and transport from the single-fracture scale to the multiple-fracture scale. The single-fracture part of the model is consistent with earlier laboratory tests and field observations. The multiple-fracture aspect of the model was verified in the constant aperture fracture limit with an earlier code. The simulated breakthrough curves obtained from the model display dispersion on two different scales as has been reported from field experiments.

Okaya, D.A., Karageorgi, E., McEvilly, T.V., and Malin, P.E., 1992. Removing vibrator-induced correlation artifacts by filtering in frequency-uncorrelated time space. Geophysics, v. 57, no. 7, p. 916–926 (LBL-30818).

Vibrator-to-ground coupling can produce resonance-induced energy that propagates with the primary sweep and produces serious artifacts in the correlated seismogram due to the frequency structure of this offending energy. For sweeps linearly increasing in frequency, the resulting artifact is observed (uncorrelated) to increase in frequency at a linear rate differing from the original sweep. Upon crosscorrelation with the pilot sweep, the artifact-producing energy becomes distributed over an extended range of time while the normal reflected sweep is compressed, by design, into a narrow correlation wavelet. The resulting traces thus exhibit strong amplitudes that increase monotonically in dominant frequency. Display of individual uncorrelated seismograms using a Fourier frequency-uncorrelated time (F-T) transformation reveals the relationship between the primary sweep and the induced artifact. "Surgical" filtering in this new F-T space provides for a first-order removal of both the artifact and the energy in sweep harmonics as induced by the strong first arrivals. Two-dimensional (2-D) spectral filtering of the modulus of the (complex) 2-D transform of the F-T data provides better rejection of the unwanted energy. Application of this trace-by-trace filtering process to a badly contaminated crustal-scale multichannel CDP profile in the southern San Joaquin Valley, California, reveals significant reflections from the middle and lower crust that were obscured in the unfiltered profile.

Oldenburg, C.M., and Spera, F.J., 1992. Hybrid model for solidification and convection. Numer. Heat Transfer B, v. 21, p. 217–229 (LBL-29899).

We present a hybrid model for continuum phase-change problems. The hybrid model accounts for flow in regions of concentrated mush, dilute mush, and single-phase liquid. Scale analysis shows that, in dilute mush, the Blake-Kozeny-Carman relation may lead to inaccuracy in the continuum formulation for certain values of the Rayleigh and Darcy numbers. The hybrid model uses arctangent switching functions to switch on the Darcy flow and variable viscosity terms depending on the local value of the fraction solid. Two-dimensional example calculations suggest that the hybrid model more accurately accounts for transport in the dilute mush region.

Pigford, T.H., Chambré, P.L., and Lee, W.W.-L., 1992. A review of near-field mass transfer in geologic disposal systems. Radioactive Waste Manage. & Nucl. Fuel Cycle, v. 16, no 3–4, p. 175–276 (LBL-27045).

In performance assessment of geologic repositories of nuclear waste, reliable predictions must be made of rates of release of radionuclides from the waste into rock, transport through the porous geologic media, cumulative release to the accessible environment and maximum concentrations in waters which may be used by people. In this paper we present a review of theoretical approaches to making the predictions of near-field release from buried nuclear waste. The calculated release rates are input to total system performance analysis. In each case we provide the conceptual model, governing equations, analytic solutions and numerical illustrations of the solutions using parameter values typical of nuclear waste repositories. We also discuss the limits of applicability of mass transfer theory. Extensions of the applications are given for radioactive decay chains, and potential repositories in salt and unsaturated rock.

Poister, D., and Tokunaga, T.K., 1992. Selenium in Kesterson Reservoir ephemeral pools formed by groundwater rise: II. Laboratory experiments. J. Environ. Qual., v. 21, no. 2, p. 252–258 (LBL-30589).

The formation of seleniferous ephemeral pools that result from shallow water table rise through seleniferous soils was studied in laboratory columns of soils from Kesterson Reservoir, Merced County, California. Variables included in the column experiments included the depth interval of the soils, the rate of shallow water table rise and temperature. The columns were packed with either surface (0–0.15 m) soils (with and without the original salt crust), or subsurface soils (0.15–0.30 m) sampled from the southwest corner of Pond 1, Kesterson Reservoir. Controlled inputs of nonseleniferous, saline water through the bottoms of the columns provided water table rise rates of 3, 10 and 30 mm d^{-1}. The soil columns were maintained at either room temperature (≈25°C) or 5°C. The amount of Se transported from the soils into the overlying ponding waters was proportional to the water–extractable soil Se content, and was positively corre-

lated with the rate of water table rise. The 5°C experiments resulted in greater Se transfers into the ponding waters in the columns subjected to 10 and 30 mm d^{-1} rates of water table rise (relative to comparable room temperature columns), while the reverse effect was observed with 3 mm d^{-1} columns.

Roy, R.N., Vogel, K.M., Good, C.E., Davis, W.B., Roy, L.N., Johnson, D.A., Felmy, A.R., and Pitzer, K.S., 1992. Activity coefficients in electrolyte mixtures: HCl + $ThCl_4$ + H_2O for 5–55°C. J. Phys. Chem., v. 96, p. 11065–11072 (LBL-32731).

The emf of the cell without liquid junction (A) was used to study the HCl + $ThCl_4$ + H_2O mixed electrolyte system. The

$$\text{Pt, } H_2(g,1\text{ atm})|HCl(m_A), ThCl_4(m_B)|AgCl,Ag \qquad (A)$$

emf was measured for solutions at constant total ionic strengths of 0.006, 0.008, 0.01, 0.05, 0.1, 0.25, 0.5, 1.0, 2.0, and 3.0 mol·kg^{-1} and at temperatures ranging from 5 to 55°C. The mean activity coefficients of HCl in the mixtures were calculated using the Nernst equation. Two detailed treatments are given of the data for 25°C. In the first, the Harned equations were fitted to the activity coefficient data using least-squares regression techniques. Results show that the quadratic equation is adequate for the full range of Y_B to 0.9 for $I \leq 2.0$ mol·kg^{-1} but only for smaller Y_B at I = 3.0. Second, an ion-interaction (Pitzer) equation treatment is given in which experimental isopiestic measurements, solubility, and the activity coefficient data are analyzed and the necessary parameters developed for the H^+-Th^{4+}-Cl^--H_2O system.

Rutqvist, J., Noorishad, J., Stephansson, O., and Tsang, C.F., 1992. Theoretical and field studies of coupled hydromechanical behaviour of fractured rocks—2. Field experiment and modelling. Int. J. Rock Mech. Min. Sci. & Geomech. Abstr., v. 29, no. 4, p. 411–419 (LBL-32255).

A series of water injection experiments were performed on four horizontal fractures intercepted by a borehole at the University of Luleå Rock Mechanics Laboratory site in Sweden. The fractures are located in a borehole section 80–350 m in depth. Three types of injection tests were carried out: (1) constant-pressure injection tests, with pressures ranging from below to above the overburden pressure, (2) constant-flowrate injection tests; and (3) step pressure tests (hydraulic jacking test). In the former two cases, the results clearly depict the coupled effect of mechanical fracture-aperture opening due to increased hydraulic pressure, even in the pre-hydrofracturing regime.

A parallel numerical study was carried out to simulate these injection tests using the computer code ROCMAS II [see Part 1, Int. J. Rock Mech. Min. Sci. & Geomech. Abstr. 29, 401–409 (1992)]. We were able to simulate closely the pre-hydrofracturing coupled effect in the step pressure and constant pressure test. The success in this attempt validates the soundness of the conceptualized constitutive relations governing the coupled hydromechanical behaviour of rock masses. The results also point out a potential methodology of using a joint field and theoretical study of fracture hydromechanical responses to extract key characterizing parameters of the rock and fractures.

Schrag, D.P., DePaolo, D.J., and Richter, F.M., 1992. Oxygen isotope exchange in a two-layer model of oceanic crust. Earth & Plan. Sci. Lett., v. 111, p. 305–317 (LBL-32293).

A numerical model is presented for the transport and exchange of oxygen isotopes in an idealized two-layer oceanic crust (basalt-carbonate) that is saturated with a non-advecting pore fluid open to the overlying ocean. The model allows for time-varying sedimentation rate, porosity, chemical diffusivity, and temperature-dependent ^{18}O fractionation factors. Reaction is modeled as solution-precipitation of calcite in the carbonate sediment and as modified solution-precipitation (basalt dissolves, smectite precipitates) in the basalt layer. Generic models, using input parameters that are typical of those measured in DSDP-ODP cores, and constant sedimentation rates, illustrate the behavior of the system sufficiently well to allow first-order effects to be discerned that have important implications for paleotemperature and ocean floor weathering studies.

The solution-precipitation reactions allow oxygen to be exchanged between the low-$\delta^{18}O$ basalt layer and the high-$\delta^{18}O$ carbonate sediment through the medium of the pore fluids. This results in $\delta^{18}O$ increasing upwards in the basalt and decreasing downwards in the sediment. Pore fluid $\delta^{18}O$ values decrease with depth from zero to values of –1 to –3‰ at the basalt-sediment interface, and to values of –7 to –15‰ within the basalt. Because reaction rates are slow relative to diffusion in the pore fluid, high-frequency $\delta^{18}O$ variations in the solid are preserved indefinitely, but the amplitude of the variations decreases as e^{-Rt} where R is the reaction rate (fraction reacted per unit time). The results suggest that the diagenetic shifts of the $\delta^{18}O$ values of benthic and high-latitude planktonic foraminifera samples younger than Oligocene age are typically negligible. For samples older than 50 Ma, diagenetic effects are typically significant, and generally cause estimates of bottom and high-latitude surface ocean temperatures in the Cretaceous and early Tertiary to be too high. On the other hand, the model suggests that diagenesis will shift the $\delta^{18}O$ values of low-latitude planktonic foraminifera to higher values, and that paleotemperature estimates of low-latitude surface waters, particularly in the Eocene and Oligocene, may be too low. Using a synthetic $\delta^{18}O$ record for DSDP Site 167, we demonstrate how numerical models can be used to correct specific measured records for diagenesis. This approach could provide a means of extracting paleotemperature information from heavily altered Late Cretaceous and older samples, and for quantifying the subtle effects of diagenesis on the $\delta^{18}O$ record at all sites.

Shan, C., Falta, R.W., and Javandel, I., 1992. Analytical solutions for steady state gas flow to a soil vapor extraction well. Water Resour. Res., v. 28, no. 4, p. 1105–1120 (LBL-30924).

Analytical solutions are developed for modeling steady state gas flow to a single vacuum extraction well in the unsaturated zone. The solutions are applicable to isotropic as well as anisotropic homogeneous subsurface media in which the ground surface is open to the atmosphere. Analytic expressions are given for the gas pressure field, and for the stream function distribution. Streamline travel times are computed using a simple numerical technique employing the analytical solutions. The pressure solution may be used to analyze in situ gas pumping tests to determine average horizontal and vertical gas permeabilities. The stream function solution and streamline travel times may be used to optimize the design of vapor extraction systems for volatile organic chemical removal from the unsaturated zone. Application of the solutions to several examples illustrates the strong effect of screen location and anisotropy on the induced gas flow field, and dimensionless type curves are given for a variety of gas well geometries.

Sterner, S.M., 1992. Synthetic fluid inclusions: Part XI. Notes on the application of synthetic fluid inclusions to high *P–T* experimental aqueous geochemistry. Am. Mineral., v. 77, p. 156–167 (LBL-31060).

A new modification to the procedure for trapping synthetic fluid inclusions effectively allows the experimenter to control the timing of the onset of inclusion formation. The main advantage of the new procedure is that inclusion trapping may be postponed until the experimental pressure and temperature are stabilized and the fluid has equilibrated at P and T to a constant and uniform composition and density throughout the capsule. Thus, *PVTX* studies may be extended to higher temperatures in cases where premature fracture healing previously resulted in volumetric and compositional heterogeneity among inclusions from a single sample.

The new method has been found to improve significantly the precision of volumetric determinations in the CO_2-H_2O system at temperatures above 600°C. Additionally, the technique shows promise in the investigation of high-salinity brines and for mixed-gas aqueous systems where fluid compositions may evolve through time. The ability to sample the fluid

phase at P and T after equilibration at P and T may prove invaluable in speciation studies at high pressures and temperatures involving kinetically slow buffers or diffusional processes and in the experimental study of H_2O-rock interactions.

Sterner, S.M., Chou, I.-M., Downs, R.T., and Pitzer, K.S., 1992. Phase relations in the system NaCl-KCl-H_2O. V. Thermodynamic–*PTX* analysis of solid-liquid equilibria at high temperatures and pressures. Geochim. Cosmochim. Acta, v. 56, p. 2295–2309 (LBL-31059).

The Gibbs energies of mixing for NaCl-KCl binary solids and liquids and solid-saturated NaCl-KCl-H_2O ternary liquids were modeled using asymmetric Margules treatments. The coefficients of the expressions were calibrated using an extensive array of binary solvus and solidus data, and both binary and ternary liquidus data. Over the *PTX* range considered, the system exhibits complete liquid miscibility among all three components and extensive solid solution along the anhydrous binary. Solid-liquid and solid-solid phase equilibria were calculated by using the resulting equations and invoking the equality of chemical potentials of NaCl and KCl between appropriate phases at equilibrium. The equations reproduce the ternary liquidus and predict activity coefficients for NaCl and KCl components in the aqueous liquid under solid-saturation conditions between 673 and 1200 K from vapor saturation up to 5 kbar. In the NaCl-KCl anhydrous binary system, the equations describe phase equilibria and predict activity coefficients of the salt components for all stable compositions of solid and liquid phases between room temperature and 1200 K and from 1 bar to 5 kbar.

Tokunaga, T.K., 1992. The pressure response of the soil water sampler and possibilities for simultaneous soil solution sampling and tensiometry. Soil Sci., v. 154, no. 3, p. 171–183 (LBL-32090).

A soil water sample may be viewed as a tensiometer with a relatively slow response time. An expression for the pressure response of a fixed volume soil water sampler is derived. The criterion for determining when the gage pressure within the soil solution sampler may be used to infer the soil water matric potential in the vicinity of the sampler tip depends upon the cup-soil conductance (K^*), the sampler's internal volume (V_Σ), the initial absolute pressure (P_o) associated with the vacuum set on the sampler, and the elapsed time since application of the vacuum (t). It was found that when the dimensionless time given by $[P_o K^* t](V_\Sigma)^{-1}$ is greater than about 5, the sampler pressure may be used in determinations of matric and/or pressure potentials (Ψ), or more generally the tensiometer pressure potential which also includes the influence of the soil air pressure potential. The essential difference in the response of tensiometers and soil water samplers arises from differences in the nature of the instrument sensitivities (S^*). In the "tensiometer-limited" response, the standard tensiometer approaches an equilibrium reading via an exponential decay of the initial pressure disturbance characterized by a response time $\tau = (K^* S^*)^{-1}$, where K^* and S^* are, in principle, constant for a particular equilibration. A nonexponential decay response of the soil water sampler on the other hand arises from time-dependent S^* and K^*. Only the time-dependent S^* effect is considered here. The S^* in the case of soil water sampler is equal to $P(V_{gas})^{-1}$, where P and V_{gas} are the instantaneous sampler gas pressure and gas phase volume, respectively. Under conditions where the ratio $P(V_{gas})^{-1}$ undergoes considerable change during the course of soil water collection, large deviations from the exponential decay response occur. Conversely, when only minor variations in $P(V_{air})^{-1}$ are experienced, the soil water sampler pressure response approaches that of the exponential decay. The time-weighting of the collected soil solution is discussed. One particular instrument design suited for simultaneous tensiometry and soil water sampling is described. Field data illustrating cases where soil and water sampler pressures may and may not be used to obtain Ψ data are provided. The possible use of this type of device for both soil solution sampling and tensiometry in deep (> 10 m) profiles is explained.

Tokunaga, T.K., and Benson, S.M., 1992. Selenium in Kesterson Reservoir ephemeral pools formed by groundwater rise: I. A field study. J. Environ. Qual., v. 21, no. 2, p. 246–251 (LBL-30588).

One of the principal initial plans for managing Se contamination at Kesterson Reservoir (Merced County, California) entailed excavation to a depth of at least 0.15 m in order to remove soils with Se concentrations higher than 4 mg kg^{-1}. Prior to implementing this plan, surface waters were collected from numerous shallow ephemeral pools that formed during the winters of 1986 to 1988. Elevated concentrations of Se were measured in all of these pools. Pools formed during this period from a combination of overland flow from adjacent nonseleniferous pond waters, rainfall ponding, and emergence of the fluctuating shallow water table above the soil surface. Selenium in these ephemeral pool waters originated primarily from dissolution of surface salt crusts and from displacement of seleniferous soil solutions up to the surface. Through the monitoring of a test plot where 0.30 m of the surface soil had been removed, the potential was demonstrated for shallow water table rise to displace seleniferous soil solutions to the surface, resulting in highly seleniferous ephemeral pools. In the test plot, ephemeral pool Se concentrations often exceeded 10^3 µg L^{-1}. This study clearly demonstrated (i) that pools formed over soils with total Se concentrations in the range of 0.5 to 1.7 mg kg^{-1} could still provide a highly seleniferous aquatic environment, (ii) that the total Se concentration in a soil can be a misleading parameter to use in determining target goals for remediation, and (iii) that the excavation strategy was inappropriate for the Kesterson Reservoir setting.

Tsang, Y.W., 1992. Usage of "equivalent apertures" for rock fractures as derived from hydraulic and tracer tests. Water Resour. Res., v. 28, no. 5, p. 1451–1455 (LBL-31244).

In the literature during the past several years there appear numerous references to the "equivalent aperture" of a rough-walled rock fracture as derived from various hydraulic and tracer tests. However, the similar or even identical terms used by different researchers for "equivalent aperture" often do not have the same meaning. This has led to some confusion in the comparison of their results. In particular, there is a serious apparent contraction in the claims of some authors that "equivalent apertures" derived from tracer tests are much larger than those derived from hydraulic tests, and the findings of others that apertures estimated from tracer tests are consistently smaller than those estimated from hydraulic tests. This apparent contradiction of the field results in fact arises from the different definitions of the so-called "tracer aperture" as employed by different researchers. In this short technical note I have attempted to sort out the different definitions, denotations and usage of the various "equivalent apertures" and show that there are mainly three alternative definitions used in the literature. The meaning of each as related to experimental measurements is explained and their interrelationship discussed. It is shown that once the specific definition of "equivalent aperture" referred to by each researcher is identified, then the relative magnitudes of these "equivalent apertures" as reported by different groups of researchers are perfectly consistent with each other.

Tsang, Y.W., and Narasimhan, T.N., 1992. Effects of periodic atmospheric pressure variation on radon entry into buildings. J. Geophys. Res., v. 97, no. B6, p. 9161–9170 (LBL-31164).

Using a mathematical model, we have investigated the temporal variations of radon entry into a house basement in the presence of time-dependent periodic variations of barometric pressure as well as a persistent small steady depressurization within the basement. The tool for our investigation is an integral finite difference numerical code which can solve for both diffusive and advective flux of radon in the soil gas which is treated as a slightly compressible fluid. Two different boundary conditions at the house basement are considered: (1) a dirt floor basement so that diffusion is equally or more important than advective transport, and (2) an "imper-

meable" cement basement except for a 1-cm-wide crack near the perimeter of the basement floor; in which case, advective transport of radon flux dominates. Two frequencies of barometric pressure fluctuation with representative values of amplitudes, based on a Fourier decomposition of barometric pressure data, were chosen in this study: one with a short period of 0.5 hour with pressure amplitude of 50 Pa, the other a diurnal variation with a period of 24 hours with the typical pressure amplitude of 250 Pa. For a homogeneous soil medium with soil permeability to air between 10^{-13} and 10^{-10} m^2, we predict that the barometric fluctuations increase the radon entry into the basement by up to 120% of the steady radon inflow into the basement owing to a steady depressurization of 5 Pa. If soil permeability heterogeneity is present, such as the presence of a thin layer of higher permeability aggregate immediately below the basement floor, radon flux due to atmospheric pumping is further increased. Effects of pressure pumping on radon entry are also compared to diffusion-only transport when the steady depressurization is absent. It is found that contribution to radon entry is significant for the basement crack configuration. In particular, for pressure pumping at 0.5-hour period and for a homogeneous medium of permeability of 10^{-10} m^2, the radon entry is a factor of 10 larger than that predicted by the diffusion-only transport. This may help to explain indoor radon concentrations during times of low steady state driving force. Extending beyond radon transport, the results of this case study establish the importance of transient advective transport resulting from atmospheric pressure variation. These results may have relevance in the estimations of the transfer of trace gases such as methane and nitrous oxide across the soil-atmosphere interface and their impact on global climate changes.

Tura, M.A.C., Johnson, L.R., Majer, E.L., and Peterson, J.E., 1992. Application of diffraction tomography to fracture detection. Geophysics, v. 57, no. 2, p. 245–257 (LBL-28466).

Two different tomography techniques are applies to crosshole field data to detect fractures in granitic rock. The techniques used are the conventional back-propagation method and a new quadratic programming method incorporating constraints. In this formulation, the Born approximation is used for linearization of the inverse problem. Two dimensional (2-D) pseudo spectral finite-difference synthetic data are generated to demonstrate the inversion methods and justify use of the Born approximation. Also, using 2-D Born synthetic data, the velocity sensitivity of the inversion algorithm and reduction of fracture generated tube waves and *S*-waves are investigated.

The inversion methods are applied to field data from the Grimsel test site in Switzerland. The data are collected from a 10×21.5 m rectangular area where fractures are known to exist. Data acquisition with 0.5 m spacing of three component receivers and a piezoelectric source is carried out so as to obtain a nearly complete coverage of the region. Crosshole inversions are performed on data from the receiver components in the plane of the rectangular region and normal to its boundary. As the result of a separate experiment conducted in a homogeneous region of the granitic rock, a cosine function was found to best fit the source radiation pattern. A background attenuation value is estimated for the region, using a simple statistical approach, and estimates of the wavelet are found by common source gathers, common receiver gathers, and averages of all traces. The preprocessing steps are: (1) source radiation correction, (2) attenuation correction, (3) removal of the incident wavefield, (4) muting beginning of the traces and windowing the ends, (5) wavelet deconvolution, and (6) two-and-a-half dimensional (2.5-D) corrections. This preprocessing is designed to enhance scattered *P*-waves that are used in the inversions.

Images obtained from the application of back-propagation and quadratic programming methods to the preprocessed data show possible fracture zones that agree well at the foundaries of the region with the fracture sets observed from core samples taken from the boreholes. Although the quadratic programming method is an order of magnitude slower than the back-propagation method, as demonstrated by the synthetic examples, it proves useful by yielding high resolution images when constraints can be imposed. Transmission ray tomography is also applied to the crosshole data, and although the resolution is not as high, general agreement with the wave equation based methods is obtained.

Wong, H., Morris, S., and Radke, C.J., 1992. Two-dimensional menisci in nonaxisymmetric capillaries. J. Colloid & Interface Sci., v. 148, no. 1, p. 284–287 (LBL-30305).

Calculation of meniscus shapes is often difficult because the contact line is usually a free boundary. We describe a method which avoids this difficulty by using a disjoining force to eliminate the free contact line. Thus, a free-boundary problem is converted to a problem with a known domain boundary. We solve numerically the augmented Young-Laplace equation and recover the solution of the Young-Laplace problem with a contact line by a limiting procedure. The method is demonstrated by calculating the shapes of two-dimensional gravity-free menisci in elliptic, eye-shaped, and star-shaped capillaries. The numerical results are confirmed by comparison with previously known analytic solutions.

Wong, H., Morris, S., and Radke, C.J., 1992. Three-dimensional menisci in polygonal capillaries. J. Colloid & Interface Sci., v. 148, no. 2, p. 317–336 (LBL-30714).

The shapes of gravity-free, three-dimensional menisci are computed from the augmented Young-Laplace equation. Incorporation of disjoining thin-film forces in the Young-Laplace relation eliminates the contact line, thereby eliminating the free boundary from the problem. To calculate a meniscus with finite contact angles, the conjoining/disjoining pressure isotherm must also contain an attractive, sharply varying, spike function. The width of this function, w, reflects the range of the thin-film forces. In the limit of w approaching zero, a solution of the Young-Laplace equation is recovered. The proposed calculation method is demonstrated for menisci in two different types of capillaries. In the first case, the capillary is regular-polygonal in cross section with either 3, 4, or 6 sides and with contact angles F ranging from 0 to 45°. In the second case, the capillary is rectangular in section with aspect ratios ranging from 1.2 to 5 and with $F = 0°$, 15°, or 30°. Gas-liquid menisci inside a square glass capillary of 0.5 mm inscribed radius are measured optically for air bubbles immersed in a solution of di-*n*-butyl phthalate and mineral oil. This liquid mixture exhibits a zero contact angle with the wall and matches the refractive index of the glass capillary, permitting precise visual location of the interface. Excellent agreement is found with the numerical results which further demonstrates that the limiting process of the proposed method is valid. Because it avoids the issue of locating the contact line, solution of the augmented Young-Laplace equation is a simple and powerful method for the calculation of three-dimensional menisci.

Zawislanski, P.T., Tokunaga, T.K., Benson, S.M., Oldfather, J.M., and Narasimhan, T.N., 1992. Bare soil evaporation and solute movement in selenium-contaminated soils of Kesterson Reservoir. J. Environ. Qual., v. 21, no. 3, p. 447–457 (LBL-31061).

Two approaches were taken to estimate evaporation of water from the surface of a salt-encrusted and Se contaminated soil in a playa-like environment at Kesterson Reservoir, California. Direct evaporation flux measurements were made using a lysimetric (gravimetric) approach and revealed a seasonal dependence of bare soil evaporation rates, which ranged from 0.1 to 1.5 mm d^{-1}. The low range is suggestive of a vapor-flux control of bare soil evaporation due to the presence of a salt crust. Temporal changes in chloride concentrations and soil moisture content were used in a quantitative assessment of a mean seasonal evaporative flux. Bare soil evaporation rates measured by these two methods compared favorably. Although concentrations of salts and Se in near-surface soil fluctuated seasonally during a drier than average year, a slight net decline in salt concentrations was observed over 12 mo due to rainfall infiltration and the associated solute transport. Increases in Se near the soil surface due to an evaporatively driven flux appear unlikely in this setting, due to low rates of

bare soil evaporation as compared with downward fluxes due to rainfall infiltration.

Zimmerman, R.W., 1992. Hashin-Shtrikman bounds on the Poisson ratio of a composite material. Mech. Res. Commun., v. 19, p. 563–569 (LBL-34186).

Hashin and Shtrikman derived upper and lower bounds on the bulk and shear moduli, K and G, of macroscopically homogeneous multi-component media. These bounds are functions of the elastic moduli and volume fractions of the different components, and are the most restrictive bounds that have been found without considering the geometry of the various components. Upper (or lower) bounds on Young's modulus E can be obtained from the H-S upper (or lower) bounds on K and G by using the usual relationship between E, K, and G. This procedure does not, however, lead to correct bounds on the Poisson ratio. In this note the correct upper and lower Hashin-Shtrikman bounds on the Poisson ratio are obtained.

Zimmerman, R.W., Chen, D.-W., and Cook, N.G.W., 1992. The effect of contact area on the permeability of fractures. J. Hydrol., v. 139, p. 79–96 (LBL-32356).

The permeability of a rock fracture is controlled primarily by the geometry of its void space. One effect of void space geometry is to cause the fluid to follow a tortuous path to flow around the asperities, which are regions where the two faces of the fracture are in contact. To examine the tortuosity induced by the contact area, we consider an idealized fracture consisting of two parallel plates propped open by isolated asperities. Boundary-element calculations, analogue electrical conductivity measurements and an effective medium approximation are used to study the permeability of fractures with circular, elliptical and irregular asperity shapes. The permeability is seen to depend not only on the amount of contact area, but also on the shape of the asperities. For circular or elliptical asperities, very accurate estimates are found by using the effective medium theory proposed by Maxwell.

APPENDIX B: OTHER PUBLICATIONS

TOPICAL REPORTS

LBL-23592
Niemi, A., Bodvarsson, G.S., and Pruess, K., 1991. Incorporation of the capillary hysteresis model HYSTR into the numerical code TOUGH.

LBL-23593
Niemi, A., Bodvarsson, G.S., and Montazer, P., 1991. Preliminary capillary hysteresis simulations for fracture rocks.

LBL-28384
Doughty, C., 1991. Users guide for SIMSOL (Version 1.0).

LBL-28613
Narasimhan, T.N., and Wang, J.S.Y., 1989. Conceptual, experimental, and computational approaches to support performance assessment of hydrology and chemical transport at Yucca Mountain.

LBL-29876
Earth Sciences Division, Geologic Repository Project, 1990. LBL studies of fractured rocks: Summary, FY 1986–1990.

LBL-30707
Lee, W.W.-L., Sadeghi, M.M., Chambré, P.L., and Pigford, T.H., 1991. Waste-package release rates for site suitability studies.

LBL-30877 (SAND92-0659)
Nitsche, H., Roberts, K., Gatti, R.C., Prussin, T., Becraft, K., Leung, S.C., Carpenter, S.A., and Novak, C.F., 1992. Plutonium solubility and speciation studies in a simulant of air intake shaft water from the Culebra dolomite at the Waste Isolation Pilot Plant.

LBL-31069
Apted, M.J., O'Connell, W.J., Lee, K.H., MacIntyre, A.T., Ueng, T.-S., Lee, W.W.-L., and Pigford, T.H., 1990. Preliminary calculations of release rates of Tc-99, I-129, Cs-135, and Np-237 from spent fuel in a potential repository in tuff.

LBL-31255
Lee, W.W.-L., Choi, J.S., and Sadeghi, M.M., 1991. Release rates from partitioning and transmutation waste packages.

LBL-31344
Wollenberg, H.A., and Smith, A.R., 1991. Baseline measurements of terrestrial gamma radioactivity at the CEBAF site.

LBL-31377
Pulliam, R.J., 1991. Imaging earth's interior: Tomographic inversions for mantle P-wave velocity structure (Ph.D. thesis).

LBL-31428
Aunzo, Z.P., Bjornsson, G., and Bodvarsson, G.S., 1991. Wellbore models GWELL, GWNACL, and HOLA: User's guide.

LBL-31534
Michelini, A., 1991. Fault zone structure determined through the analysis of earthquake arrival times (Ph.D. thesis).

LBL-31674
Wilt, M., 1991. Interpretation of time domain electromagnetic soundings near geological contacts (Ph.D. thesis).

LBL-31737
Cox, B.L., and Wang, J.S.Y., 1992. Fractal surfaces: Measurement and applications in the earth sciences.

LBL-31760
Long, J.C.S., and Karasaki, K., 1992. Simulation of tracer transport for the site characterization and validation site in the Stripa mine.

LBL-31761
Long, J.C.S., Mauldon, A.D., Nelson, K., Martel, S., Fuller, P., and Karasaki, K., 1992. Prediction of flow and drawdown for the site characterization and validation site in the Stripa mine.

LBL-31970
Lee, S., 1991. Modelling of 3-D electromagnetic responses using the time-wavenumber method.

LBL-31982.
Daley, T.M., and Majer, E.L., 1991. Seismic imaging of the SWCC.

LBL-32063
Quinn, N.W.T., 1992. San Joaquin–Tulare conjunctive use model: Detailed model description.

LBL-32194
Tsao, L., and Weres, O., 1992. Reactions of cresol in hot aqueous borate solutions.

LBL-32195
Pruess, K., 1992. Brief guide to the MINC-method for modeling flow and transport in fractured media.

LBL-32200 (EPRI TR-101218)
Narasimhan, T.N., Apps, J.A., and Zhu, M., 1992. Applications handbook for FASTCHEM. Volume 2: Chemical transport modules.

LBL-32310
Martel, S.J., 1992. Geologic characterization of fractures as an aid to hydrologic modeling of the SCV block at the Stripa mine.

LBL-32418
Pruess, K., 1992. Analysis of flow processes during TCE infiltration in heterogeneous soils at the Savannah River site, Aiken, South Carolina.

LBL-32521
Leonard, M.A., Daley, T.M., Johnson, L.R., and McEvilly, T.V., 1992. VSP site characterization at NTS: OSSY'92 — Summary report.

LBL-32611
Moridis, G.J., and Pruess, K., 1992. TOUGH simulations of Updegraff's set of fluid and heat flow problems.

LBL-32662
Quinn, N.W.T., 1992. Analysis of the potential impacts on surface water quality resulting from the proposed use of the San Luis Drain to transport agricultural drainage through the Northern Grasslands.

LBL-32729
Kiryukhin, A.V., 1992. Progress report on modeling studies: Natural state conditions and exploitation of the Dachny geothermal reservoir, Mutnovsky hydrothermal system, Kamchatka, Russia.

LBL-32907
Hadgu, T., and Bodvarsson, G.S., 1992. Supplement to "Wellbore models GWELL, GWNACL, and HOLA User's Guide."

LBL-33080
Benson, S.M., Tokunaga, T.K., and Zawislanski, P., 1992. Anticipated soil selenium concentrations at Kesterson Reservoir.

Lawrence Berkeley Laboratory
Technical Information Department
University of California
Berkeley, California 94720